Technology for liquid-liquid extraction process development

James Daniel Daglish

Submitted in accordance with the requirements for the degree of
Doctor of Philosophy

The University of Leeds
School of Mechanical Engineering

August, 2021

The candidate confirms that the work submitted is his own, except where work which has formed part of jointly-authored publications has been included. The contribution of the candidate and the other authors to this work has been explicitly indicated below. The candidate confirms that appropriate credit has been given within the thesis where reference has been made to the work of others.

Chapter 3 is based on the paper 'A High Throughput Image Processing Methodology to Determine Phase Separation Rates' which is to be submitted to a journal soon after submission of this thesis. The author of this thesis developed the algorithm and experimental setup. He also conducted the experiments discussed in Chapter 3 and the post processing analysis. The prototype mixing apparatus was developed as part of a 3rd year student project by Chong Seng (University of Leeds). The scale up experiments were completed with oversight and input from Mary Bayana (iPRD lab manager).

Chapters 4, 5 and 6 are all the authors own work. Guidance and input was provided by his supervisors.

The Benzoic extraction study in Chapter 7 was partially conducted by the author and partially by Luke Power, a PhD student in the iPRD at the University of Leeds. Luke developed the pH monitoring system and optimisation routines used throughout. He also selected the benzoic acid extraction for study and provided the foundational chemical analysis for the work. The single, two stage and three stage extractions were jointly conducted by the author and Luke. The separation rate experiments in this chapter were conducted by the author.

Acknowledgements

I would like to express my thanks to the University of Leeds for providing me with guidance and support throughout my undergraduate and masters course. The knowledge and skills I gained and opportunities afforded to me resulted in me pursuing this PhD.

This PhD would not be possible without support and funding from Astra Zeneca. I would particularly like to thank my industrial supervisory team: Anna Parsons, David Hose and Alex Crampton. They were always willing to support whichever direction we wanted to take the project and offered their expertise and input generously. Their advice for developing the lab-scale separator and about separation rate issues at scale were particularly useful. Each time we met, the conversation was interesting, insightful and motivating. The input provided by Astra Zeneca gave an industrial context to the project that enriched it throughout.

I am especially grateful for the support and guidance given to me by my supervisors at the University of Leeds: Professor Nikil Kapur, Professor John Blacker, Dr Gregory de Boer, Dr Muhammad Tausif and Professor Stephen Russell. The multidisciplinary nature of this project has meant that I have received input from several departments at the university. Nik Kapur and Greg de Boer both work in the Mechanical Engineering department, John Blacker in the Chemistry department, Muhammad Tousif and Stephen Russel in the Textiles department. I am extremely fortunate to have Nik as my main supervisor. He always provided me with suggestions and guidance that progressed my work. His knowledge and experience of developing prototype flow chemistry equipment has been invaluable; Whether it be a mechanical, electrical or process related issue that I faced, he was always able and willing to help. Not only could Nik help with any issues I faced, he was always supportive and brought a broader perspective to the project. John was another knowledgeable and experienced supervisor who had great patience for me and my lack of chemistry knowledge as a mechanical engineer. He was always able to help me understand unfamiliar concepts and point me in the right direction. I appreciate the time Greg had for me, particularly when it came to the more mathematical aspect of the project; optimisation, experimental design, fluid mechanic and filtration. He was always willing to read over my work and provide feedback when needed. I would also like to thank Stephen and Tousif for sharing their knowledge about nonwoven materials and filtration. Their advice on these aspects of the project were highly appreciated.

I would like to thank all of the members of the iPRD for providing such a great place to work. The number of great ongoing projects and willingness to share experience

Abstract

In recent years, laboratory scale equipment for flow chemistry has become both commercially available and widely used in industry and academia. There has been particular focus on reactor design, in-line analytics and performing multistage synthesis. One of the challenges that has arisen as a consequence of introducing active mixing of multiple phases and multiple reaction steps is the need to remove impurities from reaction streams and efficiently separate multiple phases from one another. The devices currently available for performing liquid-liquid separation steps at laboratory scale have limitations in performance, control and scalability. This thesis presents a new laboratory scale separation device that utilises nonwoven coalescing filters to separate challenging emulsion systems, adapt to changing system inputs and integrate with current flow technology.

A literature review of flow chemistry and its benefits, liquid-liquid system characteristics, laboratory scale separation equipment and nonwoven coalescing filters has been conducted.

In order to characterise different liquid-liquid systems an image analysis technique was developed. The image analysis technique was used to determine phase separation rates in liquid-liquid systems. The technique was used in the lab on multiple samples at once with minimal change to the algorithm input parameters. The analysis technique was tested on both fast and slow settling systems with different phase ratios. In order to demonstrate the value of the imaging technique a selection of systems were scaled up to 20 Litres so that the separation rate of the scaled up mixtures could be compared to the 10 ml samples. The scaled up systems showed good correlation with the small scale counterparts which showed that the small scale experiments could be used to predict separation behaviour at a larger scale.

A laboratory scale continuous separation device was then developed which utilised nonwoven coalescing filter media to rapidly separate liquid phases. The device has an integrated control scheme that relies on conductivity measurements and downstream valve or pump control. The user is able to specify different flow rates and phase ratios and the system adapts automatically to different solution conductivities. The device's performance was compared with a commercially available separation device based on different flow rates, phase ratios and liquid pairs. The performance depending on what filter media was used and the batch separation rate (determined by the aforementioned image analysis technique) was also considered.

The separation device was then developed further so that it could be used as a multistage extraction platform, allowing the testing of complex extraction processes at a laboratory scale. Two extraction systems were tested, an Acetone extraction from water and an extraction of Benzoic acid derivatives. Both systems provided challenges for the system such as emulsion formation and large changes in phase ratio. The device enabled the study of these two systems at laboratory scale, providing valuable insight into the system behaviour at low cost and with a small footprint.

Table of Contents

List of Tables

List of Figures

List of Abbreviations

PBT	Polybutylene terephthalate
SEM	Scanning Electron Microscope
BPR	Back pressure regulator
HPLC	High-performance liquid chromatography
FTIR	Fourier transform infrared
NMR	Nuclear Magnetic Resonance
SFR	Segmented Flow Reactor
COBR	Continuous oscillatory baffled reactor
CSTR	Continuous stirred tank reactor
DCM	Dichloromethane
RTD	Residence time distribution
HLD	Hydrophilic-Lipophilic difference
EACN	Equivalent alkane carbon number
FLLEX	Flow Liquid Liquid Extraction
HEED	High-efficiency extraction device
PTFE	Polytetrafluoroethylene
TEHP	Tris(2-ethylhexyl) phosphate
PEEK	Polyetheretherketone
DEHPA	Bis-2-ethylhexyl phosphoric acid
REM	Rare earth metal
RSD	Relative standard deviation
THF	Tetrahydrofuran
MPPS	Most penetrating particle size
HTE	High throughput experimentation
LoG	Laplacian of Gaussian method
SDBS	Sodium dodecyl benzene sulfonate
LED	Light emitting diode
HSM	High shear mixer
FIR	Finite impulse response
NaCl	Sodium Chloride
CAD	Computer-aided design
UNF	Unified national fine thread
PCD	Pitch circle diameter
PWM	Pulse width modulation
ICSP	In-circuit serial programming

UART	Universal asynchronous receiver-transmitter
I^2C	Inter-Integrated Circuit
SDA	Serial data line
SCL	Serial clock line
ACK/NACK	Acknowledge/Not Acknowledge
PVDF	Polyvinylidene fluoride
FFKM	Perfluoroelastomer
PID	Proportional-Integral-Derivative controller
DoE	Design of Experiments
MD	Machine Direction
CD	Cross direction
GSM	Grams per square metre
EDX SEM	Energy Dispersive X-Ray Scanning Electron Microscope
OWRK	Owens, Wendt, Rabel and Kaelble
GUI	Graphical user interface
NaOH	Sodium Hydroxide
NRTL-RK	Non-Random Two Liquid with Redlich-Kwong equations
UNIFAC	Universal functional group activity coefficients
UNIQUAC	Universal Quasi-chemical model
GC	Gas Chromatography
SNOBFIT	Stable Noisy Optimisation by Branch and Fit
RPM	Rotations per minute

Chapter 1

Introduction

1.1 Research gap

The economic, environmental, and safety benefits of continuous flow operations in the fine chemical industries have been widely exemplified.[1-4] Single step reactions performed in flow have resulted in increased yields and purity compared to their batch counterparts. The increased surface to volume ratio in continuous flow reactors allow for better mass transfer of molecules. Smaller overall volumes and closed systems mean higher temperatures and pressures can be explored resulting in more flexible and diverse reaction systems.[2] The development of in-line purification technology has expanded the scope of flow chemistry by allowing multiple reaction steps to be performed sequentially in flow.[5] This has increased the potential applications of continuous processes in the fine chemical industries as more complex molecules with challenging work-ups can be realised via multi-step continuous flow synthesis.[1,3,6,7] Furthermore, the development of lab-scale flow technology has enabled the exploration and optimisation of new and existing synthesis routes via automated technology and in-line analysis.[8-10]

One purification step that has attracted significant attention in the flow chemistry community is the extraction of products or impurities based on their solubility in different liquids.[5,11] Liquid-liquid extraction has several potential benefits such as operation at low temperatures and pressures which is important when heat sensitive materials require processing.[12] Extraction processes can be highly selective over multiple stages and are ideal when components are present in small quantities and require recovery or removal.[13] Green and renewable solvents such as those derived from bio-materials are generally less volatile than crude oil based solvents and are therefore separated more readily by differences in their solubilities rather than by distillation.[14,15]

A number of lab-scale devices have been designed to separate immiscible liquids in order to facilitate liquid-liquid extraction processes. Various phase separation devices have been extensively reviewed elsewhere, particularly those operating on the microscale.[5,16-18] The two most commonly encountered separation methods are gravity force driven[19-21] and surface force driven.[22-26] Gravity driven devices rely on density differences between the organic and aqueous phases while surface force

driven devices rely on different surface wettabilities. Gravity driven devices are often simple in design and can operate at a range of phase ratios. The possible operational flow rates depend on the separation rate of the two phases and tend to require larger volumes than surface force driven devices.[19-21]

One mechanism that has not been explored for continuous separations in the fine chemical industries is coalescing filtration. Coalescing filters make use of both surface forces and gravity forces to separate immiscible liquids. Coalescing filters are depth filters as opposed to surface filters and operate via the following five steps: (i) Contact between the dispersed phase droplets and filter fibres; (ii) Attachment of small droplets to individual fibres throughout the filter depth; (iii) Coalescence of droplets attached to the filter surface; (iv) Transport of the enlarged droplets through the filter media; (v) and detachment from the filter surface and removal from the fluid stream via gravity or surface filtration.[27] Figure 1.1 (a) shows a typical separation of a dispersed phase from a continuous phase through coalescing filter media. Coalescing filters are often used in the automotive and aviation industries to remove residual water from fuel[28] and separate water from crude mixtures in the petroleum industry.[29,30]

Many different materials have been employed to act as coalescing filters, including thermoplastics such as Polyurethane, Polypropylene and Polybutylene terephthalate (PBT), glass fibres[27,28,31-35] and in the case of aerosol coalescers - steel meshes.[36] Each of these filter materials are formed into nonwoven fabrics. Nonwovens are defined as a sheet or web of entangled fibres with random orientation, they can be mechanically, thermally or chemically bonded and are not weaved or knitted into a repeating structure.[37] Most nonwovens used for coalescing filtration are formed via melt-spinning processes and have high porosities and permeabilities, with a median pore sizes in the range of 10 μm and a highly tortuous fluid path through the media depth.[38] Figure 1.1(b) is an SEM image of a meltblown PBT nonwoven material used throughout this paper.

In this thesis, a device which utilizes coalescing filter media to separate liquid-liquid mixtures has been developed, characterized and applied to multiple extraction processes. A control scheme has been integrated to automate the separation process. As well as this, an image analysis methodology has been developed to characterize liquid-liquid and emulsion systems. It was evident that there is a lack of understanding of emulsion formation in pharmaceutical processes and a limited approach to analysing emulsion break-up.[39, 40-42]
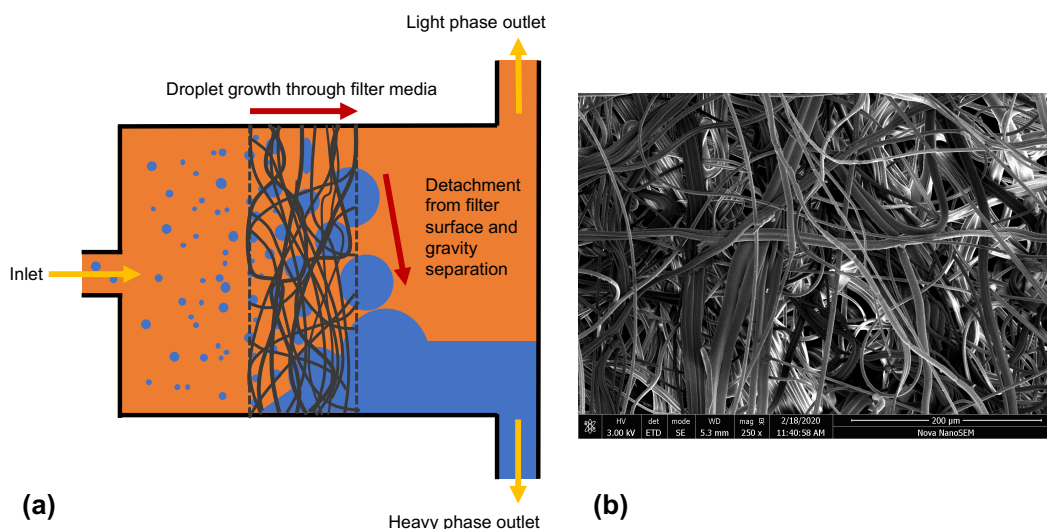
Figure 1.1: (a) diagram of how nonwoven filter media coalesces droplets that are collected on its surface and separates them from the continuous phase downstream of the filter. (b) SEM image of melt-blown PBT filter media at 250x zoom (200 μm scale for reference).

1.2 Aims and Objectives

The main aim of this research is to determine the feasibility of using nonwoven coalescing filter media to separate liquid-liquid systems in flow in pharmaceutical processes. Several objectives exist as an extension of this:

1. Develop a method of characterising liquid-liquid systems in terms of how long they take to separate.
2. Design a separation device compatible with flow chemistry equipment that can be used on a small-scale to perform separations and characterise the device, comparing it to existing technology.
3. Develop the equipment into a multistage platform capable of performing extraction processes used in the pharmaceutical industry.

1.3 Thesis layout

This thesis is divided into the following chapters:

1. Chapter 1 describes the research area to be explored and the aims and objectives of the thesis.
2. Chapter 2 provides a literature review of relevant research areas such as flow chemistry, lab scale extraction equipment, coalescing filters and filtration technology.
3. Chapter 3 describes an image analysis algorithm and experimental process which can determine emulsion settling rates of sample mixtures.

4. Chapter 4 describes a lab-scale separation device that was developed. The devices operation and design are described in this chapter.

5. In Chapter 5 the lab-scale separation devices performance is analysed and compared to a commercially available separation device.

6. In Chapter 6 the design of the separation device is expanded so that multistage extractions can be performed at lab-scale.

7. Chapter 7 uses the multistage extraction unit developed in chapter 6 to perform multistage counter-current extractions at lab-scale and compares it to a model system.

8. Chapter 8 provides a conclusion and recommends future work.

Chapter 2
Literature Review

2.1 Flow chemistry

2.1.1 Introduction

In flow chemistry chemical synthesis occurs in a continuous fluid stream as opposed to in batches. This generally requires a number of pumps, valves and tubes connected in series to perform chemical transformations.[2] In its most basic form two pumps will dose solvents and reagents at a constant flow rate to a t-piece where the two streams will mix. This mixture will then travel along a coil of tubing or 'coil reactor' so that the desired chemical reaction can take place. The residence time is dictated by the flow rate of the system and the length of the tubing. To control the temperature of the reaction the tubing coil can be placed in a heated bath and to control the pressure a back-pressure regulator (BPR) can be placed at the end of the reaction step. Extraction, purification, and analysis of the desired product can then be done offline after quenching the fluid outlet stream. More recently technology advances have allowed in-line analytics such as HPLC, FTIR and NMR spectroscopy and a multitude of purification steps to take place in-flow.[43] These technology advancements along with various reactor designs and process control techniques have led to the development of multi-step continuous processes and the production of more complex molecules under novel process conditions.

2.1.2 Advantages and disadvantages of flow chemistry

The economic, environmental, and safety benefits of continuous flow operations in the fine chemical industries have been widely exemplified and single step reactions performed in flow have resulted in increased yields and purity compared to their batch counterparts.[1-4] Some of the advantages over batch reactions are:

- Smaller overall volumes and increased process control means higher temperatures and pressures can be safely explored. This allows solvents to be used above their atmospheric boiling points, leading to more extreme processing conditions, higher reaction diversity and flexibility.[2]
- it is easier to rapidly heat and cool reactions due to high surface area to volume ratios.
- The development of in-line purification technology has expanded the scope of flow chemistry by allowing multiple reaction steps to be performed sequentially in flow.[5]

- Time between reaction stages is reduced and unstable intermediates can be rapidly transferred from one reaction to the next before degrading.[1,3,4]

- Continuous-flow systems are often 'green' in comparison to their batch counterparts, either by reducing or preventing waste, improving process safety and risk mitigation or improving overall energy efficiency.

- Flow systems operate at steady-state and require a certain degree of automation, this results in decreased process downtime.

- Waste reduction is achieved by recycling unreacted starting materials, catalysts or extraction solvents. Recycling unused reagents increases the effective residence time of the reactor and increases the overall conversion of reactants.

- Continuous processes with multiple stages reduce the amount of hazardous materials requiring storage between process steps.[1,3,4]

- Scale-up of continuous flow systems is simple in comparison to batch processes. Normally, multiple units of the small-scale equipment run in unison (scale-out rather than scale-up) This means the equipment used does not alter significantly and is therefore well characterised at the initial stages of process design.

- The reconfiguration/modular design of flow systems is also beneficial to developing multiple synthesis routes with the same equipment in different configurations.

- Another advantage of flow chemistry is the incorporation of in-line analysis, process control and automation. This not only allows for improved safety and process data collection but is useful for rapidly screening large reaction spaces and optimising process conditions with minimal product use resulting in financial and environmental gains.[1,3,4]

These benefits have resulted in more complex molecules with challenging work-ups being realised via multi-step continuous flow synthesis in the fine chemical industries.[1,3,6,7] Furthermore, the development of lab-scale flow technology has enabled the exploration and optimisation of new and existing synthesis routes via automated technology and in-line analysis.[8-10] However, there are some disadvantages to flow chemistry such as:[1,2]

- Specialist equipment is required which reduces the number of researchers and companies able or willing to adopt it due to cost and space demands.

- Flow chemistry requires a broad skillset of engineering and chemistry that creates barriers to usage of the technology.

- Much of the equipment is designed for single phase processes which limits its use.
- System complexity increases dramatically with more stages due to the need to purify streams between reaction steps without process downtime. The necessity to provide in-line monitoring and parameter adjustment also increases complexity.
- There is an added safety and commercial risk with any new flow system as it has not been used before and there can be limited data available on the process/procedure.
- Upfront costs are often larger than with batch systems as more initial process design is required as well as more specialist equipment.

2.1.3 Continuous flow process theory

In batch reactions the composition of the reaction changes with respect to time. The rate of the reaction is dependent on the temperature and pressure of the reaction vessel. In continuous processes the reaction reaches steady state and the composition of the reaction mixture at each point within the reactor remains constant with respect to time.[44]

<u>Plug Flow Reactor</u>

The plug flow reactor is a theoretical model used to describe reactions that occur while flowing down a pipe. It is theoretical because it assumes that the fluid in the pipe moves in infinitely thin "plugs" that have a uniform composition. This assumption means that the fluid is perfectly mixed in the radial direction but no mixing occurs in the axial direction.

<u>Segmented Flow Reactors</u>

One type of continuous reactor is the segmented flow reactor (SFR). In this reactor the liquid or gas phase moves in discrete 'plugs'. These plugs provide a segmented flow in which internal vortex mixing occurs (figure 2.1). The segmented flow provides three main benefits:

- No cross contamination between reaction slugs
- Increased mixing compared to laminar flow regimes
- Narrow residence time distributions
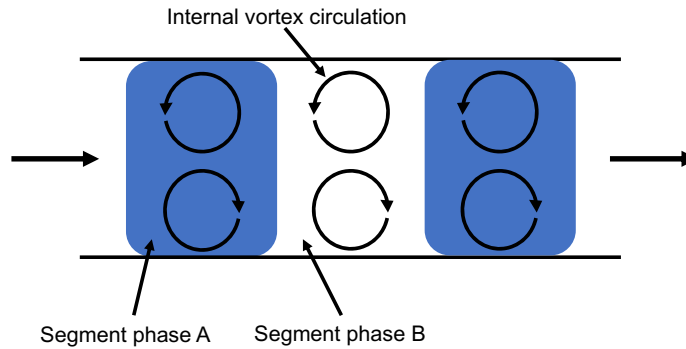
Figure 2.1: Internal vortex circulation in plug flow reactor.[45]

Continuous Oscillatory Baffled Reactors

Alternatively, continuous oscillatory baffled reactors (COBRs) can be used to introduce eddies into a reactor. COBRs are tubes/pipes that have an internal structure which encourages the formation of eddy currents (figure 2.2 (y)). The flow of fluid through these structures is oscillatory which further increases the amount of local mixing within the reactor. Figure 2.2(y) shows the stages of mixing as the flow is accelerated and decelerated. In image (a) a vortex forms downstream of the baffle, (b) as the flow is reversed the eddy detaches from the baffle and is drawn into the central streamlines (c). This produces free eddies which interact with previously produces vortices (d).[46] COBRs can have different internal structures such as Integral baffles, Central axial baffles, Round-edged helical baffles, Sharp-edged helical baffles, Sharp-edged helical baffles with a central insert or wire wool baffles as shown in figure 2.2(z). COBRs have the advantage of maintaining near plug flow while increasing local mixing.[46,47]
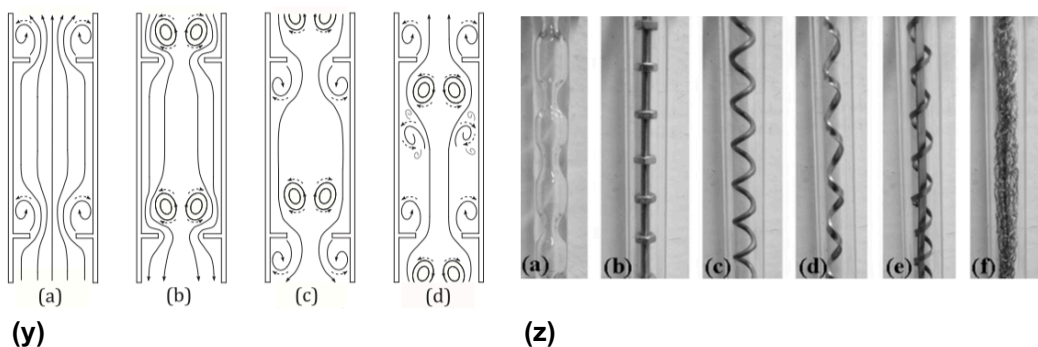
Figure 2.2: (y) Sketch of eddy formation in an oscillatory baffled reactor - Reprinted with permission from Elsevier[46] (z) Oscillatory baffled reactor configurations (a) Integral baffles, (b) Central axial baffles, (c) Round-edged helical baffles, (d) Sharp-edged helical baffles, (e) Sharp-edged helical baffles with a central insert, (f) wire wool baffles - Reprinted with permission from Elsevier[46].

<u>Continuous Stirred Tank Reactors</u>

Continuous stirred tank reactors (CSTRs) are ideally suited to the processing of multiphasic systems such as those in solid-liquid and liquid-liquid reactions. This is because active mixing minimises the formation of solid build up and clogging compared with tubular reactors and increases the interfacial area between liquid phases which increases the rate of mass transfer in liquid-liquid reactions. The active mixing produced by a stirrer also means that the mixing becomes flow rate independent, unlike with COBRs and static mixers.[48,49]

A number of CSTRs have been designed for lab-scale development of continuous processing. Jensen and Mo (2016)[50] developed a miniature CSTR cascade for reactions containing solids. Up to 8 blocks are mounted on a magnetic stirrer plate. Each block has internal dimensions of 18mm diameter x 10mm height and have a cross shaped magnetic stirrer. The device successfully managed to perform two solid forming reactions in flow. The reaction of glyoxal and cyclohexylamine to form N,N′-dicyclohexylethylenediimine which was insoluble in the reaction solvent – ethanol, and the sulfonylation of 2-octanol with methanesulfonyl chloride for which the side product triethylamine hydrochloride has limited solubility in dichloromethane (DCM).[50]
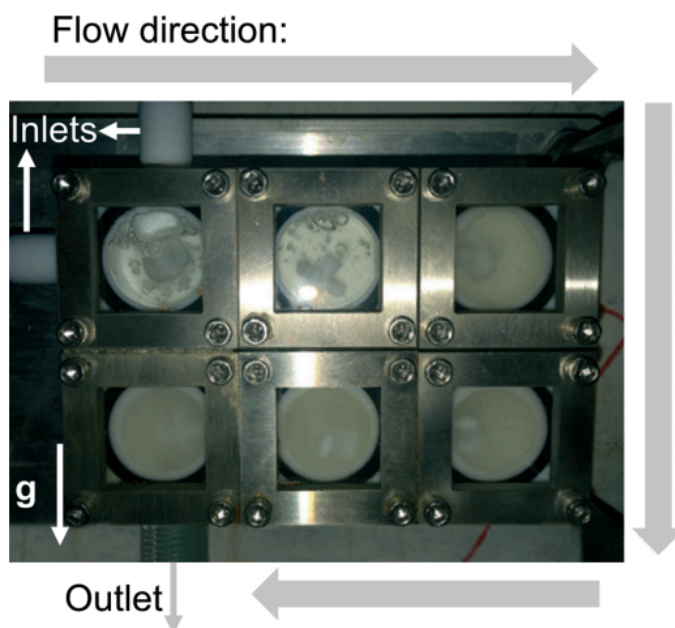
Figure 2.3: CSTR cascade during operation showing the solid fraction inside the cells increasing along the flow path. Reproduced from Jensen and Mo (2016)[50] with permission from the Royal Society of Chemistry.

Jensen et al (2017)[48] also developed a miniature CSTR for lab-scale continuous process development, this time with liquid-liquid systems in mind. The device's stirrer was fixed centrally to the fluid cell and magnets would rotate it up to speeds of 3000 RPM. The cell had four baffles located on its walls, these baffles helped increase

droplet break up in immiscible systems. The device managed to produce droplets of Hexane/Water down to 0.5 mm in diameter.[48]
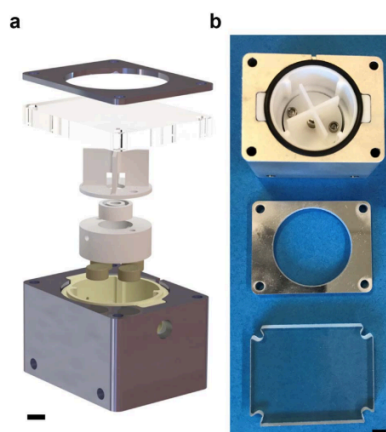
Figure 2.4: (a) Exploded view of a single CSTR unit and (b) The three main components of the CSTR unit. Reprinted with permission from Elsevier.[48]

Kapur and Blacker et al (2017)[51] developed a miniature CSTR for multiphasic continuous flow chemistry applications (shown in figure 2.5). The device has since been made commercially available. The device constitutes of a circular flow cell of approximately 2 ml volume with a cross shaped magnetic stirrer. The device was shown to provide increased productivity measured in $gL^{-1}h^{-1}$ compared to batch counterparts in 5 out of 6 reactions studied (summarised in table 2.1). The reaction phases were either L, L/L, L/S or G/L/S.[51]
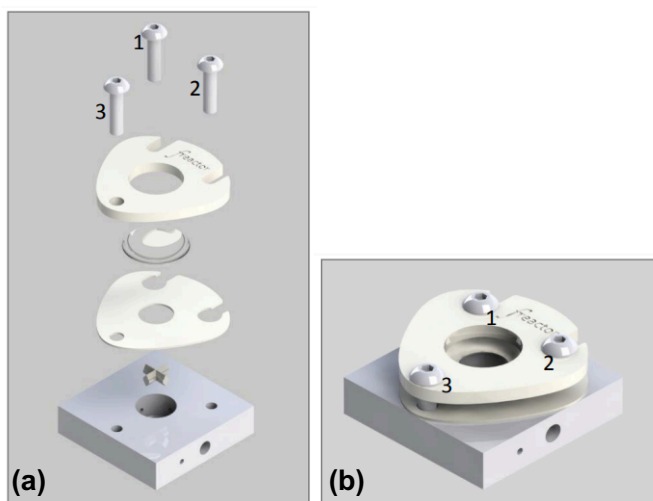
Figure 2.5: (a) Exploded view of fReactor (CSTR) and (b) assembled view of fReactor. Reproduced from Kapur and Blacker et al (2017)[51] supplementary information.

Table 2.1: Summary of multiphasic reactions evaluated by Kapur and Blacker et al (2017).[51]

| | | | Productivity | |
Reaction type	Phase (G, L, S)	τ_{res} (min)	Batch	Flow
Imine Reductase	L	19	6.4	17
N-chloroamine	L/L	5-50	198	826
Monoacetylation	L/L	30	51	173
Heterocyclization	L→L/L	2	660	1920
Crystallization	L→L/S	20	8.2	31
hydrogenation	G/L/S	180	3.5	0.12

Residence Time Distribution

The amount of time and distribution of time that molecules spend in a flow reactor can be measured by the residence time distribution (RTD). Ideally every molecule would spend the same amount of time in the reactor and therefore every molecule would have a constant amount of time to react. This behaviour is only seen in an ideal plug flow reactor. Figure 2.6 shows the residence time distribution of any point in a plug flow reactor. The composition of each 'plug' will differ along the length of the pipe but each plug will be discreate and perfectly mixed.
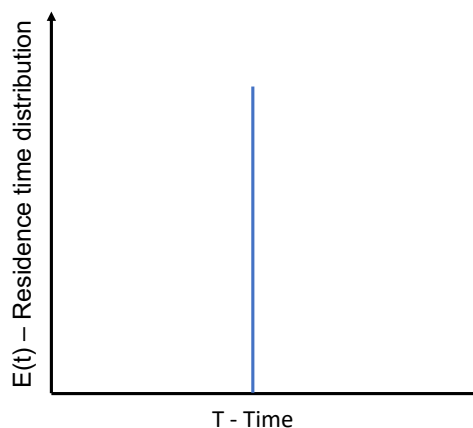
Figure 2.6: Plug flow reactor ideal residence time distribution

To calculate the residence time of a tube reactor the reactor volume and the system flow rates need to be known (figure 2.7). The reaction residence time will be dependent on the reactor cross-sectional area, length and flow rate (equation 2.1 for a cylindrical tube reaction zone).

Flow rate A (ml/min)

Reactor Zone

Flow rate A + B (ml/min)

Flow rate B (ml/min)
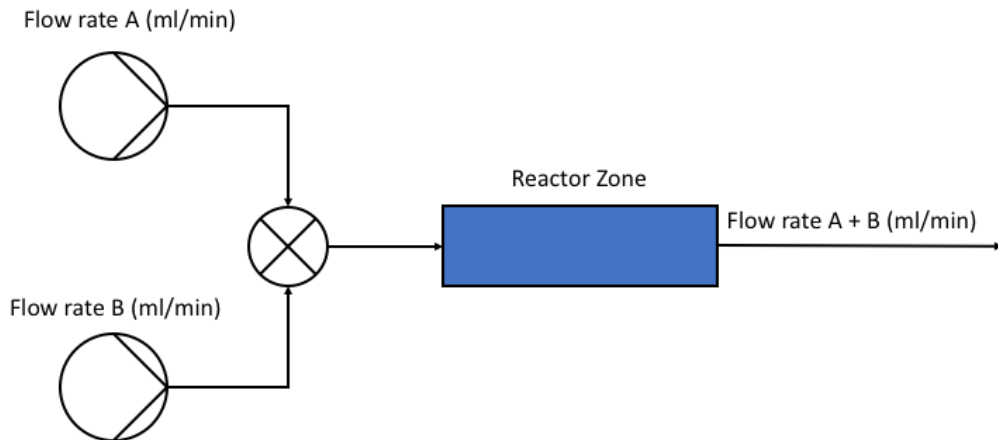
Figure 2.7: Flow rate at different points in a continuous process[52].

$$R_R = \frac{A_R \times L_R}{Q_v} \qquad (2.1)$$

$A_R =$ Cross-sectional area of the reactor (m^2)

$L_R =$ Length of reactor (m)

$Q_v =$ Volumetric flow rate (m^3/s)

$R_R =$ Residence time of the reactor (s)

This equation provides a theoretical calculation which can be used to calculate the length of pipe necessary to reach conversion for a desired product.

In practice, tubular reactors produce axial mixing which results in the movement of molecules such that concentrations vary along a given reactor length. SFR's limit the amount of axial dispersion and therefore have a narrow residence time distribution.[52, 53] COBRs and CSTRs have wider RTDs due to the greater axial dispersion components of their mixing mechanisms.[54] The residence time in a CSTR flow reactor can be modelled using equation 2.2, 2.3 and 2.4.[53] The residence time distribution in CSTRs becomes narrower with respect to the normalised time θ as more CSTRs are added in series (figure 2.8)[53, 50, 47]

$$\tau = NV_0/F \qquad (2.2)$$

$$\theta = t/\tau \qquad (2.3)$$

$$E(\theta) = \frac{N(N\theta)^{N-1}}{(N-1)!} \exp(-N\theta) \qquad (2.4)$$

$N =$ Number of CSTRs

$V_0 =$ Volume of CSTR (ml)

$F =$ Volumetric flow rate (ml)

$\tau =$ Mean residence time (MRT) (min)

$t =$ Time (min)

$\theta =$ Normalised time

$E(\theta) =$ Residence time distribution
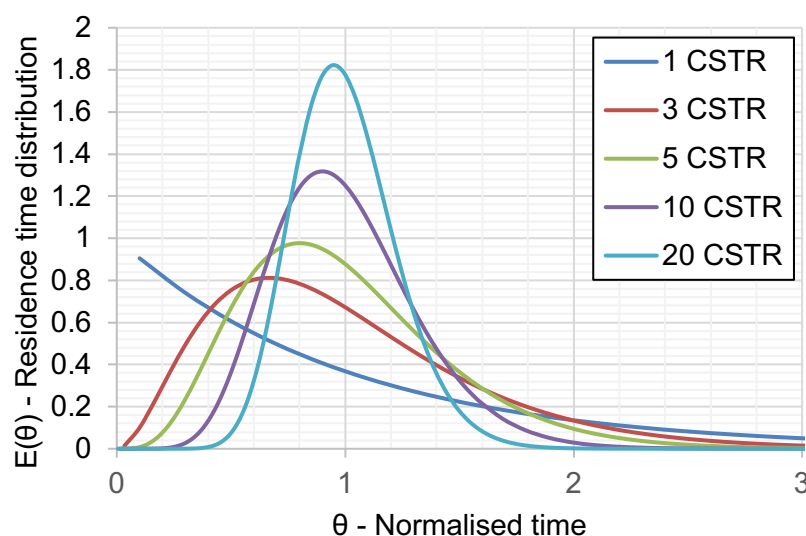
Figure 2.8: Modelled residence time distribution (RTD) depending on the number of CSTRs connected in series.

Once the desired residency time has been met a quenching agent can be added after the appropriate length of tubing to stop the reaction. Quenching can be achieved via rapid cooling, deactivating unreacted reagents or residual intermediates, neutralizing the pH or removing the product from the reaction mixture via extraction, distillation or precipitation. Alternatively, no isolation is performed and one reaction follows on from the previous after a defined amount of time within the reactor. This process becomes more complicated with each reaction step due to solvent compatibilities, impurities and process variables. Therefore, the introduction of in-line scavenger units, extraction modules, and nanofiltration membranes can support the development of multi-stage reactions by removing some of these complications before subsequent reaction steps.[5]

Reynolds Number

Most continuous reactions take place under a laminar flow regime which can be determined for a specific system by the Reynolds number (equation 2.5). If the Reynolds number is < 2000 it is laminar and above 2000 depending on the roughness of the pipe surface the flow can either be transitional or turbulent. The Reynolds number of a given fluid flow is governed by the flow rate and viscosity of the fluid. CSTRs and COBRs are designed to introduce turbulence (or at least enhanced transport) into a system in order to enhance the amount of mixing that takes place. However, the operational flow rates used with CSTRs are usually still within the

laminar flow envelope meaning that if the active mixing stops the produced turbulence would likely dissipate and laminar flow would resume.[52]

$$Re = \frac{\rho VL}{\mu}$$ (2.5)

$Re =$ Reynolds Number

$\rho =$ Fluid density (kg/m^3)

$V =$ Flow speed (m/s)

$L =$ Characteristic length (m)

$\mu =$ Dynamic viscosity $(kg/m.s)$

Damköhler number

The high surface area to volume ratio that is provided in flow reactors compared to batch reactors is beneficial for mass transfer between phases. By maximising the interfacial area, mass transfer can happen rapidly; this is particularly beneficial to fast reacting systems. If a competitive side reaction exists then 'mixing-disguised selectivity' can occur.[55] Consider the reaction of A + B → C and C + A → D where D is a side product. If the diffusion or mass transfer in this system is slower than the reaction then concentration gradients will be produced. These concentration gradients allow the side reaction to take place as unreacted A exists in the system with C. If the system had been homogenous then all of A and B would react to produce C before the side reaction C + A → D has a chance to take place. Because of the greater surface area to volume ratio in flow reactors, homogeneity is reached faster than in batch reactors. The ratio of reaction rate to mass transfer/diffusivity is given using the Damköhler number (equation 2.6).[52, 56]

$$Da = \frac{\text{rate of reaction}}{\text{rate of diffusion}} = kC_0^{n-1}\tau$$ (2.6)

$Da =$ Damköhler number

$k =$ Reaction rate constant

$C_0 =$ Initial concentration

$n =$ Reaction order

If $Da < 1$ then the system reaches near homogeneity before the reaction takes place and if $Da > 1$ the reaction is diffusion limited and concentration gradients will form.

2.2 Liquid-liquid systems

Liquid-liquid systems are common in flow chemistry. They require sustained mixing to ensure the interfacial area between phases remains large. The greater the

interfacial area between the two phases the more efficiently mass transfer can take place.[48] The drawback of increased interfacial area is the creation of fine dispersions which can cause downstream processing issues such as emulsion formation, long separation times and product inconsistencies.[12,39] Understanding how changing process variables can influence both product purity and yield as well as tendencies to form emulsions and fine dispersions must be considered simultaneously in order to optimise a process.[15,39]

2.2.1 Two phase flow

Many dimensionless numbers in fluid mechanics can be used to characterise liquid-liquid systems.[16] For two phase flow systems the Capillary number compares the viscous to surfaces forces in a given system. For a given flow rate, viscosity and interfacial tension it can be deduced whether the flow is surface force or viscous force dominated. Because the flow rates in flow chemistry are generally quite low, the surface forces tend to dominate.

$$Ca = \frac{\mu V}{\sigma} \tag{2.7}$$

$Ca =$ Capillary Number

$\mu =$ Dynamic viscosity of dispersed phase (Ns/m^2)

$\sigma =$ Interfacial Tension (N/m)

Dessimoz et al (2008)[57] compared y- and t- junction mixing optically to see if plug or laminar flow was formed depending on the Reynolds number and Capillary number of the system. Reynolds number was varied between 0.5 and 5 while the capillary number was in the 10^{-4} range. They found that an increased capillary number due to reduced interfacial tension and increased viscosity resulted in laminar over plug flow at the same Reynolds number.

The Weber number is another dimensionless number, it compares surface to inertial forces. The Weber number tends to be low in flow systems due to low flow rates during mixing. It can become > 1 (inertial force dominated) if large droplets exist and liquid or gas density differences are large.[25] In traditional batch mixing vessels the velocity is measured at the rotor tip and can be used to predict droplet sizes and power requirements.

$$We = \frac{\rho V^2 d_d}{\sigma} \tag{2.8}$$

$We =$ Weber Number

$\rho =$ Density of dispersed phase (kg/m^3)

$d_d =$ Droplet diameter (m)

The Eötvös number or bond number is the ratio of gravity to surface forces and tends to favour surface forces in flow systems. It is often used as a rationale for utilising surface driven separators such as membranes and plate separators over gravity driven separations in liquid-liquid flow systems. It can also be used to determine the nature of droplet detachment from a surface depending on the interfacial tension of the system and the contact angle between the droplet and surface in question.[58]

$$Eö = \frac{\Delta \rho g d_d^2}{\sigma} \tag{2.9}$$

$Eö$ = Eötvös number

$\Delta \rho$ = Density difference between dispersed and continuous phases (kg/m^3)

g = Acceleration due to gravity (m/s^2)

2.2.2 Emulsions
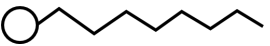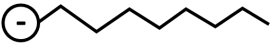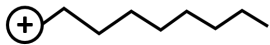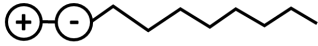
An emulsion can be defined as a liquid-liquid system consisting of a dispersed phase within another immiscible phase (continuous phase), With or without emulsifiers/stabilisers.[59] An emulsion is generated through mixing or agitation, however dispersions can be unstable once mixing or agitation stops. For many systems, the mixture will settle into two distinct phases over a period of time. The rate of separation in liquid-liquid systems can be severely limited if the dispersed phase droplets are stabilised within the continuous phase. Small particulates can cause Pickering emulsions and surface-active molecules can form stable barriers that resist coalescence.[60] Small changes in salinity, pH, temperature, or phase composition can drastically change how compounds interact at the liquid-liquid interface and subsequently the rate of separation of emulsions.[61-67] Surface-active molecules may also reduce interfacial tension, resulting in smaller droplets and longer separation times. A low volumetric ratio of one phase with another generally results in the lowest volume being the dispersed phase and the higher viscosity phase tends to be the continuous phase.

Surfactants

Surfactants are amphipathic molecules (they have both hydrophilic and hydrophobic parts). The hydrophobic group is usually a long-chain hydrocarbon, the hydrophilic group is usually an ionic or highly polar group. Surfactants can be classified depending on this hydrophilic group as shown by table 2.2. They are either, Non-ionic and have no apparent ionic charge, Anionic and have a negative charge, Cationic and have a positive charge or Zwitterionic and have both a negative and positively charged portion of the head group. The amphipathic nature of the

molecules means they tend to migrate to the interface between organic and aqueous phases. A structural and charge barrier then exists between the two phases which resists coalescence and promotes the formation of stable emulsions.[68]

Table 2.2: Surfactant classifications

Surfactant type	Head group characteristics	Illustration
Non-ionic	No apparent ionic charge	
Anionic	Negative charge	
Cationic	Positive charge	
Zwitterionic	Both oositive and negative charges	

Emulsion Types

Most emulsions are thermodynamically unstable and they separate out into two distinct phases over a period of time. These are described as macro-emulsions and generally have droplets larger than 0.1µm and interfacial tensions > 1 mN/m. Macro-emulsions are described as either type I emulsions where the oil phase is dispersed within the surfactant rich water phase (O/W) or type II emulsions where the water phase is dispersed in the surfactant rich oil phase (W/O). O/W/O and W/O/W emulsions can also be formed under certain circumstances.[69] The other type of emulsion is the micro-emulsion which is thermodynamically stable and generally has extremely low interfacial tensions in the µN/m range. Micro-emulsions are described as either type III emulsions where there is an excess oil and water phase but in between there is an indistinct dispersion where neither phase is predominantly dispersed or a type IV emulsion where the indistinct phase exists without any excess oil or water phase (as shown in figure 2.9). Type IV emulsions are simply type III emulsions where enough surfactant exists in the system to solubilise all of the water and oil.[70]
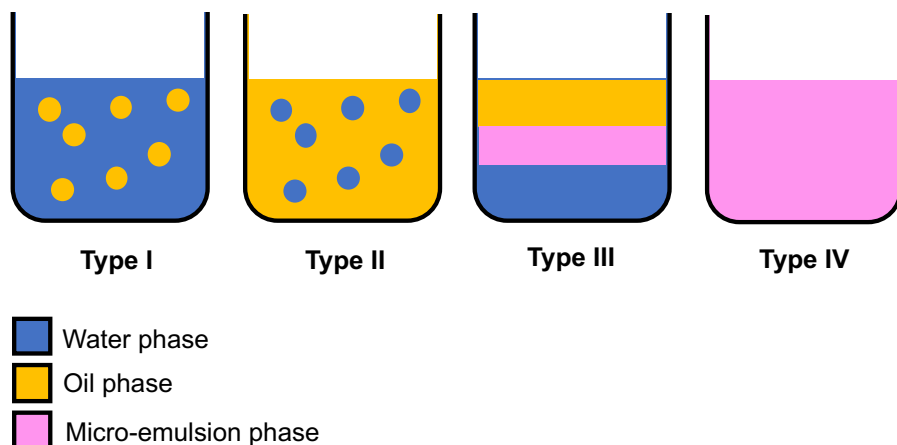
Figure 2.9: Different emulsion types

Emulsion formation

The formation of an emulsion is caused by the deformation and break-up of the to-be dispersed phase. Depending on the flow regime this occurs due to velocity gradients/shear stress or pressure difference/inertial effect and is opposed by the Laplace pressure (equation 2.10). The relationship between the velocity gradient and Laplace pressure is described by the Weber number (equation 2.8).[71]

$$P_l = 2\gamma/r \tag{2.10}$$

P_l = Laplace pressure (Pa)

γ = Interfacial tension (N/m)

r = Droplet radius (m)

In turbulent flow, the local flow velocity varies in a chaotic way with a number of eddies of various sizes. Kolmogorov theory suggests that the smaller the eddy the higher the velocity gradient. If a droplet is smaller than the smallest eddy it is unlikely to deform within the flow field. Turbulent flow results in a spread of droplet sizes and depends on mixing technique, impeller shape, size, speed, and fluid properties.[71] The maximum diameter of a droplet that can resist further breakup by eddies of a certain size is given by equation 2.11. The constant C_1 varies depending on the mixing system being used such as stirred vessel, ultrasound, or homogeniser.[72] Table 2.3 shows how the Energy dissipation (ε) affects maximum droplet size of a liquid system and the typical droplet size of various dispersion devices.[73]

$$d_{max} = C_1 \varepsilon^{-0.4} \gamma^{0.6} \rho_c^{-0.6} \tag{2.11}$$

d_{max} = Maximum droplet diameter (μm)

C_1 = Dimensionless constant

ε = Energy dissipation per unit mass (W/kg)

ρ_c = Density of continuous phase (kg/m^3)

Table 2.3: Dependence of droplet size on local power draw for different dispersion devices.[73]

Dispersion device	ε, Energy dissipation per unit mass (W/kg)	d_{max}, Maximum droplet diameter (μm)
Static mixer	$10^1 - 10^2$	100 – 1000
Agitated vessels	$10^1 - 10^4$	10 – 500
Colloid mills	$10^5 - 10^6$	7 – 10
Liquid whistles	$10^7 - 10^8$	1 – 4
Valve homogenizer	$10^8 - 10^9$	< 1
Ultrasonic	10^9	< 1

The mean surface diameter of droplets within a dispersion are shown in equation 2.12.[74] It relates the volume fraction of the dispersed phase (ϕ) and the inerfacial area (a_v). If d_i is to the power of 4 in the numerator and 3 in the denominator this is the volume mean diameter and is commonly used in particle size distributions.[75,76]

$$d_{32} = \frac{6\phi}{a_v} = \frac{\sum_{i=1}^{i=m} n_i d_i^3}{\sum_{i=1}^{i=m} n_i d_i^2} \tag{2.12}$$

d_{32} =   Surface area mean droplet diameter   (m)

ϕ =   Volume fraction of the dispersed phase

a_v =   Inerfacial area per unit volume   (m^{-1})

m =   Number of size classes describing the droplet size distribution

n_i =   Number of droplets

d_i =   Diameter of drops in size class m   (m)

For low viscosity, non-coalescing, dilute systems the mean droplet diameter can be correlated with the Weber number by equation 2.13. This is true If the systems being studied are geometrically similar. Doing this allows the prediction of droplet size depending on impeller size and speed. The Weber number calculation has been adapted for a mixing vessel by equation 2.14. As discussed earlier, inertial forces (disruptive) and surface forces (cohesive) can be compared using the Weber number (We). The relationship between mean droplet diameter and Weber number holds up across various liquid-liquid pairs and varying ratios of impeller to tank diameter.[73]

$$\frac{d_{32}}{D} = C_2 We^{-0.6} \tag{2.13}$$

D =   Impeller diameter   (m)

C_2 =   Dimensionless constant

$$We = \eta_c N^2 D^3 / \gamma \tag{2.14}$$

N =   Impeller speed   (rad/s)

The relationship described by equation 2.13 is for dilute systems $\phi < 0.01$. It assumes there is no coalescence occurring in the system, the turbulence structure is not affected, and droplet breakup forces are not impeded. However, many studies have shown that by modifying this relationship appropriately the affect an increased phase fraction ($0.01 < \phi < 0.3$) has on turbulent forces can be taken into account. These studies still assume that the emulsion is stabilized against coalescence and the rheology of the system is not effected by the increased percentage dispersed phase.[73]

Another factor to consider during the formation of an emulsion is the transient nature of droplet formation. It is generally found that as mixing time increases the

droplet size distribution narrows and the mean droplet size gradually decreases. As the mixing speed increases, time to disperse decreases and a narrower droplet size distribution can be seen; as shown in figure 2.10 for a toluene/water emulsion with dissolved surface active polymer. If the interfacial tension or dispersed phase viscosity is increased then a longer time to disperse and a wider droplet size distributions will be observed.[77]
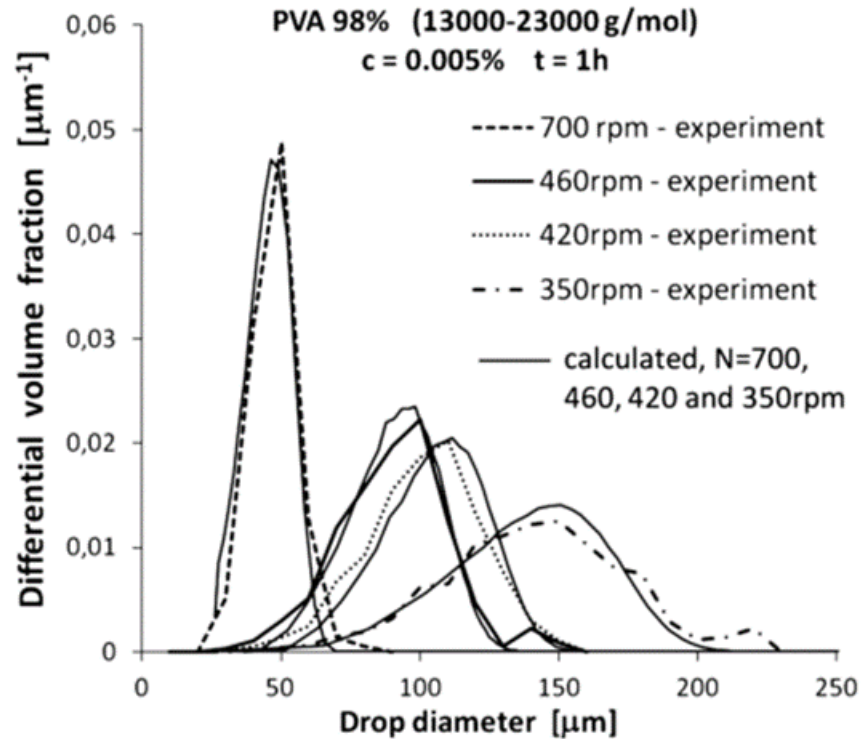
Figure 2.10: Measured and predicted drop size distribution at various impeller speeds for a toluene/water emulsion with 0.005% surface active polymer. Reprinted with permission from The Institute of Chemical Engineers (Bak and Podgorska, 2013).[77]

Emulsion Separation

An emulsion can destabilise and separate via five different phenomenon. These phenomenon are creaming, sedimentation, flocculation, coalescence, and Oswalds ripening. Creaming is when the dispersed phase has a lower density than the continuous phase and therefore floats to the top of a vessel and coalesces, forming two separate phases. If the dispersed phase has a larger density than the continuous phase then the dispersed phase falls to the bottom of the vessel; this is called sedimentation. These two processes are grouped as gravitational separation. The time it takes a droplet to separate from a bulk fluid can be estimated using stokes equation (2.15). Equation 2.15 shows that the difference in density between the two phases, $\rho_d - \rho_c$, the continuous phase viscosity, μ_c, the acceleration due to gravity,

g, and the droplet size, d influence the time it takes to separate two immiscible phases.[70,78]

$$u = \frac{2r^2(\rho_d - \rho_c)g}{9\eta} \qquad (2.15)$$

u =   Settling rate   (m/s)

r =   Droplet radius   (m)

ρ_d =   Density of dispersed phase   (kg/m³)

ρ_c =   Density of continuous phase   (kg/m³)

g =   Gravitational acceleration   (m²/s)

η_c =   Viscosity of continuous phase   (Pa.s)

Flocculation occurs when there are weak net attractions between droplets and coalescence is inhibited. The droplets collect together but do not coalesce, they retain there individual integridy. Coalescence is the merging of two or more droplets to form one larger droplet. Demulsification operations like centrifugation can promote coalescence and creaming. Temperature changes can also make emulsions less stable, therefore facilitating separation.[78]

The collision frequency $\xi(d, d')$ between drops d and d' is dependent on agitation rate, droplet size, and coalescence efficiency but independent of concentration. Coalescence frequency $\Gamma(d, d')$ is defined as the probability of coalescence per collision. It depends on the collision force, the cleanliness of the interface, and the time of contact. Coalescence efficiency $\lambda(d,d')$ depends on a set of hydrodynamic factors, physiochemical variables, drop size, contact time, and film drainage time. Coalescence frequency between two drops is calculated as $\Gamma(d, d') = \xi(d, d')\lambda(d, d')$. For turbulent flow, collision rate depends on a number of factors: motion induced by turbulent fluctuations in the continuous phase; motion induced by velocity gradients in the flow; different bubble rise velocities; motion of eddies bringing droplets into contact; and wake interactions.[79] When droplets are small in comparison to the macroscale, isotropic turbulance theory can be used to model the collision frequency using equations 2.16. The approach force can be found using equation 2.17 and the contact time between two drops can be found by equation 2.18. Both collision frequency and approach force increase with droplet size and agitation rate. Contact time increases with drop size and decreases with agitation rate.[73]

$$\xi(d, d) = C_3 d^{\frac{7}{3}} \varepsilon^{\frac{1}{3}} = C_4 d^{\frac{7}{3}} N D^{\frac{2}{3}} \qquad (2.16)$$

C_3 & C_4 =   Dimensionless constants

d =   Droplet diameter   (m)

$$F \sim (d^8\varepsilon^2)^{1/3} \tag{2.17}$$

F = Approach force (N)

$$t_c \sim (d^2/\varepsilon)^{1/3} \tag{2.18}$$

t_c = Contact time (s)

Collision efficiency is more difficult to quantify. Consider two equal sized drops as shown in figure 2.11 approaching each other with force F. Force F squeezes the film of continuous phase fluid of thickness h trapped between the drops. The contact time between the two drops should be sufficient to reach critical thickness where film rupture will take place and coalescence occurs. During contact the drops deform and flatten, creating a flat surface with radius R. This increases surface area of contact and decreases drainage of the trapped fluid. Film thinning also depends on the mobility of the interface between drops. A rigid interface resists film drainage due to the no-slip condition at the film drop interface.[73]
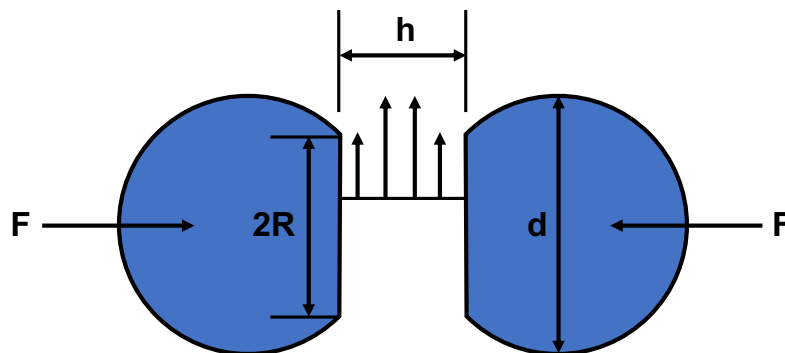
Figure 2.11: Film drainage and thinning for deformable equal-sized colliding drops.[73]

The physicochemical factors effecting coalescence and film drainage are complex. High drop viscosity promotes coalescence by reducing deformation of the droplet during impact but high viscosity also inhibits coalescence by making film drainage more difficult. By decreasing interfacial tension, coalescence is inhibited as it leads to greater flattening for a given impact force. By increasing the amount of surfactant in a system and significantly reducing the interfacial tension droplet coalescence can be strongly limited.[77] Coalescence is promoted by gentle collisions as large collision forces promote flattening and rebounding.[80] Electrostatic forces can also contribute or inhibit coalescence as droplets may attract or repulse each other.

A simple model for the coalescence of a single drop with a plane interface is shown by equation 2.19. It assumes the drainage rate is time invarient and works similar to flow between parallel disks (lubrication approximation).

$$\frac{dh}{dt} = -\alpha_3 h^3 \tag{2.19}$$

h = Separation distance after time t (m)

t = Time (s)

α = Constant accounting for factors that determine the drainage time

For two colliding drops the leading edges can be modelled as flat parallel disks as shown in figure 2.11. equation 2.20 approximates the time required for film rupture in order for coalescence to take place. h_c is normally much smaller than h_0 therefore $\left(\frac{1}{h_c^2} - \frac{1}{h_0^2}\right) \approx \frac{1}{h_c^2}$ and film rupture only occurs if τ is smaller than contact time t_c.[73]

$$\tau = \frac{3\eta_c d^2 F}{64\pi\gamma^2}\left(\frac{1}{h_c^2} - \frac{1}{h_0^2}\right) \tag{2.20}$$

τ = Time to film rupture (s)

F = Approach force (N)

h_c = Critical film thickness (m)

h_0 = Initial film thickness (m)

$$F \sim \pi R^2 \left(\frac{4\sigma}{d}\right) \tag{2.21}$$

R = Radius of disk formed on drop surface (m)

The complexity of emulsion formation and separation means that emulsions require experimental study, therefore many experimental techniques exist to characterise them.

Emulsion characterisation methods

A number of techniques have been developed to characterise emulsion stability.[70,81] Light scattering techniques are commonly used for lab scale investigations, and can predict droplet size distributions and sedimentation rates.[40-42] A monochromatic light is directed through an emulsion sample and the amount of backscattered light is measured. A large percentage of backscattered light correlates with a high concentration of droplets and therefore an emulsion. As droplets float to the top of a sample or sediment at the bottom more back scattering will be observed. As coalescence occurs, the amount of back scattering detected will decrease. Any liquid that comes out of the emulsion (clarification) will also produce less back scattering (see figure 2.12).
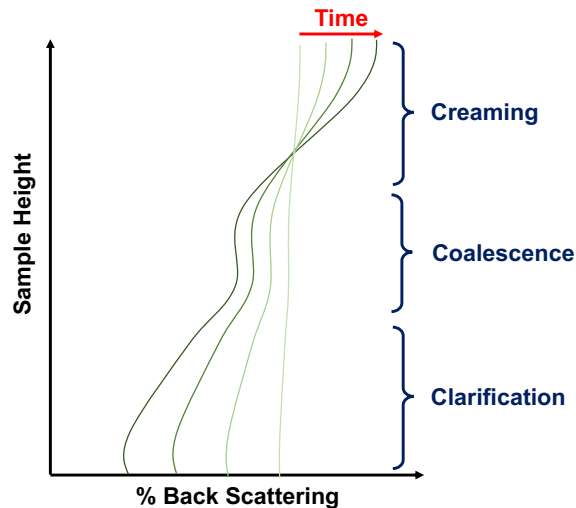
Figure 2.12: Typical back scattering profile obtained from an emulsion sample.

Light back scattering methods are sensitive to small differences in refractive index or large differences in dispersed phase concentrations, which can lead to errors.[41] There are some commercially available systems that use light backscattering techniques to analyse emulsion samples such as the Turbiscan[41] and LumiReader.[82,83] One of the main draw backs of these systems is the number of samples that can be analysed at once, this becomes an issue for analysing long lasting emulsions. Ultrasound and magnetic resonance imaging have been used in a similar way to light scattering techniques to provide droplet size distributions and volume fraction information. These techniques are non-invasive and well suited to highly stable emulsions that can be monitored over a long period of time.[84,85]

'Bottle tests' and visual observations can be used as a fast and simple method to determine creaming/sedimentation rates during separation. BS2000-412:1996 describes this method which uses standardised mixing regimes for qualitative comparison.[86] Imaging techniques have been used to augment this method and provide a quantitative measure of sedimentation/creaming rates. Novales et al (2003)[87] plotted the grayscale intensity value against height for different emulsions over time. A higher grayscale intensity correlated with an emulsion phase. Wang et al (2018)[88] integrated the grayscale intensity data with respect to height which gave a series of curves that corresponded to the clarity of emulsions and amount of phase separation that had occurred over time. Ghanbari et al (2018)[89] measured the absorbance of light by an emulsion sample and compared this to a clear sample, resulting in a 'light absorbance index'. Horozov and Binks (2004)[42] used an image analysis technique to analyse up to 24 samples at once. Image analysis techniques are suited to investigating the phase separation behaviour of relatively fast settling systems as information about the entire height of the sample can be obtained in one

instance and images can be collected at a high frequency. Image analysis techniques will be discussed further in chapter 3.

HLD theory

The semi-empirical Hydrophilic-Lipophilic difference (HLD) can be used to characterise emulsion systems and explain the influence salt concentration, solvent choice and temperature has on a surfactant systems (Equation 2.22).[61,90,91]

It was originally developed to characterise microemulsions (nano-sized thermodynamically stable drops) but can just as readily be used to create macroemulsions. When HLD=0 the emulsion system is at its lowest energy state (thermodynamically stable) and the boundary between phases becomes unstable, resulting in easy breakup of droplets. A type III or IV microemulsion can form if the surfactant is dissolved in a sufficiently high concentration. If HLD<0 then the emulsion will be an O/W emulsion and if HLD>0 the emulsion will be W/O (Figure 2.13).[92] Equation 2.22 is the calculation performed to obtain the HLD value of a given system.

$$HLD = F(S) - k.EACN - \alpha(T - 25) + Cc \qquad (2.22)$$

HLD =	Hydrophilic lipophilic difference	
F(S) =	Function of salinity	(g/100ml)
k =	Oiliness factor = 0.17	
EACN =	Equivalent alkane carbon number	
α =	Temperature factor	
T =	Temperature	(°C)
Cc =	Surfactant characteristic	

The function of salinity varies depending on the type of surfactant i.e. for a non-ionic surfactant it is 0.13 x S and for an ionic surfactant f(S) = ln(S+SurfSal) where S is the salinity in g/100ml and SurfSal is the salinity contributed by the surfactant in g/100ml NaCl. The EACN takes account of the oils hydrophilicy. α changes depending on the type of surfactant as different surfactants are effected by temperature differently and Cc describes the hydrophilic/lipophilic balance of the surfactant. HLD is a powerful tool for predicting and controlling emulsion formation. It can be used to find the solubility of one phase in another given characteristics of the surfactant such as the effective tail length, the surfactant area, and the Molecular weight. The HLD scale shows that when solubility is at a maximum, interfacial tension is at a minimum and this will always be at HLD=0 (figure 2.13b). The time required for emulsion phases to separate increases exponentially as the HLD value deviates from 0. Only when a system is situated far from the phase inversion point does the

time for separation tend to reduce again, due to increased interfacial tension, larger droplet sizes and less efficient surfactant interfacial packing (figure 2.13a).[61]
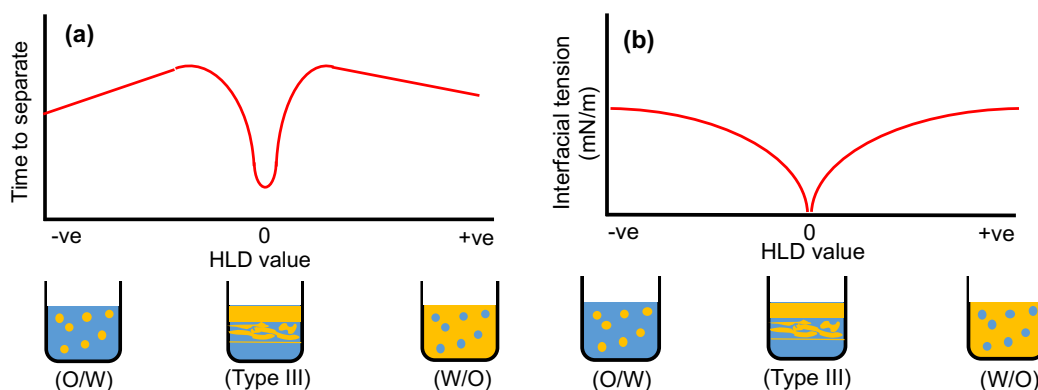
Figure 2.13: (a) The time it takes for an emulsion to separate depending on the HLD value of the emulsion. (b) The interfacial tension depending on the HLD value of the emulsion.

2.3 Lab-scale Continuous Extractions

2.3.1 Introduction

One purification step that has attracted significant attention in the flow chemistry community is the extraction of products or impurities based on their solubility in different liquids.[5,11] Liquid-liquid extraction has several potential benefits such as operation at low temperatures and pressures – important when heat sensitive materials require processing. Extraction processes can be highly selective over multiple stages and are an ideal purification technique to use when components are present in small quantities and require recovery or removal.[13] Green and renewable solvents such as those derived from bio-materials are generally less volatile than crude oil based solvents and are therefore separated more readily by differences in their solubilities rather than by distillation.[14,15]

2.3.2 Extraction process

Liquid-liquid extraction exploits the difference in miscibility of a solute between two solvents. To perform an extraction the feed solution, F comes into contact with an extracting solvent, S. F consists of a carrier solvent and a solute you wish to extract from the carrier solvent (and other solutes). Carrier A and Solvent B are immiscible and B tends to have a higher affinity for the solute than A. When A and B are mixed solute C transfers across into solvent B. Once the distribution of solute C across the two solvents reaches equilibrium the two liquids are separated. The carrier solvent depleted of solute C is called the raffinate phase and the loaded solvent B is called the extract phase.[93]
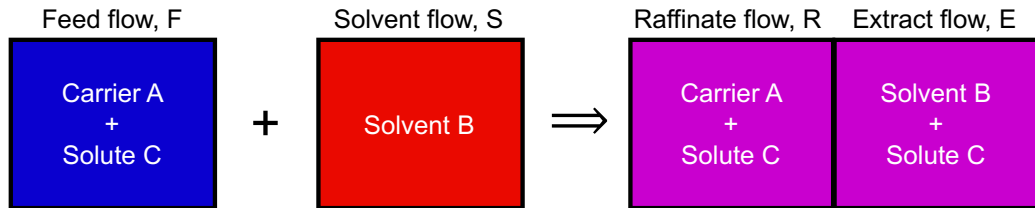
Figure 2.14: Single stage extraction process.

The efficiency and effectiveness of an extraction process is governed by the selection of extraction solvent. A number of criteria should be considered when choosing a solvent:[93]

- Distribution coefficient – A high distribution coefficient indicates high affinity of the solvent for the solute and permits lower solvent/feed ratios.

- Selectivity – If the feed mixture contains multiple components then the selectivity of the solvent for the desired solute over other components becomes important. A high selectivity reduces the number of extraction stages necessary to achieve the required extract purity.

- Density – Most extraction equipment relies on gravity separations, therefore large density differences between the extract and raffinate phase are preferred.

- Viscosity – Can influence the size of droplets during mixing and dispersion.

- Solvent recoverability – The boiling point of the solvent compared to the solute should be considered to ensure easy recovery.

- Solubility of solvent in carrier phase –The carrier and solvent phases should be as close to immiscible as possible to avoid having to perform additional solvent removal steps.

- Interfacial tension – Low interfacial tensions can lead to the formation of very fine dispersions, emulsions and long separations.

- Availability and cost – The selected solvent should be commercially available and relatively inexpensive.

- Toxicity, compatibility and flammability – Any hazard associated with the solvent will result in extra safety measures and greater costs.

- Thermal and chemical stability – If the solvent is recycled via distillation then it is important it is thermally stable.

- Corrosivity – Corrosive solvents can lead to increased equipment costs or expensive pre/post treatment of streams.

- Environmental impact – The solvent should minimise impact on the environment and be from a sustainable source where possible.

2.3.3 Extraction schemes

In many applications a single stage of extraction is not enough to recover the desired % of the solute or at a required purity, therefore multiple stages are necessary. Different arrangements of the extraction stages can be used to meet different extraction criteria. A single stage extraction has already been described above and entails two phases coming into contact, being mixed until equilibrium is reached and then separated out. This process is diagrammatically shown in figure 2.15a. If the extraction does not reach equilibrium after 1 stage of extraction, many extraction units can be placed one after another until equilibrium is reached; this is known as co-current extraction (figure 2.15b). In single stage and co-current operations the % solute extracted is limited by the equilibrium of the two phases at the phase ratios used. To overcome this a cross-current arrangement can be used. In a cross-current arrangement fresh extraction solvent is mixed with the carrier phase at each stage. This allows more solute to be extracted from the carrier phase but at the cost of additional solvent usage (figure 2.15c). A compromise between single stage/co-current and cross-current extraction is the counter-current extraction. During counter-current extraction the solvent and feed flow in opposite directions to one another (figure 2.15d). This means that the feed comes into contact with a close to fully saturated solvent. The final stage with the depleted feed stream comes into contact with fresh solvent. This means there is always a differential in solute concentration that can be exploited at each stage. In this arrangement a higher purity can be achieved than compared with single-stage but the same amount of solvent is used.[93,94]
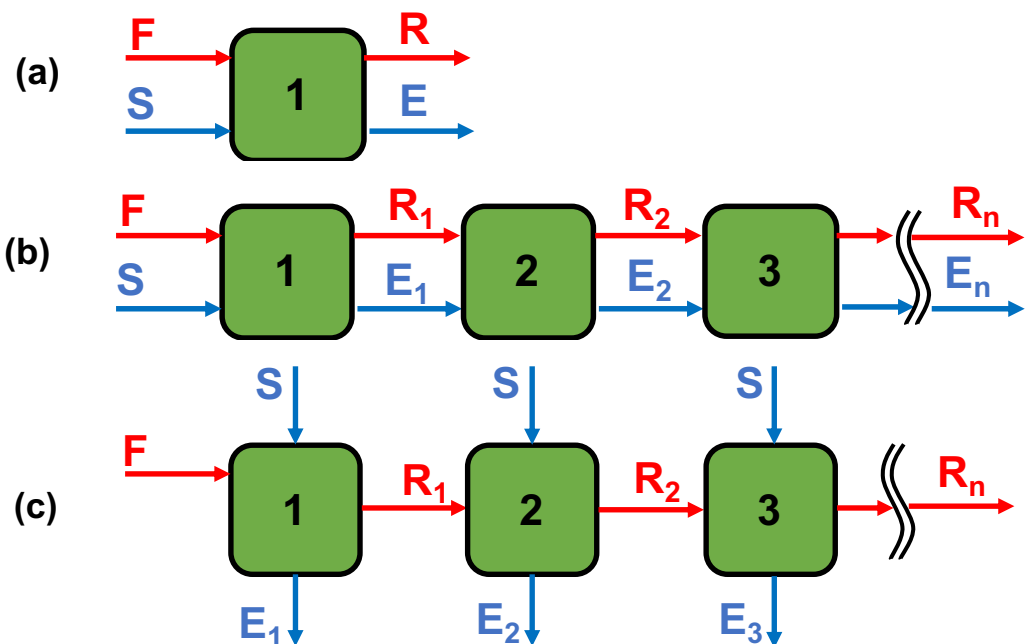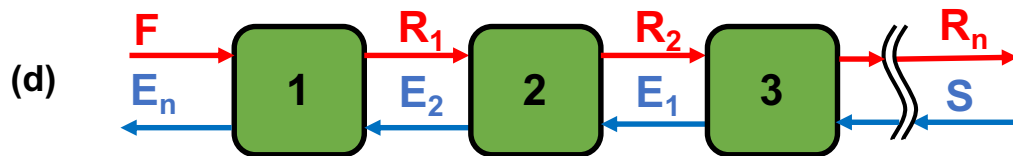
Figure 2.15: (a) Single stage extraction, (b) Co-current extraction, (c) Cross-current extraction, (d) Counter-current extraction.

2.3.4 Lab-scale continuous extraction process development equipment

To enable the development of continuous-flow extraction processes a number of milli-scale and micro-scale separators have been developed.[16-18] Xu and Xia (2017)[18] catalogued various microfluidic liquid-liquid extractors into stop flow, counter-current and co-current arrangements, laminar, droplet/slug flow and chaotic flow. Hohmann et al (2016)[17] reviewed three different separation units; a miniaturised extraction column, capillary flow separator and an in-flow crystallisation system.[17] Gürsel et al (2017)[16] reviewed a number of microstructured separation devices for flow applications and catagorised them according to flow regime. The flow regimes in different systems with maximum flow rates ranging from 12 – 1200ml/hr (0.2 – 20 ml/min) were slug, parallel, droplet, annular, deformed interface, dispersed and fully dispersed. Furthermore, slug flow regimes were reported in a multitude of systems ranging in maximum flow rates from 3ml/hr – 7200 ml/hr (0.05 – 120 ml/min). The devices/techniques used to separate these slugs were predominantly membranes/capillary force driven separations and the exploitation of different surface wettability. Separations become more difficult as droplet sizes reduce therefore the mechanism used to disperse and mix the liquid phases is important to the downstream separation process.[51,95] Two commercially available separation devices were mentioned, the Syrris Asia FLLEX (Flow liquid-liquid extraction) module[22] and the Zaiput membrane separator by Zaiput flow technologies.[96] One of the main differences between them and the prototype devices presented in the literature is more consideration for downstream pressure fluctuations, automation and outlet flow regulation.

A number of lab-scale devices have been designed to separate immiscible liquids in order to facilitate liquid-liquid extraction processes. Various phase separation devices have been extensively reviewed elsewhere, particularly those operating on the microscale.[5,16-18] The two most commonly encountered separation methods are gravity force driven[19-21] and surface force driven.[22-26]

Gravity driven technology

Gravity driven separation technology predominantly relies on the difference in densities of the aqueous and organic phases. Some systems simply match the outlet

flow rates of a small settling area with the inlet phase velocities. Sprecher et al (2012)[20] utilised a small cylindrical vessel to allow sufficient time for separation to take place and monitored the phase levels with an electrical impedance probe. The system was used to produce 100g quantities of labile diacyl azide. The separation unit had a volumetric capacity of approximately 100ml and was used at flow rates of 18.8ml/min.

A similar system was developed by O'Brien et al (2012)[21] but utilised image analysis techniques to determine the height of the interface between settling interfaces over time. A 10mm diameter cylinder with a green ball that had a density between that of the aqueous and organic phases was monitored by a webcam. The separator was attached to a 1ml/min system that used magnetic stirrers to agitate the mixture prior to separation. The 'hue' of the object was determined by image analysis and this in turn determined where the ball was within the cylinder. The outlet pump speed was then adjusted to maintain a constant interface height over time.

The High-efficiency extraction device (HEED) developed by Day et al (2016)[19] is similar in construction to the other devices described above, it is 25cm long with a 5mm diameter and feeds droplet from opposing ends of the cylinder to allow mixing to occur. The system pressure at the outlets is manually adjusted to stabilise the separation during an initial period of operation. Table 2.4 summarised these 3 gravity driven separation devices.

Table 2.4: Gravity driven continuous separation devices for lab-scale extractions.

Device	Volume (ml)	Level control
High-efficiency extraction device (HEED)[19]	3.8	Manual pressure adjustment
Computer-vision' prototype[21]	2.5	Dynamic pump control based on camera level sensing
impedance probe separator[20]	100	Dynamic pump control based on impedance probe measurement

Gravity driven devices rely on density differences between the organic and aqueous phases. These devices work best with larger internal diameters where plug flow is avoided. For continuous flow operations it is desirable to implement some form of 'level sensing' so that the interface between the two phases is kept at a specific height within the device. This avoids a phase exiting the device through the wrong outlet. Gravity driven devices are often simple in design and can operate at a range of phase ratios. The possible operational flow rates depend on the separation rate of the two phases and generally require larger volumes than surface force driven

devices.[19-21] At the microscale, surface forces dominate over gravity forces due to the small length scales and are therefore generally preferred for microscale extractions.

Three types of gravity systems that are commonly used at industrial scale for continuous extractions are: Mixer-settlers, Column extractors, and centrifugal separators. Mixer-settlers involve a mixing vessel (often mixed by an impeller) followed by a settling area (large tank over which emulsions can separate). Mixer-settler systems must balance high dispersion and mass transfer with long separations. Mixer settlers are flexible, can have high capacity and high stage efficiencies. Their main disadvantage is the large amount of material required per stage with the settler unit making up approximately 75% of this.[13]

Column separators have a light phase and heavy phase inlet at the top and bottom of the column and the two phase mix as they pass through the device in opposite directions. Column extractors can be split into agitated, unagitated and pulsed columns. Agitated columns use impellers, reciprocating or vibrating plates to create phase dispersion as the two phases pass through them. Unagitated columns generally have lower efficiency than agitated columns due to poor phase contacting. However, they are simple in design and are useful when processing corrosive systems due to there absence of moving parts. Several columns have been designed to increase unagitated column mixing by manipulating the flow path through the device such as with packed columns and perforated plate columns. Another method to increase mass transfer in column extractors is by creating a pulsed flow regime.[13]

Centrifugal extractors rotate a fluid stream at high speed in order to create a centrifugal force which increases the rate of separation due to density differences between the two phases. They are particularly useful in highly emulsified systems and systems with small density differences. The disadvantage of centrifugal separators is that they are complex with high capital and operating costs.[13]

Although these devices are commonly used at large scale for extraction processes, there is limited reference to use of these devices in the flow chemistry community at lab scale for process development. In this thesis, the focus was on devices that are already embedded in the flow chemistry community.

<u>Surface tension and capillary force driven technology</u>

The principle behind surface force devices is that part of the separator will be preferentially wetted by one of the liquids, whether this be two plates made of different materials, a porous capillary tube or membrane.[22-26] The differential pressure across the two outlets of these devices must be closely controlled to ensure proper separation and limit breakthrough or retention of the organic into the aqueous phase or vice versa. To overcome this limitation different mechanisms have been

successfully implemented (table 2.5). Surface force driven separation devices work best when interfacial tensions are large and flow rates are small. Operation at phase ratios far from 1 (organic flow rate/aqueous flow rate) can cause failure of the mechanism.[97] Scale-up can be limited as surface area to volume ratios need to remain small. Downstream pressure fluctuations and particulates that block small pores or flow channels can cause problems for these separators.[98] However, surface force driven separators have small internal volumes and simple integration at lab-scale. They can separate liquids with similar densities and in some cases break emulsions, meaning residence times are small and what are considered challenging or time consuming separations in batch can often be dramatically improved via surface force driven separations.[12]

Table 2.5: Surface tension/Capillary force driven separation devices for lab-scale separations

Device	Volume (ml)	Outlet control
Asia FFLEX[22]	0.1	Manual or automated cross membrane pressure control
Zaiput separator[96]	0.5	Automated pressure control via integrated diaphragm
Plate separator[24]	< 0.01	Manual control
Steel sieve separator[25]	0.3	Manual set pump and pressure-control valve
Porous capillary separator[26]	< 0.2	Optical transmittance sensor controls a needle valve on one outlet – controlling the outlet pressure difference
Concentric annular separator[99]	< 2.1	Adjustable back pressure regulator

Kolehmainen and Turunen (2007)[100] demonstrated the feasibility of using plates made from different materials to separate organic and aqueous phases (figure 2.16). Okubo et al (2004)[24] used a similar approach to separate surfactant laden systems. The plate coalescer works by using preferentially wetted surfaces such as glass (hydrophilic) and PTFE (Hydrophobic) to coalesce droplets within the microchannel. The success of separation was dependent on the droplets entering the device being larger than the slit height, thus allowing for wall contact and variation in flow velocities through the device due to the difference in wettabilities of the two liquids. Smaller droplets travel through the device slower compared to larger droplets due to lower surface area contacted with the wetting surface (smaller surface force). The smaller droplet also has less momentum than larger droplets in the continuous fluid stream.

Two channel sizes were tested by Kolehmainen and Turunen (100μm and 200μm). The ability for the plate coalescer to separate smaller droplets from the continuous phase was increase by the smaller slit size. However, this also increased pressure drop and increases the probability of clogging. The plate coalescer was tested at 3ml/min which equated to 3.3cm/sec in the 100μm slit and 1.7cm/sec in the 200μm slit. The aqueous phase was water and the organic phase was Shelsol + Tris(2-ethylhexyl) phosphate (TEHP).[24,100]
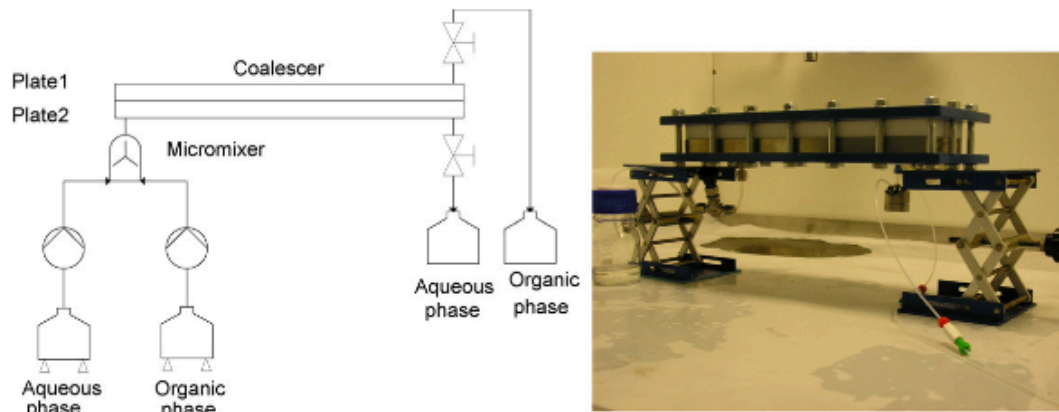
Figure 2.16: Plate coalescence experimental setup and device. Reprinted with permission from Elsevier.[100]

Holbach and Kockmann (2013)[25] utilised surface forces and capillary forces to separate organic from aqueous liquids utilising a hydrophobic outlet made from Polyetheretherketone (PEEK) and a porous hydrophilic steel sieve with 400μm holes (figure 2.17). The devices overall volume was 0.3 ml and had a 4mm diameter to allow for settling of the organic phase from the aqueous before reaching the steel sieve. The droplet generation was strictly controlled and whether slug flow or droplet 'jetting' flow or 'dripping' flow was observed. As flow rate increased the general trend was towards droplet jetting flow where multiple droplets smaller than the tube diameter were created. The tube diameter at the point of mixing was 1000μm and droplets were generated via a 200μm needle. The organic phase was n-nonane and the aqueous phase was water. The separation device was tested up to a total flow rate of 9ml/min and had good separation of the aqueous and organic phases.
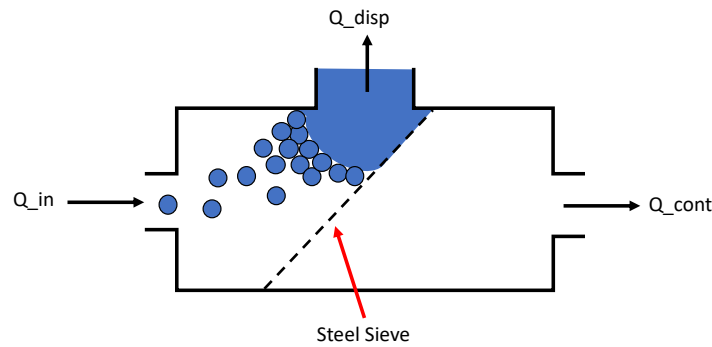
Figure 2.17: Design of metal sieve separator device.[25]

Gürsel et al (2016)[97] investigated two different separators applied to a toluene-acetone-water system and n-butyl acetate-acetone-water system. The application of these separators to scale-up, high throughput and pilot plant scale separations was under investigation. The two separation devices were a plate type separator with glass and Teflon that caused preferential wetting of the organic and aqueous phases and a PTFE membrane separator (figure 2.18).
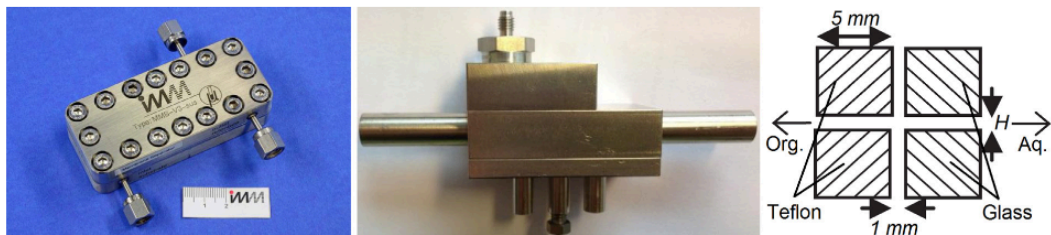
Figure 2.18: Flow separation devices, left: membrane separator, middle: slit shaped separator, right: internal cross-section view of the slit shaped flow separator. Reprinted with permission from Elsevier.[97]

The slit shaped separator gave 100% separation of phases up to 22 ml/min for the toluene-acetone-water system at a phase ratio of 1. The performance of the separator slowly decreased from 22 ml/min up to 120 ml/min where it had 20% crossover of each phase in the opposing outlets. The separator performed worse with the n-butyl acetate-acetone-water system due to the lower interfacial tension between the organic and aqueous phases. Crossover of the organic phase was seen in the aqueous outlet after 12 ml/min. At 50 ml/min there was a 40% crossover of phases. At 20 ml/min the effect of phase ratios between 0.1 and 0.9 was tested and it was shown that once the aqueous phase fraction reached 0.6 some crossover of the aqueous into the organic phase was seen.

The membrane based separator appeared to perform worse than the slit shaped device as around 20% breakthrough of the organic phase into the aqueous outlet occurred from 2 ml/min up to 20 ml/min for the toluene-acetone-water system and 30% for the n-butyl-acetate-water system. This may be due to poor back pressure

control at the aqueous outlet. The effect of changing phase ratios was investigated At 10ml/min and it was found that at low aqueous fractions the device performed much worse due to the lack of back pressure control.

Microsystems have been compared to common large-scale extraction processes to understand their performance and feasibility at scale. Leblebici et al (2016)[98] utilised a PTFE membrane separator to extract rare earth metals (REMs) yttrium and europium. The extraction process was compared to standard mixer settler units used in industry for this process via its space-time-yield (STY) using equation 2.23. The throughput of an industrial mixer settler unit was assumed to be 30 m^3 per day. The total volume of the mixer settler unit was 400 L (100 L mixer and 300 L settler). The total passage time was 19 minutes. The STY was therefore 75 L of throughput for every litre of mixer-settler volume per day (L/Ld).

$$STY = \frac{V_R}{\tau} \qquad (2.23)$$

$$STY = \quad \text{Space time yield} \qquad \text{(L/L.day)}$$

$$V_R = \frac{V_{th}}{V_{unit}} = \quad \text{Normalised unit volume} \qquad \text{(L/L.day)}$$

$$V_{th} = \quad \text{Throughput volume} \qquad \text{(L)}$$

$$V_{unit} = \quad \text{Process step unit volume} \qquad \text{(L)}$$

$$\tau = \quad \text{Time period} \qquad \text{(Days)}$$

Yttrium and Europium were extracted from dodecane using Bis-2-ethylhexyl phosphoric acid (DEHPA) as an extracting agent out of an aqueous solution containing hydrochloric acid. DEHPA is a surfactant and can cause stable emulsions to form during mixing. The organic and aqueous phases were mixed in a t-piece producing slugs. Depending on the concentration of REMs and DEHPA and the pH of the solution, the solution required a longer residence time in the membrane separator to separate. At pH2 and phase ratio 1 the Separation factor and distribution ratio of the extractants was best but the residence time required was long compared to at a pH of 0.4. Therefore, upon scale up, to reach the throughput of an industrial unit, 10000 microextractors would be needed. When the residence time equalled 10 seconds, at the highest separation factor, 25000 units were required. This demonstrates the need for fast separations to allow for more economic scale out of microsystems.

Harvie and Herrington (2019)[26] developed a separation device that utilised a porous capillary PTFE tube that allowed organic phases to pass through its pores but kept the aqueous phase within the tube. The separation was controlled by monitoring the two outlets with optical transmittance sensors, the phases were deemed to be fully separated when the two signals were invarient. To control the separation, a

restriction on one outlet is required to provide a back pressure. A needle valve on the other outlet was then controlled by a positional servo motor to determine the amount of liquid that passes through that outlet by changing the pressure difference between the two outlets (figure 2.19).
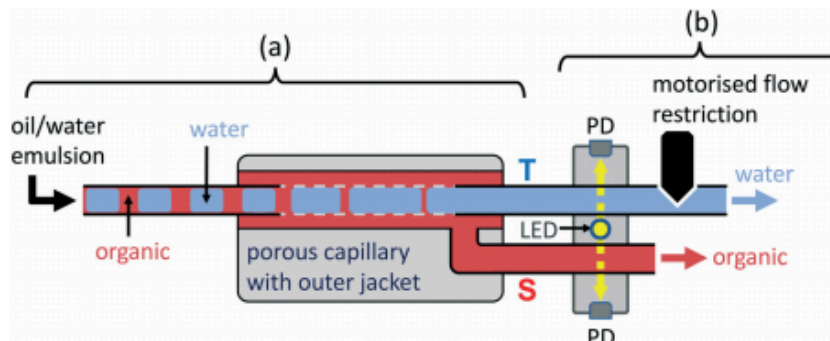
Figure 2.19: Diagram of the optically monitored porous capillary tube separator. Reproduced from Harvie and Herrington (2019) with permission from the Royal Society of Chemistry.[26]

Because of the electromechanical control of the separation, an optimisation routine was required to ensure complete separation. The T channel refers to the aqueous outlet and the S channel refers to the organic. The Transmission signal was monitored at both outlets and if it was invariant in both outlets then good separation had occurred. If the signal fluctuates then one or both of the channels had not completely separated. The relative standard deviation (RSD) was used to determine this (equation 2.24).

$$\gamma_S = \frac{\sigma}{\mu} \tag{2.24}$$

$\gamma_S =$ Relative standard deviation at S channel outlet

$\sigma =$ Standard deviation

$\mu =$ mean

A high relative standard deviation over a set time period meant a fluctuating signal and poor separation.

Four scenarios were observed:

i) RSD was high in the S channel and low in the T channel, indicating that both liquids were passing through the porous capillary wall and therefore the valve on the T channel should be opened further.

ii) RSD was low in the S channel and high in the T channel, indicating both liquids were not passing through the porous capillary wall and therefore the valve on the T channel should be further closed.

iii) RSD was low in both channels therefore good separation was occurring.

iv)   RSD was moderately high in both channels therefore full separation was not occurring but was close to the correct valve position.

The amount the valve rotated was proportionally controlled depending on how large the difference between the RSD values of each outlets was ($\Delta\gamma = \gamma_S - \gamma_T$). The servos new position and required rotation could then be determined via proportional control $\Delta V = \alpha\Delta\gamma$. Where α is the user defined proportionality constant. The maximum rotation the servo could do in one iteration was limited to avoid repeated overshooting and the valve remained stationary once the RSD went below a certain user defined threshold. A summary of the parameters used can be found in figure 2.20.

The separator was tested between 0.1 and 4.8ml/min using equal phase ratios of water and DCM. For the separator to reach complete separation a period of time was required, this varied around the 1 minute mark depending on flow rate and phase ratios. Separation was achieved at flow ratios between 1:10 and 10:1 in 126 seconds or less and the control algorithm was able to respond to changes in the flow conditions. The flow rate was changed from 0.1 and 4.8 ml/min and then back to 0.1ml/min, each time reaching a steady state and complete separation after a transitional period that lasted approximately 60 seconds.[26]

Max rotation per iteration	$\Delta V_{max} = 80°$
Proportionality constant	$\alpha = 10000°$
RSD threshold for valve rotation	$\gamma_{min} = 0.2\%$
Wait time before data acquisition	$t_d = 2$ s
Duration of data acquisition	$t_m = 4$ s
Sample rate	$f = 50$ Hz

(b) Parameters for optimisation procedure
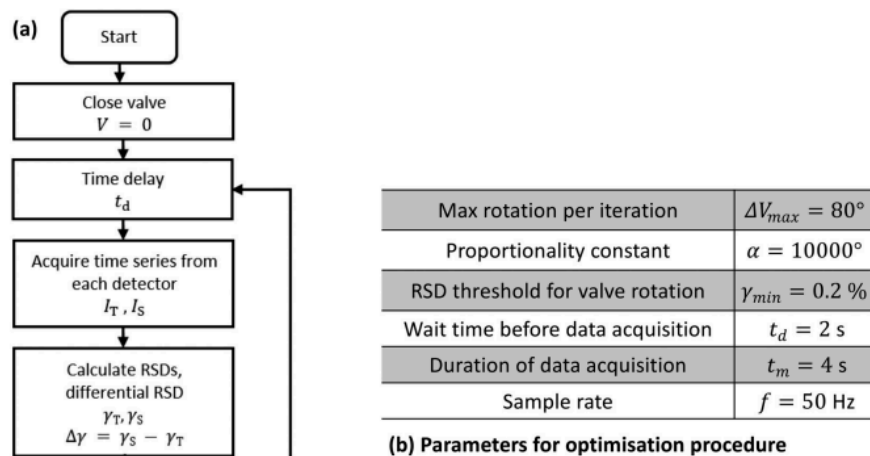
Figure 2.20: a) iterative algorithm to control the servo position and separation. b) User defined parameters for the optimisation procedure. Reproduced from Harvie and Herrington (2019) with permission from the Royal Society of Chemistry.[26]

Harding et al (2021)[99] developed a tubular membrane separator using expanded PTFE from Zeus Industrial Products (figure 2.21). The expanded PTFE membranes had between 30 and 50 % porosity. Unlike most other tubular membrane separators

the fluid flowed around the external walls of the membrane and the wetting liquid passes through the membrane into the centre of the tube. This increases the effective surface area of the membrane as the outer diameter of the membrane is greater than the inner diameter allowing for more fluid contact with the membrane for separation to take place. It was also suggested that flowing through an annulus rather than tube would maintain laminar flow at higher flow rates.
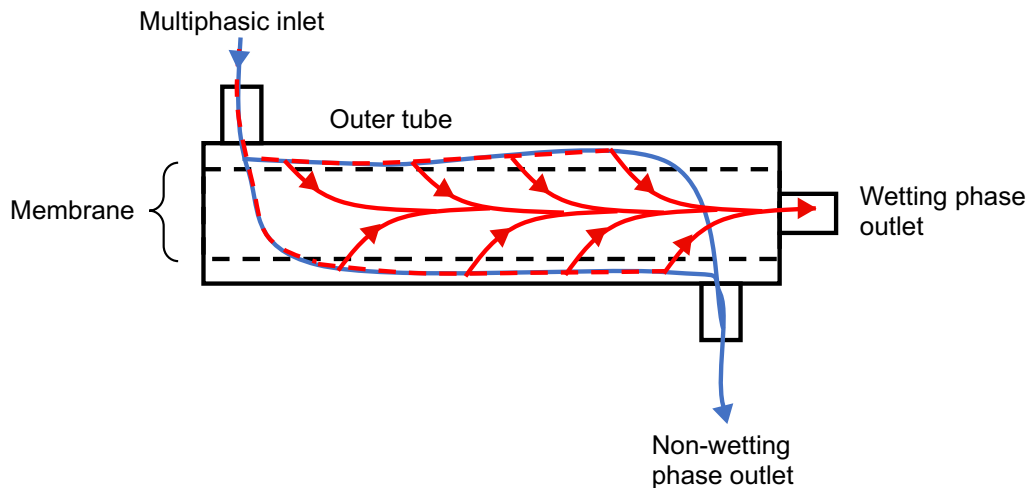
Figure 2.21: Flow through the tubular membrane separator. Redrawn from Harding et al (2021).[99]

The separator was tested using a 17.5 cm effective length separator. The membrane had an outside diameter of 6.35 mm, inner diameter of 3 mm and an annular gap of 0.7 mm. Three different mixtures were tested: Heptane/water, toluene/water and ethyl acetate/water. heptane/water had the highest interfacial tension, then toluene/water and then ethyl acetate/water at 6.8 mN/m. The operating window of each system was obtained depending on the applied back pressure. This configuration was capable of separating heptane/water without breakthrough of phases up to a total flow rate of 10.75 ml/min. Toluene/Water could be separated at 9.75 ml/min and Ethyl Acetate was separated at a maximum flow rate of 5.8 ml/min. When the annular gap was increased to 1.1 and 1.9 mm the maximum flow rate achieved without breakthrough was 41 and 63 ml/min respectively.[99]

Operating Membrane Separators

Leblebici et al (2016)[98] used a membrane separator at microscale and described the operational window theoretically using equations 2.25i – 2.25v. P_1 (aqueous channel pressure) has to be greater than P_2 (organic channel pressure) and this was controlled by adding a back pressure at the aqueous outlet. To stop the aqueous feed from passing through the hydrophobic membrane the capillary pressure needs to be below the membrane pressure. The capillary pressure varies with the size of the

membrane pores and the interfacial tension between the two liquids being separated. If the interfacial tension between the two liquids is extremely low then it is difficult to keep the membrane pressure low enough to adhere to equation 2.25iii. The two simplest ways to keep P_M below P_C are to reduce the flow rate or decrease the size of the membrane pores. Another consideration for the membrane separator is if pores become blocked due to sediment/gels forming in the liquid phases, this will reduce the number of available pores and therefore increase P_M.

$$P_M = P_1 - P_2 \qquad (2.25i)$$

$$P_1 > P_2 \qquad (2.25i)$$

$$P_c > P_M \qquad (2.25iii)$$

$$P_M = \frac{8\mu Q}{n\pi R^4} L_m \qquad (2.25iv)$$

$$P_c = \frac{2\gamma}{R} \cos\theta \qquad (2.25v)$$

$P_M =$	Pressure required for the organic phase to pass through the membrane	(Pa)
$P_C =$	Critical capillary pressure at which aqueous phase passes through the membrane	(Pa)
$P_1 =$	Aqueous channel pressure	(Pa)
$P_2 =$	Organic channel pressure	(Pa)
$\mu =$	Viscosity of organic phase	(Pa.s)
$Q =$	Flow rate of organic phase	(m³/s)
$n =$	Number of pores on membrane surface	
$R =$	Pore size	(m)
$L_m =$	Membrane thickness	(m)
$\gamma =$	Interfacial tension between liquid phases	(N/m)
$\theta =$	Contact angle between the membrane material and liquid phases	(Deg)

In the study by Lablebici et al (2016)[98] one consideration was that because DEHPA is a surfactant, as the loading of the extraction agent increased, the interfacial tension of the system reduced. The density difference also reduced and the viscosity increased. Therefore, the separation became more difficult and residence time increased.

Yang et al (2017)[101] demonstrated that the Young-Laplace equation (2.25v) and the Hagen-poiseuille equation (2.25iv) do not fully describe when retention and breakthrough occur in the membrane separator. Retention of organic phase in the aqueous phase occurs at a higher membrane pressure than the Young-Laplace equation suggests and breakthrough occurs at a lower membrane pressure than

Hagen-Poiseuille predicts. This is because the underlying assumptions in these models are not entirely true. The membrane is made of a distribution of pore sizes (some smaller and some larger than the mean pore size) and the pores are not straight cylindrical tubes, instead they follow a tortuous path through the thickness of the membrane. By taking this into consideration a tortuosity factor has been included in the Hagen-Poiseuille equation and the pore size distribution of the membrane is experimentally obtained. The new models are shown to be better predictors of the experimental results than the original theoretical models based on the simple Young−Laplace equation and the straight-channel Hagen−Poiseuille equation.

Pressure control of membrane separators is difficult due to upstream and downstream pressure fluctuations that cause breakthrough or retention of organic and aqueous phases. In extraction processes the volume ratio can change from the initial inlet flow rates due to mass transfer of species, this can also change the pressure across the membrane and affect separation if the back pressure on each outlet of the membrane separator is not selected carefully. In order to understand how the membrane separator reacts to pressure variations, different flow conditions and fluid systems, Yang et al (2017)[101] added downstream pressure gauges and installed back pressure regulators (BPRs) at each outlet. Water/toluene and water/hexane systems were then tested up to 10ml/min and the BPRs were set between 0 and 2.5 bar.

A tortuosity factor C_{tor} was added to the Hagen-Poiseuille equation (equation 2.26i) which accounts for the higher pressure at which retention occurs. C_{tor} is the average liquid path length over membrane thickness. For the membrane used in this study the factor was found to be 3.52.

$$P_M = \frac{8C_{tor}\mu Q}{n\pi R^4}L_m \tag{2.26i}$$

To understand when breakthrough occurs the Young-Laplace equation is used (equation 2.25v). As pore size is actually a distribution, R needs to be an integral across a range of sizes (equation 2.26ii).

$$N = \int_{R_1}^{R_2} n(R)dR \tag{2.26ii}$$

N = Number of pores between R_1 and R_2

N(R) = The pore distribution function

From the Young-Laplace equation every ΔP_{mem} will have a corresponding break through pore size. The aqueous flow rate through the permeate side ($Q_{aq,perm}$) is

therefore the sum of flow rates through all of the pores larger than the threshold $R_{\Delta P_{mem}}$.

By plotting normalised aqueous phase flow rate through the permeate side of membrane ($Q_{aq,perm}/Q_{org}$) against different membrane pressures controlled via the BPRs the pore size at which aqueous phase break occurs could then be calculated using the Young-Laplace equation. The aqueous phase flow through the permeate side will also vary as ΔP_{mem} increases. $Q_{aq,perm}/\Delta P_{mem}$ can be plotted against the corresponding calculated pore size for breakthrough at the given pressure. The pore size distribution can then be found using equation 2.27.

$$n(R) = -\frac{8C_{tor}\mu_{aq}L}{\pi R^4}\frac{\left(\frac{Q_{aq,perm}}{\Delta P_{mem}}\right)}{dR_{\Delta P_{mem}}} \tag{2.27}$$

$$Q_{aq,perm} = \frac{\pi}{8C_{tor}\mu_{aq}L}\Delta P_{mem}\int_{2\sigma/\Delta P_{mem}}^{\infty}n(R)R^4dR \tag{2.28}$$

From obtaining the pore size distribution function the predicted permeate breakthrough could then be obtained using the breakthrough equation 2.28. assuming the same membrane was used, any new liquid-liquid system retention and breakthrough could be determined using this equation.[101]

<u>Zaiput Membrane Separator</u>

One of the main challenge of using a membrane separator for micro and milli scale processes is control of the outlet pressures to enable complete separation. To overcome this problem Adamo et al (2013)[23] placed a diaphragm after the membrane to provide an Integrated solution to pressure control removing the need for feedback control of the pressure differential across the membrane. Generally $P_{cap} > P_{mem} > P_{per}$ (Hagen-Poiseuille > P_{mem} > Young-Laplace). If $P_{mem} > P_{cap}$ then breakthrough occurs, if $P_{mem} < P_{per}$ then retention occurs. The diaphragm that passively controls the outlet pressure differential is sealed against the retanate side of the membrane so only allows flow through if P_1 (retanate pressure) is greater than P_2 (permeate pressure). The diaphragm deforms and allows flow through on the retanate side.
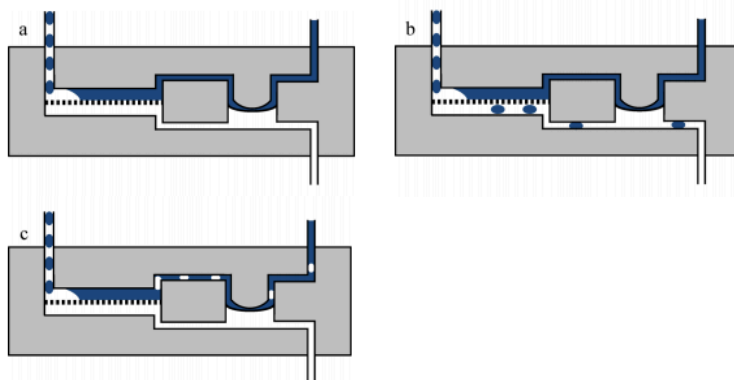
Figure 2.22: a) Complete separation b) Breakthrough c) Retention. Reprinted with permission from Adamo et al (2013).[23] Copyright 2021, American Chemical Society.

The diaphragm kept a consistent pressure across the membrane under different phase ratios and back pressures. Adamo tested two systems hexane/water and ethyl acetate/water at a total of 10ml/min with phase ratios ranging from 0.25 to 4 and from 4 to 16ml/min at a phase ratio of 1. Above 1 bar back pressure some breakthrough of the aqueous phase into the organic stream began occurring with the ethyl acetate/water system. This is due to an increased P_{dia} that pushed it past the P_{cap} limit ($P_{Cap} > P_{dia} > P_{per}$). Overall, the integration of a diaphragm allowed a more robust separation device that could operate within a larger window of flow conditions without modification to the device or the outlets. This device has now been made commercially available under the name 'Zaiput', it has been utilised in multiple flow synthesis and extraction setups.[23]

Multistage lab-scale extraction units

Some microscale extractors have been used In a counter-current arrangement to enable multistage extraction.[18] Aota et al (2007)[102] reported on a microchannel device which could perform counter-current extraction while maintaining laminar flow. The device utilised preferentially wetting surfaces to separate two phases. Laminar flow was important to ensure phase separation within the flow channels. The microchannels were 200μm deep, 300 μm wide and 20 mm long. The device successfully separated water from butylacetate at flow rates up to 8.5 μl/min. Only one stage of this arrangement was tested but showed the possibility of counter-current flow arrangements at small scale.

Hereijgers et al (2013)[103] used a Teflon (hydrophobic) or polycarbonate (hydrophilic) membrane to separate organic and aqueous mixtures in a counter-current arrangement. The membrane was spread across a 90mm long, 13mm wide area. The microchannel was either 100μm or 200μm deep. 1.3m% 1-propanol was dissolved in heptane, the 1-propanol was extracted into water. They found by

increasing the number of extraction stages/residence time they increased the fraction of 1-propanol extracted. Hereijgers et al (2015)[104] also tested the counter-current system by extracting 2 m% benzyl alcohol with water from n-heptane. They developed an analytical model to determine concentration profile as a function of residence time and performed extractions in a 3 stage system.

The steel sieve separation device developed by Holbach and Kockmann (2013)[25] (discussed earlier) was also tested in a counter-current multi-stage setup. The device produced a pressure drop per stage of 0.2 bar, therefore Interstage pumping was required as well as a pressure control valve on the dispersed phase outlet to enable continuous operation. The fine control of interstage flow rate and outlet pressure differences were one of the main challenges of the setup. Nevertheless, they managed to successfully maintained the separation of n-nonane and water over 5 counter-current stages.

Hu, O'Brien and Lay (2012)[105] demonstrated the use of the small scale gravity separation device described by O'brien et al (2012).[21] They removed diazotized amino acid from an aqueous reaction mixture of sulfuric acid and sodium nitrite using ethyl acetate. The extraction step was setup in a cross-current arrangement with three stages of extraction using ethyl acetate. Eight different diazotization reactions were performed with yields of up to 92% using the setup on a 1, 2, 8 and 20 g scale.

The Zaiput system described earlier has been developed into a multistage extraction platform. It consists of 5 Zaiputs in a counter-current arrangement with Interstage asynchronous pumping by peristaltic pumps and mixing in t-pieces (figure 2.23). A separation of THF and ethyl acetate from methanol, ethanol, iso-butanol, and tert-butanol mixtures was performed. The aqueous and organic inlets were set at 2ml/min while the interstage peristaltic pumps where set at 2.5ml/min. Q_{set} was above the Q_{ret} at each stage as this ensured a higher pressure on the permeate outlet and therefore kept the membrane pressure above the capillary pressure. The flow rates of each phase varied depending on the volume changes due to extraction at each stage. At stage 7 the interstage pumps were running at 2.5ml/min when the actual retenate flow rate was 1.4ml/min.[106]
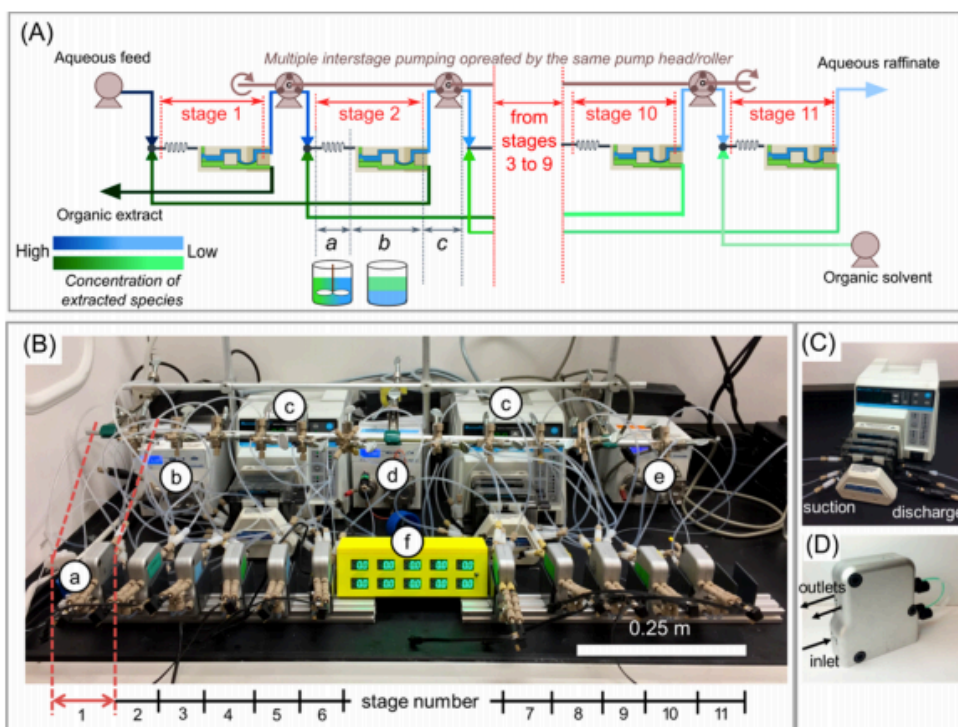
Figure 2.23: Counter-current multistage extraction Zaiput arrangement. Reprinted with permission from Weeranoppanant et al (2017)[106] Copyright 2021 American Chemical Society.

One stage extraction of THF and ethyl acetate was compared with models and a shake flask (>24hrs) to demonstrate equilibrium extraction was reached after 1 stage of the extraction module. Pulsation of the peristaltic pumps occasionally caused breakthrough or retention of phases. Nevertheless, good extraction was seen through the multiple stages as shown in figure 2.24.[106]
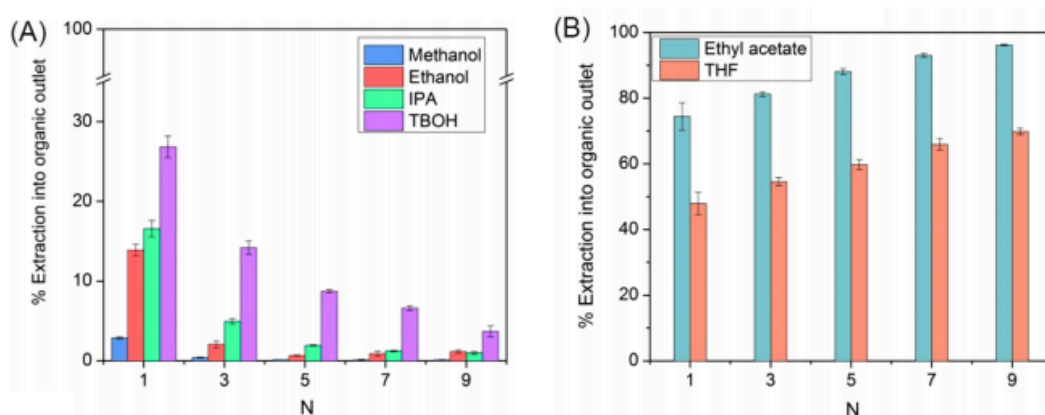
Figure 2.24: Percentage of each component in the organic phase (a) undesired components (b) desired components. Reprinted with permission from Weeranoppanant et al (2017)[106] Copyright 2021 American Chemical Society.

Membrane Separator Limitations

Membrane separators, although shown to successfully separate liquid mixtures in flow chemistry applications, are generally simple to operate and popular, they have some limitations that should be considered:

- The system flow rate generally has to remain low to maintain slug flow and avoid turbulence.

- Membrane separators operate best close to a 1:1 phase ratio as deviations from this ratio affect the system back pressure.

- Back pressure fluctuations in the system from pumping or sampling etc can cause breakthrough of one phase into the others outlet.

- Membrane separators will fail at separating very low interfacial tensions mixtures as the separation mechanism relies on a difference in interfacial tension.

- Membrane systems can easily become clogged if any particulates form in the system.

- Scale up although relatively straight forward is not very economical. The required membrane surface area is directly proportional to flow rate.

An alternative separation method to membrane separators will be discussed in section 2.4. The method uses coalescing filters which have been used in the automotive, aviation and oil and gas industries to separate emulsified water droplets from oil. Coalescing filters have not been used in flow chemistry for liquid-liquid separations before but are a potential option for consideration. In section 2.4 the mechanism by which they separate liquids, common materials and manufacturing methods as well as previous studies performed on coalescing filter media to determine their effectiveness at separating liquids and characterisation methods shall be discussed.

2.4 Coalescing filters

Although gravity separation and membrane/surface force separations have been shown to be successful at small scale there is another method that has been overlooked for continuous separations in the fine chemical industries and that is coalescing filtration. Coalescing filters make use of both surface forces and gravity forces to separate immiscible liquids. Coalescing filters are depth filters as opposed to surface filters and operate via the following five steps: (i) Contact between the dispersed phase droplets and filter fibres; (ii) Attachment of small droplets to individual fibres throughout the filter depth; (iii) Coalescence of droplets attached to the filter surface; (iv) Transport of the enlarged droplets through the filter media; (v)

and detachment from the filter surface and removal from the fluid stream via gravity or surface filtration.[27] Figure 2.25 shows a typical separation of a dispersed phase from a continuous phase through coalescing filter media. Coalescing filters are often used in the automotive and aviation industries to remove residual water from fuel and separate water from crude mixtures in the petroleum industry.[28, 29,30]
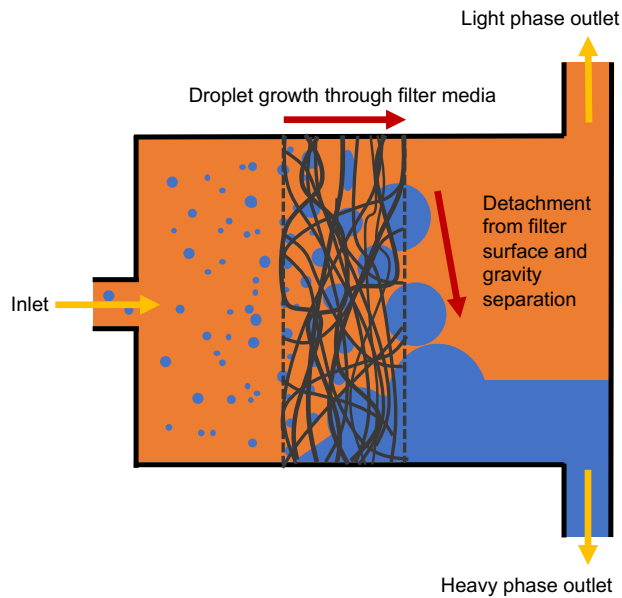
Figure 2.25: Diagram of how nonwoven filter media coalesces droplets that are collected on its surface and separates them from the continuous phase downstream of the filter.

The basis of most coalescing filters is to collect droplets on a surface so that the contact time between droplets is increased and film drainage can occur, it also allows small approach velocities as most droplets are close to stationary in comparison to the continuous phase flow.[107]

2.4.1 Filtration mechanism

Filtration and seperation can be described as the act of seperating one or more distinct phases from another in a process which uses physical differences between the phases (such as particle size, density or electric charge).[108] For separation of distinct phases such as solid from fluid and liquid from liquid the mean particle size and particle size distribution (droplet size and droplet size distribution) have a large influence on the filtration type required. Typical coalescing filters operate within the 5 – 50μm droplet size range but other filters can operate in the nm or mm size range depending on their design.[109]

There are three main ways particles/droplets collect on the surface of fibrous material. The first is direct interception where a droplet flowing along a streamline around a fibre is brought within half of its diameter of the fibre and attaches to it. The

second is inertial impaction. A large of fast moving particle may become trapped on a fibre if it has enough momentum to continue on its path towards the fibre and therefore collides with it rather than follow the fluid flow around it. The third method is by diffusion which mainly effects small particles that meander about in the flow stream due to brownian motion of the carrier fluid. Particles can also attach to fibres through electrostatic attraction and can separate from fluid through gravity seperation as shown in figure 2.26.[38,107,108]
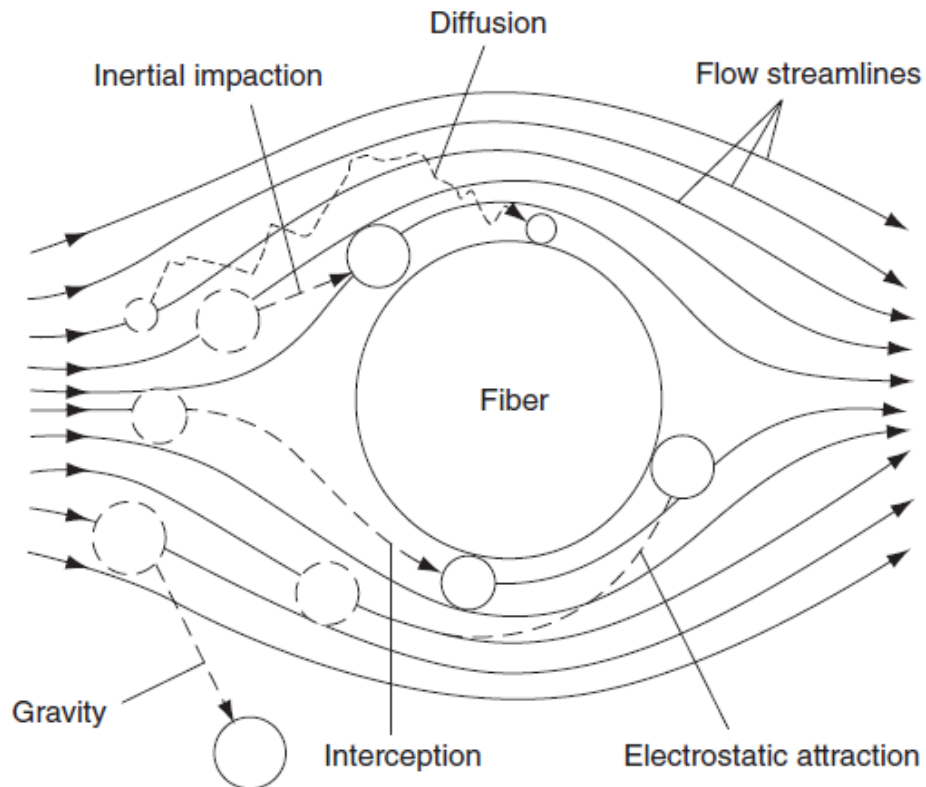
Figure 2.26: Mechanisms of particle capture. Diagram from Handbook of Nonwoven Filter Media (2nd Edition) with permission from Elsevier[38]

There are two types of filtration, surface filtration and depth filtration. Surface filtration works on the surface of the media and is reliant on the particle/droplet size being larger than the pore size unless the particles or media is deformable or viscous forces prevent the fluid from entering the filters pore structure. Almost all of the particles are collected on the upstream side of the filter and form a cake layer. The other type of filtration is depth filtration where a medium with a relatively larger thickness than those used in surface filtration collects particles/droplets throughout its thickness. This is because the tortuous path that must be followed by any particle or droplet entering the medium increases the likelyhood of capture by one of the mechanisms described in figure 2.26. A summary of droplet filtration types is given by Bansal et al (2011)[27] in figure 2.27. They suggested that depending on which

phase preferentially wets the fibres and what the pore size is compared to the droplet size you can determine weather your system will separate via a coalescing filter, surface filter, or neither.
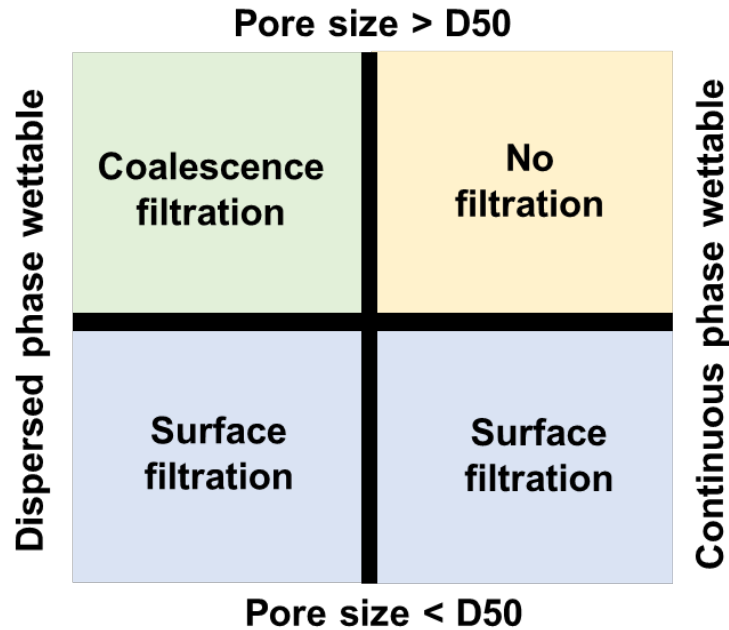
Figure 2.27: Separation mechanism for emulsions based on wettability of phases and droplet size (Redrawn from Bansal et al, 2011).[27]

The MPPS (most penetrating particle size) is normally too small for inertial effects and too large for diffusion. Velocity of the droplet/particle effects MPPS. Below the velocity of maximum penetration diffusion dominates and above inertia begins to dominate. Reentrainment occurs when particles that have been captured get 'blown' back into the stream by fluid flow. Medium migration is when small particles in the medium (fines) that were residue from the manufacturing process get 'blown' into the fluid stream. Reentrainment and medium migration are confounding effects against just increasing the velocity of the flow to increase capture of particles.[108]

The efficiency of a filter is defined as the number of particles or droplets found downstream of the filter compared to upstream of the filter and is described by equation 2.29i and 2.29ii.

$$\text{Particle filter:} \quad E = 1 - \frac{P_{out}}{P_{in}} \tag{2.29i}$$

$$\text{Coalescing filter:} \quad E = \frac{c_u - c_d}{c_u} \tag{2.29ii}$$

E = Filtration efficiency

P_{out} = Particle concentration downstream of filter   (ppm)

P_{in} = Particle concentration upstream of filter   (ppm)

c_u = Dispersed phase concentration upstream of filter   (ppm)

c_d = Dispersed phase concentration downstream of filter   (ppm)

The pressure drop across a filter is usually inversely proportional to its efficiency therefore a useful term for measuring the overall performance of a filter is the quality factor or quality coefficient shown in equation 2.30.[37] A study by Agarwal et al (2013)[30] looking at the effect different fibrous geometries had on the operating conditions of a coalescing filter demonstrates the worth of measuring quality factor alongside pressure drop and separation efficiency. Figure 2.28 shows the pressure drop, separation efficiency and quality factor for a number of different fibrous arrangements and pore sizes. The graph shows that reducing pore size does correlate with separation efficiency but pressure drop varies over the range of geometries and therefore quality factors vary largely across the range of pore sizes.

$$Q = \frac{-\ln{(1 - E)}}{\Delta p} \tag{2.30}$$

Q =   Quality factor (Pa^{-1})
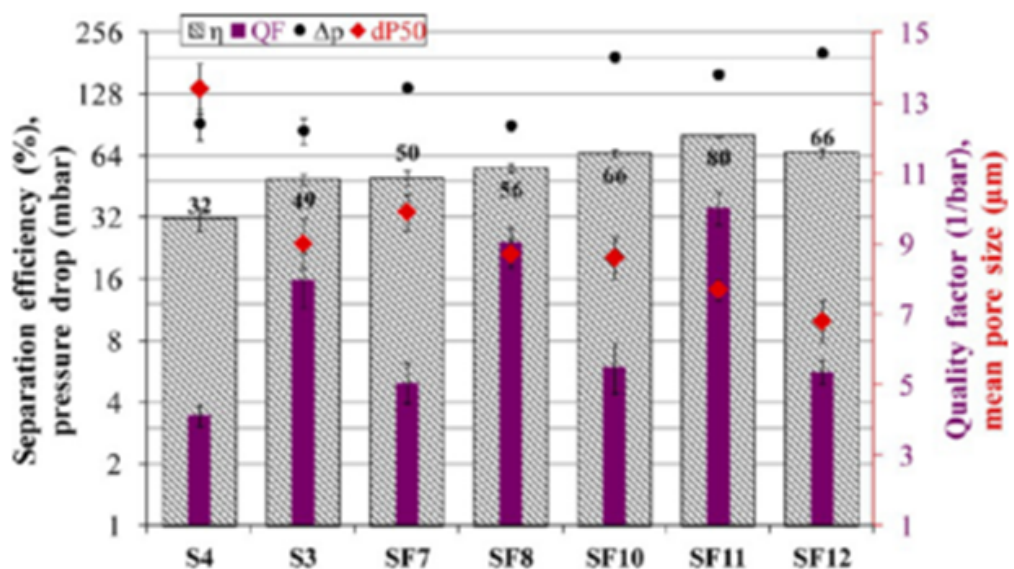
Figure 2.28: Pressure drop, separation efficiency, and quality factor depending on pore size and fibrous arrangement of coalescing filter. Reprinted with permission from Agarwal et al (2013).[30] Copyright 2013 American Chemical Society.

2.4.2 Porous media

Porous media is a solid containing many holes or voids. In the case of nonwoven filter media there are two main theories that are used to describe it: Channel theory, and cell model theory. Channel theory is also known as the capillary tube model and it assumes that the media is made up of cylindrical tubes that pass from one surface of the media to another. It is most applicable to liquid filtration through media with a high packing density. Cell model theory is more applicable to air filtration and low packing density media.[38]

Filtration theory is derived from the equations of motion and continuity, the resultant equation for flow through a flat nonwoven fabric perpendicular to the flow is known as Darcy's law and is shown in equation 2.31.[110]

$$v_0 = \frac{k}{\mu} \frac{\Delta p}{L}$$
(2.31)

v_0 =   Face velocity (volume flow per unit area)   (m/s)

k =   Permeability constant (m^2)

μ =   Fluid viscosity   (Pa.s)

Δp =   Pressure gradient across media   (Pa)

L =   Thickness of fabric   (m)

The permeability constant defined in Darcy's law is the measure of ease by which fluid can pass through the media and it is intrinsic to the media in question.[111] The permeability constant can be found for a given media by the air permeability test. In this test a known medium (air) with constant viscosity is pumped through the filter of known thickness at a constant pressure and the flow rate is then related to the permeability constant. The permeability is directly proportional to the media's properties and porous structure, the Kozeny-Carman equation (2.32) defines this for nonwovens. The Kozeny constant accounts for the tortuosity of the pore structure through the filter medium (equation 2.33) and the porosity is a ratio of the void volume to the total medium volume.

$$k = \frac{1}{KS_0^2} \frac{\varepsilon_0^3}{(1 - \varepsilon_0)^2}$$
(2.32)

K =   Kozeny constant

S_0 =   Effective surface area per unit volume of solid material (m^2/m^3)

ε_0 =   Permeable porosity (void volume) (m^3/m^3)

$$K = k_0 \left(\frac{L_e}{L}\right)^2$$
(2.33)

k_0 =   Pore shape factor

L_e =   Length of tortuous path through   (m)

L_e/L =   Tortuosity factor >1

k_0 is 2 for a perfect circle but ranges between 2 and 2.5 for rectangular or elliptical shapes. In Capillary flow one of the assumptions is that the flow through the media is at 45°, therefore the tortuosity factor is 2 and K = 5. Substituting equation 2.32 into equation 2.33 gives equation 2.34 which is applicable to filters with a permeable porosity of $0.2 < \varepsilon_0 < 0.8$ or Solidity, X_0 of $0.2 < X_0 < 0.8$ where $X_0 = (1 - \varepsilon_0)$.

$$v_0 = \frac{\varepsilon_0^3 \Delta P}{5\mu S_0^2 (1 - \varepsilon_0)^2 L} \qquad (2.34)$$

It is important to note that the permeable porosity for a porous medium is the measure of void space available for fluid flow (many porous media will have dead end pores or can swell up and trap fluid). However, in most synthetic polymer fibre or glass fibre filter substrates $\varepsilon_0 \cong \varepsilon$.[38] Porosity can be measured by determining the density of the fibres used in the nonwoven filter material and the density of the fabric. If the fabric was nonporous the density of the fibres and fabric would be the same, however the number of voids in the fabric reduces the weight of the fabric for a given volume. The porosity is calculated using equations 2.35 and 2.36.[37]

$$\phi = \frac{\rho_{fabric}}{\rho_{fibre}} \times 100 \qquad (2.35)$$

$\phi =$ Volume fraction of solid material   (%)

$\rho_{fabric} =$ Bulk density of fabric (kg/m^3)

$\rho_{fibre} =$ Density of individual fibre (kg/m^3)

$$\varepsilon(\%) = (1 - \phi) \times 100 \qquad (2.36)$$

2.4.3 Nonwoven materials

Many different materials have been employed to act as coalescing filters, including thermoplastics such as Polyurethane, Polypropylene and Polybutylene terephthalate (PBT), glass fibres[27,28,31-35] and in the case of aerosol coalescers - steel meshes.[36] Each of these filter materials are formed into nonwoven fabrics. Nonwovens are defined as a sheet or web of entangled fibres with random orientation, they can be mechanically, thermally or chemically bonded and are not weaved or knitted into a repeating structure.[37] Most nonwovens used for coalescing filtration are formed via melt-spinning processes and have high porosities and permeabilities, with a median pore sizes near 10 μm and a highly tortuous fluid path through the media depth.[38]

<u>Nonwoven manufacture</u>

The manufacture of nonwoven materials consists of three to four stages. Fiber/filament formation, web formation, web bonding and post-processing. Polymer-laid techniques are the most commonly associated with coalescing filter media in the literature, a few examples include: Ortega et al (2016)[112], Kaur et al (2014)[113], Wang et al (2017)[114], Patel and Chase (2014)[34] and Arouni (2017).[115] Polymer laying involves the extrusion and direct collection of filaments. Melt extrusion is most commonly employed. Polymer melts are stretched and carried by air onto a belt or roller where they cool and solidify.[38] Fibre diameters are typically in the range of 15

– 35 µm and the web has a thickness of 0.2 – 1.5 mm.[37] Melt blowing also utilises hot air and a polymer melt to extrude filaments. It forms fibre with diameters in the range of 2-7 µm. Entanglement of the fibres occurs through turbulance in the flow and cohesive sticking. Melt blown webs generally have better filtration properties than spun-bonded webs. Increasing the surface area of a filter can be done by manipulating the shape of the fibre cross-section during formation.[37,38]

Electrospinning can produce nanofibres (<500nm) meaning electrospun webs have extremely high surface areas. It uses a high voltage supply, a reservour with conductive elements (most commonly a syringe with a blunt needle) and a grounded collector. A polymer is disolved in a solvent or melted and a jet of liquid fibre forms when electrostatic repulsive forces overcome surface tension of the polymer solution/melt and a web is spun onto the collection plate and rapidly cools. Adding an electrospun layer to filter material has been shown to increase filtration efficiency by removing small droplets that would otherwise pass through the filter uninhibitted.[34] Electrospun media normally require a support layer as there nano-thickness results in low strength. Polymer-laying requires either a thermoplastic material for spun-laying/bonding, melt blowing, and electrospinning or a material that can be dissolved in a solvent for flash spinning (spun-bonding), or electrospinning.[37,38]

<u>Nonwoven processing</u>

Once the nonwoven web has been formed or sometimes during the web formation process itself the nonwoven is bonded to improve mechanical properties. Melt blown webs and electrospun webs may not require further bonding as the fibres bond when they contact each other during the deposition process. However, if further bonding is desired there are three main categories: Thermal bonding, chemical bonding and mechanical bonding. Thermal bonding requires melting portions of the filter media to stick them together. Chemical bonding involves the addition of binders or adhesives to a fabric web before drying and curing. The application of a binder can effect the chemical properties of a fabric as well as mechanical. Li et al (2017)[116] showed how the addition of a fluorochemical coating changed the wetting characteristics of a fabric. A number of mechanical methods also exist to entangle fibres, weather that be through water jets, needling or other mechanical apparatus.[38]

Once a web has been formed and bonded a number of post-processing techniques exist to manipulate the properties of a nonwoven. Increasing the surface roughness can be done by submerging the web in a coating that introduces additives on the fibre surface.[32] Corona treatment was used by Wang et al (2017)[114] to increase the hydrophilicy of a polypropylene/polyamide fibrous blend. The process utilises electrical discharge to influence a materials surface energy. Depending on the length

of treatment the hydrophilicy of the filter material increased. The deeper into the filter media the less change in hydrophilicy was observed, meaning a wettability gradient was produced. A number of different chemical treatments exist to change a nonwovens water repellency or oil repellency. Considerations for the penetration of the coating/immersion liquid into the fabric internal structure should also be made. In the case of polymer-laid nonwovens where the web is formed from a solution, the introduction of additives into the solution may affect the overall properties of the filter.[37] Abutaleb et al (2017)[117] tested four different additives in a solution for electrospun PEI fibres. Differing permeability, thermal stability, and mechanical strengths were reported.

Properties and Characterisation

Nonwovens can be complex to characterise as individual fibres have properties which will differ to the bulk media and the fibre arrangement cannot be fully represented by geometrically repeating patterns. Some characteristics relevant to filter media and standard measurement techniques are discussed in this section.

Grammage or basis weight refers to the weight per unit area of the media. It can be as low as 10g/m^3 for melt-blown media and measured by ISO 9073-1 (1990).[118] The 'as is' basis refers to a fabric weight per unit area with any captured moisture or volatiles in the structure. The 'bone dry' basis refers to the weight per unit area without any volatiles or moisture present.

The thickness of a nonwoven is more difficult to measure than most materials as the materials are compressible. If a material has any loose fibres then an unexpectedly high measurement will be given. Thickness tests must therefore specify size and shape of the presser and what compressive loading is applied. ISO 9073-2 (1990) contains measurements for fabric thickness.[119]

Porosity and permeability were mentioned in section 2.4 but the measurement of pore size and pore structure were only mathematically discussed. The bubble point test which is described by ASTM F316-86 (2005) is often used to determine pore size.[120] The method involves placing the filter below a liquid of known surface tension and density. Air is pushed through the filter at increasing pressure until the first bubble appears in the liquid reservoir. This is known as the bubble point and corresponds to the maximum pore size by equation 2.37.

$$d = (4\sigma\cos\theta/p) \times 10^6 \qquad\qquad (2.37)$$

d =   Maximum pore diameter   (µm)

σ =   Surface tension of reservoir fluid at 20°C   (N/m)

θ =   Contact angle between reservoir fluid and pore wall   (Deg)

p =   Pressure at bubble point   (Pa)

The bubble point, mean flow pressure, minimum pore size, pore diameter range, pore size distribution, and gas permeability can be detected using a capillary flow porometer. The mean flow pore size corresponds to the point at which 50% of the flow through a dry specimen is reached by a completely wetted specimen. It does not give the mean pore size as flow through large pores can be disproportionately greater than through smaller ones. The point at which the pressure drop across the wetted specimen is half of the dry specimen corresponds to the mean flow pore size. Other techniques exist for measuring pore size and structure, image analysis and microscopy are often used to understand the pore shape and x-ray microtomography can be used to build 2D and 3D structural arrays of specimens. Hu et al (2015)[121] used a scanning electron microscope to characterise filter media.

Strength properties of nonwoven materials can be separated into in-plane properties such as tensile strength, elongation, and tensile stiffness and out-of-plane properties such as bending stiffness, burst strength, internal bond strength, and Z-direction compression. Strength properties vary depending on the direction tested in due to the random orientation of fibres in nonwovens resulting in anisotropic behaviour.[38]

Water repellence is a measure of hydrophobicity, the most common method of determining this is through contact angle measurements. Automated contact angle testers can take a picture of a droplet on a surface and image analysis can be used to determine the angle of contact. Another method is to measure the time it takes for a drop of liquid to soak into a substrate. Absorbency can also indicate the water repellence of a media. The more water absorbed, the less repellent it is.[38]

A number of studies have shown how different filter media properties and liquid-liquid systems can affect the separation performance of coalescing filter media. Govedarica et al (2012)[29] performed a principle component analysis of a polyurethane nonwoven filter media and found strong correlations between the filter bed critical velocity (velocity at which the effluent oil concentration was above 3% of the inlet oil concentration - 500 mg/L in the aqueous phase) and bed permeability, oil viscosity, interfacial tension, emulsivity, and dielectric constant for five different oils dispersed in tap water. Bansal et al (2011)[27] showed the importance surface energy has on the droplet capture mechanism and how separation efficiency decreases with increasing pore size. As pore sizes increased, having a filter media that was preferentially wetted by the dispersed phase had a greater impact on the separation efficiency of the filter media than at smaller pore sizes. Arouni et al (2019)[28] showed how the wettability of the filter media influenced the separation efficiency as well as

the pressure drop across the filter. As the filter media became more hydrophilic the separation efficiency of water from oil improved but at the cost of an increased pressure drop across the media. This was due to water droplets being retained within the filter media. Agarwal et al (2013)[30] demonstrated that an increasing pore size gradient from influent to effluent increased the filter efficiency while reducing pressure drop compared to a media with homogenous pore sizes. Krasiński et al (2020)[35] showed pressure drop was reduced and separation efficiency was increased with a wettability gradient (inlet was wetted by incoming droplets and the outlet was nonwetting) compared to a homogenous wettability.

2.5 Summary

In this chapter a number of aspects surrounding liquid-liquid extraction process development have been explored. Firstly, key parts of flow chemistry were highlighted, such as different lab-scale devices for mixing reaction mixtures, residence time calculations, flow regimes and mass transfer rates. Secondly liquid-liquid systems were looked at in more detail. The dimensionless numbers Reynolds number, Weber number and Eotvos number were explained. Then emulsion systems were summarised in terms of how they are formed, how they separate and how they can be characterised. With an understanding of liquid-liquid systems, extraction processes were then researched. The basics of extraction processes were described and different process schemes were presented. Many different pieces of equipment for lab scale extraction studies have been presented in the literature. Section 2.3 provides a summary of these devices. The devices were split into two groups, gravity force and surface force driven devices. Devices that were used to perform extractions in a multistage arrangement were also presented. Finally, in section 2.4 an overview of coalescing filters was given. The filtration mechanism was explained and coalescing filter properties were described. How the filters can be characterised, manufactured and manipulated for different applications was shown.

Chapter 3

Development of an Automated Image Processing Methodology to Determine Phase Separation Rates

3.1 Introduction

The aim of this chapter was to develop an image analysis method which could be used to determine phase separation rates of various liquid-liquid mixtures. This was done to track the interface between settling phases and create a robust and repeatable method by which the separation rate of different liquid-liquid mixtures could be compared and characterised. The comparisons provided useful information about the separation of different liquid-liquid systems which then informed the in-flow separation/extraction experiments in chapter 5 and 7. The intention was to develop an imaging algorithm that automated the analysis of emulsion formation/separation rates in extraction systems.

Liquid-liquid extraction is used routinely as a post-reaction work-up to separate by-products, excess reagents and other impurities.[5,11] However, its optimisation is often over-looked or is quite rudimentary. If done incorrectly, the work-up can cause downstream process or product inconsistencies and impact upon crystallization. Issues such as emulsions and rag layer formation can cause long separation times, slow production and result in manufacturing inefficiencies.

In the pharmaceutical industry high throughput experimentation (HTE) is used to screen for possible drug candidates and optimise reactions and crystallizations during early process development within a reduced time frame.[122,123] However, it is far less frequently used for the optimisation of intermediate work-up steps, possibly due to the need to procure specialist equipment and adopt specialised procedures.[39,124,125] It requires less human intervention than conventional lab-scale experimentation resulting in better precision and repeatability.

One example of HTE performed on intermediate work-up steps is the work of Selekman et al (2015)[39], who demonstrated a high throughput extraction workflow and used this to identify optimum conditions for the removal of a genotoxic impurity and a residual amine base from a process stream through liquid-liquid extraction. Discrete variables included solvent, scavenger, base or acid and continuous variables included temperature, phase ratio, pH and time. The separation of the two phases (settling time, emulsion formation and phase split quality) were considered as these can affect the feasibility of process scale up and production cost. Emulsion

or rag layer formation and phase split quality was observed qualitatively between samples, and phase separation time was compared visually and recorded in minutes.

The phase separation behaviour of liquid-liquid systems is complex and depends upon the physico-chemical properties of the system. The controlling properties of the liquid includes density, viscosity and interfacial tension together with the relative phase volume. Process variables include mixing energy and vessel geometry with the link between the two being the formation of a dispersed phase of droplets suspended within the continuous phase.[73] Taken together, these variables influence the droplet size with the interfacial properties playing an important role in the subsequent behaviour. Mechanisms of liquid-liquid separation are sedimentation, creaming, flocculation, coalescence and Ostwald ripening.[70]

The rate of separation in liquid-liquid systems can be severely limited if the dispersed phase droplets are stabilised within the continuous phase such that emulsions or rag layers form. Small particulates can cause Pickering emulsions and surface-active molecules can form stable barriers that resist coalescence.[60] Surface-active molecules may also reduce interfacial tension, resulting in smaller droplets and longer separation times. Moreover, small changes in salinity, pH, temperature, or phase composition can drastically change how compounds interact at the liquid-liquid interface and subsequently the rate of separation in systems that include surface-active molecules.[61-67]

The semi-empirical relationship Hydrophilic-Lipophilic difference (HLD) can be used to characterise emulsion systems (Equation 3.1) and explain the influence salt concentration, solvent choice and temperature has on surfactant systems.[61,90,91]

$$HLD = Cc - k.\,EACN - \alpha.\,(T - 25) + f(S) \tag{3.1}$$

This equation can be used to understand a given liquid-liquid system and establish whether it is likely to result in long separation times or rag layer formation.

In chapter 2 a number of techniques used to characterise emulsion separation rate was described. Light scattering techniques are popular but often require the scanning of emulsion samples making it impractical to use on relatively fast settling systems.[40-42] 'Bottle tests' and visual observations are commonly used as a fast and simple method to determine creaming/sedimentation rates during separation. BS2000-412:1996[86] describes this method with standardised mixing regimes for qualitative comparisons. However, these methods introduce subjective measurement of interface locations. Imaging techniques have been used to augment this method and provide a quantitative measure of sedimentation/creaming rates.[87,88,89,42] Image analysis techniques are suited to investigating the phase separation behaviour of relatively fast settling systems as information about the entire height of the sample

can be obtained in one instance and images can be collected at a high frequency. However, image analysis has not yet been demonstrated in an application to determine phase heights over time other than by manual/semi-automated procedures; only Horozov and Binks (2004)[42] demonstrated the ability to analyse multiple samples at once. Furthermore, the application of image analysis techniques for the investigation of process separation rates has not been investigated.

Edge detection techniques in image analysis are ideally suited to determining phase heights over time. Edge detection is a method to find edges and boundaries between objects within an image based on differences in pixel brightness. There are three steps to edge detection algorithms (i) Filtering – to reduce noise in the image which would produce false edges (ii) Enhancement – to emphasise pixels where there is a significant change in local intensity values; this is usually done by computing the gradient of the pixel intensities (iii) Detection – to find the location of the edge via thresholds applied to the gradient function or finding the zero-crossing point of the 2nd derivative. Some commonly applied first order algorithms are the Canny[126], Roberts[127], Sobel[128] and Prewitt[129] method. A common 2nd order algorithm is the Marr and Hildreth or Laplacian of Gaussian method (LoG).[130] One of the challenges in edge detection is balancing necessary noise reduction while not over-smoothing edges and loosing detail.[131] Determining the direction of an edge and creating a function that represents the gradient creates significant challenges in many applications. Fortunately for emulsion separations we are only interested in edge detection as a 1 dimensional (1D) problem (height within a vessel) and therefore much of the complexity involved in image analysis can be reduced and a simple algorithm based on the 1st and 2nd derivatives of the image grayscale data in the vertical direction can be applied (detailed in section 3.3).

Presented in this chapter is a robust and flexible image processing algorithm that can detect the height of the interface between two liquid phases over time for both fast and slow settling systems. The nature of the dispersed phases (W/O - Aqueous dispersed in organic or O/W – Organic dispersed in aqueous) have been deduced from image data and conductivity readings. The algorithm has been designed to give results for a multitude of different systems with minimal human intervention or changes to the algorithm inputs with a view for further development and integration into high throughput experimentations of extraction processes. A number of liquid-liquid systems were studied, three liquid biphasic solutions (200ml volume) were analysed at three different phase ratios: toluene-deionised water (pH 7); toluene-acetate buffer (pH 4); toluene-glycine buffer (pH 10). Two surfactant solutions (0.01M and 0.1M SDBS) at ten different salt concentrations (15ml volume) were also

analysed. By varying the salt concentration systematically, a range of very slow through to fast settling interfaces, O/W and W/O emulsions and clear and unclear interfaces were produced. A selection of the liquid-liquid systems studied at 15ml and 200ml scale have been scaled up to 20 litres to demonstrate how variations in separation characteristics captured by the algorithm correspond to the same process at pilot scale.

3.2 Materials and Methods

3.2.1 Toluene and Aqueous Solution Experiments

All solvents and chemicals were purchased from Sigma-Aldrich, Inc. One litre of both 0.12 M, pH 4 acetate and 0.08 M, pH 10 glycine, buffer solutions were made using standard methods. 200 mL of three biphasic solutions, Toluene-Deionised water, Toluene-Acetate buffer, Toluene-Glycine buffer were prepared in phase ratios (V_{Aq}/V_{Org}) of 0.25, 1 and 4.

An illuminated LED panel was set behind a 1 litre measuring cylinder containing the test solution. A Basler acA1300-30μm area scan camera was set at a fixed distance from the centre of the measuring cylinder and horizontally in line with the 100 mL marker as shown in figure 3.1(a). A high shear mixer (HSM) was lowered halfway into the liquid and mixed for 5 minutes at 1500 rpm. Immediately after mixing, the HSM was removed to avoid obstructing the camera view and images were taken in 1 second intervals for 10 minutes after mixing ceased and the images were stored for later analysis. All experiments were conducted at room temperature.
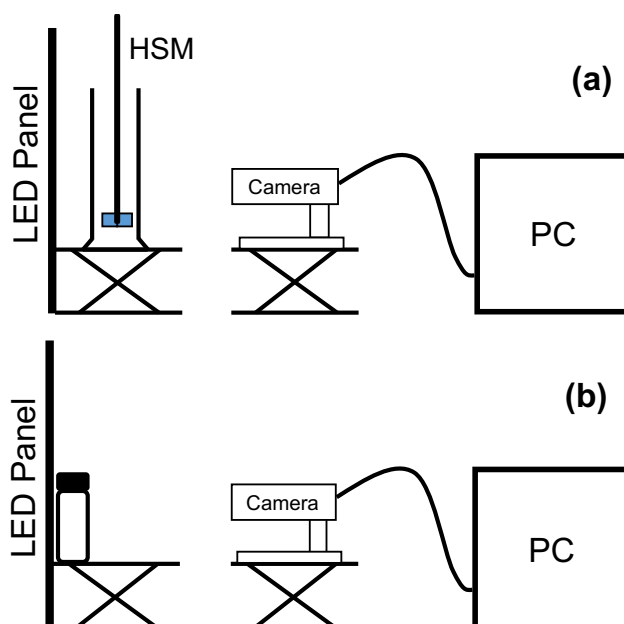
Figure 3.1: (a) Experimental setup with high shear mixer (HSM). (b) Experimental setup with hand shaken test tubes.

3.2.2 Toluene and Surfactant Solution Experiments

15 mL vials were filled with equal volumes of toluene and 0.01 M or 0.1 M solutions of sodium dodecyl benzene sulfonate (SDBS). Sodium chloride was added to each vial in aqueous phase concentrations ranging from 0.05% (w/v) to 7.8% (w/v) to create the range of HLD values found in Table 3.1. The vials were placed as in Figure 6(b) and up to five were lined up in front of the LED screen to simultaneously measure separation rates. Each vial was hand shaken for 2 minutes, left for 10 minutes and then shaken again for 2 minutes before being placed in front of the LED screen for recording. Images were taken every 10 seconds. All experiments were conducted at room temperature. Each image was then later processed according to the algorithm presented in section 3.3.

Table 3.1: NaCl concentration (mg/ml) in the aqueous phase of each vial and its corresponding HLD value.

Vial No.	NaCl concentration (mg/ml) in 0.01M SDBS solution	HLD value (0.01M solution)	Vial No.	NaCl concentration (mg/ml) in 0.1M SDBS solution	HLD value (0.1M solution)
1	0.45	-3.38	11	0.41	-2.99
2	10.76	-0.91	12	10.76	-0.87
3	16.63	-0.49	13	15.91	-0.50
4	21.72	-0.23	14	22.21	-0.19
5	27.68	0.006	15	26.8	0.007
6	33.85	0.20	16	32.87	0.19
7	43.39	0.45	17	43.48	0.46
8	57.13	0.72	18	56.59	0.72
9	66.48	0.87	19	66.51	0.88
10	78.6	1.04	20	77.93	1.04

3.2.3 Scale Up Experiments

Five experimental runs were taken from small scale and reproduced at 20 litres. Two cases from the toluene and aqueous solution experiments and three from the surfactant solution experiments. The toluene and deionised water case and the glycine buffer solution case were tested at a phase ratio of 4. 16 litres of the aqueous solution were prepared in both cases and added to the reaction vessel. 4 litres of toluene were added and stirred at 242 rpm for 10 minutes before agitation was stopped. A series of images were taken while the liquid-liquid mixtures settled in the

reaction vessel. The location of the liquid interfaces at each timestep were determined via manual image analysis.

The three surfactant experiments selected for scale up were at HLD values of - 0.49, 0 and 0.45. 0.01M of SDBS was added to 10 litres of deionised water and either 166.5, 276.7 or 433.3 grams of salt was added to each solution to reach the desired HLD value. 10 litres of Toluene was then added to the vessel and mixed at 242 rpm for 10 minutes. Once agitation stopped, a series of images were taken while the liquid-liquid mixtures settled. The location of the liquid interfaces at each timestep was determined via manual image analysis.

3.3 Interface Detection Algorithm

3.3.1 Typical separation pattern

In total, 29 separation experiments were carried out, each with a different formulation/phase ratio. A typical separation pattern and how it has been presented is described in this section. Figure 3.2 (inset images) shows separation progress at 5 timepoints. Upon initial mixing, the vial is black due to the multiple refractions at each droplet surface. In this example, a clear layer at the top of the emulsion starts to develop after 5 seconds as the suspended droplets rise and coalesce, indicating an O/W emulsion. A sharp interface is observed as only rising oil droplets form this band. There is still a dark region below this clear layer where uncoalesced droplets produce multiple refractions. Below the emulsion layer, a second clear region is observed. Since the rising droplets in this area span a range of sizes, the interface delimiting the clear continuous phase is less distinct, particularly for rapidly separating systems. Oil droplets can be seen to cling to the vessel wall in this region which further reduce clarity. Below the lower interface and above the upper interface is the separated phase and between these is the separating emulsion. Figure 3.2 shows the height of the two settling interfaces over time determined by the algorithm and by eye. The phase clarity relative to a sample of pure toluene for the top section and pure water for the bottom section is provided by a colour map.
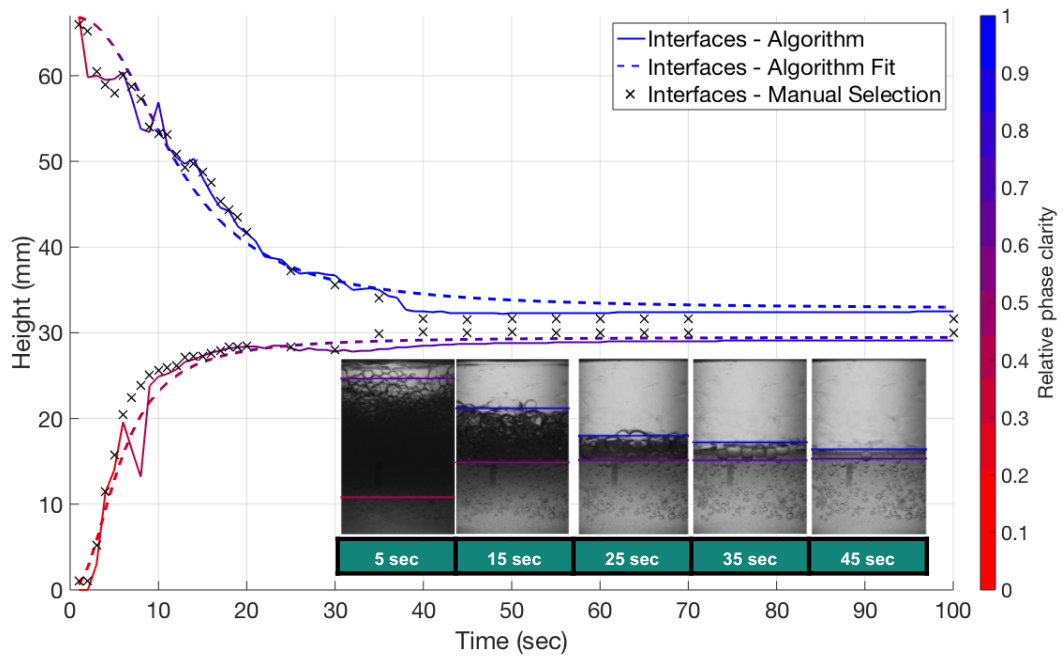
Figure 3.2. Detected interfaces and relative phase clarity over time for repeat 1 of the toluene-water time series at a phase ratio of 1 compared with values for the interface location found manually.

3.3.2 Algorithm description

The algorithm requires 24 processing steps which are broken down by the flowchart shown in figure 3.3. The algorithmic procedure is described in this section for an example image series recording the separation of toluene and water in a 15ml vial.

Load Image Grayscale Data

1. Calculate normalised grayscale data
$\Delta I_{h,t} = I_{h,t} - I_{h,t0}$

2. zero-phase low-pass FIR filter on $\Delta I_{h,t}$

3. Differentiate grayscale data:
$\frac{dI}{dH}, \frac{d^2I}{dH^2}, \frac{d^3I}{dH^3}$ and $\left|\frac{dI}{dH}\right|, \left|\frac{d^2I}{dH^2}\right|, \left|\frac{d^3I}{dH^3}\right|$

4. Find maximum and minimum points of $\frac{d^2I}{dH^2}, \frac{d^3I}{dH^3}$ and $\left|\frac{d^2I}{dH^2}\right|, \left|\frac{d^3I}{dH^3}\right|$

5. Find two largest $\left|\frac{d^2I}{dH^2}\right|$ max values in final image. Find the largest $\left|\frac{d^3I}{dH^3}\right|$ value between them. This height is h_{set}.

Crop image grayscale data to remove air/liquid and liquid/vial interfaces for this step only

6. Find average 10 $\Delta I_{h,t}$ values above h_{set} ($I_{Ave_{top}}$) and average 10 $\Delta I_{h,t}$ values below h_{set} ($I_{Ave_{bottom}}$).

If $I_{Ave_{top}} > I_{Ave_{Bottom}}$ then the upper bound of the final interface has been found

7. Find the Average of:
- $d2_{Mx_A}$ = max values of $\frac{d^2I}{dH^2}$ above h_{set}
- $d2_{Mn_A}$ = min values of $\frac{d^2I}{dH^2}$ above h_{set}
- $d2_{Mx_B}$ = max values of $\frac{d^2I}{dH^2}$ below h_{set}
- $d2_{Mn_B}$ = min values of $\frac{d^2I}{dH^2}$ below h_{set}

8. If $I_{Ave_{top}} > I_{Ave_{Bottom}}$ — True / False

9.1. If $d2_{MnA} < d2_{MnB}$ — True / False

9.2. If $d2_{MnA} < d2_{MnB}$ — True / False

10.1 Find the next $\left|\frac{d^3I}{dH^3}\right|$ value below h_{set}. This is the new h_{set}

10.2 Flip heights: $\Delta I_{h,t}, \frac{dI}{dH}, \frac{d^2I}{dH^2}, \frac{d^3I}{dH^3}$

10.3 Find the next $\left|\frac{d^3I}{dH^3}\right|$ value above h_{set}. This is the new h_{set}

10.4 Flip heights: $\Delta I_{h,t}, \frac{dI}{dH}, \frac{d^2I}{dH^2}, \frac{d^3I}{dH^3}$

11. Find the Average of:
- $d2_{Mx_A}$ = max values of $\frac{d^2I}{dH^2}$ above h_{set}
- $d2_{Mn_A}$ = min values of $\frac{d^2I}{dH^2}$ above h_{set}
- $d2_{Mx_B}$ = max values of $\frac{d^2I}{dH^2}$ below h_{set}
- $d2_{Mn_B}$ = min values of $\frac{d^2I}{dH^2}$ below h_{set}

12. Create max and min cut-off vectors from each Average d2 value
$\left[0.1 \times d2, \frac{0.1+1}{2} \times d2, \ d2, \ \frac{2+1}{2} \times d2, \ 2 \times d2\right] \times 4$

13. Find the first maximum point above h_{set} greater than the current cut-off max value at each timestep. Find the first minimum point above that which is less than the current cut-off min value and find the inflection point between these two points at each timestep and set this as Interface1 at time t. $Int_{1,t}$

14. Fit current $Int_{1,t}$ time series to sigmoidal curve:
$y = c + \frac{d-c}{1+\left(\frac{x}{b}\right)^a}$ Where: $c = Int_{1,1}$, $d = Int_{1,end}$.

15. record R^2 value of fit for each cut-off value combination (max and min above h_{set}) [5x5 matrix].

16. Select $Int_{1,t}$ series with best R^2 fit.

17. Find the first minimum point below $Int_{1,end}$ less than the current cut-off min value at each timestep. Find the first maximum point above that which is more than the current cut-off max value and find the inflection point between these two points at each timestep and set this as Interface2 at time t. $Int_{2,t}$

18. Fit current $Int_{2,t}$ time series to sigmoidal curve:
$y = c + \frac{d-c}{1+\left(\frac{x}{b}\right)^a}$ Where: $c = Int_{2,1}$, $d = Int_{2,end}$.

19. record R^2 value of fit for each cut-off value combination (max and min above h_{set}) [5x5 matrix].

20. Select $Int_{2,t}$ series with best R^2 fit.

21. Calculate average grayscale value at each timestep above $Int_{1,t}$ and below $Int_{2,t}$

22. Normalise average grayscale values with respect to pure phase values (relative phase clarity)

Under current camera settings Toluene = 197.37, Water = 226.13

23. If $I_{Ave_{top}} > I_{Ave_{Bottom}}$ — True / False

24. Flip heights: $\Delta I_{h,t}, \frac{dI}{dH}, \frac{d^2I}{dH^2}, \frac{d^3I}{dH^3}$

Save Data and Plot

Figure 3.3: Flowchart detailing the interface detection image processing algorithm.

In step 1 the average grayscale intensity is calculated (255 = white pixel, 0 = black pixel) across the width of the liquid vessel at each pixel height and each time step in the image series. The vial images were captured by 250 vertical pixels and 100 horizontal pixels, each pixel corresponded to 168µm. Each grayscale measurement, $I_{h,t}$ was normalised by subtracting the grayscale measurement at the initial time step, $I_{h,t0}$. Figure 3.4 shows the normalised grayscale intensity profile over the height of the liquid vessel at a single time step (10 seconds) and the corresponding image. Once the normalised intensity profile for each image in the time series was obtained, a zero-phase low-pass finite impulse response (FIR) filter was applied in step 2. This

smooths the normalised grayscale intensity data removing high frequency noise and leaving only the low frequency curve features. The Matlab function 'filtfilt' was used to construct the filter. Four parameters are required for this function; passband frequency, stopband frequency, passband ripple, and stopband attenuation. The values selected for each of these parameters is shown in table 3.2.

Table 3.2: Low-pass FIR filter parameters used during experiments 1 and 2

Filter Parameters	Experiment 1 – Phase ratio = 0.25, 1	Experiment 1 – Phase ratio = 4	Experiment 2
Passband Frequency	0.025	0.025	0.025
Stopband Frequency	0.1	0.6	0.3
Passband Ripple	1	1	1
Stopband Attenuation	100	100	100
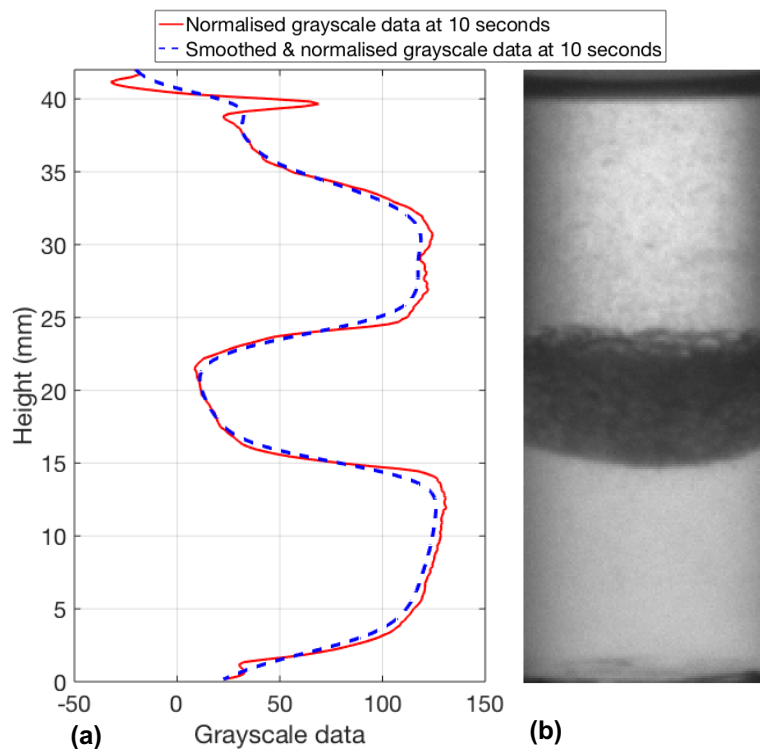
Figure 3.4. (a) Normalised and smoothed grayscale data at 10 seconds. (b) Image of toluene and deionised water separation after 10 seconds (b).

In step 3 the first, second and third derivatives of the grayscale intensity data, with respect to height, are calculated and their magnitudes found. All of the maximum and minimum peaks in $\frac{d^2 I}{dH^2}$, $\frac{d^3 I}{dH^3}$ and $\left|\frac{d^2 I}{dH^2}\right|$, $\left|\frac{d^3 I}{dH^3}\right|$ are then found in step 4. These are stored for use in steps 5, 7, 11, 13 and 17. It is assumed that two settling fronts exist in each image series, a sedimentation front and a creaming front. If one or more of the fronts

is not detected by the algorithm, then a stable emulsion has formed which does not fully separated within the timeframe of the image series. In step 5 the final image in the time series is analysed to determine the location of the interface at the final recorded time. The algorithm is set to find the most 'intense' peak in the final image. If the mixture has fully separated, then only one interface will exist but depending on the meniscus size, sample clarity and light refraction through the sample, either the top or bottom edge of the interface will be found. If both sedimentation and creaming has occurred but there still exists a rag layer between the phases, then either the top or bottom of the rag layer will be found depending on which edge provides the most 'intense' peak. If only sedimentation or only creaming occurs, then the interface will be found at the edge of the emulsion phase. If settling does not occur, then the algorithm will find the largest peak, due to noise in the data, but this will be noticeably smaller than if separation had occurred. In order to find the final interface location (h_{set}), the top and bottom 30 pixels are cropped from the data set (in step 5, 7 and 11 only). The number of pixels can be increased or decreased as needed depending on the image resolution and container height but 30 pixels was sufficient for every case in this study. This is done so that the large 2nd and 3rd derivative peaks that occur at the liquid/air interface and container bottom are ignored. The cropped portion of the data is shown in Figure 8 by the green lines. The crosses marked on the two graphs show where a peak has been found. The final interface location is selected as the largest 3rd derivative peak between the two largest 2nd derivative peaks. The two black dashed lines in Figure 3.5 show the heights of the two largest 2nd derivative peaks and the dashed red line shows the largest 3rd derivative peak located between them.
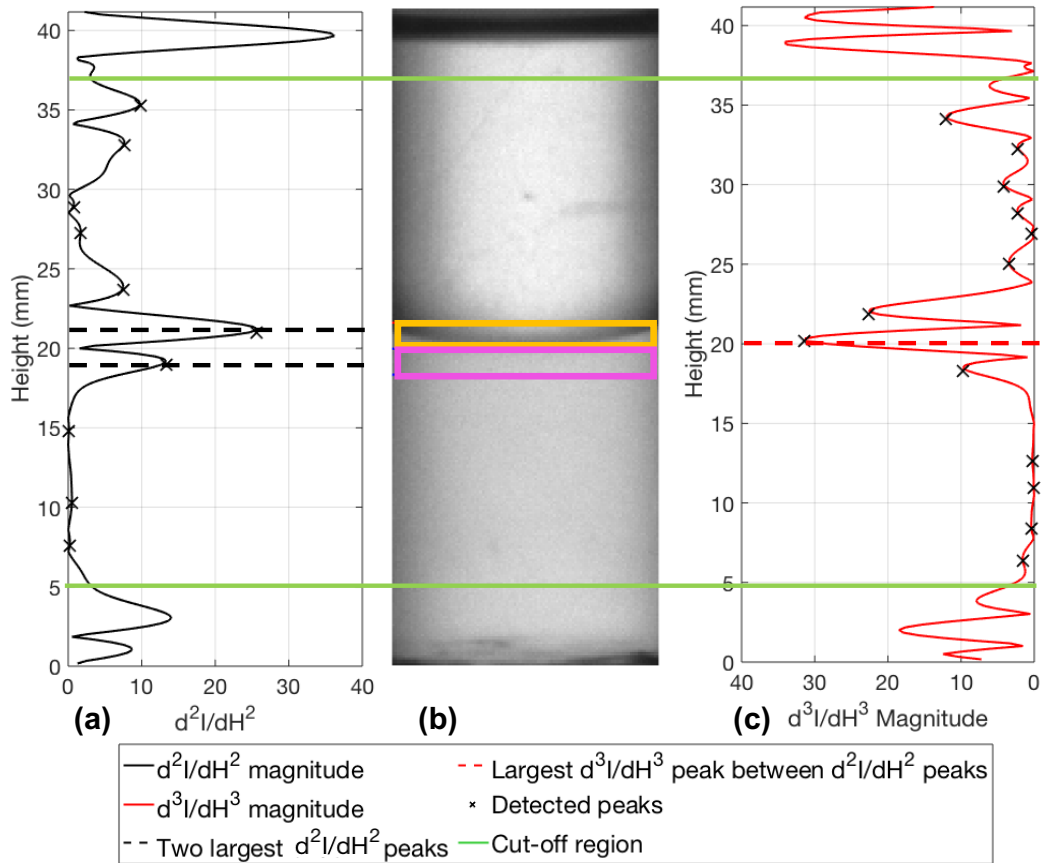
Figure 3.5. The magnitude of 2nd (a) and 3rd (c) derivatives at the final timestep. (b) is the corresponding image of toluene and water. The orange and pink areas are the areas that $I_{Ave_{top}}$ and $I_{Ave_{Bottom}}$ are calculated from.

Once h$_{set}$ has been found, the results from steps 5, 6 and 7 in the flowchart can be used to determine the first search direction and search start location via steps 8-10. In step 5, the average of the maximum and minimum 2nd derivative peaks above and below h$_{set}$, and across every timestep are calculated (d2$_{MxA}$, d2$_{MnA}$, d2$_{MxB}$, d2$_{MnB}$). The located maximum and minimum peaks above and below h$_{set}$ for the final timestep are shown in Figure 3.6.
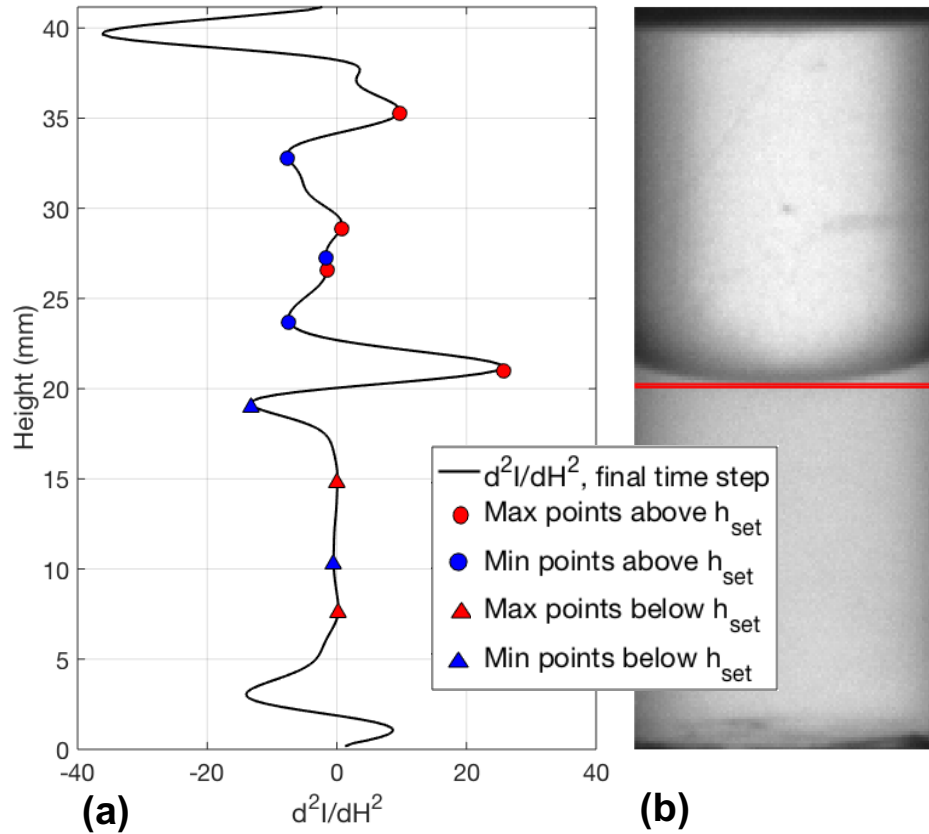
Figure 3.6. Second derivative of the final timesteps normalised and smoothed grayscale height data and the located maximum and minimum points above and below h_{set} (a). The corresponding grayscale image with h_{set} location (b).

During step 6 the average grayscale values 10 pixels above h_{set} ($I_{Ave_{top}}$) and 10 pixels below h_{set} ($I_{Ave_{bottom}}$) are calculated (shown by the orange and pink rectangles in Figure 3.5(b). If the area just above h_{set} is darker than the area just below h_{set} then h_{set} is at the lower bound of the interface (as seen in Figure 3.6) otherwise h_{set} is at the upper bound. Steps 8-10 in the flowchart are a series of logical operations depending on if $I_{Ave_{top}}$ or $I_{Ave_{bottom}}$ is larger and if d2$_{MnA}$ or d2$_{MnB}$ is smaller. The aim of this step is to ensure that the first search area passes through the interface. To do this, the result from step 6 is analysed to find out if h_{set} is at the upper or lower bound of the interface. If it is as the upper bound then the first search area is below h_{set}, if it is at the lower bound then the first search area is above h_{set}. Secondly, the search algorithm works best when the first detected interface is the most 'distinct' in the image series. To check whether the top or bottom settling fronts is more distinct d2$_{MnA}$ and d2$_{MnB}$ are compared. If d2$_{MnA}$ is less than d2$_{MnB}$ then the top settling front is more distinct than the bottom interface. To ensure that both conditions are true, h_{set} is shifted to the next 3rd derivative peak below h_{set} if $I_{Ave_{top}} >$ $I_{Ave_{bottom}}$ and d2$_{MnA} >$ d2$_{MnB}$ or to the next 3rd derivative peak above h_{set} if $I_{Ave_{top}} <$

$I_{Ave_{bottom}}$ and $d2_{MnA} < d2_{MnB}$. Shifting h_{set} in this way moves it to the other side of the interface so that the first search area can pass through the interface and detect the most distinct interface first.

At this point, to keep the algorithm universal to all cases whether the first search area is the top half or the bottom half $\Delta I_{h,t}, \frac{dI}{dH}, \frac{d^2I}{dH^2}, \frac{d^3I}{dH^3}$ are flipped with respect to their height in the vessel if the first search area is the bottom half. The data is flipped back to its original form after the search algorithm is complete. This step ensures that any logic operations within the detection algorithm based on the position of maxima or minima within the vessel is the same. The derivatives $d2_{MxA}, d2_{MnA}, d2_{MxB}, d2_{MnB}$ are then recalculated with respect to the new h_{set} (step 11). These values are used to set a cut-off value at which a given maxima or minima is decided to be significant. For example, if a maximum point above h_{set} is larger than $d2_{MxA}$, it is significant. If the cut-off values work well, they will track the interface accurately over each timestep. This is not always the case if $d2_{MxA}, d2_{MnA}, d2_{MxB}, d2_{MnB}$ are the only cut-off thresholds considered. To select a threshold that tracks the interface accurately, several threshold values should be tried. In step 12 each d2 value is multiplied by 0.1, 0.55, 1, 1.5 and 2 to produce four 5x5 vectors. This gives 25 combinations of $d2_{Mx}$ and $d2_{Mn}$ to try for each interface. These multiplication factors were set after a period of trial and error with the algorithm. The range of values produced by these vectors consistently produced at least one case from the 25 pairs that tracked the interface well, for each of the sample cases studied. Table 2 shows the vectors produced for the sample toluene and water case. The red cells correspond to the maxima and minima cut-off thresholds shown in Figure 3.7.

Table 3.3: Test Maximum and Minimum cut-off points for interface 1 and 2

Interface 1 cut-off vectors

Maximum cut-off threshold	1.01	5.55	10.08	15.13	20.17
Minimum cut-off threshold	-0.71	-3.89	-7.07	-10.61	-14.14

Interface 2 cut-off vectors

Maximum cut-off threshold	0.07	0.36	0.66	0.99	1.32
Minimum cut-off threshold	-0.52	-2.85	-5.19	-7.78	-10.37

In step 13 the algorithm searches above h_{set} (shown in Figure 3.7 (a) by the black dashed line) to find interface 1 and selects the first maximum (red dot) larger than

the maximum cut-off threshold (red dashed line) and the first minimum above this maximum (blue dot) that is less than the minimum cut-off threshold (blue dashed line). The inflection point between these two is the location of interface 1 (red line). This process is repeated for every time step and every max and min cut-off threshold combination. The best combination of maximum and minimum cut-off values is decided based on the interface height vs time data and the r^2 fit with the sigmoidal curve given by Equation 3.2 where $c = Int_{1,1}$ and $d = Int_{1,end}$ (the first and last interface heights given by the algorithm). The constants a and b are determined by the curve fit algorithm: where a determines the 'steepness' of the sigmoidal curve and was limited in the algorithm to ±5; and b is the x data point at which the curve has reached half of its final height ($Int_{1,end}/2$). There was no limit imposed on what value could be calculated for b except for repeats 1-3 of the pH 4, 0.25 phase ratio cases and the 0.46 HLD vial. Reasons for this are discussed in the relevant results sections. Interface$_{fit}$, is the interface height as determined by the sigmoidal curve fit.

$$\text{Interface}_{\text{fit}} = c + \frac{d - c}{1 + \left(\dfrac{\text{time}}{b}\right)^a}$$

(3.2)
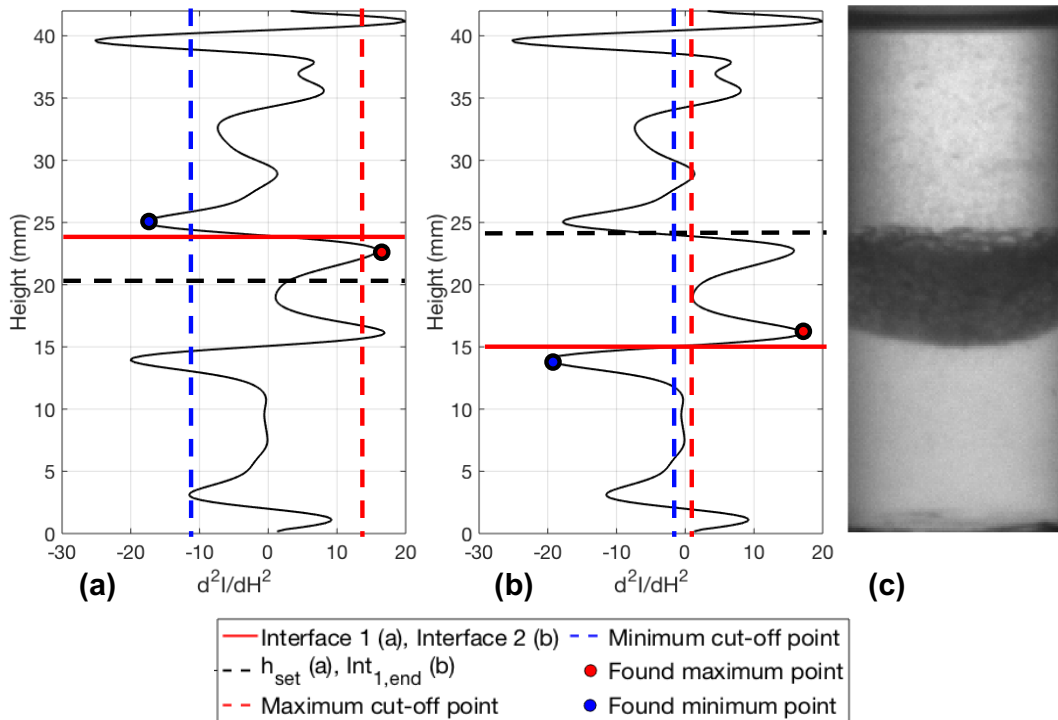
Figure 3.7. The 2nd derivative data at 10 seconds is shown with the location of interface 1 determined by the found maximum and minimum points (a). The 2nd derivative data at 10 seconds is shown with the location of interface 2 determined by the found maximum and minimum points (b). The corresponding image at 10 seconds is shown (c).

A sigmoidal curve models the settling of an emulsion well and therefore it was assumed that when the data fits the sigmoidal curve best (highest r^2 value) the algorithm has tracked the interface better than any of the other maximum and minimum cut-off threshold combinations (steps 14 – 16). A contour plot of the r^2 values obtained from the 25 maximum and minimum cut-off threshold pairs is shown in Figure 3.8 for interface 1 (a) and interface 2 (b).
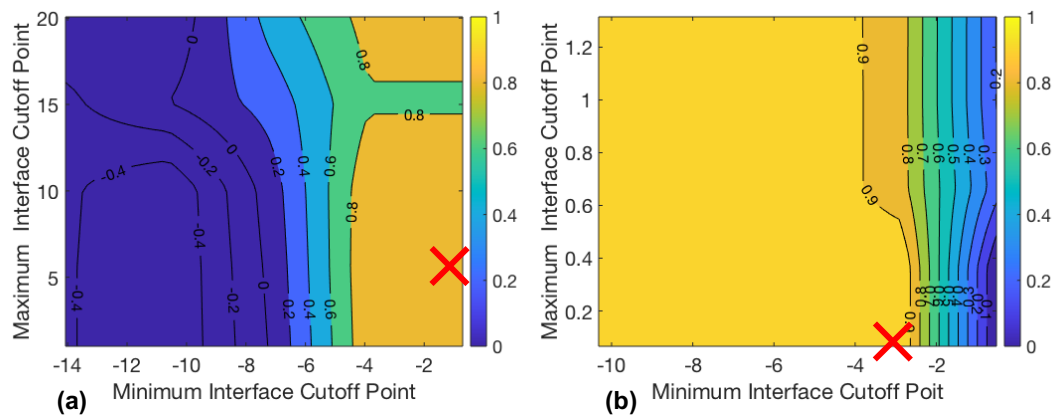
Figure 3.8. Contour plot of r^2 values for the sigmoidal curve fit for interface 1 data (a) and interface 2 data (b) depending on the maximum and minimum cut-off point combination.

There tended to be a large portion within the search area that had the same or very similar best r^2 value and therefore any of the cut-off threshold pairs within that area could be selected. The actual selected max and min cut-off values were the values closest to 0 within the area that had the same r^2 values and are shown by the red X's in Figure 3.8. Once the best maximum and minimum threshold values for interface 1 were selected a similar procedure to determine interface 2 was undertaken (steps 17-20).

The search start position for interface 2 was now $Int_{1,end}$ (black dashed line on Figure 3.7 (b)) so that any maxima and minima below the final position of interface 1 would be detected. As with interface 1 the 25 maximum and minimum cut-off thresholds combinations were tested. Figure 3.7(b) shows the cutoff points (red and blue dashed lines) for interface 2. The search for interface 2 is slightly different to the search for interface 1 as the first minimum below $Int_{1,end}$ is found first (blue dot) and then the first maximum above that (red dot). The inflection point between these two points is then selected as interface 2 (red line). This is done so that the same maximum can be selected for both interface 1 and interface 2 but the inflection points chosen are either side of that maximum, this is how the upper and lower bound of the final interface can be found. Figure 3.7 shows how the algorithm works at a single timestep (10 seconds), the process depicted here is used for all timesteps, firstly

searching for interface 1 and then interface 2. The same search procedure for the best fitting curve is applied to interface 2. The r^2 results for interface 2 are shown in Figure 3.8 (b).

Once interfaces 1 and 2 have been found, the grayscale values in the area above interface 1 and below interface 2 are averaged for each timestep and normalised with respect to the average grayscale value for pure toluene in the case of the top interface and pure water in the case of the bottom interface (steps 21 – 22). This is done to give an indication of the clarity of the 'settled' region at each timestep relative to a pure liquid phase (shown by the colour bar in figure 3.9 as the 'relative phase clarity'). A relative phase clarity of 0 indicated a very dark region that has not settled at all. A relative phase clarity of 1 indicates the settled area is very clear and has no residual droplets or fine dispersions. For example, in Figure 3.9 there are some large bubbles still below the bottom interface at 5 seconds. These bubbles darken the area below the interface (reduced average grayscale value) and therefore result in a lower relative phase clarity. In the case of stable emulsions, a settling front may be detected but fine droplets which have not settled via sedimentation or creaming may exist which cloud the area above or below the interface and reduce the relative phase clarity. This can give an indication of the emulsion type, If the bottom phase is darkest and fine droplets can be seen then that suggests the emulsion was O/W and vice versa for the top phase.
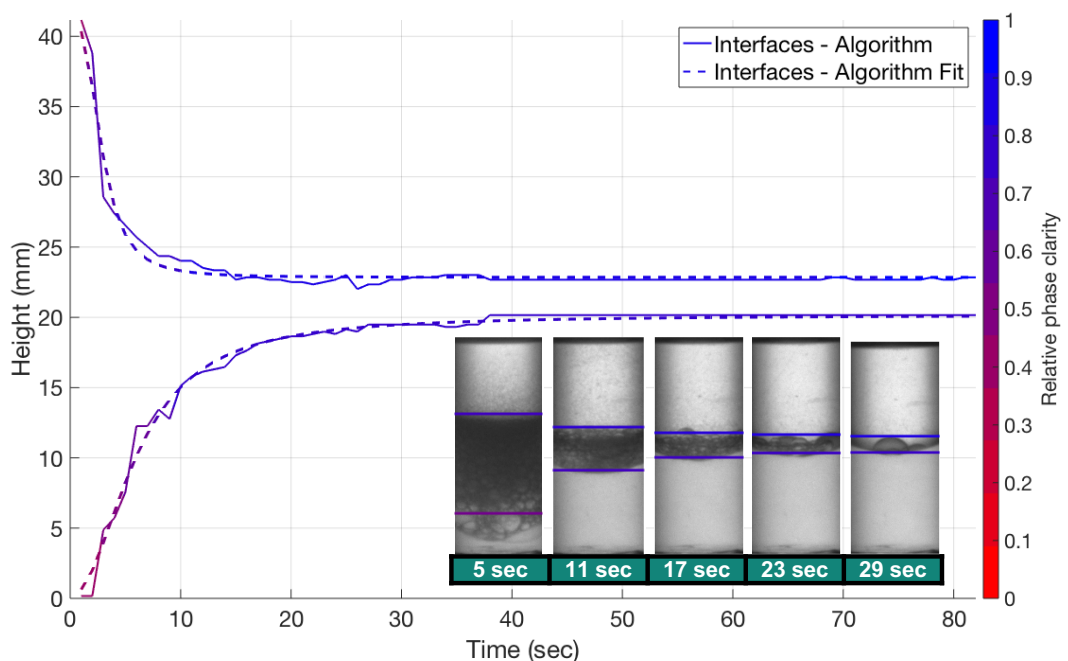
Figure 3.9. Top and bottom interface heights of example Toluene-Water case with relative phase clarity over time and sample images annotated with corresponding interface locations and relative phase clarity at selected timesteps.

The procedure described above has been applied in the same way to each case in the buffer solution experiments and the surfactant solution experiments. The overall search area changed depending on the size of the liquid vessel but was otherwise consistent. The constants detailed in table 3.4 are set before running the algorithm for each experiment. The length of a single pixel was required to convert number of pixels to a physical distance. In the buffer solution experiments this was $0.1\mu m$ and in the surfactant solution experiments this was $0.168\mu m$. The difference in pixel length depended upon the camera's zoom settings. The pure toluene and water settings were changed depending on the light level settings used for each experiment. The sample rate is the time between each image captured. The number of pixels to crop from the top and bottom of the image for steps 5,7 and 11 of the algorithm procedure remained the same except for vial 7 in experiment 2. The search distance to calculate I_{Avetop} and $I_{Avebottom}$ remained the same for both experiments.

Table 3.4: Constants used in the algorithm that are specific to each experimental setup

	Sample Rate (sec)	Average grayscale intensity of pure toluene	Average grayscale intensity of pure water	Pixel length (µm)	Number of pixels to crop (step 5,7, and 11)	Search distance for I_{Avetop} and $I_{Avebottom}$ (pxls)
Exp 1	1	172.71	182.65	100	30	10
Exp 2	10	197.38	226.13	168	30	10

An overview of the constants used for each image set and the algorithmically determined values such as the applied threshold values are given in appendix A.

3.4 Results and Discussion

3.4.1 Aqueous Solution Experiments

Nine liquid combinations were analysed using the algorithm. The three liquid biphasic solutions used were: Toluene-Deionised water (pH 7); Toluene-Acetate buffer (pH 4); Toluene-Glycine buffer (pH 10). These were prepared in three phase ratios (V_{Aq}/V_{Org}) of 0.25, 1 and 4. From the collected images it could be deduced that all of the cases at phase ratio 4 and 1 were O/W emulsions while the 0.25 phase ratio cases were W/O. For each of the 9 cases (with 3 repeats per experiment), the average time at which each interface reached 90% of its final height is shown in figure 3.10.
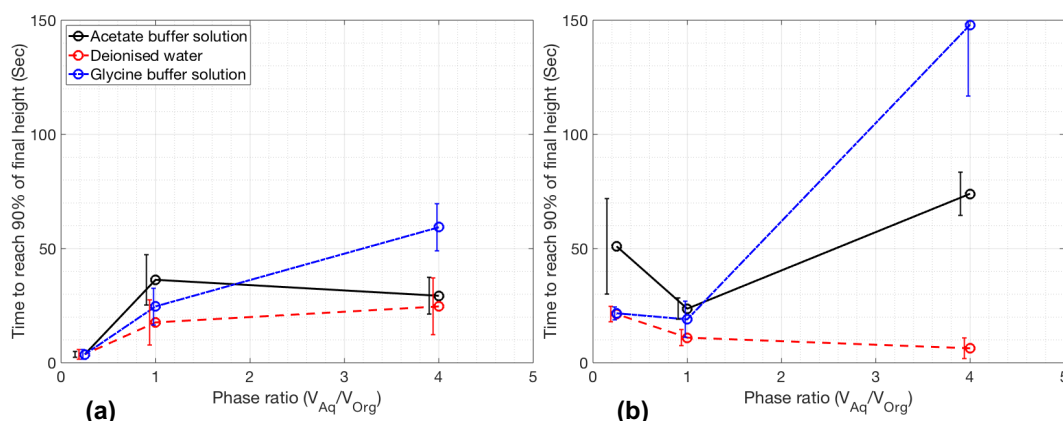
Figure 3.10. Time taken for (a) top and (b) bottom interface of each solution to reach 90 % of its final value at 3 different phase ratios.

For each case at a phase ratio of 0.25 the top interface separated in less than 10 seconds and the bottom interface took longer to separate than its corresponding top interface. This would suggest that the W/O mixture is made of very large droplets that settle to the bottom of the vessel very quickly, these droplets then require time to coalesce. The cases at a phase ratio of 4 produced the greatest difference in settling times out of the 3 phase ratios tested. The top interface in the Toluene-Acetate buffer solution and Toluene-Deionised water solution took a similar amount of time to separate (25-30 seconds) while the Toluene-Glycine buffer solution took approximately 60 seconds to separate. The bottom interface of the Toluene-Deionised water solution took less than 10 seconds to separate while the Toluene-Acetate buffer solution took 74 seconds to separate and the Toluene-Glycine buffer solution took nearly 150 seconds to separate. The deionised water solution took less time to settle than the buffered solutions. The rate of coalescence may have reduced in the buffer solutions because of a change in Zeta potential (which varies with ionic strength and pH) of the solutions. An increased Zeta potential may have increased repulsion between droplets and in turn reduced the frequency of collisions. This in turn will mean a reduced number of droplets coalescing and a slower separation[65,67]. It has also been found that sodium acetate salts can reduce the surface tension of aqueous-organic mixtures, which would result in the formation of smaller dispersed droplets[66]. The smaller percentage of toluene in the mixture at phase ratio 4 means the probability for droplet collision (and subsequent growth) is lower, thus creaming will take longer (according to Stokes law). All of the cases at phase ratio 1 took between 10 and 40 seconds to separate for both interfaces). These solutions, like the phase ratio 4 solutions are O/W mixtures, however they did not vary in separation rates as much as the phase ratio 4 solutions. This suggests that the large variation in separation rates produced by the phase ratio 4 solutions was overridden by an increase in phase ratio. This may be down to an increased number of droplets,

resulting in more collisions and more coalescence. Figures showing the individual cases interface vs time graphs, contour plots for determining the best maximum and minimum cut-off point combinations and six sample images from each case with the detected interface locations overlayed can be found in appendix A.

3.4.2 Surfactant Solution Experiments

To systematically demonstrate the performance of the imaging algorithm across a series of systems with settling performance identified *a priori*, a toluene/water system with a surfactant was adopted with the salinity of the aqueous phase used to drive the nature of the emulsion. A series of surfactant stabilised liquid bi-phases were produced by increasing the NaCl concentration to raise the HLD value of the system from approximately -3 through to 1, passing close to the 0 point, see Table 1. Twenty emulsions were formed with two different surfactant concentrations and ten salt concentrations. Both very slow and fast settling interfaces, O/W and W/O emulsions and clear and unclear interfaces where observed during the experiment. The ten salt concentrations shifted the equilibrium of the surfactant system from strongly negative on the HLD scale (O/W) through to positive (W/O) passing through a region of mixed O/W and W/O. A 3rd microemulsion phase was not observed during these experiments, possibly due to the low surfactant concentration or limited surfactant solubility in toluene. Nevertheless, a significant decrease in emulsion stability was recorded near to HLD = 0.

An example interface location graph from vial 5 (HLD ~ 0) has been presented in figure 3.11. The top interface is more distinct than the bottom, so was detected earlier than the other interface by the algorithm. Sample conductivity was measured post experiment by remixing the samples and quickly placing a conductivity probe inside the vial once mixing had ceased. The conductance of this sample was in the 10 $\mu S/cm$ range which, considering the overall salt concentration of the sample, suggests it was mostly a W/O emulsion but with some O/W. The sample lies within the transitional region of the HLD scale meaning the emulsion was expected to be partly O/W and partly W/O. However, the unclear bottom phase suggests fine toluene droplets are present in the water which would suggest the emulsion is mostly O/W. It is therefore inconclusive weather this sample is mostly O/W or W/O but as the sample lies within the transitional region of HLD space this is to be expected. The interface detected by the algorithm matched the interface locations seen in the inset images of figure 3 well and the sigmoidal curve demonstrated a good fit to this data with r^2 values of 0.997 and 0.995 for interfaces 1 and 2.
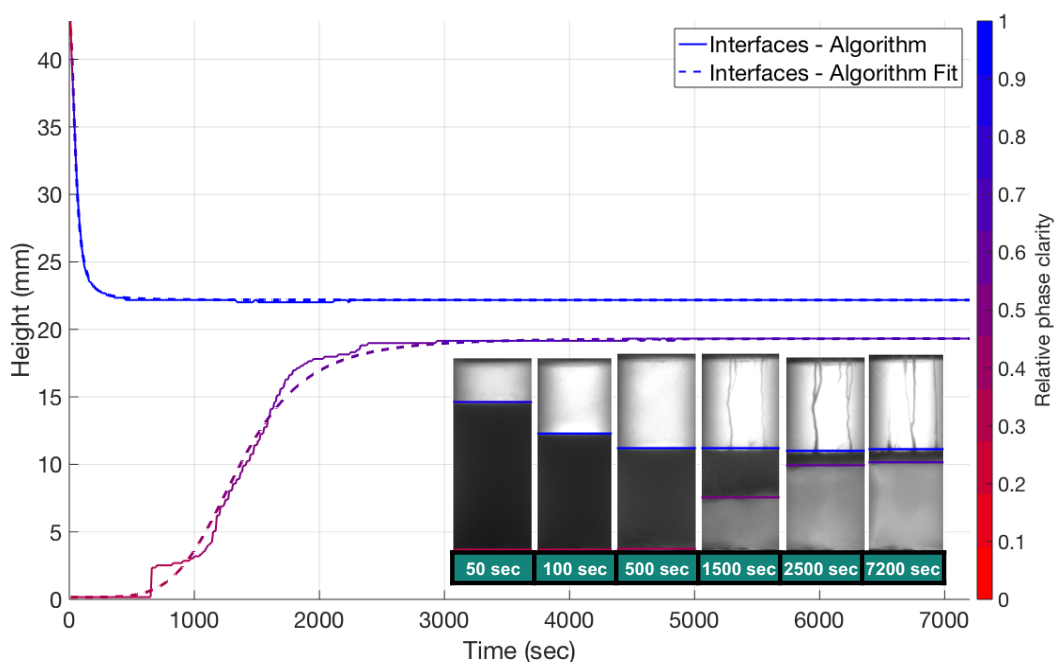
Figure 3.11. Detected interfaces and normalised grayscale intensity over time for the 0.01M solution with 27.68 mg/ml NaCl (HLD = 0.006)

Figure 3.12 (a) shows the time for both top and bottom interfaces of the 0.01M emulsions to separate depending on its location in the HLD scale. For the lower surfactant concentration, the emulsion was observed to be stable at HLD < -0.5, with long settling times for both interfaces (for this process related study, settling times were truncated at >120mins). The measurement of conductivity indicated that these are O/W emulsions. Increasing salt concentration shifts the surfactant equilibrium towards the organic phase, the system becomes less stable and the emulsion separates rapidly. At the point of HLD = 0 the emulsion enters a transitional phase and is a mixture of W/O and O/W. This transitional phase appears to span a range of HLD values from 0 up to 0.87 (vials 5-9). Both phases in vials 7, 8 and 9 remain unclear after the bulk of separation has occurred suggesting fine droplets of water and toluene are present in both phases (see appendix A). At HLD = 1, a more stable W/O emulsion forms, as suggested by the increased clarity of the bottom interface, and increased separation time of both interfaces. Theoretically, if more salt were added, the W/O emulsion would become more stable before reaching a plateau, similar to the highly negative HLD samples. However, the relationship between the HLD scale and salinity is logarithmic, so additional salt has a diminishing effect on the HLD value.
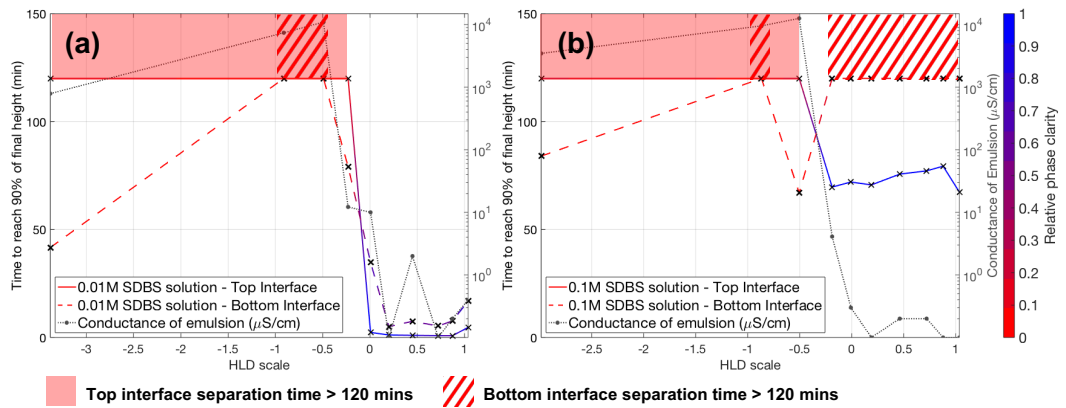
Figure 3.12. The time taken for (a) 0.01M SDBS and (b) 0.1M solutions' top and bottom interfaces to reach 90 % of their final height and the recorded conductance of each emulsion. The relative phase clarity above and below the interface at the final timestep are shown. The shaded blocks are located at the points where separation of the top or bottom interface took longer than 120 minutes to separate.

For the 0.1M SDBS surfactant solutions, Figure 3.12 (b) shows that an increase in surfactant concentration resulted in a general increased in emulsion stability, as expected. Any interface that did not settle out within the image recording time was fixed at the final recording time of 120 minutes. The shaded blocks denote where recording was stopped and separation time is longer than 120 minutes. A study over a longer period may reveal some further separation in these cases. Within the recording time investigated, the top interface can be seen to follow a similar trend to the 0.01M samples. As before, as the HLD value approaches 0 the emulsion becomes less stable. This reduction in separation time coincides with a reduction in conductivity suggesting that the emulsion is transitioning form O/W to W/O. It is clear from figures 3.12 (a) and 3.12 (b) that the separation time and emulsion type can be modified by varying salt concentration in line with HLD theory even at low surfactant concentrations. The proposed imaging algorithm can determine the separation time of emulsion systems consistently across the HLD range.

3.4.3 Scale up Experiments

5 cases from the previous experiments were scaled up to 20 litres. Two from the toluene-aqueous solutions and three from the surfactant solutions. This was done to show how the separation times changed as the cases were scaled up. The two cases from the toluene-aqueous solution experiments were the toluene-deionised water and toluene-glycine buffer solutions at a phase ratio of 4. These two cases were chosen as they showed a large difference in settling times during separation among the non-surfactant solutions at small scale (200ml). The -0.49, 0 and 0.45 solutions from the HLD emulsion study were also scaled up from small scale (15ml). The

scaled-up separation times were measured using manual image analysis as opposed to the algorithmic method used at small scale. The difference in settling times between the two scales during separation are shown in figures 3.13(a) and 3.13(b) and tables 3.5 and 3.6.
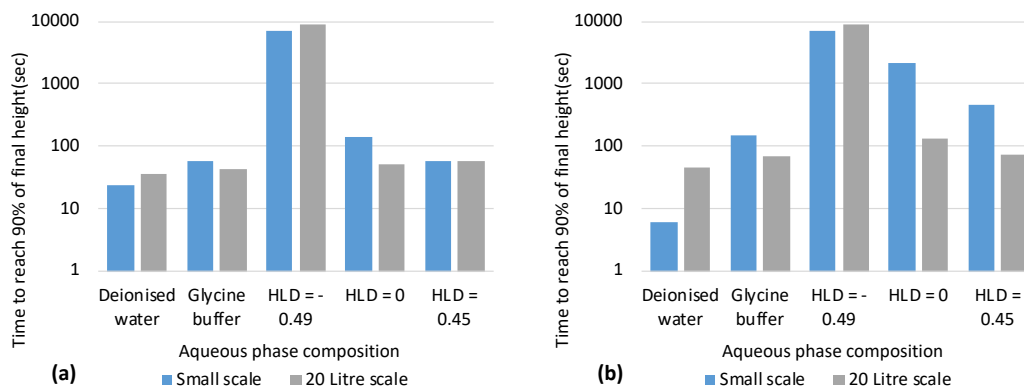
Figure 3.13. Time to reach 90% of the final height for the top interface (a) and the bottom interface (b) in the deionised water and glycine buffer solutions and three different HLD values -0.49, 0, 0.45 at small and 20L scales.

Table 3.5: Non-surfactant solution times to reach 90% of their final height at 0.2 litre scale and 20 litre scale.

Volume (L)	Height (mm)	Interface	Separation time (sec)	
			Deionised water	Glycine buffer
0.2	66	Top	24.6	59.33
		Bottom	6.33	148
20	270	Top	36	44.5
		Bottom	45.5	69

Table 3.6: Surfactant solution times to reach 90% of their final height at 0.012 litre scale and 20 litre scale.

Volume (L)	Height (mm)	Interface	Separation time (sec)		
			HLD = -0.49	HLD = 0	HLD = 0.45
0.012	43	Top	7200	140	60
		Bottom	7200	2090	450
20	270	Top	9000	51	59
		Bottom	9000	136	72

The time to reach 90% of its final height increased for both the top and bottom interface in the deionised water case upon scale-up. At small scale the deionised water solution's top interface separated after 24.67 ± 12.42 seconds and the bottom interface separated after 6.33 ± 4.51 seconds. At pilot scale the deionised water solution top interface separated after 36 seconds, which is just within the margin of

error found at small scale. The bottom interface took 45.5 seconds to separate which is larger than at small scale. Both the top and bottom phases took less time to separate in the glycine buffer solution at 20 litres than at small scale. The top interface took 59.33 ± 10.26 seconds and the bottom interface took 148 ± 31.19 seconds at small scale. At pilot scale the top interface took 44.5 seconds and the bottom interface took 69 seconds to separate. Both of these separation times fall outside of the margin of error found at small scale. However, it is important to note that at pilot scale the interface height was measured manually and therefore a level of subjectivity was introduced. Also, only one experiment was run at pilot scale for each case, meaning no variance in the separation time at pilot scale was found. The overall time the glycine buffer solution took to separate was still longer than in the deionised water solution. This could suggest that the increased ionic strength and pH of the buffer solution is still increasing the time to separate but due to the lower mixing energy (242 rpm compared to 1500 rpm at small scale) the minimum droplet size is larger and therefore the influence increased ionic strength and pH has on separation time is reduced.

The surfactant solution results are more difficult to interpret as the HLD range investigated is extremely sensitive to changes in salinity and volume ratios. A trend in decreasing separation times moving from HLD = -0.49 to HLD = 0.45 can be seen in both the small scale and pilot scale experiments that were tested. There are a couple of reasons why this might be the case, the low shear, low rpm used at pilot scale did not produce the same mixing energy as the hand shaken vials and therefore produced larger droplets that increased the separation rate, although this is difficult to quantify due to the different mixing regimes employed. A study to compare the Weber number of vial shaking and impeller mixing could provide a correlation between the two mixing methods. The agitator in the 20 litre vessel was located at the bottom of the tank, meaning the emulsion will tend towards O/W rather than W/O for cases between HLD 0 – 1. This is because the impeller draws the oil down into the aqueous phase which promotes the formation of oil droplets rather than water droplets[73]. This will result in a less stable emulsion than if the agitator was centrally located within the vessel or if hand shook like it was at small scale. Nevertheless, the two scales correlate to one another and with good understanding of process changes such as mixing regime and energy input the separation time of both surfactant free and surfactant systems can be anticipated at small scale and therefore took into consideration before scale-up. The manual interface locations found during the pilot scale experiments are shown overlayed on the corresponding small scale case data found by the algorithm in appendix A.

3.5 Conclusion

The devised algorithm has been shown to work well with a range of cases. Both O/W and W/O mixtures have been examined. Separation rates from seconds through to hours have been tracked and very subtle interfaces between the two phases have been detected. The algorithm dealt well with imperfect pictures such as in the buffer solution cases. In these cases, many droplets clung to the glass vessel which produced noise in the grayscale data, this noise was successfully ignored by the algorithm during interface detection. The use of 15 ml vials is significant, as it demonstrated the applicability of the algorithm to small samples, suiting the technique to HTE. Further developing the experimental apparatus to include an automated shaker rack would increase the number of samples that could be analysed at once. An initial prototype of such a shaker rig has been shown in appendix A.

The samples were all analysed in the same way, with little change to the algorithm or its parameters, allowing for an automated workflow. The integration of this image processing algorithm into a workup extraction analysis could provide vital and quantitative information on the feasibility of scale up due to long or challenging separations and loss of product to rag layer formation. Furthermore, small changes in salinity or aqueous and organic phases can clearly have a significant effect on separation rates and should be considered during initial process screening alongside conventional extraction efficiency studies.

A number of factors can influence the separation time of a specific liquid-liquid system upon scale up such as mixing energy and shear forces, position and type of agitator as well as the liquid-liquid system properties. The affect the liquid-liquid system properties have on separation rates can be captured at small scale and inform scale up decisions, however the mixing routine used at scale should be as closely mimicked at small scale in order to provide the most accurate predictions.

3.6 Summary

In this chapter a method for analysing the separation rate of different liquid-liquid mixtures has been devised and applied to 29 different cases with minimal manual intervention. The methodology developed in this chapter will be used in subsequent chapters to characterise and compare different continuous extraction systems. The emulsion system used in this chapter will also be used to characterise a new separator designed for continuous lab-scale extraction processes.

Chapter 4 – Design and Automation of a Liquid-Liquid Separator Utilising Coalescing Filter Media for Continuous Flow Chemistry at Laboratory Scale

4.1 Introduction

In this chapter a liquid-liquid separator has been developed for lab-scale flow chemistry applications. The aim of this chapter was to describe the developed separator and how it operated. The device utilises nonwoven coalescing filter media to collect and grow dispersed phase droplets which are then rapidly separated by gravity and surface forces downstream of the filter. The potential benefits of utilising a separator with nonwoven coalescing filter media were discussed in Chapter 2, section 2.4. The mechanical aspects of the developed separator unit are presented in section 4.2.1 and the operating conditions are presented in section 4.2.2. The devices electro-mechanical control system is then described in section 4.3. The devices various control schemes are then discussed and analysed over a range of system parameters in section 4.4.

4.2 Liquid-Liquid Separator Design

4.2.1 Mechanical Design of separator unit

Initially, the separator was designed with a volume of 6ml, however after initial testing it was evident that a smaller volume would be possible without compromising the performance within the flow ranges investigated. It was preferable to minimise volume to minimise residence time, residence time distribution and reagent use. A 2ml volume device was therefore developed and is what will be discussed in this section. An exploded view of the separator is shown in figure 4.1 (a), the assembled separator is shown in figure 4.1 (b) and a sectional view of the separator which shows how the fluid stream enters and exits the device is shown in figurer 4.1 (c).
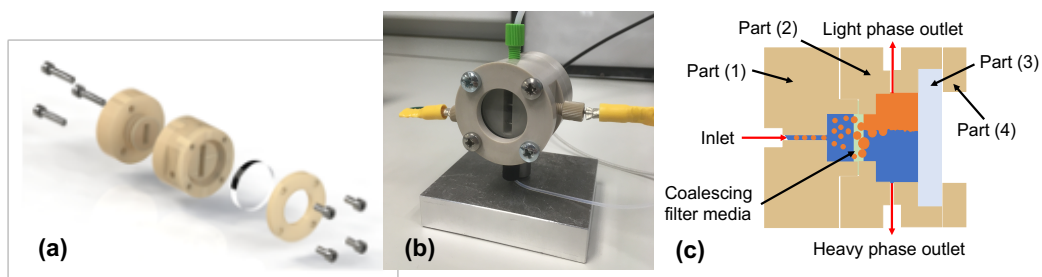
Figure 4.1: (a) Exploded view of lab-scale coalescing separator. (b) Assembled photo of lab-scale coalescing separator. (c) Sectional view of the coalescing separator annotated to show the fluid path through the device.

There are three main machined parts, all made from a 50mm diameter PEEK rod (parts 1, 2 and 4 in figure 4.1 (c). The CAD model for part 1 is shown in figure 4.2 (a). Part 1 has a single ¼-28 UNF port that connects to a 15 x 5 mm cross sectional area. This port is the fluid inlet and the coalescing filter media is compressed between the 25mm diameter face that extrudes from the 50 mm diameter body and the cut-out portion of part 2 (figure 4.2 (b)). A groove is located around the cylindrical extrusion which fits an O-ring, this O-ring creates a seal between part 1 and part 2. Three M5 holes are located on part 1 120 degrees apart. Three threaded M5 holes exist on part 2 at the same PCD which allows the two components to be screwed together, compressing the edges of the filter media to keep it in place.

Part 2 continues the 15 x 5 mm fluid path from part 1 but expands to 24 x 5 mm after 5 mm. This is to allow for a greater 'settling area' downstream of the filter media. This settling area allows more space for coalescence to occur and minimises the possibility of the aqueous or organic phases exiting through the wrong outlet. There are 4 ¼-28 UNF ports located on part 2. Two ports connect to each of the 5 mm wide internal sections. These two ports are the light and heavy phase outlets. The other two ports connect to the 24mm internal walls and house the two electrodes. It is important that the distance between the electrodes is large enough so that a 'bridge' between them does not occur during operation. A bridge between the two electrodes forms when water connects the two electrodes giving a conductance measurement even when the surrounding phase is an organic non-conducting phase. This happens due to the preferential wetting of the electrode surface with water, the further apart the electrodes are the thinner this liquid bridge becomes until the connection splits and no conductance is measured. The position of the electrodes is limited as at least one electrode should ideally be located at the centre of the rectangular section as the level control algorithm has the same distance to monitor both above and below the electrode. The second electrode is placed close to the bottom of the rectangular cell and will therefore be surrounded by the heavier phase almost all of the time. In this way, the two electrodes are far apart and only the central electrode will be of significance in the level control algorithm.

A cylindrical glass face (part (3)) is compressed against the end of part 2 in such a way that the user can see into the separator and monitor the separation on the downstream side of the filter. The glass face is compressed against part 2 using part 4 (Figure 4.2 (c)). Part 4 has Four M5 holes located 90 degrees apart. Four screws

are used to hold the glass face in place between part 2 and part 4. A groove for an O-ring is located on part 2 which seals the glass face against it.

(a)   (b)   (c)
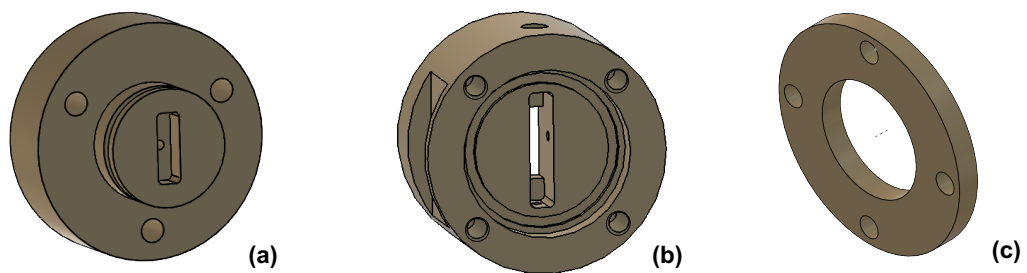
Figure 4.2: (a) CAD model of part (1) of the coalescing separator. (b) CAD model of part (2) of the coalescing separator. (c) CAD model of part (4) of the coalescing separator.

4.2.2 operating conditions

The operation of the separator is dependent on the flow rate, droplet size and distance to travel to the outlet port (as shown in figure 3.3).
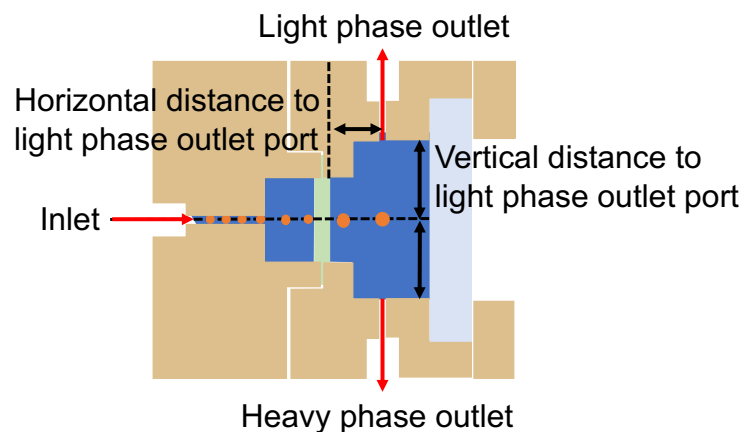
Figure 4.3: Sectional view of the coalescing separator annotated to show the vertical and horizontal distance to the light and heavy phase outlets that a droplet has to travel from the downstream side of the filter.

The time a droplet of a certain size takes to travel a vertical distance is described by Stokes law. Therefore, a simple model has been developed to determine the limitations of the device depending on the flow rate and droplet sizes downstream of the coalescing filter media. The model assumes that droplets do not interact with one another and the droplets would travel vertically through the device at the same rate as if the experiment was conducted in a batch-wise cylinder with no flow (obeys Stokes law). The model counts a successful separation as:

'A droplet of a given size that falls 12 mm vertically downstream of the filter media before it travels the horizontal distance to reach the outlet port'.

The time to travel the horizontal distance is different depending on the flow rate of the system. If the droplet is successfully separated according to this criteria then it

can be assumed that a droplet of the given size will naturally float or sink the required distance to reach the outlet. The incoming droplet size depends on the droplet size produced by the upstream mixing regime, the liquid-liquid physio-chemical properties of the system and the droplet size produced by the coalescing filter media upon detachment from its surface at the downstream face.

In figure 4.4 the horizontal red lines show the time it takes a single droplet to travel from the downstream face of the filter until it is horizontally in line with the outlet ports depending on if the inlet flow rate is 1, 5, or 10 ml/min. The black lines represent the time it takes for droplets from 10 to 1000 µm to reach the outlet ports vertically assuming the droplet starts from the centre point of the filter media. The three lines represent different dispersed phase densities. The continuous phase is assumed to be water with a density of 997 kg/m^3 and viscosity of 0.00089 Pa.s. 10ml/min is a relatively fast flow rate for a lab-scale flow system and typical droplet sizes in a flow system are around the 1500 µm size due to plug flow regimes in 1/16" ID tubing. However, as the goal is to separate the liquid phases with minimal phase carry over, the possibility of a droplet distribution lower than the typical average droplet size must be considered. Furthermore, in more complex liquid-liquid systems, surface active molecules and solids that cause pickering emulsions can drastically reduce droplet sizes, therefore a droplet size range from 1 – 1000 µm was considered during this investigation.[39,132] As can be seen in figure 4.4 if the density difference between the two phases decreases from 397 to 97 (dispersed phase density of 600 kg/m^3 and 900 kg/m^3) at a flow rate of 5 ml/min the minimum droplet size that will fully separate changes from 50 µm to 90 µm, still well below the average 1500 µm droplet size. When the density difference is changed to just 7 kg/m^3 the minimum droplet size completely separated by the device is approximately 260 µm.
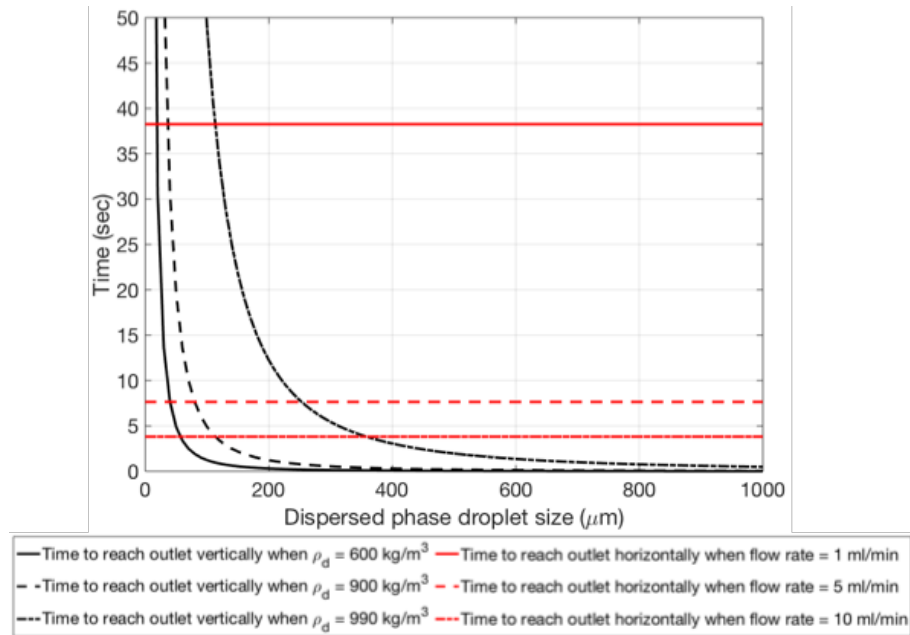
Figure 4.4: Droplet size limit of 2ml separator depending on flow rate and density difference between three different dispersed phases and water (ρ_c = 997 kg/m^3).

4.3 Liquid-Liquid Separator Automation Hardware

A system to control the outlet flow of the separator depending on the height of the interface between the two phases was vital to ensure good separation at all times during operation. Two configurations were developed, both utilised conductivity measurements to determine where the interface between the two phases were with respect to height in the separator. The conductivity circuit is described in section 4.3.2. Both systems utilised Arduino hardware and software for processing data (section 4.3.1).[133] The two configurations mainly differ in the actuation process to control the separator level. Configuration 1 uses a servo motor to open and close a needle valve depending on the conductivity measurement which in turn controls the pressure across one of the outlets and as a result the flow of liquid through it (section 4.3.3). The second configuration controls the interface location by converting the conductivity measurement to a pump rate at one of the separator outlets (4.3.4). Configuration 1 and configuration 2 are shown in figures 4.5 and 4.7.
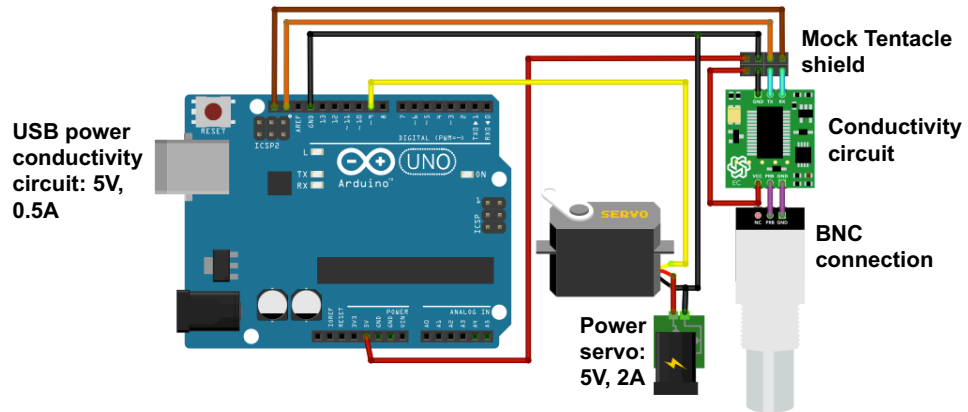
Figure 4.5: Simplified schematic of configuration 1 (Produced using Fritzing software)

Both configurations used a Whitebox labs Tentacle Shield[134] as shown in figures 4.6 and 4.8. The shield is designed to sit on top of the Arduino board and isolates the conductivity circuits preventing noise and ground loops to enable precise measurements even in closed-loop systems. The conductivity circuit is mounted on top of the tentacle shield in configuration 1 and is connected via jumper wires in configuration 2. Configuration 1 can connect two EZO circuits on the tentacle shield mini (figure 4.6) and configuration 2 can connect four EZO circuits on the tentacle shield (figure 4.8). The tentacle shield is represented by a group of pin connectors in figures 4.5 and 4.7. The relevant connections to the conductivity circuit and Arduino board are shown for configuration 1 in figure 4.6 and configuration 2 in 4.8. The communication protocol between the conductivity circuit and Arduino is discussed in section 4.3.2. Configuration 2 can be expanded to include up to 5 pumps and 4 conductivity circuits. A system which used 3 pumps and 3 conductivity circuits is demonstrated in chapter 5 & 6.
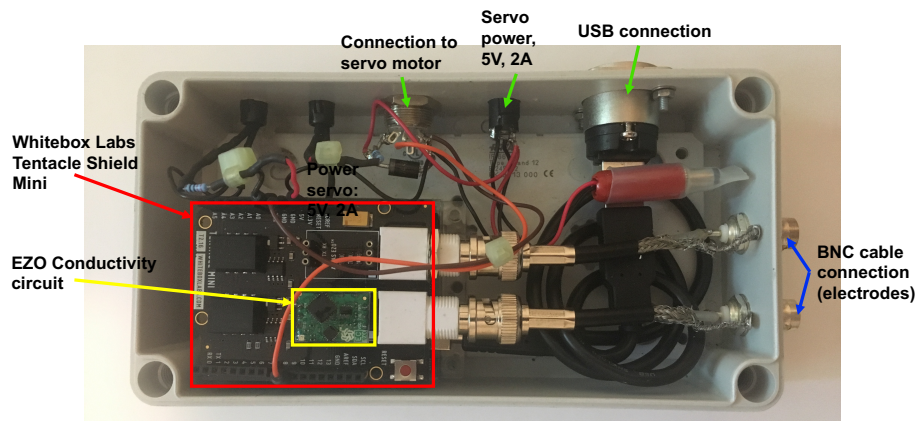
Figure 4.6: Enclosure containing electrical components of configuration 1
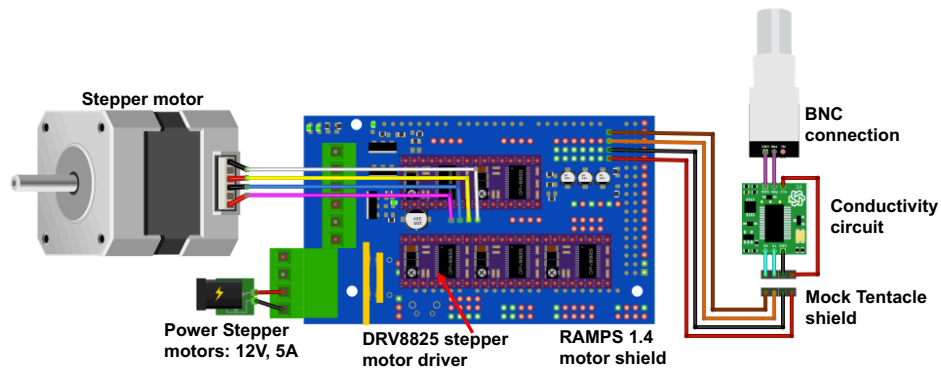
Figure 4.7: Simplified schematic of configuration 2 (Produced in Fritzing)
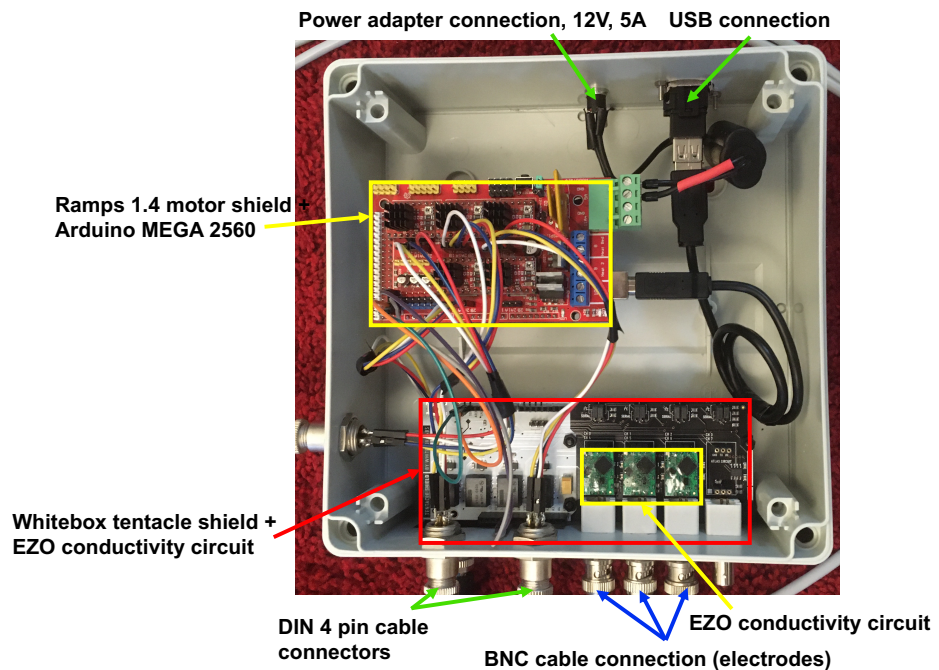
Figure 4.8: Enclosure containing electrical components of configuration 2

4.3.1 Microcontroller

The Arduino UNO is an open-source programmable board based on the ATmega328P microcontroller and was used for configuration 1. The Arduino UNO board has 14 digital input/output pins (of which 6 can be used as PWM outputs), 6 analog inputs, a 16 MHz ceramic resonator (CSTCE16M0V53-R0), a USB connection, a power jack, an ICSP (In-circuit serial programming) header and a reset button. The board can be powered from its USB connection or the input jack. The operating voltage of the board is 5V and can be powered directly from the USB connection. If the board is powered from the input jack a 6-20V can be used as the power is regulated down to 5V operating voltage.[135] For configuration 1 the Arduino was powered by the USB connection. A USB connection was required anyway as data from the sensor and servo was collected on a PC via serial communication. The

servo motor required for configuration 1 had a higher max current draw than the Arduino recommends therefore was powered externally.

The Arduino Mega 2560 is a similar open-source programmable board to the UNO and was used in configuration 2. This board uses the ATmega2560 microcontroller and has 54 digital input/output pins (of which 15 can be used as PWM outputs), 16 analog inputs, 4 UARTs (hardware serial ports), a 16 MHz crystal oscillator, a USB connection, a power jack, an ICSP header, and a reset button.[135] The same power requirements are true for the Mega board as the UNO board. As up to 5 pumps were potentially being connected to the board, an external power source would be required for them. The board itself and the conductivity circuit would be powered by the USB connection.

Both of the Arduino boards are programmed using the same language based on c/c++. All Arduino programmes consist of two main loops. A setup loop that runs once at the beginning of your programme and a main loop that continually runs while the Arduino is powered.

4.3.2 Conductivity circuit

Initially an off the shelf conductivity probe was purchased and fit into the separator but the gap between the electrodes was too small and water stuck to the glass surface of the probe. This gave false conductivity readings even when the probe (initially submersed in water) was completely submersed by Toluene. Instead, two electrodes were used for the positive and negative terminals connected to the conductivity circuit. The electrodes where 2mm diameter steel or platinum coated titanium rods and were inserted into the separator using ¼-28 UNF tubing adapters which formed a seal around the electrodes.

The conductivity of a solution is measured by providing an alternating current across two electrodes submerged in the solution. Conductivity depends on the number of ions in a solution, the more ions the higher the conductance. The conductance also depends on the surface area of the electrodes and the distance apart they are. The ratio of these two values is known as the cell constant K (equation 4.1).[136]

$$K = \frac{d}{A}$$ (4.1)

$d =$ Distance between the electrodes   (cm)

$A =$ Effective electrode area   (cm^2)

Measuring a (semi) calibrated conductivity

The conductivity is calculated by multiplying the cell constant by the conductance of the solution as shown by equation 4.2. Determining a suitable cell constant for a given system is crucial for accurate conductivity readings. Cell constants 0.1, 1, and 10 are common for commercial conductivity probes. The datasheet for the EZO conductivity circuits used recommends the K values and appropriate sized probes for a given salinity range as shown in table 4.1.[137]

$$k = G \times K \qquad\qquad (4.2)$$

$k =$ Conductivity   (S/cm)

$G =$ Conductivity of solution   (S)

Table 4.1: Conductivity measurement range depending on cell constant K

K (cm^{-1})	Conductivity measurement range (µS/cm)
0.1	0.07 - 50000
1	5 - 200000
10	10 – 1000000

The conductivity measurement will vary depending on temperature and length of cable used. The conductance of the electrodes also effects the accuracy of the conductivity measurement. Steel is not an optimum material to use as it has a low conductance, platinum or graphite are more commonly used. Platinum is more chemically resistant than graphite and would be a good option for the electrodes but is expensive. Steel rods were chosen and accuracy of the conductivity reading was sacrificed at this prototype stage – particularly as the accuracy is not operation critical, only the difference in readings between two liquids.

Different conductivity probes have been designed including 2 pole and 4 pole cells. 2 pole cells are simpler than 4 pole cells but cannot measure linearly over as large range of conductivity values. For the conductivity measurements in the separator a 2 pole system was selected for its simplicity and ease of installation. One of the main issues with 2 pole cells is polarization. Over time positive ions collect on the negative electrode and negative ions build up on the positive electrode which builds up a resistivity across the electrode surfaces, to reduce this, an alternating current is applied across the electrodes which reduces the build-up of ions on the electrode surface.

The geometry of the electrodes effects the measurement as any field lines that are impeded by the vessel walls or other structures will change the measured conductivity.[136] The area of the electrodes in the separator depends on how far they protrude into the vessel (from flush to the vessel wall up to 0.5cm). In the 6ml separator design, as the electrode is pushed further into the vessel the distance between the electrodes reduces and the surface area increases. In the 2ml separator

design as the electrodes are pushed further into the vessel they do not get closer to one another therefore only the surface area changes. Approximate values of the cell constant depending on the distance the electrode is pushed into the vessel and which separator is used are shown in table 4.2. Although it is important to ensure consistent conductivity measurements it is less important for the purpose of monitoring change in conductivity depending on if the electrodes are submerged in aqueous or organic liquids. As long as a clear relationship with enough sensitivity to detect the change in liquid was possible then the accuracy of the conductivity measurement was not a priority. What was important was providing a consistent cell constant so that scaled up versions of the separator would have the same basis for measurement. Understanding where the linear range of conductivity measurements were depending on the cell constant was also an important factor for any devised control scheme.

Table 4.2: Approximate cell constant depending on placement and surface area of the electrodes within each separator design.

6ml Separator			2ml Separator		
Electrode area (cm)	Distance between electrodes (cm^2)	Cell constant	Electrode area (cm)	Distance between electrodes (cm^2)	Cell constant
0.03	1.50	47.75	0.03	1.00	31.83
0.06	1.40	22.28	0.06	1.00	15.92
0.09	1.30	13.79	0.09	1.00	10.61
0.13	1.20	9.55	0.13	1.00	7.96
0.16	1.10	7.00	0.16	1.00	6.37
0.19	1.00	5.31	0.19	1.00	5.31
0.22	0.90	4.09	0.22	1.00	4.55
0.25	0.80	3.18	0.25	1.00	3.98
0.28	0.70	2.48	0.28	1.00	3.54
0.31	0.60	1.91	0.31	1.00	3.18
0.35	0.50	1.45	0.35	1.00	2.89

Figure 4.9: EZO conductivity circuit.[137]

Circuitry and Communication Protocol

The EZO conductivity circuit (figure 4.9) was used to measure the conductivity. The circuit processes the voltage measurement across the electrodes and converts it into

serial data ready to be passed to a device via UART or I^{2}C communication protocols. Both protocols require two signal lines for a single slave (conductivity sensor) and master (Arduino) communication.[137] However, as the number of slave devices increases the UART communication protocol requires hardware to distinguish between each slave device. In I^{2}C mode the slave device address is included in the data transfer line so that the master device knows which slave device it is currently talking to. Therefore, the I^{2}C protocol was selected as it required fewer pins on the Arduino to communicate with multiple conductivity sensors. For configuration 2 this was particularly important as the extra pins that the UART mode would require were already used by the stepper motor drivers and shield. The two signal lines required by the I^{2}C protocol are the serial data line over which serial data is read and written (SDA) and the serial clock line (SCL) which provides the transfer rate and synchronises the data transfer between the two devices. Figure 4.10 shows the structure of a single I^{2}C message.[138] The start condition for I^{2}C is when the SDA line switches from a high voltage level to a low voltage level before the SCL line switches from high to low. The stop condition is when the SDA line switches from a low voltage level to a high voltage level after the SCL line switches from low to high. After the start condition a 7 or 10 bit address is sent from the master device to the slave devices and whichever devices address matches with the sent address is the device the master device will communicate with. A read/write bit is also sent to determine whether the master device wants to read from the slave device or send data to the slave device. After each frame a acknowledge/no-acknowledge bit is sent. If the frame was successfully received, an ACK/NACK bit is returned to the sender from the receiving device. Once the device address has been identified and read or write communication established an 8 bit data packet is sent.[138,139] The device stops communication once the stop criteria has been met.
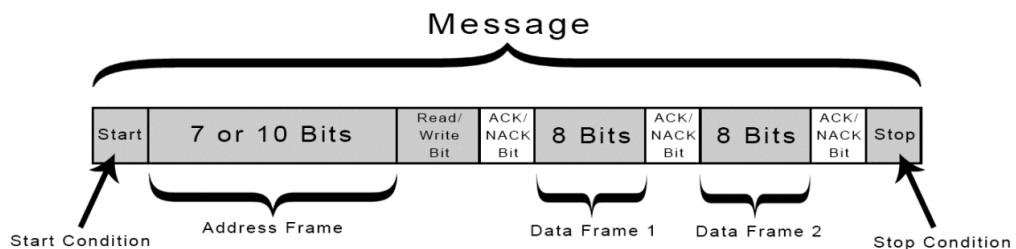
Figure 4.10: I2C communication data transfer structure [138]

As shown in figure 4.6 and 4.8 the EZO conductivity circuit was connected to the White box Tentacle shield. This device provides both voltage isolation for each of the sensors and takes care of the circuit design required for multiple I2C communications (pull up resistors on the SDA line etc). The SDA and SCL lines on the tentacle shield were connected to the Arduino.

4.3.3 Level control via needle valve actuation

Depending on the conductivity reading the outlet flow rate was changed. If the separator was left with no control at the two outlets (located at the top and bottom of the device) then all of the liquid flowed out through the bottom outlet. The needle valve was therefore attached to the bottom outlet so that when the valve was shut, no flow would pass through the it and all the fluid would travel through the top outlet. However, it was observed that without any back pressure on the top outlet the fluid streams would split between both outlets when the needle valve was fully open. This was because the narrow fluid path in the needle valve created back pressure equal to or above the static head and forced some fluid to pass through the top outlet. Therefore a 1.2 bar back pressure regulator was placed after the top outlet to account for this.

The method of controlling the needle valve required motorised actuation. A cheap and simple option was to connect a servo motor to the needle valve which could screw/unscrew the valve depending on the conductivity readings (shown in figure 4.11). The servo motor was connected via a universal joint. The block on which the needle valve was placed could move parallel to the motor in relation to the baseplate. This allowed for the change in distance between the servo and valve as it screwed/unscrewed.
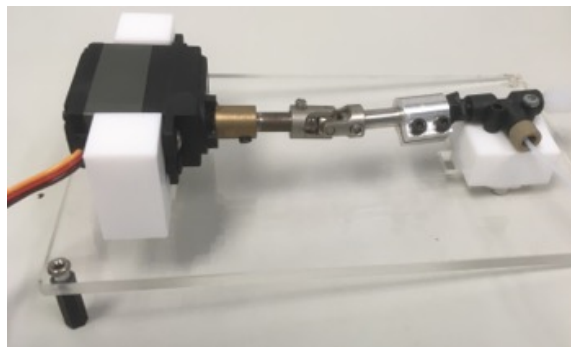
Figure 4.11: Servo to needle valve connection mounted on baseplate

Servo motors are made of 4 main parts, i) A DC motor ii) A gear train iii) A potentiometer, iv) A control circuit. The dc motor is wired to the control circuit and its shaft connects to the gear train that converts the high speed/low torque motor rotation to a low speed/high torque rotation. The potentiometer is connected to the end of the gear train and is wired to the control circuit. As the motor rotates the potentiometer resistance changes and therefore the voltage output changes. This voltage can be compared to the user input signal to determine the angle the servo shaft is away from the desired position via a feedback loop (figure 4.12)[140].
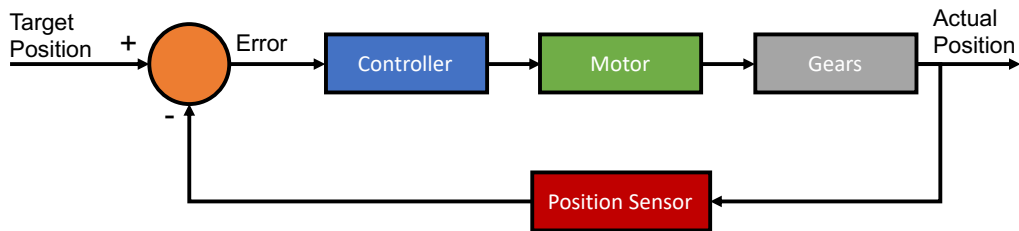
Figure 4.12: Servo control loop. Reproduced from How to Mechatronics [140]

The user input parameter is generally a pulse width modulation (PWM) signal which can be used to convert a digital signal into an analogue voltage. A PWM signal operates at a specific frequency, the servo Arduino library operates at approximately 50 Hz. This means that the digital signal turns from high to low and back 50 times a second or a single pulse occurs approximately every 2 milliseconds. The amount of time the signal is high within a single pulse determines the position of the servo. Most servos operate around the 1000 to 2000 microseconds range where 1000 microseconds = 0 degrees, 1500 microseconds = 90 degrees and 2000 microseconds = 180 degrees (figure 4.13).[140,141]
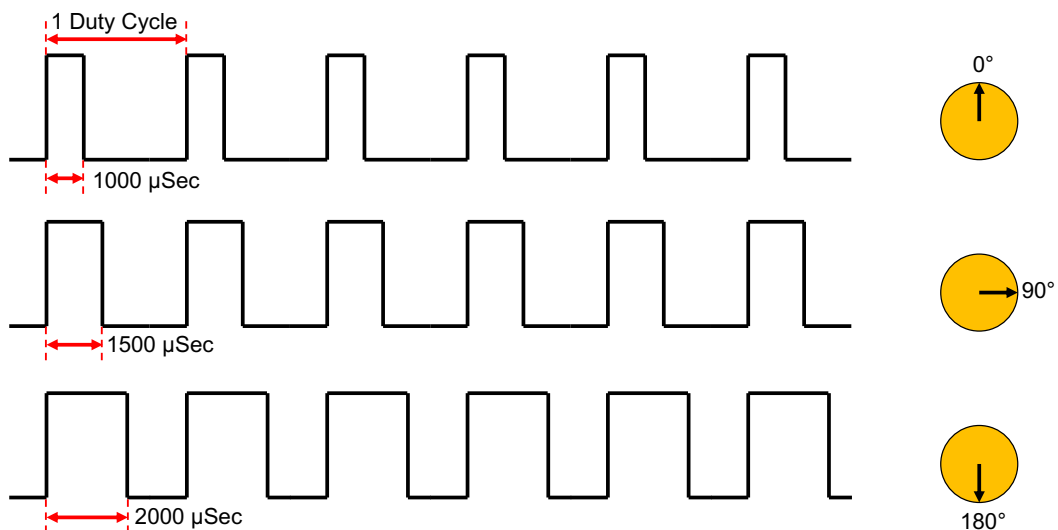
Figure 4.13: PWM servo control.

The conversion from microseconds to degrees of the selected servo was determined experimentally by incrementally changing the pulse signal microseconds until the servo motor no longer rotated. The conversion was linear and therefore a straight line equation could be used to determine the servo angular position depending on the pulse width signal and is given by equation 4.3. The servo was limited to microseconds between 1450 and 1600 which gave a rotation of 270°. This was enough rotation to fully open and fully close the valve.

$$Y = 1.8x - 2610 \tag{4.3}$$

Y = Valve position (degrees)

x = Valve position (microseconds)

The selected servo was the Turnigy TGY-6114MD [142] which unlike most servo motors could complete 6 full rotations which allowed for a larger range of valve positions than would be available with a conventional 180 degree servo motor. The operating voltage range was between 4.8 and 6 Volts and had a stall current of 1.8 to 2.2 Amps. The servo motor was powered separately to the Arduino board and conductivity circuit by a 5V, 2A - AC to DC adapter. Servo motors have 3 wires, power, ground, and signal. The power and ground wires where connected to the external power supply, the ground was also connected to one of the ground pins on the Arduino, the signal wire was connected to digital pin 9 on the Arduino which is one of the pins that can supply a PWM signal.

4.3.4 Level control via pump control

An alternate control method was devised using a pump downstream of the top outlet. This method had some advantages and disadvantages over the needle vale system:

Advantages	Disadvantages
• Accurate flow rates.	• More expensive setup.
• Better suited to a PID control system.	• Chemical compatibility of pump is limited compared with valve system.
• System pressure does not fluctuate as drastically as with opening and closing of valve.	• System pressure is limited by the pump pressure rating.

Pump Selection

Firstly, a pump suitable for the application needed to be chosen. A number of requirements needed to be met for the application of a lab scale separator and extraction system:

1. Chemically compatible with a wide range of solvents, acids and bases.
2. Capable of pumping under pressure.
3. Accurate liquid dispensing at low flow rates.
4. Capable of providing smooth continuous flow.
5. Small size for minimal lab footprint.
6. Simple integration into electrical system.

It was decided that a positive displacement pump would be ideal for this application. Axial-flow pumps are generally not suitable at the scale required due to the internal diameter required for an impeller. Furthermore, variation in pressure greatly influences the flow rate of axial pumps and the need for an impeller

mechanism within the fluid path means a greater number of materials requiring contact with the fluid, resulting in less chemical compatibility. Centrifugal pumps have similar issues, although they are better suited to lower flow rates and higher pressures than axial-flow pumps.[143] One of the main issues with a centrifugal pump is the chemical resistance of the materials in the rotational mechanism, particularly when exposed to aggressive media at elevated temperatures. Positive displacement pumps operate by trapping a volume of liquid and 'displacing' it via some mechanism. The flow rate variation due to pressure differences in positive displacement pumps is minimal because of this mechanism. Positive displacement pumps can be operated at very low flow rates as the pocket of fluid trapped before dispensing can be extremely small (µL) and the rate of dispensing is dependent on the actuation method. Many positive displacement pumps are highly chemically resistant as minimal contact between the actuation mechanism and the fluid is required. In the case of a piston pump only the fluid channel, piston head and check valves. Similarly diaphragm pumps only require the diaphragm, fluid channel and check valves to be in contact with the fluid. A peristaltic pump only requires the tubing to be in contact with the fluid. Positive displacement pumps have consistent flow rates even with multiphase flow. Arguably, the downside of using a positive displacement pump is that the dispensing mechanism means that fluid transfer is not entirely smooth. Some pumps diminish this problem by doubling up the pumping mechanism so as one fluid path is emptied the other fills and vice versa.[144]

The selection of a suitable pump at around 0.1 – 10 ml/min flow rates was undertaken and a number of options were identified. The IWAKI electromagnetic diaphragm pump from the HRP series[145] was a potential candidate because it is capable of flow rates from 0.055 – 38 ml/min, maximum pressures of 2 bar and 4 – 20mA or 1-5V proportional control. Most of the pumps wetted components were highly resistant to chemical attack such as PEEK, PTFE, and PVDF, however there was a slight concern over the valve material – aluminium ceramic which is susceptible to acid attack. Furthermore, there was limited data available for its compatibility with a number of common solvents. Another option was the Biochem Fluidics solenoid operated micropump.[146] The pump is simple in operation requiring a voltage supply that can be switched on or off at specific intervals (on for 250 milliseconds, off for 350 milliseconds) via a relay switch. The highest flow rate the pump can achieve with appropriate material selections was 6ml/min. The maximum pressure the pump could run at was 0.34 Bar which was considered too low for our application. The Williamson 150 series peristaltic pump[147] was also considered as an option. The pump could run up to 90ml/min depending on the inner diameter of the selected tubing. The pump is

controlled with a stepper motor which is an ideal control method for connecting to an Arduino as many hobbyists use stepper motors for robotics applications, therefore there is a wealth of information and components available to make integration easier. There was two issues with this pump, one was having a maximum pressure rating of 1 Bar and the other was the chemical compatibility of the tubing. One of these pumps was tested in the labs with a variety of tubing but none with sufficient chemical compatibility where able to produce a consistent fluid flow. This was likely due to the more chemically inert tubing being much stiffer than its less compatible counterparts and as a result the rotating mechanism that compresses the tubing walls was not producing a seal that could carry fluid from the pump inlet to its outlet. The pump that was selected was the KNF FEM 1.02 diaphragm metering pump.[148] The pumps wetted components are PTFE, FFKM and PVDF which are all highly resistant, although PVDF can be susceptible to swelling in the presence of Acetone at elevated temperatures. The flow rate range is from 0.2 – 20ml/min and has a maximum pressure rating of 6 Bar. The pump is actuated with a bipolar stepper motor which can be controlled with relative ease from an Arduino.

<u>Pump Drive</u>

Stepper motors work by applying current to coils of wire that are at specific angles around a magnetic or iron core. As the coils are activated the magnet rotates in specific step-wise motions. A number of different stepper motor configurations exist such as permanent magnet, variable reluctance and hybrid rotors and 4 pole, 6 pole, 8 pole stator, toothed and untoothed. Stepper motors can also be unipolar or bipolar, unipolar refers to circuitry that only applied one polarity to the coil/s at a time while bipolar can apply negative and positive polarities to different coils in a single instance. Because of this bipolar stepper motors are often seen as more efficient and can produce higher torques but at the expense of more complicated circuitry.[139,141]

Stepper motors move in discrete increments depending on the number of coils, usually in increments of 1.8° meaning 200 individual steps occur per revolution. The step resolution can be further increased by utilizing microstepping. Microstepping makes use of PWM signals to vary the voltage level going to each coil and hence provide smaller changes in angle (Figure 4.14).[139,149] The PWM signal is applied in an approximation of a sine wave and depending on the controller can go into 1/32 microsteps and less. For a 1.8° stepper motor, applying microstepping at 1/32 of a step would result in a step angle of 0.05625° and 6400 steps per revolution.
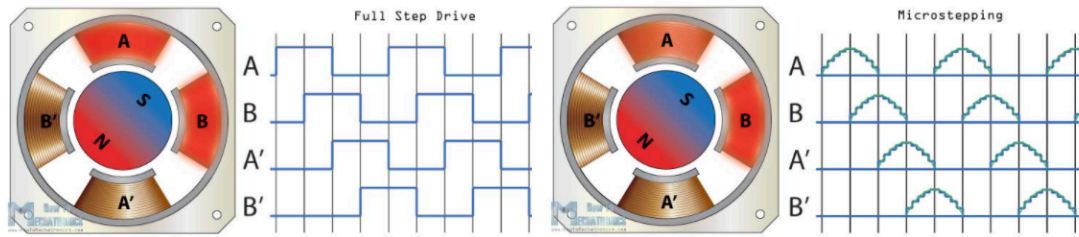
Figure 4.14: a) Full step rotor stator voltage control, b) Microstepping rotor stator voltage control.[149]

The KNF FEM 1.02 uses a 4-wire bipolar stepper motor with 200 steps per revolution, its max rpm is 200. It requires a nominal voltage of 3.52 V and has a maximum current load of 0.6 Amps. A suitable driver was required to run up to five of these pumps simultaneously. The main requirements of the driver were:

- Ease of integration with the Arduino interface.
- Able to provide sufficient current to each motor without overheating.
- Able to change the microstepping size depending on requirements.

The selected driver was the DRV8825 which can be seen in figure 4.15. The driver can supply between 8.2 and 45V to a motor from an external power source and requires a 2.5-5.25 V supply for the logic control system. The driver can draw it's logic power supply from the Arduino but requires an external power source for the stepper motors.[150]
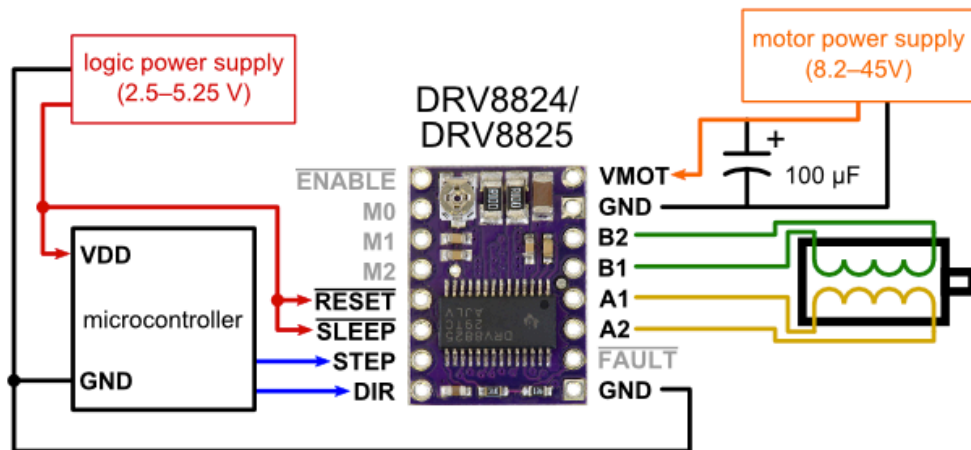
Figure 4.15: Wiring diagram to connect a microcontroller to a DRV8825 stepper motor driver (full-step mode).[150]

To enable multiple drivers to be connected to the Arduino the RepRap RAMPS 1.4 motor shield board[151] was utilized. The board fits five DRV8825 stepper motors and connects directly with an Arduino MEGA 2560 as seen in figure 4.8. A diode (1) is fitted to the 5A power supply input which was removed so that the Arduino is powered by USB and not the RAMPS 1.4 power input, this ensured the Arduino power supply to the conductivity circuit was separate to the motor power supply as it was sensitive to current spikes. The microstepping configuration could be adapted by adding

specific jumper wires located underneath the DRV8825 drivers on the RAMPS 1.4 board as seen in table 4.3.

Table 4.3: Jumper wire configurations

Jumper wire connections			Step Size
MS1	MS2	MS3	
No	No	No	Full step
Yes	No	No	half step
No	Yes	No	1/4 step
Yes	Yes	No	1/8 step
No	No	Yes	1/16 step
Yes	No	Yes	1/32 step
No	Yes	Yes	1/32 step
Yes	Yes	Yes	1/32 step

A 12V, 5A power supply was used which had sufficient current to supply 5 0.6A motors. A variable resistor is located on each DRV8825 and could be manually changed via a potentiometer to a suitable level for the connected motor. The circuit manufacturer recommends setting the reference voltage across the potentiometer to ½ the current rating of the motor – in this case 0.6 A, therefore a reference voltage of 0.3 V was set.[150]

4.4 Liquid-Liquid Separator Automation and Control

In this section the automation and control algorithm developed for the separator is described. The methods used at each stage of development to reach the final control algorithm are discussed and the rationale behind each additional feature are provided. Figure 4.16 presents an overview of what is covered in this section and why it has been included in the separator control algorithm design. As is shown, an on/off algorithm was initially developed, this algorithm provided an initial proof of concept and baselined the design. Hardware issues (such as selecting the right conductance probe) were solved at this stage. A PID controller was then used instead of the off/on algorithm. A number of development stages followed, such as providing a method to initialise the PID setpoint, selecting suitable PID constants and automating the setpoint selection process during operation. Sections 4.4.1 and 4.4.2 will discuss these automation and control algorithms in more detail.

System development	Justification
On/Off control	Simplest level control method – Used for proof of concept and initial system understanding.
PID controller – Setpoint initialisation	The closer the setpoint was to the actual solution conductivity the less variance in valve position was observed.
PID controller – PID constant setting	Optimising the PID setpoint meant a reduction in valve position variance (good for reducing valve/servo wear and providing a smoother flow regime).
PID controller – Setpoint automation	Setpoint setting was automated to ensure if system flow rates and conductivities change, the system will respond accordingly and find a new 'optimum' setpoint.
PID controller – Setpoint automation testing	The setpoint automation algorithm was tested to ensure an appropriate setpoint could be found within a reasonable time frame at different flow rates.

Figure 4.16: Flow chart showing the stages of development of the separator's automation and control algorithm and the justification for each stage of development.

4.4.1 on/off control

The first control scheme developed during testing was an on/off control system. This was the simplest design and required minimal programming. It was predominantly used with the valve control system. The interaction between the control system, sensors and actuators is shown in
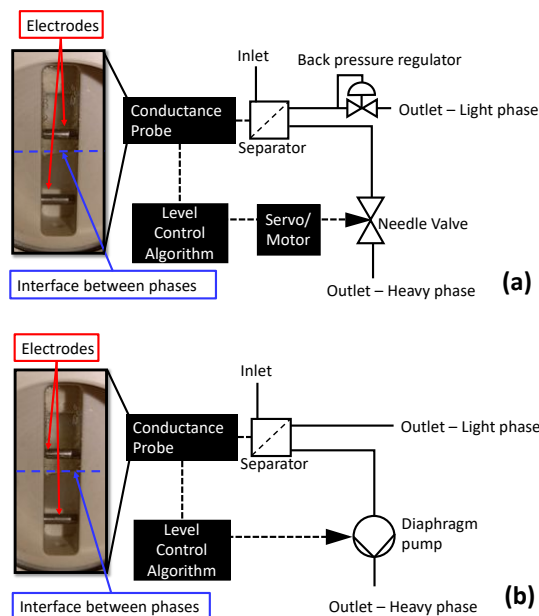
Figure 4.17: P&ID Diagram of (a) actuated valve separator system and (b) pump actuated separator system.

The algorithm code is programmed onto the Arduino Uno which receives conductance measurements from the electrodes situated inside the separator flow cell. If the measured conductance k is above the conductance threshold k_{set} then the valve which is attached to the bottom outlet (heavy liquid phase outlet) is opened and the fluid stream exits the separator via this outlet. If the measured conductance is below the conductance threshold then the valve is closed and the fluid stream exits via the top outlet. By doing this the two liquid phases that have separated into two distinct layers downstream of the filter face will cyclically be removed from the separator. The conductance threshold is a manually set parameter and should be set depending on the conductivity of the aqueous phase. As the valve opened and closed the interface between the two liquids inside the separator would move up and down creating a change in conductivity reading as the interface passed the electrodes. The off/on algorithmic procedure for this control method is shown in figure 4.18.
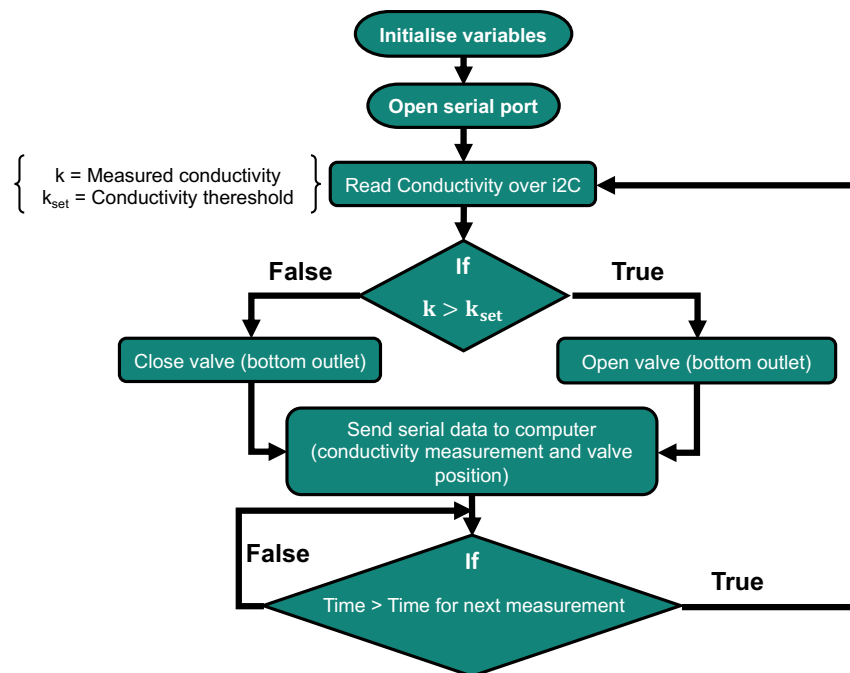
Figure 4.18: Flow chart showing off/on algorithm operational procedure

4.4.2 PID control

<u>PID Theory</u>

The second control scheme tested was a proportional integral derivative (PID) control system. A PID controller is a closed loop system and is made up of three parts. The first part, the proportional control part specifies the amount of actuation required depending on the error in the system. A larger K_p gain value results in a larger change in actuation (pump speed or valve position) per deviation of the conductance measurement from the conductance setpoint (representation of a proportional controller is shown in figure 4.19.[139]
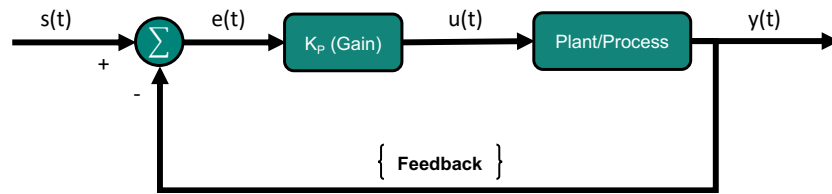
Figure 4.19: Proportional controller feedback loop

Simple proportional controllers can result in steady state errors, which is when the system has reached steady state (fluctuates about a constant measurement value) but this measurement value does match the setpoint value. This occurs in a lot of systems when the measurement value is not a linear relationship as the controller has no way of knowing that an increase in actuation at any given point does not result in the same change in the measurement value as it did at a previous point. That is when the integration part of the PID controller becomes useful. The integration term in a PID controller integrates the error term with respect to time. This results in the PID controller summing the error in the system over time and can therefore respond to correct any steady state errors until the setpoint minus the measured process variable equals 0 (SP – PV = 0). As the integral term gain is increased, the control system tends to resemble an underdamped system as the actuator overcompensates for the deviation from the setpoint and has to perpetually compensate for its own overshoot. To dampen the control system the derivative term of a PID system can be introduced. This is particularly important in systems that require a fast response (e.g large proportional and integral terms). The derivative term calculates the rate of change of the error term and correspondingly reduces or increases the actuator response. This means that as a system approaches its setpoint the derivative path will acknowledge this and reduce the process actuation prematurely in order to avoid overshooting the setpoint. PID control is therefore described by equation 4.4. Figure 4.20 presents the PID control system in a flow diagram. s(t) is the setpoint at time t, u(t) is the PID output. In our system the PID output needs to be converted to a valve position, equation 4.5 does this. Equation 4.5 uses the maximum and minimum valve positions (or pump rates) and a range of conductivities (0 to 2 x PID setpoint) and finding the linear relationship between them. v(t) is the calculated valve position and y(t) is the new conductance measurement at this iteration. This conductance is then compared to the setpoint in the next iteration to calculate u(t) once again.

$$\text{Output} = K_p e(t) + K_I \int e(t)\, dt + K_D \frac{d}{dt} e(t)$$

(4.4)

Where: e = Setpoint – Input

$$v(t) = v_{min} + u(t) \frac{v_{max} - v_{min}}{0 - 2s(t)}$$

(4.5)
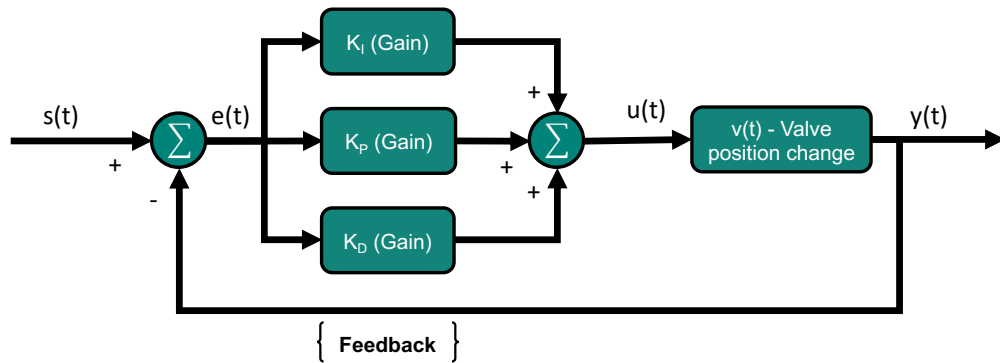
Figure 4.20: PID controller feedback loop

A PID library developed by Beauregard (2011)[152] is available to use with the Arduino software package. This library was utilised with the separator where the setpoint was a conductivity and the system level was controlled by varying the valve position or pump flow rate. Beauregard outlines a number of aspects of the PID controller and how to integrate it effectively:

1. Ensure the PID is being called at regular intervals as this simplifies the integration and derivative calculations.

2. To eliminate 'derivative kick' when the setpoint is changed the derivative of the PID performs the derivative calculation on the measurement value instead of the error value. This can occur because $\frac{de(t)}{dt} = \frac{ds(t)}{dt} - \frac{dy(t)}{dt}$ and at every instant except for when the setpoint is changed $\frac{de(t)}{dt} = -\frac{dy(t)}{dt}$. The result is that the large peak in the derivative term that occurs when a change in setpoint happens is eliminated while mathematically giving the same result at every other point.

3. In the basic PID controller if the gain values are changed while running the controller then issues with the integration term arise. This is because if K_I is changed, the entire integration series is multiplied by a new factor which in turn skews the resultant output $K_I \int e(t)dt \approx K_{I_n}[e_n + e_{n+1}+\dots]$. If the K_I term is brought inside the integral then this problem is eliminated as each change in K_I does not change the K_I values at previous time steps.

4. To avoid 'reset windup' which is what happens when the PID output is above the physical limitations of the controller, output limits are imposed on the PID output and integration term. Reset windup results in a lag between the PID response to the error in the system as the PID thinks it is increasing (or decreasing) the control variable when in reality it has reached its limit and cannot increase (or decrease) any further. Then when the error term changes the PID output has to reduce (or increase) an amount proportional to the

difference between the physical output limit and PID output value before any actual change to the control variable occurs.

5. Ensure the PID is not turned off via adjusting the output to equal 0. This does not stop the PID operating and will result in large jumps in the output once it is turned back on.

PID Tuning

The PID controller was initially integrated into the valve system and the parameters were tuned to best suit the system behaviour (detailed later in this section). The system also appeared to behave more smoothly when the setpoint was close to the conductance value of the aqueous phase and therefore the variance in the output value was determined with relation to the overall conductivity of the aqueous solution and the setpoint. An automation algorithm was then added to the PID controller to automatically set an appropriate setpoint depending on the maximum conductivity measurement.

In order to select appropriate values for the PID constants K_P, K_i and K_d, the flow system shown in figure 4.21 was setup. Tap water (low conductivity) and Toluene were pumped into a series of 3 miniature continuously stirred tank reactors (CSTR's) at 2ml/min each. The two phases are mixed in the CSTR's and then flow into the 2ml separator. The 2ml separator was used without a filter and with the valve-controlled outlet configuration (attached to the aqueous outlet). The valve position and conductivity measurement were continuously monitored in order to determine the deviation of the conductivity from the PID setpoint and the variance in the valve position.

c = Conductivity circuit
S = Sample point
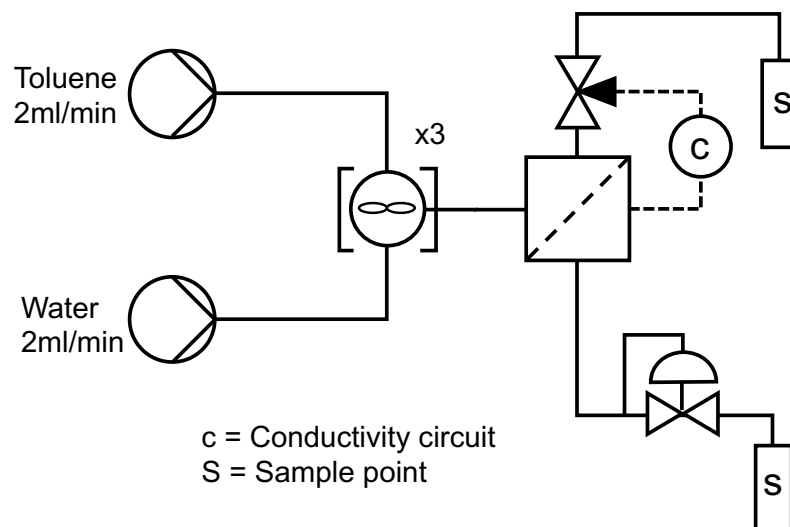
Figure 4.21: Experimental setup for PID tuning tests

Establishing the Conductivity Setpoint

In preliminary experiments it was clear that the valve position varied less when the conductivity setpoint was close to the actual conductivity of the solution. To ensure

that the setpoint was always close to the solutions conductivity value an 'initialisation' procedure was developed:

1. Start PID control with a low setpoint (e.g. 30 µS/cm).

2. Wait until valve position has changed from its maximum position to its minimum position (signifies that the liquid level in the separator has dropped below the conductivity sensor). Also wait long enough for the system to reach steady state.

3. At any point after this, press the 'Automate Setpoint' button which will fully open or close the valve (depending on valve & BPR configuration) allowing the aqueous phase level to increase in the separator. This allows the conductivity probe to become fully submersed in the aqueous phase and therefore provide a value at or close to the actual conductivity of the solution.

4. To ensure that the aqueous phase does not exit the separator via the organic outlet the time that the valve remains open is set so that only a 0.4 ml volume increase of the aqueous phase occurs in the separator (aqueous level is assumed to be at approximately half way up the vessel (1ml volume) at the beginning of the 'automate setpoint' operation and so a maximum aqueous volume of 1.4 ml occurs during this operation (aqueous phase would escape via the organic outlet if it filled the separator to 2 ml volume). The time at which this occurs is calculated by equation 4.6.

$$T = (60 \times V_{Lim})/v_{Aq} \tag{4.6}$$

$\quad T =$ Time $\hfill$ (sec)

$\quad V_{Lim} =$ Additional volume limit $\hfill$ (ml)

$\quad v_{Aq} =$ Flow rate $\hfill$ (ml/min)

5. Once this time period has elapsed the system returns to PID control but with the updated setpoint which is $0.9 \times$ Maximum conductivity measured during the initialisation procedure.

The maximum conductivity was multiplied by a factor of 0.9 to ensure the setpoint was below the maximum conductivity of the solution. If the setpoint is too close to the maximum conductivity then it is possible for the aqueous phase level to increase indefinitely without the PID realising. This procedure was used at the beginning of every experimental run from this point onwards unless otherwise stated, an example initialisation from one case is shown in figure 4.22.
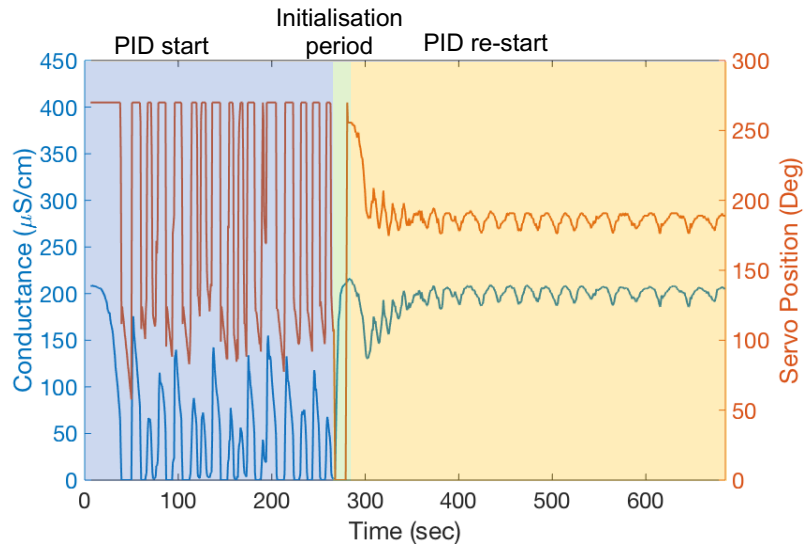
Figure 4.22: Conductivity measurement and valve position before, during and after 'initialisation' procedure.

Identify the PID Variables

Once a consistent method for initialising the setpoint had been devised the PID constants could be optimised to ensure minimal variation occurred in the conductivity measurements and valve position. This was done for two reasons:

1. One was to realise a smoother flow regime throughout the system

2. The second was to reduce wear on the valve over time.

To begin with, the differentiation term in the PID was ignored (K_d = 0). K_d would be experimentally obtained once K_P and K_i were set. K_P was set at either 0.1, 1 or 10 and K_i was set at either 0.01, 0.1, 1 or 10 resulting in 12 experiments in total. The standard deviation of the valve position and the conductance was calculated over a sample size of 200 points during the PID re-start period for each K_P and K_i combination. A surface plot of the standard deviation of the conductivity measurements and the valve positions over the sample period are presented in figures 3.23 (a) and (b).
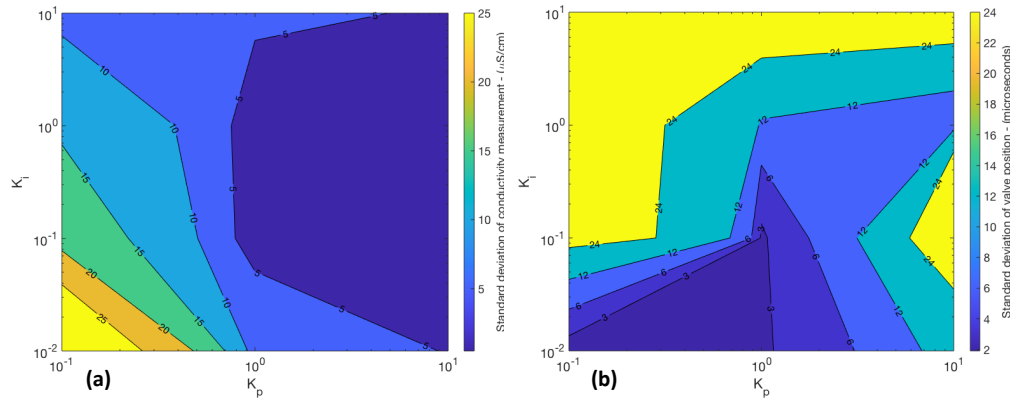
Figure 4.23: Standard deviation of (a) conductivity measurement and (b) valve position depending on K_P and K_i.

Figure 4.23 (a) shows that increasing K_P from 0.1 to 10 generally reduced the standard deviation of the conductivity and at lower K_P values increasing K_i from 0.01 to 10 reduced the standard deviation. Figure 4.23 (b) shows that the standard deviation of the valve position was lowest when K_P was between 0.1 and 1 and K_i was less than 0.1. It was more important to have minimal valve position standard deviation as this reduced the mechanical wear on the servo motor but also resulted in a smoother flow at the aqueous and organic outlets. To reach a suitable compromise between minimising the conductivity variance and the valve position variance a K_P value of between 0.5 and 2 and a K_i value of 0.05 was selected. At this point the variation in the conductivity was between 5 and 10 and the variation in the valve position was approximately 3.

The K_d constant was now introduced. K_P was set at either 0.5, 1 or 2. K_i was fixed at 0.05 and K_d was set at either 0.1, 0.5 or 1. A reduction in both the conductivity and valve position standard deviation were achieved by introducing the K_d constant. The conductivity standard deviation (figure 4.24 (a)) was reduced the most between K_P values of 1 and 2 and K_d values of 0.5 and 0.9. The valve position standard deviation (figure 4.24 (b)) was reduced the most between K_P values of 0.5 and 1.2 and K_d values of 0.6 and 1. The PID constant were therefore set at K_P = 1, K_i = 0.05 and K_d = 0.5. K_d was the only constant that wasn't set at its theoretical optimum (although the difference was marginal – Valve standard deviation = 2.5 compared to 2). This was done to limit the effect the differential term has during less-than-optimal conditions such as when the setpoint is low, or high flow rates are required. Under these conditions, the gradient of the conductivity measurements can become very large in which case K_d increases the valve position response by a large amount resulting in overshoot of the valve position and unstable PID behaviour. These PID parameters were also set on the pump system and was found to give a reasonably

smooth response with variation in pumping flow rate of 0.0553 ml/min and a variation in conductance of 2.54 at a total flow rate of 4 ml/min.
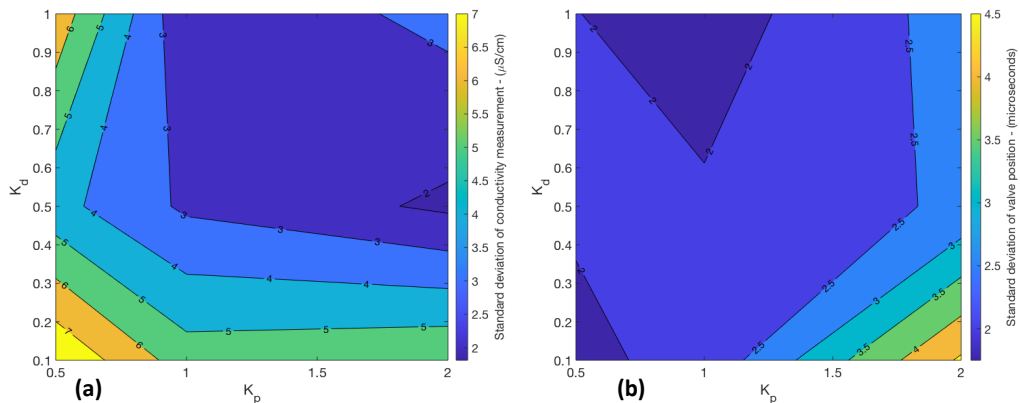
Figure 4.24: Standard deviation of (a) conductivity measurement and (b) valve position depending on K_P and K_d.

PID setpoint automation

Now that the PID constants were set, the effect of flow rate and setpoint on the variance of the valve position could be investigated. The same setup was used as shown in figure 4.21 and the setpoint was incrementally changed in relation to the maximum conductivity of the solution. Two solutions were tested, a 'low conductivity' solution and a 'high conductivity' solution and two flow rates were tested, 4 ml/min and 16 ml/min both at a phase ratio of 1 (Table 4.4).

Table 4.4: Summary of experiment conditions to investigate variance in valve position depending on flow rate and solution conductivity.

Flow rate (ml/min)	Low Conductivity solution (µS/cm)	High Conductivity solution (µS/cm)
4	129.3	9396
16	182.6	8750

To compare the results from each of these experimental runs, the setpoint was normalised with respect to the solution conductivity and plotted on figure 4.25. The pumping system had a different response to a change in flow rate or conductivity compared to the valve system. The pump rate standard deviation is shown in figure 4.26.
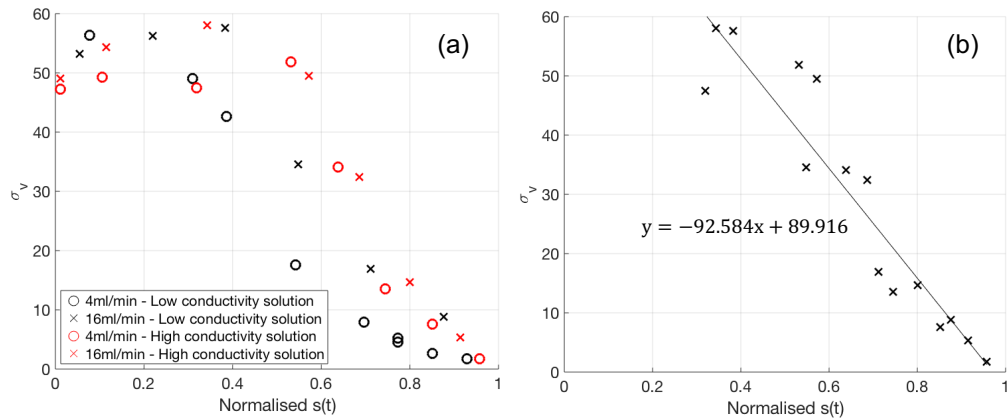
Figure 4.25: Standard deviation of the valve position at different PID setpoints depending on the flow rate and solution conductivity. (b) Linear relationship between standard deviation of valve position and PID setpoint above Normalised s(t) = 0.3 and discounting the 4ml/min low conductivity solution run.
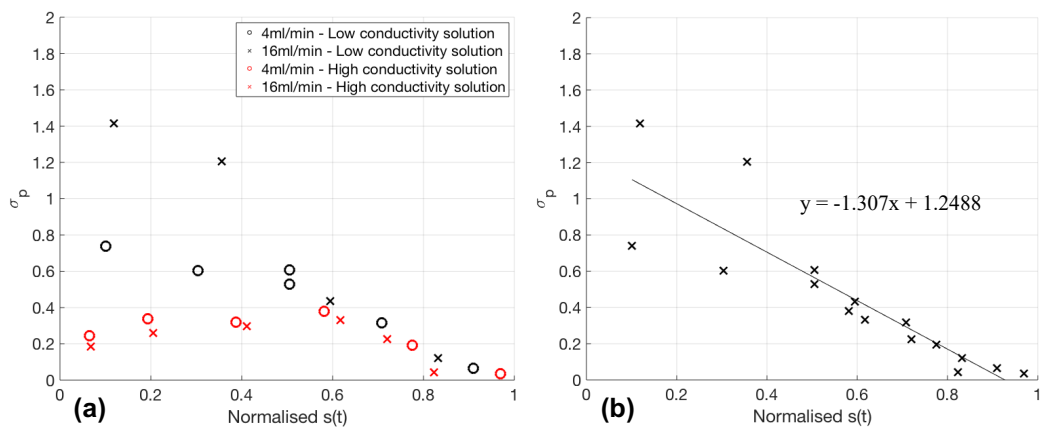
Figure 4.26: (a) Standard deviation of the pump flow rate at different PID setpoints depending on the flow rate and solution conductivity. (b) Linear relationship between the standard deviation of pump rate and normalised PID setpoint of the low conductivity solution.

From figure 4.25 (a) it is clear that there was a negative correlation between a normalised conductivity setpoint of 0.3 and 1 and the standard deviation of the valve position. Below 0.3 the standard deviation remained relatively constant – suggesting that below a setpoint of 0.3 the valve was opening and closing between its maximum and minimum positions resulting in the same standard deviation across this range. The linear relationship between a normalised setpoint of 0.3 and 1 was used to predict the amount a setpoint should be adjusted to reduce the variance in the PID output to a reasonable value for a given flow rate. Equation 4.7 defined the linear relationship between the normalised setpoint and valve position standard deviation. Figure 4.25 (b) shows the trend line plotted on the data from figure 4.25 (a) without the points acquired at setpoint below 0.3. The 4 ml/min low conductivity solution points were also excluded from figure 4.25(b) as that set of experiments generally produced lower variance than the other experimental runs and it was preferable to

get a relationship that represented the 'worst case' scenario. Figure 4.26 (a) shows the pump response to a change in setpoint or conductivity. It can be observed that the pump flow rate standard deviation was lower when the conductivity was high compared to when it was low, at normalised setpoints less than 0.5. Above this setpoint the standard deviation was very similar. Like the valve system, a trend line was fitted to the data. The high conductivity solution data was ignored below a normalised setpoint of 0.5. This was done to provide a 'worst case scenario' relationship between the pump standard deviation and normalised setpoint. The linear relationship for the pump system is given by equation 3.8 and is plotted on figure 4.26 (b).

$$\sigma_V = -92.6 S_{Norm} + 89.9 \qquad (4.7)$$

$\sigma_V = $ Valve position standard deviation

$S_{Norm} = $ Normalised PID setpoint $\qquad$ (µS/cm)

$$\sigma_p = -1.307 S_{Norm} + 1.2488 \qquad (4.8)$$

$\sigma_p = $ Outlet pump flow rate standard deviation

To determine what constituted as a sensible value for the standard deviation of the valve position, a series of experimental runs were performed at various flow rates for the two conductive solutions. The setpoint was set with the initialisation procedure described above and the standard deviation of a sample period was obtained. The standard deviation value found during this sample period was considered as 'sensible' as it was a value found with a setpoint close to the maximum conductivity of the solution but not so close that the PID might allow the aqueous phase to pass through the organic outlet.

The separator was tested at 1, 4, 8, 12 and 16 ml/min with and without a filter inserted in the separator. The results from these experimental runs are shown in figure 4.27 (a) for the valve system and (b) for the pump system. It was clear that the inclusion of the filter media meant that the standard deviation of the valve position at higher flow rates (above 8 ml/min for low conductivity solutions and above 4 ml/min for high conductivity solutions) increased, while without filter media the standard deviation reached a plateau at $\sigma_V = 6$ and $\sigma_V = 3$ respectively. A maximum and minimum acceptable limit for the standard deviation of the valve position could then be selected. As the rate of change of the liquid level in the separator is only dependent on the aqueous flow rate the equations that defined the upper and lower limits were calculated based on only the aqueous flow rate (i.e. half of the total flow rate). Equations 4.9 and 4.10 calculate the upper and lower limits that were set for

the valve standard deviation depending on the aqueous flow rate. The lower limit had all of the points in figure 4.27 (a) above it and the upper limit had all of the points on figure 4.27 (a) below it. The pump system did not show a clear difference between no filter or filter use or low or high conductance solution. The system did however show a general increase in standard deviation as flow rate increased. The selected standard deviation limits for the pump system are given by equations 4.11 and 4.12
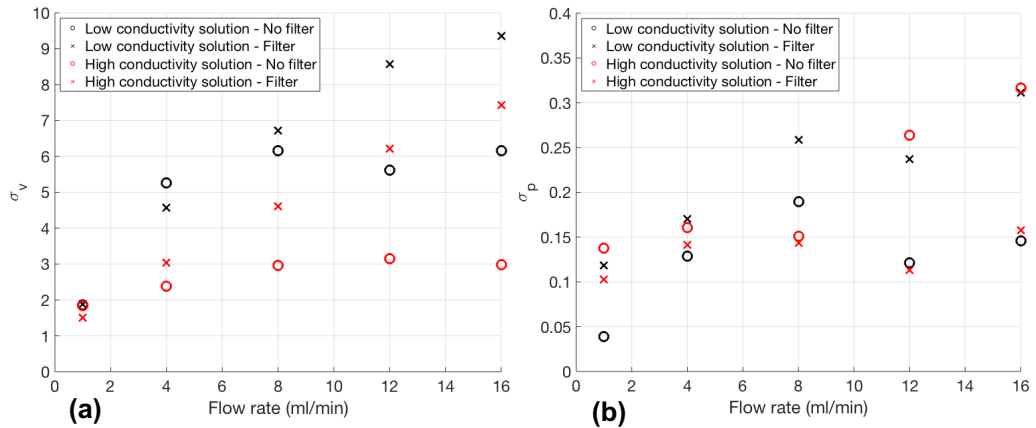
Figure 4.27: (a) Standard deviation of valve position and (b) standard deviation of pump flow rate depending on flow rate and if a filter was used in the separator.

$$\sigma_{up} = 0.733v_{Aq} + 8.133 \tag{4.9}$$

$$\sigma_{low} = 0.16v_{Aq} + 0.122 \tag{4.10}$$

v_{Aq} =   Aqueous flow rate   (ml/min)

σ_{up} =   Valve position standard deviation upper limit

σ_{low} =   Valve position standard deviation lower limit

$$\sigma_{up} = 0.02v_{Aq} + 0.19 \tag{4.11}$$

$$\sigma_{low} = 0.07 \tag{4.12}$$

v_{Aq} =   Aqueous flow rate   (ml/min)

σ_{up} =   Pump flow rate standard deviation upper limit

σ_{low} =   Pump flow rate standard deviation lower limit

One more instance that needed to be considered was if the setpoint automation algorithm calculates a new setpoint that is above the solutions maximum conductivity. If this occurs the system needs to recognise this and reduce the setpoint accordingly. It was found that when the setpoint was above the maximum conductivity of the solution, σ_c would be less than when the setpoint was below the maximum solution conductivity. Figure 3.28 shows the σ_c for the different cases run during earlier tests and what happened at different flow rates when the setpoint was increased above the solution maximum conductivity. In figure 4.28, σ_c was divided by the setpoint to

make the different conductivities of the solutions comparable. This meant that a single equation for any solution with any conductance that was below the lower acceptable limit of σ_c could be used to adjust the setpoint. If this occurred the setpoint would be set at 0.3 x Current conductance. The new setpoint was set a lot lower than the current conductance for two reasons. If during an optimisation routine the solution conductance was dropping significantly a larger drop in conductivity would be necessary and it was more efficient to do that in one large step than many small steps. Secondly, if the system cannot reach the setpoint then the aqueous phase will pass through the organic outlet. It is therefore beneficial to cut the setpoint dramatically if this is in danger of happening and then allow the system to work back up to a reasonable setpoint. The equations found during these experiments were used to set up the automation logic diagram found in figure 4.39. The lower conductivity standard deviation limit equation for the valve system was y = 0.0022x + 0.0077 and for the pump system was 0.0025x + 0.045 (as shown in figures 4.28 (a) and (b)). It can be seen in figure 4.28 (a) that there is a clear distinction between the conductivity variance when the setpoint is above the conductivity of the solution and when it is not. The pump system shown in figure 4.28 (b) however does not show as clear a distinction as multiple points with a setpoint below the solution conductivity exist below the imposed limit. As a result, the conductivity limit is not as effective in the pump system as it is in the valve system at reacting to changing conductivities. However, the pump system was still capable of maintaining a reasonably smooth flow rate. The variance in the pump system was therefore maintained at a value that cut off some lower standard deviation setpoints that would produce a smooth flow rate. However, this was deemed acceptable as the alternative is potentially letting crossover of one phase into the others outlet.
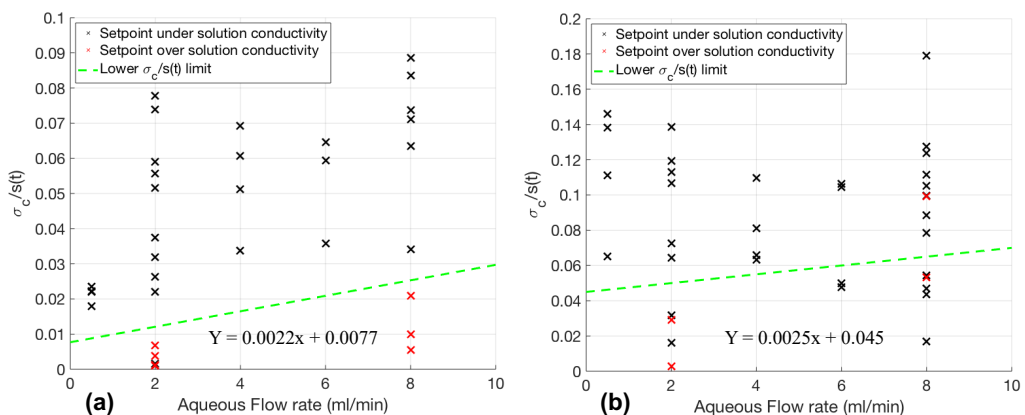
Figure 4.28: How $\sigma_c/s(t)$ changes depending on flow rate and whether the setpoint is greater or less than the solution maximum conductivity. The applied $\sigma_c/s(t)$ lower limit is shown by the green dashed line. (a) valve actuated system (b) pump actuated system.

Setpoint automation flow chart

Introducing these limits allowed an additional control to be implemented into the PID controller so that after initialising the setpoint, the system would periodically check the standard deviation of the valve system and adjust the setpoint if it was outside of its defined limits. This is particularly useful for lab-scale applications as the parameters of the system can be changed frequently during an optimisation or Design of Experiments (DoE) and as a result the conductivity of the solution may change during experimental runs. The control algorithm produced by introducing these standard deviation limits is shown in the flow chart of figure 4.29.
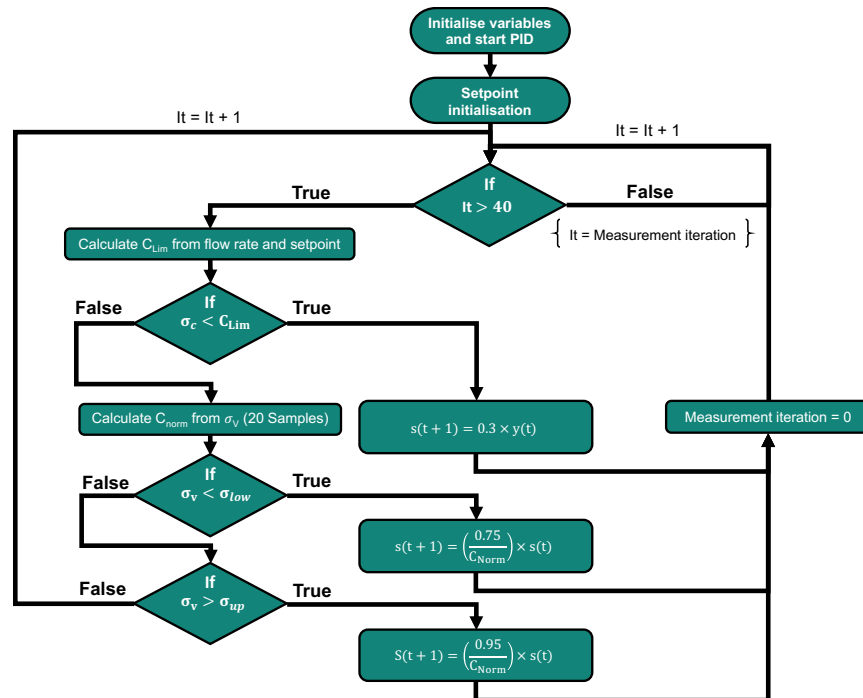
Figure 4.29: Logic diagram of the control algorithm used to automatically adjust the PID setpoint over time.

Setpoint automation testing

To test the automated setpoint adjustment algorithm the separator was set up according to figure 4.21. Toluene and low conductivity tap water were pumped through the system at 2 ml/min each. After a period of time the tap water was switched with higher conductivity water (added NaCl) until a new stable setpoint was reached, the aqueous phase was switched back to tap water and the algorithm re-adjusted the setpoint to a lower value suitable to the conductivity of the solution. Figure 4.30 shows how the setpoint changed according to the valve position and solution conductivity at 4 ml/min. When the aqueous phase was switched to a high conductivity solution at just over 500 seconds the variation in valve position increased dramatically. The change in valve position variance meant that $\sigma_v > \sigma_{up}$ was true and therefore the conductivity setpoint was increased. This repeatedly occurred for approximately 600 seconds until a setpoint of 7156 µS/cm was reached. At this point

the valve position variation had reduced enough so that $\sigma_v > \sigma_{up}$ was no longer true and the setpoint was deemed acceptable. The aqueous phase was switched back to the low conductivity solution at 1750 seconds. Over the next 500 seconds $\sigma_c < C_{Lim}$ and $\sigma_v < \sigma_{low}$ were true at different points which reduced the setpoint until a setpoint of 300 was reached. Figure 4.31 shows a similar response but at 16 ml/min. At 16 ml/min the variance in the system is generally higher and as a result automation is more challenging. We can see that the system changed the setpoint 6 times in the 10 minute period in which the high conductivity solution was used. Nevertheless, the conductance and valve position variation was kept in check during this period and no crossover of phases was seen. The response to a change in conductivity that the algorithm gave demonstrated its successful implementation and the ability to adjust the PID setpoint automatically without any manual intervention.
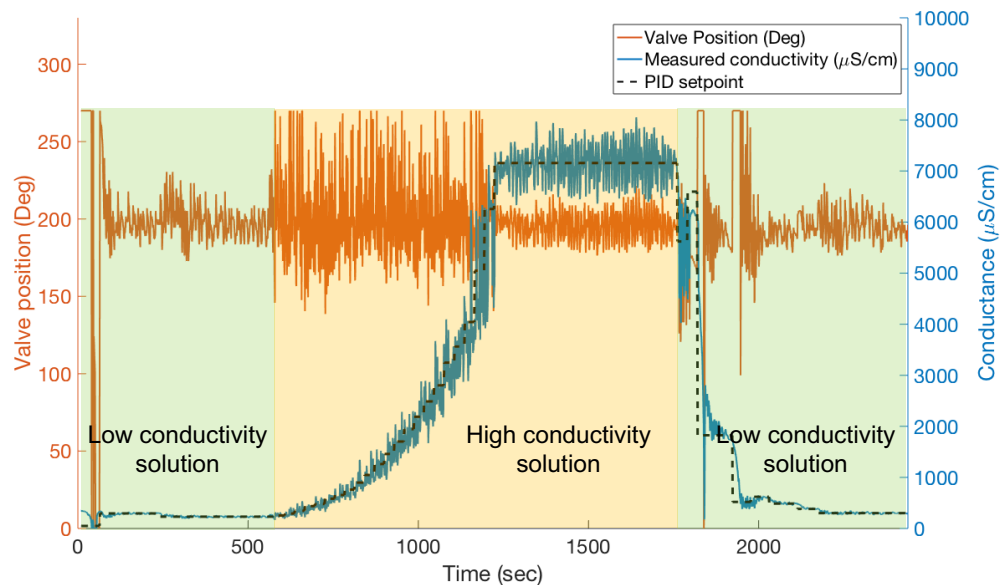
Figure 4.30: Change in setpoint over time at 4 ml/min depending on the conductance of the aqueous phase. Left axis – Valve position plot over time. Right axis – Measured conductance in the separator over time and the setpoint determined by the automation algorithm.
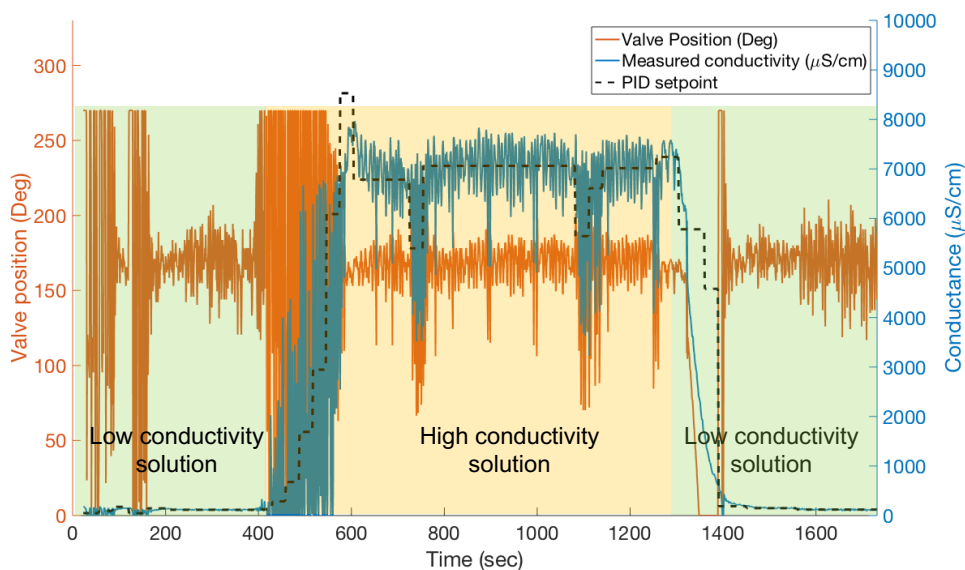
Figure 4.31: Change in setpoint over time at 16 ml/min depending on the conductance of the aqueous phase. Left axis – Valve position plot over time. Right axis – Measured conductance in the separator over time and the setpoint determined by the automation algorithm.

4.5 Summary

This chapter focused on the design and development of an automated separator for continuous flow chemistry use. The device had a small 2 ml volume, was 50 mm in diameter and 50 mm in length, suitable for lab-scale use. The device was predominantly made from chemically resistant PEEK material and could be mounted on a steel baseplate. The device utilised coalescing filter media to separate liquid phases and an automated control scheme to maintain constant separation. Two control methods have been presented; a pump controlled outlet system and a valve controlled outlet system. Both systems utilise Arduino hardware and conductivity measurements.

The control system was initially tested with a simple on/off control system but was later switched to a PID control scheme. The PID constants were selected after experimentally determining which set of constants resulted in the lowest standard deviation conductance measurement and valve position. The system was then tested at different setpoints, flow rates, conductivities and with or without filter media. The response of the system to a change in these parameters provided a framework around which an automation routine was developed. The automation routine changed the setpoint of the system depending on the variance in the valve

position/pump rate and conductance measurement. The automatic setpoint adjustment algorithm was integrated into the PID control scheme and was demonstrated at 4 ml/min and 16 ml/min.

As a result of the work completed in this chapter a new piece of separation equipment has been developed which can separate liquid-liquid systems in continuous flow and can automatically adjust its control parameters to different system conductivities. This means it can easily be integrated into lab-scale screening experiments and optimisations without manual intervention between experimental points. In the next chapter, the performance of the separator will be under investigation depending on the system flow rate, phase ratio and liquid-liquid systems in use. The device will be compared to a commercially available membrane separator.

Chapter 5 – Performance Comparison Between a Liquid-Liquid Separator Utilising Coalescing Filter Media and a Commercial Membrane Separator

5.1 Introduction

In this chapter, results from characterising the coalescing filter media and a method for tuning its hydrophobicity are presented. The separator that was described in chapter 4 has been compared to a commercial membrane separator commonly used for lab-scale separations and extractions – the Zaiput.[23] The separators were tested with different liquid-liquid systems consisting of pure organic and aqueous phases at different flow rates and phase ratios. The properties of the liquid phases have been considered during the subsequent analysis, along with the different wettability of the filter media. The separators ability to break an emulsion has also been investigated and the influence varying the number of filter media layers has on the separator's performance has been studied. The aim of comparing the separator to the commercially available separator was to demonstrate the separators performance against a benchmark system. The separator was also tested with and without any filter media which allowed a comparison of the performance of the coalescing filter media against a purely gravity based system.

5.2 Filter media characterisation

Many different materials have been employed to act as coalescing filters, including thermoplastics such as polyurethane, polypropylene and polybutylene terephthalate (PBT), glass fibres[27,28,31-35] and in the case of aerosol coalescers - steel meshes.[36] Each of these filter materials are formed into nonwoven fabrics. Nonwovens are defined as a sheet or web of entangled fibres with random orientation, they can be mechanically, thermally or chemically bonded and are not weaved or knitted into a repeating structure.[37] Most nonwovens used for coalescing filtration are formed via melt-spinning processes and have high porosities and permeabilities, with median pore sizes in the 10µm range and a highly tortuous fluid path through the media depth.[38] The nonwoven material used in this study was a meltblown PBT provided by Mogul Co. The manufacturer supplied weight, thickness and air permeability data is reported in table 5.1. A number of standard techniques have been used to characterised the filter media. In section 5.2.1 to 5.2.6: (i) the area density (grams per square metre - GSM), (ii) the filter media thickness, (iii) air permeability and

intrinsic permeability, (iv) porosity, and (v) pore size distribution is measured. A method to treat the filter media to make it more hydrophilic is described in section 5.2.7 alongside semi-quantitative measurement of the hydrophobicity of the filter media.

Table 5.1: Manufacturer provided weight, thickness and air permeability data of melt-blown PBT sample

	Lower Limit	Target	Upper Limit
Weight (g/m^2)	36	40	44
Thickness (mm)	0.3	0.4	0.5
Air Permeability (L/m2.s @125 PA)	750	920	1050

5.2.1 Area density measurement (GSM)

Ten samples were used for the area density measurements. Area density was measured by modifying BS EN 29073-1:1992[153] by testing ten 5x25cm rectangles which gave a total area of 12500 mm^2 rather than the recommended 50000 mm^2 due to availability of material. Five of the samples were cut in the machine direction (MD) and 5 in the cross direction (CD). The samples were left for an hour to acclimatize to the environment which was at standard atmospheric conditions for textile testing (described in BS EN 20139:1992[154]). The measured sample weights and resultant GSMs can be found in table 5.2. The Mean GSM value for both the machine direction samples and the cross-direction samples is 40.42 ± 0.8 g/m^2.

Table 5.2: Measured weight and calculated grams per square metre (GSM) of melt-blown PBT sample

Machine Direction			Cross Direction		
Sample No	Weight (g)	GSM (g/m^2)	Sample No	Weight (g)	GSM (g/m^2)
1	0.514	41.12	1	0.513	41.04
2	0.49	39.2	2	0.505	40.4
3	0.508	40.64	3	0.495	39.6
4	0.502	40.16	4	0.507	40.56
5	0.496	39.68	5	0.523	41.84
Mean:	0.502	40.16		0.5086	40.688

5.2.2 Thickness

The sample thickness measurement method was adopted from BS EN 29073-2:1992.[119] The thickness of textiles is measured while a specified mass is placed on top of it. This is to compress loose strands that may give a larger thickness measurement than is actually the case. For 'normal nonwovens' (non-bulky) a

pressure of 0.02 kPa is sufficient to compress the nonwoven and measure the thickness. The presser foot had a diameter of 80 mm and area of 5026mm^2 (twice as much as the recommended area). A total pressure force of 97.58 Pa was applied to the nonwoven (50 g mass attached to pressure foot). The sample thickness was measured 10 times at random locations across its 1m^2 surface. The measured thickness, mean and standard deviation is given in table 5.3.

Table 5.3: Melt-blown PBT sample thickness measurements

Pressure foot weight (g):	50
Sample number	**Thickness (mm)**
1	0.42
2	0.4
3	0.44
4	0.4
5	0.43
6	0.42
7	0.44
8	0.43
9	0.41
10	0.43
Mean:	**0.422**
Standard deviation:	**0.0148**

5.2.3 Air permeability

The air permeability which is a measure of how easily a fluid (air) can pass through a material was measured with modification of BS EN ISO 9073-15:2008[155] using a FX 3300 LabAir IV. A 5cm^2 circular test area was measured and the vacuum pump pressure was set at 125 Pa. Eight samples from the 1m^2 sample were measured and the mean and standard deviation of the sample measurements has been presented in table 5.4. In BS EN ISO 9073-15:2008[155] air permeability is expressed in litres per square centimetre per second (l/cm^2.s). In this text l/cm^2.s will be converted to the equivalent unit m/s.

Table 5.4: Melt-blown PBT air permeability measurements

Test pressure (Pa):	125
Test area (cm^2):	5

test no	Air permeability (m/s)
1	0.888
2	0.786
3	0.975
4	0.819
5	0.1210
6	0.901
7	0.932
8	0.973
Mean:	935
Standard deviation:	129.67

The intrinsic permeability of the sample was calculated using Darcy's Law (equation 5.1) which describes the flow of fluid through a porous medium. The intrinsic permeability of the PBT sample was calculated to be 5.74×10^{-11}m^2 using the mean air permeability value given in table 5.4.

$$k = \frac{U\mu t}{\Delta p} \qquad (5.1)$$

$k =$	Intrinsic permeability	(m^2)
$U =$	Air permeability (air velocity)	(m/s)
$\mu =$	Air viscosity	(Pa.s)
$t =$	Media thickness	(m)
$\Delta p =$	Pressure drop across the sample	(Pa)

The air permeability of the filter media when it was stacked to create a thicker filter was also measured. 10 different samples to those used to measure the air permeability of the PBT filter media were used for this test. 1 – 10 layers of the samples were tested and the air permeability along with the thickness of the layered media and the calculated intrinsic permeability of samples is shown in table 5.5.

Table 5.5: Air permeability of the PBT nonwoven filter media when layered.

number of filter layers	thickness (mm)	air permeability (m/s)	intrinsic permeability (m^2)
1	0.4	842	4.88 x 10^{-11}
2	0.8	408	4.73 x 10^{-11}
3	1.2	285	4.95 x 10^{-11}
4	1.6	212	4.91 x 10^{-11}
5	1.95	173	4.88 x 10^{-11}
6	2.38	143	4.93 x 10^{-11}
7	2.75	124	4.94 x 10^{-11}
8	3.12	107	4.83 x 10^{-11}
9	3.5	92.8	4.70 x 10^{-11}
10	3.9	83.1	4.69 x 10^{-11}

Table 5.5 shows that the air permeability reduces as more layers are stacked and the reduction in air permeability is less with each additional layer. Multiplying each air permeability value by the number of filter layers used gives a mean value of 847.42 ± 16.37. Multiplying each air permeability value by the media thickness gives a mean value of 334.58 ± 6.96 which is effectively a constant. The path that the air has to flow through will become longer and more tortuous as more layers are added, resulting in the reduction in air permeability. The intrinsic permeability stays very similar as more layers are added as this is intrinsic to the material structure. This suggests the interface between layers has an insignificant effect on the intrinsic permeability of the samples but the gross thickness controls the air permeability of the sample.

5.2.4 Porosity

The porosity is a measure of how much void space is in a sample. It was calculated from the mean values of area density (GSM) and thickness found in sections 5.2.1 and 5.2.2 using equation 5.2 and knowing that the density of PBT is 1310 kg/m^3. The porosity was calculated to be 92.7 %.

$$\emptyset = \left[1 - \left(\frac{\text{GSM}}{\rho t}\right)\right] \times 100 \qquad (5.2)$$

$\emptyset =$	Porosity	(%)
$\rho =$	Density of PBT	(g/m^3)
GSM $=$	Grams per square metre of sample	(g/m^2)

5.2.5 Pore size characterisation

The mean flow pore size and cumulative pore size distribution was found using a POROLUX 100FM. The mean flow pore size and pore size distribution test uses the known relationship between the surface tension of a liquid in contact with a wall and the radius of a tube in which the fluid resides (capillary pressure equation – equation 5.3). In the mean flow pore test, the filter media is soaked in a liquid that completely wets it and air is forced through the filter at an increasing pressure until the first flow of gas is detected through it. This point represents the point at which the exerted pressure was high enough to overcome the capillary pressure in the largest pore in the filter media. After this point the pressure is steadily increased and the flow rate is measured until a predetermined pressure is reached.

$$\gamma = \frac{h\rho gr}{2\cos(\phi)B} \tag{5.3}$$

$\gamma =$	Surface tension of test liquid	(mN/m)
$h =$	Height of rise	(m)
$\rho =$	Density of fluid	(kg/m^3)
$g =$	Acceleration due to gravity	(m/s^2)
$r =$	Radius of tube	(m)
$\phi =$	Contact angle between liquid and pore wall material	(°)
$B =$	Capillary constant	

The relationship between the pressure across the filter media and the diameter of the filter pores can then be obtained by adapting equation 5.3. The pressure across the filter media is equivalent to $h\rho g$, the radius is changed to a diameter and the Capillary constant is replaced with a 'shape factor' which relates to the shape of the pore structure. This gives us the 'Washburn equation' (equation 5.4). For most filter membranes the shape factor is selected as 0.715, The POROLUX 100FM uses this value as standard. The fluid used to wet the filter media was 'Galpore' with a surface tension of 19 Dyne/cm. The contact angle between this fluid and the membrane material was assumed to be 0 and therefore $\cos(\phi) = 1$ in equation 5.4.

$$d = \frac{4S\gamma\cos(\phi)}{P} \tag{5.4}$$

$d =$	Diameter or pore	(m)
$S =$	Shape factor	

In order to determine how much of the air passes through each pore size a 'dry run' of the test is also required. The pressure-flow rate curves produced by the wet

and dry runs are analysed using equation 5.5 to determine the % air passed between two specified flow rates (which correspond to two specified pore sizes).

$$Q = \left[\left(\frac{\text{wet flow}_h}{\text{dry flow}_h}\right) - \left(\frac{\text{wet flow}_l}{\text{dry flow}_l}\right)\right] \times 100 \qquad (5.5)$$

$Q =$ Percentage of flow passing through the specified pore size range   (%)

$l =$ Lower limit

$h =$ Upper limit

The pore sizes of the filter media have been plotted against the percentage of flow passing through that specified pore range. The cumulative flow percentage has been plotted on the same graph (figure 5.1). The results from the other 4 samples are shown figures 5.2 – 5.5. The mean flow pore size is defined as the pore size at which 50% of the fluid that can flow through the filter does. All pores smaller than the mean flow pore size will be blocked by the wetting liquid and all pores larger than this size will be open to air flow. The mean pore size distribution was measured according to ASTM F316 – 03 (2011)[120] and averaged across five samples. The mean flow pore size, smallest pore size and largest pore size for each sample are given in table 5.6.
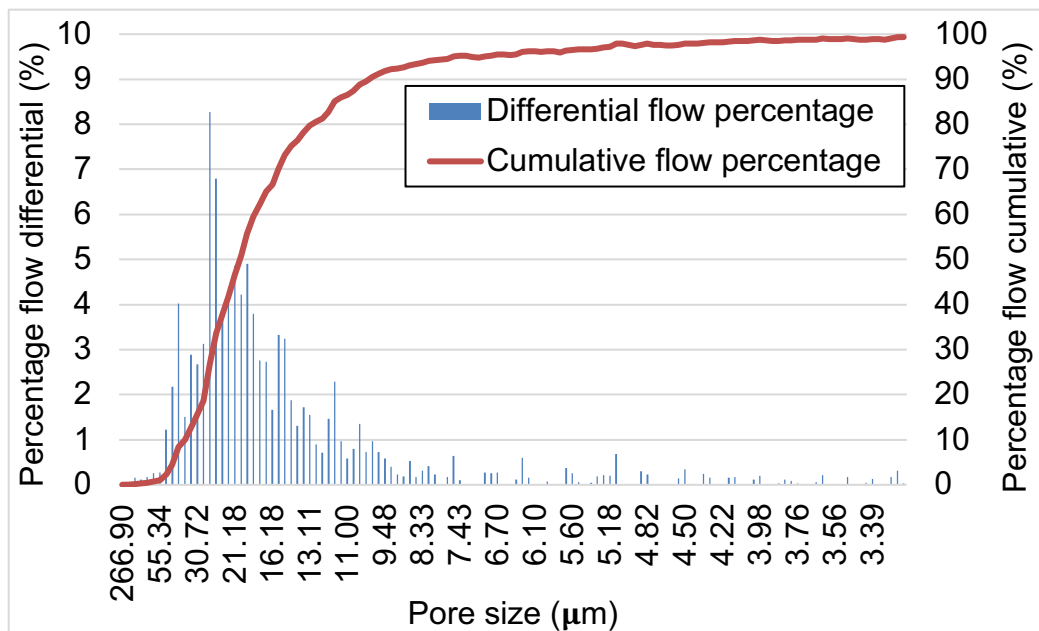
Figure 5.1: Cumulative and differential percentage flow of sample 1.
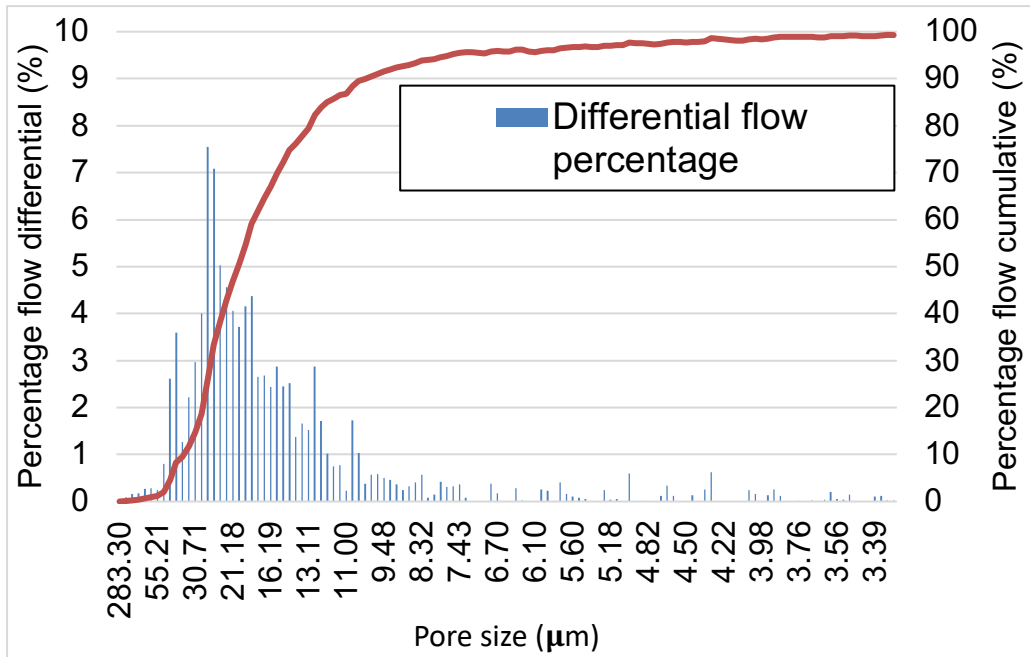
Figure 5.2: Cumulative and differential percentage flow of sample 2
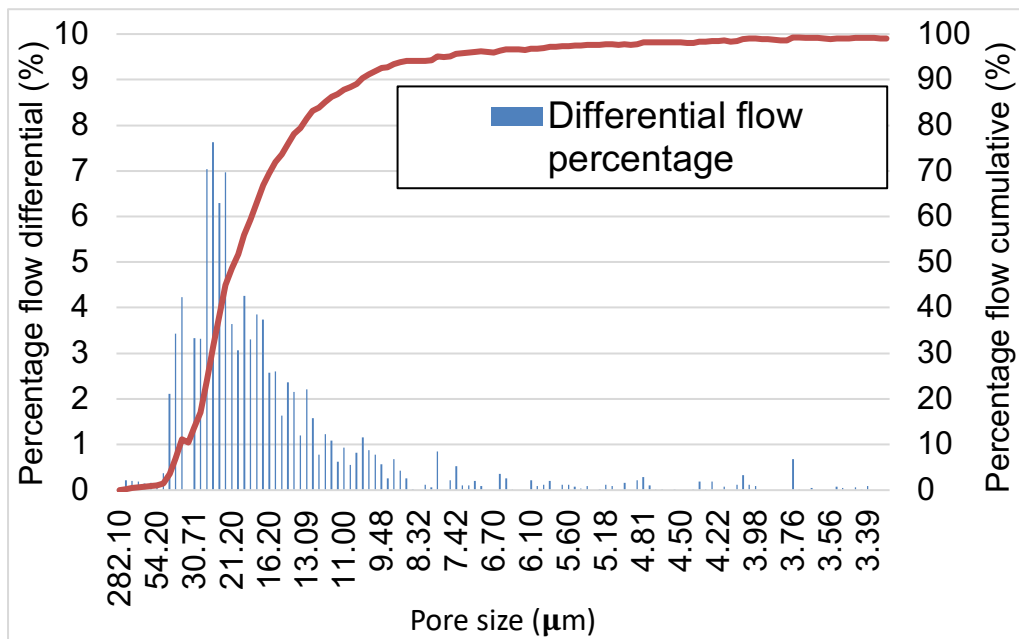
Figure 5.3: Cumulative and differential percentage flow of sample 3
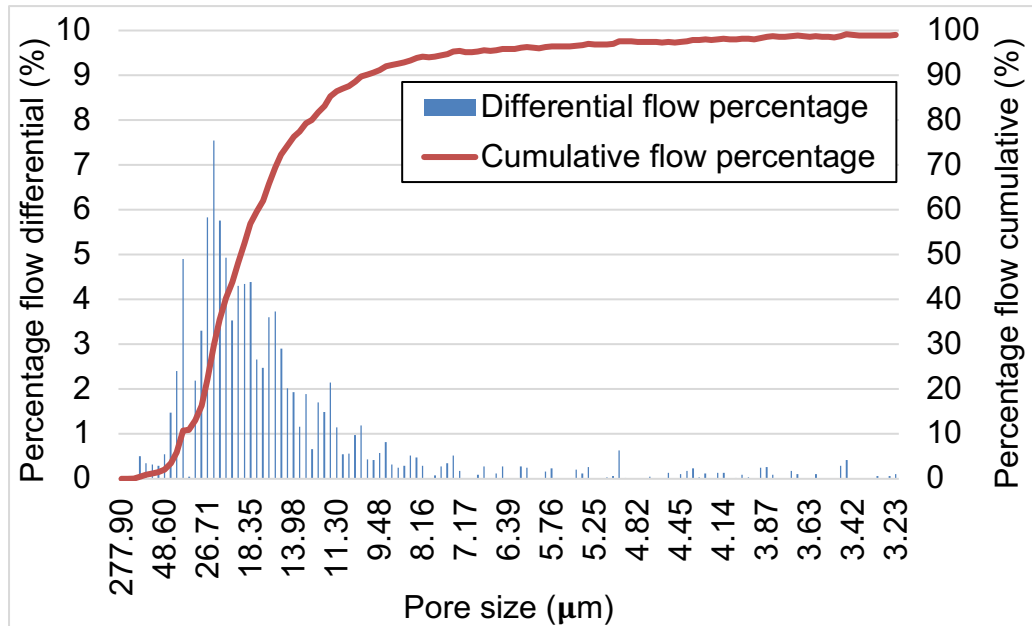
Figure 5.4: Cumulative and differential percentage flow of sample 4
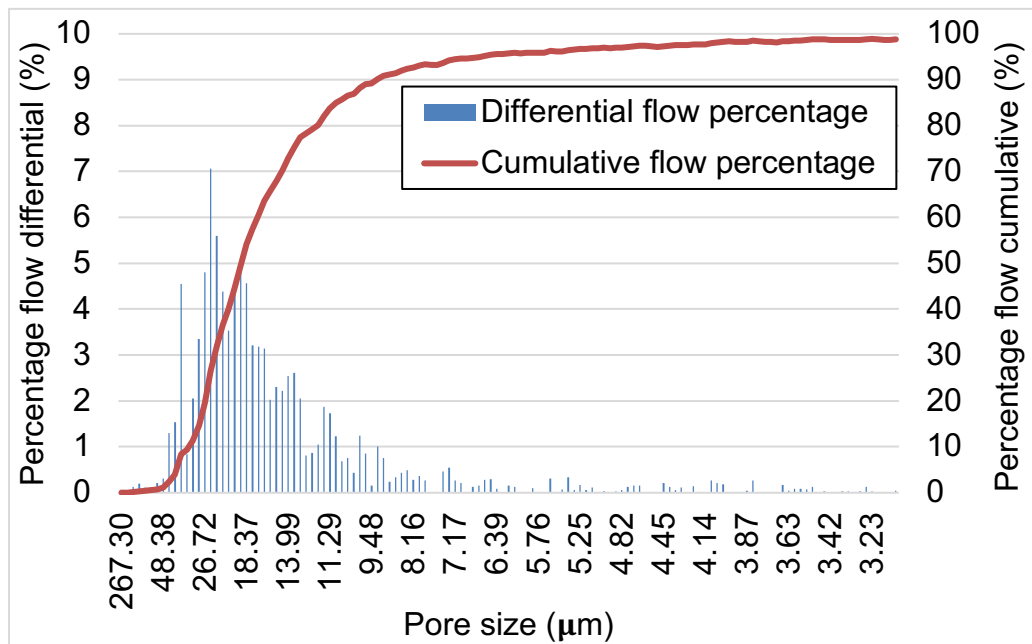
Figure 5.5: Cumulative and differential percentage flow of sample 5

Table 5.6: Mean flow pore size, smallest detected pore size and largest pore size of each sample.

Sample No:	1	2	3	4	5	Mean	Standard deviation
Mean flow pore size (µm)	20.35	20.33	20.71	19.76	19.16	20.06	0.61
Smallest pore size (µm)	3.25	3.31	3.76	3.44	3.23	3.40	0.22
Largest pore size (µm)	266.9	283.3	282.1	277.9	267.3	275.5	7.93

5.2.6 Filter media structure

Energy Dispersive X-Ray Scanning Electron Microscope (EDX SEM) was used to take micro-scale images of the filter media structure. This was used to determine the

average fibre diameter and the general structure of the fibrous mesh. Figure 5.6 (a), (b), (c) and (d) show the filter surface at 500, 200, 100 and 50 µm scale. 10 fibres from (c), five from (b) and five from (d) were measured by converting the number of pixels in the x and y direction between the two edges of a fibre to a distance measurement in µm. The resulting mean fibre size was 5.4 µm with a standard deviation of 2.7 µm.

As can be seen in figure 5.6 (a) and (c) some of the fibres tend to clump together, particularly after excessive handling, this creates the impression of larger diameter fibres. Nonwovens do not have a consistent pattern or weave which is clear from figure 5.6. However, due to the melt-blown manufacturing method, it is expected that the fibres have preferred orientation. The fibres tend to align along the conveyor belt direction. This creates a fabric that is stronger in the machine direction (MD) than the cross-direction (CD). This orientation preference can be seen in figure 5.6 (a) as the large clumps of fibre all run horizontally through the fabric.

(a)

(b)

(c)

(d)
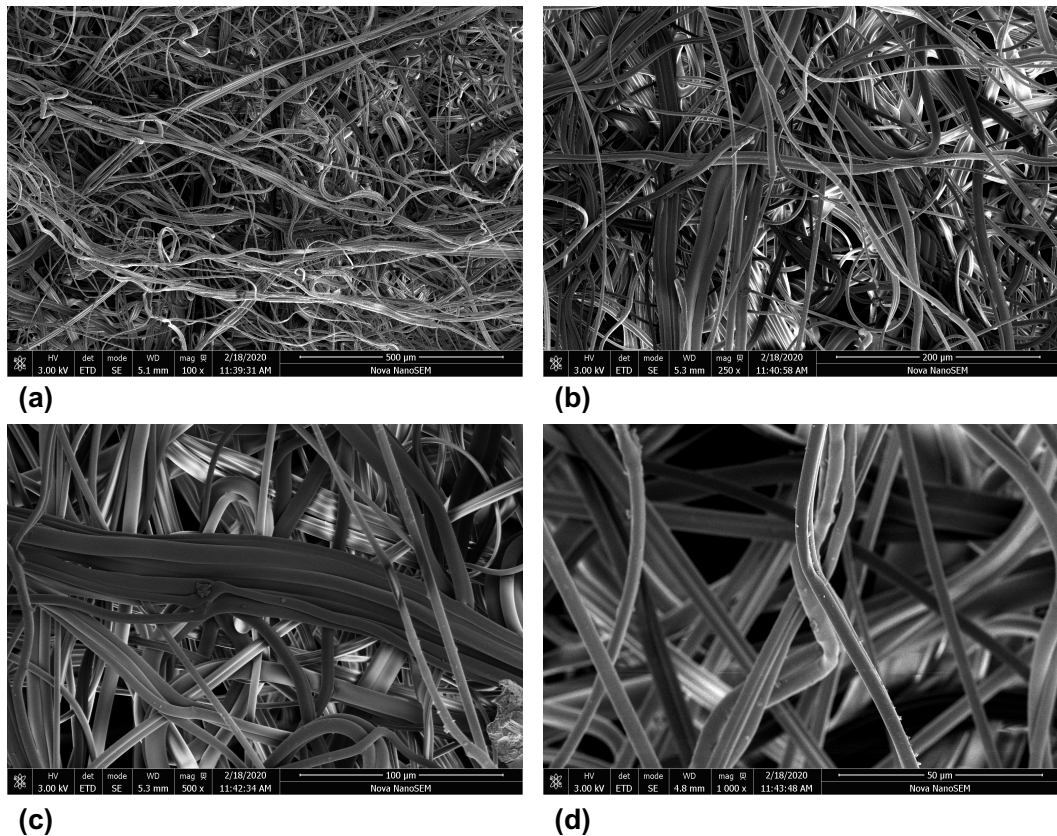
Figure 5.6: SEM EDX images of the filter media sample at (a) 500 µm scale (b) 200 µm scale (c) 100 µm scale (d) 50 µm.

5.2.7 Filter media wettability

The PBT filter media was hydrophobic which is beneficial when the dispersed phase is the organic phase as the filter fibres will have an affinity for the incoming droplets. This will allow the filter to retain the droplets which increases the probability

that another incoming droplet will come into contact with it and coalesce (benefits of tuning the filter media wettability are discussed in chapter 2). It may be beneficial to increase the hydrophillicy of the filter media so that aqueous droplets wet the filter surface for 'Water-in-Oil' (W/O) systems. Furthermore, fine tuning the filter media wettability depending on the interfacial tension between the organic and aqueous phases and whether or not the system forms a stable emulsion is a simple yet effective way to improve the separation of difficult to separate liquids. In order to make the filter media more hydrophilic it was treated with a Sodium Hydroxide solution which hydrolysed the filter surface. hydroxide ions (OH-) released in the solution add hydroxyl end groups to the polymer, which in turn increases its hydrophillicy. This treatment method was adopted from the method performed by Arouni et al (2019)[28] and Wang et al (2014)[156]. The method entails adding 12g of NaOH to a 100ml 1:1 ratio solution of methanol and water to produce a 3M solution which is then placed in a water bath with the filter material at 40ºC for 10 minutes. The filter media is then removed from the solution and rinsed with multiple washes of distilled water until the wash has a neutral pH. This treated filter media or 'hydophillic' filter media provided a comparison to the untreated 'hydrophobic' filter media during separation performance experiments.

To ensure the treatment process did not significantly alter the filter media mass, it was weighed before and after soaking in the sodium hydroxide solution. The mean and standard deviation of the mass before and after soaking are shown in figure 5.7. As figure 5.7 shows, the mass of the sample before and after soaking was well within 1 standard deviation of each another meaning that a significant mass loss was not observed during the treatment process.
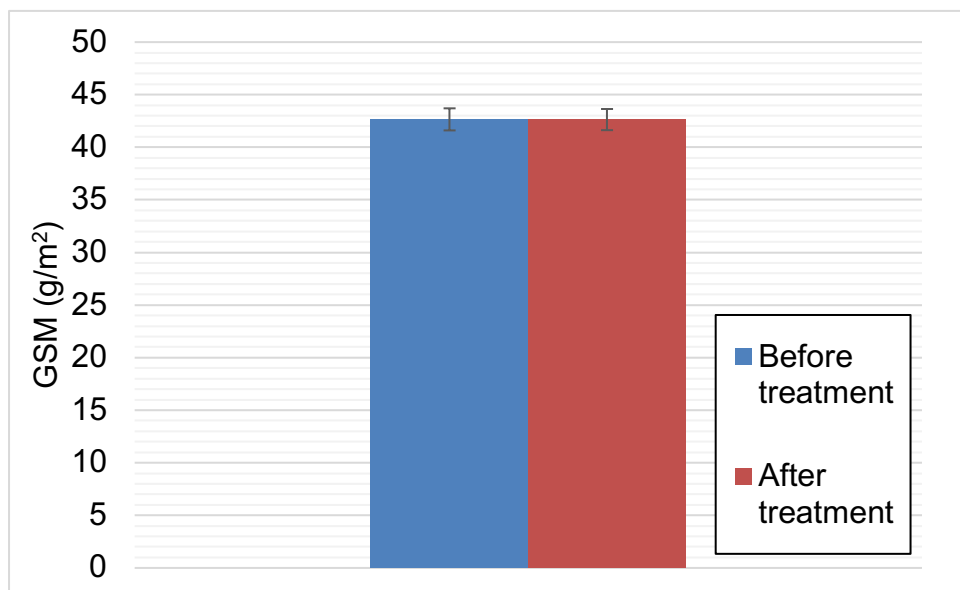
Figure 5.7: Difference in GSM between the treated and untreated filter media.

It was confirmed that the filter media was more hydrophilic after soaking by measuring the advancing contact angle. A Kruss droplet shape analyser was used to measure the advancing contact angle on the samples. The contact angle between a droplet of liquid and a surface is a measure of wettability. A large contact angle (greater than 90°) indicates low wetting of the surface and a small contact angle indicates high wetting of a surface. The protocols and best practices for contact angle analysis is set out by Huhtamäki et al (2018)[157]. The sample was prepared by leaving it to reach equilibrium with the atmosphere and cleaning any particulates from the surface. A syringe was filled with the liquid of choice (deionised water) and mounted on the dispensing unit after ensuring no air bubbles were present. The camera alignment, focus and brightness were checked and the image scale was calibrated. 2 µl of the fluid was dispensed onto the filter surface, making sure that the droplet is centred on the screen and the syringe is located to a depth of approximately half way into the droplet along the axis of symmetry. Another 1 µl is dispensed at 0.05 µl/s until the drop volume is 3 µl before waiting for 30 seconds. Subsequently, the camera starts recording the droplet and the dispensing unit starts dispensing liquid at 0.05 µl/s until the droplet reaches 10µl, at which point the test is finished and the video is saved for analysis. For contact angle measurements the base of the droplet (Baseline) has to be set, this was done manually for the first image in the video series. The Owens, Wendt, Rabel and Kaelble (OWRK) fitting method was used to analyse the droplet shape.[158-160] The OWRK method is commonly used when investigating the effect polar and dispersive interactions have on the wettability of a surface. This is particularly useful when looking at the change coating or treating a surface makes. The contact angle measurement from one test on the untreated filter media is shown in figure 5.8.
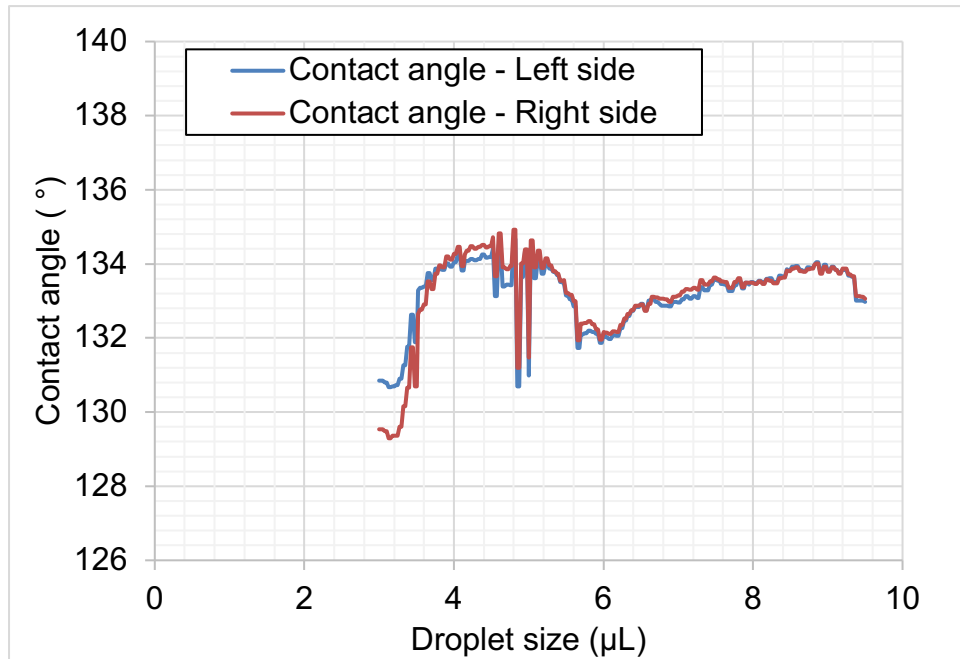
Figure 5.8: Contact angle measurement of water on the untreated filter media surface.

As can be seen in figure 5.8, the left and right droplet contact angles are very similar and therefore represent a gradual increase in droplet size throughout the experiment. The mean contact angle was 133.19° with a standard deviation of 1.03°. This is particularly important for filter media as it is a non-ideal surface for contact angle measurements (many peaks and troughs, holes and loose strands). After testing the untreated media, a treated media was tested. However, the treated media had become so hydrophilic that any water droplet that came into contact with the filter surface was immediately adsorbed into its pores. Therefore, a contact angle measurement on the treated filter media was not possible. However, it is clear from the study that the treated filter media must have a contact angle with the filter media of < 90° and is hydrophilic in nature. A different method such as the washburn capillary rise technique[161] should be used for a more detailed analysis of the filter media wettability with different liquid phases.

5.2.8 Discussion

The properties of the nonwoven PBT sample detailed in sections 5.2.1 – 5.2.7 have been presented as a baseline for discussing the results from sections 5.3 and 5.4. In section 5.3, treated and untreated media will be used to establish separator performance and to show effects of surface chemistry. In section 5.4, different numbers of layers of filter media are used to show the influence that different thicknesses have on emulsion separation and coalescence rates.

5.3 Liquid-liquid separations

In order to determine how well the separator performed at various flow rates and phase ratios, a series of test runs were conducted using different liquid-liquid pairs and the results from these tests were compared with the performance of a commercial membrane separator (the Zaiput[96]). The Zaiput was used as the device to compare to as it is the most referenced separation device in flow chemistry studied and therefore can be considered as a baseline for performance of separation devices at lab-scale. Along with measuring the amount of each phase in each outlet, the different liquids and flow conditions were analysed based on face velocity, Reynolds number, Capillary number and Eötvös number. The two separator devices will be compared and their operational windows (as a function of interfacial tension and flow rate) will be investigated. The amount of 'emulsion' downstream of the separation will also be qualitatively compared.

5.3.1 Experimental setup

The tests were carried out using the setup shown in figure 5.9 (a) and 5.9 (b). Two Jasco PU 1580 1585 HPLC pumps were used to transfer the organic and aqueous phases. The pumps were connected to three miniature CSTR's (fReactor[51]) connected in series which actively mixed the two phases. The outlet from the third CSTR was connected to either (a) the coalescing separator or (b) membrane separator depending on which test was being conducted. The coalescing separator was set up with the pump controlled outlet scheme. The outlet pump was connected to the aqueous outlet in each test. Four liquid-liquid pairs were tested, their properties are summarised in table 5.7. The four organic phases were chosen to give a range of interfacial tensions, densities and viscosities which would theoretically influence the separators performance.
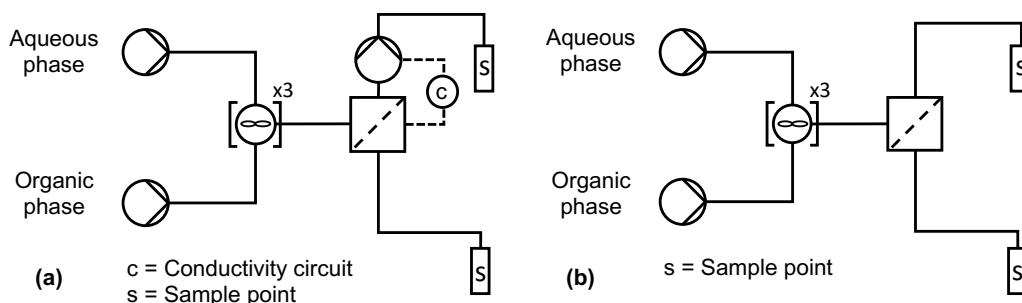
Figure 5.9: Experimental setup for liquid-liquid separation study consisting of two inlet pumps, three CSTR's and (a) a coalescing separator with the pump controlled outlet configuration detailed in chapter 3 or (b) a Zaiput membrane separator.

Table 5.7: Properties of the organic liquids used during experimentation

Aqueous phase	Organic phase	Interfacial tension (mN/m)	Density (Organic) (kg/m^3)	Viscosity (Organic) (mPa.s @ 25°C)
Water	Toluene	36.5	867	0.56
Water	Ethyl Acetate	6.4	902	0.426
Water	1-Butanol	1.8	810	0.26
Water	Dichloromethane	28.9	1330	0.413

The coalescing separator was tested without a filter, with 10 layers of the untreated filter media and with 10 layers of the treated filter media. The membrane separator was tested with both a hydrophobic and hydrophilic membrane with 'medium' pore sizes (OB-900 and IL-900[96]). Each liquid-liquid pair was tested at 4, 10 and 16 ml/min (total flow rate) at a phase ratio of 1 and at 10 ml/min (total flow rate) at a phase ratio of 0.25 and 4. When the separator is used without any filter media it can be considered equivalent to a gravity settling system. A combination of coalescing filter media and the membrane system were not studied in this chapter. This was because the focus of this study was on characterising the separator developed in chapter 4. Understanding how an upstream coalescing filter could enhance the Zaiput separator did not form part of this investigation.

The performance of the separator was determined by the percentage volume of each phase that crossed over into the other phase's outlet, i.e. a perfect separation would have 0 % aqueous phase in the organic outlet and 0 % organic phase in the aqueous outlet. A 12ml sample was taken from each outlet once the system had reached steady state. The volume of each phase in the sample was calculated under the assumption that the vials were of consistent cross-sectional area. A picture of each outlet sample was taken for analysis. The sample from each outlet could be split into 'top phase' and 'bottom phase'. The vertical length of the top and bottom phase in each vial was measured according to the number of pixels between the top of the top phase and the top of the bottom phase and the top of the bottom phase and the bottom of the bottom phase as seen in figure 5.10. This was done for both the organic and aqueous outlet and equation 5.6 was used to calculate the % crossover. The results from these experiments are given in section 5.3.4.

Top Pixel length$_{Org}$

Bottom Pixel length$_{Org}$
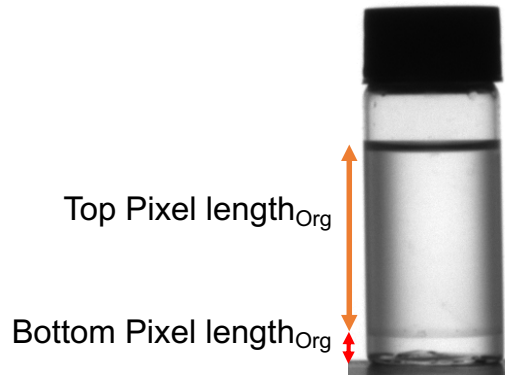
Figure 5.10: Example image of a sample from the organic outlet and the measured distances used to calculated percentage crossover.

$$\% \text{ Crossover} = \frac{\text{Bottom Pixel Length}}{\text{Top Pixel Length} + \text{Bottom Pixel Length}} \tag{5.6}$$

5.3.2 Results: Characteristic flow numbers

The separator cross-section was rectangular, therefore the characteristic length/hydraulic diameter of the system was calculated using equation 5.7 to be 7.5 mm. The hydraulic diameter could be used to calculate the Reynolds number of the different liquids at different flow rates/face velocities. Table 5.8 gives the Reynold number and capillary number for each of the liquid mixtures at each flow rate.

$$D_h = \frac{4ab}{2(a + b)} \tag{5.7}$$

D_h = Hydraulic diameter (m)

a = Rectangle width (m)

b = Rectangle height (m)

Table 5.8: Reynolds number and Capillary number of each of the tested organic phases at each flow rate

Flow rate (ml/min)	4	10	16
Face velocity (mm/s)	0.9	2.2	3.6
Toluene			
Reynolds number	10.3	25.8	41.3
Capillary number	1.4×10^{-5}	3.4×10^{-5}	5.5×10^{-5}
Ethyl Acetate			
Reynolds number	14.1	35.3	56.5
Capillary number	5.9×10^{-5}	1.5×10^{-4}	2.4×10^{-4}
1-Butanol			
Reynolds number	20.8	51.9	83.1
Capillary number	1.3×10^{-4}	3.2×10^{-4}	5.1×10^{-4}

Dichloromethane			
Reynolds number	21.5	53.7	85.9
Capillary number	1.3×10^{-5}	3.2×10^{-5}	5.1×10^{-5}

The Reynolds number of each organic phase at each flow rate is < 2000 and therefore the flow through the filter during each experiment should be laminar.

The Capillary number is important when considering the detachment of a droplet from a fibre. If an oil droplet is attached to a fibre and an aqueous phase is flowing past it at a constant flow rate, the interfacial forces will keep the droplet attached to the fibre. If the droplet grows due to coalescence with another droplet, the greater droplet size will result in a greater viscous force (drag force) trying to detach the droplet from the fibre. If the droplet reaches a critical size it will then detach from the droplet. Similarly, if the size of the droplet is fixed and the flow rate is increased, the drag force on the droplet will increase and detachment can occur. It has been found that residual oil mobilizes due to increased water injection at a Capillary number of 2 $\times 10^{-5}$.[162] The range of capillary numbers in table 4.8 vary between 1.3×10^{-5} and 5.1×10^{-4} showing that both droplet retainment and detachment will be found in this system.

Figure 5.11 plots the droplet size against Eötvös/Bond number for each of the four liquid systems. As can be seen in figure 5.11, toluene, ethyl acetate and dichlormoethane are all influenced more by interfacial forces than gravity forces, however 1-butanol is more heavily influenced by gravity when the droplets are larger than 1 mm in diameter. This may be significant in attempting to separate 1-butanol from water as it has a very low interfacial tension, meaning surface tension-based separation techniques are less effective. If the droplet size can be increased/kept above 1 mm then gravity forces will have a dominant role in the separation process.
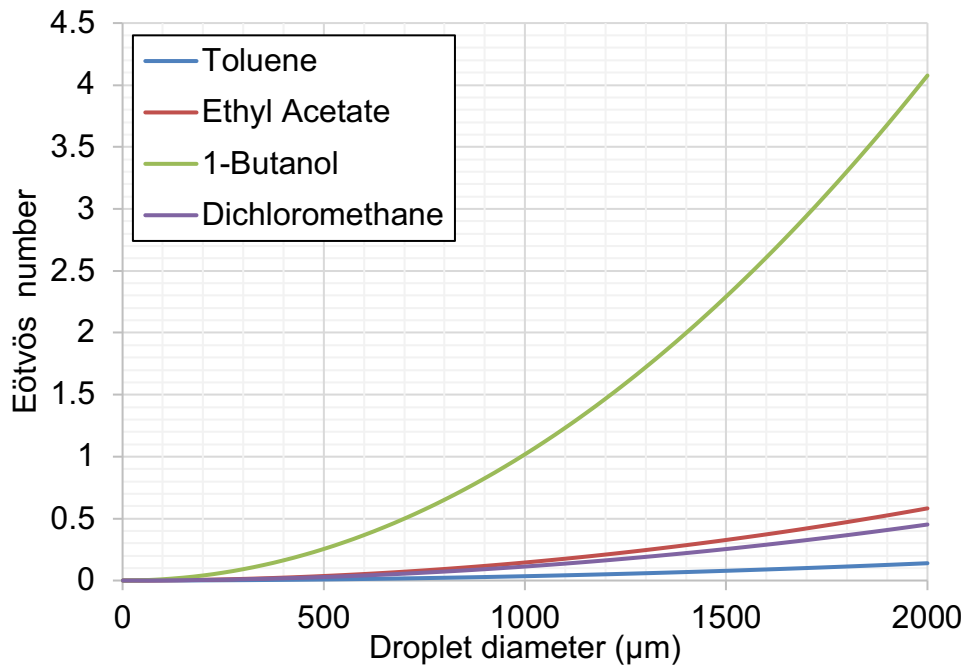
Figure 5.11: Eötvös number of each liquid system depending on the droplet size in water.

5.3.3 Results: Face velocity comparison

The efficiency of a coalescing filter is significantly affected by the flow rate of the fluid passing through it. The face velocity is the flow rate perpendicular to the filter face and can be used to compare the performance of filters at different flow rates and filter areas. Table 5.9 shows the 'critical face velocity' of 7 different coalescing filters found in the literature. The critical face velocity is the velocity above which the filter media shows significantly worse separation performance and therefore represents an upper limit of throughput for a given filter. The flow rates reported ranged between 5.8 and 16.67 mm/sec. These values will be heavily dependent on the phase ratio of oil and water as well as filter orientation, organic and aqueous phases and properties of the filter media. However, they do give some indication as to what flow rates may be possible through the coalescing separator. fThe maximum face velocity tested during our experiments was 3.56 mm/sec, which is below even the lowest critical face velocity seen in the literature. From literature, it is suggested that the upper limit of the flow rate for our system is at least twice what was tested (due to limitations on the flow rates of the pumps used here). This highlights the potential throughput that could be achieved with this system and its suitability for application at a much higher processing scale.

What is unknown is the influence increasing the dispersed phase concentration will have on the separation. The maximum dispersed phase concentration (L/L) in these literature examples was 0.8 %. This is significantly lower than what was used in our experiments (20 % or 50 %). On the one hand, the increased phase concentration

means the probability for coalescence increases. While on the other hand, over saturation of the filter media may limit the amount of coalescence that can take place.

Table 5.9: Critical face velocity of different coalescing filters reported in the literature

Reference:	Critical face velocity (mm/s)	Dispersion
Šećerov Sokolović et al (2006)[163]	8.33	500 mg/L Naphthenic-base oil in water
Šećerov Sokolović et al (2014)[33]	13.89	500 mg/L Naphthenic-base oil in water
Ma et al (2014)[164]	4.87	200 – 3000 mg/L Diesel oil in water
Lu et al (2016)[165]	16.67	2500-2857 mg/L Water in Diesel Oil
Lu et al (2016)[166]	11.67	2500-2857 mg/L Water in Diesel Oil
Han and Kang (2017)[167]	4.8	500-8000 mg/L Water with 0.01 % Span80 emulsifier in Diesel oil

5.3.4 Results: Separation of pure systems using the coalescing filter vs membrane separator

Separating toluene, ethyl acetate, dichloromethane and 1-Butanol from water was investigated at 4, 10 and 16 ml/min for the cases using no filter, untreated or treated filter media in the coalescing separator and a hydrophobic or hydrophilic membrane in the Zaiput. Figures 5.12 and 5.13 show images of the organic and aqueous samples taken from the outlets of the coalescing separator and membrane separator at each flow rate and phase ratio tested.
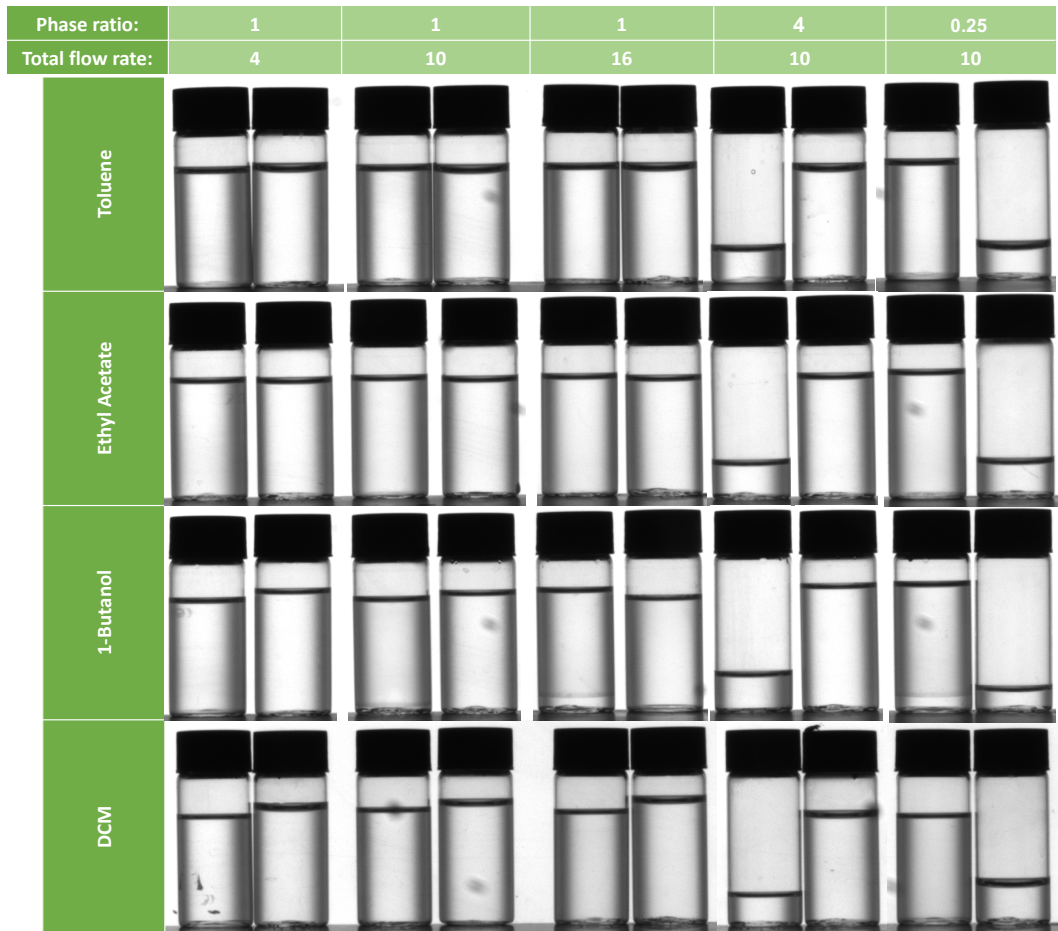
Figure 5.12: Sample images from the coalescing separator at each flow rate and phase ratio tested.
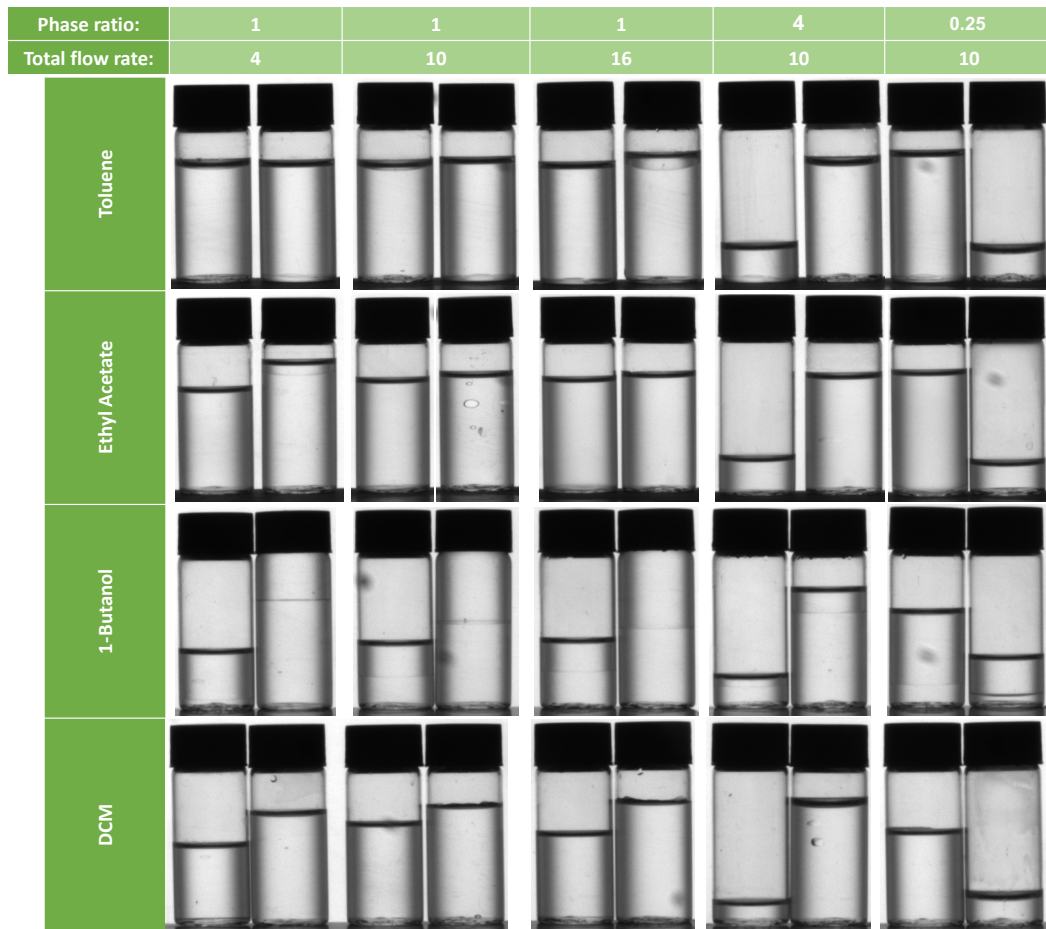
Figure 5.13: Sample images from the membrane separator at each flow rate and phase ratio tested.

The method described in section 5.3.1 was used on the images in figures 5.12 and 5.13 to calculate the % crossover of each phase in each outlet. Table 5.10 provides a summary of these values for each separator. In each case, the membrane type and filter media type that performed the best depending on the flow rate and phase ratio is given. The time it took a 10ml sample of each mixtures to separate in batch was measured using the methods described in chapter 3 and is given in table 5.10. Whether the sample formed a majority O/W or W/O emulsion during the batch experiments has also been provided in table 5.10.

Table 5.10: Summary of coalescing separator performance compared with the membrane separator

% Volume - Colour scale
91-100
81-90
71-80
61-70
51-60
41-50
31-40
21-30
11-20
1-10
0

Aqueous Phase	Organic Phase	Aqueous flow rate (ml/min)	Organic flow rate (ml/min)	Batch Separation		Coalescing filter separator			Membrane separator		
				Time to separate (sec)	Emulsion type	Filter type	% Volume of aqueous phase in organic outlet	% Volume of organic phase in aqueous outlet	Membrane type	% Volume of aqueous phase in organic outlet	% Volume of organic phase in aqueous outlet
Water	Toluene	2	2	25	O/W	Untreated	0	0	Hydrophobic	0	0
		5	5	25	O/W	Untreated	0	0	Hydrophobic	0	0
		8	8	25	O/W	Untreated	0	0	Hydrophobic	0	11
		2	8	15	W/O	Untreated	0	0	Hydrophobic	0	0
		8	2	55	O/W	Untreated	0	0	Hydrophilic	0	0
	Ethyl Acetate	2	2	41	W/O	Untreated	0	0	Hydrophobic	0	8
		5	5	41	W/O	Untreated	0	0	Hydrophobic	0	0
		8	8	41	W/O	Untreated	0	0	Hydrophobic	0	0
		2	8	19	W/O	Untreated	0	0	Hydrophobic	0	0
		8	2	15	O/W	Untreated	0	0	Hydrophilic	0	0
	1-Butanol	2	2	23	O/W	Treated	0	0	Hydrophobic	12.5	31.1
		5	5	23	O/W	Treated	0	0	Hydrophobic	45.7	46.2
		8	8	23	O/W	Treated	0	10	Hydrophobic	52.1	50.4
		2	8	190	W/O	Treated	0	10	Hydrophobic	65	19.5
		8	2	84	O/W	Treated	0	0	Hydrophilic	22.9	75.8
	Dichloromethane	2	2	26	W/O	Untreated	0	0	Hydrophobic	0	0
		5	5	26	W/O	Untreated	0	0	Hydrophobic	0	0
		8	8	26	W/O	Untreated	0	0	Hydrophobic	0	0
		2	8	13	W/O	Untreated	0	0	Hydrophilic	0	0
		8	2	93	O/W	Untreated	0	0	Hydrophobic	0	0

Toluene-water

The toluene case that took the longest to separate in batch was at a phase ratio of 4 (aq/org), it took 55 seconds compared to 25 seconds at a phase ratio of 1. Both separators could separate this mixture in flow with 0 % crossover at 10 ml/min, however the membrane separator gave 11 % organic crossover at a flow rate of 16 ml/min due to the increased demand as a result of the higher flow rate.

Ethyl acetate-water

The ethyl acetate-water mixture took 41 seconds to separate in batch at a phase ratio of 1, the membrane separator had 8 % organic crossover at 4 ml/min but not any other flow rate. This was odd as it is expected that as flow rate increases, separation becomes more difficult. Two factors may have contributed to this result. One is that the CSTR's create finer droplet dispersions than when a t-piece or similar static mixer is used, at lower flow rates, the droplets will have a longer residence time in the mixers, this in turn will create more small droplets and produce a more challenging emulsion to separate. The other factor is the internal pressure control diaphragm that controls the outlet flow streams from the membrane. If there were any particulates that gathered on the membrane or other disturbances to the back pressure in the system, some amount of phase crossover could occur.

Dichloromethane

Both separators were able to separate all of the dichloromethane tests, even the phase ratio = 4 case that took 93 seconds to separate in batch. Dichloromethane has a larger density than water, this meant that dichloromethane sunk to the bottom outlet of the coalescing separator, unlike with the other three solvents. To avoid continuously pumping solvent through the outlet pump, the pump was attached to the top outlet of the separator. The results show that this change in configuration did not impact the separation performance of the separator.

Butanol-water

The coalescing separator had some crossover of phases when 1-butanol was separated. As shown in figure 5.14, the separator performed the worst with no filter media. At the lowest flow rate there was crossover of the aqueous phase into the organic and as the flow rate increased this became larger. At the medium and high flow rates, there was also an increasing crossover of organic phase into the aqueous. Once 10 layers of untreated filter media was used in the separator there was no more crossover of organic phase into the aqueous outlet, however there was still some crossover of aqueous phase into the organic at 10 ml/min and 16 ml/min. Using the treated filter media improved the separation further so that there was only 10 % crossover of aqueous phase into the organic at 16 ml/min.
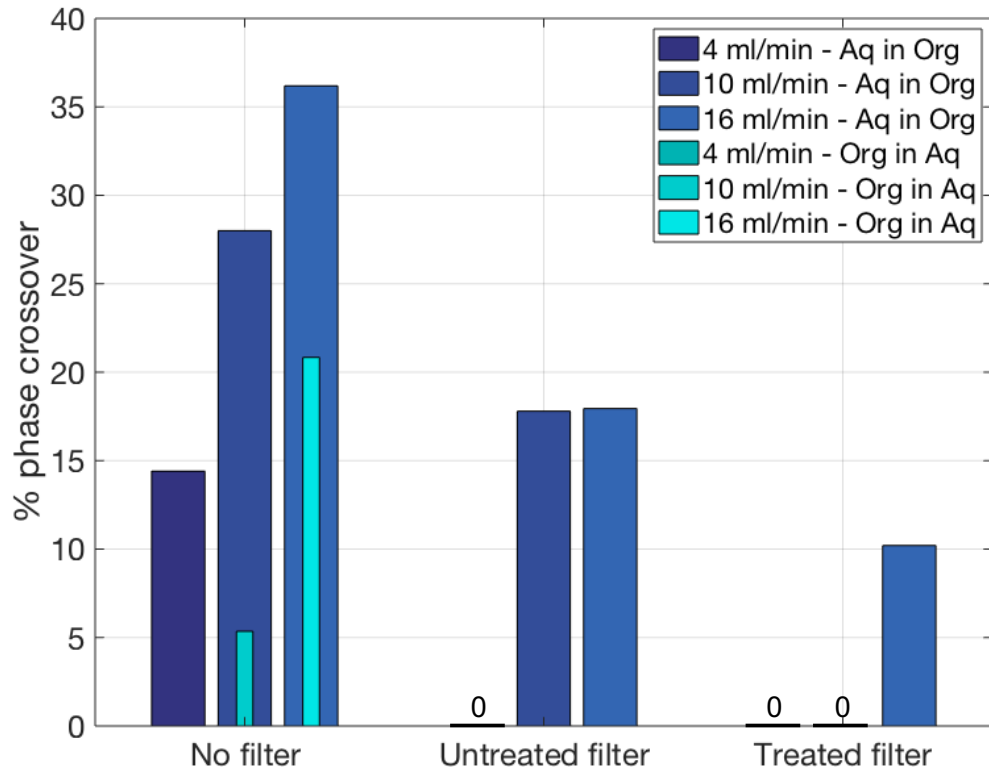
Figure 5.14: Percentage of aqueous phase found in the organic phase outlet and percentage of organic phase found in the aqueous outlet sample depending on flow rate and filter type in the coalescing separator. 1-Butanol

Figure 5.15 shows the same cases but while using the Zaiput membrane separator with a hydrophobic and hydrophilic membrane. Figure 5.15 shows that the hydrophilic membrane was not suitable for this separation as there was a 50% crossover of both phases into the other at each flow rate that was tested. The hydrophobic membrane on the other hand did separate the two liquids to some extent. At each flow rate there was some crossover of both phases into the other but less so than with the hydrophilic membrane. At 4 ml/min the separator had 30% crossover of organic phase into the aqueous and 12 % crossover of aqueous phase into organic. This percentage increased at 10 ml/min so that approximately 45 % of both phases crossed over into the other outlet and at 16 ml/min 50 % of both phases crossed over into the other.
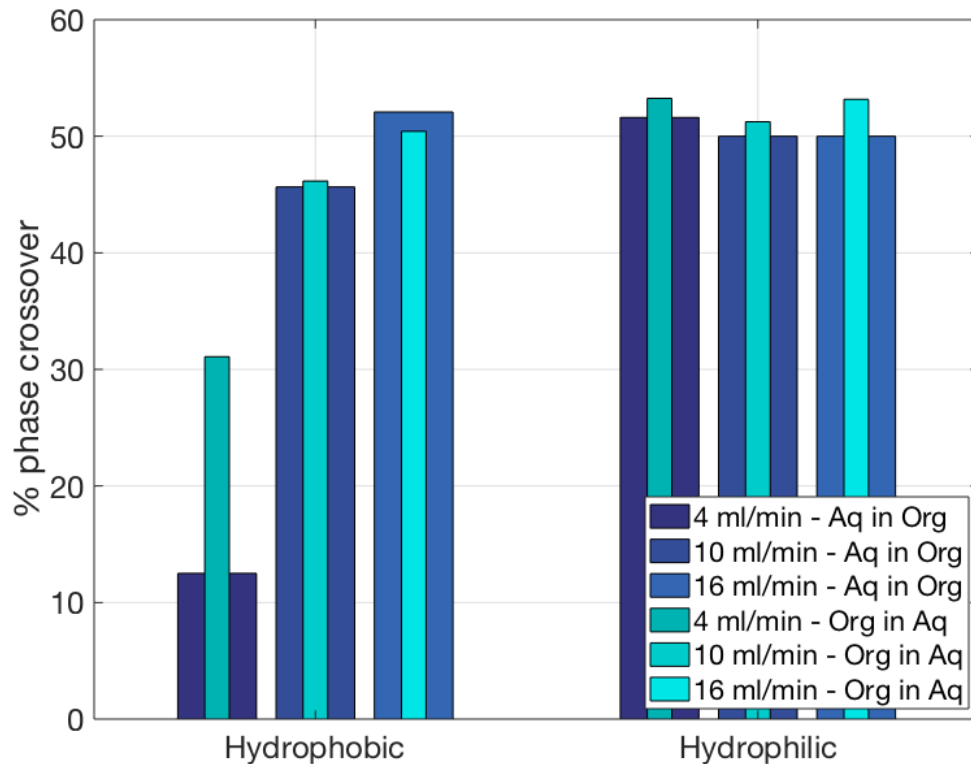
Figure 5.15: Percentage of aqueous phase found in the organic phase outlet and percentage of organic phase found in the aqueous outlet sample depending on flow rate and what membrane was used in the Zaiput.

The results for the 1-butanol case are as expected if considering the Eötvös number of the system as 1-butanol was influenced more by gravity forces than by surface forces, particularly above droplet sizes of 1 mm. As the tubing in this flow system was 1/32" ID (0.79 mm) we can expect several droplets to be close to 1 mm in size or bigger if any coalescence occurs before reaching the separator, meaning both surface forces and gravity forces will influence the separation process. As the membrane separator only utilises surface forces it would struggle to separate the low interfacial tension 1-butanol-water mixture. The coalescing separator however can utilise surface forces to grow the 1-butanol droplets into larger ones (1 mm or more) which are then significantly affected by gravity forces. As the coalescing separator has a settling area, gravity can be utilised to separate the two liquids before reaching their respective outlets. However, the additional gravity separation is evidently not the only reason the coalescing separator is able to separate 1-Butanol from water as the experimental run with no filter media would perform largely the same as the filtered runs if the separation was purely driven by gravity. Instead, the combined effect of gravity separation and droplet coalescence through a filter media increased separation significantly.

Figure 5.16 shows the difference in the height of the emulsion layer inside the coalescing separator depending on whether no filter, untreated or treated filter media

was used at a flow rate of 10 ml/min. It is clear from this the significant difference the filter media and filter media treatment process has on the separation of 1-butanol and water. The treated filter media has almost no emulsion layer downstream of the filter media which suggests the majority of the dispersed phase droplets have coalesced as they pass through the filter and only a few larger droplets require settling out via gravity separation. The fact that the treated media performs better than the untreated media suggests that in flow at least the 1-butanol-water mix forms a W/O emulsion which responds well to the hydrophilic treated filter media. However, the batch separation indicated a preference for O/W at a phase ratio of 1, if this is the same in flow than the improved separation with hydrophilic filter media may be because 1-butanol has such a small interfacial tension with water that a material that has an affinity for water may well collect its droplets more readily than a hydrophobic filter media.

No filter   Untreated filter   Treated filter
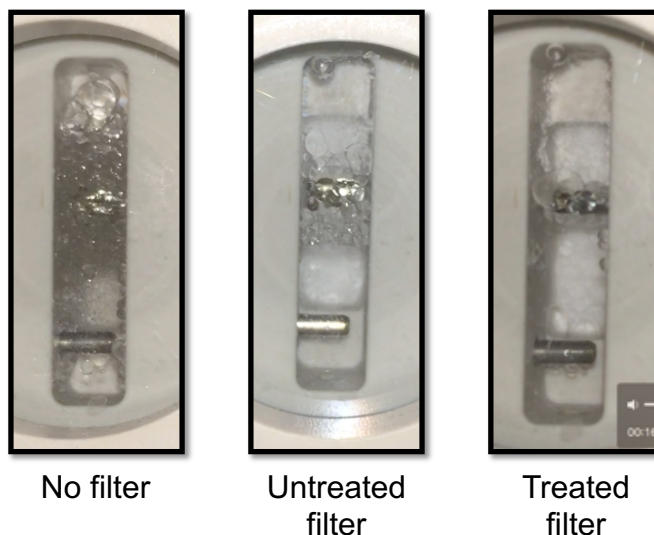
Figure 5.16: 3 images showing the difference in size of the emulsion layer inside the separator depending on if no filter, untreated or treated filter media was used at 10 ml/min.

5.3.5 Summary of separating pure systems

In this section it has been shown that the designed separator has an improved performance in comparison to a commercial membrane separator, particularly for liquid-liquid mixtures with low interfacial tensions (such as 1-butnaol-water). It has also been shown that the coalescing filter media utilised in the separator has a positive effect on the separation of binary liquid mixtures. For challenging separations, tuning the filter media wettability can have a significant positive impact on the separator performance. The separator has the potential to be operated at high flow rates and throughputs as well as low and high phase ratios for numerous systems. The system can also be easily adapted for organic liquids that are denser

than water by simply flipping the coalescer 180° so that the lower electrode is still in contact with the aqueous phase.

5.4 Emulsion separations

Coalescing filter media has previously been shown to be good at removing fine emulsified droplets from a fluid stream.[27-30,35] In the pharmaceutical industry, emulsions can form as a result/combination of phase composition, mixing regime, acids/base addition, by-products, additives, catalysts, solvents and impurities.[39,63,132] The undesirable formation of an emulsion cannot always be avoided without reworking a manufacturing method or compromising on yield/purity. It is therefore desirable to rapidly separate emulsions when they do form. In this section the toluene-water-SDBS surfactant system characterised in chapter 3 has been used to test the coalescing filters ability to separate stable emulsions depending on the number of filter layers used and the HLD value of the emulsion.

5.4.1 Experimental setup

The setup shown in figure 5.17 (a) and 5.17 (b) was used during the emulsion separation experiments. Two Jasco PU 1580 1585 HPLC pumps were used to transfer the organic and aqueous phases. The pumps were connected to three miniature CSTR's (fReactor[51]) connected in series which actively mixed the two phases. The outlet from the third CSTR was connected to either (a) the coalescing separator or (b) membrane separator depending on which test was being conducted. The coalescing separator was setup with the valve-controlled outlet scheme. The valve was connected to the organic outlet and the BPR to the aqueous outlet. Both inlet pumps were set at 5 ml/min and the separator had either 0, 1, 5 or 10 layers of untreated filter media installed.
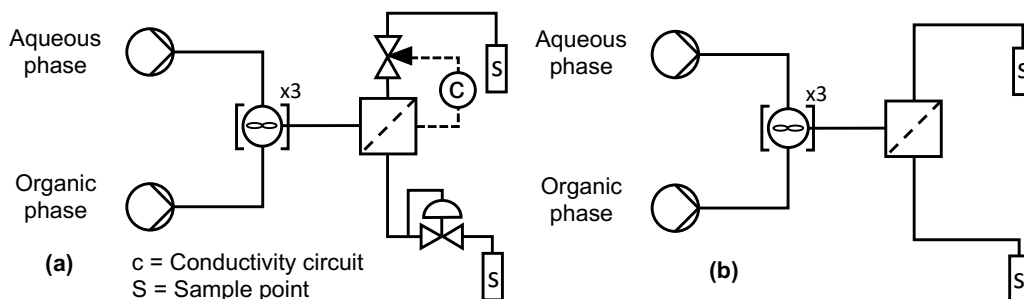
Figure 5.17: Experimental setup for the emulsion separation study consisting of two inlet pumps, three CSTR's and (a) a coalescing separator with the valve-controlled outlet configuration detailed in chapter 3 or (b) a Zaiput membrane separator.

The organic phase was toluene and the aqueous phase was a 0.01M solution of SDBS surfactant (previously detailed in chapter 3). Table 5.11 details the 10 SDBS surfactant solutions tested in chapter 3 and the batch separation rates of those solutions when mixed with toluene. The emulsion type is also shown in table 5.11.

Table 5.11: Aqueous phase solution formation and batch separation results from chapter 3

Sample No.	NaCl concentration (M)	HLD value	Emulsion type	Top phase separation time (min)	Bottom phase separation time (min)
1	0.0078	-3.38	O/W	> 120	41.67
2	0.18	-0.91	O/W	> 120	> 120
3	0.28	-0.49	O/W	> 120	> 120
4	0.37	-0.23	Mixed	> 120	79.19
5	0.47	0.01	Mixed	2.33	34.83
6	0.58	0.20	W/O	1.17	5
7	0.74	0.45	W/O	1	7.5
8	0.98	0.72	W/O	0.83	5.33
9	1.14	0.87	W/O	0.83	7.67
10	1.34	1.04	W/O	4.67	16.83

Four of the solutions (corresponding approximately to samples 1, 2, 4 and 5) were made up for these experiments and the HLD value was calculated for them. It was expected that the first three solutions would be O/W solutions with decreasing interfacial tension and the fourth solution would be a mixed phase emulsion with the lowest interfacial tension (according to HLD theory). The interfacial tension of the four solutions were measured using the pendant drop technique on a Kruss DSA100. However, because the pendant drop technique is only accurate to 1 mN/m, only approximate interfacial tension values can be given for each of the four cases. The four interfacial tensions are gives as:

1. Sample 1 ≈ 3 mN/m
2. sample 2 ≈ 1 mN/m
3. sample 4 < 1 mN/m
4. sample 5 << 1 mN/m.

To measure the separation performance, a sample from both the aqueous and organic outlets were taken. The samples were collected over a period of 2 minutes, meaning if perfect separation occurred both vials would have a 10ml volume each; this was done three times for each case with five minutes between taking each sample. Before running the experiments, an image of a 10ml sample was taken and

the number of pixels from the top to the bottom of the liquid within the sample vial was calculated. The sample height measured 214 pixels. This number of pixels corresponds with a perfect separation.

The actual volume (pixel height) of each sample from each outlet was measured using the same camera setup after each experimental run. The sample from the organic outlet was always much clearer than the sample from the aqueous outlet and had no aqueous crossover except in sample 5. The aqueous sample normally contained a significant portion of emulsified droplets that made it hard to get an accurate measure of the volume of each phase. Only the volume of organic phase collected in the organic outlet was measured during this experiment as an accurate measure of the volume could be obtained. Once the images of the samples had been taken and the pixel height measured, the pixel height was then divided by the expected pixel height (214) of a perfect separation, resulting in a fraction that related to the amount of liquid successfully separated by the device.

The amount of organic phase collected in the organic outlet has been presented in section 5.4.2 when using the coalescing separator. The difference between separation of emulsions at different points on the HLD scale has been determined, along with the impact different numbers of filter layers has on separation.

The separation performance of the membrane separator was also evaluated with these systems as a point of comparison. However, the separations could not be determined using the same imaging technique because a large amount of the outlet samples were still emulsified. Therefore, the sample images from the coalescing separator and membrane separator have been visually compared.

5.4.2 Results: Separation of emulsion systems using the coalescing separator

Figure 5.18 shows how the separator coped with an emulsion systems. Figure 5.18 (a) shows how an increased number of filter layers generally improved the amount of organic phase collected in the organic outlet at different HLD values. The only exception being at HLD = -0.03. This is because the interfacial tension is so low that there is virtually no preferential wetting on the filter surface and therefore little additional separation compared to when no filter media was used. At this HLD point the system separates relatively quickly in batch due to fast coalescence, therefore there was still some separation seen but it does not follow the same trend as the other solutions. Figure 5.18b shows that the most challenging separation was at HLD = -0.26 (sample 4). At this point the emulsion formed was extremely stable over a long period of time and the interfacial tension was also extremely low, meaning only a small improvement in separation could be achieved when additional filter layers were added.

These tests where done with the untreated filter as no W/O systems where studied. However, as seen in the 1-butanol case from the previous section, a more hydrophilic filter media may have improved the separation performance in these low interfacial tension systems. It appears that the benefits of additional filter layers has diminishing returns as the 5 layer and 10 layer results are broadly similar in each case. The best separation occurred when HLD = -3.35 and 5 filter layers where used, however 10 filter layers provided the same separation within margins of error.
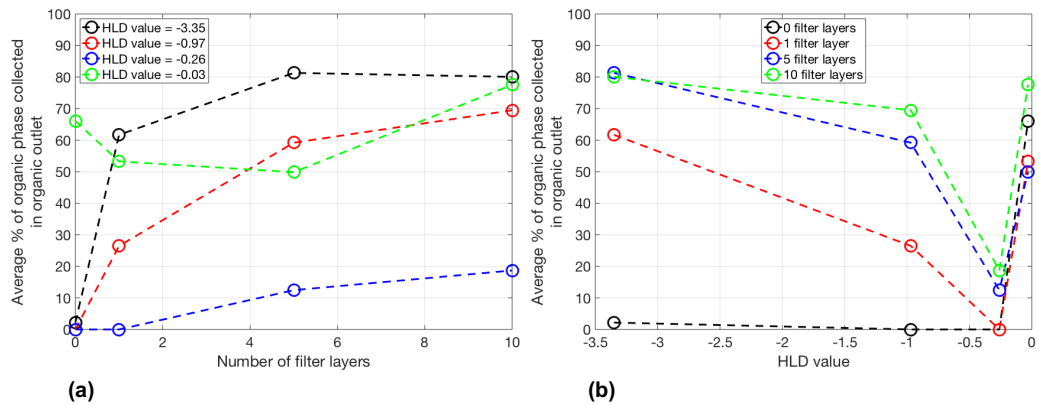
Figure 5.18: Average percentage of organic phase collected at the organic outlet depending on (a) the number of filter layers and (b) the HLD value of the emulsion.

The improvement in separation as more filter layers are added can be explained by the increase in tortuosity of the fluid path, this is shown by the decreased air permeability when the filter thickness is increased (table 5.5). The increased tortuosity means more droplets come into contact with the filter media and are retained for long enough to allow coalescence to occur before being deposited downstream. The % separated could be increased further with optimisation of the filter media wettability and pore size distribution through the filter thickness.

5.4.3 Results: Separation of emulsion systems using the coalescing filter vs membrane separator

Figure 5.19 shows the sample images from the outlets of the coalescing separator for each emulsion system that was tested. Figure 5.20 shows the sample images from the outlets of the membrane separator from each of the emulsion systems tested. During the membrane separator tests a hydrophobic and hydrophilic membrane was tested. In both figures 5.18 and 5.19 the left three images are from the organic outlet and the right three from the aqueous outlet in each block.
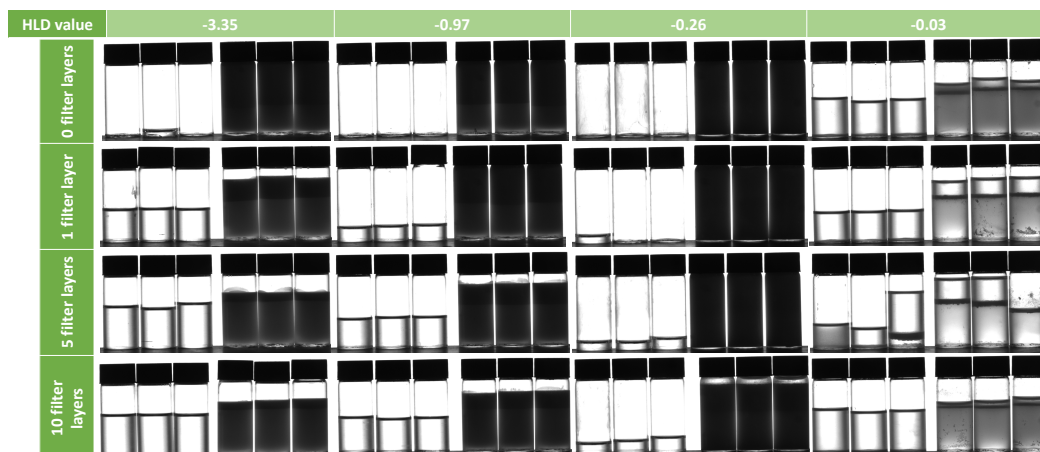
Figure 5.19: Images of samples taken from Organic and Aqueous outlets (left 3 - organic, right 3 – aqueous in each block) of the coalescing separator during the emulsion separation experiments.
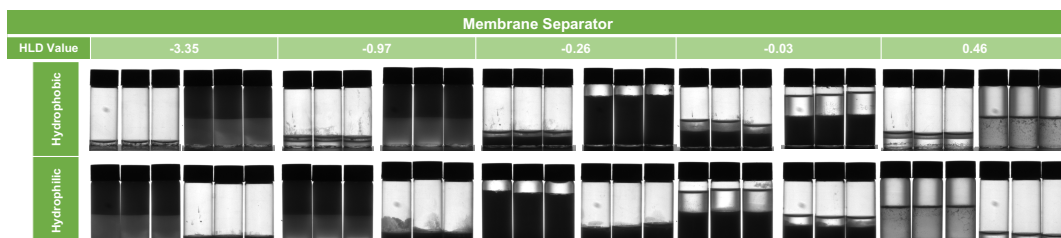
Figure 5.20: Images of samples taken from Organic and Aqueous outlets (left 3 - organic, right 3 – aqueous in each block) of the membrane separator during the emulsion separation experiments.

As can be seen in figure 5.20 the membrane separator with hydrophilic filter media struggled to de-emulsify any of the solutions. The majority of the emulsion passed through the organic phase outlet while a small amount passed through the aqueous. As the HLD value approached zero more of the emulsion passed through the hydrophilic membrane and went out through the aqueous outlet, presumably because the low interfacial tension meant that the capillary pressure in the membrane was lessened. The hydrophobic membrane seemed to perform better. Most of the emulsion passed through the aqueous outlet (retentate) but the fluid that did pass through the membrane and out through the organic outlet was less emulsified than what passed through the hydrophilic membrane. Even though the permeate phase was less emulsified there was still some aqueous phase that passed through the organic outlet during each experiment. The coalescing separator on the other hand was able to distinguish between the organic and aqueous phases so that in all cases except one (HLD = -0.03 and 5 layers of filter media) only organic phase was collected in the organic outlet. This is a significant improvement over the membrane separator as this system could now use a recycling fluid stream from the aqueous outlet to separate the remaining organic phase from the aqueous. With 10 layers of filter media there was also a clear increase in collected organic phase in comparison

to the membrane separator, suggesting that the coalescing separator was better at breaking up challenging emulsion systems.

A fifth HLD value (0.46) was tested with the membrane separator. This was because the downstream samples at HLD = -0.03 were very emulsified for the membrane separator, unlike in the coalescing separator experiments. In the coalescing separator experiments, fast separation was seen with and without a filter at this HLD value. Around the HLD = 0 point the system is very sensitive to differences in temperature, salinity and surfactant concentrations, therefore, the HLD value was increased to 0.46 to ensure this change in emulsion characteristic was captured. At HLD = 0.46 the fast settling characteristics observed during the coalescing separator experiments at HLD = -0.03 were observed for the membrane separator. It can be seen by comparing the HLD = 0.46 case in figure 5.20 to the HLD = -0.03 case in figure 5.19 that the coalescing separator performed better than the Zaiput system under these conditions as more organic phase was separated without crossover of the aqueous phase.

The imaging method used to determine phase crossover was sufficient to show bulk changes in the system depending on the filter or membrane configuration used. However, for a more detailed investigation of phase crossover, other methods should be considered such as Gas Chromatography or Karl Fischer titration. The emulsion would likely need to be solubilised in a third liquid which would add complexity to the analysis method but a more precise measurement could be obtained as a result.

5.4.4 Summary of separations involving emulsion systems

In this section we have used an SDBS surfactant system that was characterised in terms of separation rate, HLD value and emulsion type (O/W, W/O or mixed) to test the coalescing separators ability to break up stable emulsion systems. The coalescing separator was able to separate some of the organic phase from the emulsion without aqueous crossover at up to 81 % efficiency. The HLD value (and interfacial tension) of the system impacted the separation significantly, as did the number of filter media layers. The coalescing separator performed better across all test cases than the Zaiput membrane separator.

5.5 Summary

In this chapter we have characterised a nonwoven PBT coalescing filter media. We have then integrated this filter media into a lab-scale separation device and its performance in comparison to a commercial membrane separator device has been investigated. It was found that the coalescing separator performed better than the

membrane separator, particularly with significantly low interfacial tension systems such as 1-butanol-water. The coalescing separator was also better at separating emulsion systems over a range of HLD values in comparison to the membrane separator. The number of filter layers has a significant impact on the separator performance as well as the wettability of the filter media. A simple wettability tuning method was used to make the filter media more hydrophilic and therefore separate a low interfacial tension system more effectively than it could otherwise.

Chapter 6 – Design and development of a multistage extraction platform

6.1 Introduction

A single stage separation device was designed and developed in chapter 4 and tested in chapter 5. In this chapter the single stage system has been expanded so that 3 stages of separation can occur in sequence. This means that lab-scale multistage continuous extractions can be studied at lab-scale in cross-current or counter-current arrangements before scale up. The pump control outlet system from chapter 4 was used for the multistage system. Three single stage 'modules' have been developed. A touchscreen prototype has been designed as an alternative to the laptop connected control system so that an independent system can be used in the lab without external software.

- Section 6.2 will discuss the mechanical design and component layout of the stage modules.
- In Section 6.3 the changes to the electrical design from the single stage design will be described.
- Section 6.4 explains the updated control scheme for a multistage system.
- Section 6.5 discusses a concept to move the control from a PC to a touchscreen controller.

The aim of this chapter was to demonstrate the feasibility of using the separator in a counter-current extraction arrangement and optimise the control system before testing a real system in chapter 7.

6.2 Mechanical Design

6.2.1 Module design

The mechanical design of a single extraction stage (module) within the 3 stage system consisted of 6 different components, each of which is listed in table 6.1 along with the number of each component within a single module. A stainless steel case was used to house each of the components, measuring 150 mm x 150 mm x 80 mm when including the lid; Which is well suited to operation within fume hoods. The box had two internal mounting rails and a screw on lid. Figure 6.1 shows the dimensions of the box as given by the manufacturer.

Table 6.1: Components of a single module in the multistage extraction platform

Component name:	Number per stage:
Coalescing separator	x1
F-reactor (CSTR)	x2
Separator mount	x1
Diaphragm pump	x1
Fan/magnetic stirrer	x2
Stainless steel case	x1

SECTION A-A   FRONT VIEW

DETAIL OF
MOUNTING RAIL

TOP VIEW
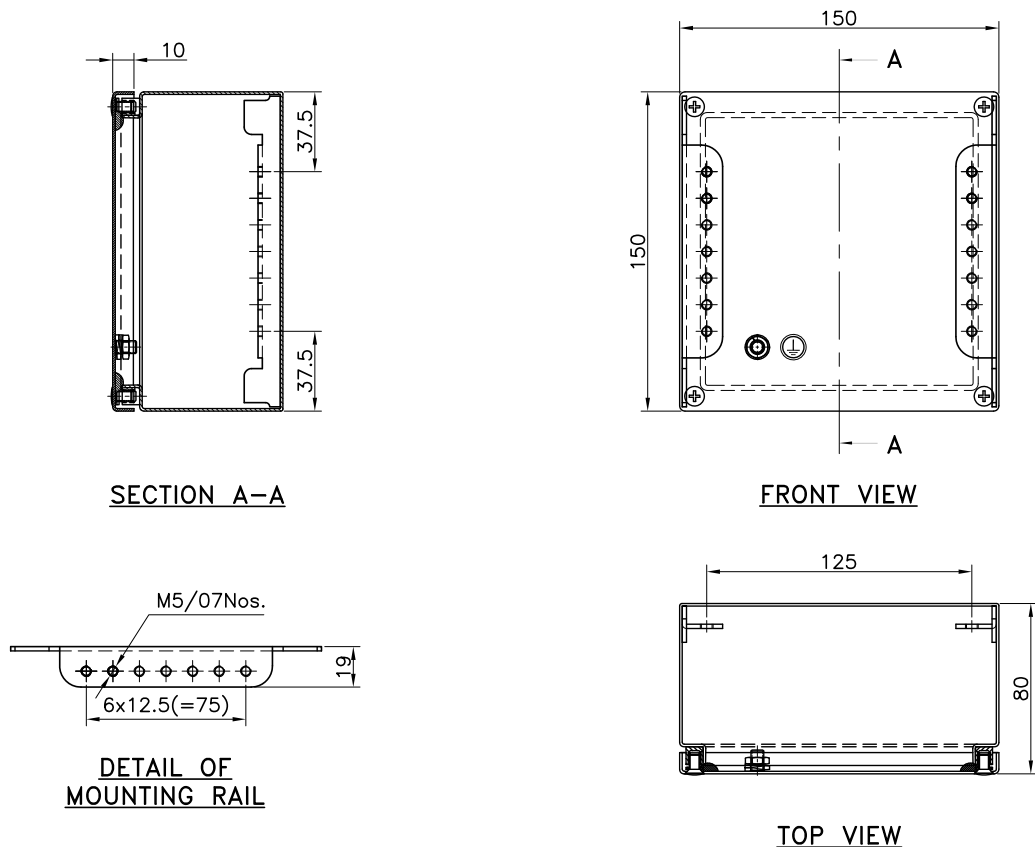
Figure 6.1: Dimensional drawing of the stainless steel case used to house a single module from the multistage extraction platform.[168]

Figure 6.2 shows the arrangement of the components in the stainless stell case. It was decided that two fReactors[51] (CSTRs) between each stage was sufficient to allow equilibrium to be reached. The two reactors sat on top of the stainless steel case, held in place by a 1 mm thick circular groove. The coalescing separator was mounted on a 50 mm long, 12.7 mm diameter post. The magnetic stirrers were mounter inside the stainless steel case close to the lid and below the fReactor grooves. The diaphragm pump was mounted inside the stainless steel case. A 30 mm x 30 mm hole was cut into the lid of the stainless steel case. The pump head slotted into this hole so that the connections for tubing were accessible without having

to open the box. The magnetic stirrer assembly was based on the design developed by Chapman et al (2017)[51]. The magnetic stirrers use a computer fan with two small magnets attached to the top of the fan. Once the fan has power going to it, it rotates the magnets which in turn rotate the stirrer bar inside the fReactors.
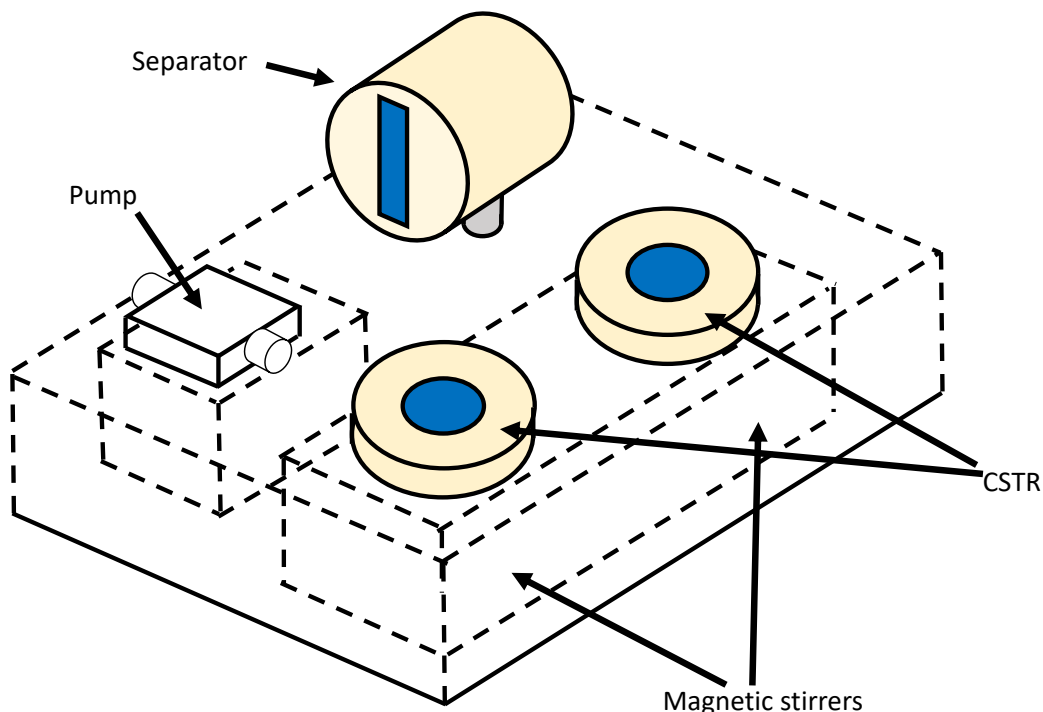
Figure 6.2: Arrangement of components in a single module of the multistage extraction platform.

Figure 6.3 shows the single module assembled and annotated to show the flow path through it. Each of the inlets and outlets could be connected to subsequent modules to expand the system from one stage to multiple stages. The module could also be connected in counter-current or cross-current arrangements. The organic and aqueous phases flow into the 1st fReactor where they are mixed. They then flow through the second fReactor and into the separator. The separator then separates the two phases back into organic and aqueous streams and the pump removes the aqueous phase from the separator while the organic phase leaves the separator via a separate outlet at a flow rate equal to:

Organic outlet flow rate = Total inlet flow rate – pump flow rate
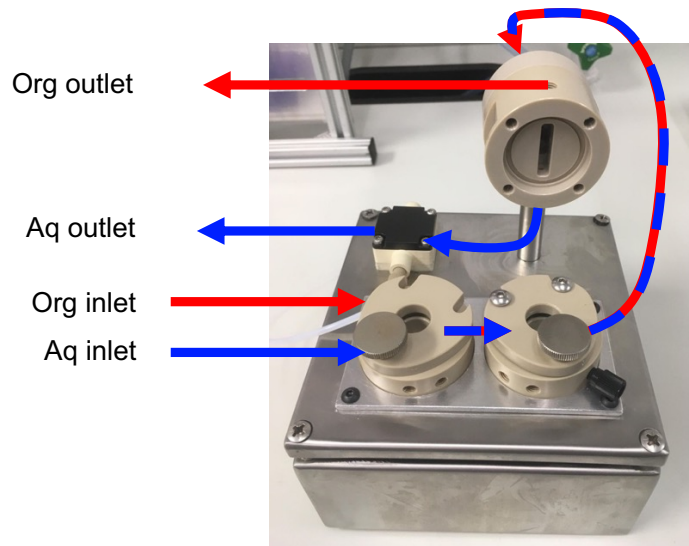
Figure 6.3: Assembled module from multistage unit labelled with the inlets and outlet of the module.

6.3 Electrical design

In figure 6.4 the Matlab controlled systems electrical design is shown. A 12V, 5A power supply is connected to the 12V input on the RAMPS 1.4 stepper motor driver shield. This supply powers up to 5 pumps (3 used in practice), the Arduino controller and the connected tentacle shield (conductivity circuitry). A laptop is connected to the Arduino USB serial port to allow communication between the user and the Arduino via a Matlab GUI. This design is broadly similar to the single stage pump system design. The only difference is the inclusion of multiple pumps and conductivity sensors.
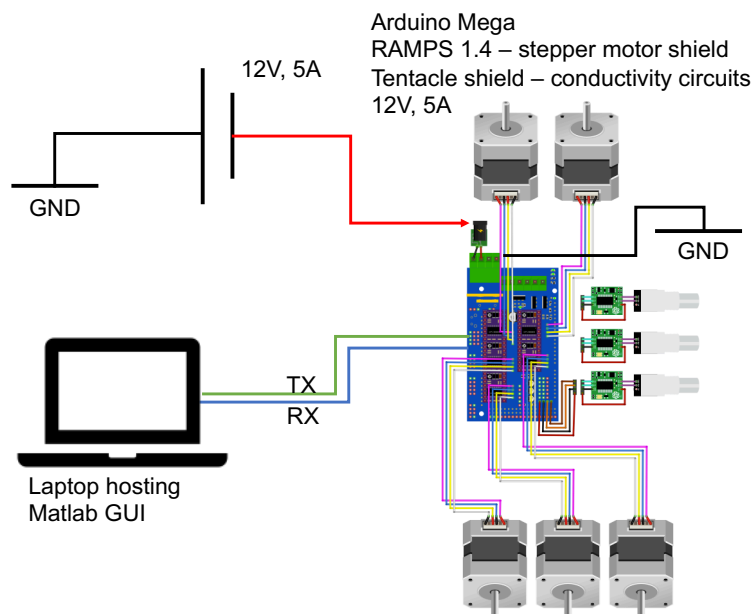
Figure 6.4: Electrical connections in the multistage extraction system - Matlab GUI version.

6.4 Control system

In order to optimally control the multistage platform the user could change various parameters of the system such as flow rates, number of stages and PID setpoint. To do this a user interface was required.

6.4.1 Matlab control system

The matlab based user interface was ideal in several ways:

- Matlab is a familiar tool with a wide range of functionality built in making building and testing fast.
- The electronic design had already been proven with a single stage system.
- The Matlab GUI allows for real-time plotting of the incoming data from pumps and conductivity probes.

Some of the draw backs of the Matlab system were:

- A laptop was required for use in the lab which is at risk of damage from chemicals.
- Matlab was required which is expensive if the organisation using the multistage platform does not already have a license.
- An additional power cable is required for the laptop.
- An additional power cable is required for the magnetic stirrers.

Figure 6.5 shows the graphical user interface as seen upon start-up of the system. To perform a standard run with the multistage platform the following steps should be taken:

1. The user should set the various parameters on the GUI. These parameters include: the inlet flow rates, an initial estimate of the PID setpoint and PID constants, which phase is heavier (aqueous or organic), if external pumps are being used at the inlets, the flow rate limits, which pumps are in use, which outlets the pumps are connected to, what microstepping is set on the pump stepper motors and which separator is attached to the system (2ml version or 6ml version). The system has set default values for each of these parameters but can be changed.
2. Once the user has set the variables they can click 'Start'. This will begin pumping the interstage pumps, start measuring conductivity within the separators and initialise the PID controller. The measured conductance and pump rates will appear on the graphs on the righthand side of the GUI.

3. Once a steady rate of fluctuation in the pump and conductivity readings is seen the user can press the 'Automate setpoint' button. This button will run the automate setpoint algorithm described in chapter 4 and provide a new 'optimum' setpoint for the PID controller. At any point the user can adjust the parameters manually on the GUI.

4. Once the experimental run has completed the user should click 'Start' again to stop the pumps and conductivity readings.

5. To save the pump and conductivity reading data click the 'save data' button at the bottom of the GUI.
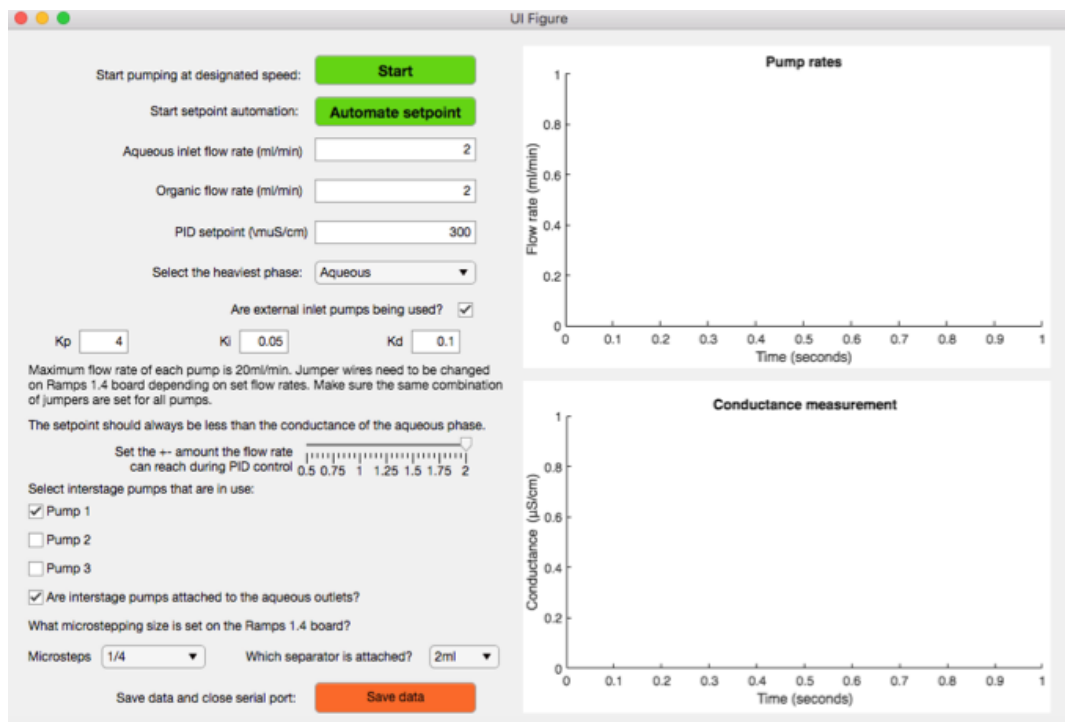
Figure 6.5: Matlab GUI for multistage extraction unit

Figure 6.6 shows the steps involved in controlling the multistage platform when using the Matlab GUI and what communication/interaction the Matlab interface has with the Arduino host. When plugged in, both Matlab and the Arduino initialise the various required parameters. The Arduino will then wait until it receives data from Matlab before it does anything else. At this point the user is at step 1 (steps above) and can change the parameters as they see fit and move onto step 2. Once start has been pressed the Matlab GUI will send the most recent set of parameters and a start bit to the Arduino. The Arduino recognises that it has serial data to read and then decomposes it and allocates the data to the correct variables on the Arduino. Because start has been pressed the Arduino will then start reading the conductivity for each of the in-use pumps, calculate the required pump flow rates from the PID controller, set these flow rates and then send this data back to Matlab. Matlab will receive this data and plot it on the GUI graphs. Matlab will check if the user has

changed any of the system parameters and send serial data back to the Arduino to do the next lot of sensor readings and PID calculations. This cycle will continue until the user presses stop (step 4). If the user presses the 'Automate setpoint' button (step 3) the communication stays the same as if it had not been pressed. Only the pump flow rates are overwritten with a value until the automation is completed and then a new setpoint value is sent to the Arduino.
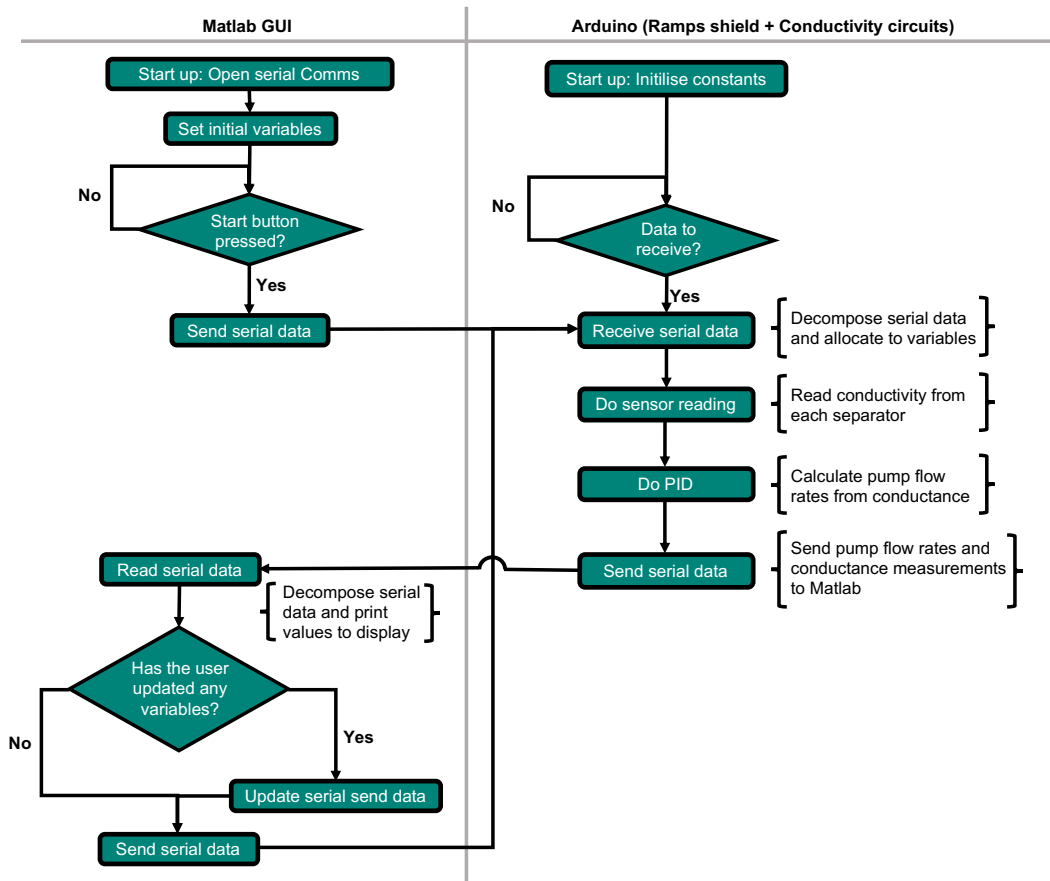
Figure 6.6: Communication flow chart between Matlab and Arduino

6.4.2 Multistage control algorithm

The control system for the multistage extraction platform is based on the control system developed for the single stage system. It was evident from early testing that arranging the separators in counter-current had a significant impact on the pump and conductivity variance over time. This is because each stage input is influenced by the previous, meaning any variation in stage one is accentuated in stage 2. Therefore, the PID constants used for a single stage separation were adjusted for counter-current flow systems. After this, three different methods of smoothing the input and output of the PID were investigated to try and reduce the variation in the PID output and finally an additional user controlled constraint was introduced into the system to reduce variation in the system and create a smoother overall flow.

Counter-current PID constants

A similar process to select the optimum PID constants for a single stage were deployed to select the optimum PID constants for multistage. A range of values for K_P and K_d values were tested to determine which gave the lowest variance in the pump standard deviation (σ_P) and conductance standard deviation (σ_c). When testing the 2 stage system K_P was tested at values of 1, 2.5, 5, 7.5 and 10, K_i and K_d were unchanged. Figure 6.7 show the difference in σ_P depending on the K_p value when K_i = 0.05 and K_d = 0.5. ρ_P did not differ significantly when K_P was adjusted, nevertheless a K_P value of 7.5 gave the best response with a standard deviation of 0.8 for both stages. Figure 6.8 shows the change in σ_c when K_P = 1, 2.5 5, 7.5 or 10 and K_i and K_d were unchanged. The conductance standard deviation reduced as K_P was increased. At K_P = 1, $\rho_c \approx 600$ and at K_P = 10, $\rho_c \approx 80$.
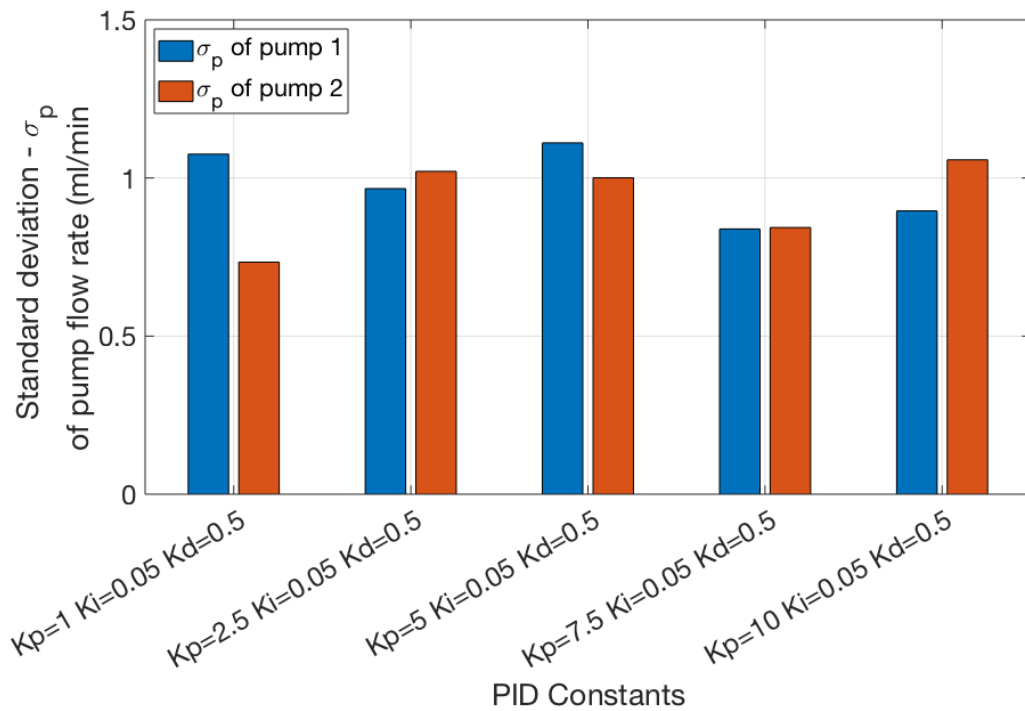
Figure 6.7: Pump standard deviation (σ_P) of the first and second stage separators in a counter current arrangement depending on the K_P value of the PID controller.
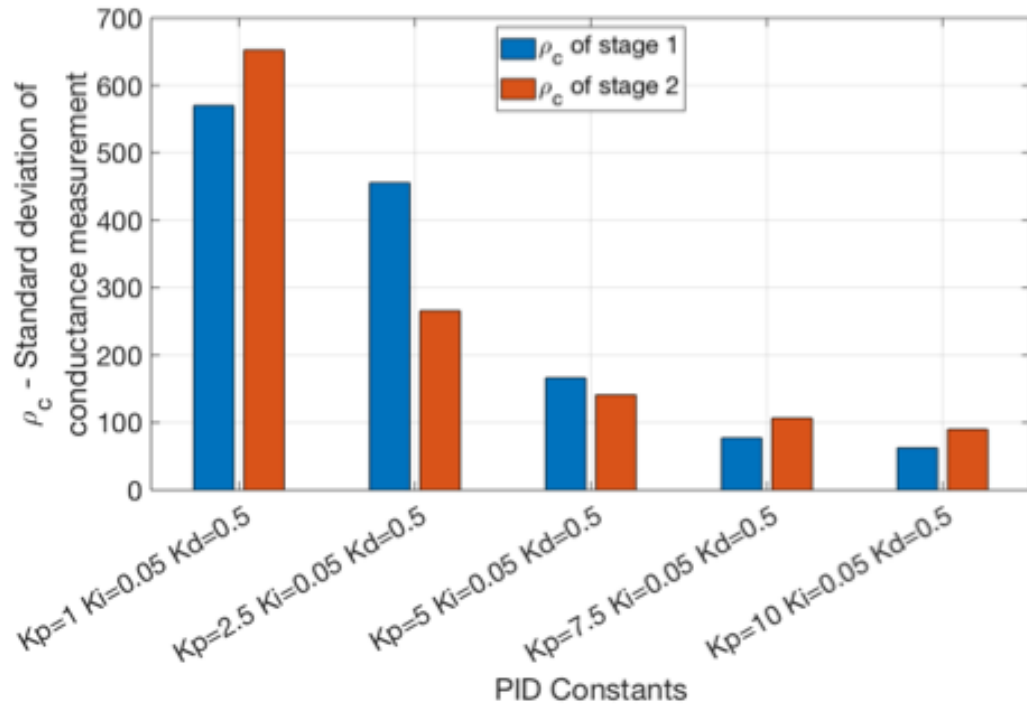
Figure 6.8: Conductance measurement standard deviation (σ_c) of the first and second stage separators in a counter current arrangement depending on the K_P value of the PID controller.

Figures 6.9 and 6.10 show the conductance measurement and outlet pump response over time for both of the extraction stages when K_P = 2.5 and when K_P = 7.5. In both of these cases the standard deviation of the pump rate was poor (1 and 0.8). The response over time was significantly different when K_P was changed from 2.5 to 7.5. At K_P = 2.5 the pump response to the measured conductance going above the PID setpoint followed the shape of a sinusoidal wave, whereby the pump flow rate increased until the conductance level dropped, the pump rate then decreased and the conductance level rose again at which point the pump flow rate began to rise again over a period of approximately 125 seconds. When K_P = 7.5 the response to a change in conductance was more aggressive and so the pump flow rate increased, decreased and increased again over a period of 10 seconds. The more aggressive response was preferable as it did not allow the conductance value to plateau (meaning the water level is above both probes) which may lead to phase crossover at the outlets.
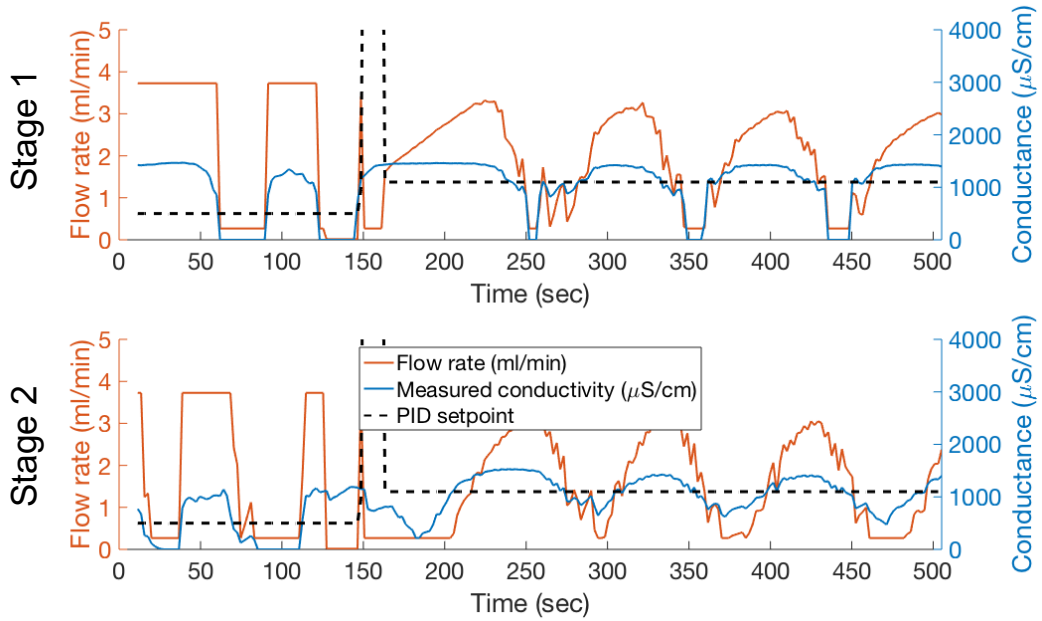
Figure 6.9: The outlet pump flow rate and corresponding conductance measurement for both stages of the counter-current flow setup when K_P = 2.5, K_i = 0.05 and K_d = 0.5.
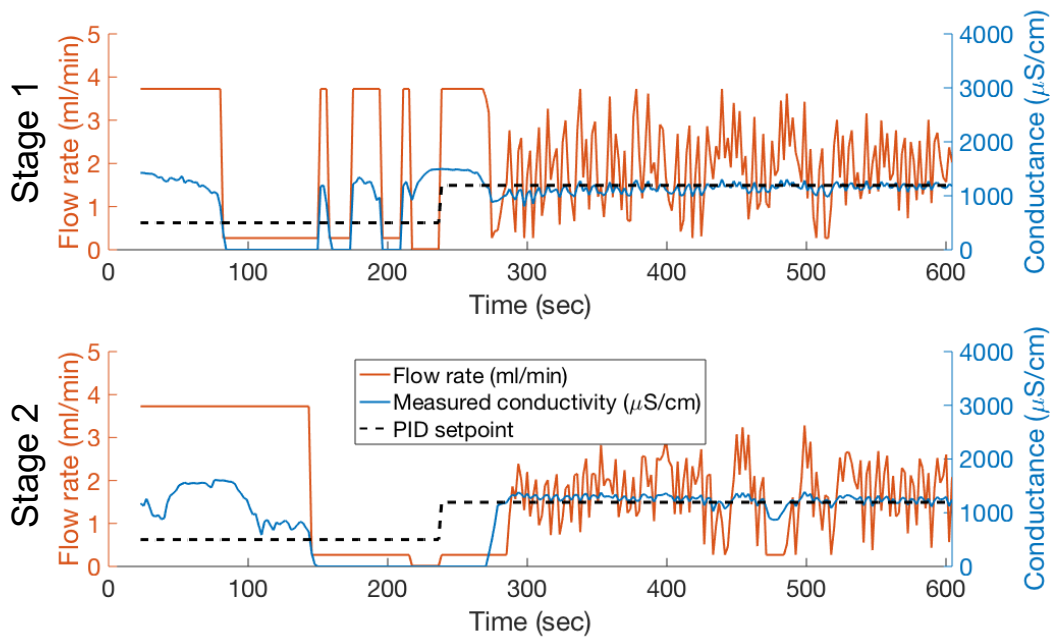
Figure 6.10: The outlet pump flow rate and corresponding conductance measurement for both stages of the counter-current flow setup when K_P = 7.5, K_i = 0.05 and K_d = 0.5.

K_d controls the PID response to the rate of change of the conductivity measurement. Because the conductance value changes quickly around the setpoint, the gradient is often steep. The K_d value was therefore reduced to stop the pump response from being overly aggressive (particularly since K_P had been increased). Figures 6.11 and 6.12 show how changing K_d from 0.5 to 0.1 affected σ_P and σ_c.
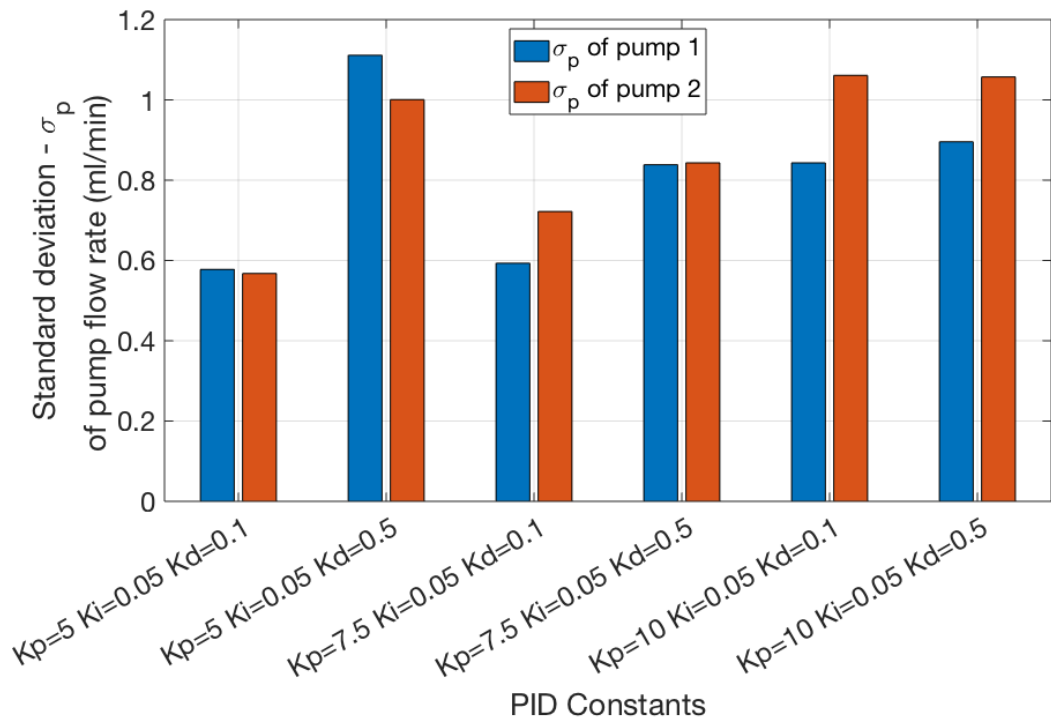
Figure 6.11: Pump standard deviation (σ_P) of the first and second stage separators in a counter current arrangement depending on the K_P and K_d value of the PID controller.
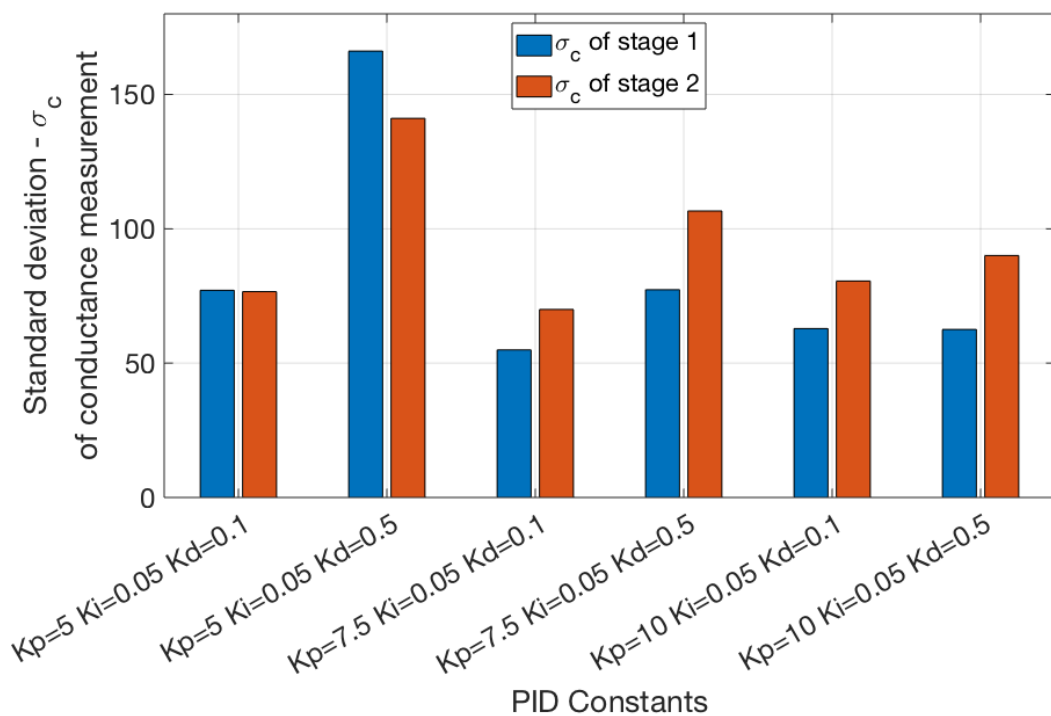
Figure 6.12: Conductance standard deviation (σ_c) of the first and second stage separators in a counter current arrangement depending on the K_P and K_d value of the PID controller.

As can be seen in figure 6.11 changing K_d to 0.1 reduced the standard deviation of the pump flow rate when $K_P = 5$ and when $K_P = 7.5$. Changing K_d to 0.1 also reduced

the conductance standard deviation when $K_P = 5$. The PID constants $K_P = 5$, $K_i = 0.05$ and $K_d = 0.1$ now gave the lowest standard deviation in pump flow rate compared to the other values tested and also kept the conductance standard deviation low. Figure 6.13 shows the response over time of the pumps and conductance measurement when $K_P = 5$, $K_i = 0.05$ and $K_d = 0.1$. The pump has a smaller response to a change in conductance than when $K_d = 0.5$.
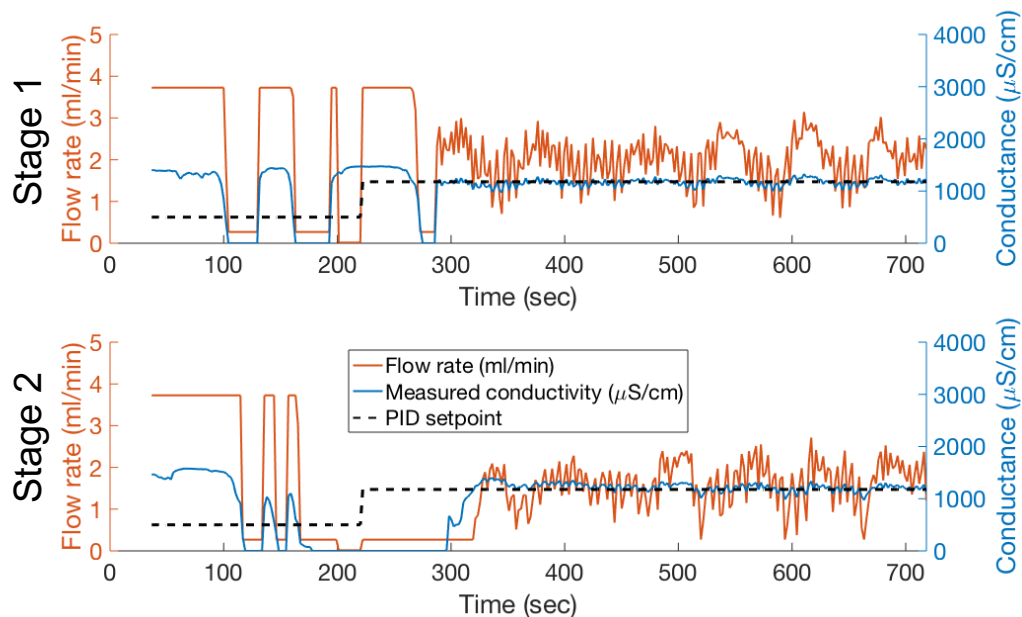
Figure 6.13: The outlet pump flow rate and corresponding conductance measurement for both stages of the counter-current flow setup when $K_P = 5$, $K_i = 0.05$ and $K_d = 0.1$.

Once the PID constants had been selected, the system was tested at different setpoints to see how the pump flow rate standard deviation varied. Figure 6.14 shows the system response at 4 ml/min and 16 ml/min and with a high and low conductivity solution. As figure 6.14 (a) and (b) show, the system gives very high variance unless the setpoint was close to the maximum conductivity of the solution (e.g. normalised $s(t) > 0.8$). This meant the system only operated well within a small window of conductivities relative to the conductance of the solution. To create a more robust system that could operate well at lower setpoints, two measures were introduced: Smoothing was applied to the PID input/output and adjustment to the flow rate limits.
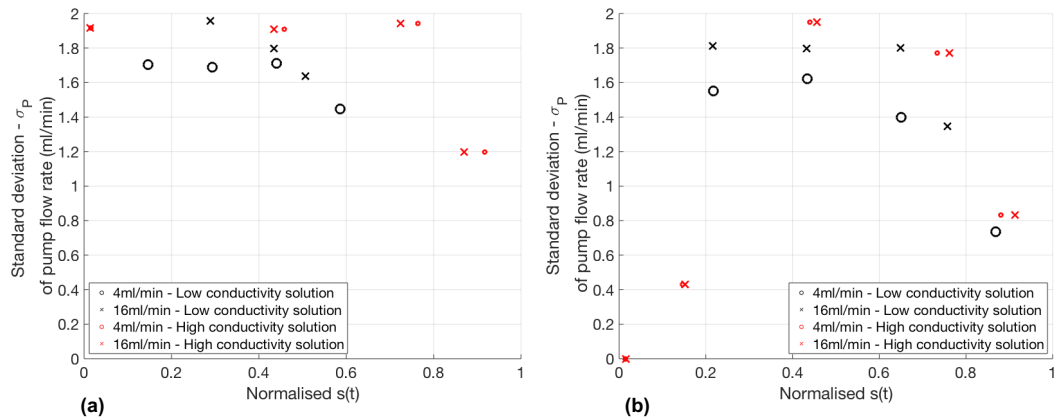
Figure 6.14: (a) Standard deviation of pump flow rate during stage 1 and (b) standard deviation of pump flow rate during stage 2 in counter-current arrangement at 4 ml/min and 16 ml/min and using either a low or high conductivity solution.

Smoothing

Two types of filters were applied to the PID output and input to examine their potential to reduced the variance in the pump flow rates. The first was a moving average filter which takes the mean of a defined number of inputs from the current and previous timesteps to calculate the average. Equation 6.1 shows the calculation applied to the filter input value to provide a smoothed output value. The moving average filter was applied to either the input, output or both input and output of the PID controller. The moving average filter was applied across either 3 or 5 timesteps.

$$y(n) = \frac{1}{N} \sum_{i=0}^{N-1} x(n - i) \tag{6.1}$$

$y(n) =$ Current output

$N =$ Number of inputs to average

$x(n) =$ Current input

The second type of filter applied was a low-pass finite impulse response filter. This type of filter is designed to remove high frequency 'noise' in a signal while keeping the low frequency data. This is achieved by multiplying the input data (unfiltered conductivity measurement) by the impulse response of the filter. This is shown in equation 6.2.

$$y(n) = \sum_{j=0}^{N-1} h(j). x(n - j) \tag{6.2}$$

$y(n) =$ Current output

$N =$ Number of inputs to filter

$x(n) =$ Current input
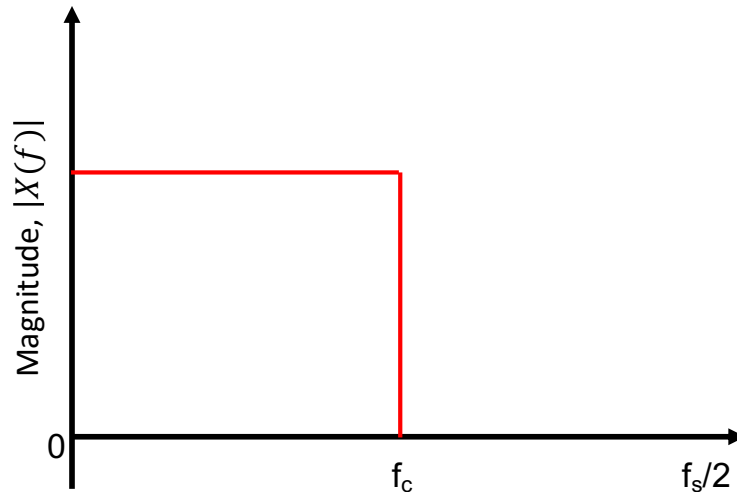
Figure 6.15: Ideal amplitude response for a low-pass filter

An ideal lowpass filter will look like figure 6.15 in the frequency domain. The filter will keep all of the low frequency data below the cut-off frequency f_c where f_s is the sampling frequency and remove all of the frequencies higher than f_c. The fourier transform of the filter impulse response is the frequency response of the filter (e.g. figure 6.15). Therefore, taking the inverse fourier transform of the filter frequency response results in the impulse response of the filter as shown in equation 6.3 and 6.4.[169]

$$h(t) = \frac{1}{2\pi} \int_{-\infty}^{+\infty} X(\omega) \cdot e^{j\omega t}\, d\omega \xrightarrow[\omega = 2\pi t]{} h(t) = \frac{1}{2\pi} \int_{-f_c}^{+f_c} e^{j2\pi ft}\, df \tag{6.3}$$

$$h(t) = \frac{\sin(2\pi f_c t)}{\pi t} \tag{6.4}$$

$h(t) =$ Impulse response of ideal lowpass filter

$t =$ time

$f_c =$ Cut-off frequency
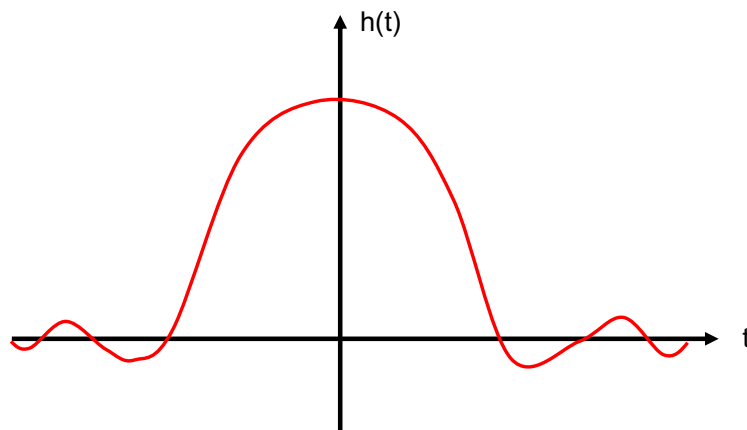
Figure 6.16: Impulse response from an ideal low pass filter

The impulse response of this filter looks like figure 6.16. There are some issues with this filter design:

- It is non-causal (has t values < 0)
- It has infinite length
- It is continuous

To implement a lowpass filter, several operation need to be carrier out. The response needs to be shifted to the right, removing the t < 0 portion of the graph, the response needs to be truncated so that it is not of infinite length and the response needs to be split into discrete sections so that it can be sampled at fixed periods. By doing these operations the filter frequency response no longer looks like the ideal filter, there are several discontinuities introduced and there is no longer a steep reduction in magnitude at the cut-off frequency, the frequency response now reduces with a gradient. Some of the issues are reduced by smoothing/windowing the impulse response. There are several methods of windowing/smoothing and changing the applied frequency response to reach a desired low-pass filter design. There are several tools available to determine the h(t) values of a desired filter design such as 'T-filter' - an online tool for calculating the impulse response of a filter.[170] T-filter was used to determine the filter coefficients (h(t) values which could then be integrated into a code to filter a given input). An FIR filter library is available on Arduino and was integrated into the PID controller when testing the low-pass filter. The designed filter from T-filter produced the following filter coefficients: 0.024 0.12 0.267 0.343 0.267 0.12 0.024. This meant the filter smoothed over 7 samples.

Once the low-pass filter had been developed, each of the smoothing methods could be tested on the PID control system. The moving average filter was applied over 3 or 5 samples of the conductivity measurement or 3 samples of both the conductivity and pump flow rate. The low pass filter was applied to the conductivity measurement. Figure 6.17 shows how the pump flow rate standard deviation changed depending on the filter type used in comparison to no filtering. Figure 6.18 shows how the conductivity measurement changed when filtering was introduced.

It can be seen in figures 6.17 and 6.18 that for both the pump flow rate and the conductivity measurement the moving average filter over 3 samples reduced the standard deviation by the greatest amount. The higher number of samples in the other cases introduced lag into the system which resulted in large variations in conductivity and flow rate over long oscillating periods.
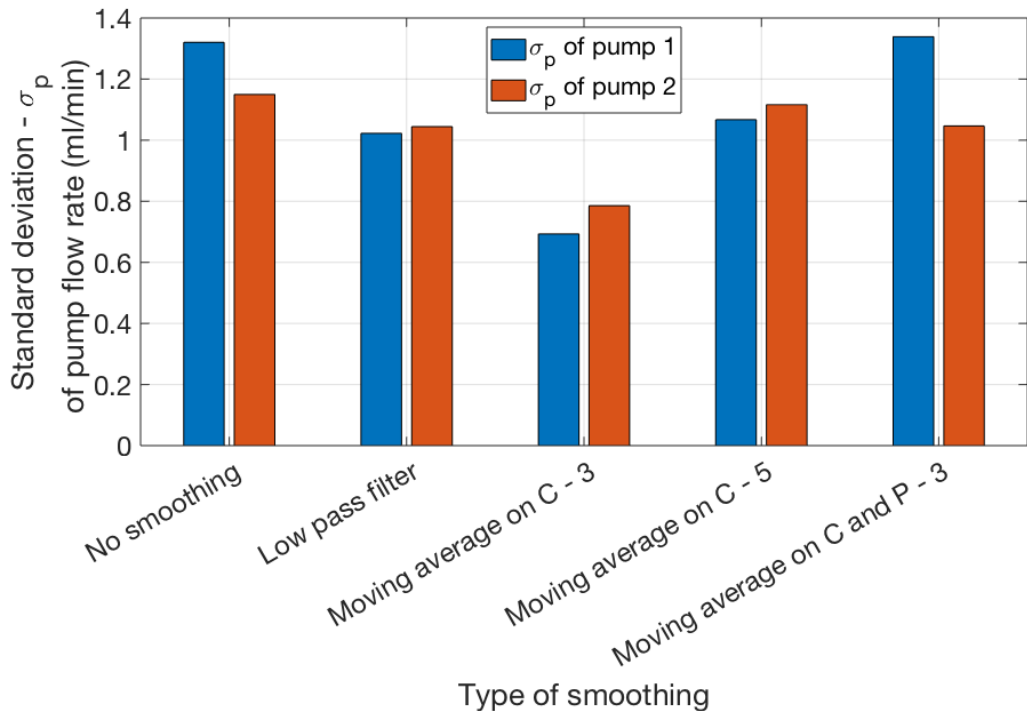
Figure 6.17: Standard deviation of stage 1 and stage 2 outlet pump flow rate depending on the type of smoothing applied to the PID controller.
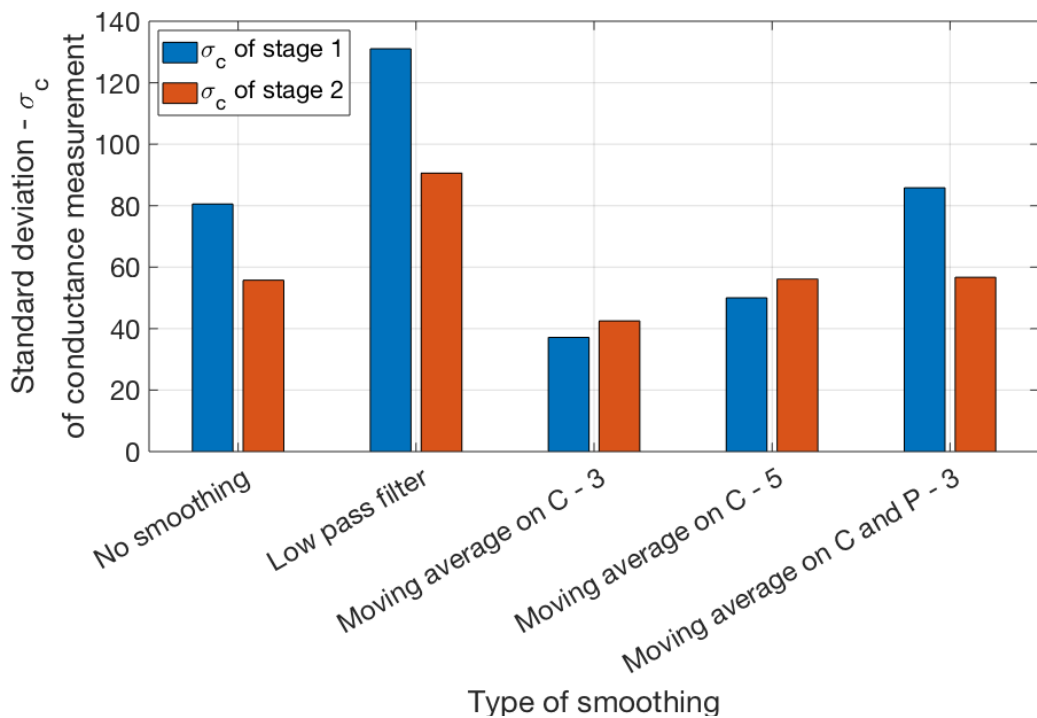
Figure 6.18: Standard deviation of stage 1 and stage 2 conductivity measurement depending on the type of smoothing applied to the PID controller.

Figure 6.19 shows the change in standard deviation of stage 1 and stage 2 outlet pump flow rate depending on (a) normalised setpoint of the system and (b) flow rate of the system. In 6.19 (b) the setpoint has been set using the initialisation procedure described in chapter 4. If we compare figure 6.19 (a) to figure 6.14 we can see that

the flow rate standard deviation is lower across a wider range of setpoints. When using the initialisation procedure the flow rate standard deviation never went above 1 whether the flow rate was 2 ml/min or 16 ml/min, however there was an upwards trend in the data as flow rate increased.
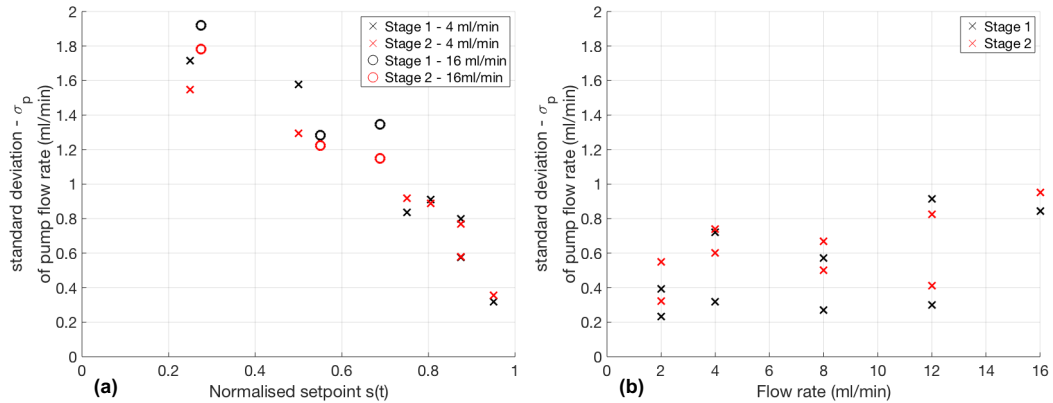
Figure 6.19: change in standard deviation of stage 1 and stage 2 outlet pump flow rate depending on (a) normalised setpoint of the system and (b) flow rate of the system.

<u>Flow limit adjustment</u>

The second method investigated to reduce the variance in the outlet control system was adjusting the flow rate limits. In every test so far the flow rate limit of the PID controller was set at ± 2 ml/min of the inlet flow rates. In the next test the flow rate limit was changed between ± 2, ± 1 and ± 0.5 ml/min. reducing the flow rate limits would artificially reduce the variance in the outlet flow rate as the PID could not increase or decrease as much as it could before. It would also mean a smaller change in flow rate would occur per change in conductance measurement. Both of these effects would reduce the overall variance in the outlet pump system. The downside of reducing the flow rate limits, particularly when multiple stages are involved is that if the system is partially soluble or the species to be transported from one phase to the other is highly concentrated then a large change in flow rate at the outlet compared to the inlet can be observed. If the flow rate limits are too small, this may mean that the pumps cannot pump fast enough to remove all of the phase which has increased in volume from stage to stage. Therefore, this method has been left as a user input, if the system requires a larger flow rate limit then ±2 ml/min can be used, otherwise a smaller value can be used.

Figures 6.20 through 6.22 show the outlet flow rate and conductance measurement of a 3 stage system when the flow rate limit is set at ± 2, ± 1 and ± 0.5 ml/min respectfully. As can be seen in the figures, as the flow rate limit reduces, the variance in the flow rate and the conductance measurement reduces in all 3 stages.
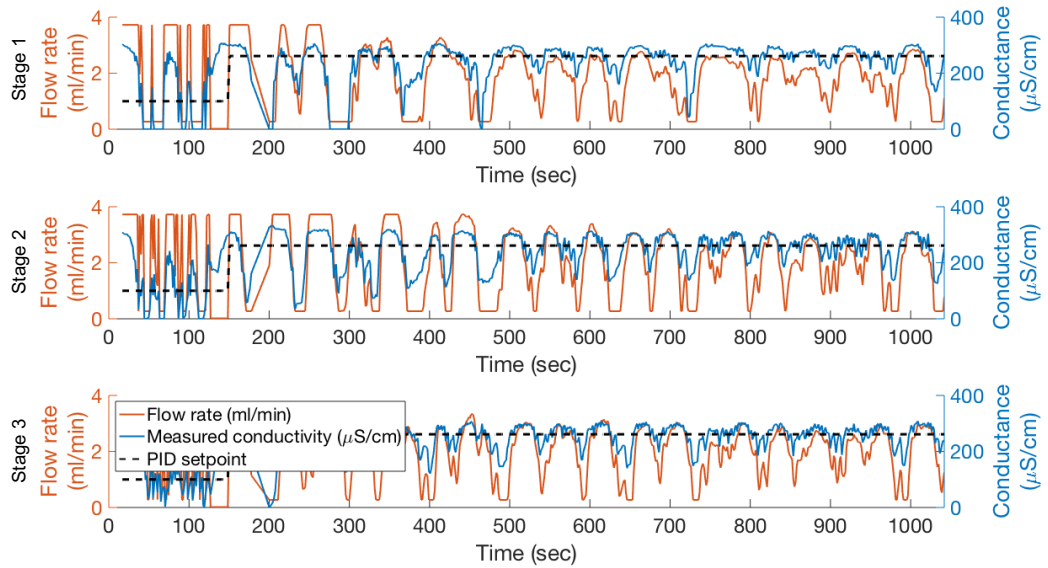
Figure 6.20: The outlet pump flow rate and corresponding conductance measurement for 3 stages of the counter-current flow setup when the flow limit was set at ± 2.
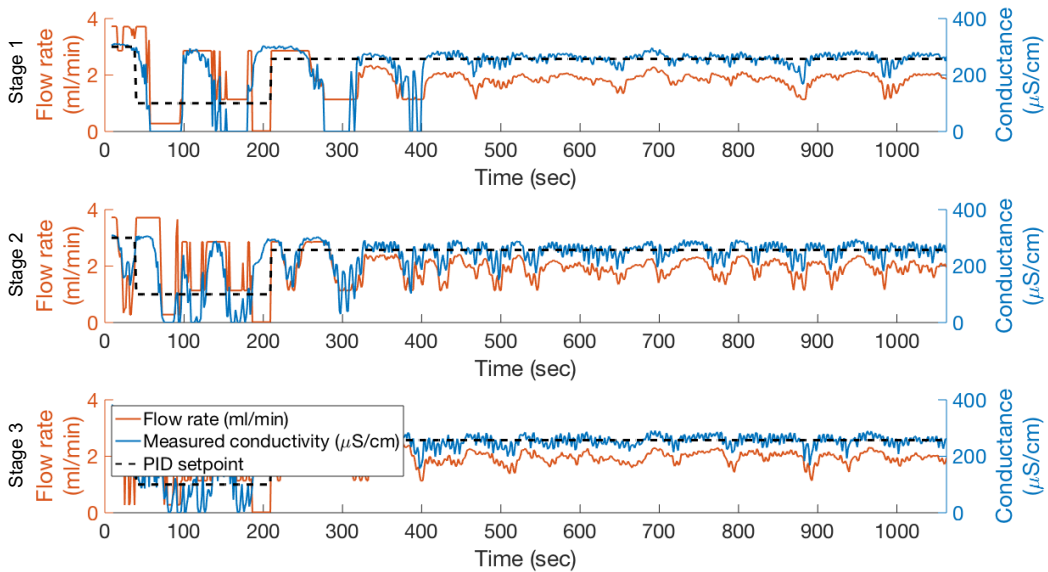
Figure 6.21: The outlet pump flow rate and corresponding conductance measurement for 3 stages of the counter-current flow setup when the flow limit was set at ± 1.
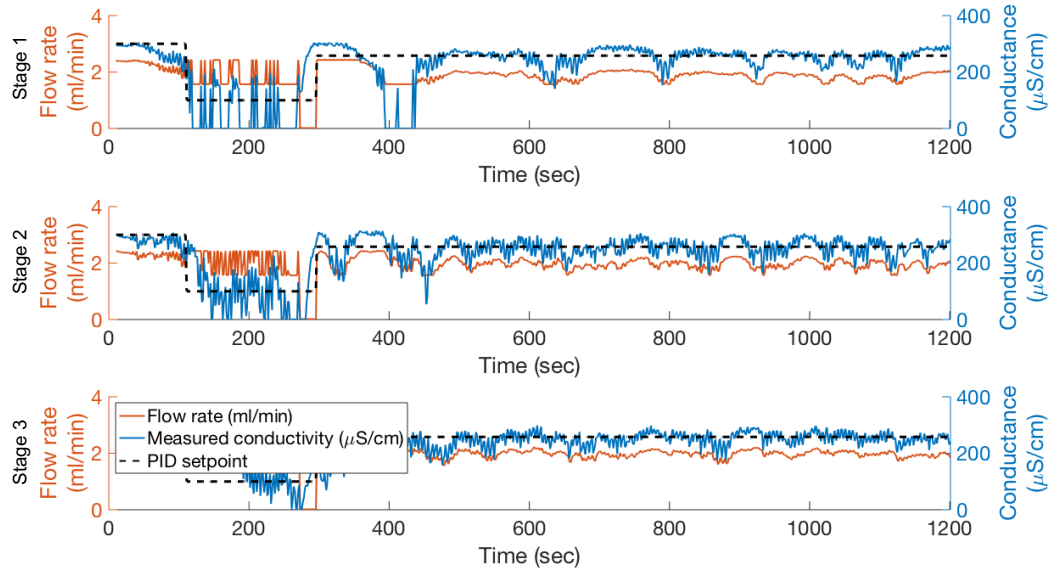
Figure 6.22: The outlet pump flow rate and corresponding conductance measurement for 3 stages of the counter-current flow setup when the flow limit was set at ± 0.5.

Figure 6.23 shows how the pump flow rate and conductance measurement varies at different setpoints. From figure 6.23(a) there is a clear and significant reduction in flow rate standard deviation when the flow rate limit is changed from ± 2 to ± 0.5. This is true for flow rates of 4 ml/min and 10 ml/min. When the flow rate limit was set at ± 0.5 there was not a significant difference in pump flow rate standard deviation when the flow rate was 4 ml/min compared to 10 ml/min. The reduction in conductivity measurement values shown in figure 6.23(b) is not very significant but there is a small change, particularly when s(t) is low.
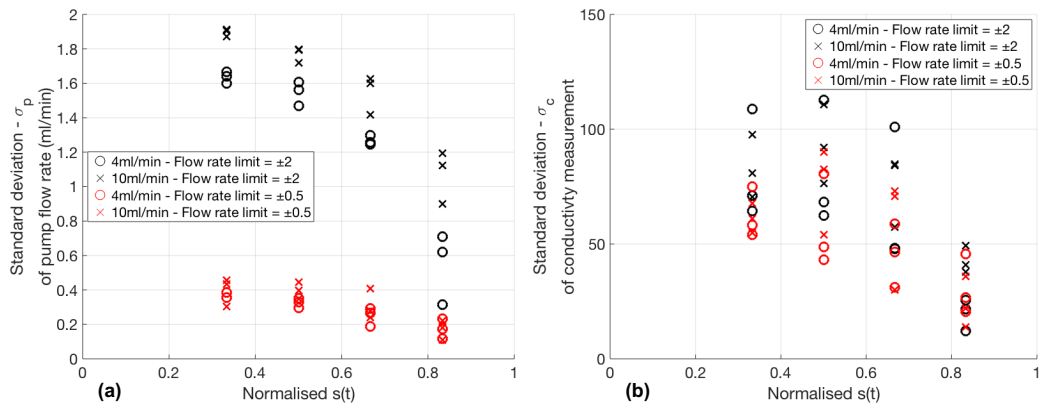
Figure 6.23: Standard deviation of (a) pump flow rate over 3 stages in counter-current arrangement and (b) standard deviation of conductance measurement in counter-current arrangement at 4 ml/min or 10 ml/min and with a flow rate limit of either ± 2 or ± 0.5.

6.5 Touchscreen

In this section a concept to use a touchscreen controller instead of the laptop connected controller is described. The differences between the touchscreen controller and laptop controllers electrical components, circuitry and GUI are presented.

6.5.1 Electrical housing

The electrical components were housed similarly to the single stage and multistage pump system except for the addition of mounting the touchscreen and additional power connections to the magnetic stirrers. The differences between the laptop connected system and the touchscreen system are as follows:

Touchscreen model	Laptop connected model
• 6 pin DIN connectors were used to connect the 4 wires needed to control the pumps and the two wires needed for the magnetic stirrers.	• 4 pin DIN connectors were used to connect the 4 wires needed to control the pumps. Externally powered magnetic stirrers were used.
• To power and communicate with the touchscreen a second Arduino was used. This Arduino relayed messages to and from the touchscreen to the Arduino controlling the pumps and conductivity sensors.	• The Arduino controlling the pumps and conductivity sensors is connected to Matlab through a USB serial connection which sends and receives messages.
• The touchscreen is mounted on the enclosure lid as shown in figure 6.24.	• No touchscreen, the user interface for the control system is on a Matlab GUI.

Figure 6.24: Touchscreen mounted on electrical enclosure lid.

6.5.2 Touchscreen circuit diagram

The touchscreen system used a 12V, 8A power supply to ensure enough power was supplied to the additional components included in this design. The power supply connected to the RAMPS 1.4 stepper motor driver shield in the same way as in the Matlab controlled system. This supplied power to the pumps, conductivity circuit and Arduino. The magnetic stirrers were connected in parallel to the 12V supply. Up to six were expected to be connected but in theory more could be connected. A 5V regulator was also connected to the 12V supply in order to power the second Arduino, which hosted the 4DSystems gen4-uLCD-43DT-AR resistive touchscreen display. This Arduino communicates via a serial connection between the touchscreen display and the Arduino hosting the RAMPS 1.4 board as shown in figure 6.25.
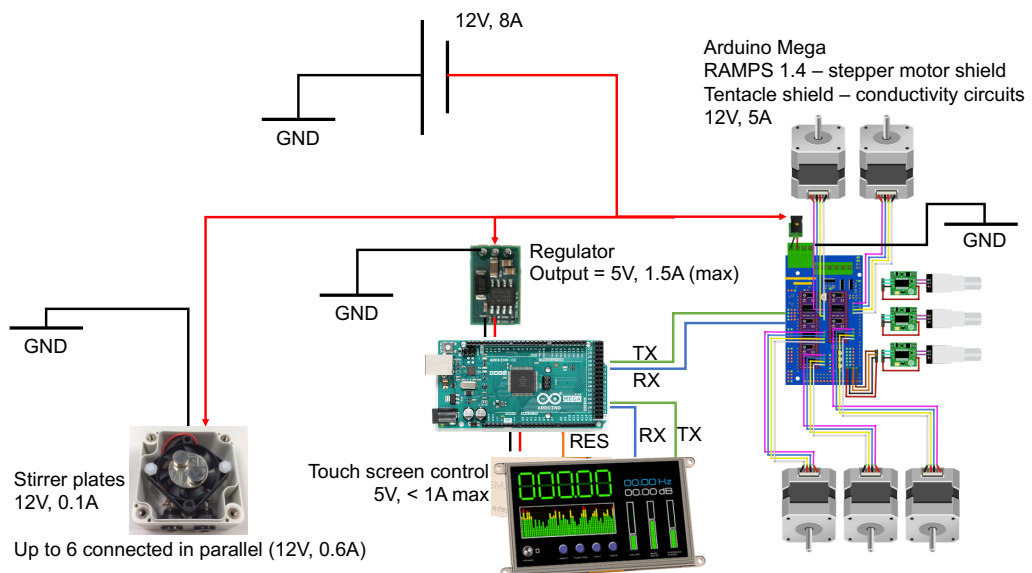
Figure 6.25: Electrical connections in the multistage extraction system – touchscreen version.

6.5.3 Touchscreen control system

The touchscreen controlled system operates in much the same way as the matlab controlled system. The main differences come from the addition of the second Arduino and different layout of the GUI. The touchscreen based system was preferable because:

- The system was standalone, no additional power sockets or laptops/computers were required to operate the system.
- The touchscreen is cheap compared to a laptop.
- The touchscreen coding interface is opensource and free to use.

Some of the draw backs of the touchscreen system were:

- The touchscreen coding lacks functionality making the graphical interface less user friendly.

- The touchscreen electronic design is more complex due to the additional Arduino.

The touchscreen module display is split into three screens (as seen in figures 6.26, 6.27 and 6.28). In the same way as with the Matlab GUI, the user can set each of the parameters before starting the pumps and PID controller. There are pre-set values for each of these that can be used. Upon start up page 1 (figure 6.26) will be displayed and the user can set the aqueous and organic flow rates and allowable flow rate deviation. The user can also set which interstage pumps are in use. The pump microstepping is set to ¼ step as default but can be changed. Once the user is happy with these values they can click next to go to page 2 (figure 6.27).
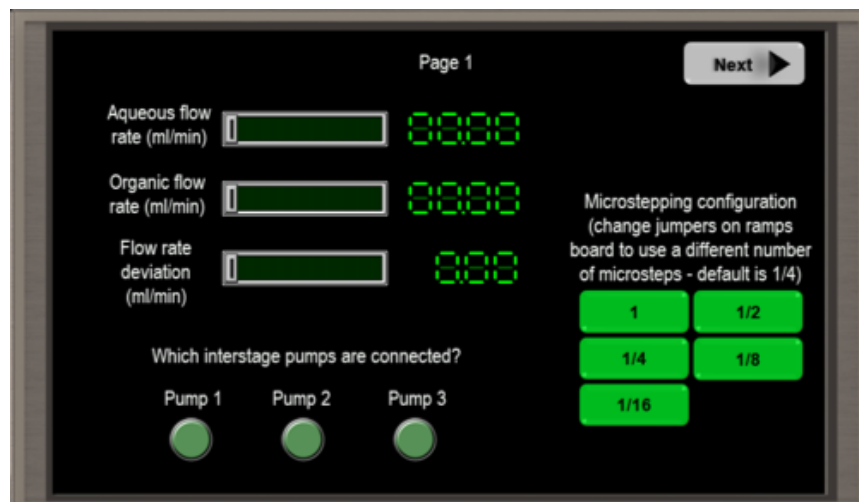
Figure 6.26: Touchscreen GUI for multistage extraction unit (Page 1)

In page 2 the user tells the system which phase is the heaviest and which phase the interstage pumps are connected to. The user can also set the PID constants to something other than the default values if they wish. The PID setpoint is set to 100 as default but can be changed using the setpoint multiplier and setpoint knob. Once happy with the values the user can click next to go to page 3 (figure 6.28).
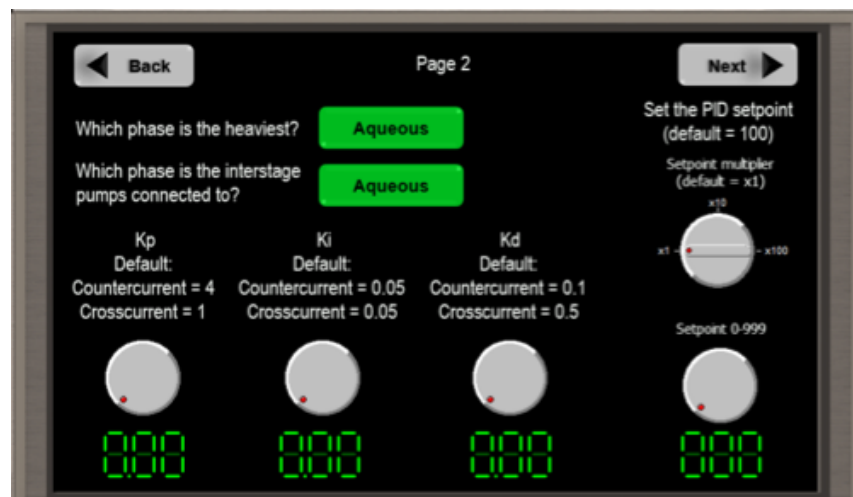
Figure 6.27: Touchscreen GUI for multistage extraction unit (Page 2)

In figure 6.28 the user can select whether the system is connected in cross-current or counter-current. This changes the PID constants accordingly. The user can start the pumps, conductivity readings and PID control from this page as well as perform the setpoint automation if they wish. The measured conductance will appear on the bottom graph (scaled between 0 and 1000) and the pump flow rates will appear on the top graph in microseconds (between 0 and 1000).
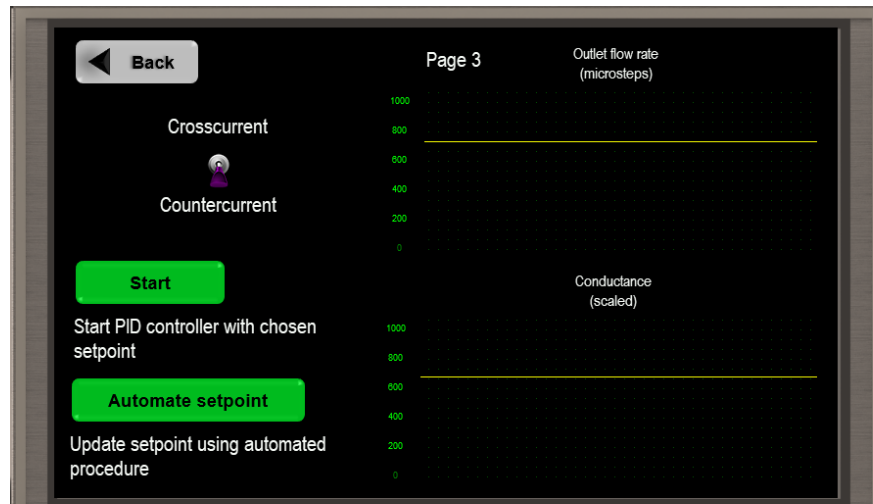
Figure 6.28: Touchscreen GUI for multistage extraction unit (Page 3)

Figure 6.29 shows the flow of information between the touchscreen, Arduino connected to the touchscreen and the Arduino connected to the Ramps shield. Upon start up the Arduinos initialise the default variables required to run the system. These variables are sent to the touchscreen to be displayed to the user. At this point the Arduino connected to the Ramps shield will do nothing until it received serial data from the other Arduino. It will not receive any serial data until the start button has been pressed by the user on the touchscreen. The user can update the variables they wish to change and click start. The pumps, conductivity sensor readings and PID controller will then begin. The pump flow rates and conductivity readings will be sent to the touchscreen to be displayed to the user on the graphs. If the user updates one or multiple variables after this point the controller will be updated accordingly. The PID controller will continue until the stop button is pressed.
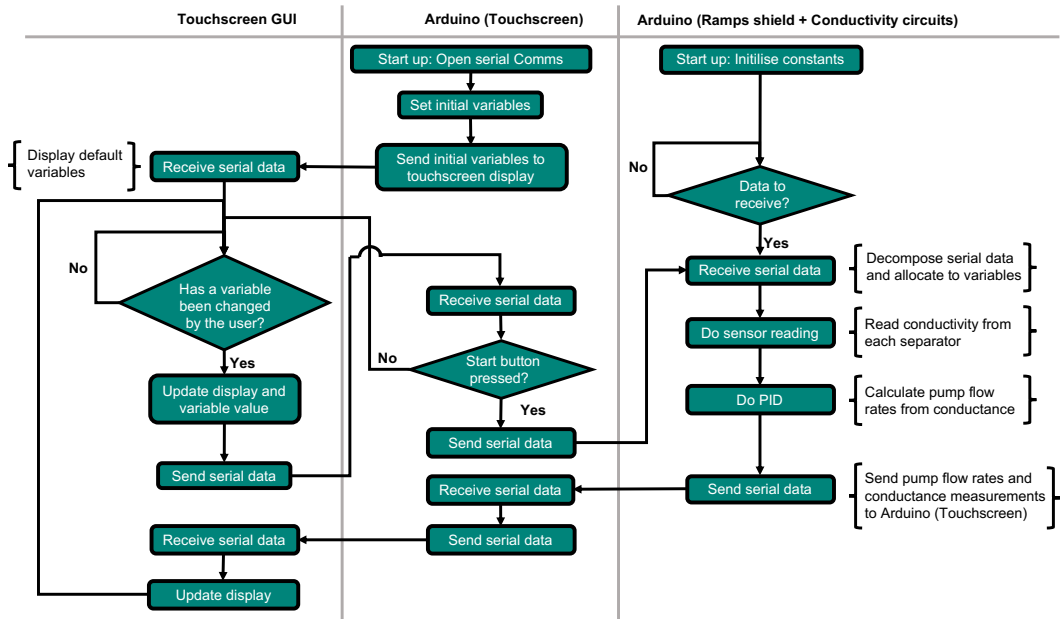
Figure 6.29: Communication flow chart between Touchscreen and two Arduinos

6.5.4 Conclusion

The touchscreen system has significant advantages over the Matlab/laptop controlled system. The system is standalone and no additional power sockets or laptops/computers are required to operate the system. Using a touchscreen also represents a cost reduction in comparison to the Matlab/laptop system. By removing the necessity of a laptop connection the electrical design has increased in complexity. The touchscreen system was not tested in the lab due to time constraints. However, the developed electrical design and GUI have been designed to operate with similar control logic as the Matlab/laptop control and therefore should operate in the same way.

6.6 Summary

In this chapter we have expanded upon the separator design developed in chapter 4 into a multistage separation platform complete with active mixing and automated separation. A touchscreen control system has been developed to replace the laptop controlled system to make the unit stand-alone. The multistage platform can currently control up to 3 stages but can be expanded to 5 with minimal change to the underlying control system. The platform is modular in design so that 1-3 stages can be easily connected together. The standard PID controller has been optimised for use in a counter-current system and further improved upon by introducing a filter to smooth the input data from the conductance probe and a flow rate limit adjustment parameter to minimise variance in the pump output. In the next chapter the 3 stage system will be used to study two different extraction systems.

Chapter 7 – Lab-scale multistage extractions in flow

7.1 Introduction

The aim of this chapter was to demonstrate the separator working during an extraction process and analyse the extraction depending on the number of stages used and the stability of any emulsion formed during processing.

The lab-scale multistage extraction platform developed in chapter 6 is used to perform two extractions in flow. The first is the removal of acetone from water with toluene. This system has been modelled in ASPEN Hysis as a single stage extraction as well as two and three stage counter-current extraction. This allowed the extraction platform developed in chapter 6 to be analysed with respect to equilibrium stages during an extraction process.

The second system under investigation is the extraction of 2-chlorobenzoic acid from benzoic acid and 2,6-dichlorobenzoic acid in 2-MethylTHF using different concentrations of NaOH solution. Firstly, the separation rate of the system at different phase ratios and NaOH concentrations was studied in batch. The system was then tested in flow as a single stage extraction as well as two and three stage counter-current. The extraction efficiency and purity found during experimentation has been presented for each configuration. The extraction was optimised with respect to inlet flow rates (phase ratios) and NaOH concentration.

The two example systems studied in this chapter demonstrate how the multistage platform can be utilised to characterise and optimise simple and complex systems in flow at lab-scale. The analysis of the benzoic acid systems separation rates in batch provides an understanding of the systems behaviour which can inform the selection of process variables for the scale-up of flow processes.

7.2 Water-Toluene-Acetone Extraction modelling

7.2.1 Introduction

The fraction of a solute left in the carrier phase can be determined with some simple equations if the feed carrier and extracting solvent are immiscible and the solute concentration is low (< 1%). The system is assumed to reach equilibrium after 1 stage. For a single extraction stage equation 6.1 can be used.[13]

$$\frac{x_R}{x_F} = \frac{1}{1 + E}$$

(7.1)

$x_R =$ Mole fraction of solute in raffinate

$x_F =$ Mole fraction of solute in feed

$E = \dfrac{KS}{F}$ Extraction factor

$K = \dfrac{x_{i,E}}{x_{i,R}}$ Distribution coefficient

$S =$ Solvent flow (s^{-1})

$F =$ Feed flow (s^{-1})

$x_{i,E} =$ Mole fraction of solute in extractant

If the system is arranged in a cross-current mode then N number of stages results in $\frac{S}{N}$ solvent per stage. The extraction factor per stage becomes $\frac{E}{N}$. The fraction of solute not extracted after N number of stages is then given by equation 7.2.[13]

$$\frac{x_N}{x_F} = \frac{1}{\left(1 + \frac{E}{N}\right)^N} \qquad (7.2)$$

$x_N =$ Mole fraction of solute after stage N

In a counter-current arrangement the fraction of solute not extracted is found from equation 6.3.[13]

$$\frac{x_R}{x_F} = \frac{E - 1}{E^{N-1} - 1} \qquad (7.3)$$

In the Water-Acetone-Toluene system, acetone is found in high concentrations (50 % weight in water). This means that the assumptions inherent in equations 7.1 to 7.3 are not satisfied and a different approach to find the fractions of solute in the raffinate and extract phases after each stage is required. A graphical method can be used to determine the required solvent flow rate and number of stages required to reach a desired concentration of solute in the raffinate phase in a counter-current arrangement assuming each stage reaches equilibrium. To do this, the ternary phase diagram of the system is necessary. In this section we examine the extraction of acetone from water into toluene using a graphical method as well as process simulation using Aspen plus V10 software.

7.2.2 Modelling method

Selection of a thermodynamic model suitable to the system in question is important for obtaining an accurate representation of that system. Al-Malah, 2017[171] recommends the use of an activity coefficient model as they tend to perform well for systems with polar compounds at low pressures away from the critical region. Three such models were used to create a ternary phase diagram of toluene-acetone-water. These phase diagrams were compared to the extraction results obtained experimentally in batch to find the model that represented the real system most

closely. The phase diagram that matched the batch results most closely was used in the subsequent process simulations for counter-current extraction.

The three thermodynamic models tested were:

- NRTL-RK (Non-Random Two Liquid with Redlich-Kwong equations)
- UNIFAC (Universal functional group activity coefficients)
- UNIQUAC (Universal Quasi-chemical model)

The three system components were set as water, acetone and toluene. When producing the ternary phase diagram the temperature was set at 25 ºC and a pressure of 1 bar. It was found that the UNIFAC model fit the batch experimental data best and so this method was used for the counter-current simulation. The ternary phase diagram produced by Aspen Plus V10 is given in figure 7.1.
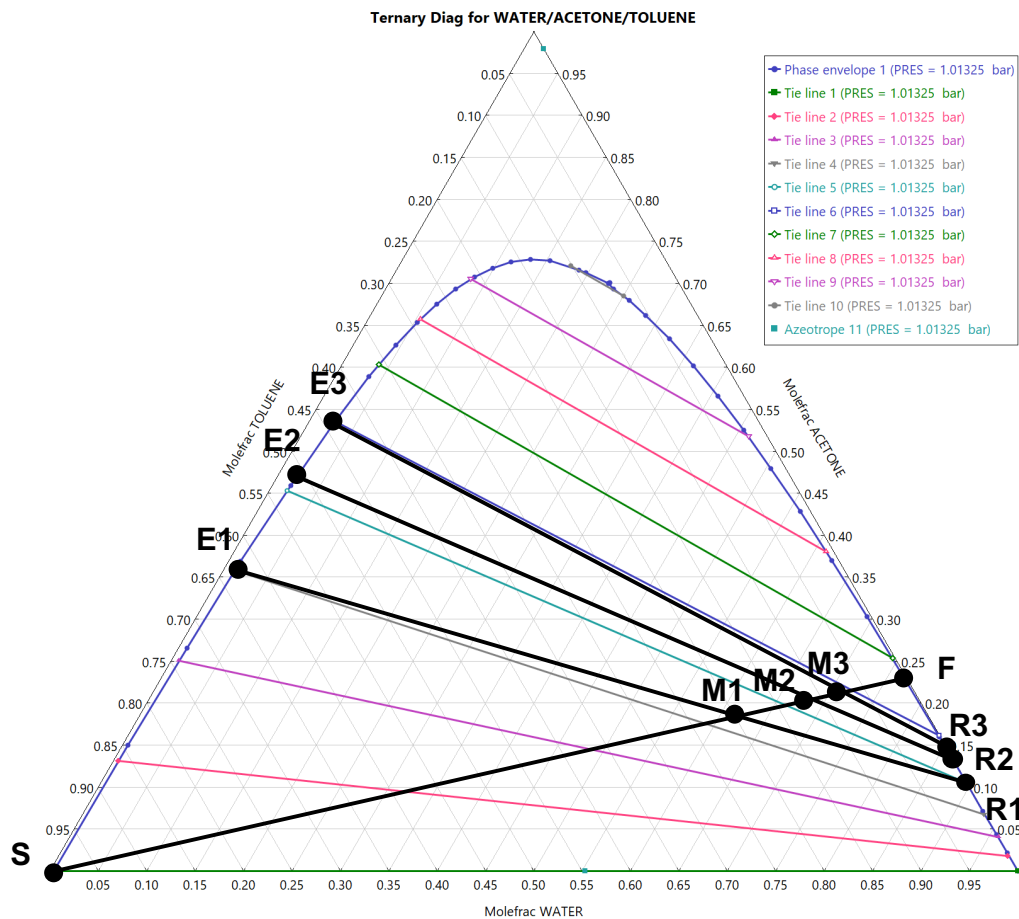
Figure 7.1: Ternary phase diagram of toluene-acetone-water system with overlayed extract and raffinate mole fractions at three phase ratios and the mixing point of each system.

The results from the batch extraction are overlayed on the ternary diagram so that the extract and raffinate found via experiments can be compared to the tie lines on the ternary diagram. The closer the direction of the tie lines matched with the extraction results, the better the model was deemed to be. In figure 7.1 S = Solvent composition, F = Feed composition, M_1, M_2, and M_3 are the mixing points found at

phase ratios of 1, 2 and 3. E_1, E_2 and E_3 and R_1, R_2 and R_3 are the extract phase and raffinate phase compositions when the solvent and feed were mixed at phase ratios of 1, 2 or 3. As can be seen from figure 7.1 the tie lines produced by the UNIFAC model match closely the experimental data found at phase ratios 2 and 3 well. However, the model data deviates from the experimental data at a phase ratio of 1 as the raffinate phase had a higher concentration of acetone than predicted by the model. Out of the three models tested, this model fit the experimental data best and was therefore used for the counter-current extraction simulation.

The simulation model was tested at a phase ratio of 1, 2 and 3 (Aq/Org). The simulation was also set up as either a single stage extraction, 2 or 3 stages in counter-current. Figure 7.2 shows the 3 different flow configurations and table 7.1 summarises the inlet stream compositions.
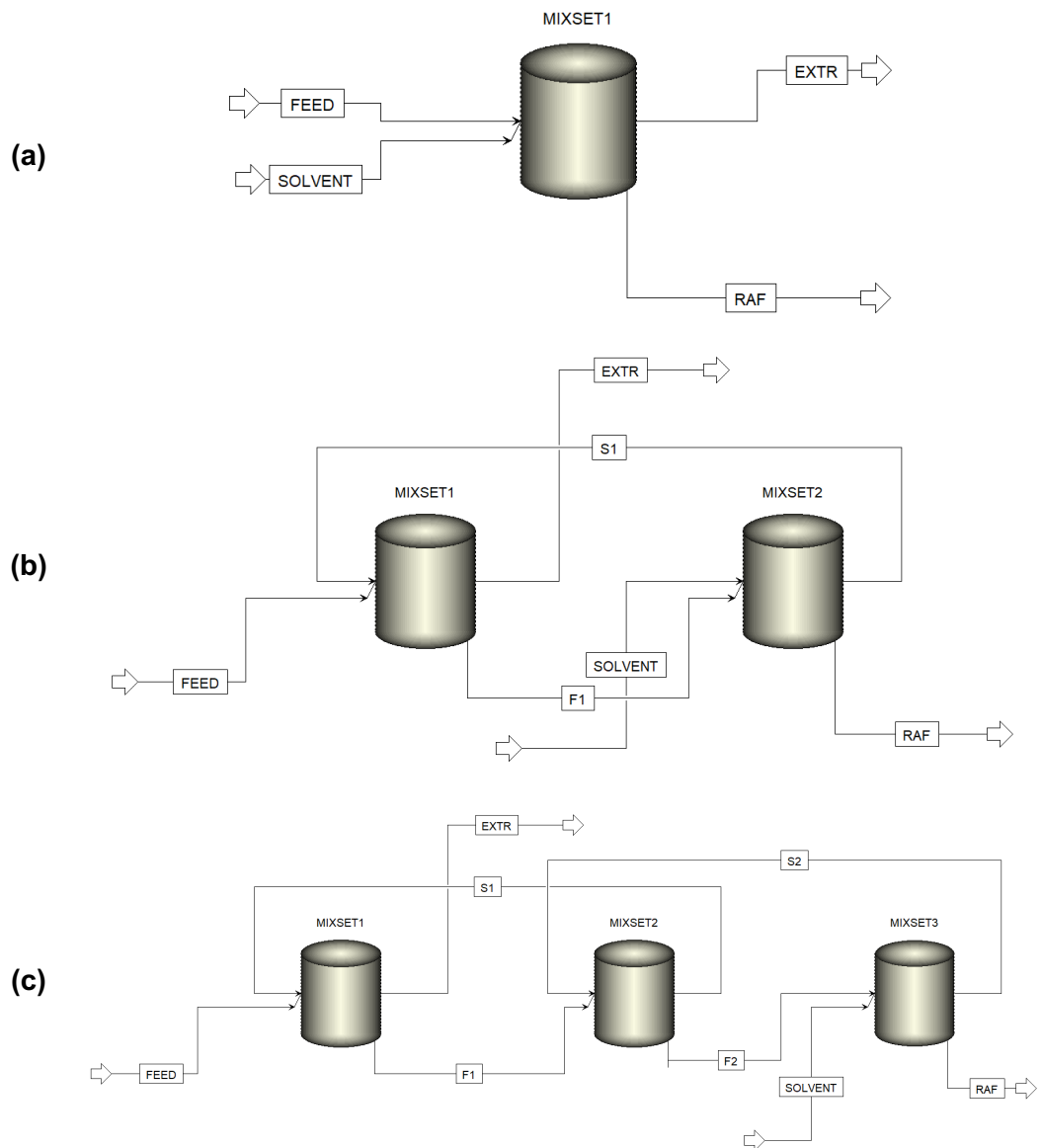
Figure 7.2: Counter-current flow simulation as (a) single stage, (b) two stage and (c) three stage extraction.

Table 7.1: Inlet flow compositions for each phase ratio and number of stages.

No of stages	Phase ratio (Aq/Org)	Feed flow rate (L/min)	Solvent flow rate (L/min)	Feed composition (kg/kg)	
1	1	1.5	1.5	Water	0.5
1	2	2	1	Acetone	0.5
1	3	2.25	0.75	**Solvent**	
2	1	1.5	1.5	**composition (kg/kg)**	
2	2	2	1	Toluene	1
2	3	2.25	0.75		
3	1	1.5	1.5		
3	2	2	1		
3	3	2.25	0.75		

The outlet streams ('extr' and 'raf') composition was collected from the model output data and has been presented in section 7.2.3. The weight fraction of the extract and feed streams combined with the stream flow rates gave the % of acetone extracted from the feed stream using equation 7.4.

$$\% \text{ acetone extracted} = \frac{C_{Acetone,Ex} \times Q_{Ex}}{C_{Acetone,F} \times Q_F} \times 100 \qquad (7.4)$$

$C_{Acetone,Ex} =$ Concentration of acetone in extract stream (kg/kg)

$C_{Acetone,F} =$ Concentration of acetone in feed stream (kg/kg)

$Q_{Ex} =$ Flow rate of extract stream (L/min)

$Q_F =$ Flow rate of feed stream (L/min)

7.2.3 Results

The mole and weight fractions of the extract and raffinate phases are given in the appendix C along with the total flow rates of each stream. Using the total flow rates of the feed and extract phases the percentage of acetone extracted from the feed can be found using equation 7.4. The % extracted for each phase ratio and number of stages tested using the UNIFAC model is summarised in figure 7.3.
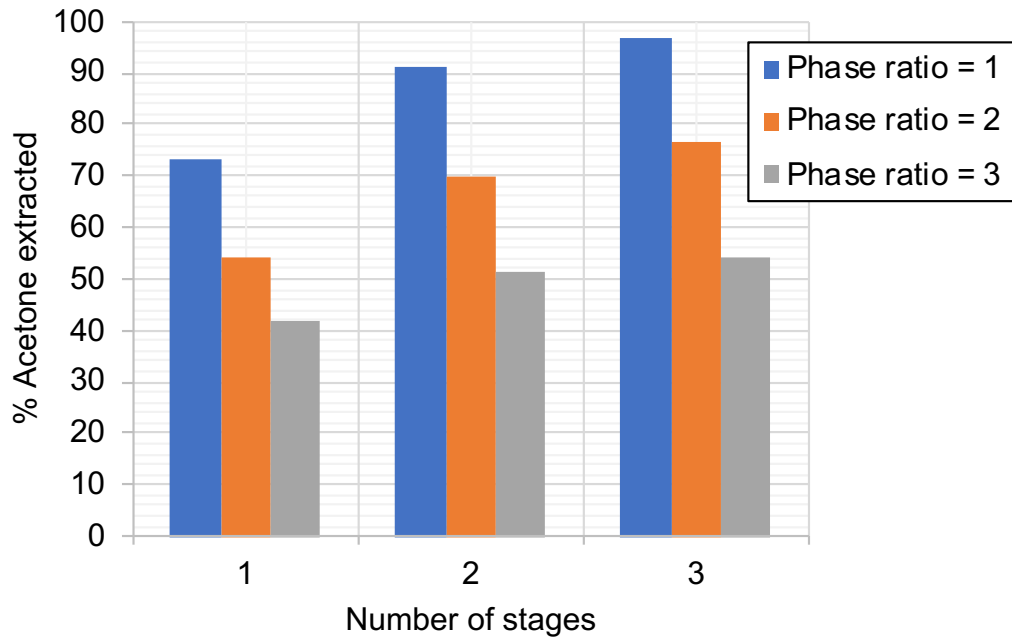
Figure 7.3: Percentage of acetone extracted from water using toluene depending on the number of stages and phase ratio of the inlet feeds.

7.2.4 Discussion

It is clear from figure 7.3 that, as the phase ratio is increased, the % of acetone extracted is reduced. This is logical as there is less toluene per kg of aqueous phase, therefore less solvent to extract the acetone. This is also shown in the ternary diagram in figure 7.1 by following the tie lines. At lower mole fractions of toluene (left hand side of triangle) the raffinate side (right hand side) contains more acetone and therefore less acetone has been extracted. An increase in the number of stages also resulted in an increase in % of acetone extracted at every phase ratio. The highest % of acetone extracted was 96.98 % at a phase ratio of 1 and 3 stages of extraction. After 1 stage at a phase ratio of 1 the % extracted was 73.05 % and after 2 stages was 91.05 %. This was a 33. 2 % reduction in the amount of acetone in the raffinate by increasing the number of stages from 1 to 2 and a further 33.7 % reduction from 2 to 3 stages.

7.2.5 Conclusion

From this model the number of stages required for a certain reduction in acetone concentration can be estimated. The number of stages required and the mass flow rate of solvent can be varied depending on the system economics, practicality and environmental impact. The model employed to give these extraction values are based on thermodynamic models and are assumed to reach equilibrium which is often not the case in reality. This does however mean it is a good benchmark to measure a

real extraction systems efficiency. In the next section the water-acetone-toluene system explored in this chapter will be studied experimentally, both in batch and as a continuous counter-current extraction, and compared to the model system.

7.3 Water-Toluene-Acetone Extraction

7.3.1 Introduction

The removal of acetone from water has been used multiple times as a standard test system to characterise extraction equipment and processes.[97,106,172] The system is inexpensive to use and is well understood thermodynamically, making it simple to model and obtain equilibrium data for single or multiple stages of extraction.

In this study the multistage extraction platform developed in chapter 6 was tested at three phase ratios as a single stage, two stage and three stage continuous extraction. We compare the obtained extraction efficiencies to a single wash batch extraction as well as to the modelled extraction efficiencies found in section 7.2. The high concentration of acetone in water meant that the separator would be challenged to deal with large changes in organic and aqueous flow rates between stages as the acetone transferred from one phase to another.

7.3.2 Experimental setup

In all experiments the aqueous phase and solvent solutions were made in the same way. 400g of Acetone was added to 400g of de-ionised water for the aqueous solution and the solvent was 99.8 % anhydrous toluene. 100 mg of NaCl was added to the aqueous solution so that a conductivity measurement was available during the flow experiments. The batch solutions were prepared as 10 ml samples with either 5, 6.66 or 7.5 ml aqueous solution and 5, 3.33 or 2.5 ml toluene depending on the required phase ratio. The solutions were hand shaken for 2 minutes, left to rest for 10 minutes and then shook again for 2 minutes and then left to rest for a further 30 minutes before a sample of the organic phase was taken for analysis via GC (Gas Chromatography).

In the flow setup, two Jasco PU 1580 1585 HPLC pumps were used to pump the organic and aqueous phases. The system was in either a single stage, two or three stage counter-current arrangement as shown in figure 7.4. Each stage consisted of two miniature CSTRs to mix the two phases and a 2ml separator with 10 layers of hydrophobic PBT filter media with an interstage pump connected to its aqueous outlet. Stage 1 was labelled as the stage at which the organic inlet entered and stage 3 was the stage at which the organic/extract stream exited the system.
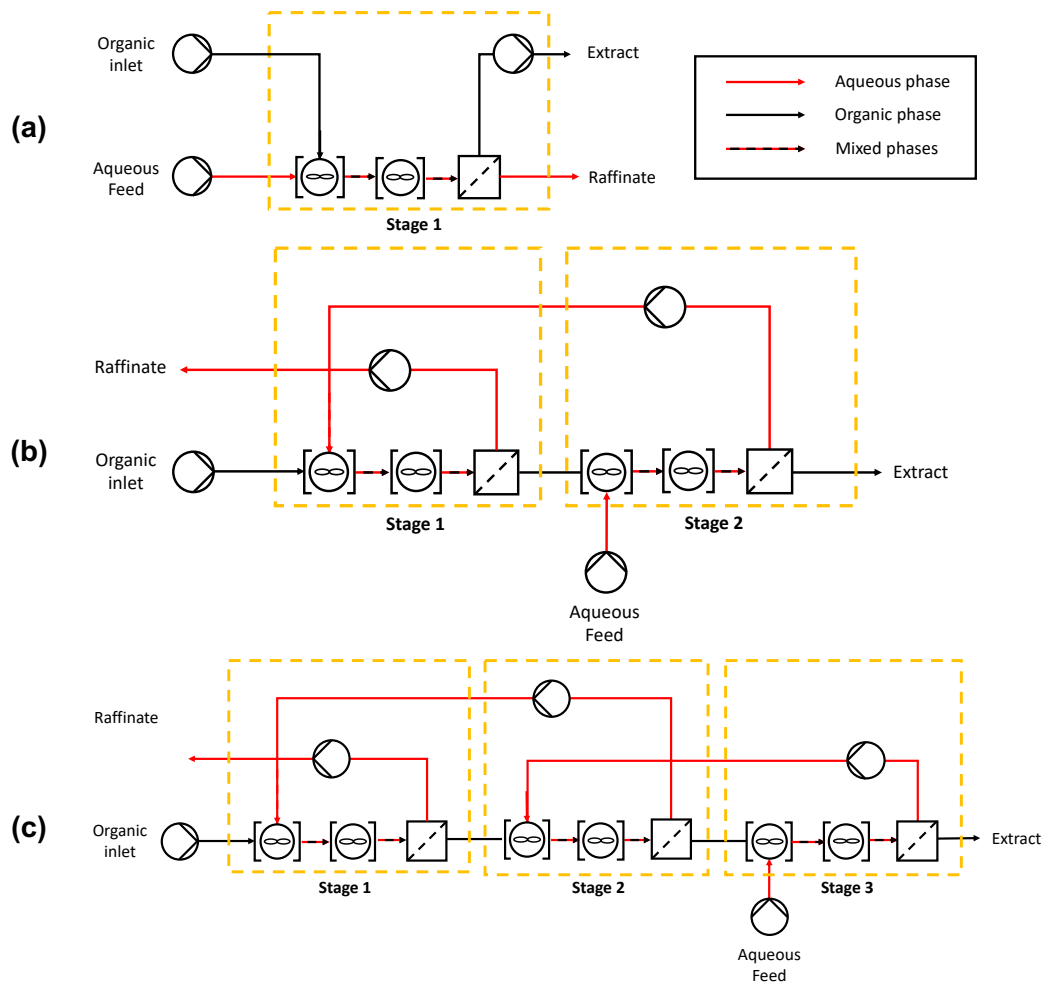
Figure 7.4: Arrangement of experimental system for (a) 1 stage, (b) 2 stage or (c) 3 stages

The total flow rate of the system was 3 ml/min for every experiment but the ratio of aqueous to organic flow rates changed between 1, 2 and 3 as was done for the model system. The flow rates of the streams at each of the phase ratios is given in table 7.2.

Table 7.2: Inlet flow rates at each phase ratio tested

Phase ratio (Aq/Org)	Aqueous/feed flow rate (ml/min)	Organic/solvent flow rate (ml/min)
1	1.5	1.5
2	2	1
3	2.25	0.75

Each of the phase ratios were tested for a single stage extraction, then two stages and then three stages. At each flow rate combination, the system was left to run for 30 minutes before a sample of the organic outlet (extract) was taken to allow the system to reach steady state. In order to determine the organic outlet flow rate, an 8 ml sample was collected and the time required to collect this sample was recorded.

A separate 5 ml sample of the organic outlet (extract) was collected for analysis using gas chromatography (GC).

7.3.3 Analysis method

To measure the amount of acetone extracted into toluene a GC method was created. This required a calibration curve in order to determine what peak area corresponded to what concentration of acetone. Therefore, a range of solutions with different concentrations of acetone and toluene were produced. Each sample was 10 ml in volume and had a different ratio of toluene to acetone. The weight and volume of acetone and toluene in each calibration sample has been presented in table 7.3 along with the peak area of each given by the GC method and the concentration of acetone in mg/ml calculated from the weight measurements of each solution. Figure 7.5 (a) plots acetone concentration against peak area in order to determine the straight line equation that describes the relationship between them and figure 7.5 (b) does the same but for the toluene concentration. The sample with concentration 39.43 mg/ml was omitted from the calibration curve because it was at a low concentration, much less than what was found during the actual extractions and it produced a large lever arm that influenced the straight lines angle (m in the straight-line equation y = mx + c).

Table 7.3: Weight, volume and concentration of calibration samples and their corresponding peak areas using GC

Toluene weight (mg)	Acetone weight (mg)	Toluene volume (ml)	Acetone volume (ml)	Concentration of acetone (mg/ml)	Toluene peak area	Acetone peak area
8235	8234	9.5	0.5	39.4	1348347	20092
7802	7800	9	1	78.6	1253709	40211
6938	6935	8	2.02	157.9	1096463	82086
6069	6065	7	3	235.4	966134	127331
5204	5199	6	4	313.5	816104	172058
4336	4330	5	5.01	392.2	693249	227873
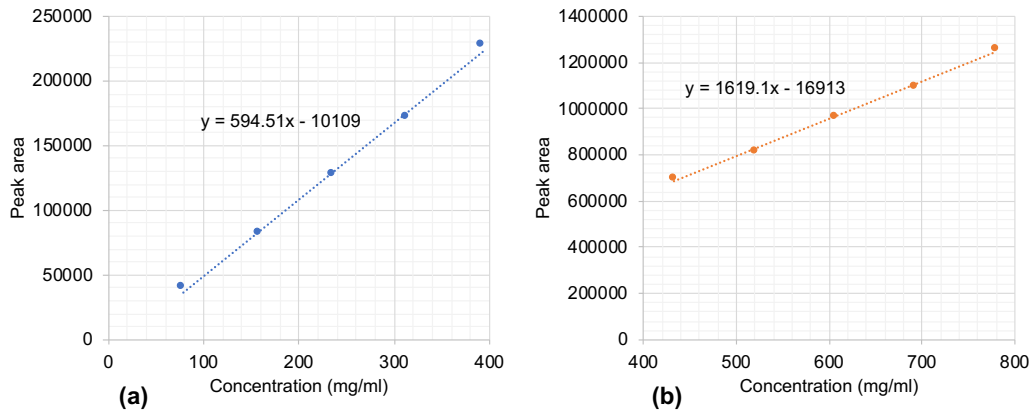
Figure 7.5: Calibration curve for (a) acetone concentration in acetone + toluene solution (omitting 39.42 mg/ml sample) and (b) toluene concentration in acetone + toluene solution (omitting the same sample).

The batch results were calculated under the assumption that toluene and water were immiscible, therefore all of the toluene would be present in the organic phase. Based on this assumption the volume of acetone in the organic phase after mixing with the aqueous could be calculated. Firstly the concentration of toluene was found using the toluene calibration curve and peak areas. As the mass of toluene added to the solution was known for each phase ratio, dividing this value by the concentration would yield the total volume of the organic sample after mixing. Taking this value and multiplying it by the concentration of acetone in the organic phase (found via the acetone calibration curve) gave the weight of acetone in the organic phase. To obtain the percentage of acetone extracted, this weight was divided by the weight of acetone in the aqueous phase before mixing and multiplied by 100. Equation 7.5 describes this procedure.

$$\% \text{ Acetone extracted} = \frac{C_{Acetone,Ex} \times Weight_{Toluene,S}}{C_{Toluene,Ex} \times Weight_{Acetone,F}} \times 100 \qquad (7.5)$$

$C_{Acetone,Ex}$ = Concentration of acetone in the extract phase (mg/ml)

$C_{Toluene,Ex}$ = Concentration of toluene in the extract phase (mg/ml)

$Weight_{Toluene,S}$ = Weight of toluene (solvent phase) (mg)

$Weight_{Acetone,F}$ = Weight of acetone (feed) (mg)

To calculate the % of acetone extracted in the counter-current flow experiments equation 7.4 was used. The only difference was that concentration was calculated in mg/ml instead of kg/kg and flow rate in ml/min rather than L/min. The organic outlet (extract) flow rate was calculated from the time it took to fill an 8 ml volume and the aqueous feed flow rate was specified by the inlet aqueous pump speed.

7.3.4 Results

The results from the 9 experimental runs are shown in figure 7.6. The x axis label S1PR1 corresponds to 1 stage (S1) of extraction at a phase ratio of 1 (PR1). The three single stage extractions carried out in flow are compared to the batch extraction results and all nine flow extractions are compared to the Aspen thermodynamic model.
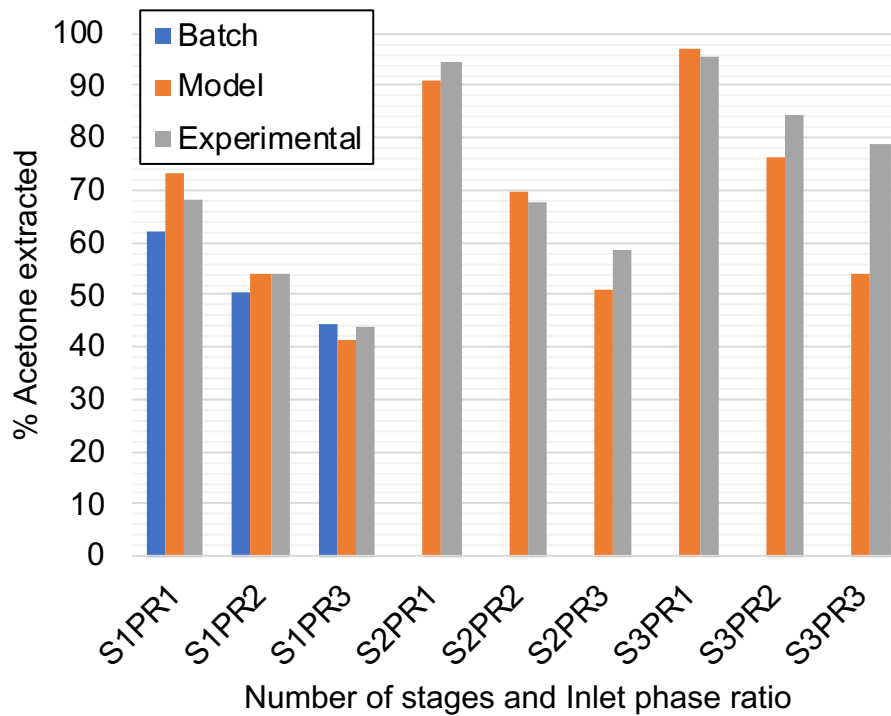
Figure 7.6: % of acetone extracted from the aqueous phase depending on phase ratio and number of extraction stages. The extraction percentage is compared to the % found in batch as well as by the Aspen thermodynamic model.

7.3.5 Discussion

The single stage batch extractions showed a reduction in the percentage of acetone extracted as the phase ratio was increased. The same trend was seen in both the model results and the flow results. The largest difference between the three sets of results was seen at a phase ratio of 1 where the model predicted an extraction percentage of 73 % while the batch results gave an extraction of 62 % and the flow experiments gave an extraction of 68 %. In this case the model seemed to over-estimate the amount of acetone extracted. There was a 6 % difference between the batch experiments and the single stage flow experiments at a phase ratio of 1. At a phase ratio of 2 the difference was 4 % and at a phase ratio of 3 the batch results were 0.6 % higher than the flow experiments. The fact that the batch experiments give a lower extraction efficiency than the in-flow results at a phase ratio of 1 and a higher extraction efficiency than the in-flow results at a phase ratio of 3 suggests

there may be some discrepancies in the inlet flow rates. The addition of salt to the flow experiments may also have changed the extraction efficiency of the flow experiments due to the salting out effect compared to the batch and model results.[173] Despite the potential discrepancies between the systems, the three sets of results gave similar values of extraction percentage and provide validation that the flow extraction system worked well and reached equilibrium after a single stage.

Much like in the model multistage extraction, as the number of stages in the experimental setup were increased, the percentage of acetone extracted also increased. A maximum of 95.6 % acetone was extracted from the aqueous phase after 3 stages, this was achieved at a phase ratio of 1. This was an improvement of 1.3 % on 2 stages and an improvement of 27.7 % on 1 stage. This suggests that the improvement in extraction percentages reduces quickly after 2 stages of extraction for this system when the phase ratio is 1. This is also seen in the model system as the final extraction percentage after 3 stages at a phase ratio of 1 is 97 %, after two stages it is 91 % and after 1 stage it is only 73 %. At lower phase ratios the percentage extracted increased more steadily with extraction stages. At a phase ratio of 2 the extraction percentages for 1, 2 and 3 stages are 53.9, 67.5 and 84.4 % and at a phase ratio of 3 the extraction percentages are 43.8, 58.6 and 78.7 %. The largest deviation in the experimentally obtained extraction percentages from the model system occurred at 3 stages and a phase ratio of 3. The model predicted an extraction percentage of 54 % where the experimental value was 78.7, a difference of 24.7 %. This difference has again been attributed to inaccuracies in the pump inlet flow rates as well as the flow rate measurement technique. Performing some inlet flow rate measurements and repeat extractions could help explain this difference. The difference may also be due to the model not fully representing the real system, as shown with the differences in the batch experimental results and the model ternary diagram (figure 7.1) they do not match up perfectly and therefore some differences in the results from the model and real system are to be expected.

The inlet and outlet flow rates have been given in table 7.4. The differences between the two values at each phase ratio and number of stages shows that the algorithm was capable of adjusting the interstage flow rate over a wide range of values. The largest change in organic phase flow rate was found after 3 stages at a phase ratio of 3. The flow rate increased from 0.75 ml/min at the inlet to 1.94 ml/min at the outlet, this was a percentage increase of 158 %. Within the algorithm, the interstage pumps are allowed to pump ± 2 ml/min from the inlet flow rate, therefore 1.94 ml/min is well within the range of flow rates the system was capable of dealing with (i.e. 0 – 2.75 ml/min).

Table 7.4: Inlet and outlet flow rates of the continuous extraction system and the % increase in organic phase flow rate.

No of stages	Phase ratio (Aq/Org)	Feed flow rate (ml/min)	Solvent flow rate (ml/min)	Extract flow rate (ml/min)	% Organic flow rate increase
1	1	1.5	1.5	1.79	19
1	2	2	1	1.41	41
1	3	2.25	0.75	1.17	56
2	1	1.5	1.5	2.05	37
2	2	2	1	1.50	50
2	3	2.25	0.75	1.32	76
3	1	1.5	1.5	2.40	60
3	2	2	1	2.11	111
3	3	2.25	0.75	1.94	158

7.3.6 Conclusion

In conclusion, a 3 stage counter-current extraction platform has been successfully applied to a high concentration extraction system and analysed. The designed system has a small lab footprint and can be used for process development under a range of phase ratios and flow rates. The system has been compared to batch experiments and to a thermodynamic model. The flow system was found to give similar results to the batch extraction and model system barring the 3 stage, phase ratio = 3 system where a significant deviation between the model and experimental results was seen. These differences could be due to differences in the inlet pump flow rates and therefore more careful validation of the inlet pump flow rates is necessary to investigate this potential error source. The system had higher extraction efficiencies as the number of stages increased for each phase ratio tested and a decrease in phase ratio resulted in a higher percentage of acetone extracted from the aqueous phase.

7.4 Multistage extraction of benzoic acid derivatives in flow

7.4.1 Introduction

Many chemical reaction systems contain impurities that require removing from the product stream. From 1993 to 2012 there was an increase in publications about 'genotoxicity' and 'genotoxic impurities' which coincided with an increased awareness of what they are, how to monitor, regulate and remove them from pharmaceutical process streams.[174] The main source of impurities come from

unreacted starting material, side-products, ligands and catalysts.[174,175] In pharmaceutical and fine chemical industries, the number of potential impurities increases due to the complexity of the molecules being manufactured and the number of process steps required to make them.[174-176]

Impurities can cause issues for downstream work up processes such as reduced purity and reduced yield as well as extended processing times and expensive purification steps.[5,12,177] Significant process optimisation is often required to improve purity and yields as well as develop a process work-up suitable for scale-up. In this section, we examine an example extraction system that contains impurities from which the product requires isolating. The system in question is based on a reaction reported by Erbing et al, 2018[178] in which C−H activation/iodination of benzoic acid was achieved. The benzoic acid was transformed into an ortho-iodobenzoic acid using an iridium catalyst and NIS (N-iodosuccinimide) as a halogenating agent as seen in figure 7.7. Numerous derivatives of the benzoic acid were also transformed in high yields, however one common issue was the over iodation of the benzoic acid which would result in the production of diortho-iodobenzoic acid. This results in the ortho-iodobenzoic acid being the middle extracting component (middle pK_a value) between the unreacted benzoic acid and diortho-iodobenzoic acid.
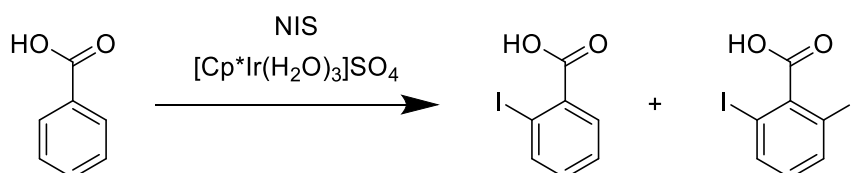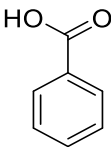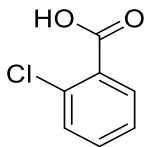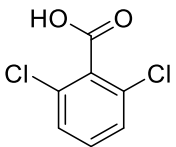
Figure 7.7: The ortho-iodation reaction performed by Erbing et al, 2018[178] to make ortho-iodobenzoic acid and a common side product of diortho-iodobenzoic acid.

The chlorobenzoic acid derivatives of this reaction were selected for investigation because of their prevalence in the pharmaceutical and agrochemical industry.[179] The extraction of 2-chlorobenzoic acid from a mixture of benzoic acid and 2,6-dichlorobenzoic acid were performed. The 2-chlorobenzoic acid was assumed to be produced at 70 % conversion and 80% selectivity resulting in the molar distributions given in table 7.5. The benzoic acids were dissolved in 2-methyl tetrahydrofuran and were extracted using an aqueous phase of water and varying amounts of sodium hydroxide.

Table 7.5: Concentration, molar distribution and pK$_a$ value of benzoic acids in 2-methyl tetrahydrofuran

	Benzoic acid	2-chlorobenzoic acid	2,6-dichlorobenzoic acid
Molar Distribution (%)	30	56	14
Concentration (M)	0.18	0.336	0.084
pK$_A$ Value[180,181]	4.193	2.73	1.84

Using this system an investigation of the systems separation characteristics has been undertaken, including emulsion type (W/O, O/W or mixed) as well as the separation time depending on phase ratio of the organic and aqueous phases and the concentration of sodium hydroxide in the aqueous phase. Using this information, a single stage continuous extraction of the system was performed at various phase ratios and sodium hydroxide concentrations. The extractions were studied in flow using the multistage separator developed in chapter 6 and its ability to separate the aqueous and organic phases were observed. The extraction efficiency and purity at each design point were also analysed in order to characterise the extraction system. In-line analytics were used to measure the system pH at strategic points and sampling of the aqueous and organic phases was done using online HPLC. The single stage extraction system was expanded to two and three stages and the extraction results were compared.

The extraction of 2-chlorobenzoic acid can be analysed with two metrics, the system extraction efficiency and the system purity. Equation 7.6 gives the purity of the aqueous extract and equation 7.7 gives the extraction efficiency (fraction of solute extracted into the extract phase).

$$\text{Purity} = \frac{[2-\text{chlorobenzoic Acid}]_{\text{Aq}}}{\sum[\text{Benzoic Acids}]_{\text{Aq}}} \tag{7.6}$$

$$\text{Extraction efficiency} = \frac{1}{1 + \frac{C_{\text{raf}}}{C_{\text{ext}}}} \tag{7.7}$$

$C_{\text{ext}} = $ Concentration of solute in the extract phase   (mol/l)

$C_{\text{raf}} = $ Concentration of solute in the raffinate phase   (mol/l)

7.4.2 Batch separation rates

The system separation characteristics were found using the techniques developed in chapter 3. A range of 10 ml samples were made up of the benzoic acid/2-methyltetrahydrofuran and sodium hydroxide solutions. Six different base concentrations and five different phase ratios were tested as shown in table 7.6.

Table 7.6: Design space used during the batch separation rate experiments.

Phase ratio (Org/Aq)	Extractant concentration (M)					
	0	0.05	0.1	0.2	0.3	0.4
0.5						
0.75						
1						
1.25						
1.5						

Each sample was mixed for 2 minutes by hand and then left for 10 minutes before being mixed for a further 2 minutes. The vials were placed in front of a camera and recorded until each phase had fully settled out. Once the recording ended, a conductance measurement of the aqueous phase was taken. The vials were shaken for a further 2 minutes and a second conductance measurement of each sample was taken in order to determine if the emulsion was O/W or W/O. The emulsion type depending on phase ratio and extractant concentration is given in figure 7.8.
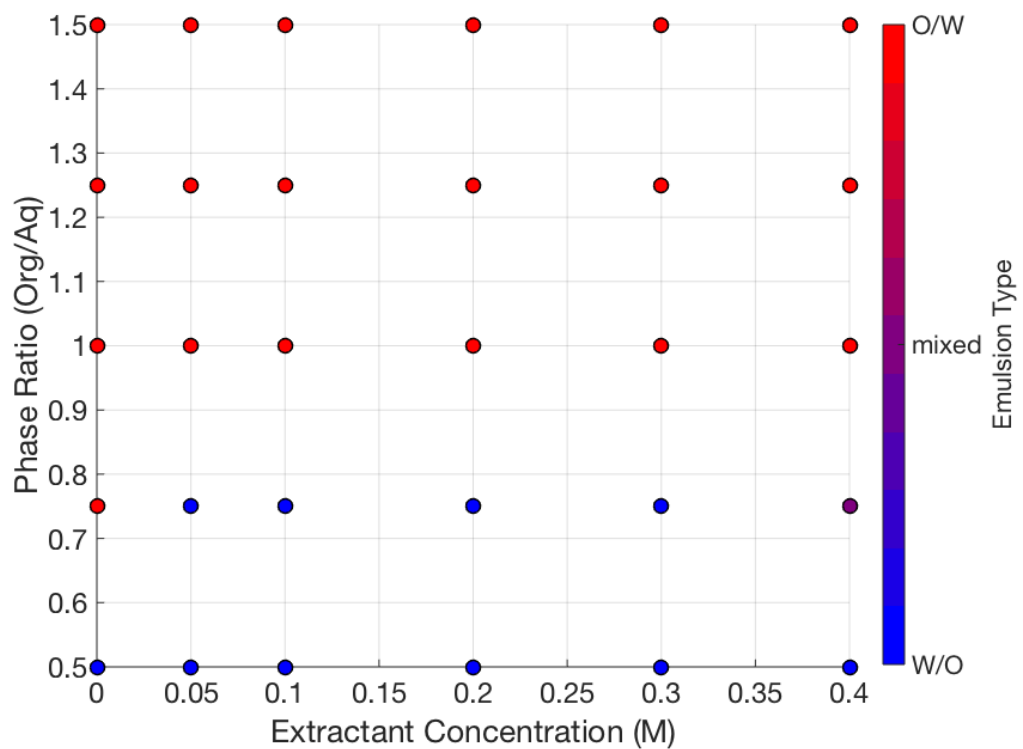
Figure 7.8: Emulsion type depending on phase ratio and extractant concentration.

Figure 7.8 shows that the emulsion type is mostly dependent on the phase ratio. Below a phase ratio of 1 the system tends to be a W/O type emulsion and from a phase ratio of 1 it is a O/W emulsion. Only at an extractant concentration of 0.4 and phase ratio of 0.8 was the formed emulsion a mixed O/W and W/O emulsion. When 0 M of sodium hydroxide was used the emulsion formed an O/W emulsion at a phase ratio of 0.8 as opposed to 1. Figure 7.8 shows that for the majority of cases a hydrophobic filter will most likely perform best in the separator as most of the formed emulsions within the design space are O/W. At low phase ratios a more hydrophilic filter media may be perform better.

As well as understanding the type of emulsion, knowledge of how stable the emulsion is allows those points in the design space to be identified that may cause separation issues. The time at which 90 % of the emulsion had settled out after mixing has been recorded and plotted in figure 7.9 and 7.10. Both the top and bottom interfaces generally took much longer to separate at low extractant concentrations (below 0.1M). The emulsion took between 30 minutes and 2 hours to separate below 0.1M extractant and below a phase ratio of 1.3. Above an extractant concentration of 0.1M and above a phase ratio of 1 the emulsion generally took between 3 and 14 minutes to separate. Above an extractant concentration of 0.1 and below a phase ratio of 1, the emulsion took less than 2 minutes to separate. For an ideal separation

that does not cause processing issues such as emulsion or rag layer formation, this would be the region in which to operate.
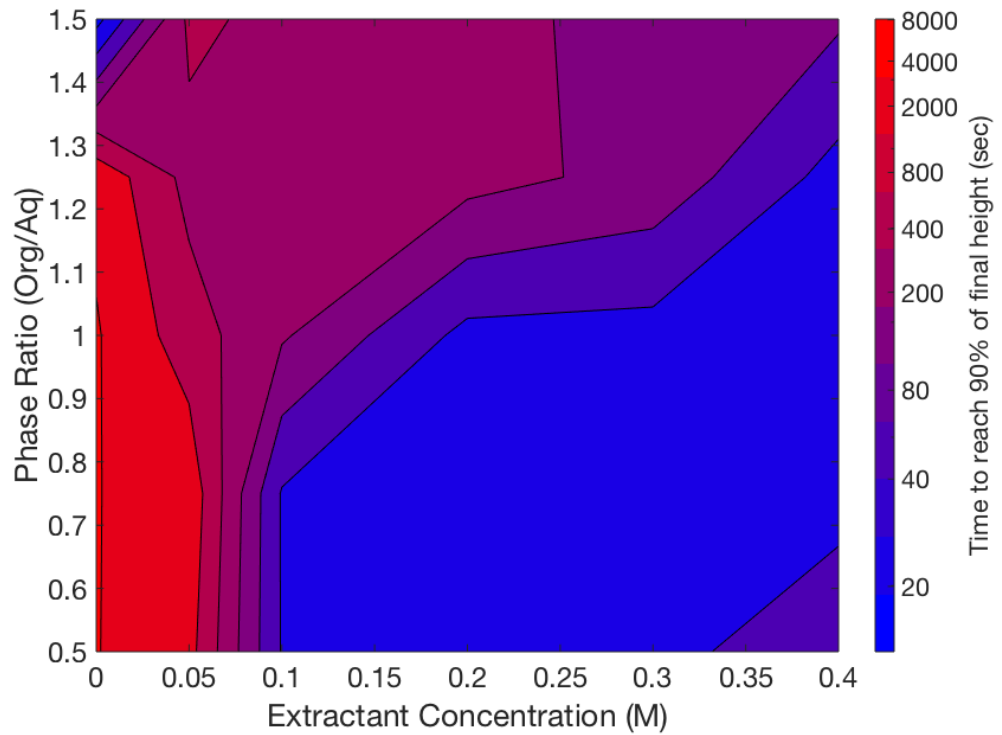
Figure 7.9: Time for the top interface to reach 90% of final separation height depending on phase ratio and extractant concentration.
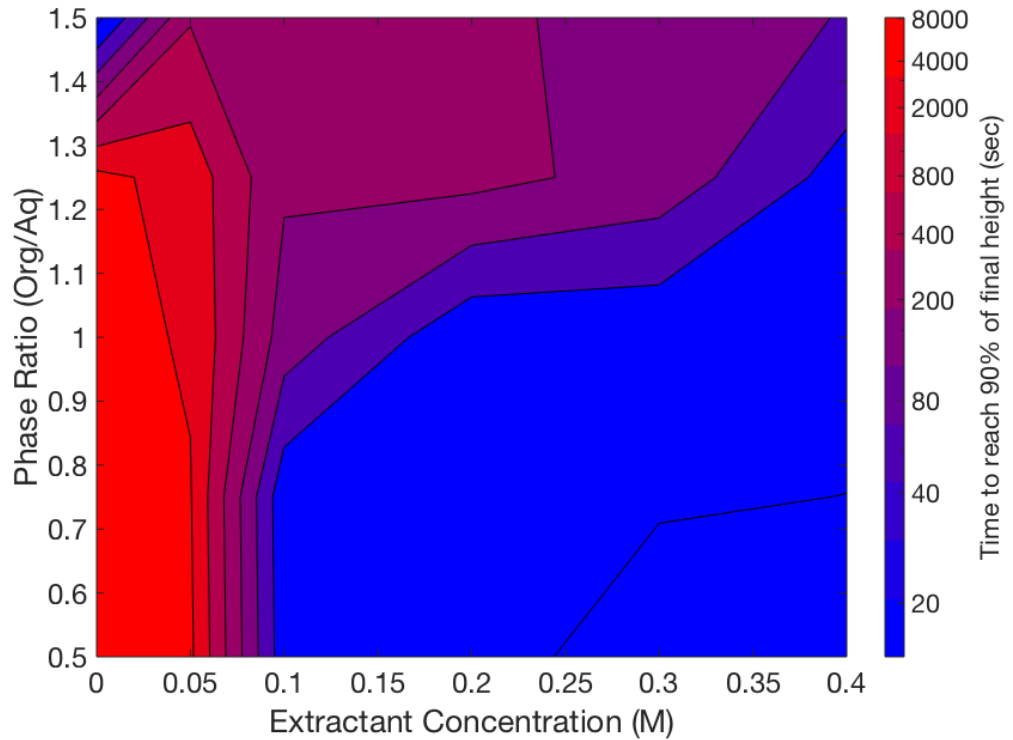
Figure 7.10: Time for the bottom interface to reach 90% of final separation height depending on phase ratio and extractant concentration.

7.4.3 Single stage extraction

Now that the systems separation characteristics are established, the extraction of 2-chlorobenzoic acid was investigated. Ideally the optimum point of extraction would lie within the region of fast separation. To investigate, a flow system was set up as shown in figure 7.11. Two aqueous inlets were mixed in a single CSTR, these two aqueous phases were deionised water and 1M solution of sodium hydroxide. By varying these two pump flow rates, the inlet sodium hydroxide concentration could be controlled. The other inlet pumped the benzoic acid solution to the CSTR's that would mix the organic and aqueous phases. After the two phases had mixed, the separator developed in chapters 4 was used to split the two phases. The aqueous outlet from the separator was pumped through an in-line pH probe and through a sample loop that would feed to the online HPLC. The sample loop also collected a sample from the organic phase after it exited the separator and sent it to the HPLC. In this way the concentration of the acids in both the raffinate and extract phase were collected.
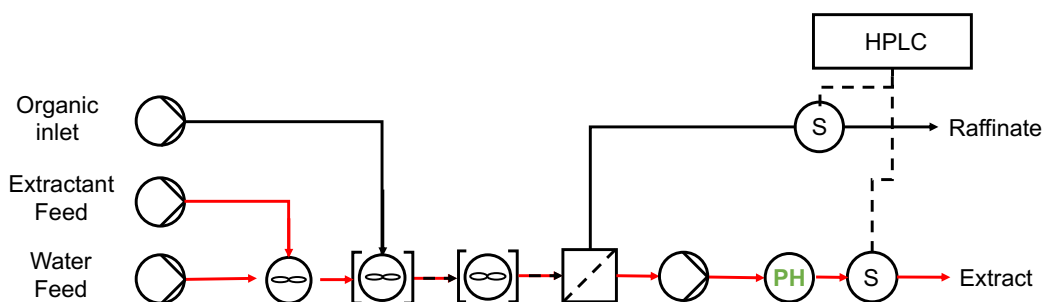
Figure 7.11: Process flow diagram of the Single stage extraction system.

Two variables were examined within the extraction. (i) phase ratio and (ii) extractant concentration. The phase ratio was varied between 0.5 and 1.5 (Org/Aq) and the extractant concentration was varied between 0 and 0.8. The design space was initially explored using a latin hypercube sampling method. 15 data points were collected and analysed using this method. An optimisation method known as SNOBFIT (Stable Noisy Optimisation by Branch and Fit)[182] was also used to find an optimum extraction point. SNOBFIT is an optimisation method suitable for optimisation of noisy objective functions. The purity of the 2-chlorobenzoic acid in the aqueous phase was used as the objective function and the algorithm ran over 22 data points. As well as determining the optimum purity of the single stage extraction, the extraction efficiency was calculated. Each data point was checked to ensure no crossover of phases was seen in the separator outlets, particularly relevant at the data points that coincided with long separation times in batch.

The Extraction efficiency of benzoic acid, 2-chlorobenzoic acid and 2,6-dichlorobenzoic acid depending on phase ratio and sodium hydroxide concentration

are shown in figures 7.12, 7.13 and 7.14. The extraction efficiency values have been overlayed on top of the batch separation rate data where it was available. As would be expected, as more base was added into the system, more of the acids were extracted into the aqueous phase. Thus, the area of long separation times when only a small amount of base was used can be avoided without compromise to the extraction efficiency of any of the solutes. As the phase ratio decreased the amount of extraction increased. This was because the quantity of aqueous phase available per unit volume of organic phase increased, so the effective amount of solute that could be transferred increased. The benzoic acid required more base in the aqueous phase to extract than the 2-chlorobenzoic acid, similarly the 2-chlorobenzoic acid required more base than the 2,6-dichlorobenzoic acid. This was expected based on their pK_a values (given in table 7.5).
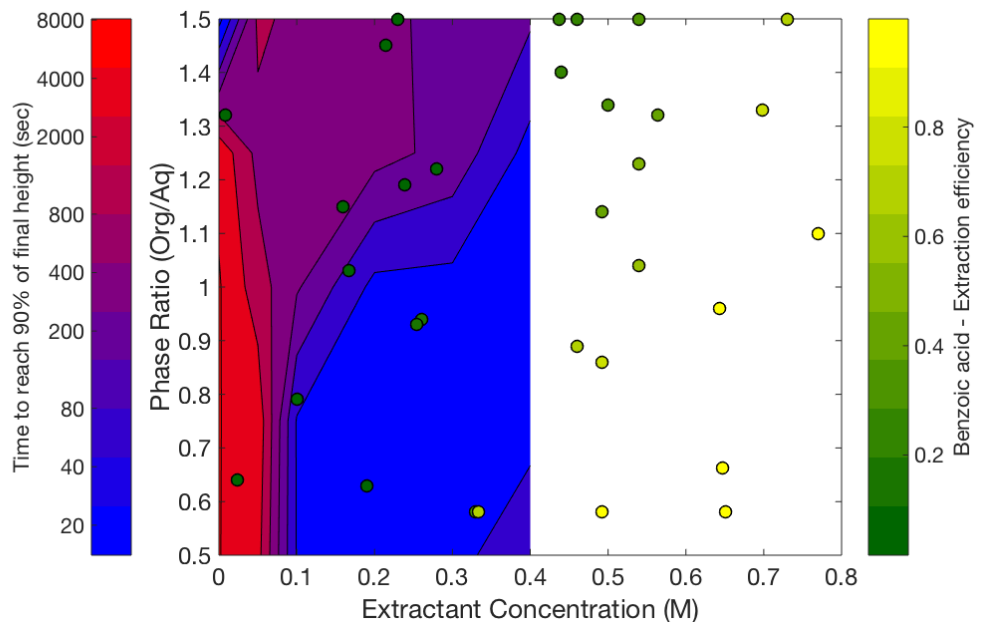
Figure 7.12: Extraction efficiency of benzoic acid from 2-methyltetrahydrofuran depending on the phase ratio and extractant concentration in the aqueous phase. The batch separation rate of the organic and aqueous phases has been included in the figure.
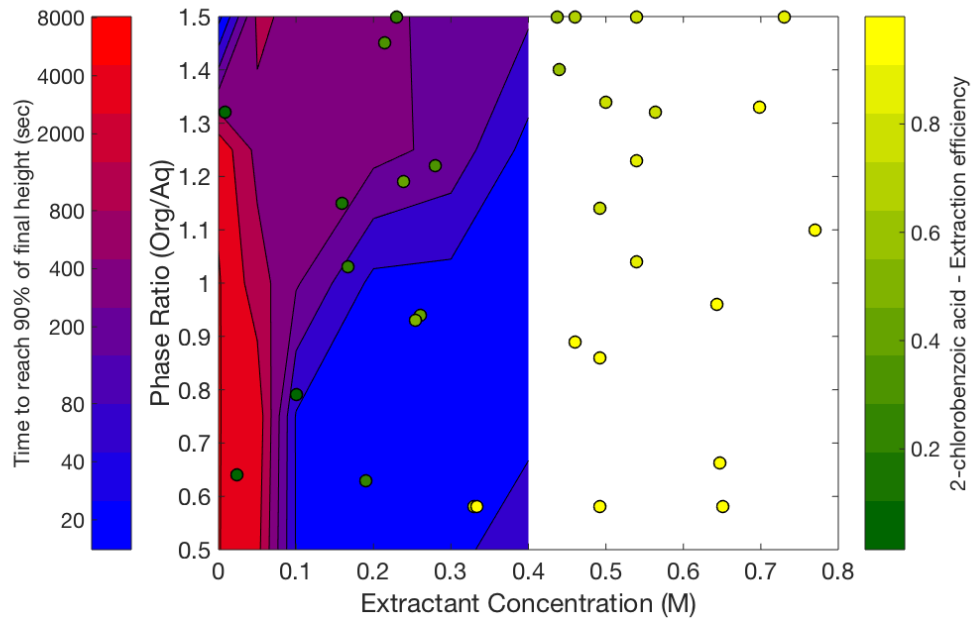
Figure 7.13: Extraction efficiency of 2-chlorobenzoic acid from 2-methyltetrahydrofuran depending on the phase ratio and extractant concentration in the aqueous phase. The batch separation rate of the organic and aqueous phases has been included in the figure.
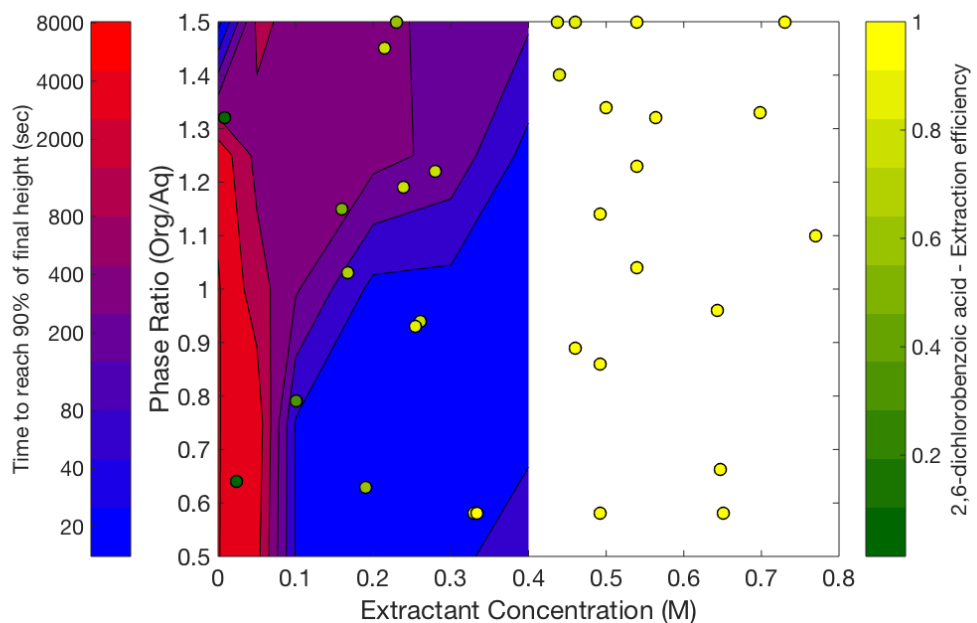
Figure 7.14: Extraction efficiency of 2,6-dichlorobenzoic acid from 2-methyltetrahydrofuran depending on the phase ratio and extractant concentration in the aqueous phase. The batch separation rate of the organic and aqueous phases has been included in the figure.

To ensure separation had fully occurred within the design space, images of separation within the separator were taken, these images are shown in table 7.7. The images are rotated 90º anticlockwise so that the two outlets are on the left and right side of the image. It is clear that no emulsion layer formed in the separator and no

phase crossed over into the opposite outlet. Samples 3 and 9 sat within the challenging separation region and showed emulsion droplets attached to the filter surface, these droplets appeared to travel up the filter surface and detach at the interface between the two phases where they coalesced with the bulk organic phase. From these sample images it was concluded that no separation issues occurred with 10 layers of PBT filter media in the separator and that the entire design space could be explored.

Table 7.7: Images *(rotated 90° anticlockwise)* of the phase separation occurring in the separator at various sample points.

Sample No	Phase ratio (Org/Aq)	Base concentration (M)	2-chlorobenzoic acid extraction efficiency	Phase separation
1	0.66	0.65	0.99	
2	1.45	0.21	0.31	
3	0.64	0.024	0.021	
4	1.5	0.73	0.90	
5	1.14	0.49	0.82	
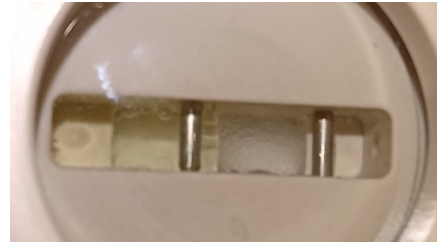
6	1.03	0.17	0.26	
8	1.1	0.77	0.97	
9	1.32	0.0079	0.014	
11	0.58	0.65	0.998	
12	1.19	0.24	0.37	
13	1.5	0.46	0.66	
15	1.32	0.56	0.82	
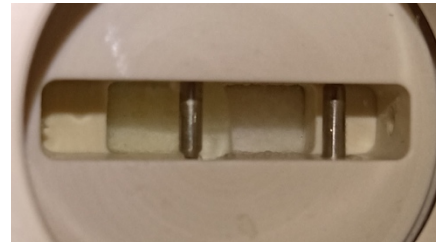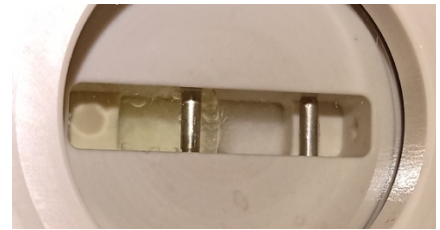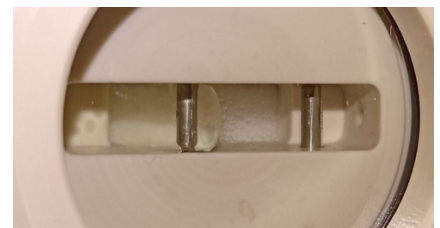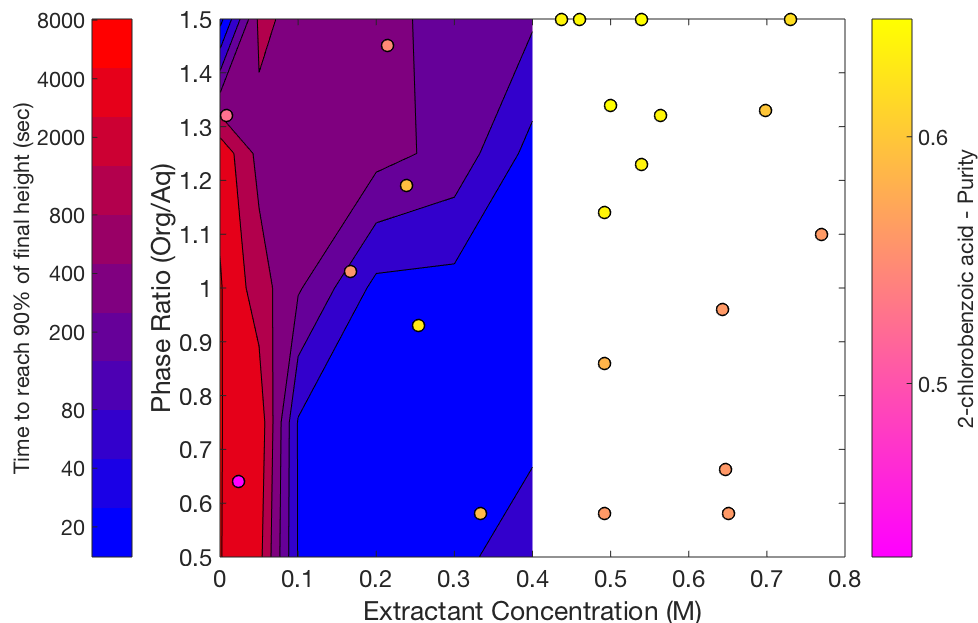
Figure 7.15: Purity of 2-chlorobenzoic acid in the aqueous phase depending on the phase ratio and extractant concentration. The batch separation rate of the organic and aqueous phases has been included in the figure.

Figure 7.15 shows the purity of 2-chlorobenzoic acid in the extract phase depending on phase ratio and extractant concentration. It can be seen that an optimum 'band' of extractant concentration and phase ratio exists. As either the phase ratio increases or as the organic feed flow rate increases, more extractant is required to obtain the same purity in the extract phase. This band of optimum purity appears to coincide with the faster separation rate area. By dividing the base concentration by phase ratio, the 3D graph of extraction efficiency of each acid can be presented on a 2D axis as shown in figures 7.16. As can be seen in figure 7.16, each of the acids follows a curve as extractant concentration increases or phase ratio decreases. The 2,6-dichlorobenzoic acid is extracted from the organic phase with the least amount of base due to its higher pK_a value, the 2-chlorobenzoic acid is second and benzoic acid third. It is clear that at no proportion of base or phase ratio can the 2-chlorobenzoic acid be extracted without some of the 2,6-dichlorobenzoic acid or benzoic acid also being extracted at the same time.
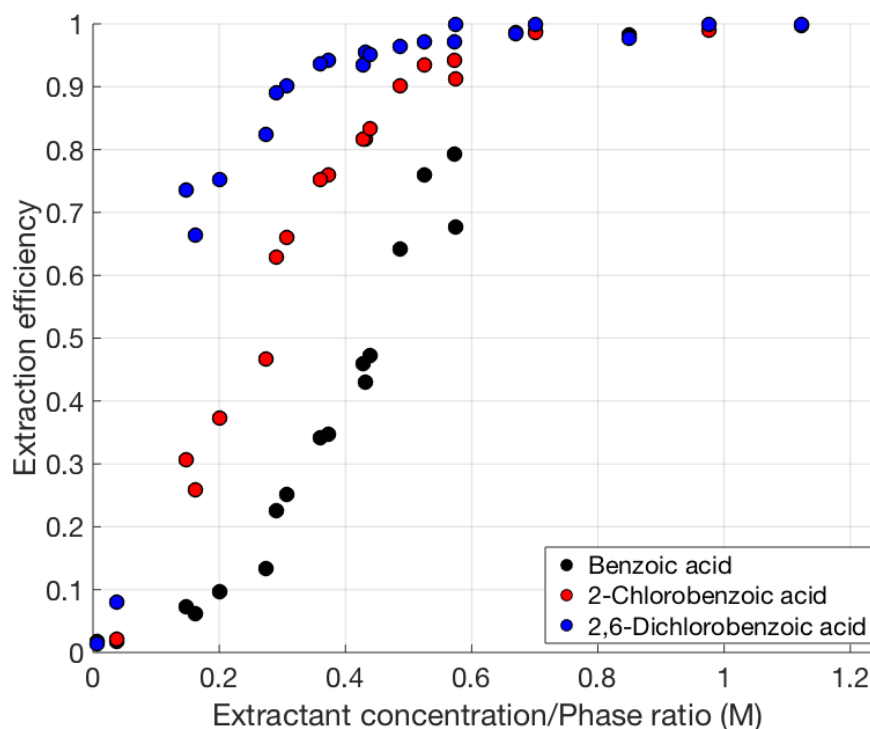
Figure 7.16: Extraction efficiency of benzoic acid, 2-chlorobenzoic acid and 2,6-dichlorobenzoic acid in the aqueous phase depending on the extractant concentration/phase ratio.

It is therefore important to look at the point at which optimum purity is achieved as this is the point at which the 2-chlorobenzoic acid is extracted with the least amount of the other components being extracted at the same time. Figure 7.17 shows the purity and the extraction efficiency of 2-chlorobenzoic acid plotted against base concentration/phase ratio. The maximum purity obtained was 0.65, at this point 75% of the 2-chlorobenzoic acid was extracted. To reach 95 % extraction efficiency the base concentration/phase ratio needs to be at least 0.58 M, however at this point the purity of the extracted 2-chlorobenzoic acid is 0.58.

By monitoring the pH of the aqueous outlet, the point at which all of the acids have been extracted can be deduced. Figure 7.18 shows the pH of the aqueous extract phase at each base concentration and phase ratio. A large jump in pH from 7 to 12.5 can be seen from a base concentration/phase ratio of 0.6 onwards. This point coincides with the point at which all of the benzoic acid has been extracted (see figure 7.16). This can therefore be used as a marker for the maximum base concentration required to extract all of the acid in one stage. However, a trade-off between the percentage of product extracted and the purity of the extracted product is inevitable. To improve the overall purity of the system without compromising on extraction efficiency, multiple stages of extraction can be used. The benzoic acid system studied as a single stage extraction in this section will now be studied as a two and three stage counter-current extraction.
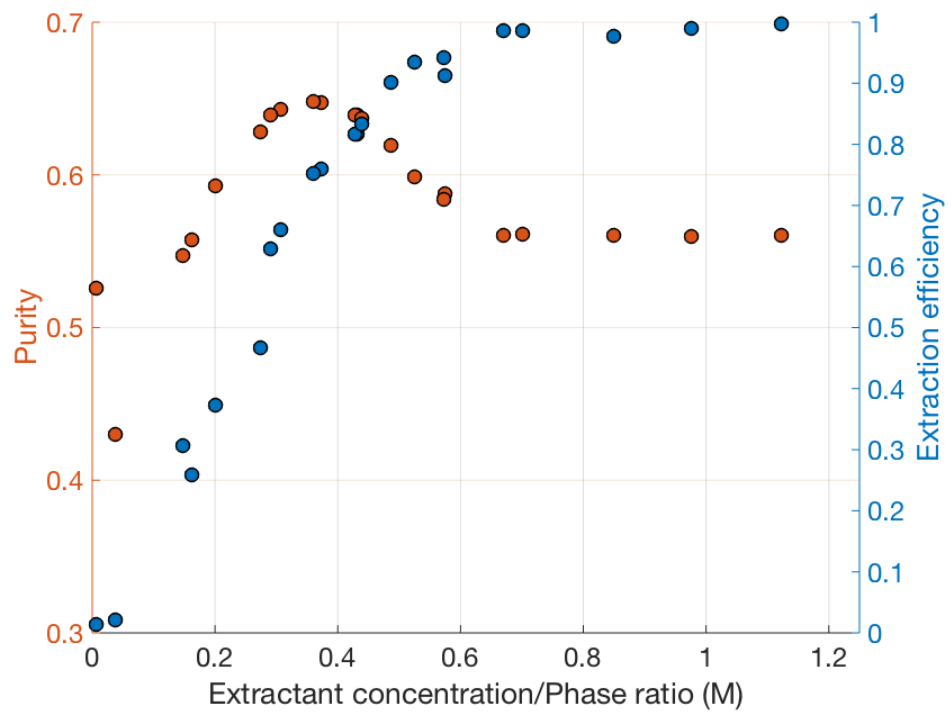
Figure 7.17: Purity and Extraction efficiency of 2-chlorobenzoic acid in the aqueous phase depending on the extractant concentration/phase ratio.
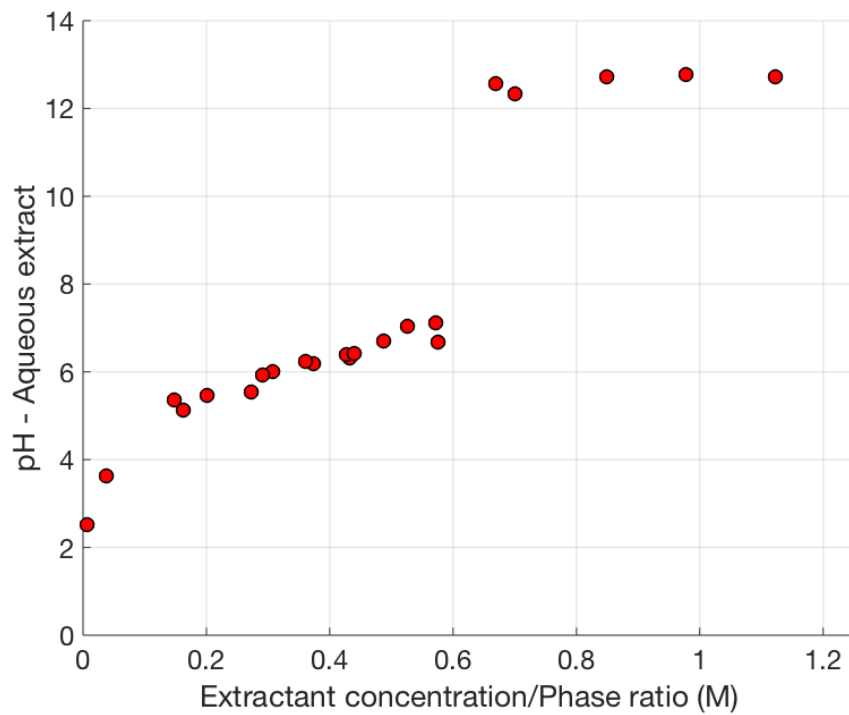
Figure 7.18: pH measurement of the aqueous extract phase depending on the extractant concentration/phase ratio.

7.4.4 Multistage extraction

A counter-current extraction was conducted across two and three stages. Theoretically, this provides an improvement in extraction efficiency for the same input conditions compared to single stage. The setup for the two stage counter-current experiment is shown in figure 7.19 and for the three stage counter-current experiment in figure 7.20.
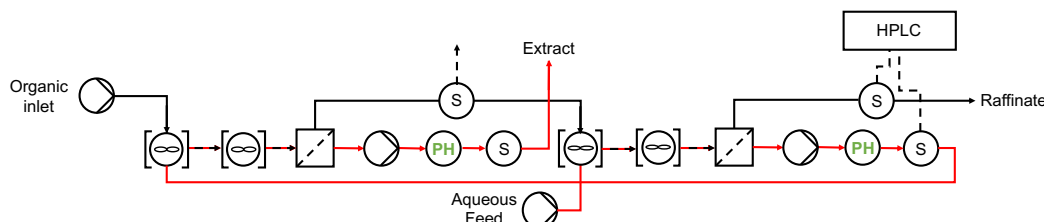
Figure 7.19: Process flow diagram of the two stage counter-current extraction system.
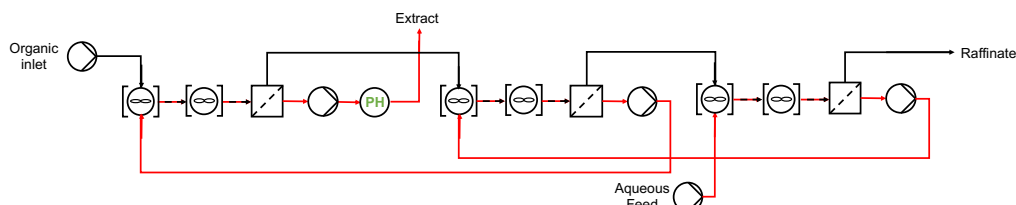
Figure 7.20: Process flow diagram of the three stage counter-current extraction system.

The two-stage extraction experiment was tested at a fixed phase ratio of 1 and base concentrations between 0 and 0.6M. The concentration of each solute was found via sampling and subsequent measurement using offline HPLC after the first stage of extraction (relative to the organic inlet) and via online HPLC after the second stage. The pH after each stage was also recorded. The extraction efficiency and purity after two stages of extraction was compared to a single stage extraction. The three-stage extraction was tested at a fixed phase ratio of 1 and base concentrations between 0 and 0.8M. The concentration of each solute was found via sampling and offline measurement using HPLC of the raffinate and extract phases. The pH of the extract phase was also recorded using an in-line pH probe. The extraction efficiency and purity after three-stages of extraction were compared to the results from the single stage and two stage experiments.

Figure 7.21 shows the extraction efficiency of each solute for 1, 2 or 3 stages of extraction. A similar amount of 2-chlorobenzoic acid was extracted at each base concentration tested whether 1, 2 or 3 stages were used. With additional stages more 2,6-dichlorobenzoic acid was extracted with the same base concentration and less benzoic acid was extracted at the same base concentration. As the equilibrium point of the system is shifted as more stages are added, the proportion of each component

that gets extracted changes and the amount of base required to obtain the highest purity extract changes.
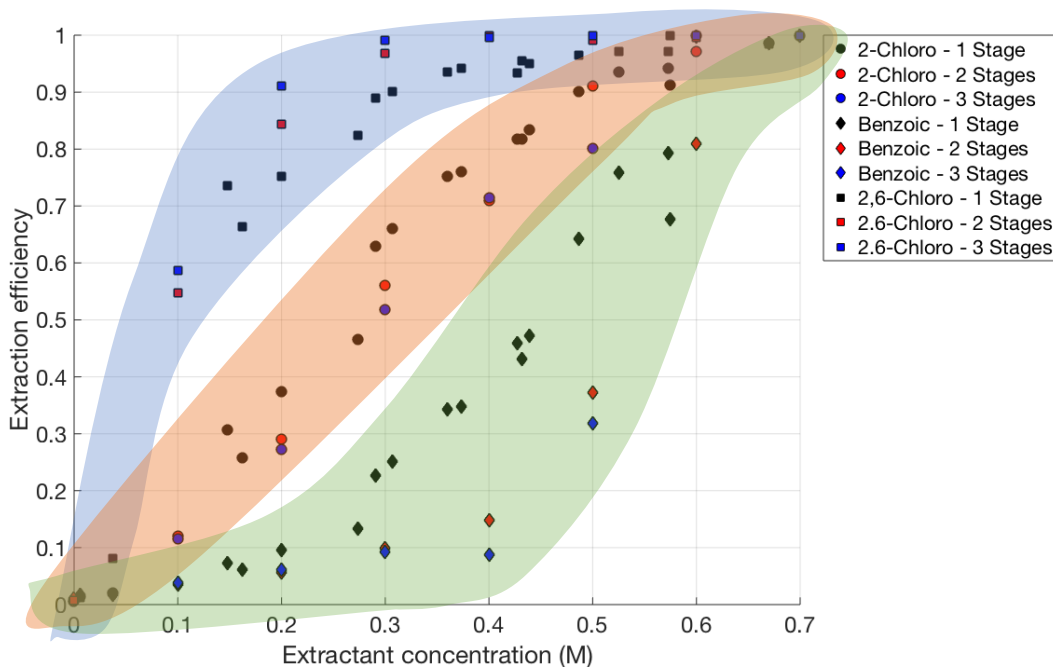
Figure 7.21: Extraction efficiency of each component depending on the number of extraction stages

This can be seen in figure 7.22, the maximum achievable purity of 2-chlorobenzoic acid increases as more stages are added and the maximum peak shifts to the right (more base) as the number of stages increase. After one stage the maximum purity is 0.648 at a base concentration of 0.36M. After 2 stages the maximum purity increases to 0.69 at a base concentration of 0.4M and after 3 stages this increases to 0.716 at a base concentration of 0.5M. By looking at figure 7.21, it is evident that most of this increase in purity happens because of the reduction in Benzoic acid being transferred into the aqueous phase as more stages are added. A similar amount of 2-chlorobenzoic acid is carried across at a base concentration of 0.5 and 99-100% of the 2,6-dichlorobenzoic acid is carried across.

By multiplying the extraction efficiency and purity we can define a balance between a pure product and extracting as much of the product as possible. For example after 3 stages the optimum purity is 0.716 but only 80.1% of the product is extracted and therefore 19.9% is lost. If we multiply the purity by extraction efficiency we get an optimum point at a base concentration of 0.6M (see figure 7.23). At this point the purity is 0.678 which is better than what was achieved after a single stage but less than the optimum purity of 0.716. The extraction efficiency increases from 80.1% to 99%. Under these conditions almost all of the 2-chlorobenzoic acid is extracted while an improvement in extract purity compared to single stage extraction is still achieved.
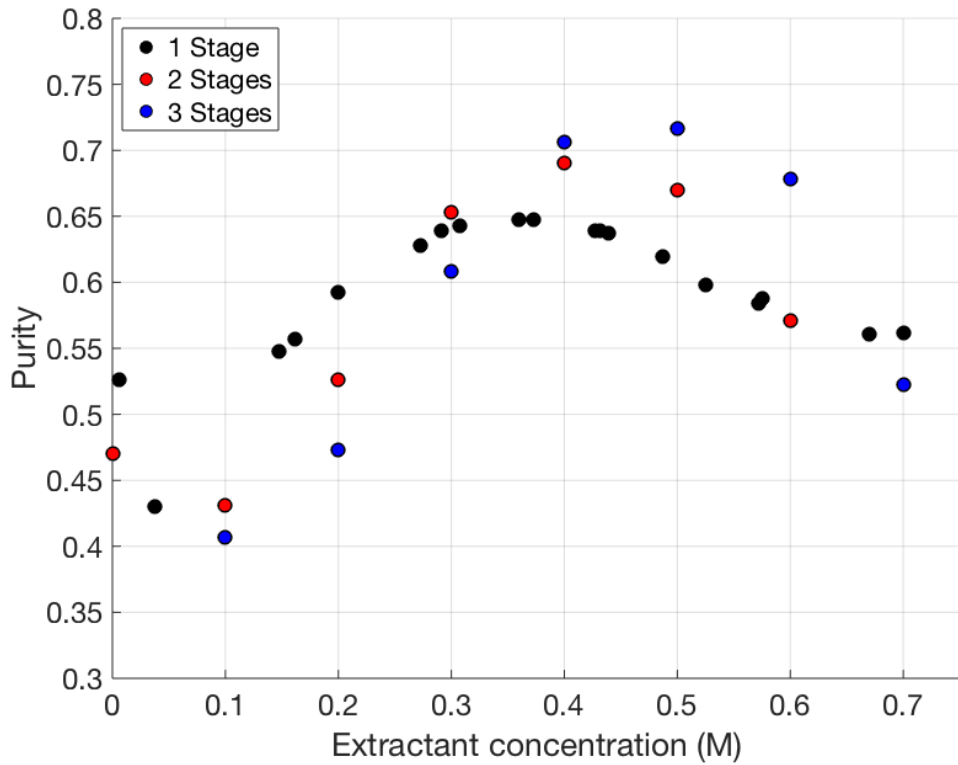
Figure 7.22: Purity of 2-chlorobenzoic Acid depending on the number of extraction stages
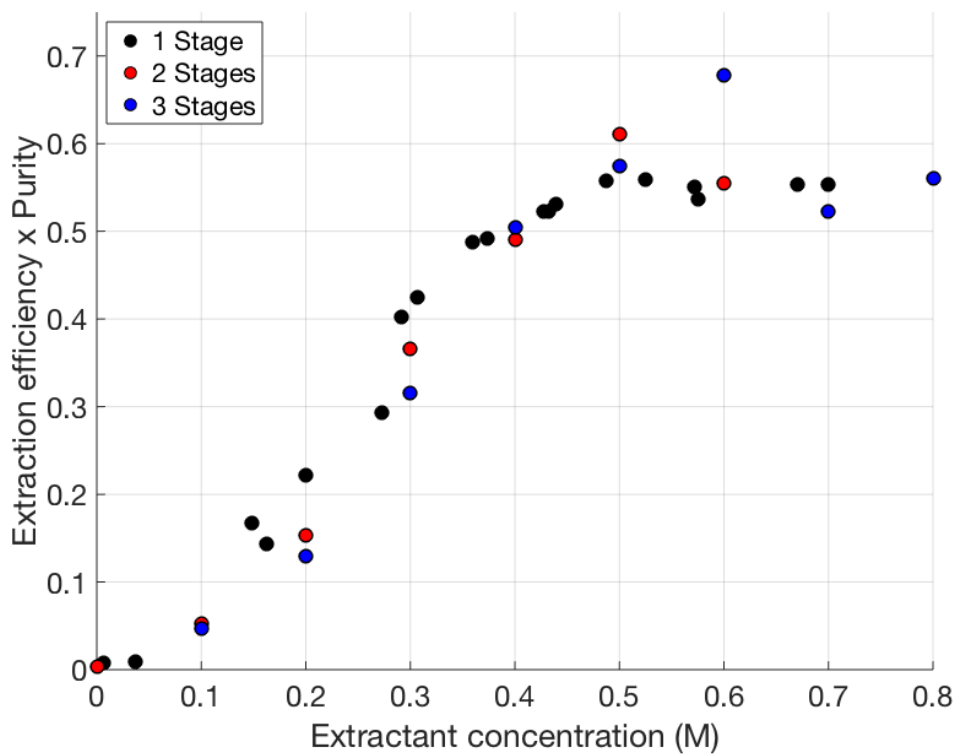
Figure 7.23: Extraction efficiency x Purity of 2-chlorobenzoic Acid depending on the number of extraction stages

It is clear from figure 7.20 that an increase in extract purity can be achieved for a given base concentration by increasing the number of counter-current extraction

stages. It is clear from figure 7.23 that as extractant concentration increases so does extraction efficiency x purity up to an extractant concentration of approximately 0.5 for 1 and 2 stages and 0.6 for 3 stages. It would therefore be beneficial to run further experiments around this point in order to discern the optimum concentration with more precision.

In figure 7.24 the purity is plotted against the extraction efficiency for 1, 2 and 3 stages of extraction. The optimum point on this graph would be at the top right hand corner (Extraction efficiency = 1, Purity = 1). It is clear that as more extraction stages take place the data points move closer to this point. What is unclear is which point (labelled point 1 and point 2 in figure 7.24) is the optimum point or whether it is likely to be a point somewhere between these two. By calculating the distance of these points from point (1 , 1) and doing the same for the midpoint of these two points we can make a decision on where the optimum point for 3 stages of extraction is likely to be. Table 7.8 shows these distances for the three points under consideration. This shows that point two is closer to point (1 , 1) but there is likely a third point between point 1 and 2 that is closer.

Table 7.8: Distance of point 1, 2 and the midpoint between them from point (1 , 1) on figure 6.22.

Point	X position	Y position	Distance from point (1,1)
1	0.72	0.80	0.346
2	0.68	1	0.322
Midpoint	0.70	0.90	0.319
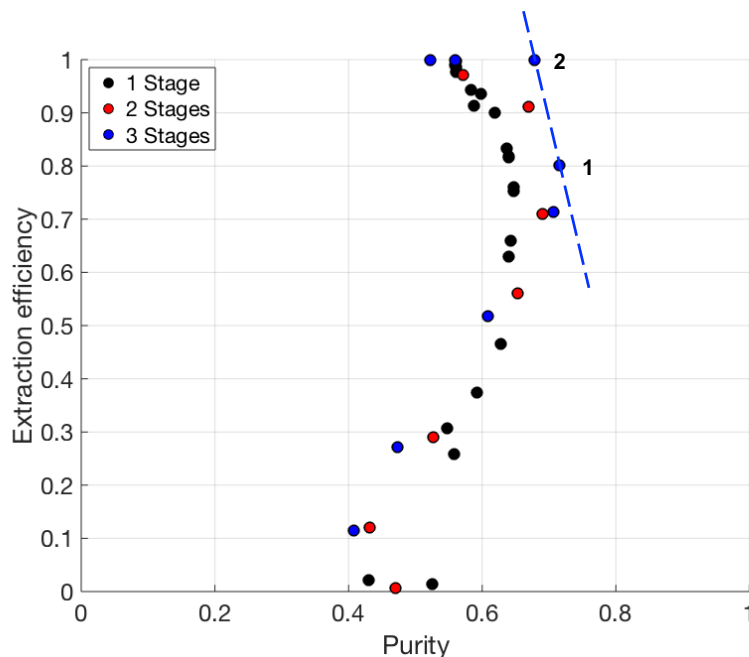
Figure 7.24: Extraction efficiency plotted against purity of the 2-chlorobenzoic Acid during 1, 2 and 3 stages of extraction.

7.4.5 Conclusion

In this section a separation rate algorithm for batch systems was tested on an extraction system with unknown separation rates. 30 samples were tested with different phase ratios and base concentrations in order to screen the experimental space. Using the knowledge gained during these experiments a more informed decision on the processability of the extraction system could be made. Including where within the experimental space there is likely to be significant emulsions forming and at what phase ratio the emulsion will be O/W or W/O. A continuous extraction was then performed using the lab-scale separator developed in previous chapters. The separator used 10 layers of nonwoven PBT which was shown to be able to separate even the most challenging base concentration/phase ratio combinations in terms of emulsion formation. The extraction efficiency and purity of the system for 1, 2 or 3 counter-current stages of extraction were compared. It was found that an increase in number of stages resulted in increased purity of the extract phase. By analysing the extraction efficiency and purity of the extract phase a compromise between extracting the maximum amount of product and achieving high purity could be made. The decision of what extractant concentration and phase ratio is selected depends on the commercial requirements of the project. The above analysis shows that the developed extraction platform provides a method to make these decisions and shows the feasibility of the extraction process before scale-up.

7.5 Summary

In this chapter the lab-scale separator has been tested as a single stage, 2 and 3 stage unit. It has been tested on a high concentration system (50% acetone to extract) and a multicomponent system (benzoic acid derivatives). A range of phase ratios and flow rates were successfully tested in both cases. In the acetone extraction case the system was compared to batch experiments and to a thermodynamic model with generally good agreement across the models. The benzoic acid derivative multicomponent system formed a stable emulsion (lasting up to 2 hours) under certain conditions, nevertheless the separator successfully separated the organic and aqueous phases. An improvement in purity of the product was achieved by using multiple stages.

Chapter 8
Conclusions and future work

8.1 Project outcomes

Lab-scale separation devices have been utilised in numerous papers to separate product and waste streams after reaction steps. However, many of these devices place limitations on the system in the form of maximum flow rates, phase ratios close to 1, high interfacial tension and/or a large density difference between the two phases. In this project, we aimed to develop a device which improved the range of flow rates and phase ratios that could be used and increase the number of liquid-liquid pairs that could be separated.

In order to achieve this, objective 1 from Chapter 1 needed to be addressed:

'Develop a method of characterising liquid-liquid systems in terms of how long they take to separate.'

This is necessary as measuring the performance of separation devices is difficult without a clear picture of the liquid-liquid system involved. There are many variables to consider, such as: Flow rate, phase ratio, mixing energy, emulsion type (O/W or W/O) and separation time. An image analysis technique was developed to determine the influence phase ratio, base concentration and surfactant concentration has on the time it took liquid-liquid samples to separate. The technique was used to characterise 29 different cases with minimal manual intervention. Within the range of cases studied were simple liquid-liquid pairs with varying interfacial tensions and densities as well as an emulsion system with different salt concentrations and surfactant concentrations. This resulted in both O/W and W/O samples and separation times less than 1 minute to up to several hours.

The image processing algorithm allowed for an automated workflow and analysis of multiple samples at once. It gave a robust method of comparing samples and was able to provide vital and quantitative information on the feasibility of scale up due to long or challenging separations. The algorithm was later used to determine the separation rate of different liquid-liquid pairs before they were used in flow as part of an extraction process. This gave information about the type and stability of emulsions formed in flow that would not otherwise be known.

Once a method of analysing liquid-liquid pairs had been developed. The lab-scale device which utilised coalescing filter media to separate liquid-liquid pairs was designed. Objective two refers to this part of the project:

'Design a separation device compatible with flow chemistry equipment that can be used on a small-scale to perform separations and characterise the device, comparing it to existing technology.'

The developed device had a small 2 ml volume, was 50 mm in diameter and 50 mm in length suitable for lab-scale use. The device was predominantly made from chemically resistant PEEK material and could be mounted on a steel baseplate. The device utilised coalescing filter media to separate liquid phases and had an automated control scheme to maintain constant separation. The control system was optimised to reduce deviations in conductance measurement and valve position. The automation routine was able to change the PID setpoint of the system depending on the variance in the valve position/pump rate and conductance measurement. The automatic setpoint adjustment algorithm was demonstrated at 4 ml/min and 16 ml/min. This means it can easily be integrated into lab-scale screening experiments and optimisations without manual intervention between experimental points.

The separator was tested by comparing its performance with a commercial membrane separator device. It was found that the coalescing separator performed better than the commercial membrane separator, particularly with significantly low interfacial tension systems such as 1-butanol-water and at higher flow rates and phase ratios. The coalescing separator was also better at separating emulsion systems over a range of HLD values in comparison to the membrane separator. The number of filter layers in the device had a significant impact on the separator performance. The wettability of the filter media also impacted the performance of the separator. A simple wettability tuning method was used to make the filter media more hydrophilic and therefore separate a low interfacial tension system more effectively than it could otherwise.

Once the device had been fully characterised it was utilised in an extraction process. Two extraction processes were studied as single stage, two stage and three stage counter-current extractions. This work covered objective three of the project:

'Develop the equipment into a multistage platform capable of performing extraction processes commonly used in pharmaceutical processes.'

A multistage separation platform was developed based on the single stage device, complete with active mixing and automated separation. The multistage platform could control up to 3 stages. The platform is modular in design so that 1-3 stages could be easily connected in either cross-current or counter-current arrangements. The standard PID controller was optimised for use in a counter-current system and further improved upon by introducing a filter to smooth the input data from the conductance

probe and a flow rate limit adjustment parameter to minimise variance in the pump output.

The multistage platform was then tested on a high concentration system (50% acetone to extract) and a multicomponent system (benzoic acid derivatives). A range of phase ratios and flow rates were successfully tested in both cases. In the acetone extraction case the system was compared to batch experiments and to a thermodynamic model with generally good agreement across the models. The benzoic acid derivative multicomponent system formed a stable emulsion (lasting up to 2 hours) under certain conditions, nevertheless the separator successfully separated the organic and aqueous phases and an improvement in purity of the product was achieved by using multiple stages.

8.2 Recommended further work

The recommended further work is split into three sections. 8.2.1 discusses the image analysis algorithm and the potential to develop a shaker rig to accompany the algorithm. In 8.2.2 the design and development of the single stage and multistage equipment is discussed and in 8.2.3 further extraction studies that make use of the equipment are considered.

8.2.1 Image analysis and shaker rig

The image analysis algorithm has been developed to a point where it requires little to no human intervention while running. Any poor quality interface tracking results can be improved by adjustments to in-built parameters post experiment. The largest variation in data sets is as a consequence of the experimental setup described in Chapter 3, section 3.2. There are two main areas to improve in this regard. One is to have a fixed apparatus that consists of:

- A series of mounting points for vials a fixed distance apart from one another.
- A fixed distance between the camera and vials and LED screen.
- Programmable/consistent camera settings
- Consistent LED light settings – This could be replaced with a strobe lighting system that connects to the camera.

The second area to improve upon is the mixing procedure. Currently the vials are shaken by hand. Ideally this would be done robotically to ensure consistency between batches. An initial prototype shaker rig is shown in appendix A. The prototype only holds one vial but shows that sufficient mixing energy can be imparted on the vial contents while not impairing the camera view of it. Expanding this design to multiple vials would be a step forward in creating a high throughput system capable of

analysing multiple samples at once in a consistent manner. If the experimental rig was improved in these ways the algorithm code could be expanded to automatically perform the interface detection procedure on multiple samples one after another as the location of the vials within the cameras field of view would be identical every time.

8.2.2 Separator future design iterations

The current separator design relies on a laptop connection and Matlab to run. In order to reduce cost and create a stand-alone system, a touchscreen model was designed. The touchscreen controlled system was not tested, therefore a repeat experiment of some of the extraction processes conducted in chapter 7 should be undertaken with the touchscreen setup. Further developments to the system include:

- Integrating magnetic stirrer speed control into the system.
- Minimising the electronics housing size.
- Eliminate the need for a second Arduino in the touchscreen control system.
- Reduce the number of connections between the electronics box and separator module. This could be achieved by running one cable for the magnetic stirrer, pump, and conductivity sensor. Currently two cables are required for these connections.

Any future design iterations should focus on simplifying the system for the user and enabling greater control of the system input parameters. The system has capacity to operate 5 pumps at once. An additional tentacle shield would be required to house the extra conductivity circuits necessary to run 5 separators but this is a feasible mode of operation and should be tested and verified in future work.

8.2.3 Future extraction studies

Two extractions were studied in depth in the project. The extraction of acetone from water using toluene and the extraction of 2-chlorobenzoic acid from benzoic acid and 2,6-dichlorobenzoic acid. Both systems posed challenges for the extraction module. Acetone was in water in high concentrations, therefore there were large changes in phase ratios between extraction stages as a result. 2-chlorobenzoic acid could not be extracted without extracting some 2,6-dichlorobenzoic acid and therefore there were challenges relating to the purity of the extract. There are several other aspects of extraction processes that could be considered in future work:

- Processes that include a gaseous component – either produced as a result of an upstream process or as part of the extraction process itself.
- Processes that include a solid component – either produced as a result of an upstream process or as part of the extraction process itself.

- Integration into optimisation routines. This was explored to a certain degree in chapter 7 but the possibility of running multi-objective studies considering both reaction productivity and extraction efficiency/purity could be explored.
- Integration of other in-line monitoring and feedback control systems such as the pH system utilised in chapter 7.

Bibliography

1.   Britton J, Raston CL. Multi-step continuous-flow synthesis. 10.1039/C6CS00830E. *Chemical Society Reviews*. 2017;46(5):1250-1271. doi:10.1039/C6CS00830E

2.   Plutschack MB, Pieber B, Gilmore K, Seeberger PH. The Hitchhiker's Guide to Flow Chemistry. *Chemical Reviews*. 2017/09/27 2017;117(18):11796-11893. doi:10.1021/acs.chemrev.7b00183

3.   Webb D, Jamison TF. Continuous flow multi-step organic synthesis. 10.1039/C0SC00381F. *Chemical Science*. 2010;1(6):675-680. doi:10.1039/C0SC00381F

4.   Bennett JA, Campbell ZS, Abolhasani M. Role of continuous flow processes in green manufacturing of pharmaceuticals and specialty chemicals. *Current Opinion in Chemical Engineering*. 2019;26:9-19. doi:10.1016/j.coche.2019.07.007

5.   Weeranoppanant N, Adamo A. In-Line Purification: A Key Component to Facilitate Drug Synthesis and Process Development in Medicinal Chemistry. *ACS Medicinal Chemistry Letters*. 2020;11(1):9-15. doi:10.1021/acsmedchemlett.9b00491

6.   Dennehy OC, Lynch D, Collins SG, Maguire AR, Moynihan HA. Scale-up and Optimization of a Continuous Flow Synthesis of an α-Thio-β-chloroacrylamide. *Organic Process Research & Development*. 2020/05/19 2020;doi:10.1021/acs.oprd.0c00079

7.   Heider PL, Born SC, Basak S, et al. Development of a Multi-Step Synthesis and Workup Sequence for an Integrated, Continuous Manufacturing Process of a Pharmaceutical. *Organic Process Research & Development*. 2014/03/21 2014;18(3):402-409. doi:10.1021/op400294z

8.   Clayton AD, Schweidtmann AM, Clemens G, et al. Automated self-optimisation of multi-step reaction and separation processes using machine learning. *Chemical Engineering Journal*. 2020/03/15/ 2020;384:123340. doi:https://doi.org/10.1016/j.cej.2019.123340

9.   Coley CW, Thomas DA, Lummiss JAM, et al. A robotic platform for flow synthesis of organic compounds informed by AI planning. *Science*. 2019;365(6453):eaax1566. doi:10.1126/science.aax1566

10.   Bédard A-C, Adamo A, Aroh KC, et al. Reconfigurable system for automated optimization of diverse chemical reactions. *Science*. 2018;361(6408):1220. doi:10.1126/science.aat0650

11.   Silvestre CIC, Santos JLM, Lima JLFC, Zagatto EAG. Liquid–liquid extraction in flow analysis: A critical review. *Analytica Chimica Acta*. 2009/10/12/ 2009;652(1):54-65. doi:https://doi.org/10.1016/j.aca.2009.05.042

12.   Peer M, Weeranoppanant N, Adamo A, Zhang Y, Jensen KF. Biphasic Catalytic Hydrogen Peroxide Oxidation of Alcohols in Flow: Scale-up and Extraction. *Organic Process Research & Development*. 2016/09/16 2016;20(9):1677-1685. doi:10.1021/acs.oprd.6b00234

13.   André BDH, Bosch H. *Industrial Separation Processes: Fundamentals*. Walter De Gruyter; 2013.

14.   Ullmann F. *Ullmann's encyclopedia of industrial chemistry*. Fifth completely revised edition. ed. Water to Zirconium and Zirconium compounds. VCH Verlagsgesellschaft; 1996.

15.   Lebl R, Murray T, Adamo A, Cantillo D, Kappe CO. Continuous Flow Synthesis of Methyl Oximino Acetoacetate: Accessing Greener Purification

Methods with Inline Liquid–Liquid Extraction and Membrane Separation Technology. *ACS Sustainable Chemistry & Engineering*. 2019;7(24):20088-20096. doi:10.1021/acssuschemeng.9b05954

16. Vural Gürsel I, Kockmann N, Hessel V. Fluidic separation in microstructured devices – Concepts and their Integration into process flow networks. *Chemical Engineering Science*. 2017/09/21/ 2017;169(Supplement C):3-17. doi:https://doi.org/10.1016/j.ces.2017.03.023

17. Hohmann L, Kurt SK, Soboll S, Kockmann N. Separation units and equipment for lab-scale process development. *Journal of Flow Chemistry*. 2016;6(3):181-190. doi:10.1556/1846.2016.00024

18. Xu C, Xie TL. Review of Microfluidic Liquid-Liquid Extractors. *INDUSTRIAL & ENGINEERING CHEMISTRY RESEARCH*. 2017;56(27):7593-7622. doi:10.1021/acs.iecr.7b01712

19. Day C, Saldarriaga A, Tilley M, Hunter H, Organ MG, Wilson DJ. A Single-Stage, Continuous High-Efficiency Extraction Device (HEED) for Flow Synthesis. *Organic Process Research & Development*. 2016/10/21 2016;20(10):1738-1743. doi:10.1021/acs.oprd.6b00226

20. Sprecher H, Payán MNP, Weber M, Yilmaz G, Wille G. Acyl Azide Synthesis and Curtius Rearrangements in Microstructured Flow Chemistry Systems. *Journal of Flow Chemistry*. 2012/01/01 2012;2(1):20-23. doi:10.1556/jfchem.2011.00017

21. O'Brien M, Koos P, Browne DL, Ley SV. A prototype continuous-flow liquid–liquid extraction system using open-source technology. 10.1039/C2OB25912E. *Organic & Biomolecular Chemistry*. 2012;10(35):7031-7036. doi:10.1039/C2OB25912E

22. Syrris. Asia FLLEX (Flow Liquid-Liquid EXtraciton) module. https://syrris.com/modules/asia-fllex-flow-liquid-liquid-extraction/

23. Adamo A, Heider PL, Weeranoppanant N, Jensen KF. Membrane-Based, Liquid–Liquid Separator with Integrated Pressure Control. *Industrial & Engineering Chemistry Research*. 2013/08/07 2013;52(31):10802-10808. doi:10.1021/ie401180t

24. Okubo Y, Toma M, Ueda H, Maki T, Mae K. Microchannel devices for the coalescence of dispersed droplets produced for use in rapid extraction processes. *Chemical Engineering Journal*. 2004/08/01/ 2004;101(1):39-48. doi:https://doi.org/10.1016/j.cej.2003.10.025

25. Alexander H, Norbert K. Counter-current arrangement of microfluidic liquid-liquid droplet flow contactors. *Green Processing and Synthesis*. 2013;2(2):157-167. doi:https://doi.org/10.1515/gps-2013-0006

26. Harvie AJ, Herrington JO, deMello JC. An improved liquid–liquid separator based on an optically monitored porous capillary. 10.1039/C9RE00144A. *Reaction Chemistry & Engineering*. 2019;doi:10.1039/C9RE00144A

27. Bansal S, von Arnim V, Stegmaier T, Planck H. Effect of fibrous filter properties on the oil-in-water-emulsion separation and filtration performance. *Journal of Hazardous Materials*. 2011/06/15/ 2011;190(1):45-50. doi:https://doi.org/10.1016/j.jhazmat.2011.01.134

28. Arouni H, Farooq U, Goswami P, Kapur N, Russell SJ. Coalescence efficiency of surface modified PBT meltblown nonwovens in the separation of water from diesel fuel containing surfactants. *Results in Engineering*. 2019/12/01/ 2019;4:100048. doi:https://doi.org/10.1016/j.rineng.2019.100048

29. Govedarica DD, Šećerov Sokolović RM, Sokolović DS, Sokolović SM. Evaluation of the Separation of Liquid–Liquid Dispersions by Flow through Fiber Beds. *Industrial & Engineering Chemistry Research*. 2012/12/12 2012;51(49):16085-16091. doi:10.1021/ie3026967

30. Agarwal S, von Arnim V, Stegmaier T, Planck H, Agarwal A. Effect of Fibrous Coalescer Geometry and Operating Conditions on Emulsion Separation. *Industrial & Engineering Chemistry Research*. 2013/09/11 2013;52(36):13164-13170. doi:10.1021/ie4018995

31. Kulkarni PS, Patel SU, Chase GG. Layered hydrophilic/hydrophobic fiber media for water-in-oil coalescence. *Separation and Purification Technology*. 2012/02/02/ 2012;85(Supplement C):157-164. doi:https://doi.org/10.1016/j.seppur.2011.10.004

32. Agarwal S, von Arnim V, Stegmaier T, Planck H, Agarwal A. Role of surface wettability and roughness in emulsion separation. *Separation and Purification Technology*. 2013/04/02/ 2013;107:19-25. doi:https://doi.org/10.1016/j.seppur.2013.01.001

33. Šećerov Sokolović RM, Govedarica DD, Sokolović DS. Selection of Filter Media for Steady-State Bed Coalescers. *Industrial & Engineering Chemistry Research*. 2014/02/12 2014;53(6):2484-2490. doi:10.1021/ie404013e

34. Patel SU, Chase GG. Separation of water droplets from water-in-diesel dispersion using superhydrophobic polypropylene fibrous membranes. *SEPARATION AND PURIFICATION TECHNOLOGY*. 2014;126:62-68. doi:10.1016/j.seppur.2014.02.009

35. Krasiński A, Sołtan Ł, Kacprzyńska-Gołacka J. Effect of fiber surface modifications on the coalescence performance of polybutylene terephthalate filter media applied for the water removal from the diesel fuel. *Separation and Purification Technology*. 2020/04/01/ 2020;236:116254. doi:https://doi.org/10.1016/j.seppur.2019.116254

36. Manzo GM, Wu Y, Chase GG, Goux A. Comparison of nonwoven glass and stainless steel microfiber media in aerosol coalescence filtration. 2016;162:14-19. doi:10.1016/j.seppur.2016.02.006

37. Russell SJ, Textile I. *Handbook of nonwovens*. CRC Press; 2007.

38. Hutten IM. *Handbook of nonwoven filter media*. 1st ed. Butterworth-Heinemann; 2007.

39. Selekman JA, Tran K, Xu Z, et al. High-Throughput Extractions: A New Paradigm for Workup Optimization in Pharmaceutical Process Development. *Organic Process Research & Development*. 2016/10/21 2016;20(10):1728-1737. doi:10.1021/acs.oprd.6b00225

40. Mengual O, Meunier G, Cayre I, Puech K, Snabre P. Characterisation of instability of concentrated dispersions by a new optical analyser: the TURBISCAN MA 1000. *Colloids and Surfaces A: Physicochemical and Engineering Aspects*. 1999/07/15/ 1999;152(1):111-123. doi:https://doi.org/10.1016/S0927-7757(98)00680-3

41. Mengual O, Meunier G, Cayré I, Puech K, Snabre P. TURBISCAN MA 2000: multiple light scattering measurement for concentrated emulsion and suspension instability analysis. *Talanta*. 1999/09/13/ 1999;50(2):445-456. doi:https://doi.org/10.1016/S0039-9140(99)00129-0

42. Horozov TS, Binks BP. Stability of suspensions, emulsions, and foams studied by a novel automated analyzer. *Langmuir*. Oct 12 2004;20(21):9007-13. doi:10.1021/la0489155

43.   Fabry DC, Sugiono E, Rueping M. Online monitoring and analysis for autonomous continuous flow self-optimizing reactor systems. 10.1039/C5RE00038F. *Reaction Chemistry & Engineering*. 2016;1(2):129-133. doi:10.1039/C5RE00038F

44.   Levenspiel O. *Chemical Reaction Engineering*. Wiley VCH Imprint; 1998.

45.   Ahmed-Omer B, Barrow DA, Wirth T. Heck reactions using segmented flow conditions. *Tetrahedron Letters*. 2009/07/01/ 2009;50(26):3352-3355. doi:https://doi.org/10.1016/j.tetlet.2009.02.133

46.   McDonough JR, Phan AN, Harvey AP. Rapid process development using oscillatory baffled mesoreactors – A state-of-the-art review. *Chemical Engineering Journal*. 2015/04/01/ 2015;265:110-121. doi:https://doi.org/10.1016/j.cej.2014.10.113

47.   McGlone T, Briggs NEB, Clark CA, Brown CJ, Sefcik J, Florence AJ. Oscillatory Flow Reactors (OFRs) for Continuous Manufacturing and Crystallization. *Organic Process Research & Development*. 2015/09/18 2015;19(9):1186-1202. doi:10.1021/acs.oprd.5b00225

48.   Mo Y, Lin H, Jensen KF. High-performance miniature CSTR for biphasic C–C bond-forming reactions. *Chemical Engineering Journal*. 2018/03/01/ 2018;335:936-944. doi:https://doi.org/10.1016/j.cej.2017.10.114

49.   Browne DL, Deadman BJ, Ashe R, Baxendale IR, Ley SV. Continuous Flow Processing of Slurries: Evaluation of an Agitated Cell Reactor. *Organic Process Research & Development*. 2011/05/20 2011;15(3):693-697. doi:10.1021/op2000223

50.   Mo Y, Jensen KF. A miniature CSTR cascade for continuous flow of reactions containing solids. 10.1039/C6RE00132G. *Reaction Chemistry & Engineering*. 2016;1(5):501-507. doi:10.1039/C6RE00132G

51.   Chapman MR, Kwan MHT, King G, et al. Simple and Versatile Laboratory Scale CSTR for Multiphasic Continuous-Flow Chemistry and Long Residence Times. *Organic Process Research & Development*. 2017/09/15 2017;21(9):1294-1301. doi:10.1021/acs.oprd.7b00173

52.   Darvas F, Hessel V, Dormán G. *Flow chemistry: Volume 1, Fundamentals*. De Gruyter Textbook; 2014.

53.   Gao Y, Muzzio FJ, Ierapetritou MG. A review of the Residence Time Distribution (RTD) applications in solid unit operations. *Powder Technology*. 2012/09/01/ 2012;228:416-423. doi:https://doi.org/10.1016/j.powtec.2012.05.060

54.   Fogler HS. *Elements of chemical reaction engineering*. Fourth edition. ed. Prentice-Hall PTR international series in the physical and chemical engineering sciences. Prentice Hall PTR; 2006.

55.   Rys P. The Selectivity of Chemical Reactions Disguised by Diffusion. Part I: Chemical Selectivity Disguised by Mixing. https://doi.org/10.1002/anie.197708073. *Angewandte Chemie International Edition in English*. 1977/12/01 1977;16(12):807-817. doi:https://doi.org/10.1002/anie.197708073

56.   Nagy KD, Shen B, Jamison TF, Jensen KF. Mixing and Dispersion in Small-Scale Flow Systems. *Organic Process Research & Development*. 2012/05/18 2012;16(5):976-981. doi:10.1021/op200349f

57.   Dessimoz A-L, Cavin L, Renken A, Kiwi-Minsker L. Liquid–liquid two-phase flow patterns and mass transfer characteristics in rectangular glass

microreactors. *Chemical Engineering Science*. 2008/08/01/ 2008;63(16):4035-4044. doi:https://doi.org/10.1016/j.ces.2008.05.005

58.	Chatterjee J. Shape analysis based critical Eotvos numbers for buoyancy induced partial detachment of oil drops from hydrophilic surfaces. *Advances in Colloid and Interface Science*. 2002/10/21/ 2002;99(2):163-179. doi:https://doi.org/10.1016/S0001-8686(02)00036-2

59.	Mikula RJ. Emulsion Characterization. *Emulsions*. American Chemical Society; 1992:79-129:chap 3. *Advances in Chemistry*; vol. 231.

60.	Gonzalez Ortiz D, Pochat-Bohatier C, Cambedouzou J, Bechelany M, Miele P. Current Trends in Pickering Emulsions: Particle Morphology and Applications. *Engineering*. 2020/02/15/ 2020;doi:https://doi.org/10.1016/j.eng.2019.08.017

61.	Kiran SK, Acosta EJ. HLD–NAC and the Formation and Stability of Emulsions Near the Phase Inversion Point. *Industrial & Engineering Chemistry Research*. 2015/07/01 2015;54(25):6467-6479. doi:10.1021/acs.iecr.5b00382

62.	Kiran SK, Acosta EJ, Moran K. Evaluating the hydrophilic–lipophilic nature of asphaltenic oils and naphthenic amphiphiles using microemulsion models. *Journal of Colloid and Interface Science*. 2009/08/01/ 2009;336(1):304-313. doi:https://doi.org/10.1016/j.jcis.2009.03.053

63.	Pogrzeba T, Schmidt M, Hohl L, et al. Catalytic Reactions in Aqueous Surfactant-Free Multiphase Emulsions. *Industrial & Engineering Chemistry Research*. 2016/12/21 2016;55(50):12765-12775. doi:10.1021/acs.iecr.6b03384

64.	Hohl L, Knossalla M, Kraume M. Influence of dispersion conditions on phase separation in liquid multiphase systems. *Chemical Engineering Science*. 2017/11/02/ 2017;171:76-87. doi:https://doi.org/10.1016/j.ces.2017.05.005

65.	Wojciechowski K, Bitner A, Warszyński P, Żubrowska M. The Hofmeister effect in zeta potentials of CTAB-stabilised toluene-in-water emulsions. *Colloids and Surfaces A: Physicochemical and Engineering Aspects*. 2011/02/20/ 2011;376(1):122-126. doi:https://doi.org/10.1016/j.colsurfa.2010.09.033

66.	Lima ERA, Melo BMd, Baptista LT, Paredes MLL. Specific ion effects on the interfacial tension of water/hydrocarbon systems. *Brazilian Journal of Chemical Engineering*. 2013;30(1):55-62. doi:10.1590/S0104-66322013000100007

67.	Berg JM, Romoser A, Banerjee N, Zebda R, Sayes CM. The relationship between pH and zeta potential of ~ 30 nm metal oxide nanoparticle suspensions relevant to in vitro toxicological evaluations. *Nanotoxicology*. 2009/12/01 2009;3(4):276-283. doi:10.3109/17435390903276941

68.	Rosen MJ, Kunjappu JT. *Surfactants and interfacial phenomena*. 4th ed. Wiley; 2012.

69.	Chakraborty M, Bart H-J. Emulsion liquid membranes: Role of internal droplet size distribution on toluene/ n-heptane separation. *Colloids and Surfaces A: Physicochemical and Engineering Aspects*. 2006;272(1):15-21. doi:10.1016/j.colsurfa.2005.07.002

70.	Goodarzi F, Zendehboudi S. A Comprehensive Review on Emulsions and Emulsion Stability in Chemical and Energy Industries. *The Canadian

Journal of Chemical Engineering. 2019;97(1):281-309. doi:10.1002/cjce.23336

71. Walstra P. Principles of emulsion formation. *Chemical Engineering Science*. 1993;48(2):333-349. doi:10.1016/0009-2509(93)80021-H

72. Lemenand T, Della Valle D, Zellouf Y, Peerhossaini H. Droplets formation in turbulent mixing of two immiscible fluids in a new type of static mixer. *International Journal of Multiphase Flow*. 5// 2003;29(5):813-840. doi:https://doi.org/10.1016/S0301-9322(03)00032-6

73. Calabrese DELRV. *Handbook of Industrial Mixing*. Wiley-Interscience; 2004.

74. Albright LF. *Albright's chemical engineering handbook*. 1 ed. CRC Press; 2009.

75. Scientific H. Understanding and Interpreting Particle Size Distribution Calculations. 13/11/2021, https://static.horiba.com/fileadmin/Horiba/Products/Scientific/Particle_Characterization/Downloads/Technical_Notes/TN156_Understanding_and_Interpreting_PSD_Calculations.pdf

76. Li M, Wilkinson D. Determination of non-spherical particle size distribution from chord length measurements. Part 1: Theoretical analysis. 2005;60(12):3251-3265. doi:10.1016/j.ces.2005.01.008

77. Bak A, Podgorska W. Drop breakage and coalescence in the toluene/water dispersions with dissolved surface active polymers PVA 88% and 98. *CHEMICAL ENGINEERING RESEARCH & DESIGN*. 2013;91(11):2142-2155. doi:10.1016/j.cherd.2013.06.011

78. Varzakas T, Tzia C. *Food Engineering Handbook: Food Process Engineering*. 1 ed. CRC Press LLC; 2015.

79. Liao Y, Lucas D. A literature review on mechanisms and models for the coalescence process of fluid particles. *Chemical Engineering Science*. 2010;65(10):2851-2864. doi:10.1016/j.ces.2010.02.020

80. Lehr F, Mewes D. A transport equation for the interfacial area density applied to bubble columns. *Chemical Engineering Science*. 2001;56(3):1159-1166. doi:10.1016/S0009-2509(00)00335-3

81. Hu Y-T, Ting Y, Hu J-Y, Hsieh S-C. Techniques and methods to study functional characteristics of emulsion systems. *Journal of Food and Drug Analysis*. 2017/01/01/ 2017;25(1):16-26. doi:https://doi.org/10.1016/j.jfda.2016.10.021

82. GmbH L. LumiReader. Accessed 19th December, 2021. https://www.lumireader.com/

83. Chen H, Jin X, Li Y, Tian J. Investigation into the physical stability of a eugenol nanoemulsion in the presence of a high content of triglyceride. 10.1039/C6RA16270C. *RSC Advances*. 2016;6(93):91060-91067. doi:10.1039/C6RA16270C

84. Onuki Y, Horita A, Kuribayashi H, Okuno Y, Obata Y, Takayama K. Non-destructive monitoring of creaming of oil-in-water emulsion-based formulations using magnetic resonance imaging. *Drug Development and Industrial Pharmacy*. 2014;40(7):937-943. doi:10.3109/03639045.2013.790903

85. Newling B, Glover PM, Keddie JL, Lane DM, McDonald PJ. Concentration Profiles in Creaming Oil-in-Water Emulsion Layers Determined with Stray Field Magnetic Resonance Imaging. *Langmuir*. 1997/07/01 1997;13(14):3621-3626. doi:10.1021/la9610056

86.   Pti. *BS 2000-412:1996, ISO 6614:1994 - Methods of test for petroleum and its products. Petroleum products. Determination of water separability of petroleum oils and synthetic fluids*. Mineraloelerzeugnisse Bestimmung des Wasserabscheidevermoegens von Mineraloelen und synthetischen Fluessigkeiten. 1996.

87.   Novales B, Papineau P, Sire A, Axelos MAV. Characterization of emulsions and suspensions by video image analysis. *Colloids and Surfaces A: Physicochemical and Engineering Aspects*. 2003/07/15/ 2003;221(1):81-89. doi:https://doi.org/10.1016/S0927-7757(03)00102-X

88.   Wang H, Tan P, Barona D, et al. Characterization of the suspension stability of pharmaceuticals using a shadowgraphic imaging method. *International Journal of Pharmaceutics*. 2018/09/05/ 2018;548(1):128-138. doi:https://doi.org/10.1016/j.ijpharm.2018.06.053

89.   Ghanbari M, Esmaeilzadeh F, Binazadeh M. An experimental investigation of creaming phenomenon using a novel optical method: A case study of mineral oil-in-water emulsion. *Journal of Dispersion Science and Technology*. 2018/05/04 2018;39(5):634-643. doi:10.1080/01932691.2017.1379019

90.   Acosta EJ, Yuan JS, Bhakta AS. The Characteristic Curvature of Ionic Surfactants. *Journal of Surfactants and Detergents*. 2008/05/09 2008;11(2):145. doi:10.1007/s11743-008-1065-7

91.   Salager JL, Morgan JC, Schechter RS, Wade WH, Vasquez E. Optimum Formulation of Surfactant/Water/Oil Systems for Minimum Interfacial Tension or Phase Behavior. *Society of Petroleum Engineers Journal*. 1979/4/1/ 1979;19(02):107-115. doi:10.2118/7054-PA

92.   Abbott S. *Surfactant Science: Principles and Practice*. DEStech Publications; 2016.

93.   De Haan A, Bosch H. Liquid-Liquid Extraction. De Gruyter; 2013. p. 1-1.

94.   Ahmad Abdul L, Fernando WJN. Liquid-Liquid Extraction. Penerbit Universiti Sains Malaysia; 2012. p. 1-1.

95.   Yang Z, Matsumoto S, Goto H, Matsumoto M, Maeda R. Ultrasonic micromixer for microfluidic systems. *Sensors and Actuators A: Physical*. 2001/10/15/ 2001;93(3):266-272. doi:https://doi.org/10.1016/S0924-4247(01)00654-9

96.   technologies Zf. Zaiput liquid-liquid-gas separator. https://www.zaiput.com/product/liquid-liquid-gas-separators/

97.   Vural Gürsel I, Kurt SK, Aalders J, et al. Utilization of milli-scale coiled flow inverter in combination with phase separator for continuous flow liquid–liquid extraction processes. *Chemical Engineering Journal*. 2016/01/01/ 2016;283:855-868. doi:https://doi.org/10.1016/j.cej.2015.08.028

98.   Leblebici ME, Kuhn S, Stefanidis GD, Van Gerven T. Milli-channel mixer and phase separator for solvent extraction of rare earth elements. *Chemical Engineering Journal*. 2016/06/01/ 2016;293:273-280. doi:https://doi.org/10.1016/j.cej.2016.02.083

99.   Harding MJ, Feng B, Lopez-Rodriguez R, et al. Concentric annular liquid–liquid phase separation for flow chemistry and continuous processing. 10.1039/D1RE00119A. *Reaction Chemistry & Engineering*. 2021;doi:10.1039/D1RE00119A

100.   Kolehmainen E, Turunen I. Micro-scale liquid–liquid separation in a plate-type coalescer. *Chemical Engineering and Processing: Process*

Intensification.   2007/09/01/   2007;46(9):834-839. doi:https://doi.org/10.1016/j.cep.2007.05.027

101. Yang L, Weeranoppanant N, Jensen KF. Characterization and Modeling of the Operating Curves of Membrane Microseparators. *Industrial & Engineering Chemistry Research*. 2017/10/25 2017;56(42):12184-12191. doi:10.1021/acs.iecr.7b03207

102. Aota A, Nonaka M, Hibara A, Kitamori T. Countercurrent Laminar Microflow   for   Highly   Efficient   Solvent   Extraction. https://doi.org/10.1002/anie.200600122. *Angewandte Chemie International Edition*.   2007/01/29   2007;46(6):878-880. doi:https://doi.org/10.1002/anie.200600122

103. Hereijgers J, Callewaert M, Lin X, et al. A high aspect ratio membrane reactor for liquid–liquid extraction. *Journal of Membrane Science*. 2013/06/01/ 2013;436:154-162. doi:https://doi.org/10.1016/j.memsci.2013.02.020

104. Hereijgers J, van Oeteren N, Denayer JFM, Breugelmans T, De Malsche W. Multistage counter-current solvent extraction in a flat membrane microcontactor. *Chemical Engineering Journal*. 2015/08/01/ 2015;273:138-146. doi:https://doi.org/10.1016/j.cej.2015.03.025

105. Hu DX, O'Brien M, Ley SV. Continuous Multiple Liquid–Liquid Separation: Diazotization of Amino Acids in Flow. *Organic Letters*. 2012/08/17 2012;14(16):4246-4249. doi:10.1021/ol301930h

106. Weeranoppanant N, Adamo A, Saparbaiuly G, et al. Design of Multistage Counter-Current Liquid-Liquid Extraction for Small-Scale Applications. *INDUSTRIAL & ENGINEERING CHEMISTRY RESEARCH*. 2017;56(14):4095-4103. doi:10.1021/acs.iecr.7b00434

107. Hazlett RN. Fibrous Bed Coalescence of Water. Steps in the Coalescence Process. *Industrial & Engineering Chemistry Fundamentals*. 1969/11/01 1969;8(4):625-632. doi:10.1021/i160032a005

108. Sutherland K. *Filters and filtration handbook*. 5th / Ken Sutherland. ed. Elsevier; 2007.

109. Sparks T, Chase G. *Filters and Filtration Handbook*. 6th.;Sixth; ed. Butterworth-Heinemann; 2013.

110. Johnson RW. *Handbook of fluid dynamics*. Second ed. CRC Press; 2016.

111. Kokal SL, Maini BB, Woo R. Flow of Emulsions in Porous Media. *Emulsions*. American Chemical Society; 1992:219-262:chap 6. *Advances in Chemistry*; vol. 231.

112. Ortega RA, Carter ES, Ortega AE. Nylon 6,6 Nonwoven Fabric Separates Oil Contaminates from Oil-in-Water Emulsions. *PLOS ONE*. 2016;11(7):e0158493. doi:10.1371/journal.pone.0158493

113. Kaur S, Sundarrajan S, Rana D, et al. Review: the characterization of electrospun nanofibrous liquid filtration membranes. *Journal of Materials Science*. 2014;49(18):6143-6159. doi:10.1007/s10853-014-8308-y

114. Wang J, Ponting M, Zhang C, Olah A, Baer E. Fuel filtration properties and mechanism of a novel fibrous filter produced by a melt-process. *JOURNAL OF MEMBRANE SCIENCE*. 2017;526:229-241. doi:10.1016/j.memsci.2016.12.040

115. Arouni H. *Nonwoven Coalescing Fuel-Water Filter Media for Diesel Engines*.   University   of   Leeds   U6   -   ctx_ver=Z39.88-2004&ctx_enc=info%3Aofi%2Fenc%3AUTF-8&rfr_id=info%3Asid%2Fsummon.serialssolutions.com&rft_val_fmt=info%3A

ofi%2Ffmt%3Akev%3Amtx%3Abook&rft.genre=dissertation&rft.title=Nonwoven+Coalescing+Fuel-Water+Filter+Media+for+Diesel+Engines&rft.DBID=0DL&rft.au=Arouni%2C+Hamidreza&rft.date=2017-06-01&rft.pub=University+of+Leeds&rft.externalDBID=n%2Fa&rft.externalDocID=oai_etheses_whiterose_ac_uk_18692&paramdict=en-US U7 - Dissertation; 2017. http://leeds.summon.serialssolutions.com/2.0.0/link/0/eLvHCXMwlV09T8MwED0VJgRDESA-Jf-BoMR2Erlw0DRiqBhKBaNlOzcgokRqEvXvc2daVLH1B1g-3fDe-Z3vHYCSj3H0DxMy5TLtZJHGHgtbaHzKiYmJbX0qMbWs778v9OpFLz_S5QR2CwZ55rWnB-OGJXVijd2AFe9RItw9Ujnb5cflgkrLhtC-3-OGagqn5V5P-xwm2F7A81vXbjoCEjHrLFsmEUOIasQm-qTibi2qL-5Si7DKXlDdKEp2a2jErz1gfwl5NV_NXqNwnUFW34ZeGnZp3kZr_qI11pvx24Ro1RWcWf603g5huK2-BkEpSVxOnO1Qa68SVzsiErTS14n3SXYD8aHX3B5-5A5OJHNVkBbu4XhYj_iwzecPYGyNhw

116. Li YX, Cao LX, Hu D, Yang CF. Uncommon wetting on a special coating and its relevance to coalescence separation of emulsified water from diesel fuel. *SEPARATION AND PURIFICATION TECHNOLOGY*. 2017;176:313-322. doi:10.1016/j.seppur.2016.11.058

117. Abutaleb A, Lolla D, Aljuhani A, Shin HU, Rajala JW, Chase GG. Effects of Surfactants on the Morphology and Properties of Electrospun Polyetherimide Fibers. *Fibers*. 2017 2017-10-19 2017;5(3):33. doi:http://dx.doi.org/10.3390/fib5030033

118. BS EN 29073-1:1992, ISO 9073-1:1989: Methods of test for nonwovens. Methods of test for nonwovens. Determination of mass per unit area. British Standards Institute; 1990.

119. BS EN 29073-2:1992, ISO 9073-2:1989: Methods of test for nonwovens. Methods of test for nonwovens. Determination of thickness. British Standards Institute; 1990.

120. International A. ASTM F316-03(2019), Standard Test Methods for Pore Size Characteristics of Membrane Filters by Bubble Point and Mean Flow Pore Test. West Conshohocken, PA2011.

121. Hu D, Li X, Li L, Yang C. Designing high-caliber nonwoven filter mats for coalescence filtration of oil/water emulsions. *Separation and Purification Technology*. 2015;149:65-73. doi:10.1016/j.seppur.2015.05.014

122. Selekman JA, Qiu J, Tran K, et al. High-Throughput Automation in Chemical Process Development. *Annual Review of Chemical and Biomolecular Engineering*. 2017/06/07 2017;8(1):525-547. doi:10.1146/annurev-chembioeng-060816-101411

123. Mennen SM, Alhambra C, Allen CL, et al. The Evolution of High-Throughput Experimentation in Pharmaceutical Development and Perspectives on the Future. *Organic Process Research & Development*. 2019/06/21 2019;23(6):1213-1242. doi:10.1021/acs.oprd.9b00140

124. Gonzalez FL, Wisniewski SR, Katipally K, et al. Systematic Optimization of a Robust Telescoped Process for a BTK Inhibitor with Atropisomer Control by High-Throughput Experimentation, Design of Experiments, and Linear Regression. *Organic Process Research & Development*. 2019/06/21 2019;23(6):1143-1151. doi:10.1021/acs.oprd.8b00398

125. Welch CJ, Albaneze-Walker J, Leonard WR, et al. Adsorbent Screening for Metal Impurity Removal in Pharmaceutical Process Research. *Organic Process Research & Development*. 2005/03/01 2005;9(2):198-205. doi:10.1021/op049764f

126. Canny J. A Computational Approach to Edge Detection. *IEEE Transactions on Pattern Analysis and Machine Intelligence*. 1986;PAMI-8(6):679-698. doi:10.1109/TPAMI.1986.4767851

127. Tippett JT, Berkowitz D, Clapp LC, Koester CJ, Vanderburgh Jr A. *Machine Perception of 3-D Solids, Optical and Electro-Optical Information Processing*. MIT Press; 1965.

128. Sobel I. An isotropic 3×3 image gradient operater. *Machine vision for three-dimensional scenes*. 1990:376-379.

129. Prewitt JMS. Object enhancement and extraction. *Picture Processing and Psychopictorics*. 1970 1970;

130. Marr D, Hildreth E, Brenner S. Theory of edge detection. *Proceedings of the Royal Society of London Series B Biological Sciences*. 1980;207(1167):187-217. doi:doi:10.1098/rspb.1980.0020

131. Jain RC, Kasturi R, Schunck BG. *Machine vision*. Internat.ed. ed. McGraw-Hill; 1995.

132. Hiebler K, Lichtenegger GJ, Maier MC, et al. Heterogeneous Pd catalysts as emulsifiers in Pickering emulsions for integrated multistep synthesis in flow chemistry. *Beilstein journal of organic chemistry*. 2018;14:648-658. doi:10.3762/bjoc.14.52

133. Arduino. https://www.arduino.cc/en/main/boards. Accessed 05/10/2020, 2020.

134. Labs W. https://www.whiteboxes.ch/. 2020.

135. Getting Started and Understanding the Arduino Landscape. *Exploring Arduino®*. 2019/10/22 2019:1-21. Wiley Online Books. doi:doi:10.1002/9781119405320.ch1
10.1002/9781119405320.ch1

136. SAS RA. *Conductivity Theory and Practice*. 2004.

137. Scientific A. https://atlas-scientific.com/circuits/ezo-conductivity-circuit/. 2020.

138. Campbell S. https://www.circuitbasics.com/basics-of-the-i2c-communication-protocol. 2020.

139. Bolton W. *Mechatronics: Electronic control systems in mechanical and electrical engineering*. Pearson Education UK; 2015.

140. Dejan HtM. https://howtomechatronics.com/how-it-works/how-servo-motors-work-how-to-control-servos-using-arduino/. Accessed 2020,

141. Driving Stepper and Servo Motors. *Exploring Arduino®*. 2019/10/22 2019:99-124. Wiley Online Books. doi:doi:10.1002/9781119405320.ch5
10.1002/9781119405320.ch5

142. HobbyKing. https://hobbyking.com/en_us/turnigytm-tgy-6114md-digital-sail-winch-servo-drum-type.html?gclsrc=aw.ds&gclid=CjwKCAjwiOv7BRBREiwAXHbv3EqmDtTGciU39pV4-xCLiH-FG5YhGwiOUgIqzHYY4f1gLHJCGBgc_RoCIL4QAvD_BwE&_store=en_us.

143. Hall Stephen M. Pumps. 6th Edition ed: Elsevier; 2018. p. 1-1.

144. Khan KM. *Fluid mechanics and machinery*. Oxford University Press; 2015.

145. Ltd I. https://www.iwakipumps.jp/en/products/metering/elec/hrp-oem/.
146. Fluidics B. https://biochemfluidics.com/products/solenoid-operated-micro-pumps. 2020.
147. Pumps W. http://wmcpumps.com/index.php/series-150.
148. Group K. https://knf.com/en/uk/solutions/pumps/series/diaphragm-liquid-pump-fem-102. 2020.
149. Dejan HtM. https://howtomechatronics.com/how-it-works/electrical-engineering/stepper-motor/. 2020.
150. Corporation P. https://www.pololu.com/product/2133. 2020.
151. RepRap. https://www.reprap.org/wiki/RAMPS_1.4. 2020.
152. Beauregard B. http://brettbeauregard.com/blog/2011/04/improving-the-beginners-pid-introduction/. 2020.
153. BS EN 29073-1:1992, ISO 9073-1:1989: Methods of test for nonwovens. Methods of test for nonwovens. Determination of mass per unit area. British Standards Institute; 1990.
154. BS EN 20139:1992, ISO 139:1973: Textiles. Standard atmospheres for conditioning and testing. British Standards Institute; 1992.
155. BS EN ISO 9073-15:2008: Textiles. Test methods for nonwovens. Determination of air permeability. British Standards Institute; 2008.
156. Wang Z, Macosko CW, Bates FS. Tuning Surface Properties of Poly(butylene terephthalate) Melt Blown Fibers by Alkaline Hydrolysis and Fluorination. *ACS Applied Materials & Interfaces*. 2014/07/23 2014;6(14):11640-11648. doi:10.1021/am502398u
157. Huhtamäki T, Tian X, Korhonen JT, Ras RHA. Surface-wetting characterization using contact-angle measurements. *Nature Protocols*. 2018/07/01 2018;13(7):1521-1538. doi:10.1038/s41596-018-0003-z
158. Owens DK, Wendt RC. Estimation of the surface free energy of polymers. https://doi.org/10.1002/app.1969.070130815. *Journal of Applied Polymer Science*. 1969/08/01 1969;13(8):1741-1747. doi:https://doi.org/10.1002/app.1969.070130815
159. Kaelble DH. Dispersion-Polar Surface Tension Properties of Organic Solids. *The Journal of Adhesion*. 1970/04/01 1970;2(2):66-81. doi:10.1080/0021846708544582
160. Habenicht G. Kleben der Kunststoffe und weiterer nichtmetallischer Werkstoffe. In: Habenicht G, ed. *Kleben: Grundlagen, Technologie, Anwendungen*. Springer Berlin Heidelberg; 1997:583-648.
161. Alghunaim A, Kirdponpattara S, Newby B-mZ. Techniques for determining contact angle and wettability of powders. *Powder Technology*. 2016/01/01 2016;287:201-215. doi:https://doi.org/10.1016/j.powtec.2015.10.002
162. Ding M, Kantzas A. Capillary Number Correlations for Gas-Liquid Systems. *Journal of Canadian petroleum technology*. 2007;46(2):27-32. doi:10.2118/07-02-03
163. Šećerov Sokolović RM, Vulić TJ, Sokolović SM. Effect of Fluid Flow Orientation on the Coalescence of Oil Droplets in Steady-State Bed Coalescers. *Industrial & Engineering Chemistry Research*. 2006/05/01 2006;45(11):3891-3895. doi:10.1021/ie051189w
164. Ma S, Kang Y, Cui S. Oil and Water Separation Using a Glass Microfiber Coalescing Bed. *Journal of Dispersion Science and Technology*. 2014/01/02 2014;35(1):103-110. doi:10.1080/01932691.2013.767209

165.   Lu H, Yang Q, Xu X, Wang HL. Effect of the Mixed Oleophilic Fibrous Coalescer Geometry and the Operating Conditions on Oily Wastewater Separation. *Chemical Engineering & Technology*. 2016;39(2):255-262. doi:10.1002/ceat.201400773

166.   Lu H, Yang Q, Liu S, Xie L-s, Wang H-l. Effect of fibrous coalescer redispersion on W/O emulsion separation. *Separation and Purification Technology*. 2016/02/08/ 2016;159(Supplement C):50-56. doi:https://doi.org/10.1016/j.seppur.2015.12.049

167.   Han Q, Kang Y. Separation of water-in-oil emulsion with microfiber glass coalescing bed. *Journal of Dispersion Science and Technology*. 2017;38(11):1523-1529. doi:10.1080/01932691.2016.1259073

168.   Ltd RC. Junction box dimensional drawing. Accessed 22nd December, 2021. https://uk.rs-online.com/web/p/junction-boxes/7491857

169.   Siqueira MG, Diniz PSR. 2 - Digital Filters. In: Chen W-K, ed. *The Electrical Engineering Handbook*. Academic Press; 2005:839-860.

170.   Isza P. T-filter. 2021. http://t-filter.engineerjs.com/

171.   Al-Malah KIM. *Aspen plus : chemical engineering applications*. Wiley; 2017.

172.   Mísek T, European Federation of Chemical E, Working Party on Distillation and A. *Standard test systems for liquid extraction*. Institution of Chemical Engineers; 1985.

173.   Hasseine A, Meniai AH, Korichi M. Salting-out effect of single salts NaCl and KCl on the LLE of the systems (water + toluene + acetone), (water + cyclohexane + 2-propanol) and (water + xylene + methanol). *Desalination*. 2009/06/01/ 2009;242(1):264-276. doi:https://doi.org/10.1016/j.desal.2008.05.006

174.   Szekely G, Amores de Sousa MC, Gil M, Castelo Ferreira F, Heggie W. Genotoxic Impurities in Pharmaceutical Manufacturing: Sources, Regulations, and Mitigation. *Chemical Reviews*. 2015/08/26 2015;115(16):8182-8229. doi:10.1021/cr300095f

175.   Roy J. Pharmaceutical impurities--a mini-review. *AAPS PharmSciTech*. 2002;3(2):E6-E6. doi:10.1208/pt030206

176.   Ahuja S. Assuring quality of drugs by monitoring impurities. *Advanced Drug Delivery Reviews*. 2007/01/10/ 2007;59(1):3-11. doi:https://doi.org/10.1016/j.addr.2006.10.003

177.   Bédard A-C, Longstreet AR, Britton J, et al. Minimizing E-factor in the continuous-flow synthesis of diazepam and atropine. *Bioorganic & Medicinal Chemistry*. 2017/12/01/ 2017;25(23):6233-6241. doi:https://doi.org/10.1016/j.bmc.2017.02.002

178.   Erbing E, Sanz-Marco A, Vázquez-Romero A, et al. Base- and Additive-Free Ir-Catalyzed ortho-Iodination of Benzoic Acids: Scope and Mechanistic Investigations. *ACS Catalysis*. 2018/02/02 2018;8(2):920-925. doi:10.1021/acscatal.7b02987

179.   Cantillo D, Kappe CO. Halogenation of organic compounds using continuous flow and microreactor technology. 10.1039/C6RE00186F. *Reaction Chemistry & Engineering*. 2017;2(1):7-19. doi:10.1039/C6RE00186F

180.   Davis MM, Hetzer H. The Ionic Dissociation of 2,4-, 2,6- and 3,4-Dichlorobenzoic Acids in Water. *The Journal of Physical Chemistry*. 1957;61:123-125.

181. Streitwieser A, Klein HS. Isotope Effects on Acidity of Deuterated Formic, Acetic, Pivalic, and Benzoic Acids. *Journal of the American Chemical Society*. 1963/09/01 1963;85(18):2759-2763. doi:10.1021/ja00901a019

182. Huyer W, Neumaier A. SNOBFIT -- Stable Noisy Optimization by Branch and Fit. *ACM Trans Math Softw*. 2008;35(2):Article 9. doi:10.1145/1377612.1377613

Appendix A

Supplementary Information - Automated Image Processing Methodology to Determine Phase Separation Rates

A.1 Algorithm inputs

A.1.1 Pixel starting locations

Table A1 catalogues the horizontal and vertical starting pixel and the horizontal and vertical number of pixels (width and height) that the algorithm used for each experiment run in experiment 1, table A2 catalogues the same values for experiment 2. Ideally these values would not change within a single experiment as the liquid volume would be closely controlled along with the vessel location within the cameras field of view. However, as the focus of this work was on the algorithm development, creating an experimental apparatus that kept these parameters consistent was not a priority. The development of such an apparatus would remove the variance in start position of the vessel within the cameras field of view and would eliminate variance in the values stated in Table A1 and A2

Table A1: Horizontal and vertical starting pixel and the horizontal and vertical number of pixels (width and height) for each case in experiment 1.

Aqueous solution	Phase ratio	Repeat no	x start	y start	x length	y length
toluene:acetate	0.25	1	700	230	420	660
toluene:acetate	0.25	2	700	230	420	660
toluene:acetate	0.25	3	700	230	420	660
toluene:deionised water	0.25	1	690	240	420	660
toluene:deionised water	0.25	2	690	225	420	660
toluene:deionised water	0.25	3	690	220	420	660
toluene:glycine	0.25	1	690	235	420	670
toluene:glycine	0.25	2	690	220	420	670
toluene:glycine	0.25	3	690	220	420	670
toluene:acetate	1	1	675	235	420	660
toluene:acetate	1	2	680	230	420	660
toluene:acetate	1	3	680	225	420	660
toluene:deionised water	1	1	690	230	420	670
toluene:deionised water	1	2	680	225	420	670
toluene:deionised water	1	3	675	225	420	670

toluene:glycine	1	1	690	235	420	670
toluene:glycine	1	2	680	225	420	670
toluene:glycine	1	3	680	220	420	670
toluene:acetate	4	1	680	235	420	670
toluene:acetate	4	2	680	220	420	670
toluene:acetate	4	3	680	220	420	670
toluene:deionised water	4	1	700	230	420	670
toluene:deionised water	4	2	670	225	420	670
toluene:deionised water	4	3	665	220	420	670
toluene:glycine	4	1	695	235	420	670
toluene:glycine	4	2	685	225	420	670
toluene:glycine	4	3	685	225	420	670

Table A2: Horizontal and vertical starting pixel and the horizontal and vertical number of pixels (width and height) for each case in experiment 2.

Vial Number	SDBS Concentration (M)	Salinity (g/100ml)	HLD value	x start	y start	x length	y length
1	0.01	0.0453	-3.38	365	275	100	255
2	0.01	1.076	-0.91	505	275	100	255
3	0.01	1.6627	-0.49	645	275	100	255
4	0.01	2.172	-0.23	785	275	100	255
5	0.01	2.768	0.006	925	275	100	255
6	0.01	3.372	0.2	335	280	100	255
7	0.01	4.3387	0.45	475	280	100	255
8	0.01	5.7133	0.72	615	280	100	255
9	0.01	6.6480	0.87	755	275	100	260
10	0.01	7.86	1.04	895	275	100	260
11	0.1	0.0413	-2.99	315	275	100	255
12	0.1	1.076	-0.87	455	275	100	255
13	0.1	1.5907	-0.5	595	275	100	255
14	0.1	2.2213	-0.19	740	275	100	255
15	0.1	2.68	0.007	880	275	100	255
16	0.1	3.2867	0.19	390	275	100	255
17	0.1	4.348	0.46	530	275	100	255
18	0.1	5.6587	0.72	670	275	100	255
19	0.1	6.6507	0.88	810	275	100	255
20	0.1	7.7937	1.04	950	275	100	255

A.1.2 Sigmoidal curve fitting inputs

Table A3 shows the imposed limits on the sigmoidal curve fitting equation for experiment 1. All of the cases in experiment 1 had the same limits imposed on constant a (±5), only the toluene:acetate cases at a phase ratio of 0.25 had a different limit imposed on constant b (±20). Table A4 shows the imposed limits on the sigmoidal curve fitting equation for experiment 2. All of the cases in experiment 2 had the same limits imposed on constant a (±5), only vial 7 had a different limit imposed on constant b (±100). Constants c and d were set by the algorithm depending on the 1st and last interface height detected by the algorithm in both experiments.

Table A3: Imposed limits on the sigmoidal curve fitting equation constants a, b, c, and d for interface 1 and 2 in experiment 1.

Aqueous solution	Phase ratio	Repeat no	a (limits)	b (limits)	Interface 1 c (fixed)	Interface 1 d (fixed)	Interface 2 c (fixed)	Interface 2 d (fixed)
toluene:acetate	0.25	1	±5	±20	0.05	5.58	64.51	9.20
toluene:acetate	0.25	2	±5	±20	0.15	5.70	65.26	9.20
toluene:acetate	0.25	3	±5	±20	0.90	6.64	64.42	10.20
toluene:deionised water	0.25	1	±5	±600	0.00	6.20	65.87	9.70
toluene:deionised water	0.25	2	±5	±600	0.00	7.10	64.74	10.30
toluene:deionised water	0.25	3	±5	±600	0.24	7.40	58.32	10.90
toluene:glycine	0.25	1	±5	±600	0.00	7.50	59.05	11.40
toluene:glycine	0.25	2	±5	±600	0.00	7.20	66.85	10.40
toluene:glycine	0.25	3	±5	±600	0.00	7.50	66.22	10.90
toluene:acetate	1	1	±5	±600	0.00	29.80	65.90	32.70
toluene:acetate	1	2	±5	±600	66.00	32.30	0.10	29.40
toluene:acetate	1	3	±5	±600	66.00	32.60	0.10	29.80
toluene:deionised water	1	1	±5	±600	0.59	29.50	66.82	32.80
toluene:deionised water	1	2	±5	±600	1.98	30.40	66.75	33.70
toluene:deionised water	1	3	±5	±600	5.12	30.90	66.89	34.10
toluene:glycine	1	1	±5	±600	0.00	30.20	66.90	33.20
toluene:glycine	1	2	±5	±600	0.03	29.80	66.54	33.00
toluene:glycine	1	3	±5	±600	0.09	30.10	66.89	33.30
toluene:acetate	4	1	±5	±600	66.98	53.30	0.14	52.16
toluene:acetate	4	2	±5	±600	66.99	52.80	0.11	51.65
toluene:acetate	4	3	±5	±600	66.98	52.50	0.10	50.28

toluene:deionised water	4	1	±5	±600	65.06	51.37	6.52	50.70
toluene:deionised water	4	2	±5	±600	65.86	50.91	4.11	50.40
toluene:deionised water	4	3	±5	±600	65.08	52.91	0.32	51.50
toluene:glycine	4	1	±5	±600	66.78	52.57	0.10	50.72
toluene:glycine	4	2	±5	±600	66.96	53.22	0.10	52.23
toluene:glycine	4	3	±5	±600	66.93	53.61	0.10	52.67

Table A4: Imposed limits on the sigmoidal curve fitting equation constants a, b, c, and d for interface 1 and 2 in experiment 2.

Vial Number	SDBS Concentration (M)	HLD value	a (limits)	b (limits)	Interface 1		Interface 2	
					c (fixed)	d (fixed)	c (fixed)	d (fixed)
1	0.01	-3.38	±5	±7200	0.00	15.57	42.67	42.67
2	0.01	-0.91	±5	±7200	0.00	10.98	42.58	26.05
3	0.01	-0.49	±5	±7200	42.13	23.41	3.61	20.33
4	0.01	-0.23	±5	±7200	0.00	13.10	38.29	21.67
5	0.01	0.006	±5	±7200	42.33	22.18	0.17	19.31
6	0.01	0.2	±5	±7200	42.62	22.85	0.18	20.16
7	0.01	0.45	±5	±100	42.56	23.02	13.75	21.28
8	0.01	0.72	±5	±7200	41.91	23.35	0.17	20.33
9	0.01	0.87	±5	±7200	42.35	23.35	0.17	20.50
10	0.01	1.04	±5	±7200	0.00	19.15	42.96	22.69
11	0.1	-2.99	±5	±7200	0.00	7.49	37.87	25.03
12	0.1	-0.87	±5	±7200	41.76	40.37	6.21	39.65
13	0.1	-0.5	±5	±7200	0.00	12.73	36.61	23.02
14	0.1	-0.19	±5	±7200	42.84	29.47	4.19	15.12
15	0.1	0.007	±5	±7200	42.84	31.08	5.91	16.46
16	0.1	0.19	±5	±7200	42.84	31.93	0.24	21.67
17	0.1	0.46	±5	±7200	42.84	32.20	6.81	20.33
18	0.1	0.72	±5	±7200	42.84	31.92	6.35	17.81
19	0.1	0.88	±5	±7200	42.84	31.63	7.21	7.22
20	0.1	1.04	±5	±7200	42.84	30.35	4.53	19.32

A.2 Algorithm outputs

In this section the outputs of the algorithm are detailed. This includes the r^2 value of each sigmoidal fit and the constants determined by the curve fit a and b, the selected maximum and minimum cut-off values for interface 1 and 2 and the d2 multiplication factor used to set those maximum and minimum cut-off values.

A.2.1 *Sigmoidal curve fitting outputs*

Table A5 shows the constants a and b and the r^2 value determined by the curve fitting process for each interface in each case for experiment 1. The same values are shown in table A6 for experiment 2.

Table A5: Outputs of the sigmoidal curve fit for experiment 1.

Aqueous solution	Phase ratio	Repeat no	Interface 2			Interface 2		
			a (fit)	b (fit)	r2	a (fit)	b (fit)	r2
toluene:acetate	0.25	1	1.64	18.41	0.49	3.33	3.02	0.91
toluene:acetate	0.25	2	1.73	7.97	0.90	5.00	2.44	0.94
toluene:acetate	0.25	3	1.02	6.22	0.84	5.00	2.05	0.97
toluene:deionised water	0.25	1	5.00	14.12	0.94	5.00	4.46	0.94
toluene:deionised water	0.25	2	4.15	10.64	0.99	5.00	2.16	0.98
toluene:deionised water	0.25	3	1.74	7.12	0.93	5.00	1.44	0.96
toluene:glycine	0.25	1	4.10	12.00	0.96	5.00	1.43	0.94
toluene:glycine	0.25	2	5.00	16.75	0.99	5.00	4.03	0.96
toluene:glycine	0.25	3	5.00	13.03	0.98	5.00	2.41	0.94
toluene:acetate	1	1	3.33	15.25	0.99	3.27	25.14	0.95
toluene:acetate	1	2	3.33	15.43	0.98	4.63	13.36	0.99
toluene:acetate	1	3	3.92	17.89	0.97	5.00	13.91	0.98
toluene:deionised water	1	1	2.25	5.62	0.96	2.44	12.03	0.97
toluene:deionised water	1	2	2.27	3.23	0.98	3.13	5.57	0.96
toluene:deionised water	1	3	1.74	2.53	0.96	4.18	8.08	0.98
toluene:glycine	1	1	3.87	16.07	0.96	3.32	17.15	0.97
toluene:glycine	1	2	3.49	6.94	1.00	2.36	6.86	0.94
toluene:glycine	1	3	2.88	7.50	1.00	3.14	12.11	0.96
toluene:acetate	4	1	2.47	14.02	0.97	2.25	23.93	0.88
toluene:acetate	4	2	2.70	15.26	0.97	2.38	31.91	0.95
toluene:acetate	4	3	2.97	9.76	0.98	2.68	34.92	0.94
toluene:deionised water	4	1	1.16	5.43	0.87	5.00	1.47	0.96
toluene:deionised water	4	2	1.65	4.76	0.95	2.48	2.68	0.95
toluene:deionised water	4	3	1.46	3.55	0.89	3.11	5.79	0.98
toluene:glycine	4	1	1.48	16.57	0.93	3.48	94.79	0.97
toluene:glycine	4	2	1.95	20.40	0.97	3.21	77.22	0.96
toluene:glycine	4	3	1.93	15.54	0.95	3.21	58.49	0.97

Table A6: Outputs of the sigmoidal curve fit for experiment 2.

Vial Number	SDBS Concentration (M)	HLD value	a (fit)	b (fit)	r²	a (fit)	b (fit)	r²
			Interface 1			Interface 2		
1	0.01	-3.38	1.89	855.86	0.99	0.00	0.00	-1.21
2	0.01	-0.91	3.14	2576.42	0.62	1.16	983.11	0.21
3	0.01	-0.49	1.42	100.80	0.34	5.00	13.71	0.16
4	0.01	-0.23	3.60	2796.22	0.98	5.00	13.05	0.11
5	0.01	0.006	2.24	51.84	1.00	5.00	1353.27	1.00
6	0.01	0.2	3.24	39.90	0.97	2.85	141.92	0.94
7	0.01	0.45	3.36	35.53	0.95	0.62	4.07	0.33
8	0.01	0.72	3.08	26.44	0.98	3.70	178.59	0.97
9	0.01	0.87	2.87	25.29	0.99	3.23	237.43	0.97
10	0.01	1.04	5.00	653.09	0.99	1.75	78.94	1.00
11	0.1	-2.99	2.69	2743.66	0.99	5.00	12.17	0.01
12	0.1	-0.87	0.67	15.27	0.00	5.00	14.08	0.78
13	0.1	-0.5	2.16	1736.40	0.99	5.00	11.75	0.00
14	0.1	-0.19	2.10	1811.27	0.99	5.00	12.22	0.00
15	0.1	0.007	1.95	1843.20	0.98	5.00	11.29	-0.48
16	0.1	0.19	2.23	1908.48	0.99	5.00	30.96	0.46
17	0.1	0.46	2.13	2085.45	0.99	5.00	11.53	-0.52
18	0.1	0.72	2.00	2104.10	0.98	5.00	11.31	-0.46
19	0.1	0.88	2.17	2281.81	0.99	4.81	2.66	-3.77
20	0.1	1.04	1.82	1584.09	0.99	5.00	12.77	-0.40

A.2.2 *Maximum and minimum thresholds*

Table A7 and A8 list the maximum and minimum cut-off values selected by the algorithm during steps 13 – 20 in the interface detection process for experiment 1 and experiment 2.

Table A7: Maximum and minimum cut-off thresholds for interface 1 and 2 in experiment 1.

Aqueous solution	Phase ratio	Repeat no	Max Cut-off	Min Cut-off	Max Cut-off	Min Cut-off
			Interface 1		Interface 2	
toluene:acetate	0.25	1	7.58	-7.03	0.63	-0.52
toluene:acetate	0.25	2	6.93	-5.50	0.77	-0.72
toluene:acetate	0.25	3	8.99	-4.32	0.87	-1.03
toluene:deionised water	0.25	1	2.01	-5.77	0.90	-0.82
toluene:deionised water	0.25	2	9.82	-13.10	0.83	-1.34
toluene:deionised water	0.25	3	11.09	-14.78	1.04	-1.50
toluene:glycine	0.25	1	7.69	-11.68	0.82	-1.21
toluene:glycine	0.25	2	8.56	-13.06	0.43	-0.89

toluene:glycine	0.25	3	9.26	-14.04	0.64	-1.13
toluene:acetate	1	1	4.25	-2.69	1.08	-2.26
toluene:acetate	1	2	4.43	-3.46	1.65	-2.87
toluene:acetate	1	3	3.12	-2.43	0.96	-1.41
toluene:deionised water	1	1	4.67	-2.72	1.04	-2.27
toluene:deionised water	1	2	4.80	-3.91	0.83	-1.59
toluene:deionised water	1	3	5.29	-4.25	1.46	-2.73
toluene:glycine	1	1	5.24	-3.55	0.71	-1.86
toluene:glycine	1	2	5.85	-4.54	0.63	-1.65
toluene:glycine	1	3	5.71	-4.31	0.91	-2.12
toluene:acetate	4	1	17.83	-14.02	2.29	-2.40
toluene:acetate	4	2	11.07	-10.73	2.16	-2.39
toluene:acetate	4	3	11.05	-7.28	2.84	-2.82
toluene:deionised water	4	1	19.08	-9.81	3.68	-6.34
toluene:deionised water	4	2	13.31	-10.58	2.25	-4.83
toluene:deionised water	4	3	16.28	-11.81	2.25	-4.12
toluene:glycine	4	1	17.36	-17.32	2.26	-2.18
toluene:glycine	4	2	17.25	-11.82	2.26	-4.10
toluene:glycine	4	3	23.80	-11.95	2.54	-4.89

Table A8: Maximum and minimum cut-off thresholds for interface 1 and 2 in experiment 2.

			Interface 1		Interface 2	
Vial Number	SDBS Concentration (M)	HLD value	Max Cut-off	Min Cut-off	Max Cut-off	Min Cut-off
1	0.01	-3.38	0.60	-0.45	0.03	-0.03
2	0.01	-0.91	0.06	-0.04	0.03	-0.04
3	0.01	-0.49	0.04	-0.04	0.06	-0.03
4	0.01	-0.23	0.11	-0.07	0.05	-0.03
5	0.01	0.006	10.49	-10.10	1.26	-6.14
6	0.01	0.2	8.85	-9.28	0.49	-1.67
7	0.01	0.45	5.80	-5.05	0.22	-0.99
8	0.01	0.72	7.00	-5.25	0.25	-1.70
9	0.01	0.87	7.41	-4.59	1.60	-2.97
10	0.01	1.04	10.91	-11.84	1.69	-10.64
11	0.1	-2.99	3.46	-2.86	0.04	-0.03
12	0.1	-0.87	0.12	-0.17	0.14	-0.13
13	0.1	-0.5	2.06	-2.29	0.05	-0.02
14	0.1	-0.19	18.11	-24.67	0.05	-0.02

15	0.1	0.007	20.02	-25.09	0.07	-0.01
16	0.1	0.19	19.66	-28.99	0.11	-0.04
17	0.1	0.46	22.07	-29.39	0.10	-0.02
18	0.1	0.72	25.69	-35.73	0.07	-0.01
19	0.1	0.88	26.57	-22.56	0.07	0.00
20	0.1	1.04	21.54	-35.80	0.07	-0.02

A.3 Case Figures and Images

A.3.1 Experiment 1

Toluene-acetate – Phase ratio = 0.25, Repeat 1

Figure A1: Detected interfaces and normalised grayscale intensity over time for repeat 1 of the toluene-acetate time series at a phase ratio of 0.25.

Figure A2: Contour plot of r^2 values for the sigmoidal curve fit for interface 1 data (a) and interface 2 data (b) depending on the maximum and minimum cut-off point combination – Toluene-acetate, phase ratio = 0.25, repeat 1.
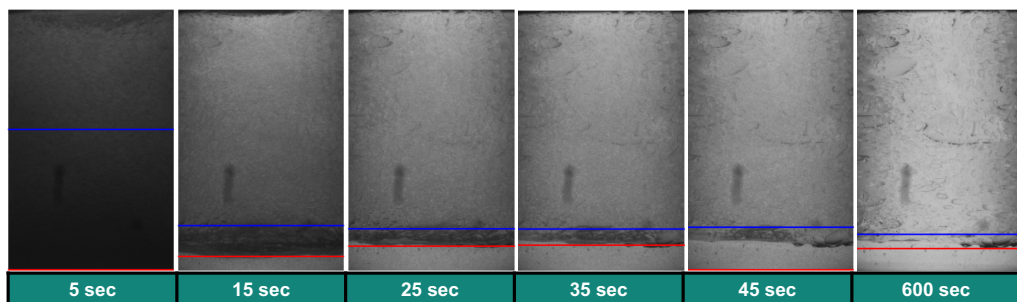
Figure A3: Sample images from toluene-acetate, phase ratio = 0.25, repeat 1 case with location of detected interfaces.

Toluene-acetate – Phase ratio = 0.25, Repeat 2
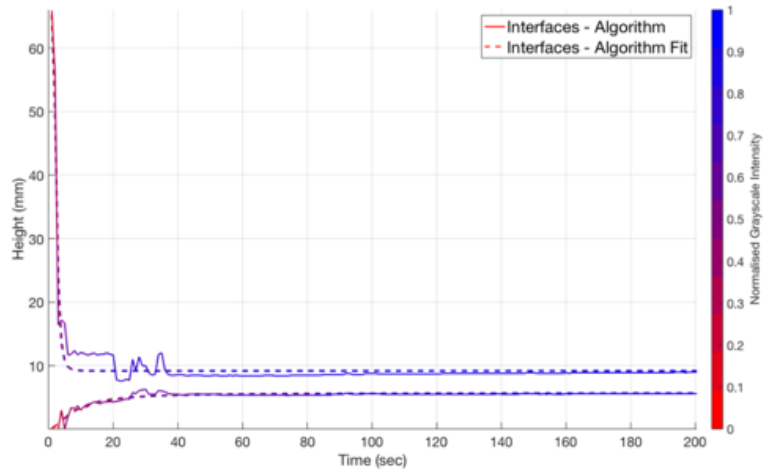
Figure A4: Detected interfaces and normalised grayscale intensity over time for repeat 2 of the toluene-acetate time series at a phase ratio of 0.25.

Figure A5: Contour plot of r² values for the sigmoidal curve fit for interface 1 data (a) and interface 2 data (b) depending on the maximum and minimum cut-off point combination – Toluene-acetate, phase ratio = 0.25, repeat 2.

| 5 sec | 15 sec | 25 sec | 35 sec | 45 sec | 600 sec |

Figure A6: Sample images from toluene-acetate, phase ratio = 0.25, repeat 2 case with location of detected interfaces.

Toluene-acetate – Phase ratio = 0.25, Repeat 3

Figure A7: Detected interfaces and normalised grayscale intensity over time for repeat 3 of the toluene-acetate time series at a phase ratio of 0.25.

Figure A8: Contour plot of r^2 values for the sigmoidal curve fit for interface 1 data (a) and interface 2 data (b) depending on the maximum and minimum cut-off point combination – Toluene-acetate, phase ratio = 0.25, repeat 3.

Figure A9: Sample images from toluene-acetate, phase ratio = 0.25, repeat 3 case with location of detected interfaces.

Toluene-acetate – Phase ratio = 0.25, Average

Figure A10: Averaged interface locations and normalised grayscale intensity over time for the toluene-acetate time series at a phase ratio of 0.25.

Toluene-deionised water – Phase ratio = 0.25, Repeat 1

Figure A11: Detected interfaces and normalised grayscale intensity over time for repeat 1 of the toluene-deionised water time series at a phase ratio of 0.25.

Figure A12: Contour plot of r^2 values for the sigmoidal curve fit for interface 1 data (a) and interface 2 data (b) depending on the maximum and minimum cut-off point combination – Toluene-deionised water, phase ratio = 0.25, repeat 1.

Figure A13: Sample images from toluene-deionised water, phase ratio = 0.25, repeat 1 case with location of detected interfaces.

Toluene-deionised water – Phase ratio = 0.25, Repeat 2

Figure A14: Detected interfaces and normalised grayscale intensity over time for repeat 2 of the toluene-deionised water time series at a phase ratio of 0.25.

Figure A15: Contour plot of r^2 values for the sigmoidal curve fit for interface 1 data (a) and interface 2 data (b) depending on the maximum and minimum cut-off point combination – Toluene-deionised water, phase ratio = 0.25, repeat 2.

Figure A16: Sample images from toluene-deionised water, phase ratio = 0.25, repeat 2 case with location of detected interfaces.

Toluene-deionised water – Phase ratio = 0.25, Repeat 3

Figure A17: Detected interfaces and normalised grayscale intensity over time for repeat 3 of the toluene-deionised water time series at a phase ratio of 0.25.

Figure A18: Contour plot of r^2 values for the sigmoidal curve fit for interface 1 data (a) and interface 2 data (b) depending on the maximum and minimum cut-off point combination – Toluene-deionised water, phase ratio = 0.25, repeat 3.

| 2 sec | 6 sec | 10 sec | 14 sec | 18 sec | 600 sec |

Figure A19: Sample images from toluene-deionised water, phase ratio = 0.25, repeat 3 case with location of detected interfaces.

Figure A20: Averaged interface locations and normalised grayscale intensity over time for the toluene-deionised water time series at a phase ratio of 0.25.

Toluene-glycine – Phase ratio = 0.25, Repeat 1

Figure A21: Detected interfaces and normalised grayscale intensity over time for repeat 1 of the toluene-glycine time series at a phase ratio of 0.25.

Figure A22: Contour plot of r^2 values for the sigmoidal curve fit for interface 1 data (a) and interface 2 data (b) depending on the maximum and minimum cut-off point combination – Toluene-glycine, phase ratio = 0.25, repeat 1.

Figure A23: Sample images from toluene-glycine, phase ratio = 0.25, repeat 1 case with location of detected interfaces.

Figure A24: Detected interfaces and normalised grayscale intensity over time for repeat 2 of the toluene-glycine time series at a phase ratio of 0.25.

Figure A25: Contour plot of r^2 values for the sigmoidal curve fit for interface 1 data (a) and interface 2 data (b) depending on the maximum and minimum cut-off point combination – Toluene-glycine, phase ratio = 0.25, repeat 2.

Figure A26: Sample images from toluene-glycine, phase ratio = 0.25, repeat 2 case with location of detected interfaces.

Toluene-glycine – Phase ratio = 0.25, Repeat 3

Figure A27: Detected interfaces and normalised grayscale intensity over time for repeat 3 of the toluene-glycine time series at a phase ratio of 0.25.

Figure A28: Contour plot of r^2 values for the sigmoidal curve fit for interface 1 data (a) and interface 2 data (b) depending on the maximum and minimum cut-off point combination – Toluene-glycine, phase ratio = 0.25, repeat 3.
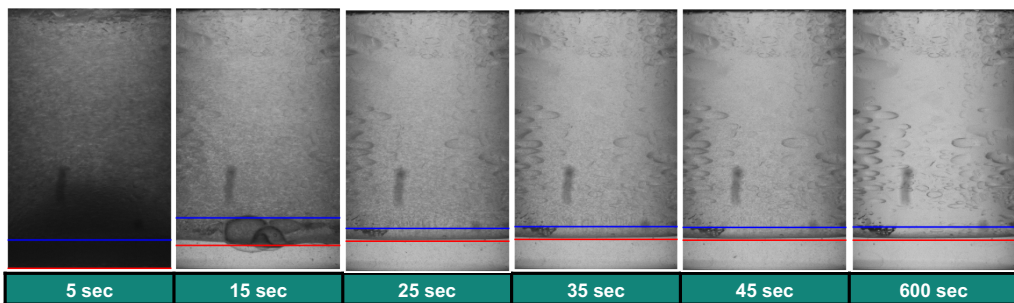
Figure A29: Sample images from toluene-glycine, phase ratio = 0.25, repeat 3 case with location of detected interfaces.
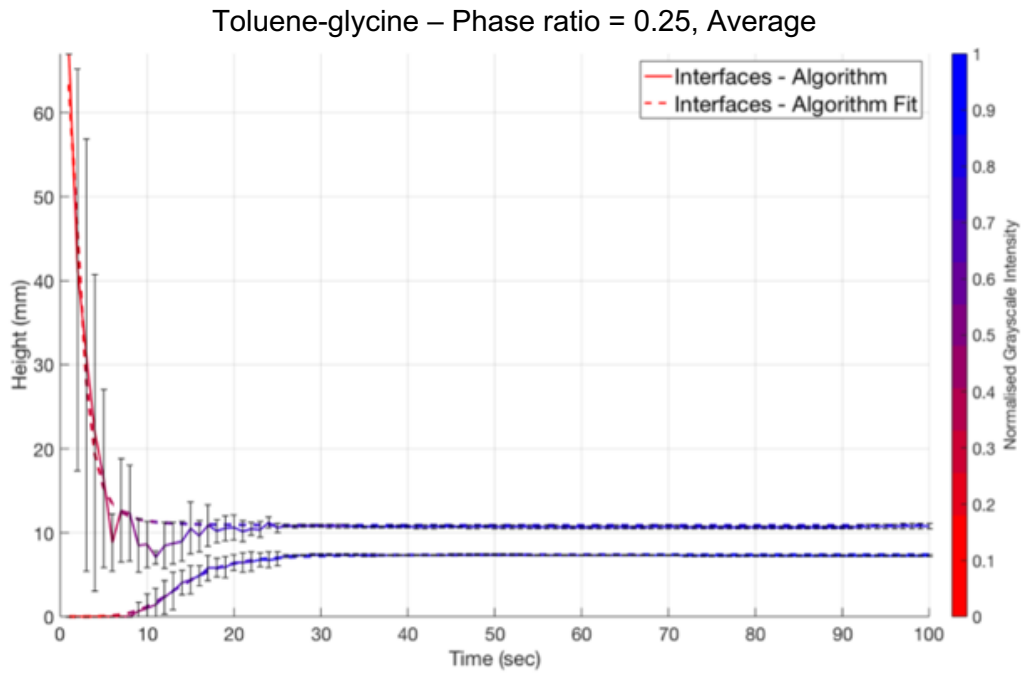
Figure A30: Averaged interface locations and normalised grayscale intensity over time for the toluene-glycine time series at a phase ratio of 0.25.

Toluene-acetate – Phase ratio = 1, Repeat 1
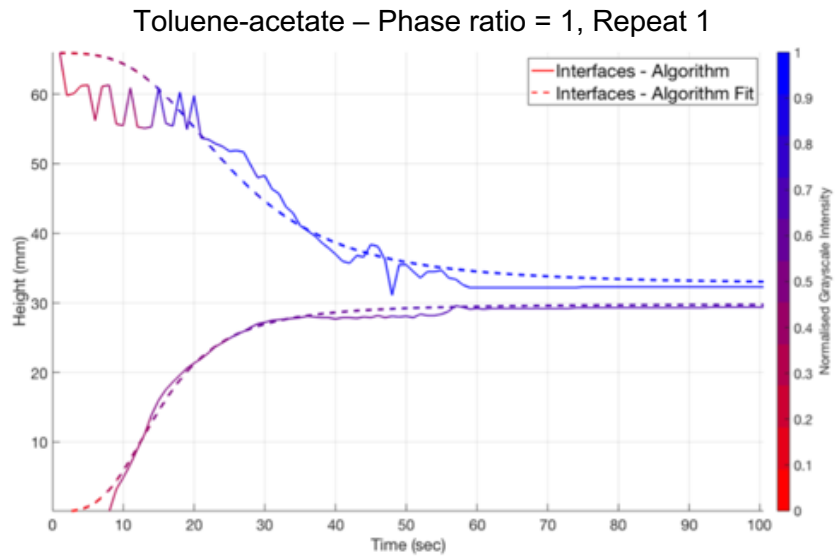
Figure A31: Detected interfaces and normalised grayscale intensity over time for repeat 1 of the toluene-acetate time series at a phase ratio of 1.

Figure A32: Contour plot of r^2 values for the sigmoidal curve fit for interface 1 data (a) and interface 2 data (b) depending on the maximum and minimum cut-off point combination – Toluene-acetate, phase ratio = 1, repeat 1.
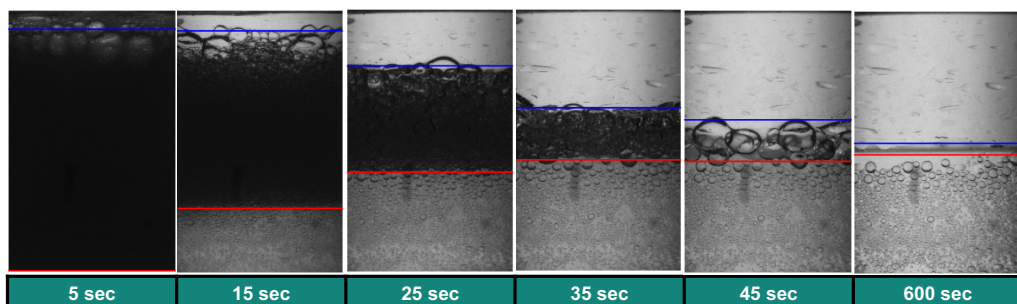
Figure A33: Sample images from toluene-acetate, phase ratio = 1, repeat 1 case with location of detected interfaces.

Toluene-acetate – Phase ratio = 1, Repeat 2
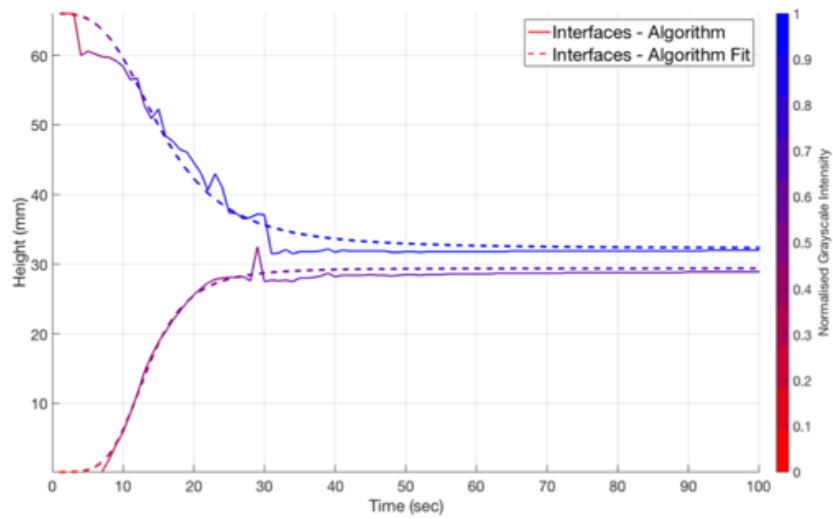
Figure A34: Detected interfaces and normalised grayscale intensity over time for repeat 2 of the toluene-acetate time series at a phase ratio of 1.

Figure A35: Contour plot of r^2 values for the sigmoidal curve fit for interface 1 data (a) and interface 2 data (b) depending on the maximum and minimum cut-off point combination – Toluene-acetate, phase ratio = 1, repeat 2.
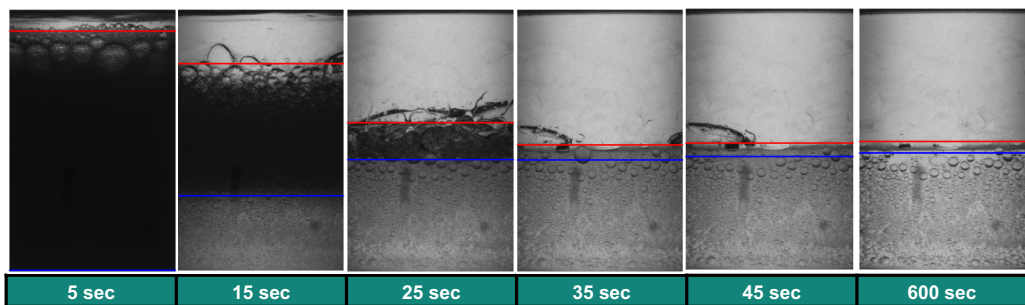
Figure A36: Sample images from toluene-acetate, phase ratio = 1, repeat 2 case with location of detected interfaces.

Toluene-acetate – Phase ratio = 1, Repeat 3
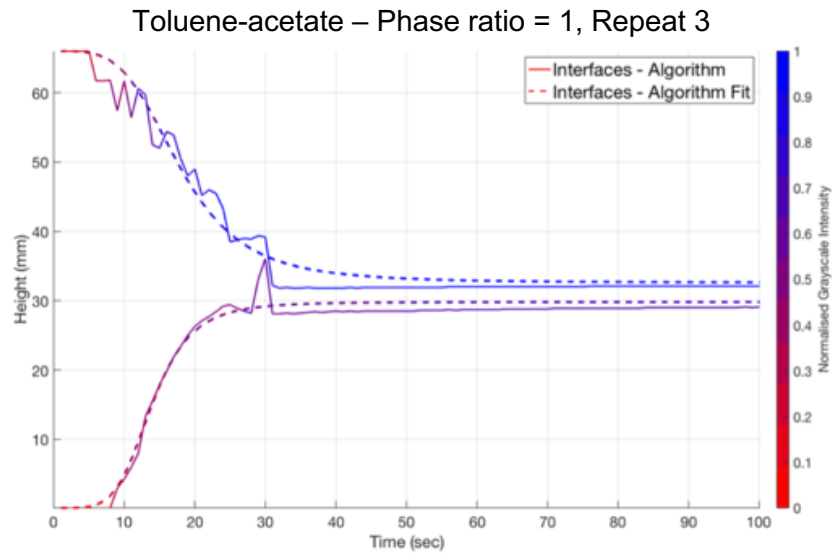
Figure A37: Detected interfaces and normalised grayscale intensity over time for repeat 3 of the toluene-acetate time series at a phase ratio of 1.

Figure A38: Contour plot of r^2 values for the sigmoidal curve fit for interface 1 data (a) and interface 2 data (b) depending on the maximum and minimum cut-off point combination – Toluene-acetate, phase ratio = 1, repeat 3.

| 5 sec | 15 sec | 25 sec | 35 sec | 45 sec | 600 sec |
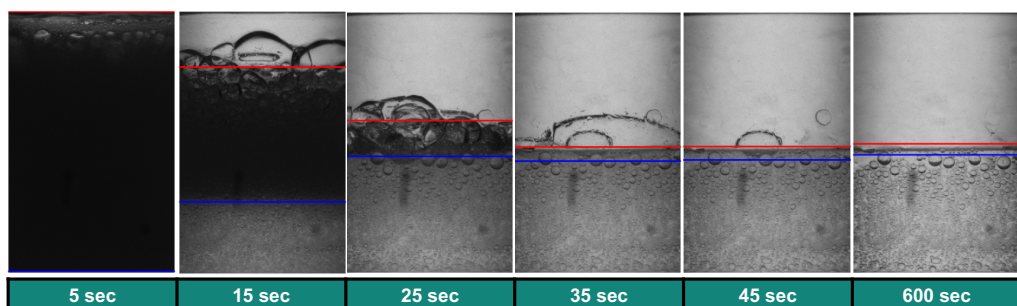
Figure A39: Sample images from toluene-acetate, phase ratio = 1, repeat 3 case with location of detected interfaces.
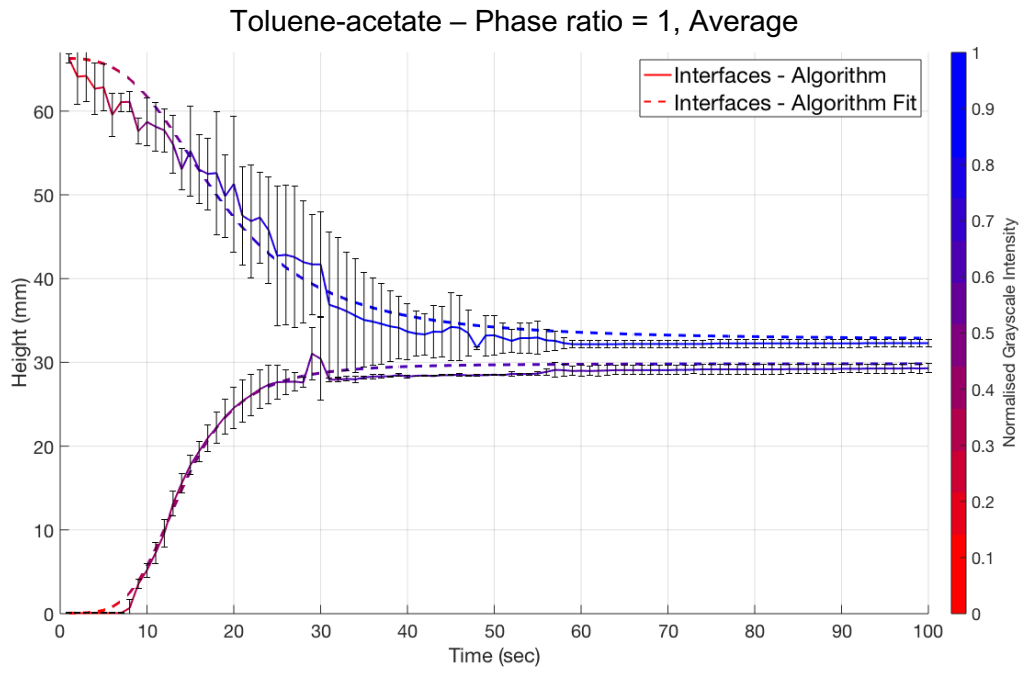
Figure A40: Averaged interface locations and normalised grayscale intensity over time for the toluene-acetate time series at a phase ratio of 1.

Toluene-deionised water – Phase ratio = 1, Repeat 1
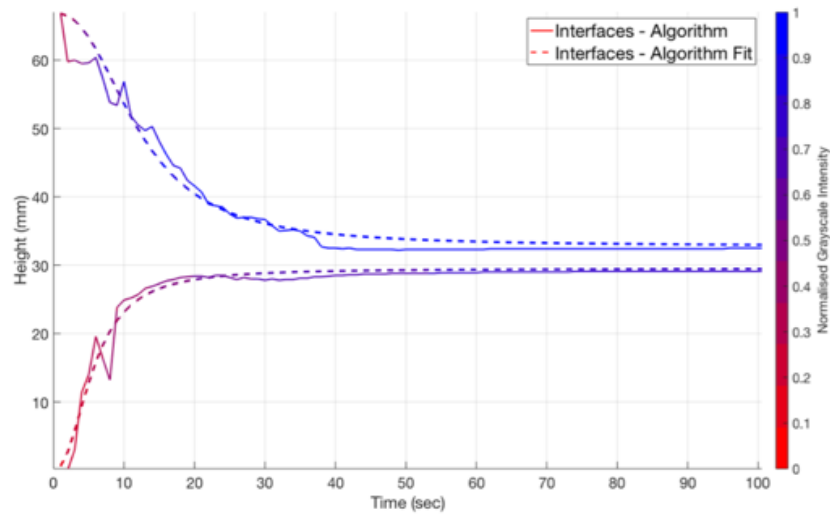
Figure A41: Detected interfaces and normalised grayscale intensity over time for repeat 1 of the toluene-deionised water time series at a phase ratio of 1.

Figure A42: Contour plot of r² values for the sigmoidal curve fit for interface 1 data (a) and interface 2 data (b) depending on the maximum and minimum cut-off point combination – Toluene-deionised water, phase ratio = 1, repeat 1.

| 5 sec | 15 sec | 25 sec | 35 sec | 45 sec | 600 sec |
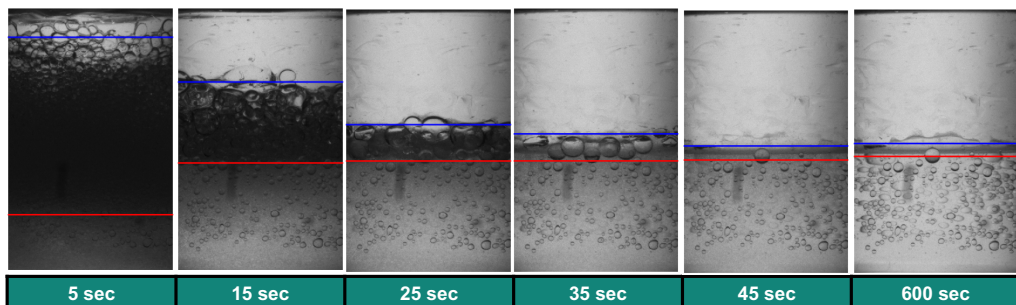
Figure A43: Sample images from toluene-deionised water, phase ratio = 1, repeat 1 case with location of detected interfaces.

Toluene-deionised water – Phase ratio = 1, Repeat 2
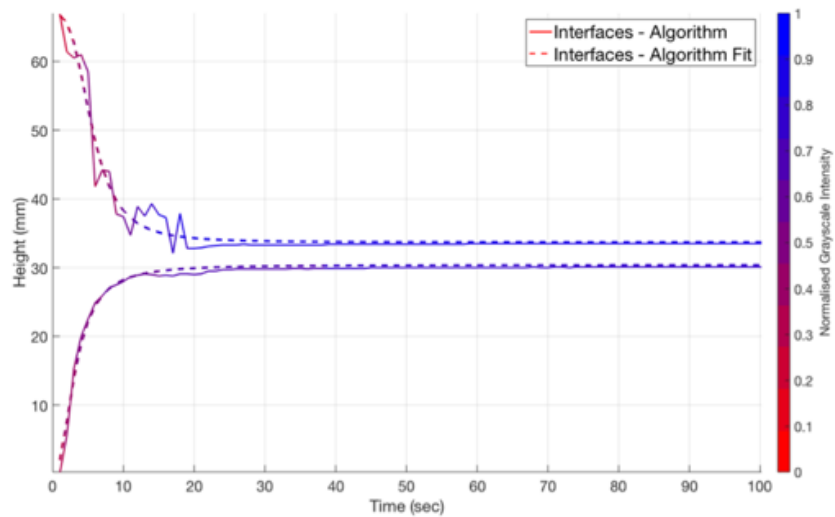
Figure A44: Detected interfaces and normalised grayscale intensity over time for repeat 1 of the toluene-deionised water time series at a phase ratio of 2.

Figure A45: Contour plot of r^2 values for the sigmoidal curve fit for interface 1 data (a) and interface 2 data (b) depending on the maximum and minimum cut-off point combination – Toluene-deionised water, phase ratio = 1, repeat 2.

| 5 sec | 15 sec | 25 sec | 35 sec | 45 sec | 600 sec |
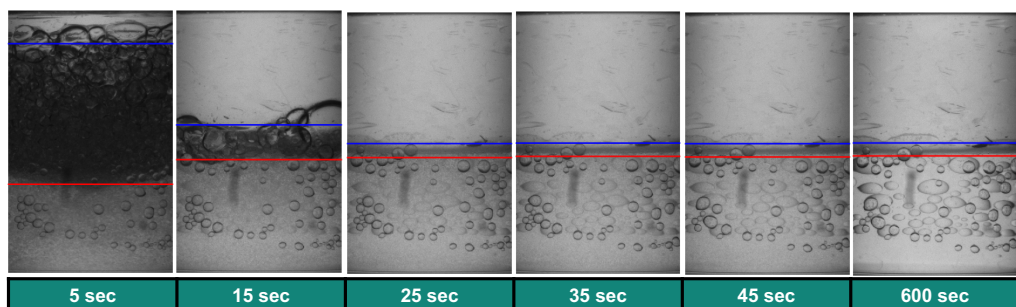
Figure A46: Sample images from toluene-deionised water, phase ratio = 1, repeat 2 case with location of detected interfaces.

Toluene-deionised water – Phase ratio = 1, Repeat 3
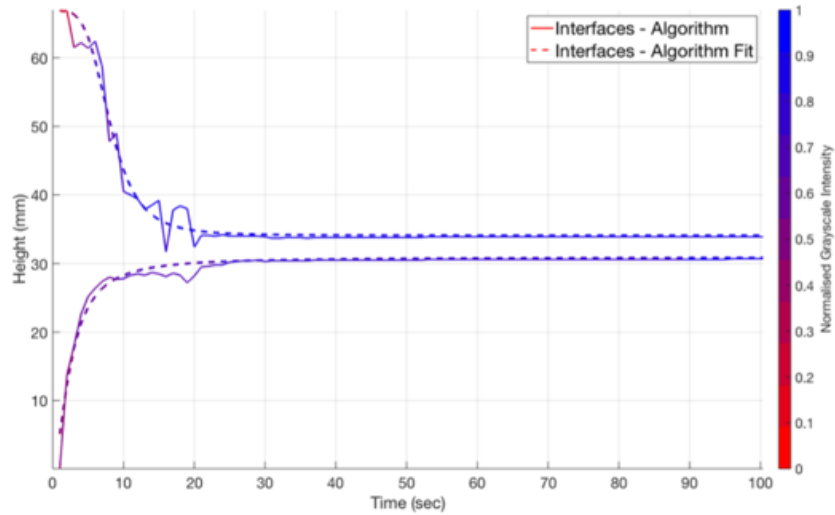
Figure A47: Detected interfaces and normalised grayscale intensity over time for repeat 3 of the toluene-deionised water time series at a phase ratio of 1.

Figure A48: Contour plot of r^2 values for the sigmoidal curve fit for interface 1 data (a) and interface 2 data (b) depending on the maximum and minimum cut-off point combination – Toluene-deionised water, phase ratio = 1, repeat 3.

| 5 sec | 15 sec | 25 sec | 35 sec | 45 sec | 600 sec |
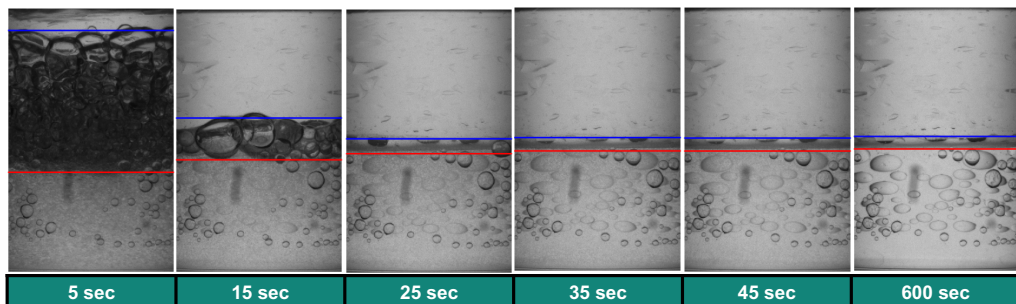
Figure A49: Sample images from toluene-deionised water, phase ratio = 1, repeat 3 case with location of detected interfaces.
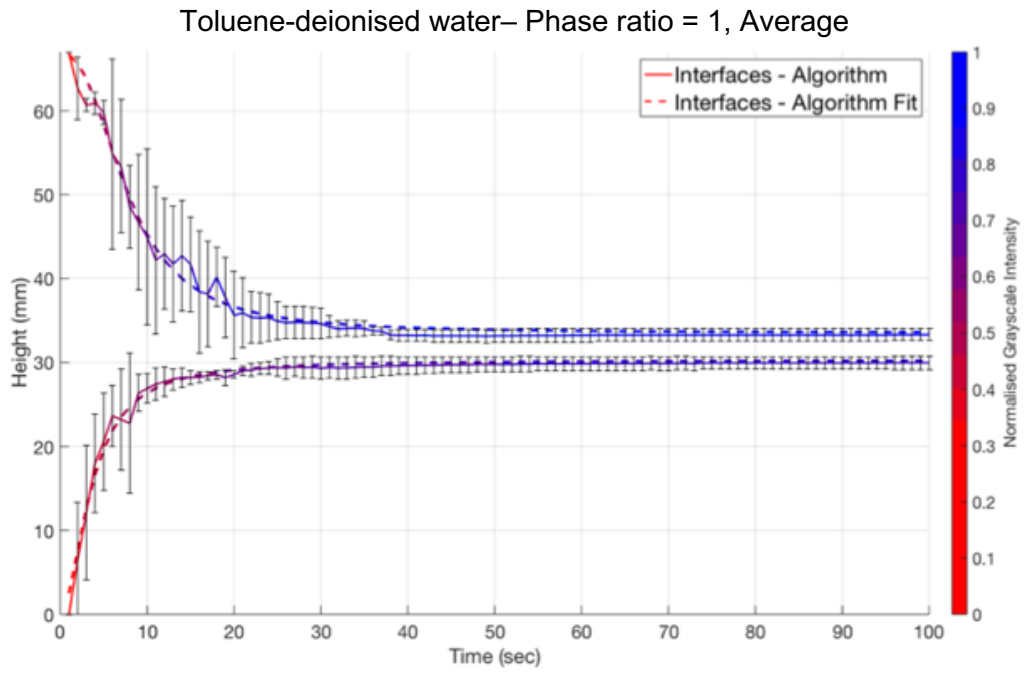
Figure A50: Averaged interface locations and normalised grayscale intensity over time for the toluene-deionised water time series at a phase ratio of 1.
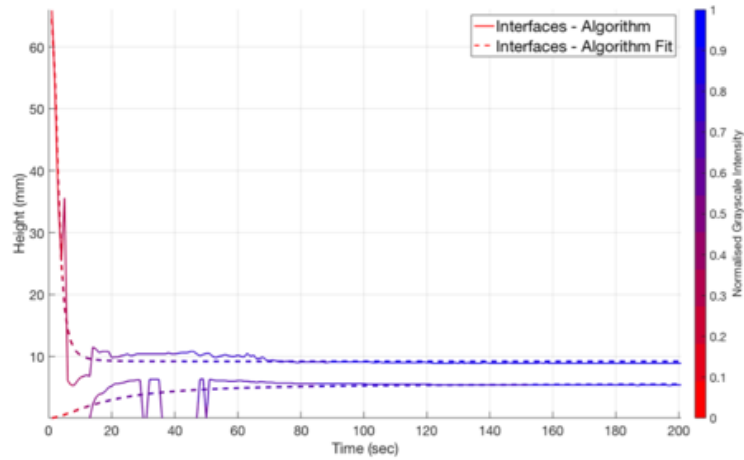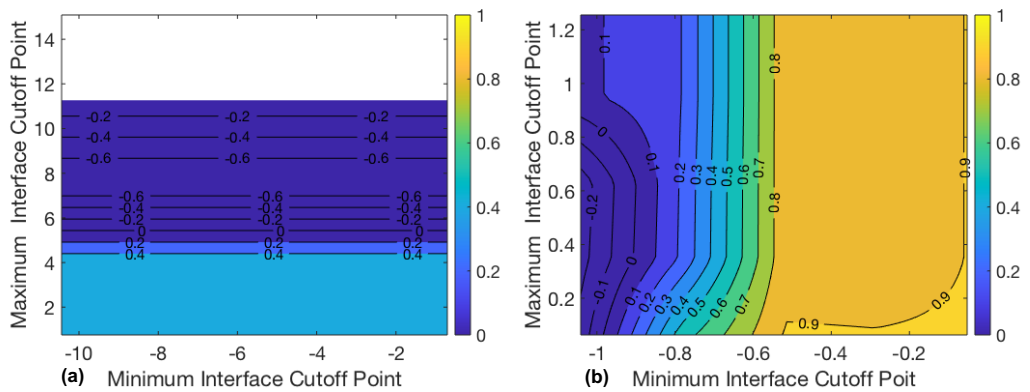
Toluene-glycine – Phase ratio = 1, Repeat 1
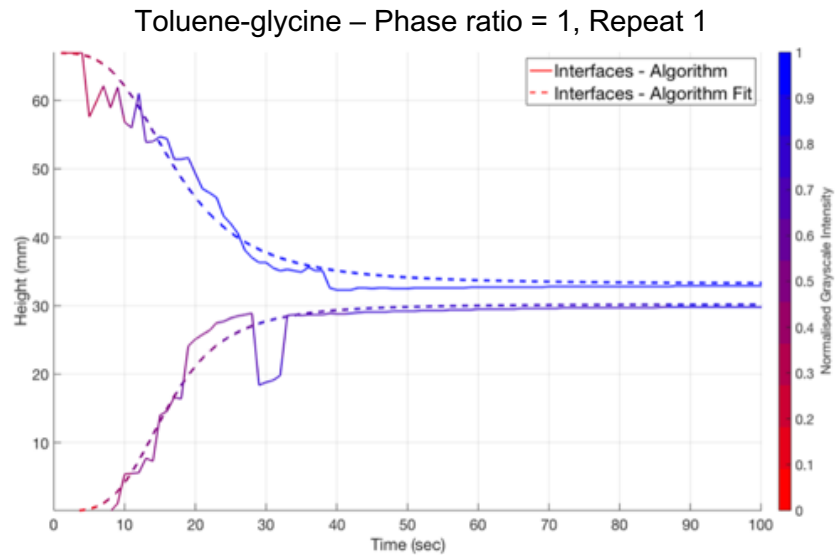
Figure A51: Detected interfaces and normalised grayscale intensity over time for repeat 1 of the toluene-glycine time series at a phase ratio of 1.

Figure A52: Contour plot of r^2 values for the sigmoidal curve fit for interface 1 data (a) and interface 2 data (b) depending on the maximum and minimum cut-off point combination – Toluene-glycine, phase ratio = 1, repeat 1.


| 5 sec | 15 sec | 25 sec | 35 sec | 45 sec | 600 sec |
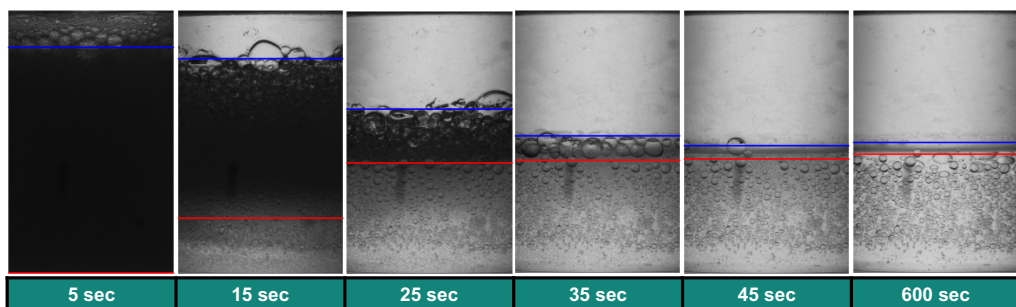
Figure A53: Sample images from toluene-glycine, phase ratio = 1, repeat 1 case with location of detected interfaces.

Toluene-glycine – Phase ratio = 1, Repeat 2
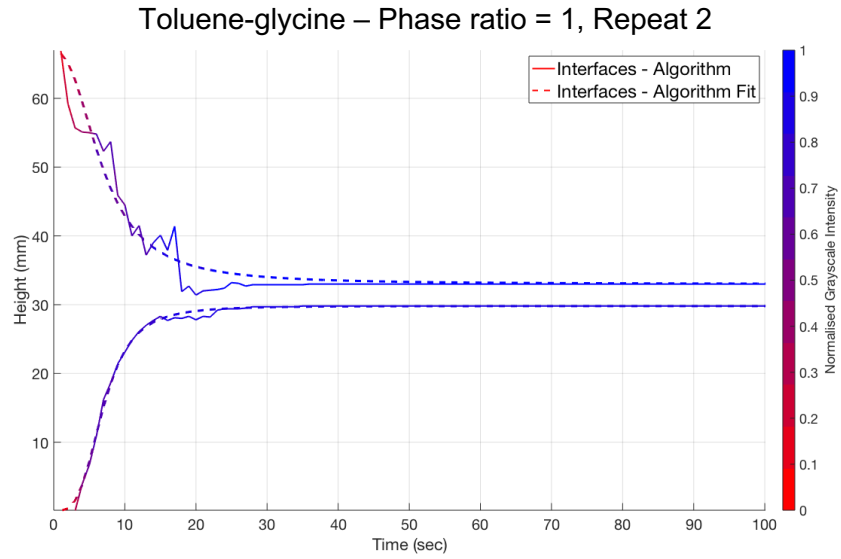
Figure A54: Detected interfaces and normalised grayscale intensity over time for repeat 2 of the toluene-glycine time series at a phase ratio of 1.
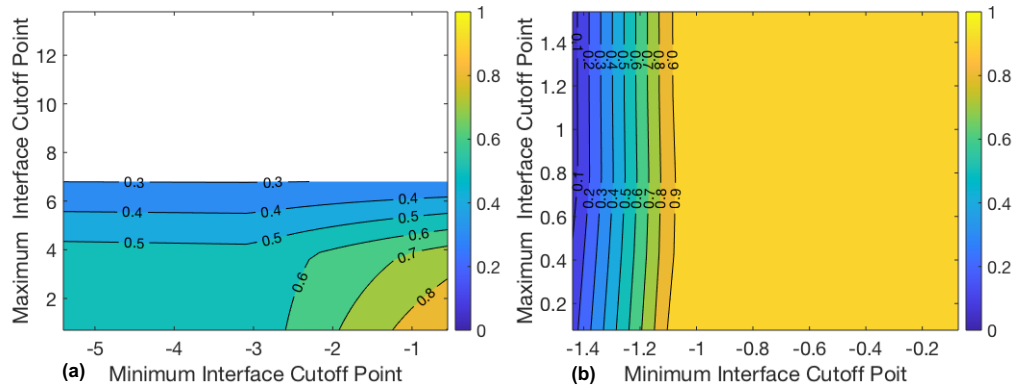

Figure A55: Contour plot of r^2 values for the sigmoidal curve fit for interface 1 data (a) and interface 2 data (b) depending on the maximum and minimum cut-off point combination – Toluene-glycine, phase ratio = 1, repeat 2.
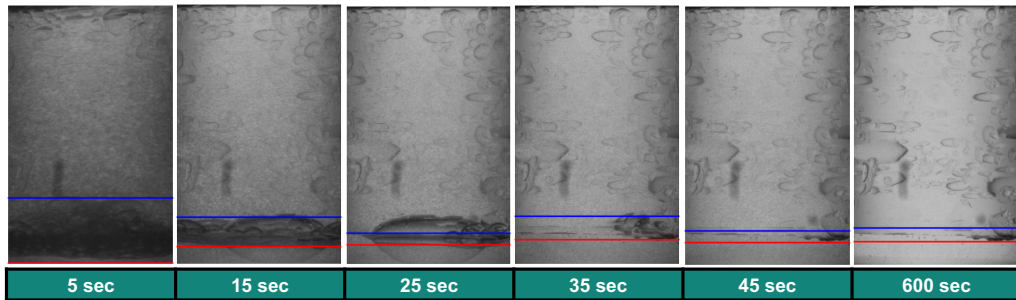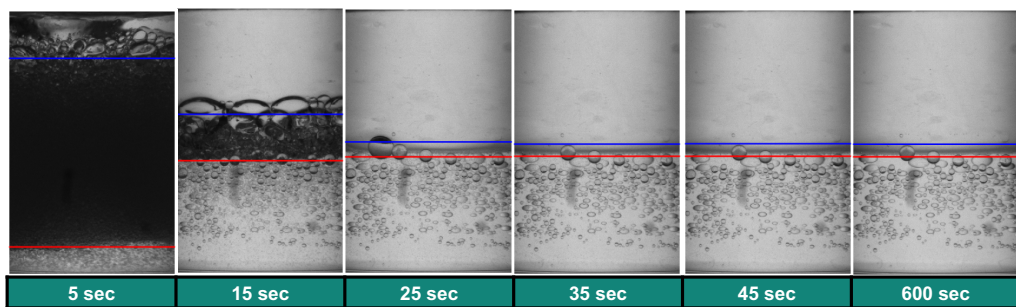

Figure A56: Sample images from toluene-glycine, phase ratio = 1, repeat 2 case with location of detected interfaces.
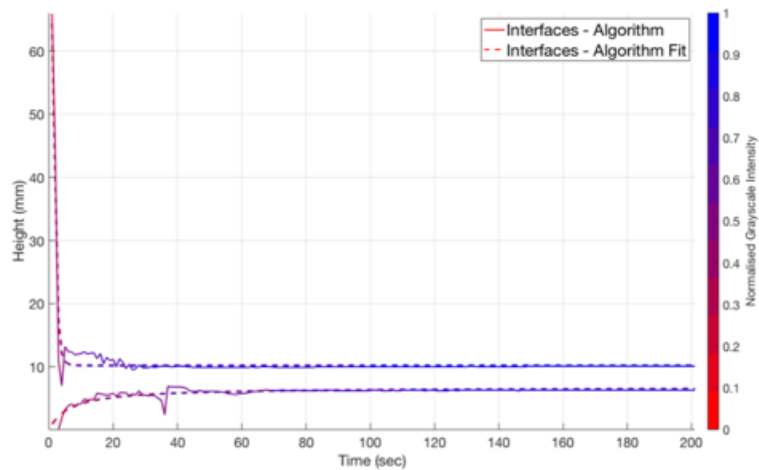
Toluene-glycine – Phase ratio = 1, Repeat 3
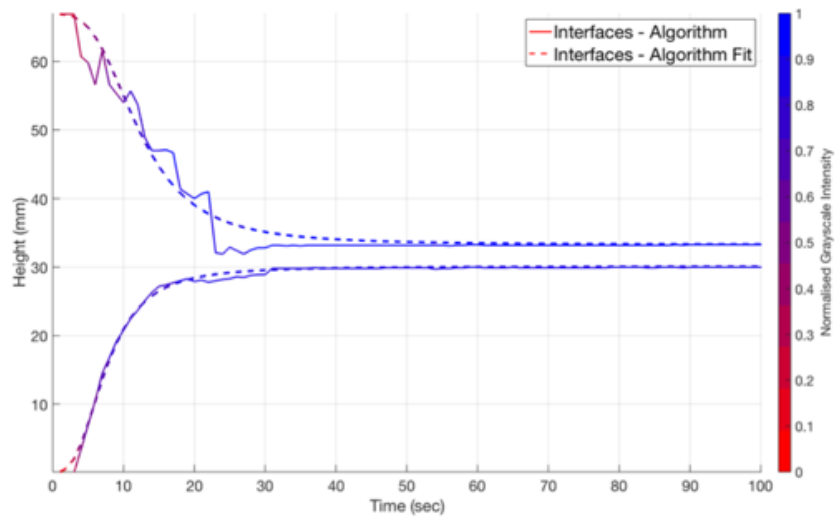
Figure A57: Detected interfaces and normalised grayscale intensity over time for repeat 3 of the toluene-glycine time series at a phase ratio of 1.
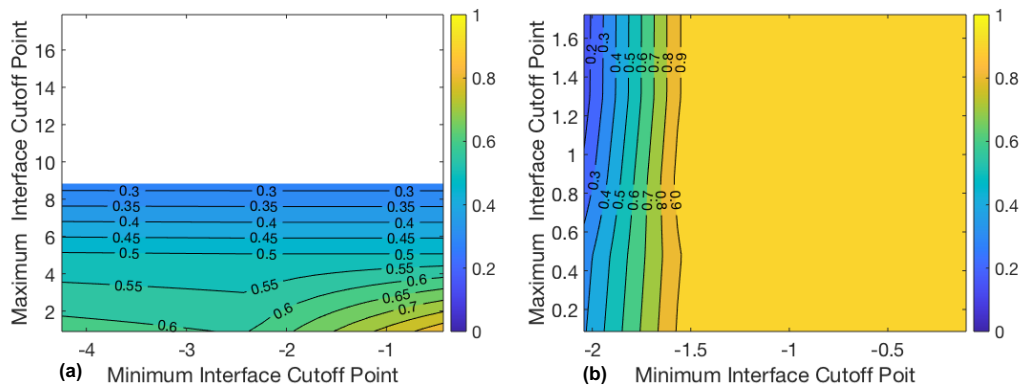

Figure A58: Contour plot of r^2 values for the sigmoidal curve fit for interface 1 data (a) and interface 2 data (b) depending on the maximum and minimum cut-off point combination – Toluene-glycine, phase ratio = 1, repeat 3.
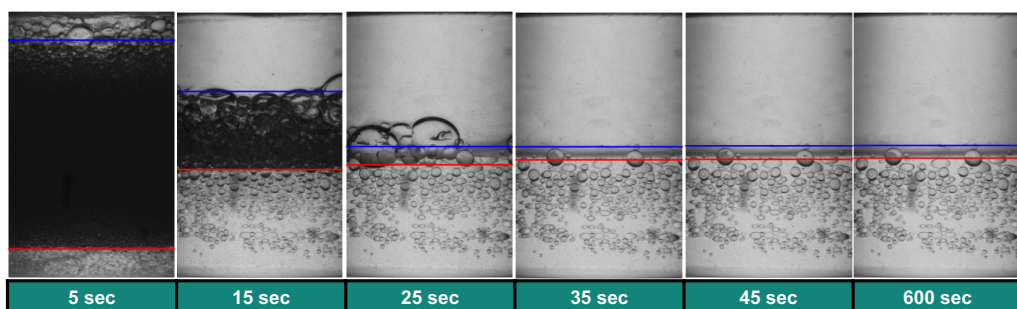
Figure A59: Sample images from toluene-glycine, phase ratio = 1, repeat 3 case with location of detected interfaces.
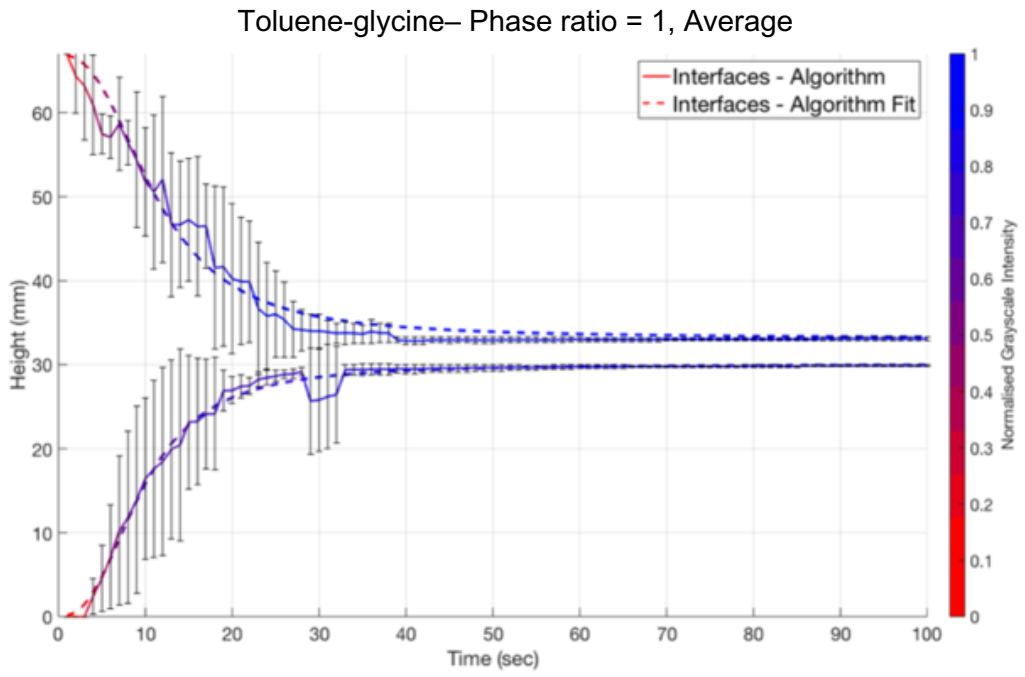
Figure A60: Averaged interface locations and normalised grayscale intensity over time for the toluene-glycine time series at a phase ratio of 1.

Toluene-acetate – Phase ratio = 4, Repeat 1
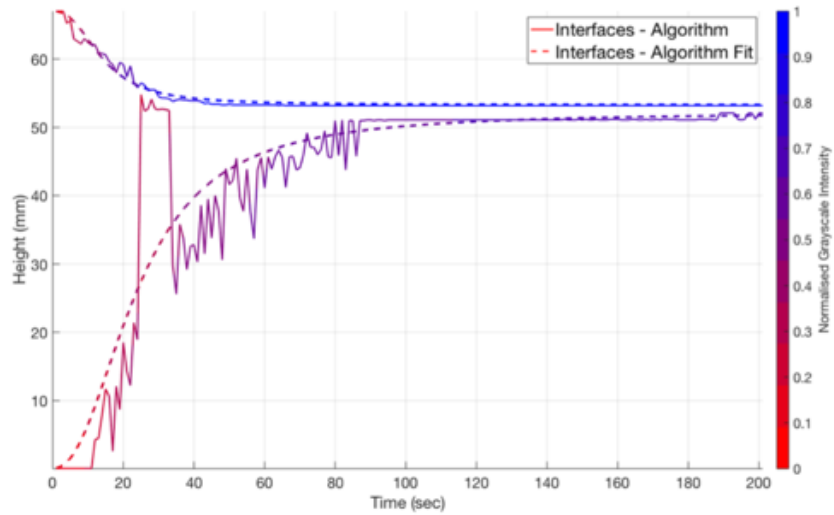
Figure A61: Detected interfaces and normalised grayscale intensity over time for repeat 1 of the toluene-acetate time series at a phase ratio of 4.

Figure A62: Contour plot of r^2 values for the sigmoidal curve fit for interface 1 data (a) and interface 2 data (b) depending on the maximum and minimum cut-off point combination – Toluene-acetate, phase ratio = 4, repeat 1.
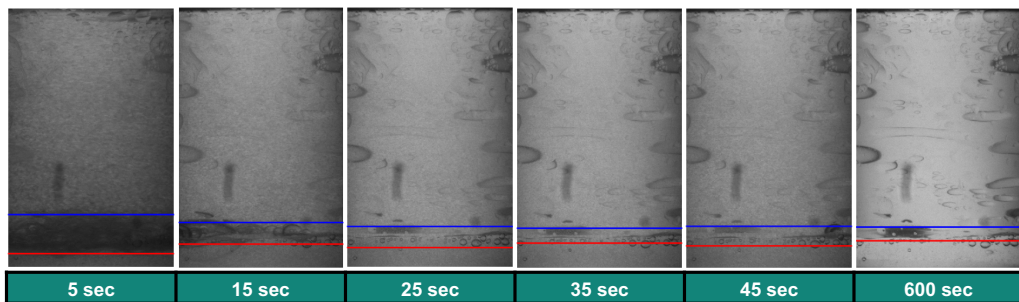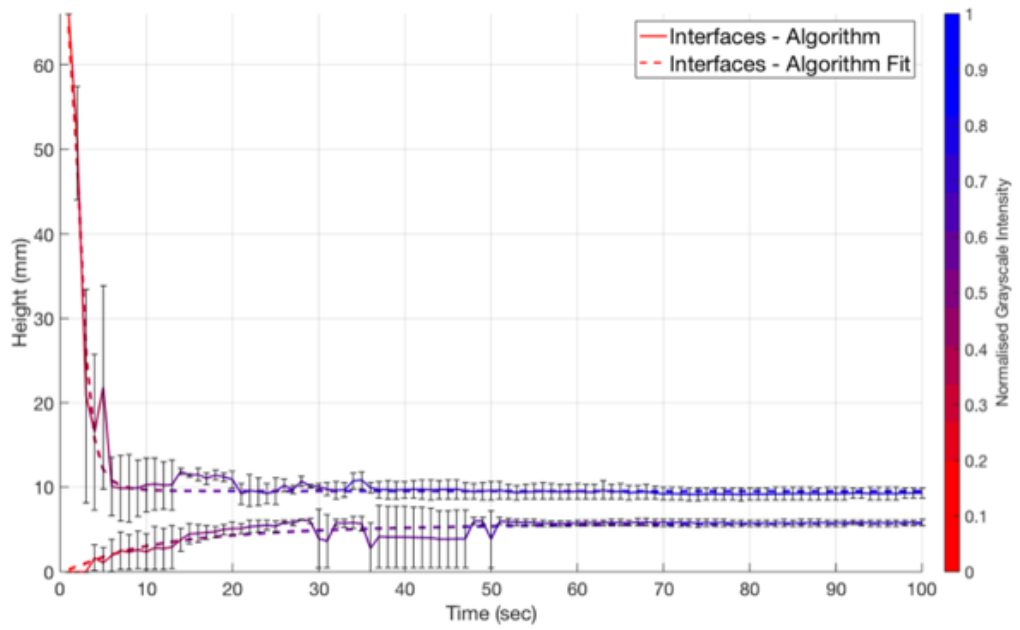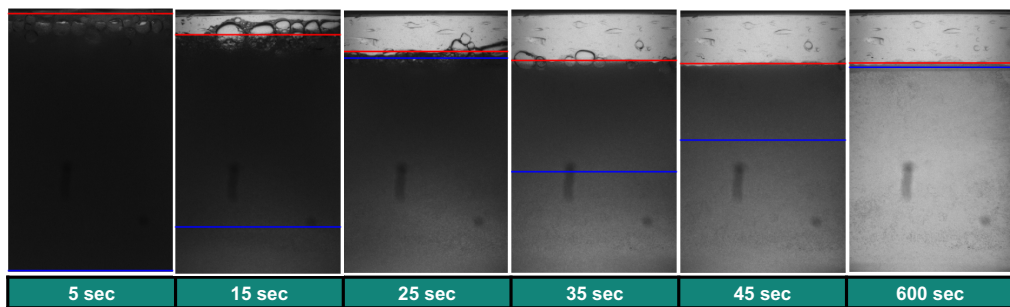

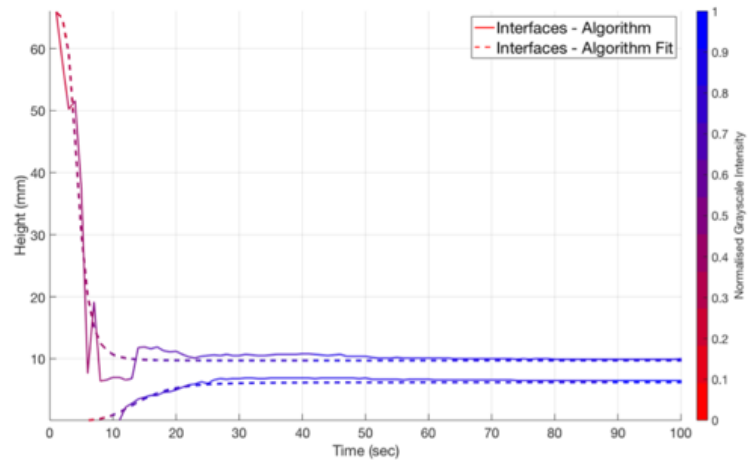**Figure A63:** Sample images from toluene-acetate, phase ratio = 4, repeat 1 case with location of detected interfaces.
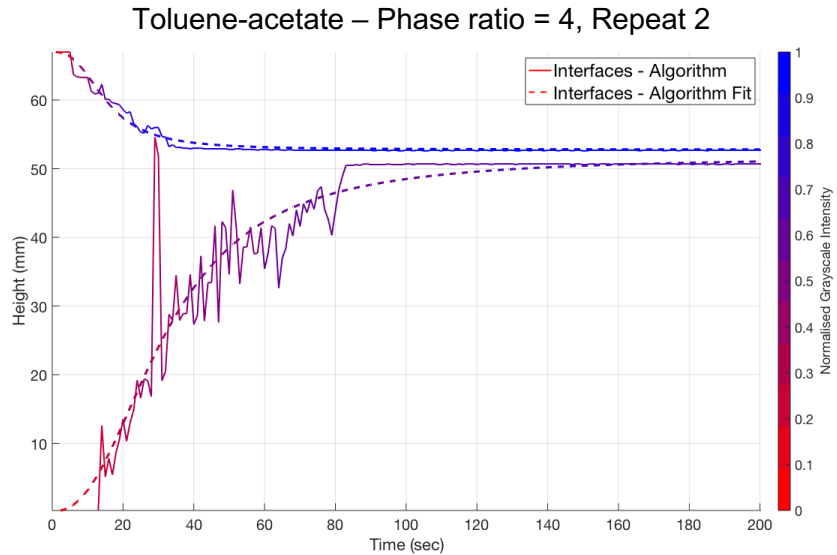
Figure A64: Detected interfaces and normalised grayscale intensity over time for repeat 2 of the toluene-acetate time series at a phase ratio of 4.
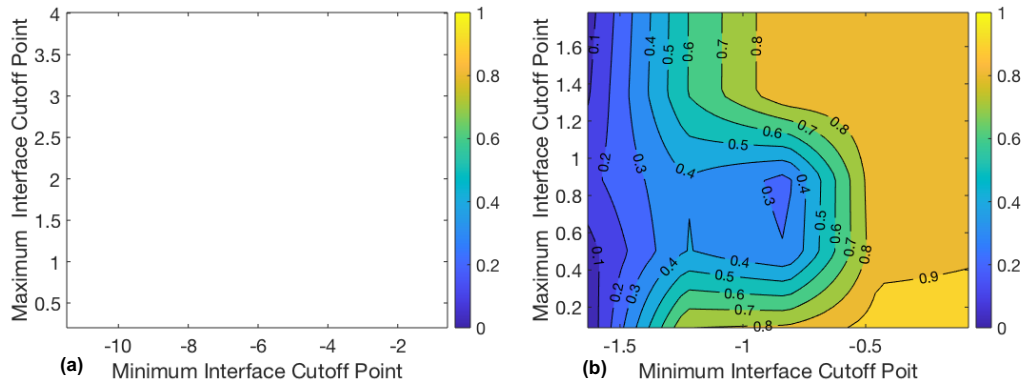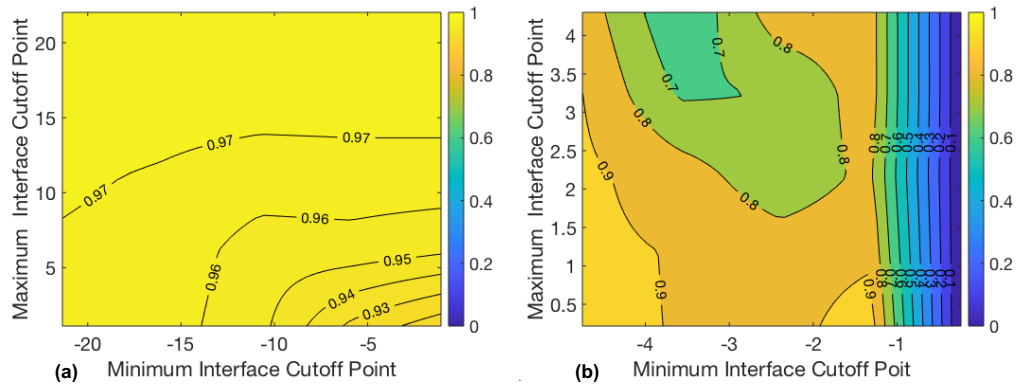

Figure A65: Contour plot of r^2 values for the sigmoidal curve fit for interface 1 data (a) and interface 2 data (b) depending on the maximum and minimum cut-off point combination – Toluene-acetate, phase ratio = 4, repeat 2.
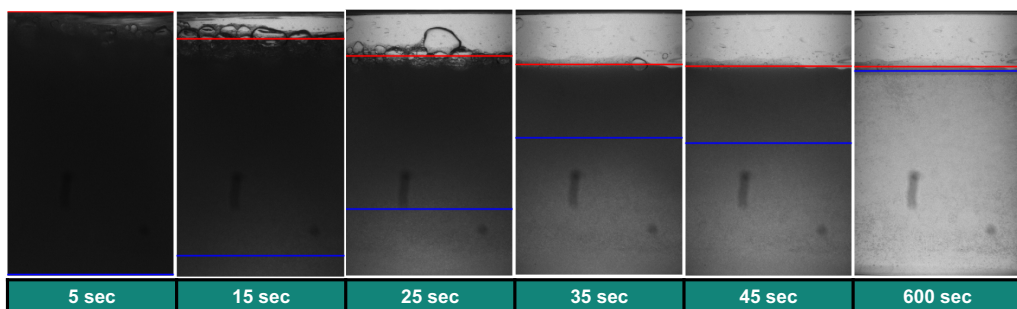
Figure A66: Sample images from toluene-acetate, phase ratio = 4, repeat 2 case with location of detected interfaces.

Toluene-acetate – Phase ratio = 4, Repeat 3
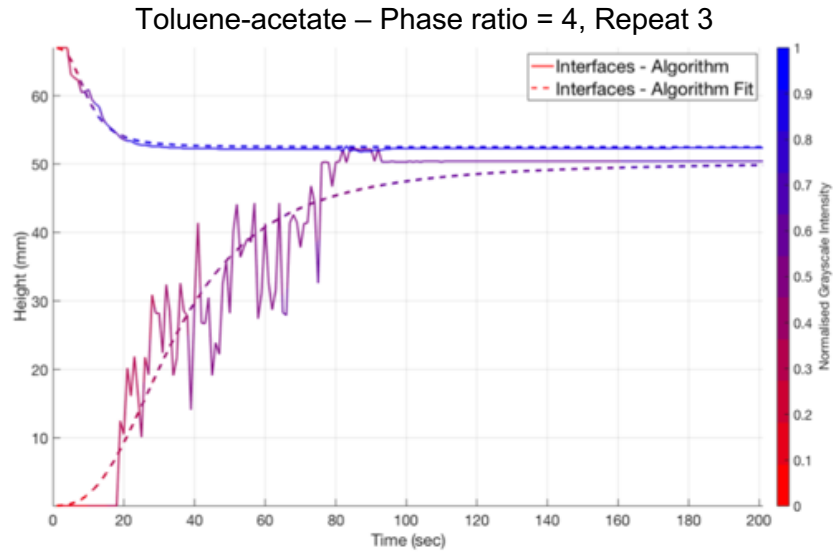
Figure A67: Detected interfaces and normalised grayscale intensity over time for repeat 3 of the toluene-acetate time series at a phase ratio of 4.
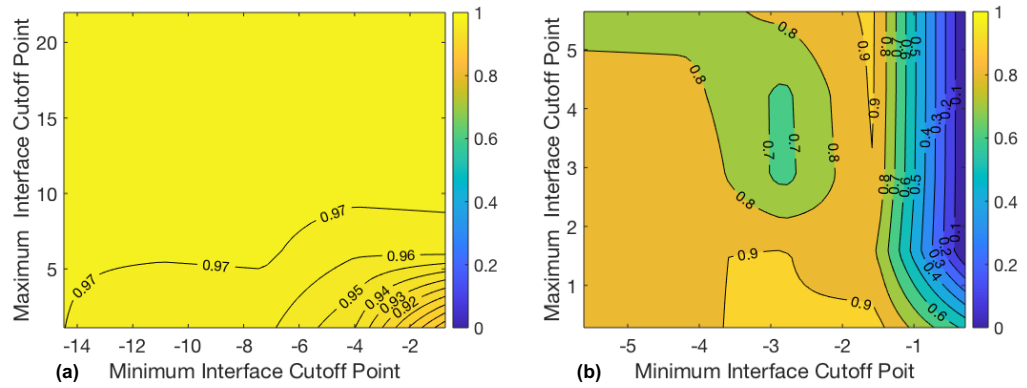
Figure A68: Contour plot of r^2 values for the sigmoidal curve fit for interface 1 data (a) and interface 2 data (b) depending on the maximum and minimum cut-off point combination – Toluene-acetate, phase ratio = 4, repeat 3.
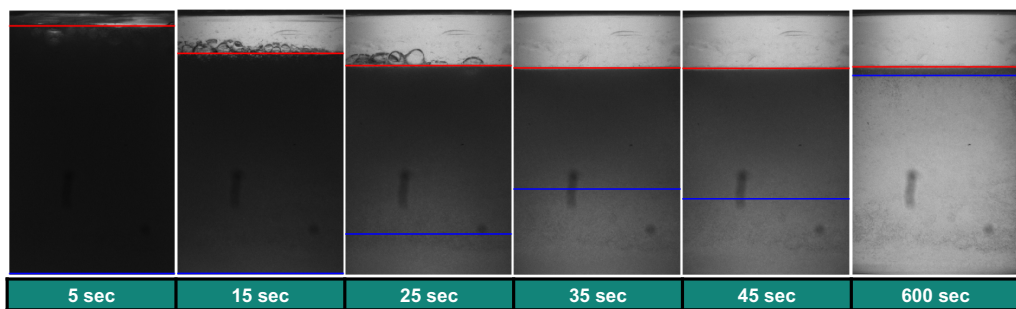
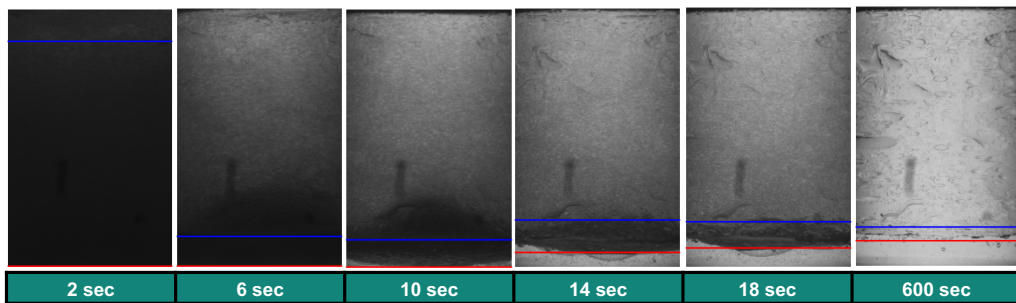**Figure A69:** Sample images from toluene-acetate, phase ratio = 4, repeat 3 case with location of detected interfaces.

Toluene-acetate – Phase ratio = 4, Average
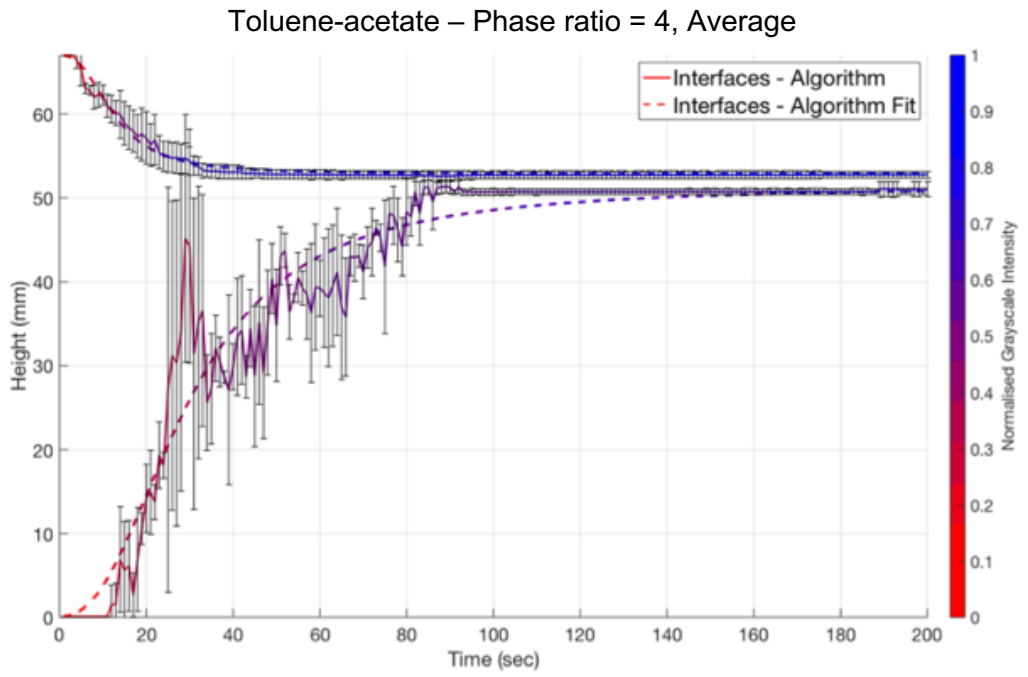
Figure A70: Averaged interface locations and normalised grayscale intensity over time for the toluene-acetate time series at a phase ratio of 4.

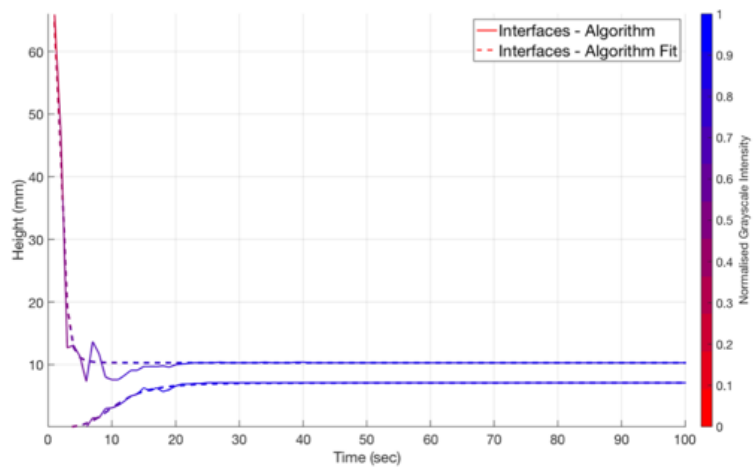Toluene-deionised water – Phase ratio = 4, Repeat 1
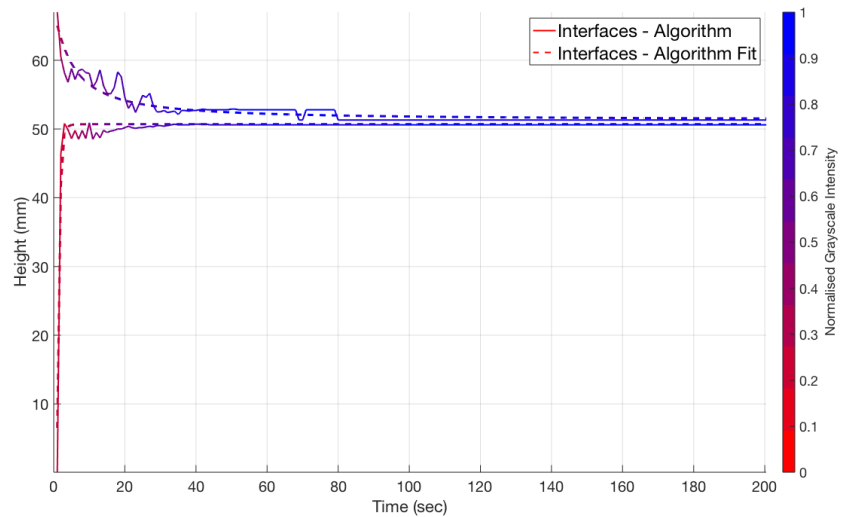
Figure A71: Detected interfaces and normalised grayscale intensity over time for repeat 1 of the toluene-deionised water time series at a phase ratio of 4.
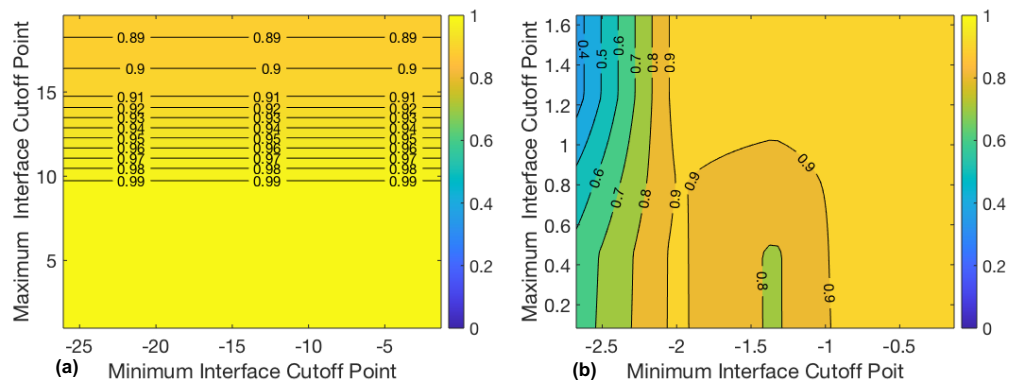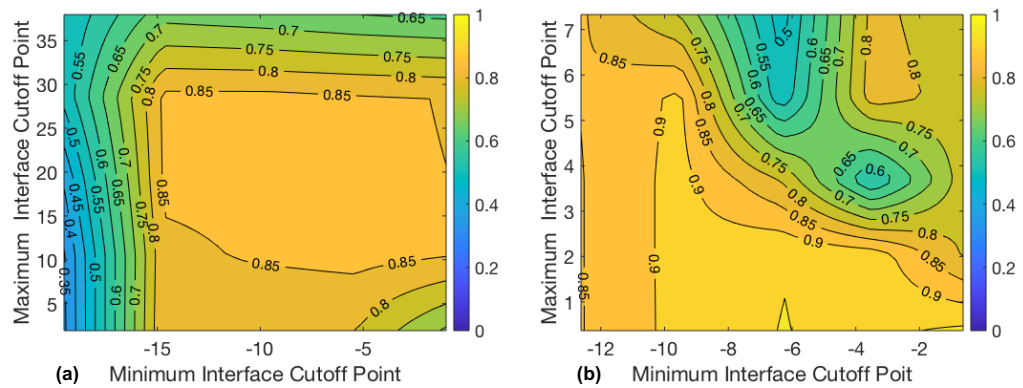

Figure A72: Contour plot of r^2 values for the sigmoidal curve fit for interface 1 data (a) and interface 2 data (b) depending on the maximum and minimum cut-off point combination – Toluene-deionised water, phase ratio = 4, repeat 1.
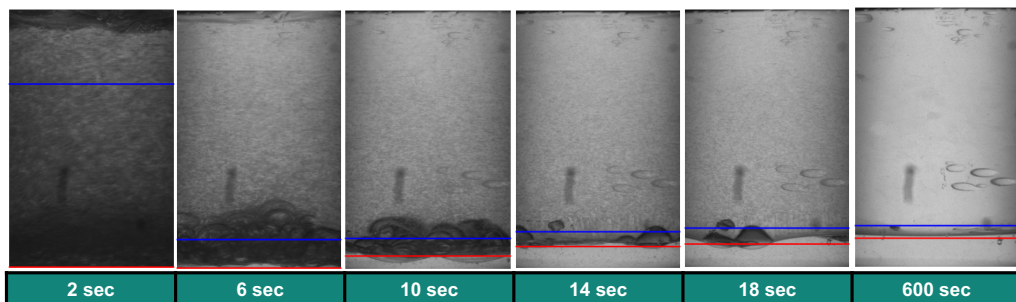

| 5 sec | 15 sec | 25 sec | 35 sec | 45 sec | 600 sec |
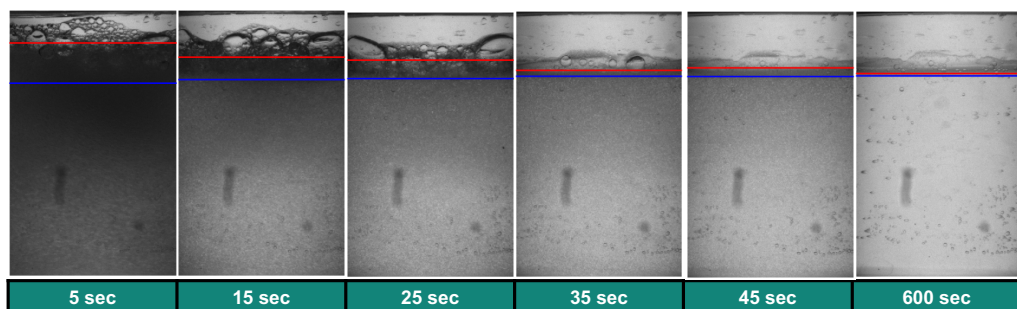
Figure A73: Sample images from toluene-deionised water, phase ratio = 4, repeat 1 case with location of detected interfaces.

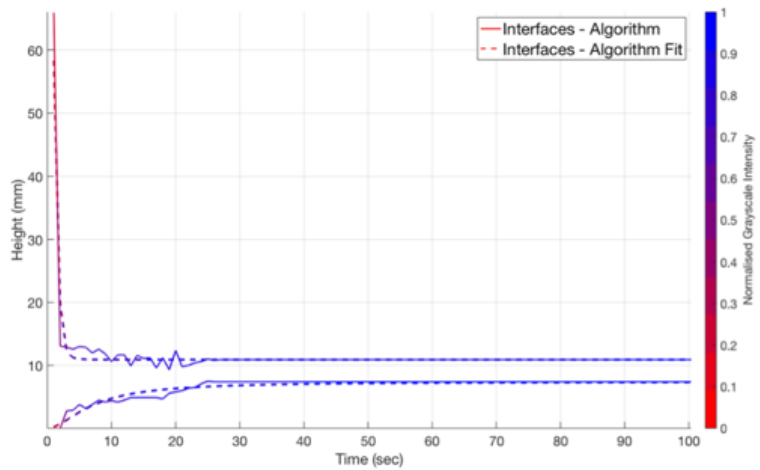Toluene-deionised water – Phase ratio = 4, Repeat 2
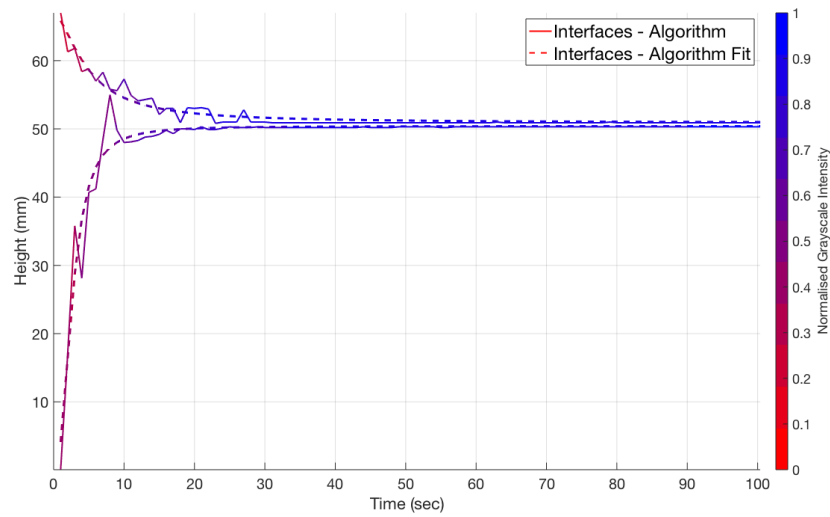
Figure A74: Detected interfaces and normalised grayscale intensity over time for repeat 2 of the toluene-deionised water time series at a phase ratio of 4.
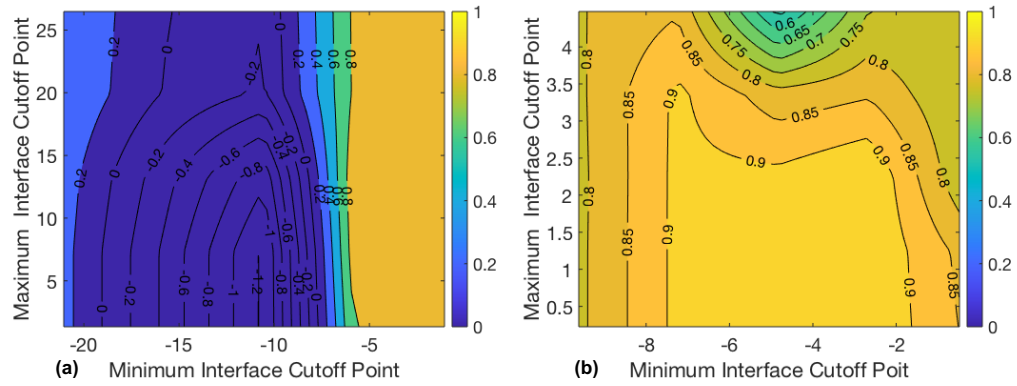
Figure A75: Contour plot of r^2 values for the sigmoidal curve fit for interface 1 data (a) and interface 2 data (b) depending on the maximum and minimum cut-off point combination – Toluene-deionised water, phase ratio = 4, repeat 2.
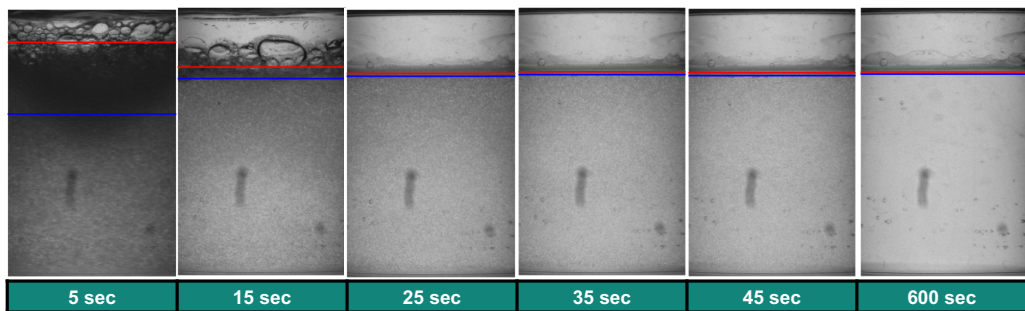
Figure A76: Sample images from toluene-deionised water, phase ratio = 4, repeat 2 case with location of detected interfaces.

Toluene-deionised water – Phase ratio = 4, Repeat 3
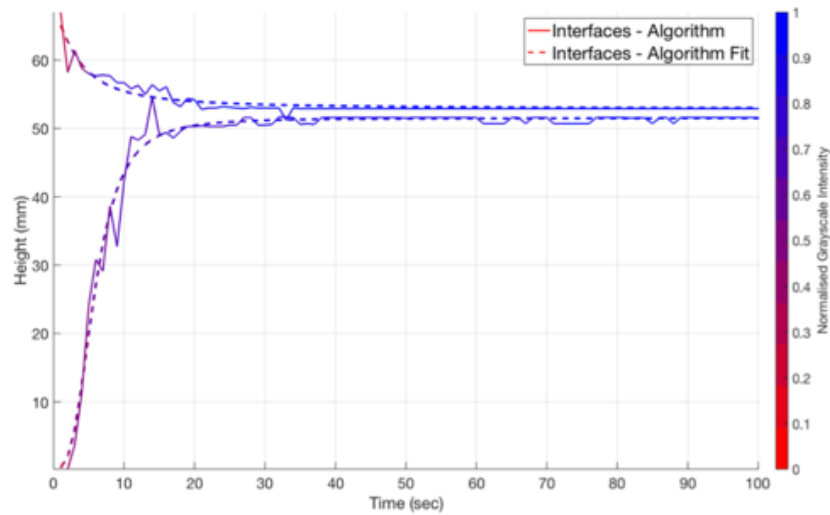
Figure A77: Detected interfaces and normalised grayscale intensity over time for repeat 3 of the toluene-deionised water time series at a phase ratio of 4.
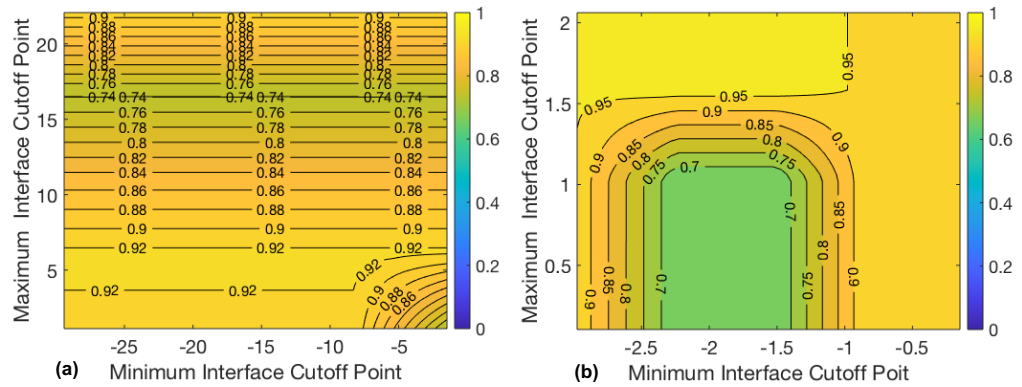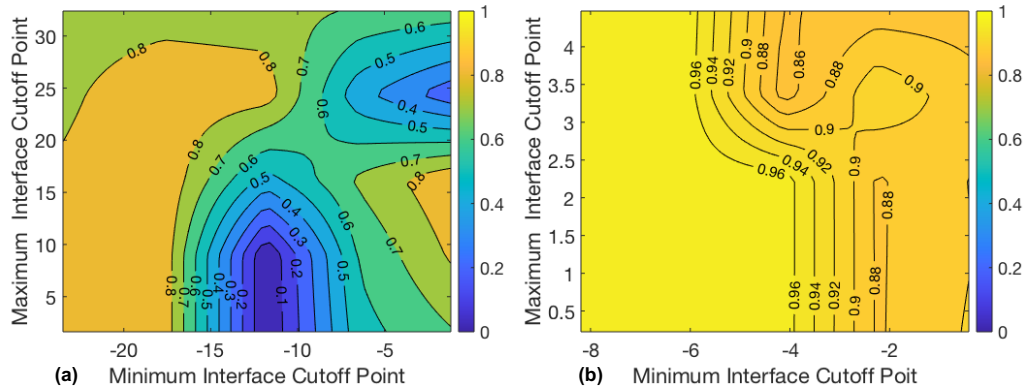

Figure A78: Contour plot of r^2 values for the sigmoidal curve fit for interface 1 data (a) and interface 2 data (b) depending on the maximum and minimum cut-off point combination – Toluene-deionised water, phase ratio = 4, repeat 3.
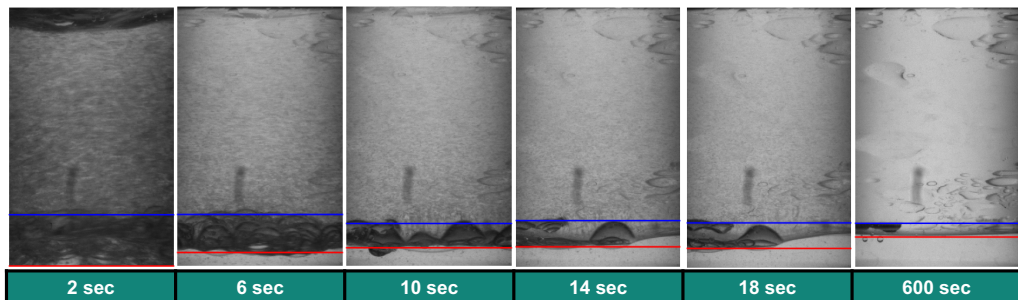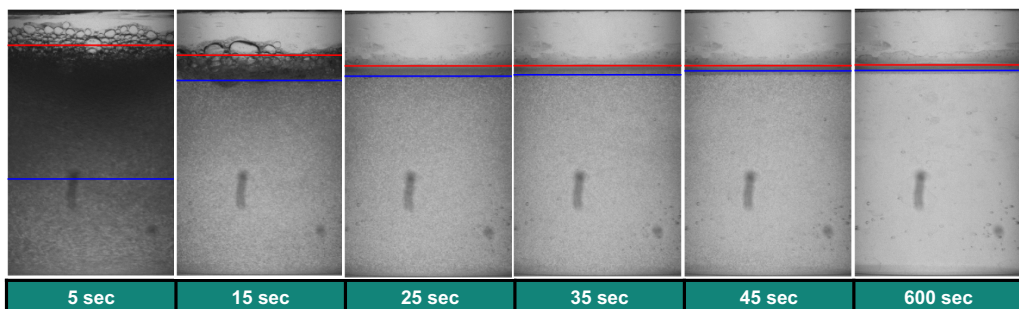

Figure A79: Sample images from toluene-deionised water, phase ratio = 4, repeat 3 case with location of detected interfaces.
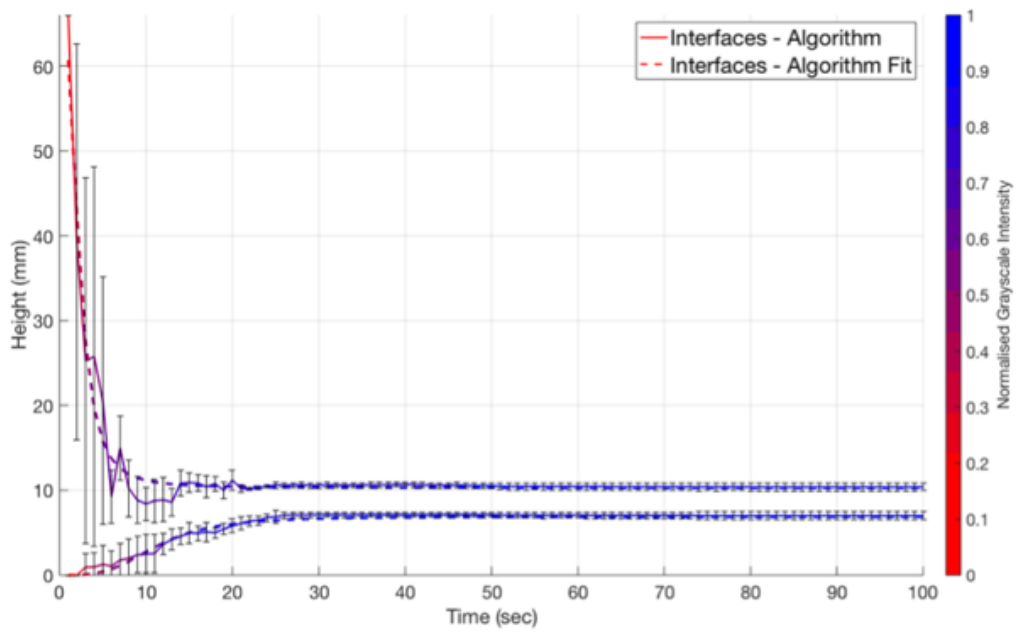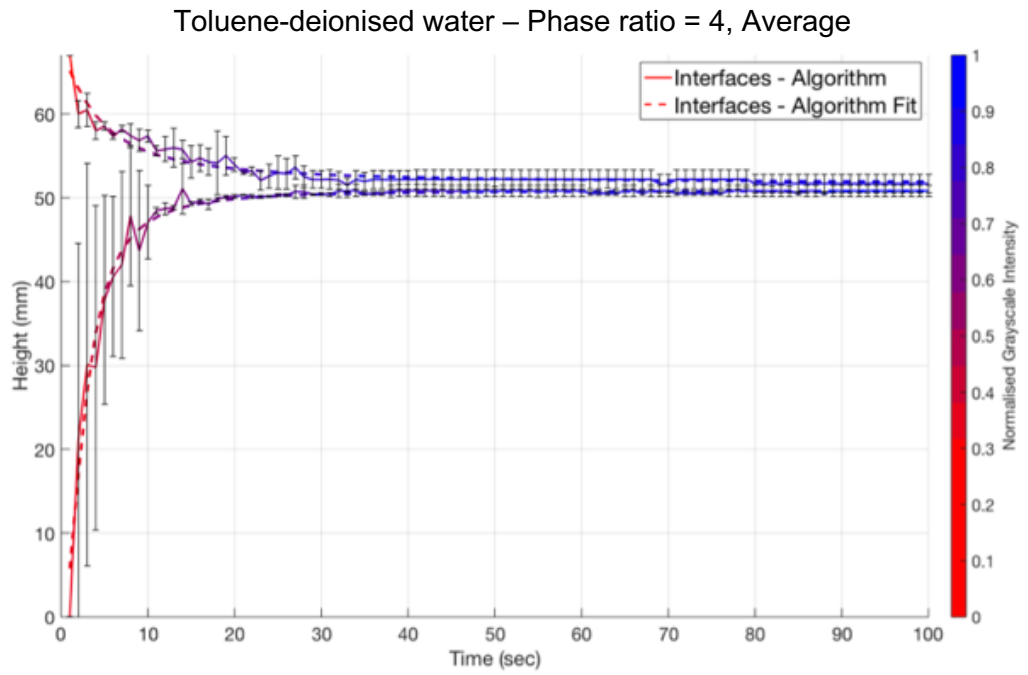
Figure A80: Averaged interface locations and normalised grayscale intensity over time for the toluene-deionised water time series at a phase ratio of 4.
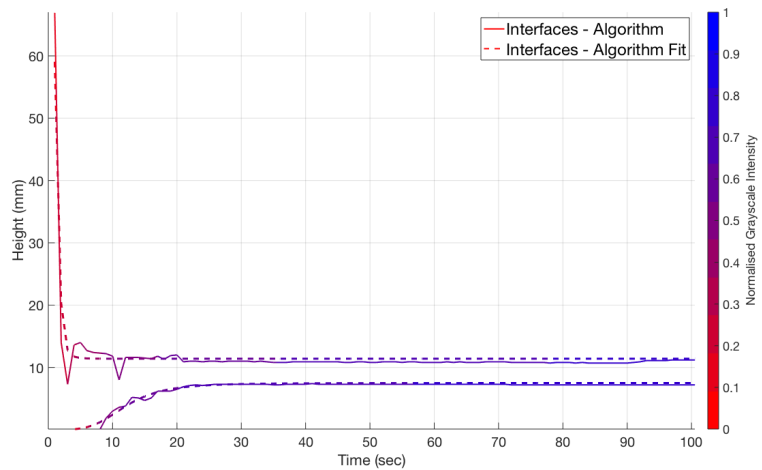
Toluene-glycine – Phase ratio = 4, Repeat 1
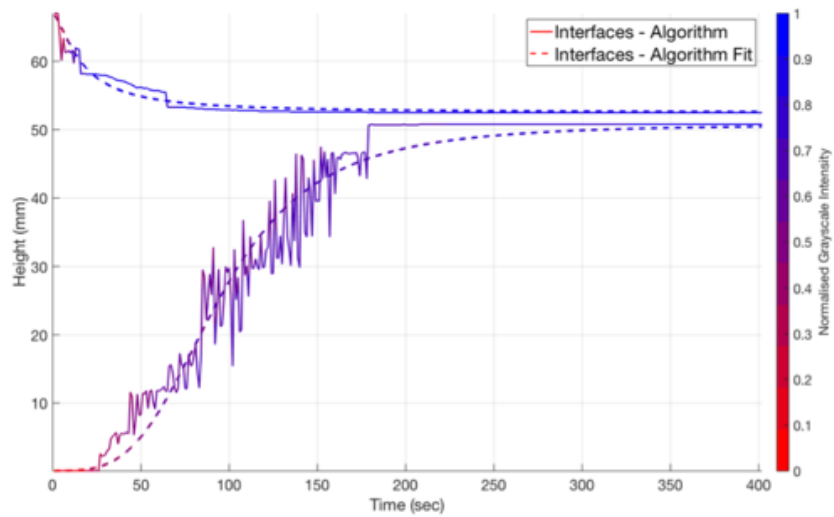
Figure A81: Detected interfaces and normalised grayscale intensity over time for repeat 1 of the toluene-glycine time series at a phase ratio of 4.
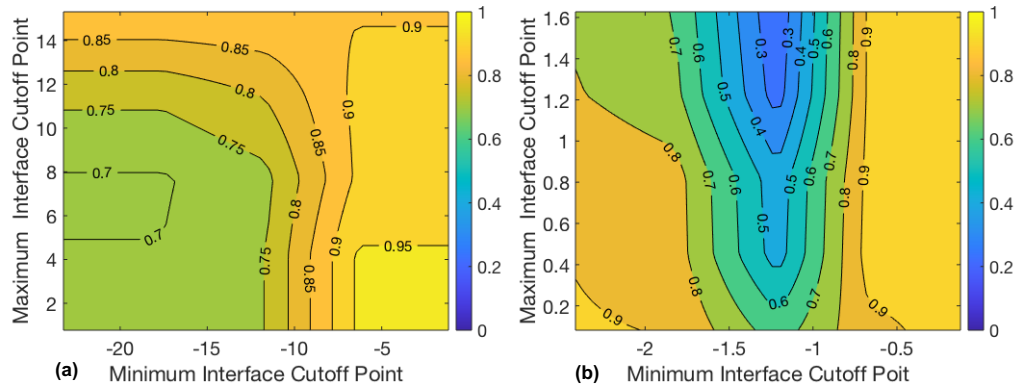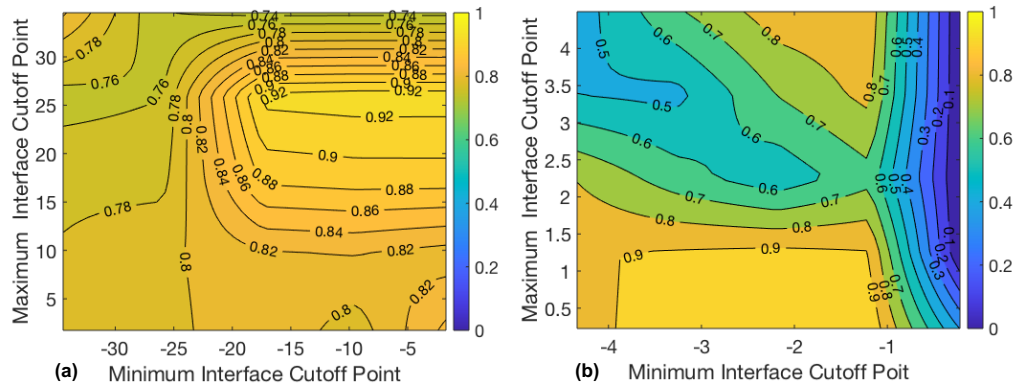

Figure A82: Contour plot of r^2 values for the sigmoidal curve fit for interface 1 data (a) and interface 2 data (b) depending on the maximum and minimum cut-off point combination – Toluene-glycine, phase ratio = 4, repeat 1.

| 20 sec | 60 sec | 100 sec | 140 sec | 180 sec | 600 sec |
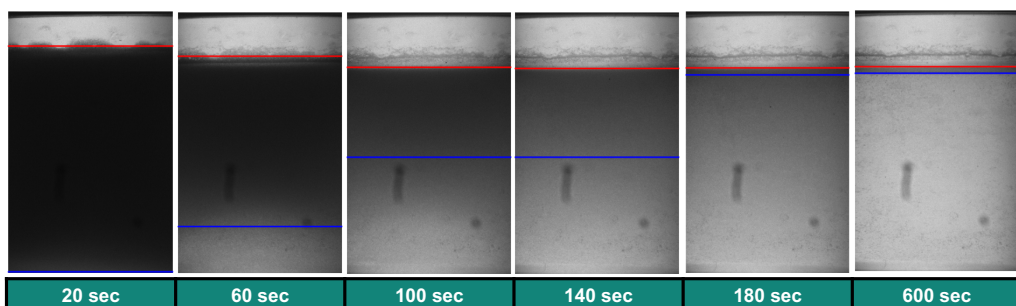
Figure A83: Sample images from toluene-glycine, phase ratio = 4, repeat 1 case with location of detected interfaces.
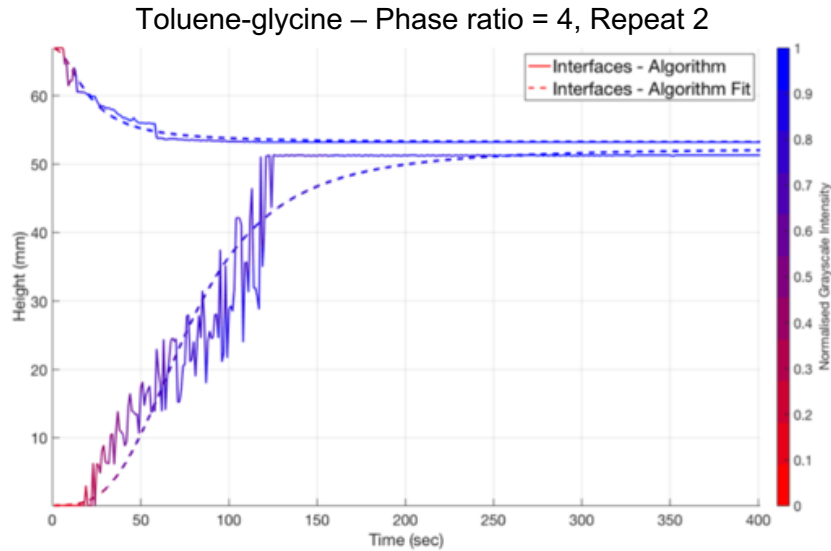
Figure A84: Detected interfaces and normalised grayscale intensity over time for repeat 2 of the toluene-glycine time series at a phase ratio of 4.
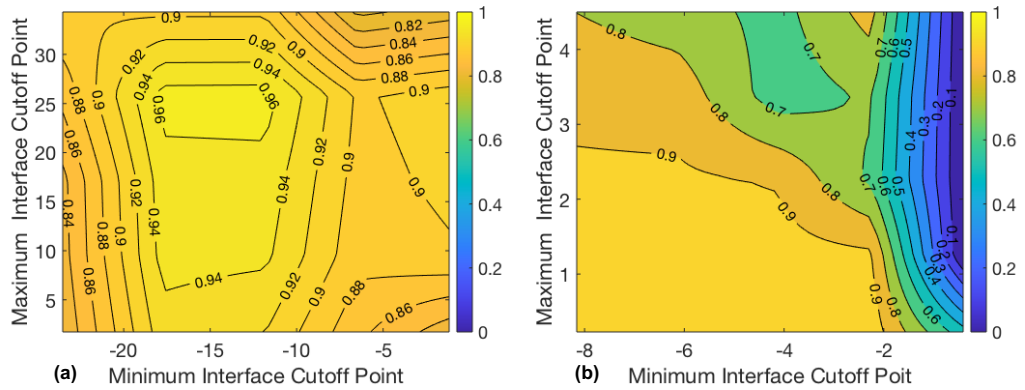
Figure A85: Contour plot of r^2 values for the sigmoidal curve fit for interface 1 data (a) and interface 2 data (b) depending on the maximum and minimum cut-off point combination – Toluene-glycine, phase ratio = 4, repeat 2.
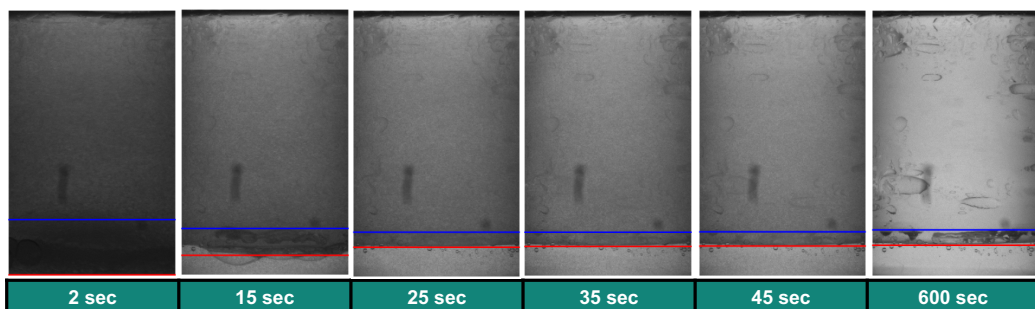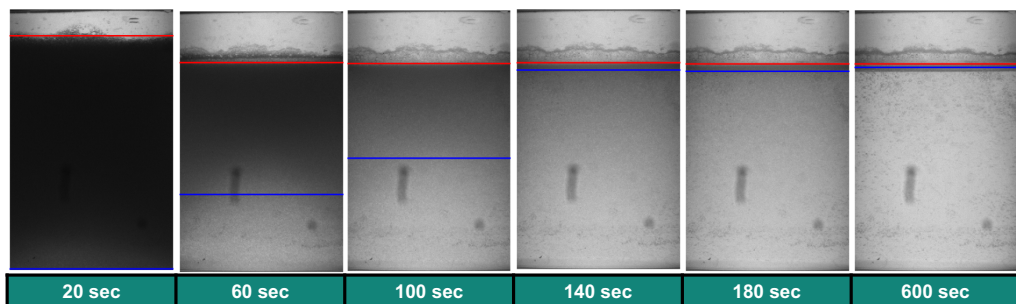

Figure A86: Sample images from toluene-glycine, phase ratio = 4, repeat 2 case with location of detected interfaces.
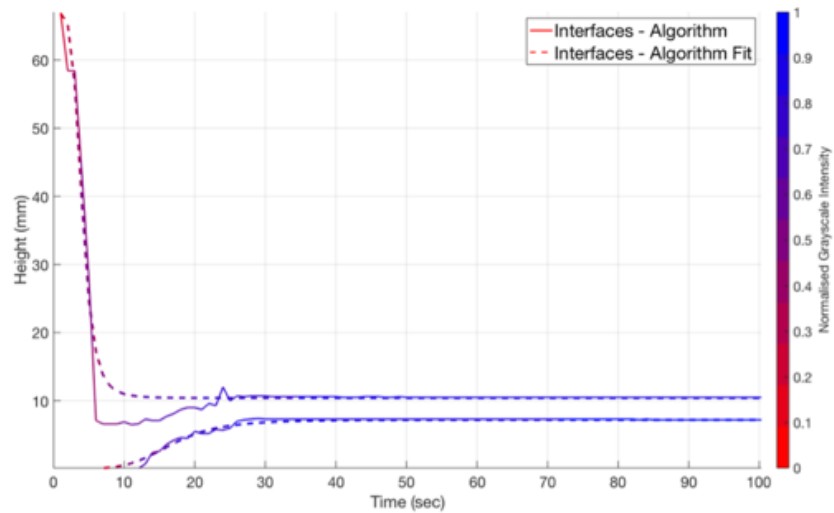
Toluene-glycine – Phase ratio = 4, Repeat 3
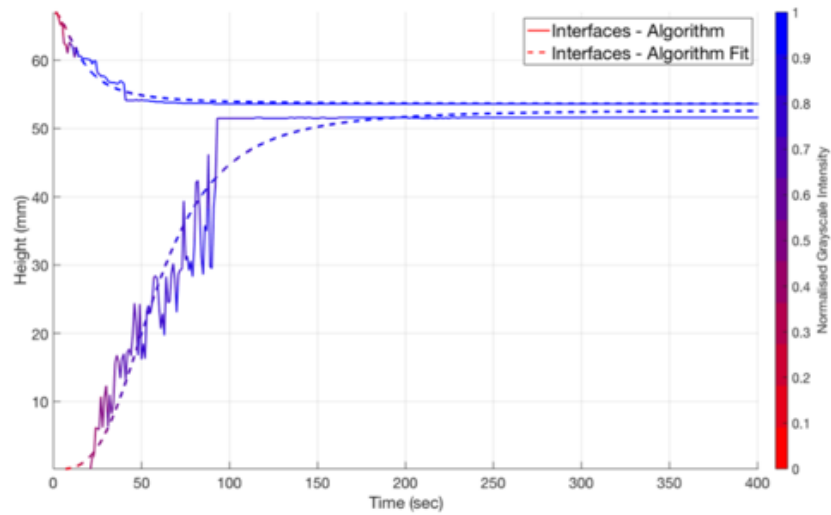
Figure A87: Detected interfaces and normalised grayscale intensity over time for repeat 3 of the toluene-glycine time series at a phase ratio of 4.
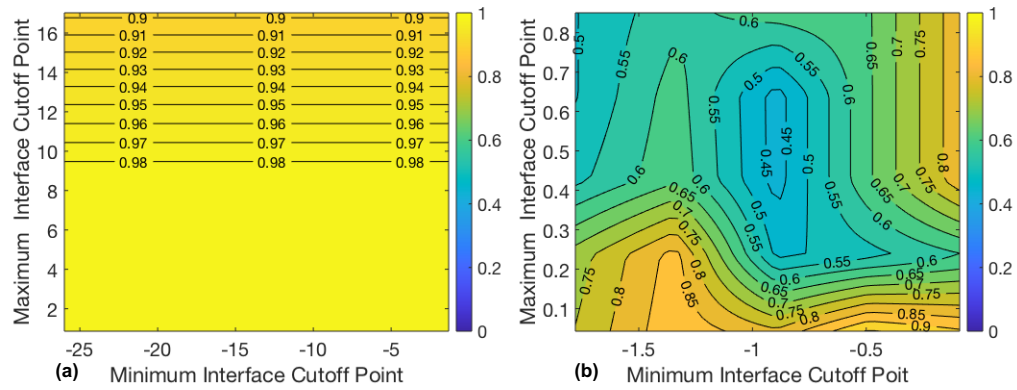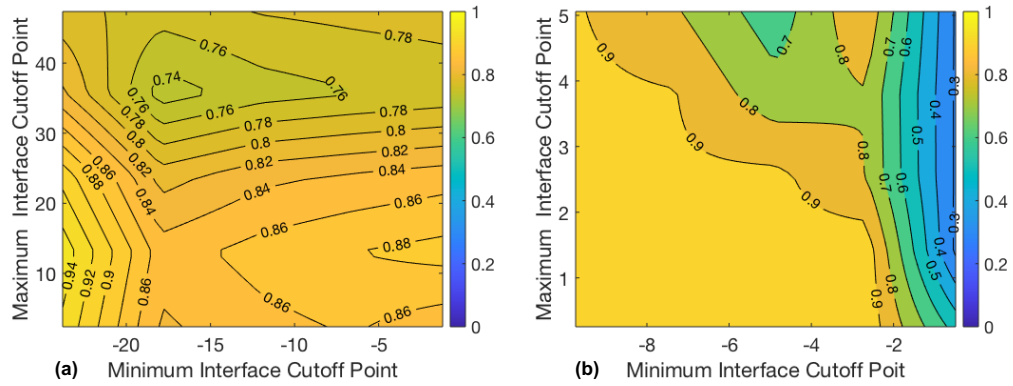

Figure A88: Contour plot of r^2 values for the sigmoidal curve fit for interface 1 data (a) and interface 2 data (b) depending on the maximum and minimum cut-off point combination – Toluene-glycine, phase ratio = 4, repeat 3.
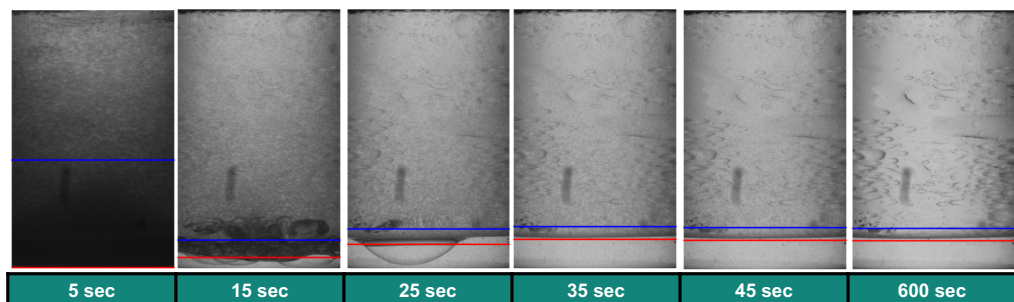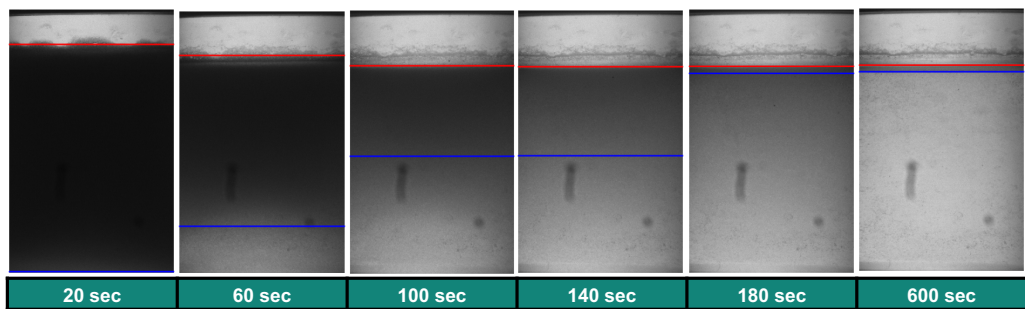

Figure A89: Sample images from toluene-glycine, phase ratio = 4, repeat 3 case with location of detected interfaces.
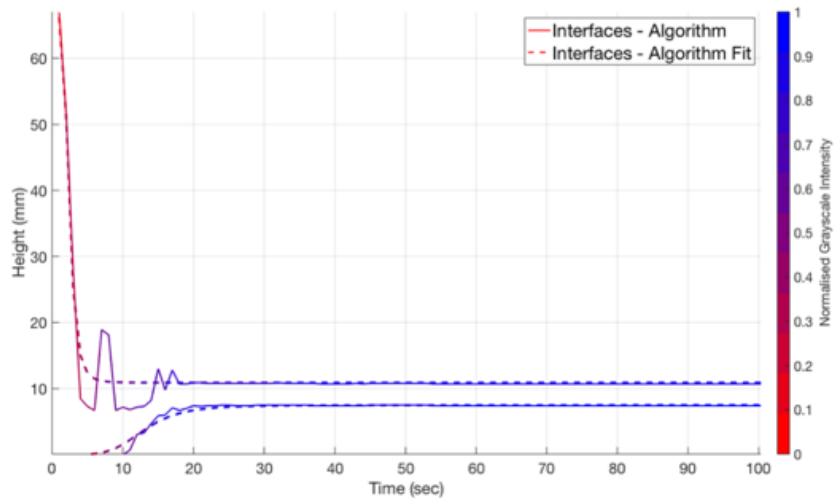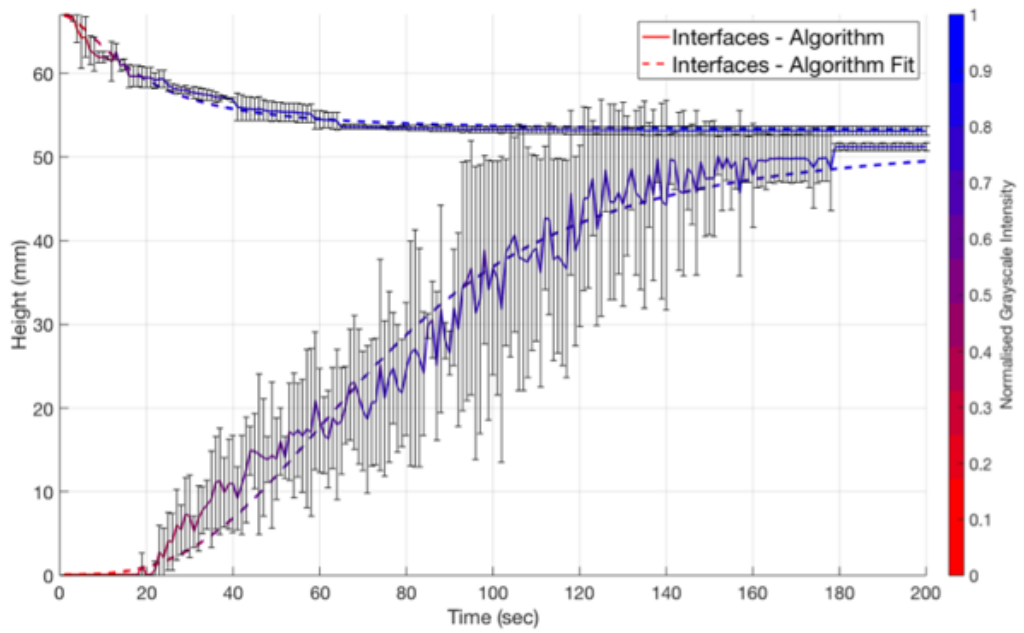
Figure A90: Averaged interface locations and normalised grayscale intensity over time for the toluene-glycine time series at a phase ratio of 4.

A.3.2 *Experiment 2*

Vial 1 - Toluene-water, 0.01M SDBS, 0.0453g/100ml NaCl
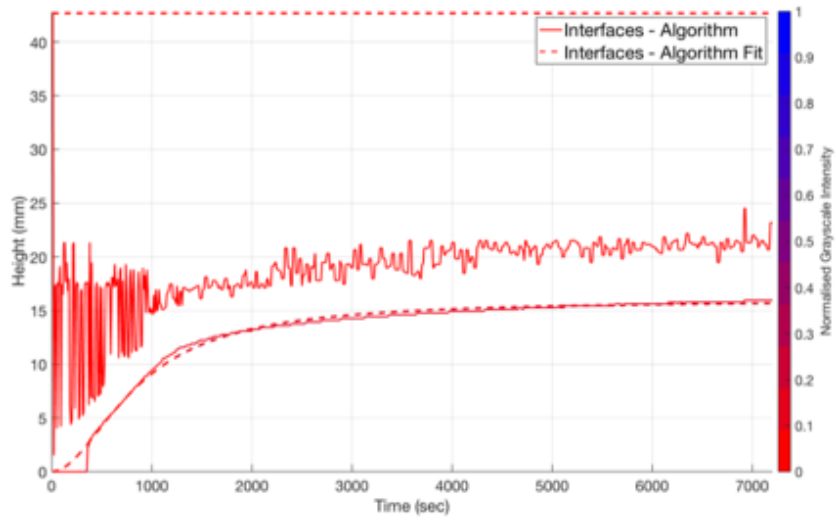
Figure A91: Detected interfaces and normalised grayscale intensity over time of the 0.01M SDBS solution (0.453g/100ml NaCl).
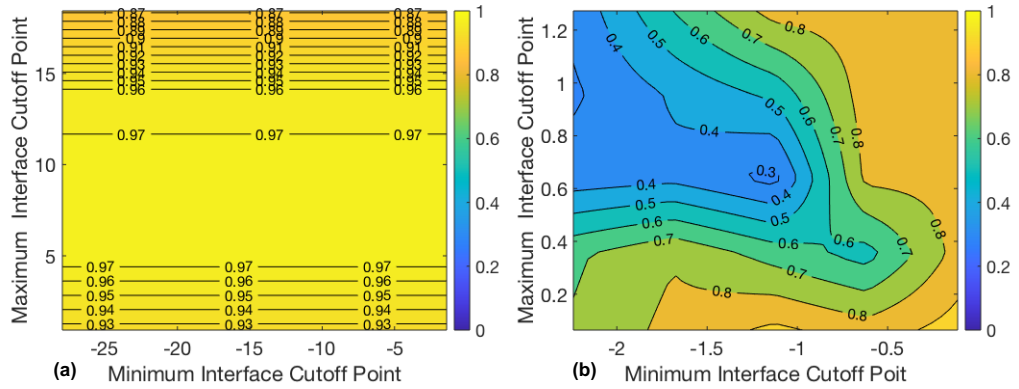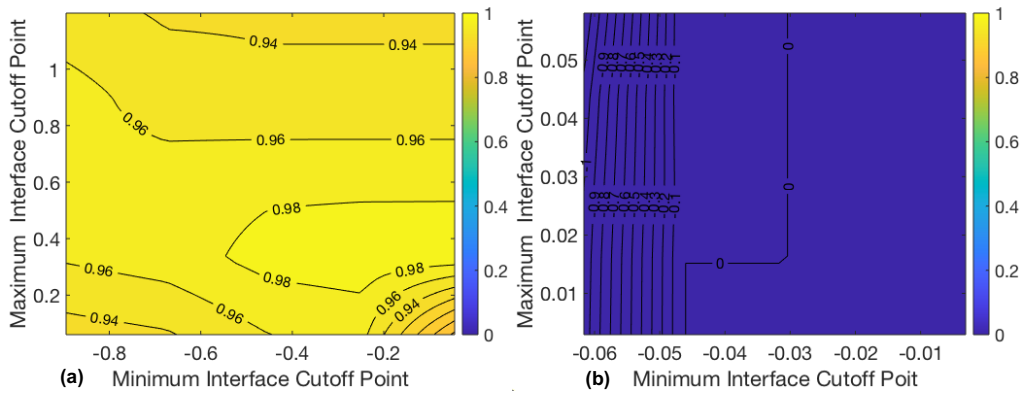

Figure A92: Contour plot of r^2 values for the sigmoidal curve fit for interface 1 data (a) and interface 2 data (b) depending on the maximum and minimum cut-off point combination – 0.01M SDBS solution (0.453g/100ml NaCl).
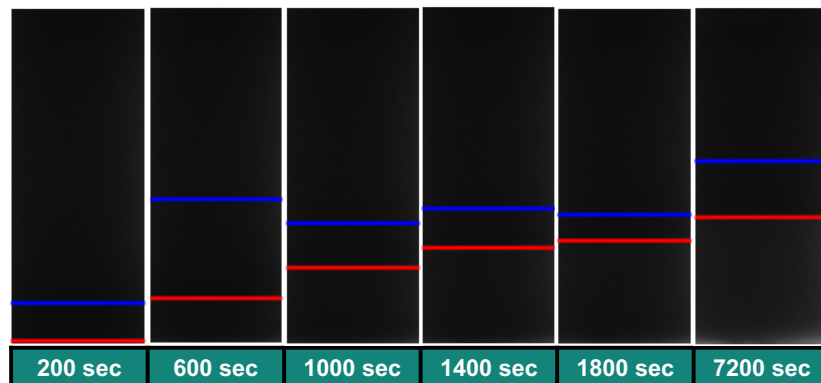
Figure A93: Sample images from 0.01M SDBS solution (0.453g/100ml NaCl) with location of detected interfaces.

Vial 2 - Toluene-water, 0.01M SDBS, 1.076g/100ml NaCl
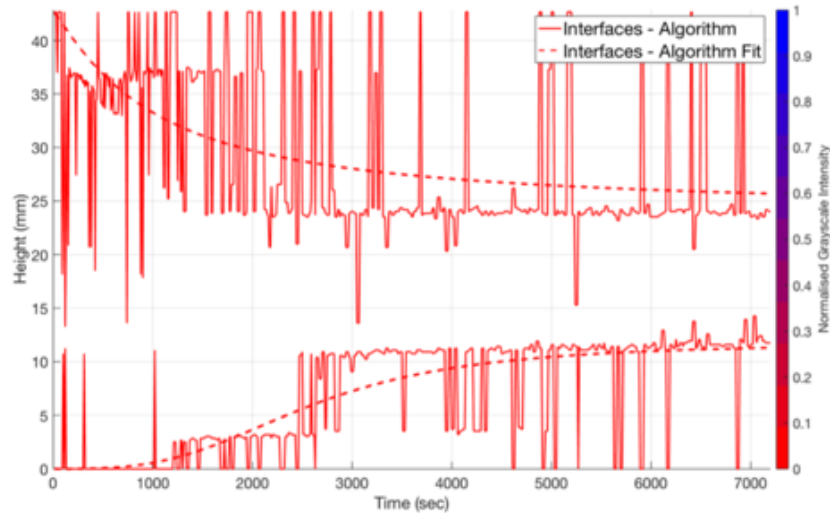
Figure A94: Detected interfaces and normalised grayscale intensity over time of the 0.01M SDBS solution (1.076g/100ml NaCl).
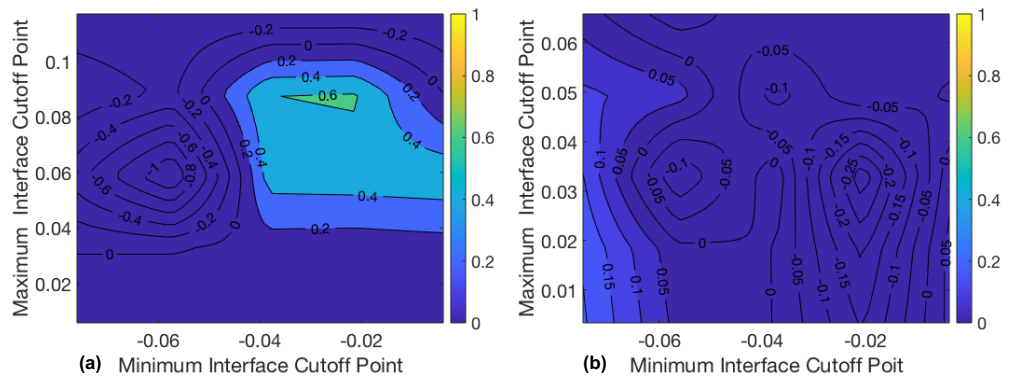
Figure A95: Contour plot of r^2 values for the sigmoidal curve fit for interface 1 data (a) and interface 2 data (b) depending on the maximum and minimum cut-off point combination – 0.01M SDBS solution (1.076g/100ml NaCl).
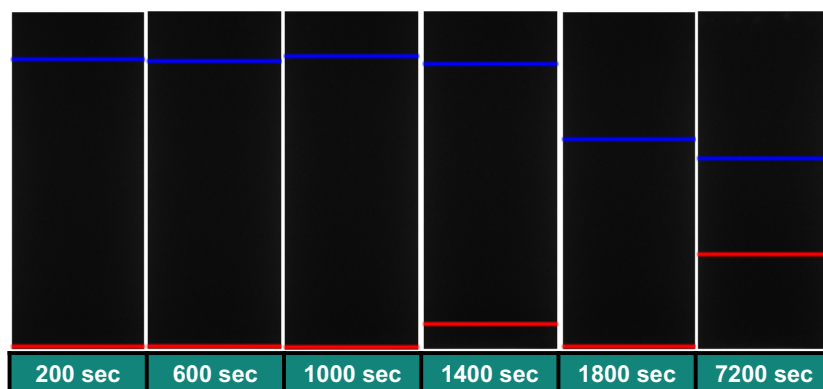
Figure A96: Sample images from 0.01M SDBS solution (1.076g/100ml NaCl) with location of detected interfaces.

Vial 3 - Toluene-water, 0.01M SDBS, 1.6627g/100ml NaCl
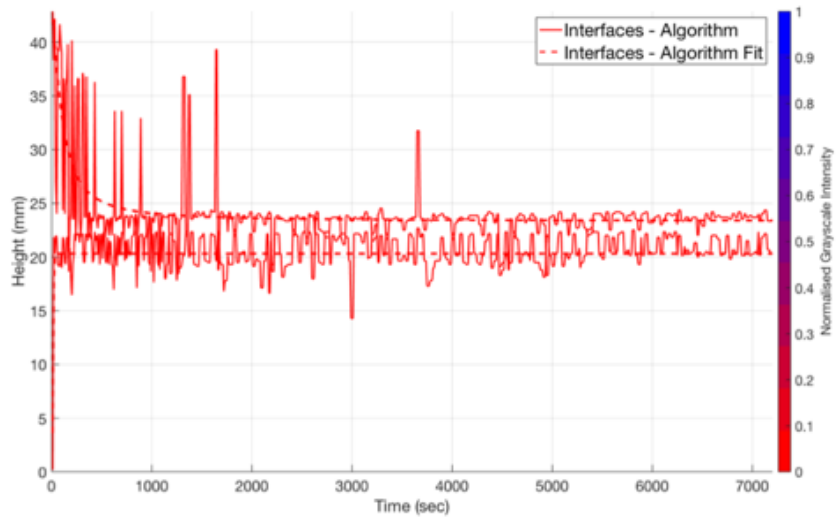
Figure A97: Detected interfaces and normalised grayscale intensity over time of the 0.01M SDBS solution (1.6627g/100ml NaCl).
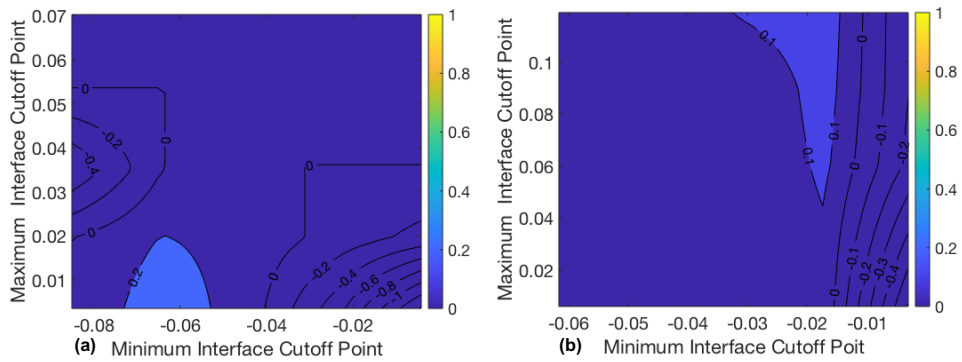
Figure A98: Contour plot of r^2 values for the sigmoidal curve fit for interface 1 data (a) and interface 2 data (b) depending on the maximum and minimum cut-off point combination – 0.01M SDBS solution (1.6627g/100ml NaCl).
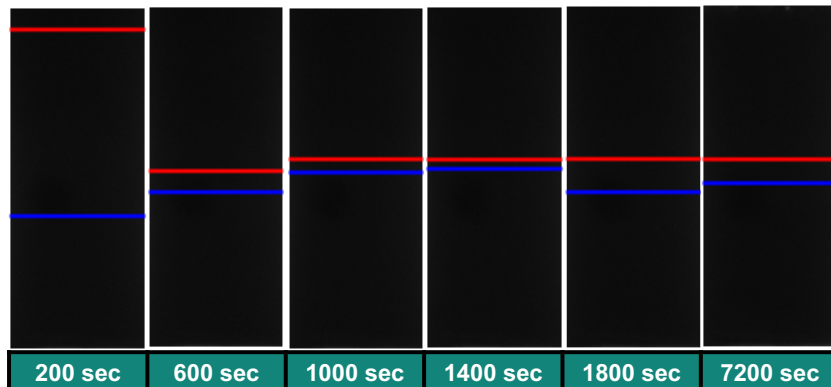
Figure A99: Sample images from 0.01M SDBS solution (1.6627g/100ml NaCl) with location of detected interfaces.

Vial 4 - Toluene-water, 0.01M SDBS, 2.172g/100ml NaCl
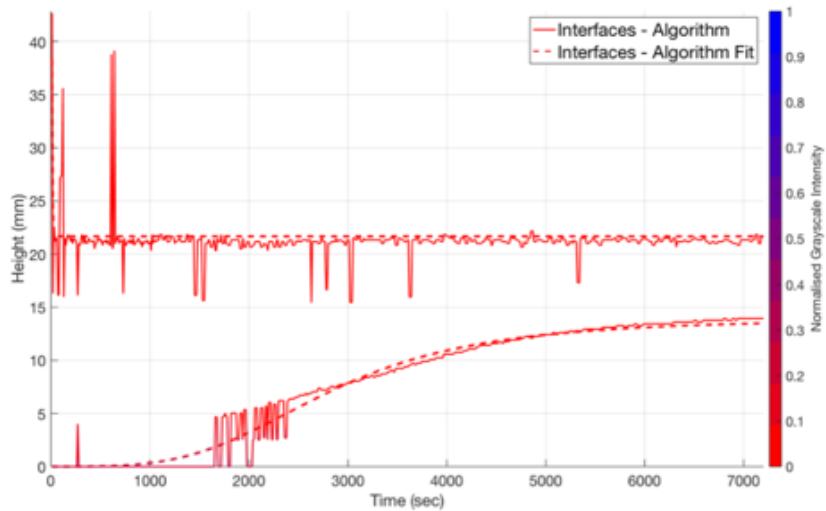
Figure A100: Detected interfaces and normalised grayscale intensity over time of the 0.01M SDBS solution (2.172g/100ml NaCl).
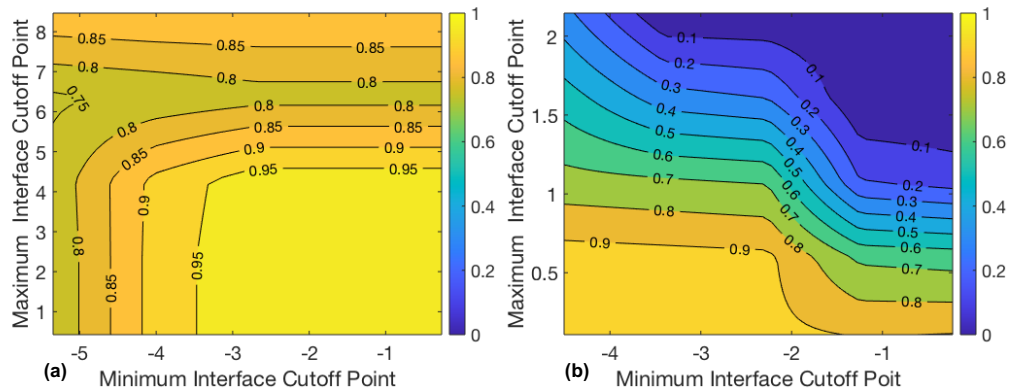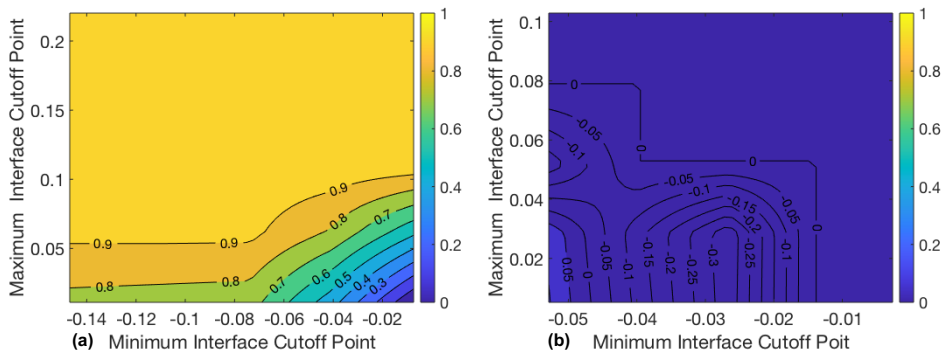

Figure A101: Contour plot of r^2 values for the sigmoidal curve fit for interface 1 data (a) and interface 2 data (b) depending on the maximum and minimum cut-off point combination – 0.01M SDBS solution (2.172g/100ml NaCl).

| 700 sec | 2100 sec | 3500 sec | 4900 sec | 6300 sec | 7200 sec |
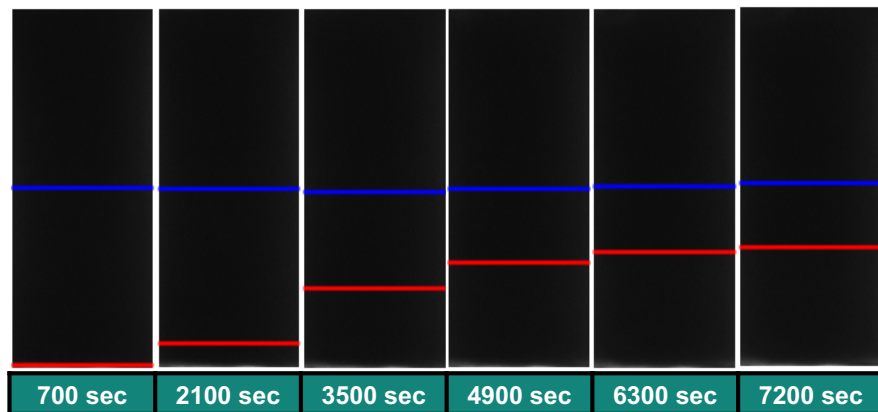
Figure A102: Sample images from 0.01M SDBS solution (2.172g/100ml NaCl) with location of detected interfaces.

Vial 5 - Toluene-water, 0.01M SDBS, 2.768g/100ml NaCl
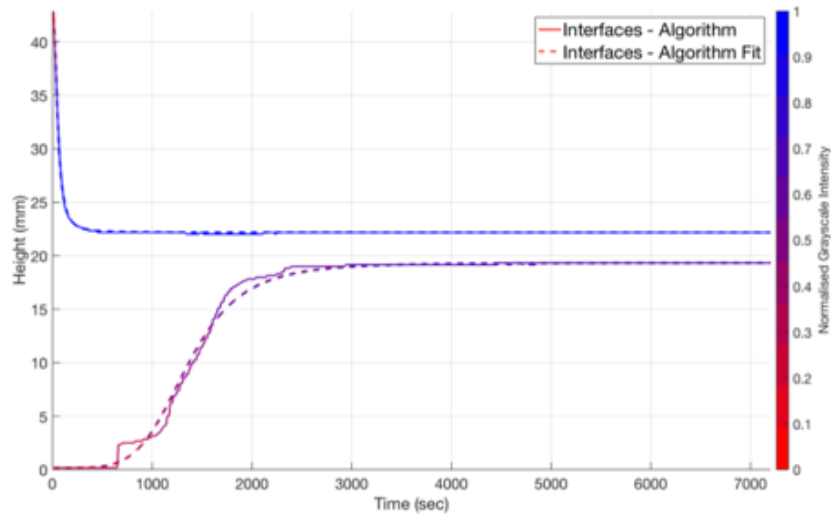
Figure A103: Detected interfaces and normalised grayscale intensity over time of the 0.01M SDBS solution (2.768g/100ml NaCl).
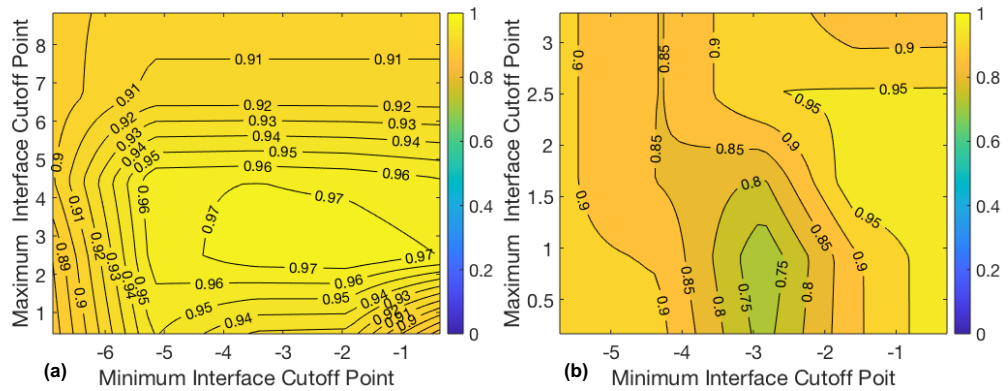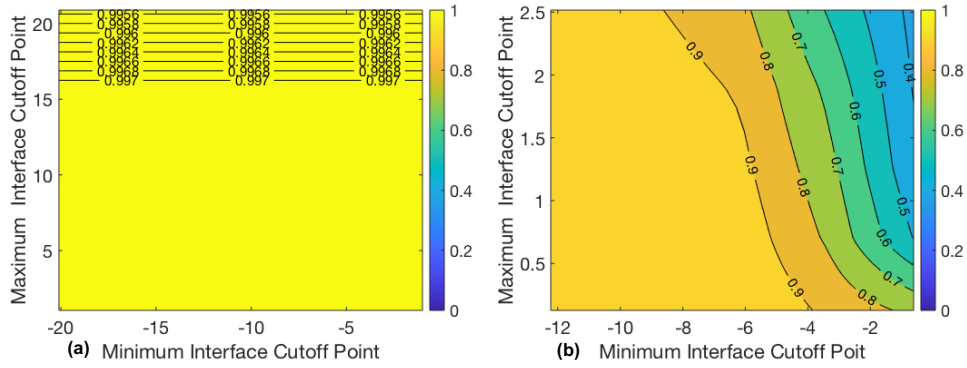

Figure A104: Contour plot of r^2 values for the sigmoidal curve fit for interface 1 data (a) and interface 2 data (b) depending on the maximum and minimum cut-off point combination – 0.01M SDBS solution (2.768g/100ml NaCl).

| 200 sec | 600 sec | 1000 sec | 1400 sec | 1800 sec | 7200 sec |
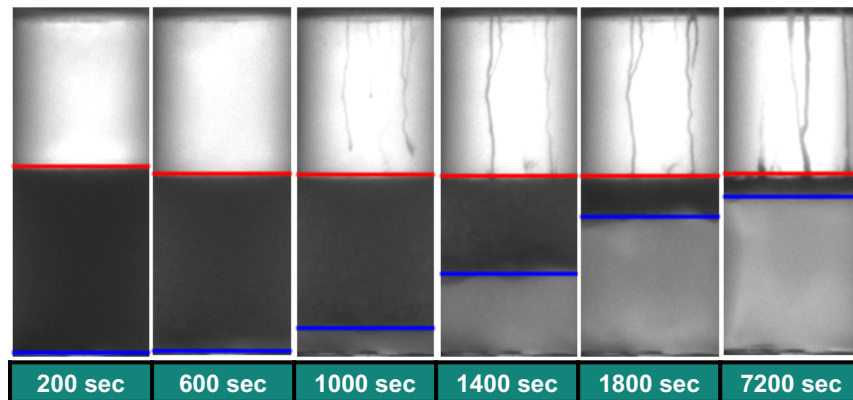
Figure A105: Sample images from 0.01M SDBS solution (2.768g/100ml NaCl) with location of detected interfaces.

Vial 6 - Toluene-water, 0.01M SDBS, 3.372g/100ml NaCl
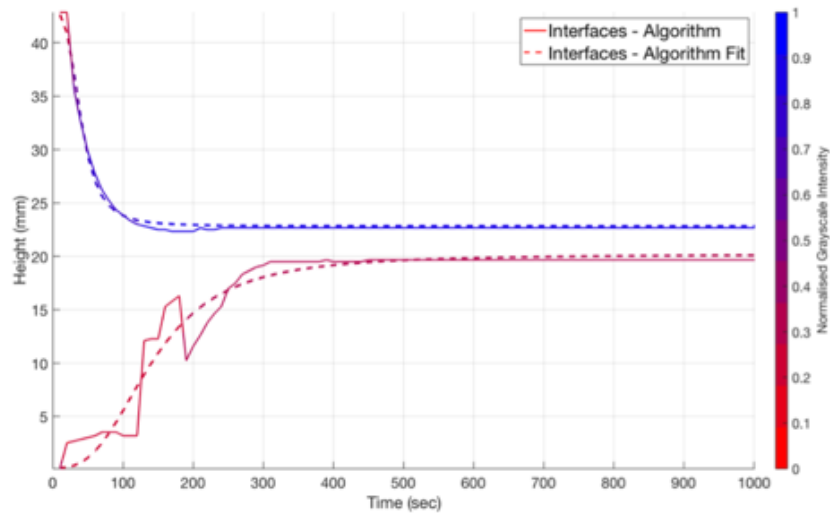
Figure A106: Detected interfaces and normalised grayscale intensity over time of the 0.01M SDBS solution (3.372g/100ml NaCl).
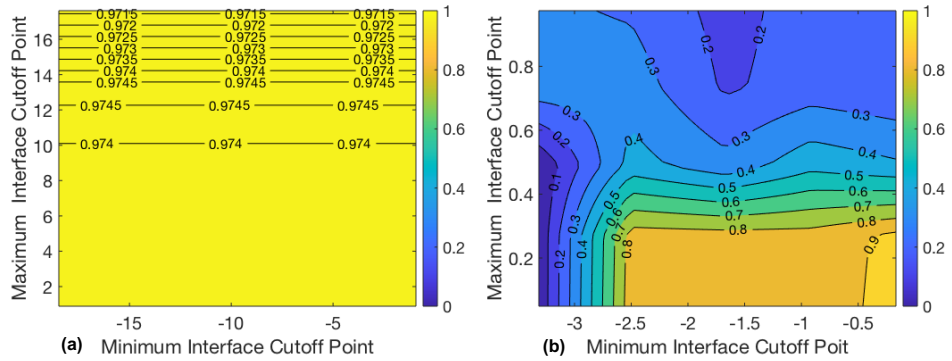
Figure A107: Contour plot of r^2 values for the sigmoidal curve fit for interface 1 data (a) and interface 2 data (b) depending on the maximum and minimum cut-off point combination – 0.01M SDBS solution (3.372g/100ml NaCl).

| 30 sec | 90 sec | 150 sec | 210 sec | 270 sec | 7200 sec |
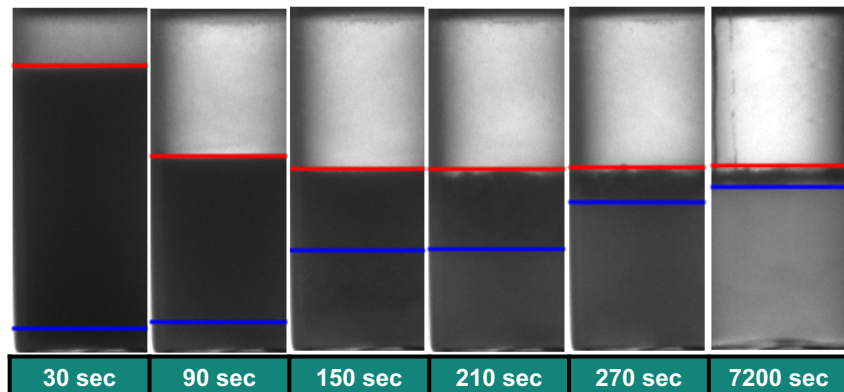
Figure A108: Sample images from 0.01M SDBS solution (3.372g/100ml NaCl) with location of detected interfaces.

Vial 7 - Toluene-water, 0.01M SDBS, 4.3387g/100ml NaCl
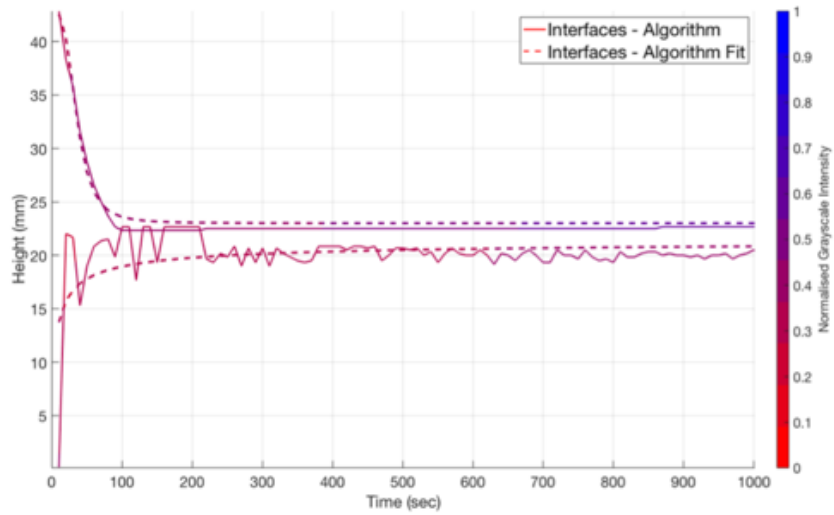
Figure A109: Detected interfaces and normalised grayscale intensity over time of the 0.01M SDBS solution (4.3387g/100ml NaCl).
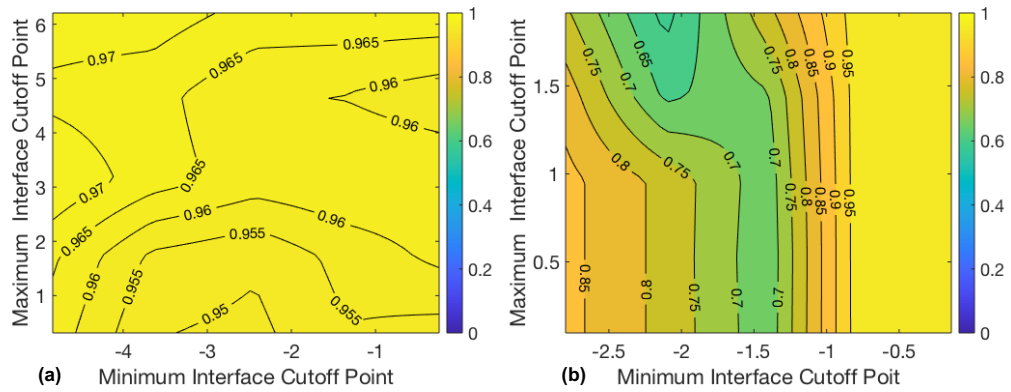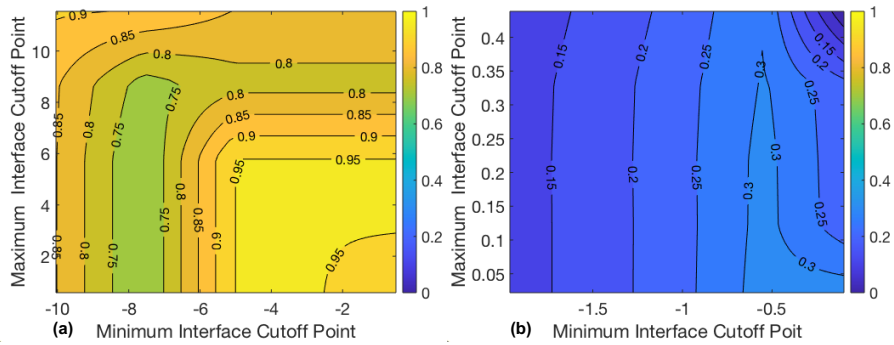
Figure A110: Contour plot of r^2 values for the sigmoidal curve fit for interface 1 data (a) and interface 2 data (b) depending on the maximum and minimum cut-off point combination – 0.01M SDBS solution (4.3387g/100ml NaCl).

| 10 sec | 30 sec | 50 sec | 70 sec | 90 sec | 7200 sec |
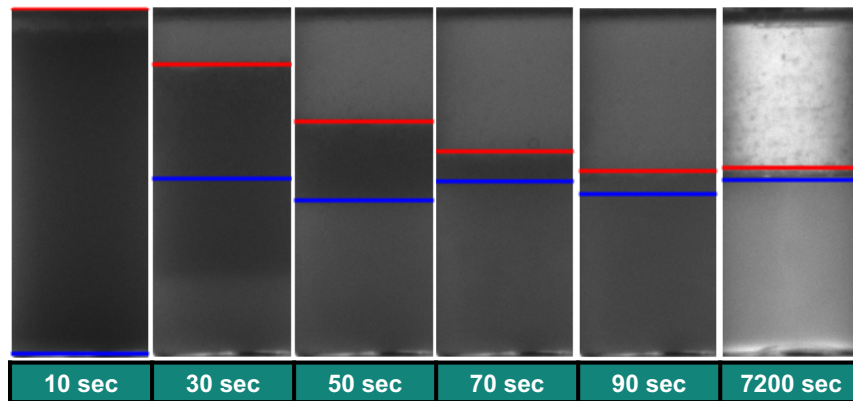
Figure A111: Sample images from 0.01M SDBS solution (4.3387g/100ml NaCl) with location of detected interfaces.

Vial 8 - Toluene-water, 0.01M SDBS, 5.7133g/100ml NaCl
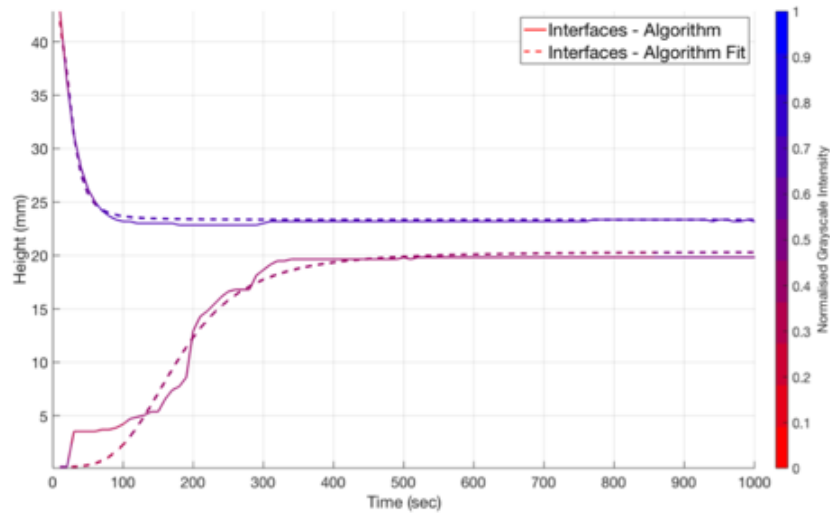
Figure A112: Detected interfaces and normalised grayscale intensity over time of the 0.01M SDBS solution (5.7133g/100ml NaCl).
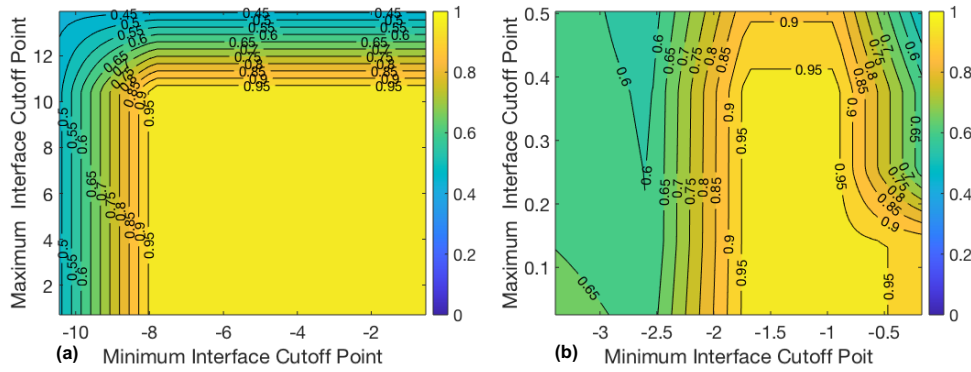
Figure A113: Contour plot of r^2 values for the sigmoidal curve fit for interface 1 data (a) and interface 2 data (b) depending on the maximum and minimum cut-off point combination – 0.01M SDBS solution (5.7133g/100ml NaCl).

| 20 sec | 60 sec | 100 sec | 140 sec | 180 sec | 7200 sec |
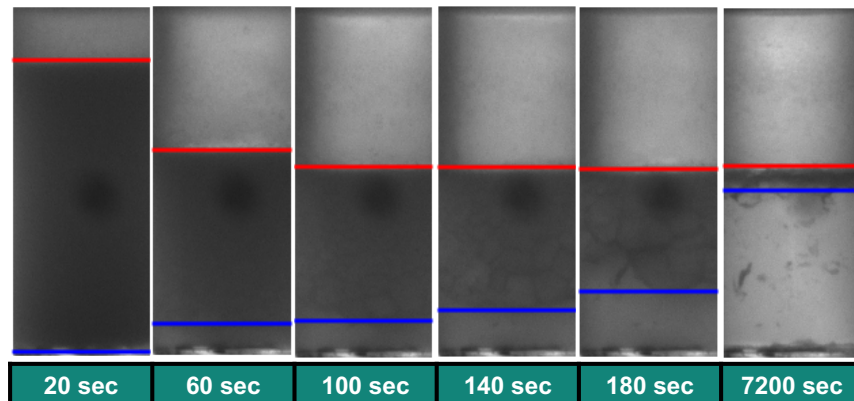
Figure A114: Sample images from 0.01M SDBS solution (5.7133g/100ml NaCl) with location of detected interfaces.

Vial 9 - Toluene-water, 0.01M SDBS, 6.648g/100ml NaCl
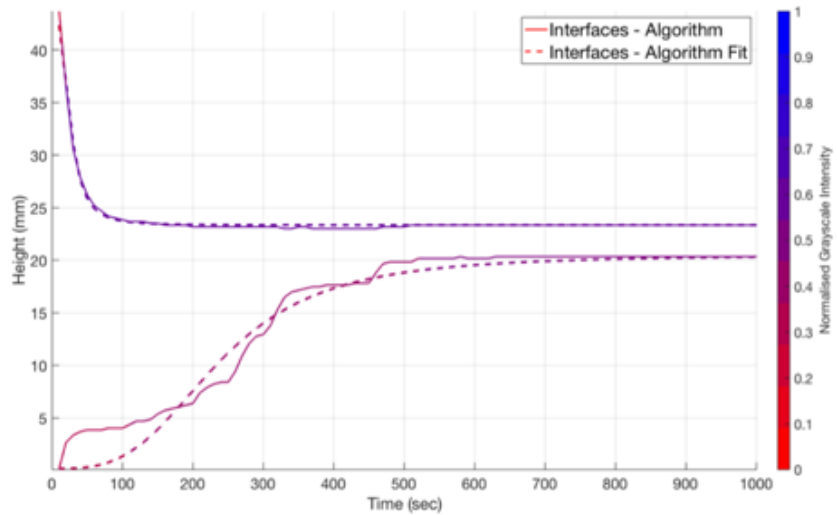
Figure A115: Detected interfaces and normalised grayscale intensity over time of the 0.01M SDBS solution (6.648g/100ml NaCl).
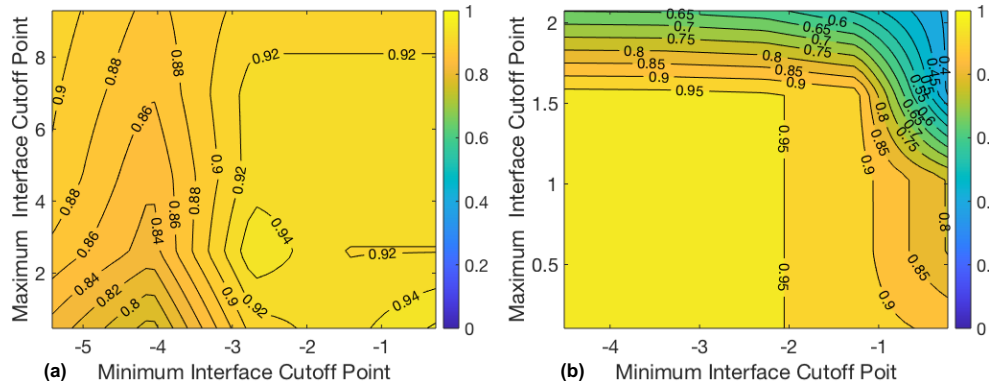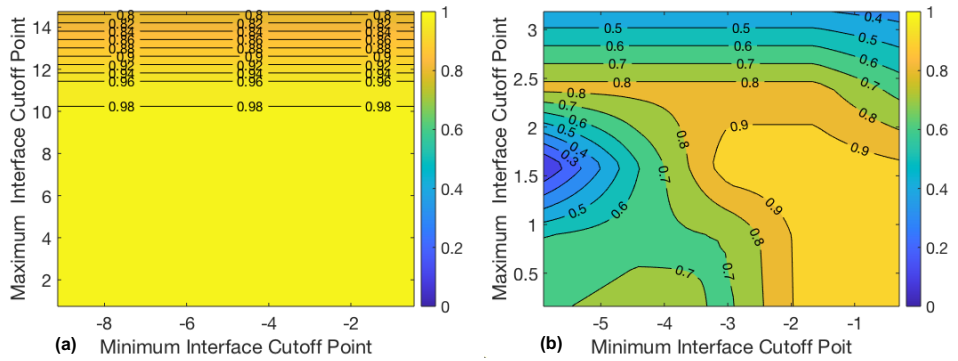

Figure A116: Contour plot of r^2 values for the sigmoidal curve fit for interface 1 data (a) and interface 2 data (b) depending on the maximum and minimum cut-off point combination – 0.01M SDBS solution (6.648g/100ml NaCl).
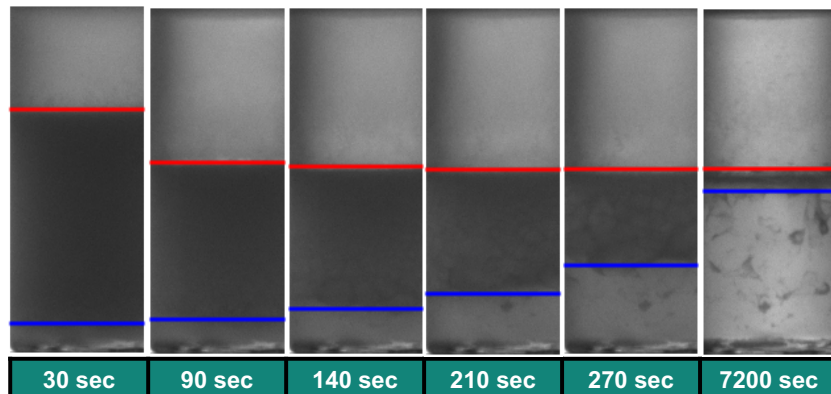
Figure A117: Sample images from 0.01M SDBS solution (6.648g/100ml NaCl) with location of detected interfaces.

Vial 10 - Toluene-water, 0.01M SDBS, 7.86g/100ml NaCl
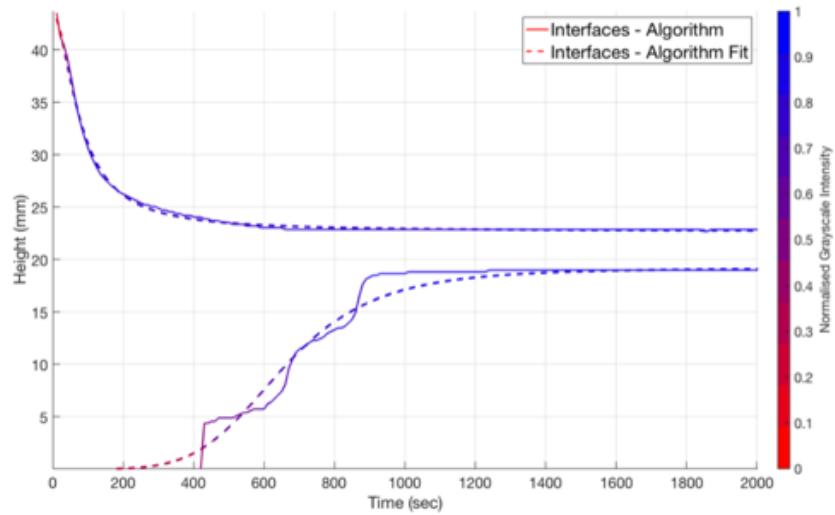
Figure A118: Detected interfaces and normalised grayscale intensity over time of the 0.01M SDBS solution (7.86g/100ml NaCl).
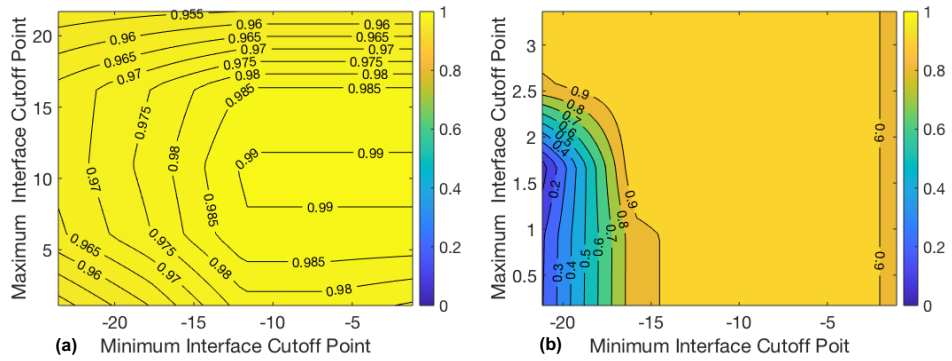
Figure A119: Contour plot of r^2 values for the sigmoidal curve fit for interface 1 data (a) and interface 2 data (b) depending on the maximum and minimum cut-off point combination – 0.01M SDBS solution (7.86g/100ml NaCl).
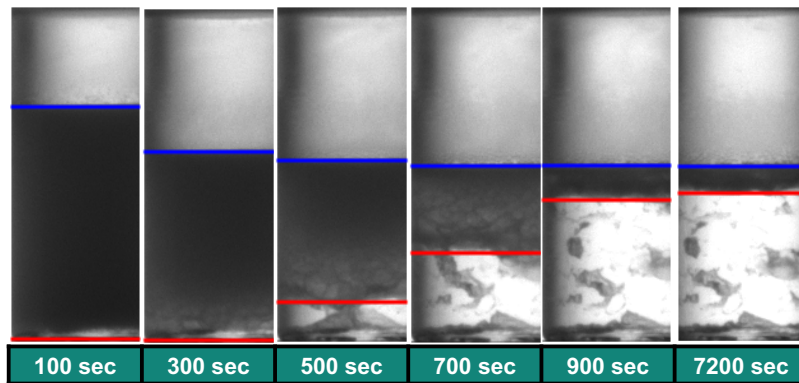
Figure A120: Sample images from 0.01M SDBS solution (7.86g/100ml NaCl) with location of detected interfaces.

Vial 11 - Toluene-water, 0.1M SDBS, 0.0413g/100ml NaCl
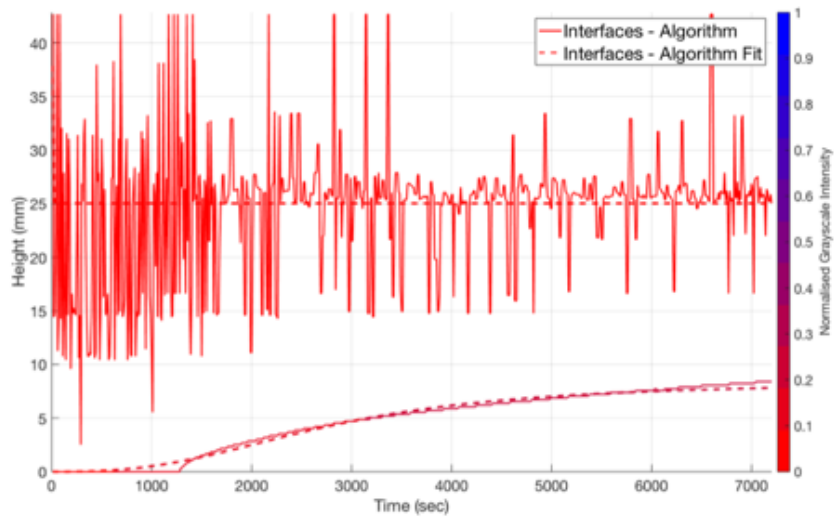
Figure A121: Detected interfaces and normalised grayscale intensity over time of the 0.1M SDBS solution (0.0413g/100ml NaCl).
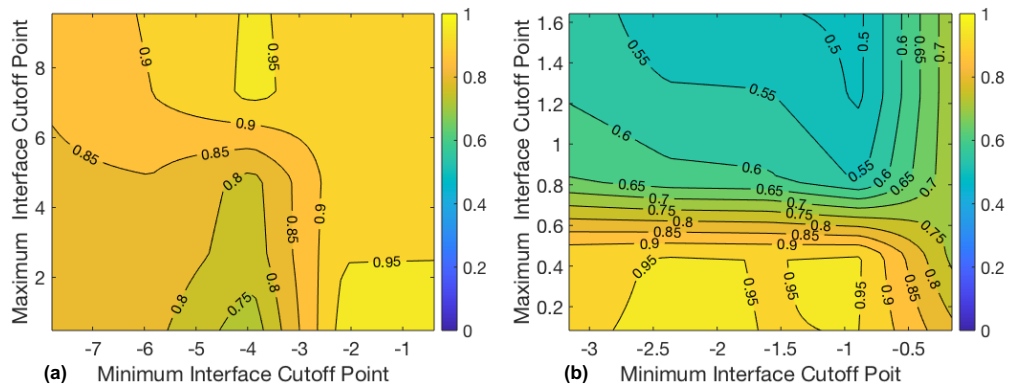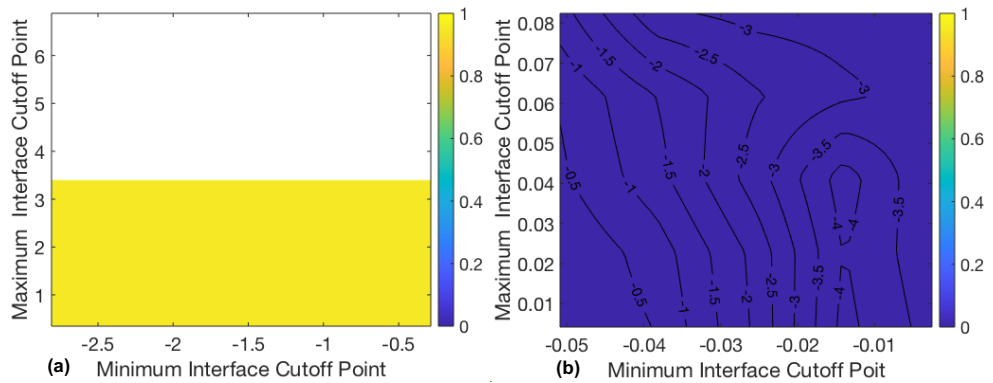

Figure A122: Contour plot of r^2 values for the sigmoidal curve fit for interface 1 data (a) and interface 2 data (b) depending on the maximum and minimum cut-off point combination – 0.1M SDBS solution (0.0413g/100ml NaCl).
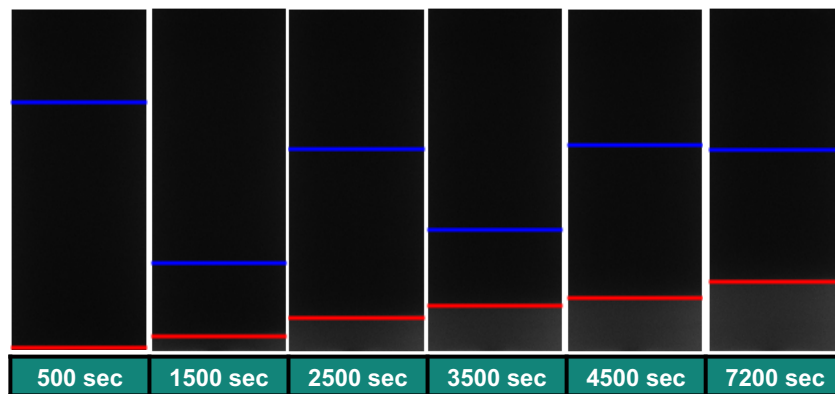
Figure A123: Sample images from 0.1M SDBS solution (0.0413g/100ml NaCl) with location of detected interfaces.

Vial 12 - Toluene-water, 0.1M SDBS, 1.076g/100ml NaCl
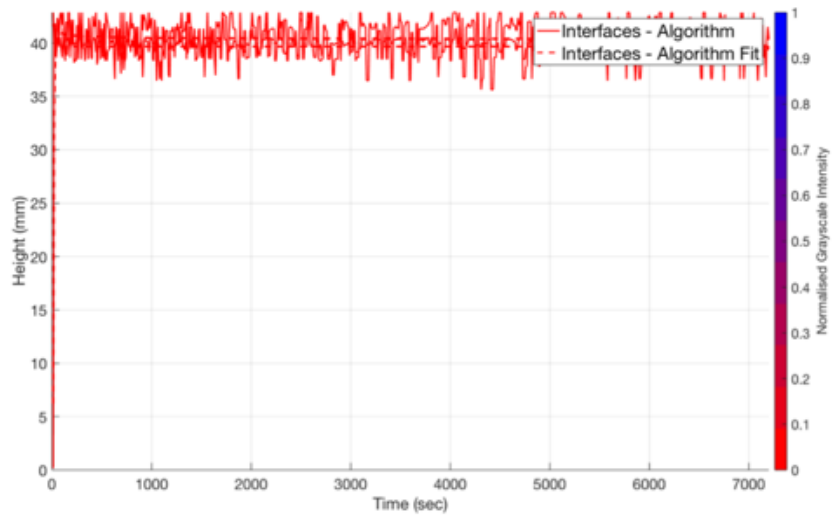
Figure A124: Detected interfaces and normalised grayscale intensity over time of the 0.1M SDBS solution (1.076g/100ml NaCl).
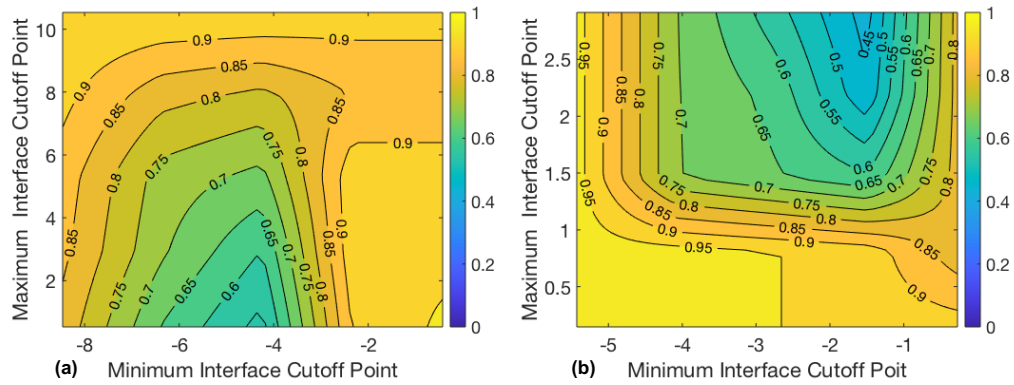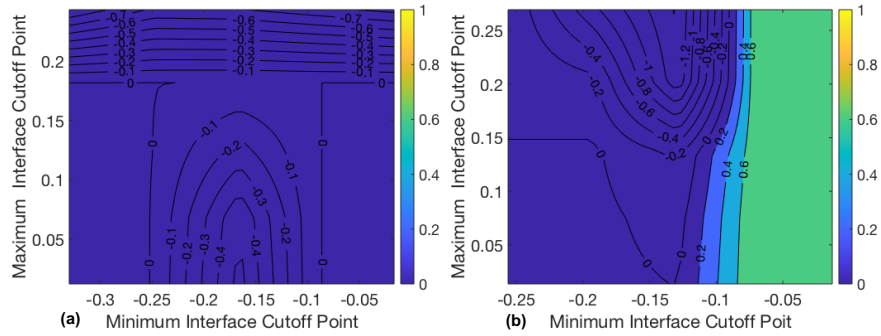

Figure A125: Contour plot of r^2 values for the sigmoidal curve fit for interface 1 data (a) and interface 2 data (b) depending on the maximum and minimum cut-off point combination – 0.1M SDBS solution (1.076g/100ml NaCl).

| 500 sec | 1500 sec | 2500 sec | 3500 sec | 4500 sec | 7200 sec |
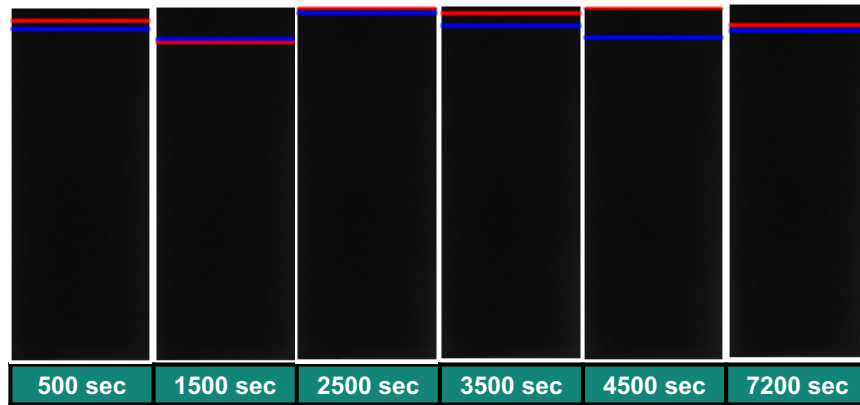
Figure A126: Sample images from 0.1M SDBS solution (1.076g/100ml NaCl) with location of detected interfaces.

Vial 13 - Toluene-water, 0.1M SDBS, 1.5907g/100ml NaCl
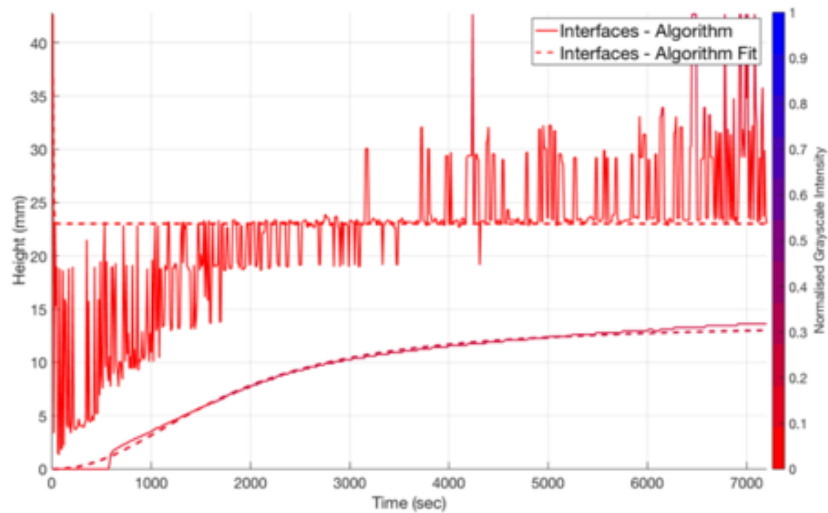
Figure A127: Detected interfaces and normalised grayscale intensity over time of the 0.1M SDBS solution (1.5907g/100ml NaCl).
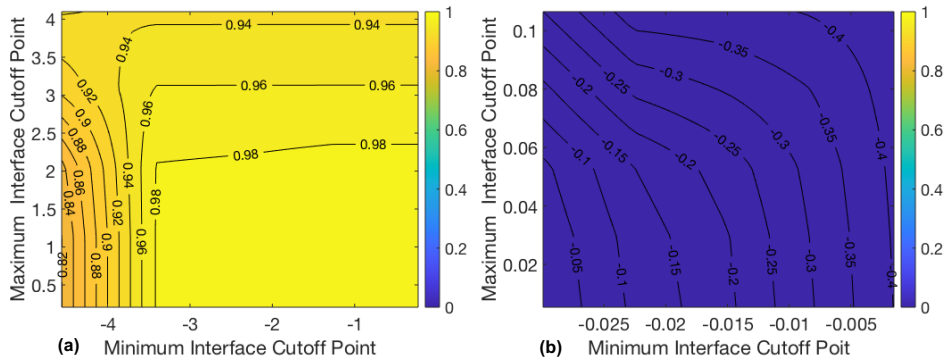
Figure A128: Contour plot of r^2 values for the sigmoidal curve fit for interface 1 data (a) and interface 2 data (b) depending on the maximum and minimum cut-off point combination – 0.1M SDBS solution (1.5907g/100ml NaCl).

| 500 sec | 1500 sec | 2500 sec | 3500 sec | 4500 sec | 7200 sec |
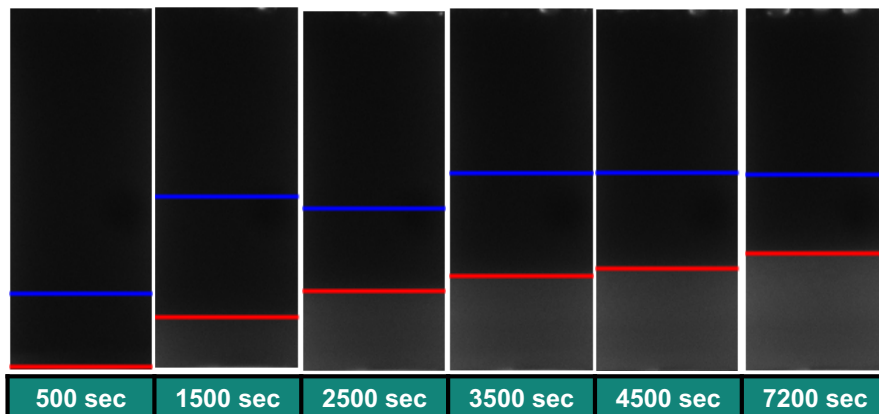
Figure A129: Sample images from 0.1M SDBS solution (1.5907g/100ml NaCl) with location of detected interfaces.

Vial 14 - Toluene-water, 0.1M SDBS, 2.2213g/100ml NaCl
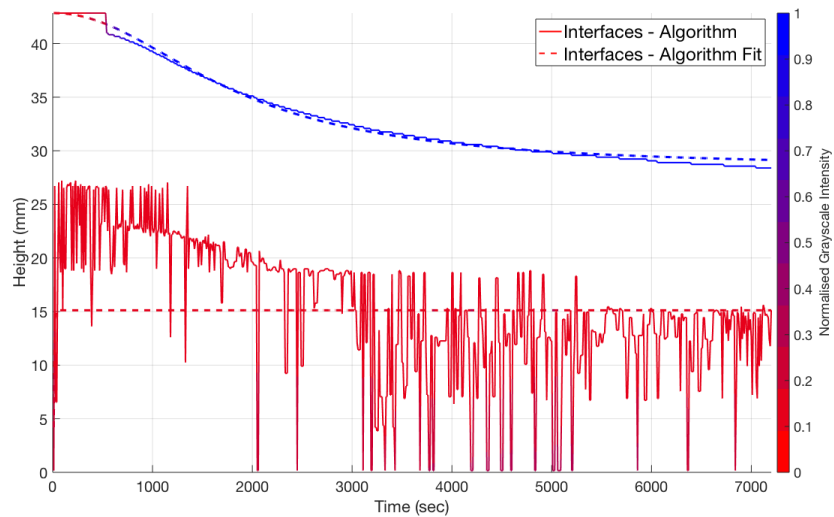
Figure A130: Detected interfaces and normalised grayscale intensity over time of the 0.1M SDBS solution (2.2213g/100ml NaCl).
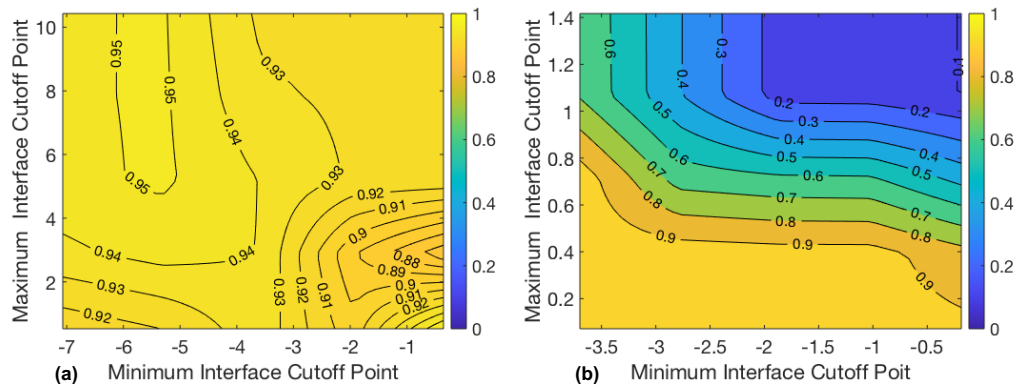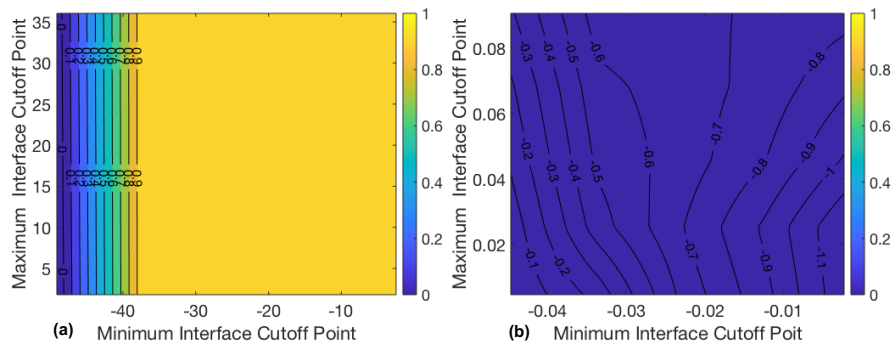
Figure A131: Contour plot of r^2 values for the sigmoidal curve fit for interface 1 data (a) and interface 2 data (b) depending on the maximum and minimum cut-off point combination – 0.1M SDBS solution (2.2213g/100ml NaCl).

| 500 sec | 1500 sec | 2500 sec | 3500 sec | 4500 sec | 7200 sec |
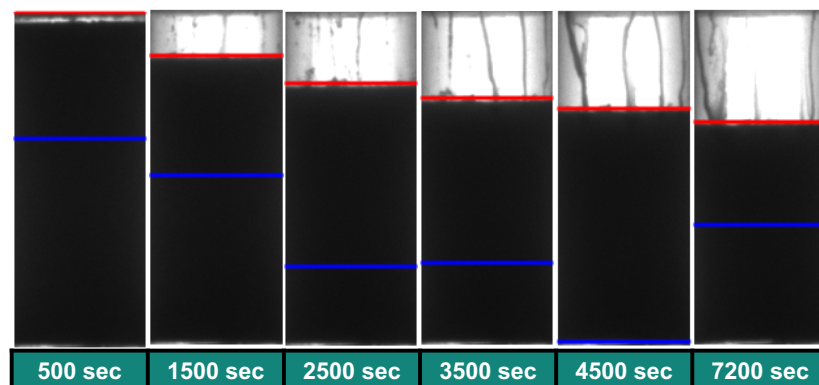
Figure A132: Sample images from 0.1M SDBS solution (2.2213g/100ml NaCl) with location of detected interfaces.

Vial 15 - Toluene-water, 0.1M SDBS, 2.68g/100ml NaCl
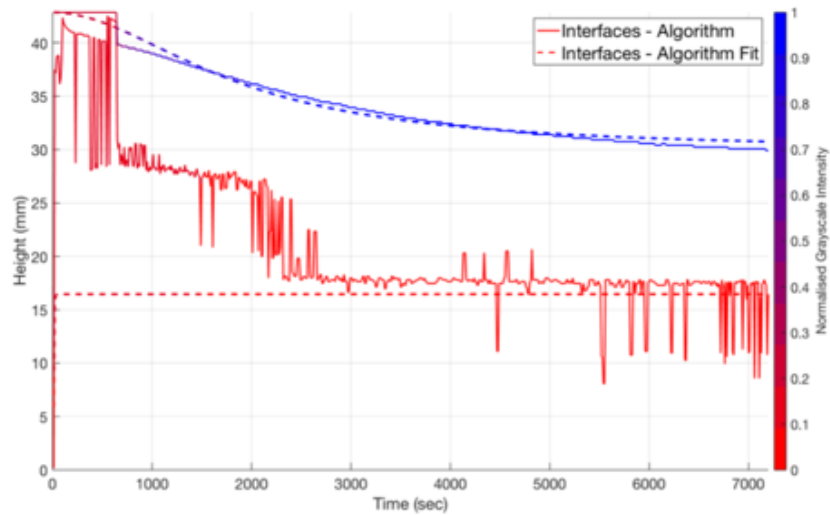
Figure A133: Detected interfaces and normalised grayscale intensity over time of the 0.1M SDBS solution (2.68g/100ml NaCl).
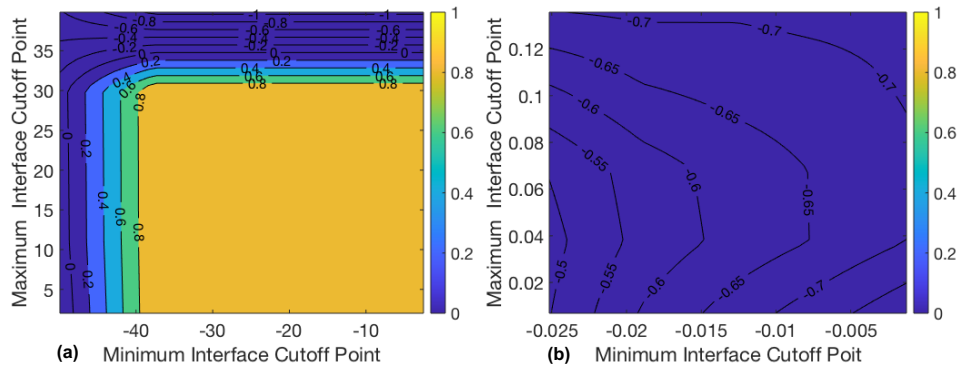
Figure A134: Contour plot of r^2 values for the sigmoidal curve fit for interface 1 data (a) and interface 2 data (b) depending on the maximum and minimum cut-off point combination – 0.1M SDBS solution (2.68g/100ml NaCl).

| 500 sec | 1500 sec | 2500 sec | 3500 sec | 4500 sec | 7200 sec |
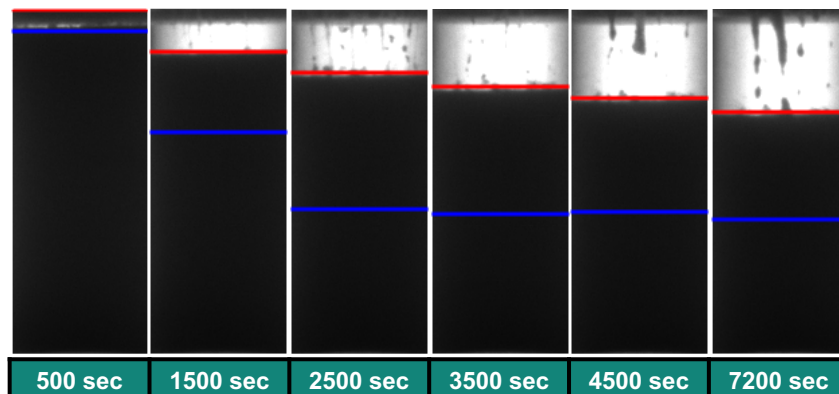
Figure A135: Sample images from 0.1M SDBS solution (2.68g/100ml NaCl) with location of detected interfaces.
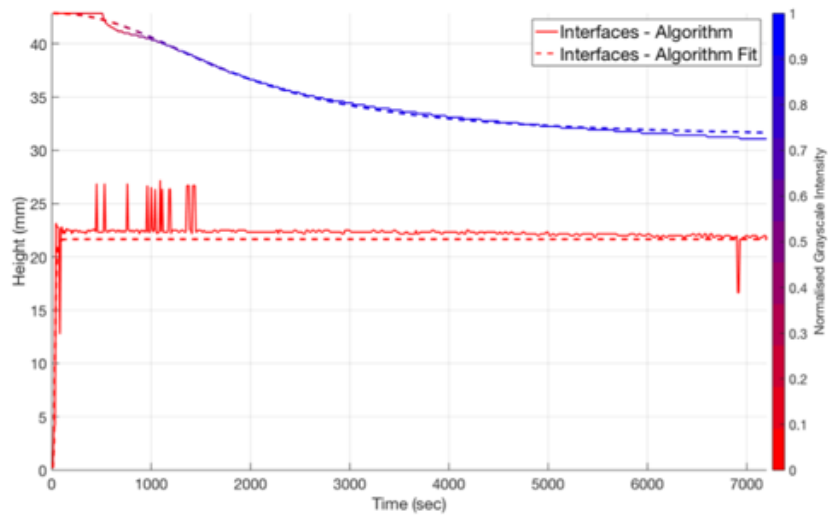
Figure A136: Detected interfaces and normalised grayscale intensity over time of the 0.1M SDBS solution (3.2867g/100ml NaCl).
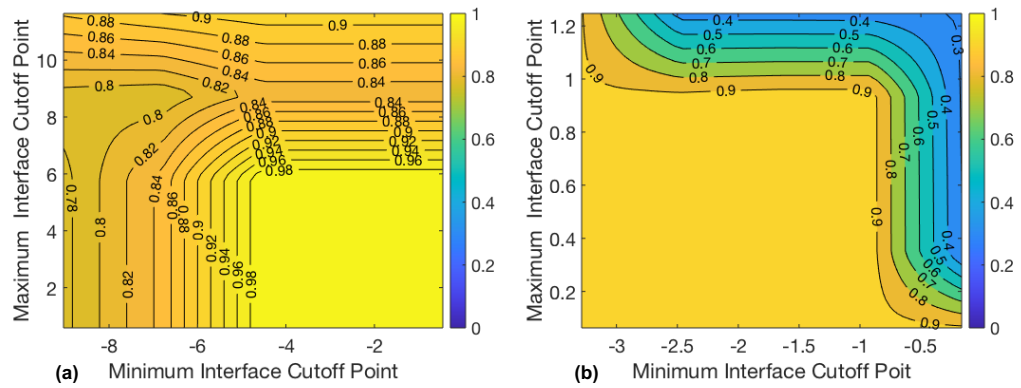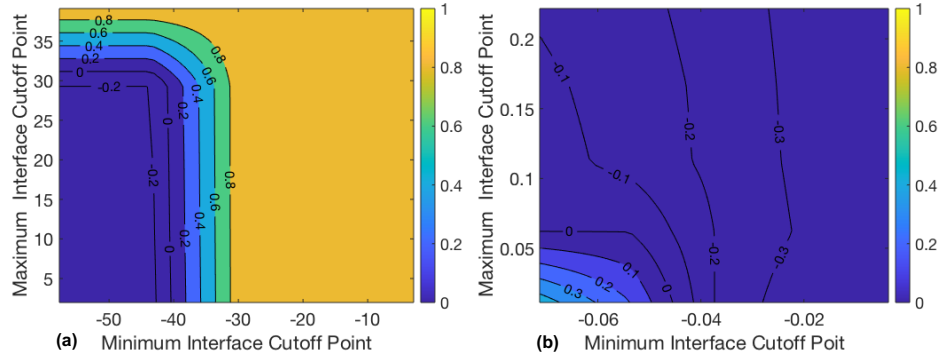

Figure A137: Contour plot of r^2 values for the sigmoidal curve fit for interface 1 data (a) and interface 2 data (b) depending on the maximum and minimum cut-off point combination – 0.1M SDBS solution (3.2867g/100ml NaCl).
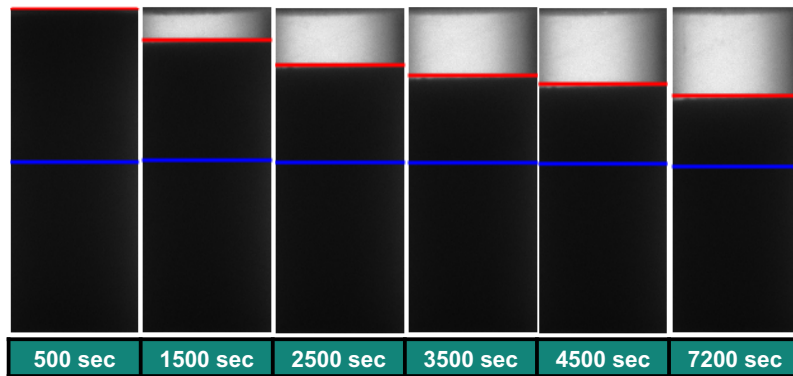
Figure A138: Sample images from 0.1M SDBS solution (3.2867g/100ml NaCl) with location of detected interfaces.

Vial 17 - Toluene-water, 0.1M SDBS, 4.348g/100ml NaCl
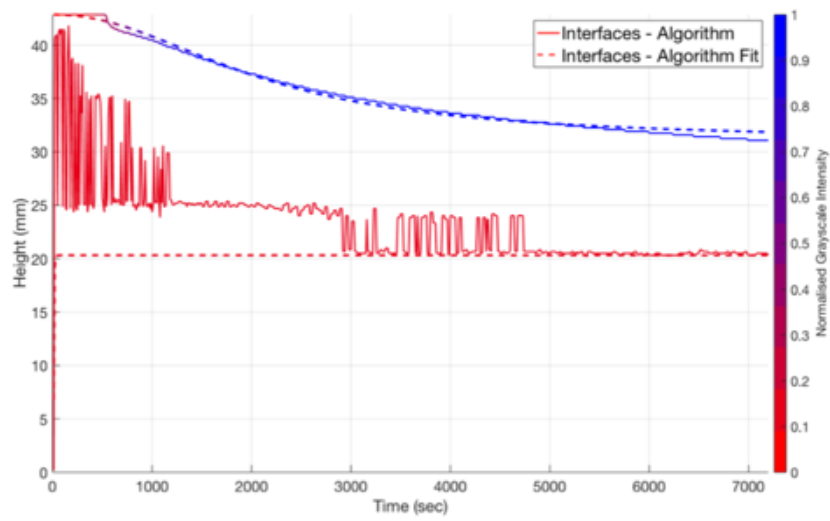
Figure A139: Detected interfaces and normalised grayscale intensity over time of the 0.1M SDBS solution (4.348g/100ml NaCl).
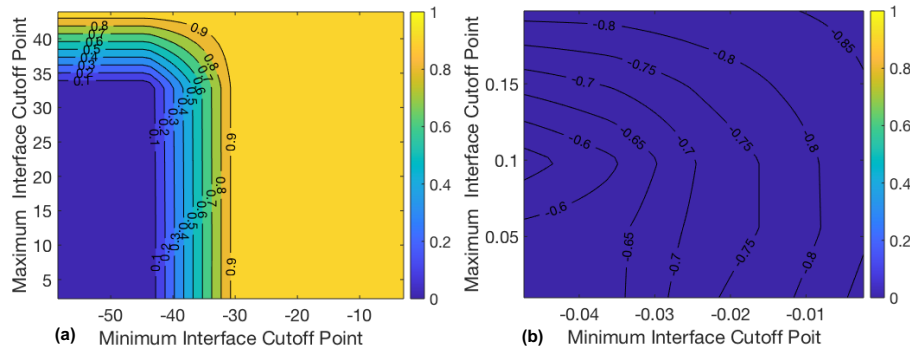
Figure A140: Contour plot of r^2 values for the sigmoidal curve fit for interface 1 data (a) and interface 2 data (b) depending on the maximum and minimum cut-off point combination – 0.1M SDBS solution (4.348g/100ml NaCl).

| 500 sec | 1500 sec | 2500 sec | 3500 sec | 4500 sec | 7200 sec |
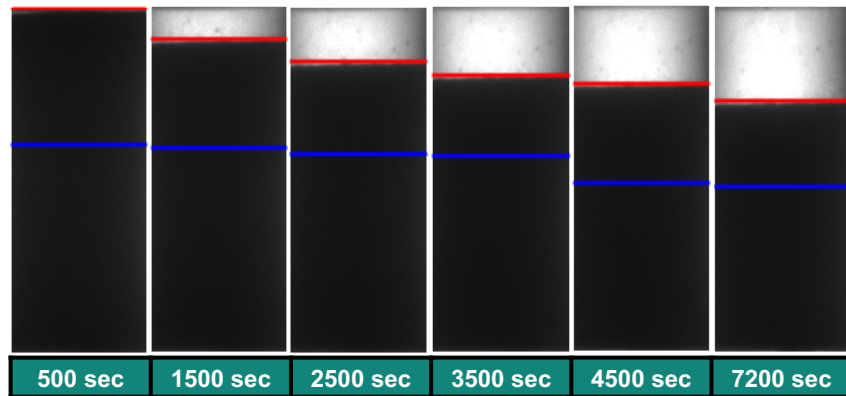
Figure A141: Sample images from 0.1M SDBS solution (4.348g/100ml NaCl) with location of detected interfaces.

Vial 18 - Toluene-water, 0.1M SDBS, 5.6587g/100ml NaCl
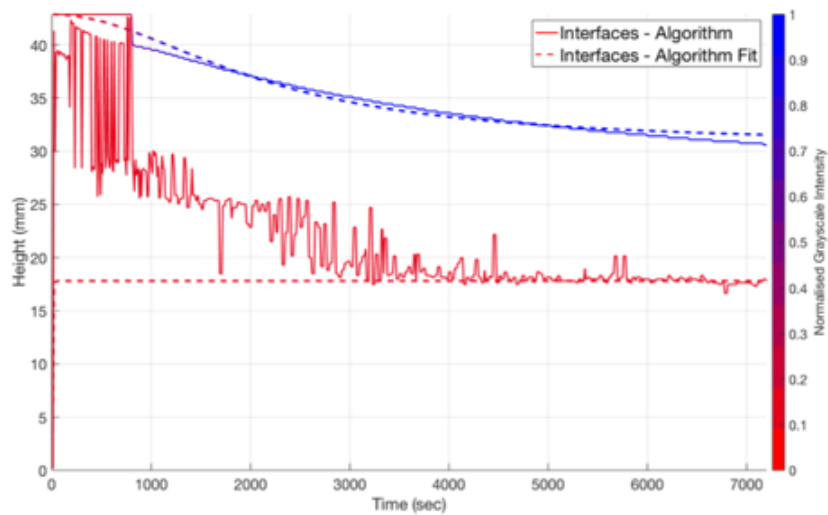
Figure A142: Detected interfaces and normalised grayscale intensity over time of the 0.1M SDBS solution (5.6587g/100ml NaCl).
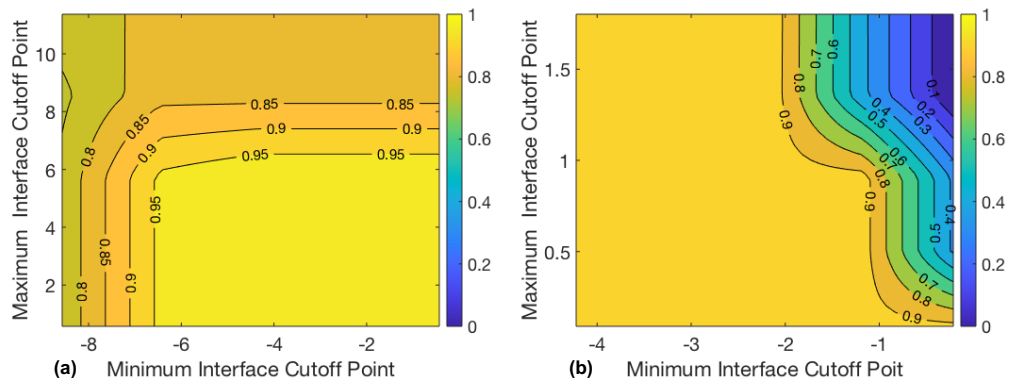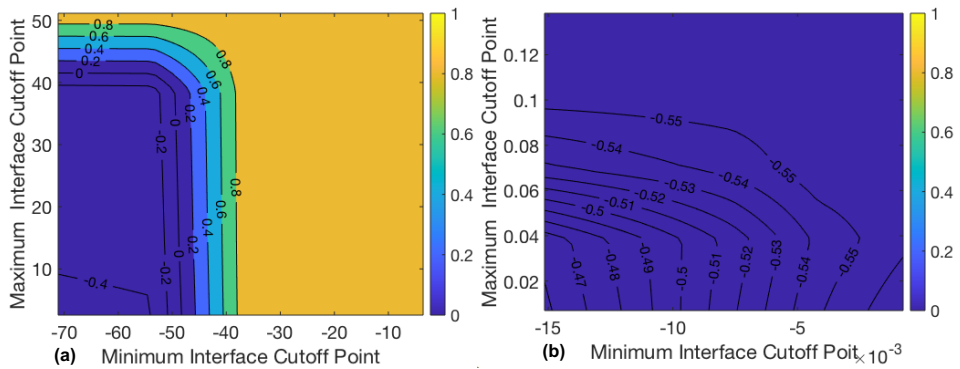

Figure A143: Contour plot of r^2 values for the sigmoidal curve fit for interface 1 data (a) and interface 2 data (b) depending on the maximum and minimum cut-off point combination – 0.1M SDBS solution (5.6587g/100ml NaCl).

| 500 sec | 1500 sec | 2500 sec | 3500 sec | 4500 sec | 7200 sec |
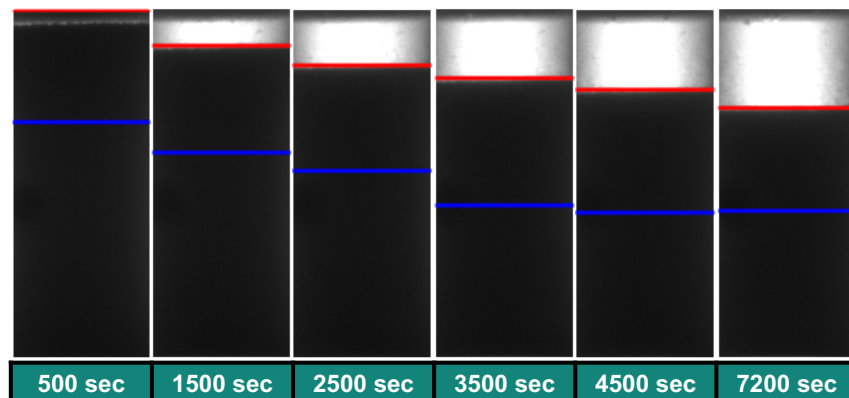
Figure A144: Sample images from 0.1M SDBS solution (5.6587g/100ml NaCl) with location of detected interfaces.

Vial 19 - Toluene-water, 0.1M SDBS, 6.6507g/100ml NaCl
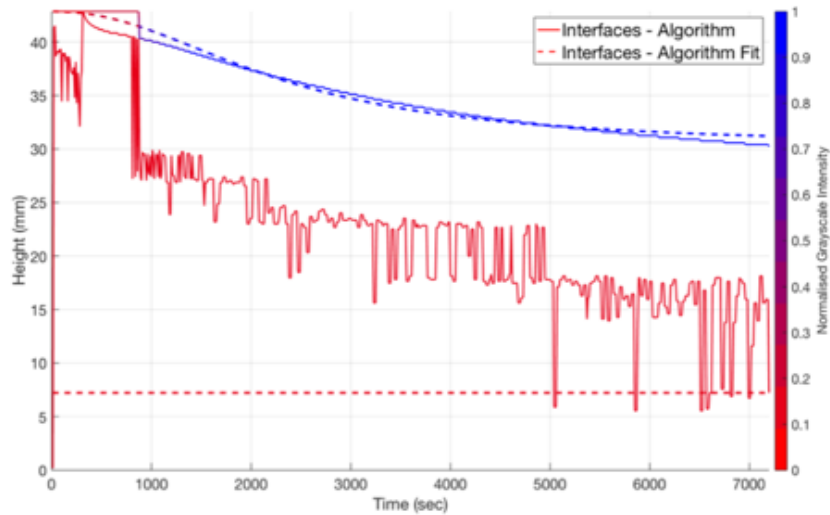
Figure A145: Detected interfaces and normalised grayscale intensity over time of the 0.1M SDBS solution (6.6507g/100ml NaCl).
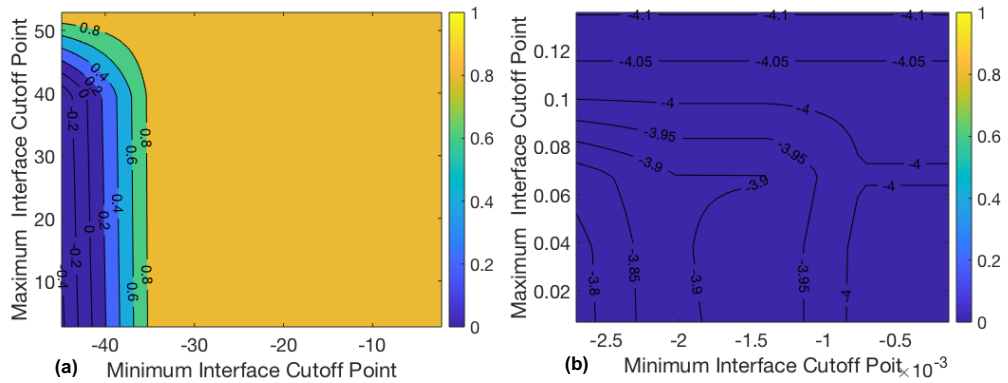
Figure A146: Contour plot of r^2 values for the sigmoidal curve fit for interface 1 data (a) and interface 2 data (b) depending on the maximum and minimum cut-off point combination – 0.1M SDBS solution (6.6507g/100ml NaCl).

| 500 sec | 1500 sec | 2500 sec | 3500 sec | 4500 sec | 7200 sec |
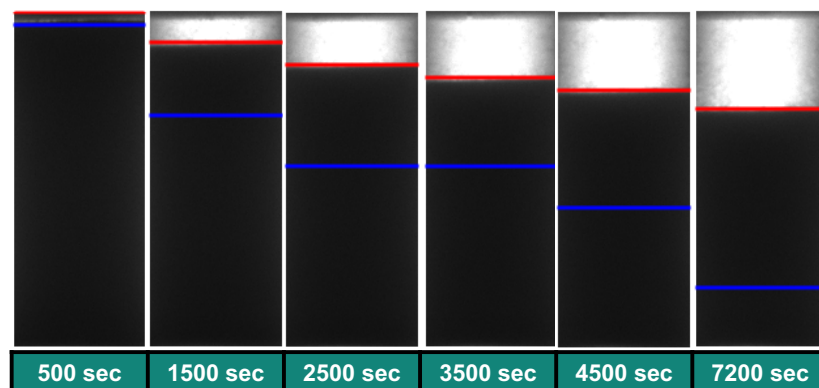
Figure A147: Sample images from 0.1M SDBS solution (6.6507g/100ml NaCl) with location of detected interfaces.

Vial 20 - Toluene-water, 0.1M SDBS, 7.7937g/100ml NaCl
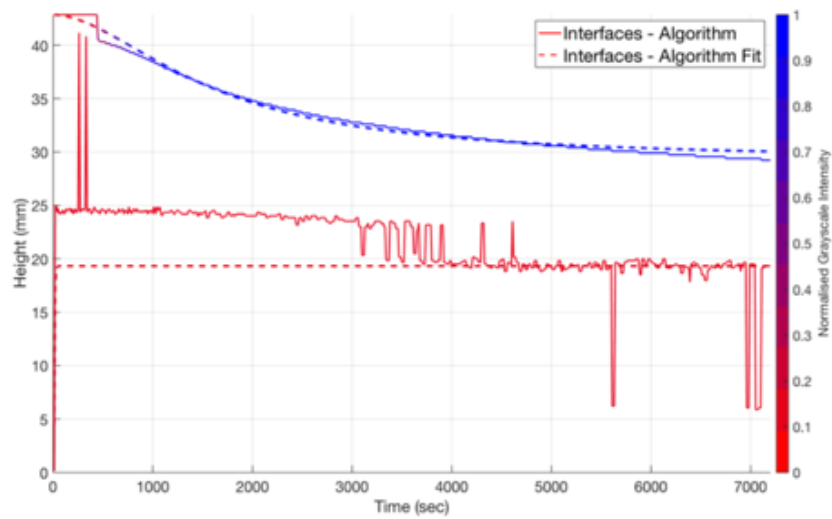
Figure A148: Detected interfaces and normalised grayscale intensity over time of the 0.1M SDBS solution (7.7937g/100ml NaCl).
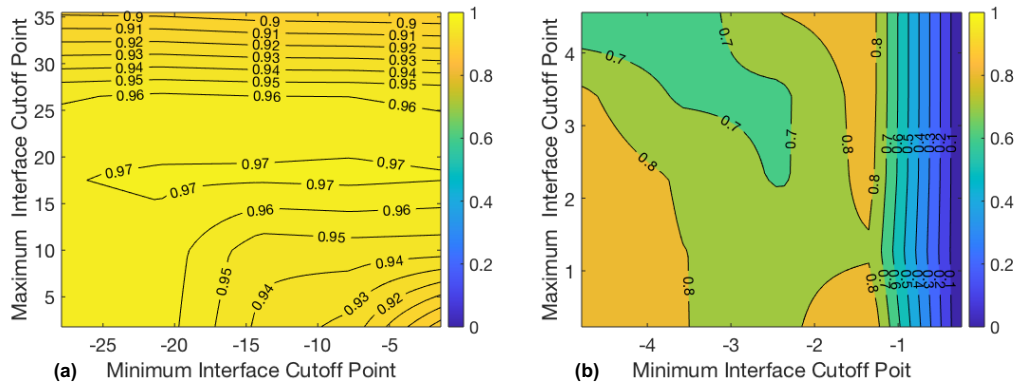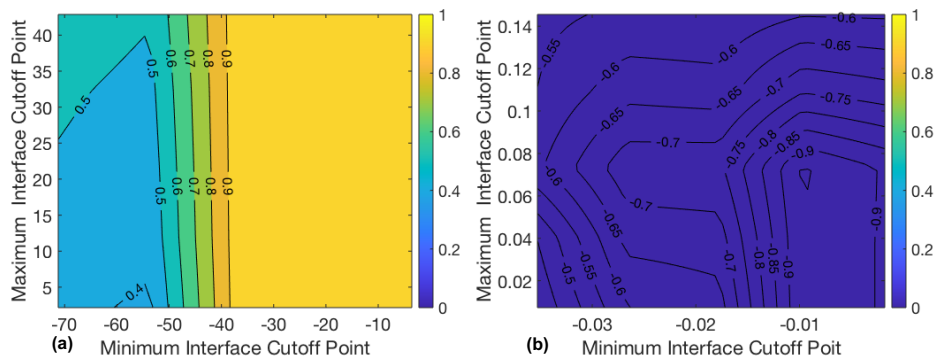

Figure A149: Contour plot of r^2 values for the sigmoidal curve fit for interface 1 data (a) and interface 2 data (b) depending on the maximum and minimum cut-off point combination – 0.1M SDBS solution (7.7937g/100ml NaCl).


| 500 sec | 1500 sec | 2500 sec | 3500 sec | 4500 sec | 7200 sec |
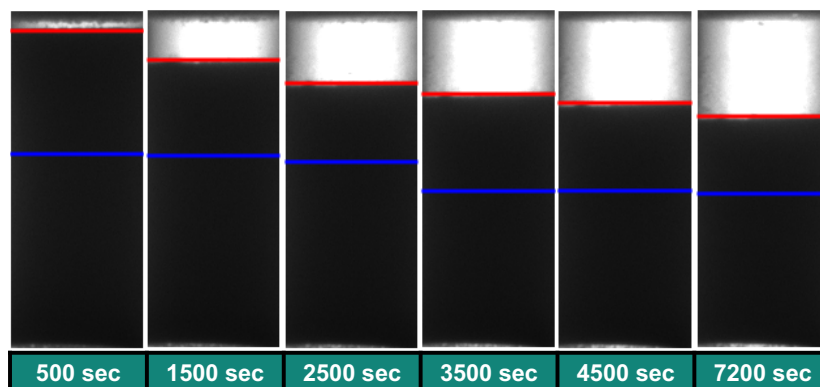
Figure A150: Sample images from 0.1M SDBS solution (7.7937g/100ml NaCl) with location of detected interfaces.

A.4 Scale up experiments

A.4.1 Scale up experiment figures and images
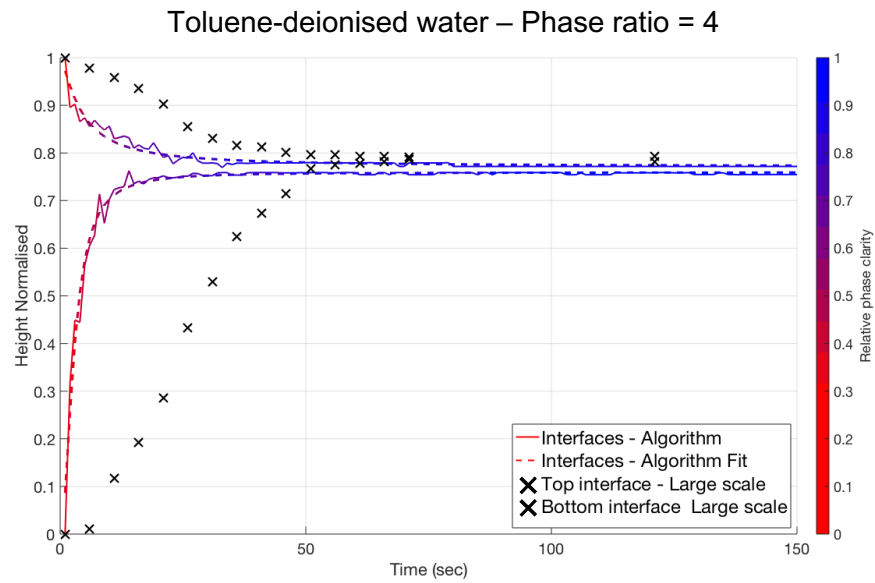
Figure A151: Normalised Height of interfaces over time of the toluene-deionised water case at a phase ratio of 4 at 20 litre scale and small scale.

Figure A152: Sample images from toluene-deionised water, phase ratio = 4, 20 litre separation
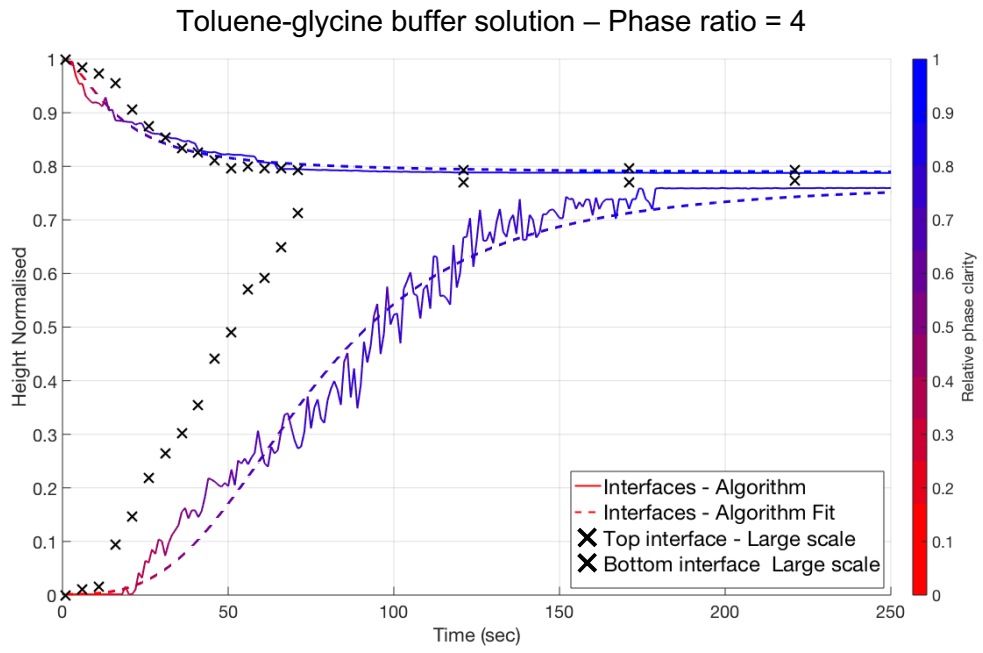
Figure A153: Normalised Height of interfaces over time of the toluene-glycine buffer solution at a phase ratio of 4 at 20 litre scale and small scale.
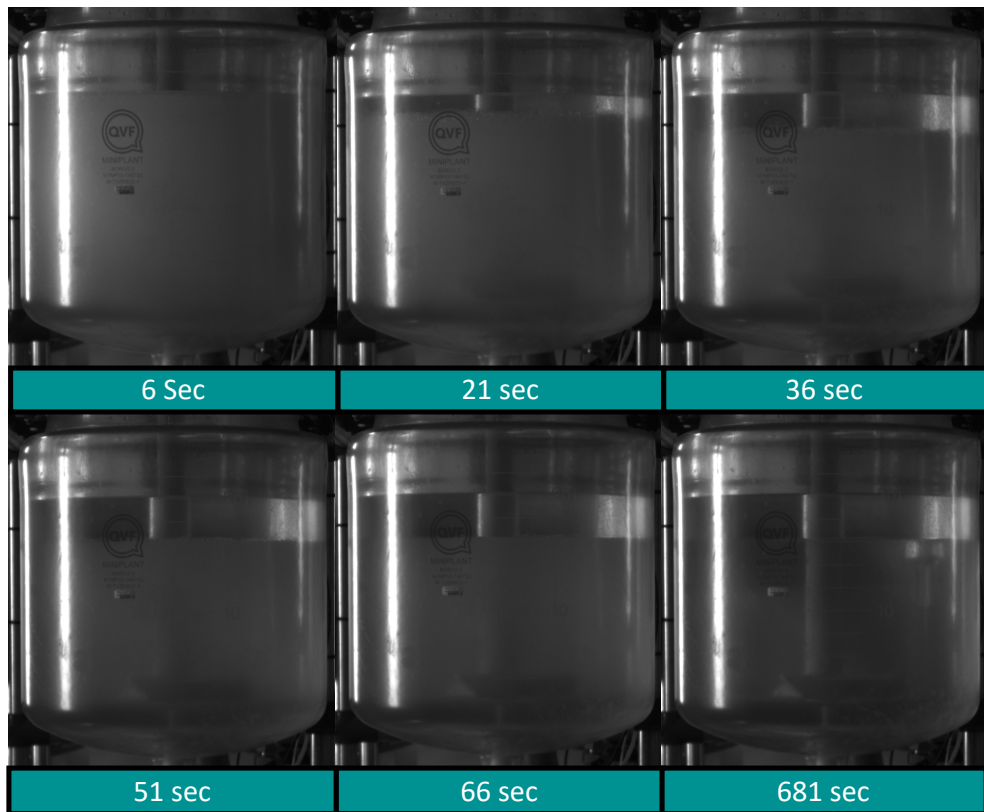
Figure A154: Sample images from toluene-glycine buffer solution, phase ratio = 4, 20 litre separation.
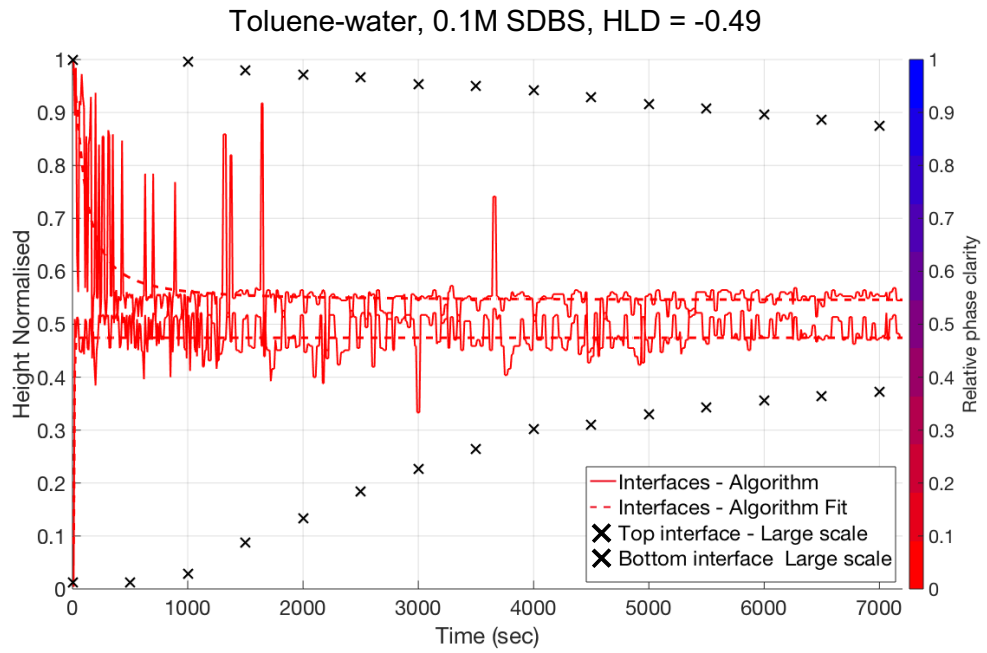
Figure A155: Normalised Height of interfaces over time of the toluene-SDBS surfactant solution, HLD = -0.49 at a phase ratio of 1 at 20 litre scale and small scale.

Figure A156: Sample images from toluene-SDBS surfactant solution, HLD = -0.49, phase ratio = 1, 20 litre separation.
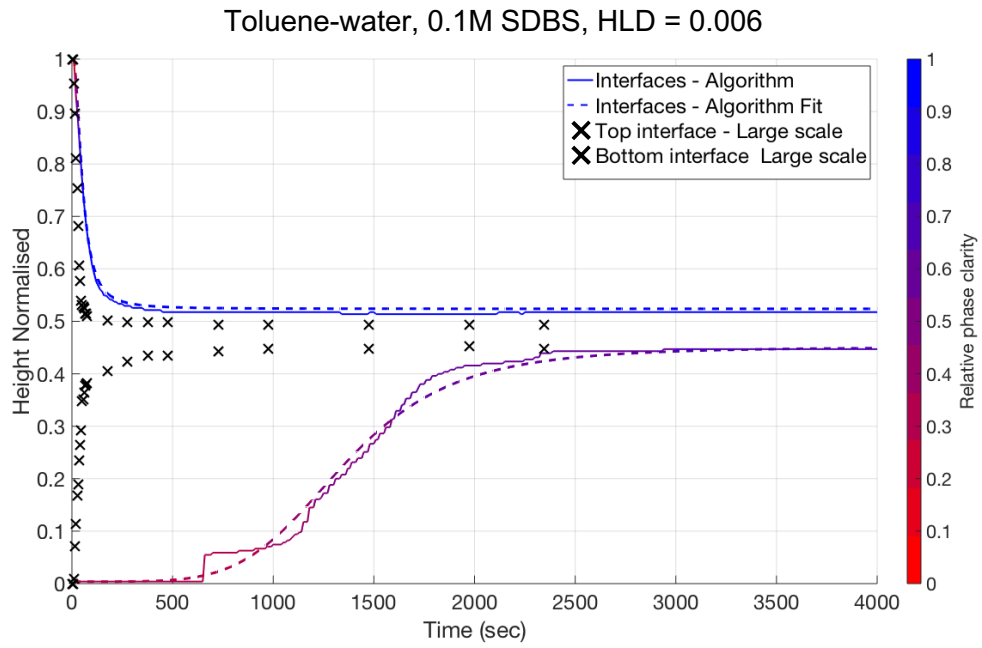
Figure A157: Normalised Height of interfaces over time of the toluene-SDBS surfactant solution, HLD = 0.006 at a phase ratio of 1 at 20 litre scale and small scale.
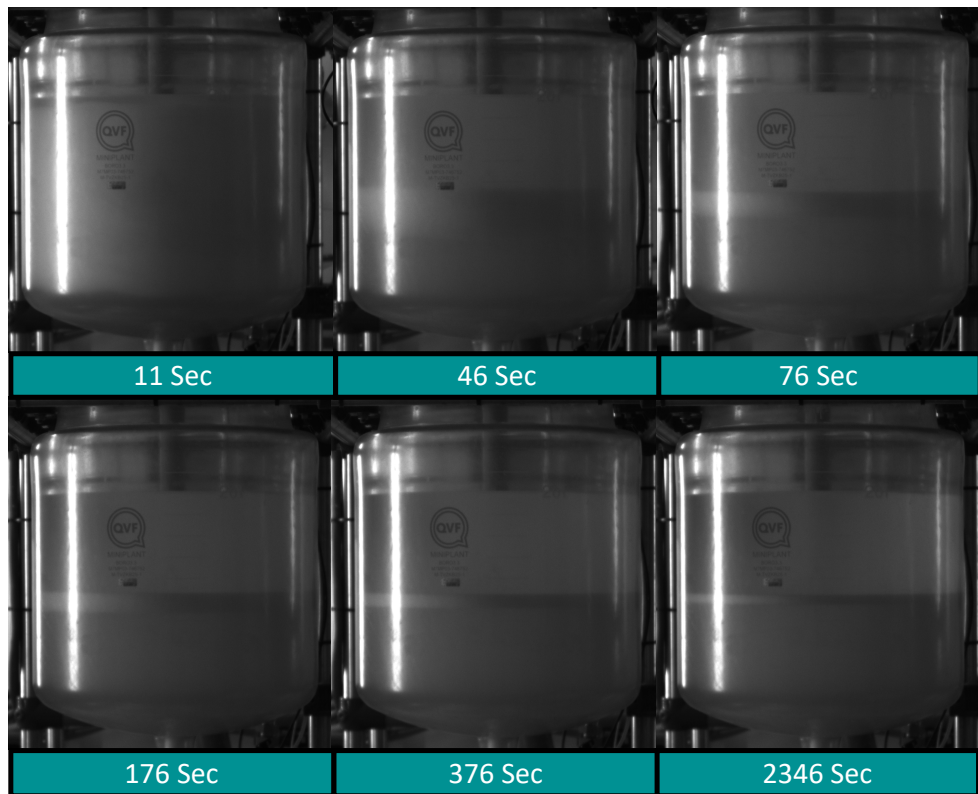
Figure A158: Sample images from toluene-SDBS surfactant solution, HLD = 0.006, phase ratio = 1, 20 litre separation.

Toluene-water, 0.1M SDBS, HLD = 0.45
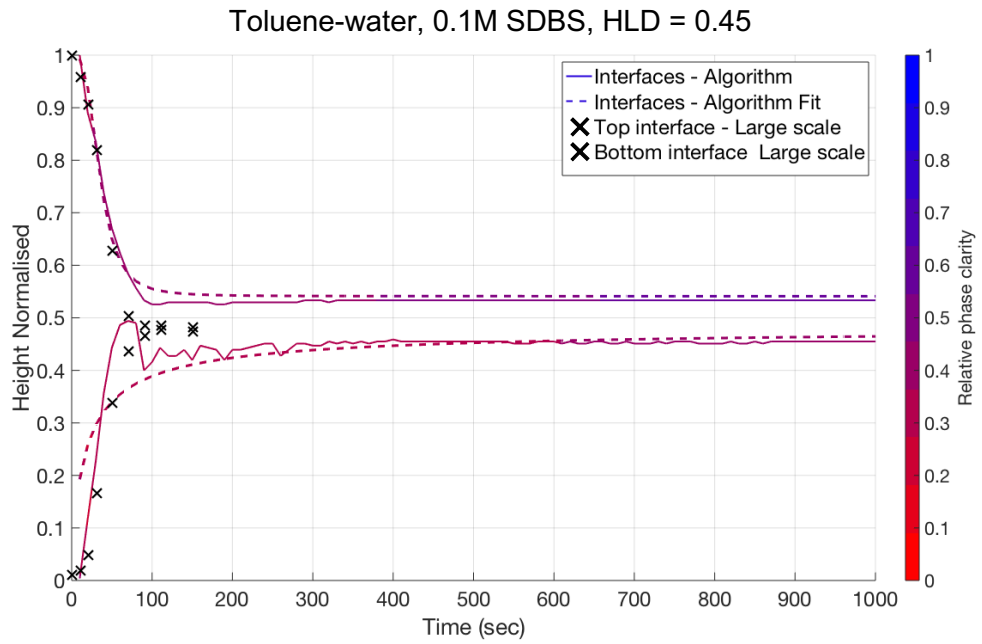
Figure A159: Normalised Height of interfaces over time of the toluene-SDBS surfactant solution, HLD = 0.45 at a phase ratio of 1 at 20 litre scale and small scale.
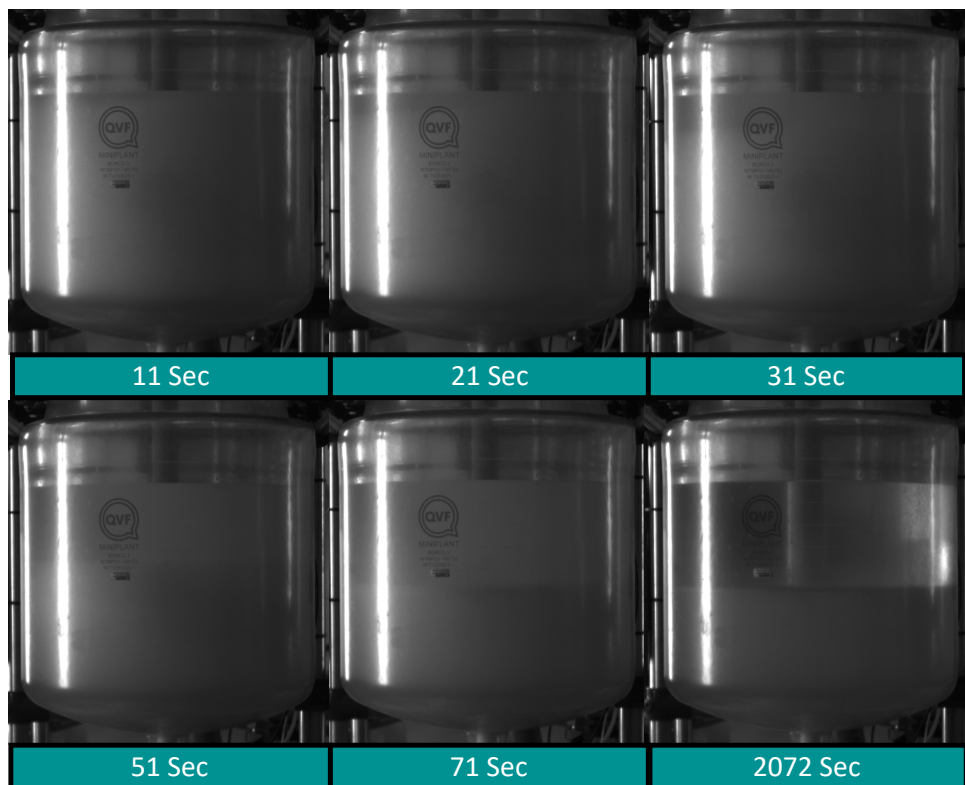
Figure A160: Sample images from toluene-SDBS surfactant solution, HLD = 0.45, phase ratio = 1, 20 litre separation.

A.5 Experimental rig development

During development of the interface detection algorithm an initial prototype of an automatic shaker rig was developed. The shaker would consist of a rack which could hold 8-12 samples in place and be shook for a period of time using a motor and suitable control system. The shaker rack could be stacked to multiply the number of samples that can be analysed at once by n – number of stacks. As an initial proof of concept a single vial containing sunflower oil and water was shook using an Arduino and stepper motor at up to 362 rpm. Figure A161 shows the level of emulsification in the vial at various rpms. The successful emulsification of sunflower oil and water shows that the shaker provides enough mixing energy to successfully and consistently emulsify a liquid-liquid mixture.

(a) 94 RPM

(c) 257 RPM

(b) 165 RPM

(d) 362 RPM
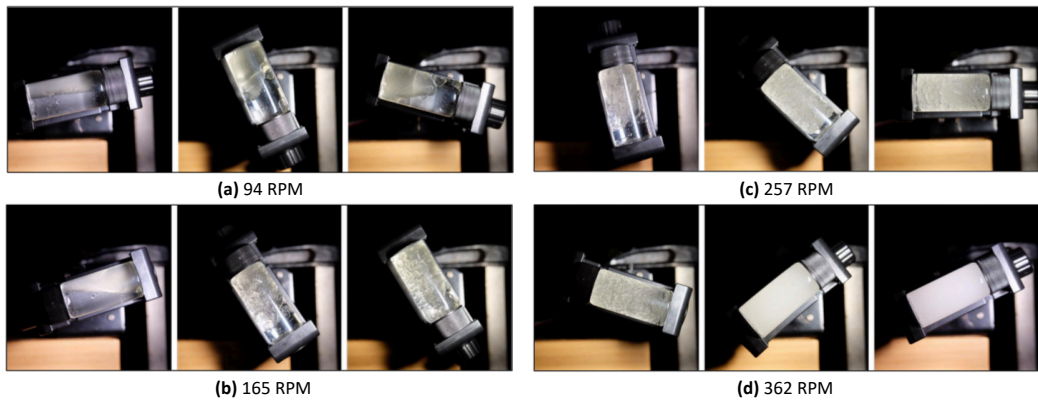
Figure A161: Vial shaker prototype demonstration at various RPM's. Each image at each RPM is taken 30 seconds apart.

Appendix B
Separator Control Algorithm - Code

In this appendix, the Arduino and Matlab code used for the separator control algorithm is presented as a flow chart for both the single stage and multistage systems. The flow chart in chapter 4, figure 4.29 gives a summary of the PID control and setpoint adjustment algorithm. Chapter 6, figure 6.6 provides a summary of the logic flow between Matlab and Arduino. The flow charts presented in this appendix (figure B1 and B2) are a more detailed expression of the code used to control the single stage and multistage systems. Most of the algorithm operates in the same way for the single stage and multi-stage systems. The main difference comes after the automate setpoint button has been pressed and the new setpoint has been set. A brief description of some of the logic diagram is given below:

- **Matlab GUI: Set initial variables:** The variables have default values but can be adjusted on the GUI before pressing the start button.

- **Matlab GUI: Open serial comms:** The serial communication port is opened between Matlab and the Arduino and the baud rate is set (9600).

- **Matlab GUI: Send serial data:** The send serial data only occurs after the start button has been pressed. Matlab packages up all of the current variables (such as: inlet pump speed, setpoint, outlet connection, flow rate limit) and a start/stop bit and sends this to the Arduino over the serial port.

- **Arduino: Do sensor reading:** After the Arduino has received the current variables from Matlab and decomposed the serial string into each variable and allocated it within the Arduino code, the Arduino reads values from each of the conductivity sensors. In the single stage code there is only 1 conductance probe so one value is read. In the multi-stage code there can be 1, 2 or 3 probes attached and read.

- **Arduino: Do PID:** Do PID is the point at which the algorithm takes the conductivity readings (input) and calculates the PID controller output. The PID output is transposed into a valve position which is then applied to the servo motor.

- **Arduino: PIDpause = 0?:** At this point the code will do something different depending on what the value of PIDpause is. In the single stage code PIDpause can be either 0, 1 or 2. In the multi-stage code PIDpause can only be 0 or 1. PIDpause is used as a value to indicate whether the automate setpoint functionality has been pressed or not. If PIDpause = 0 the automate setpoint button has not been pressed yet or has been pressed and the

initialise setpoint routine has finished. If PIDpause = 1 then the initialise setpoint routine is currently running. These statements are true for both the single stage and multistage control algorithm. PIDpause = 2 is unique to the single stage system and only occurs if the conductivity measurement standard deviation falls below the conductivity limit. It stays at PIDpause = 2 until the conductivity measurement falls below the setpoint again.

- **Z = 0?:** z is a single digit which indicates what the algorithm does in relation to PIDpause. It can be either 0, 1 or 2 in both the single stage and multi-stage systems. Z = 0 is the default value. It will stay equal to 0 until the automate setpoint button is pressed. When the automate setpoint button is pressed and z = 0 the amount of time the PID will be paused is calculated and PIDpause is changed to 1. The PID is paused so that the separator can fill with aqueous liquid and a maximum conductivity can be measured. Once the PID pause time has been calculated z is made equal to 2. While PIDpause = 1 the valve is either fully closed or fully open (depending on which outlet the valve is connected to). The valve will remain this way until the PID pause time has elapsed. Once it does, z is made equal to 1 and serial data is sent to Matlab. Matlab then changes PIDpause to be equal to 0 again, it calculates the new setpoint from the initialisation algorithm and changes z to be equal to 2. It then updates and sends the serial data back to the Arduino. The setpoint initialisation procedure is now complete and the algorithm does something different depending on if the single stage or multi-stage algorithm is in use.

- **Single stage setpoint adjustment algorithm:** This portion of the algorithm only occurs when PIDpause = 0 and z = 2 (after setpoint initialisation). This portion of figure B1 is the same as figure 4.29 and so will not be described in detail here. One addition of note is that when the conductivity falls below the conductivity limit PIDpause is made equal to 2 and the PID Kp value is changed to 10. This is done so that the new setpoint (calculated as a response to falling below the conductivity limit) can be reached quicker (because of the more aggressive proportional constant Kp). Kp stays equal to 10 until the conductivity measurement falls below the setpoint. When this happens, Kp will be changed back to 1 and PIDpause will be made equal to 0 once again.

- **Multi-stage conductivity smoothing algorithm:** The multi-stage system does not perform any setpoint adjustment. Instead, when PIDpause = 0 and z = 2 the system smooths incoming conductivity data. It takes the last 3 conductivity readings and averages them out. It only does this after 20

conductivity readings have been taken. The smoothed conductivity data is then used as the input to the PID controller as shown in figure B2.
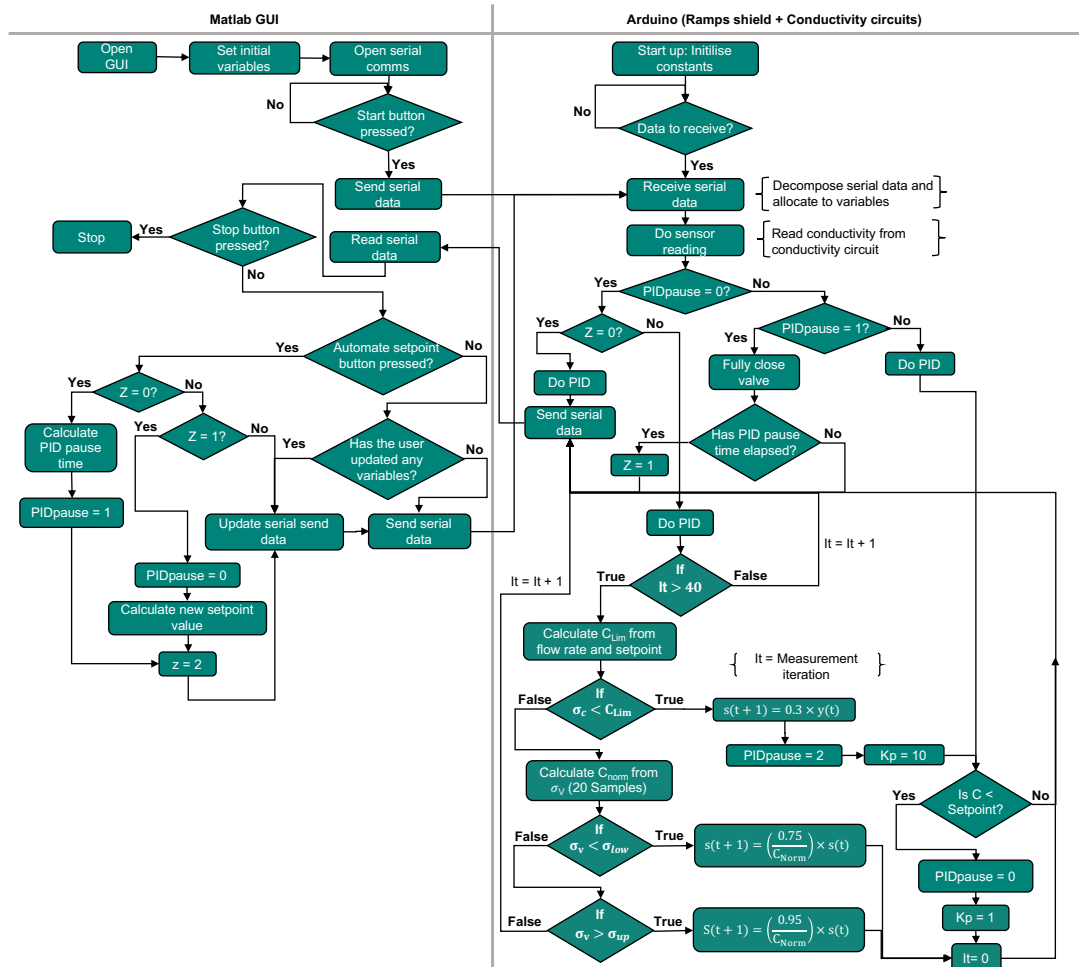
Figure B1: Single stage separator control algorithm.
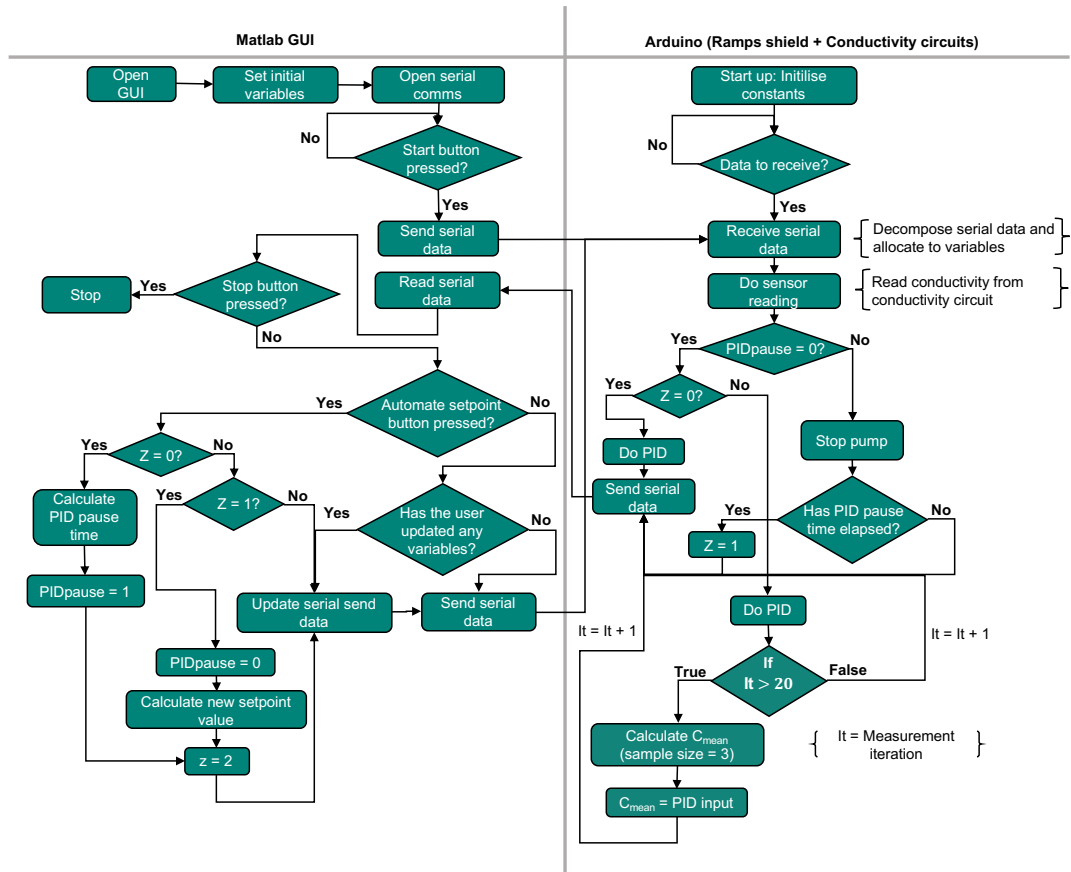
Figure B2: Multi-stage separator control algorithm.

Appendix C

Results Tables

C1.1 Results tables from Chapter 4

C1.1.1 Valve controlled system

In this section the graphs used to create figures 4.25, 4.26, 4.27 and 4.28 are presented. Where a row is red, this rows setpoint is above the conductance of the solution. The red rows were only used in figure 4.28.

Table C1: Setpoint, Normalised setpoint. Valve position standard deviation, conductance standard deviation and solution conductance during the 4 ml/min – low conductance experiment (Data plotted in figures 4.25 & 4.28(a)).

4 ml/min – low conductance solution

Normalised Setpoint	Setpoint	Valve position standard deviation (σ_V)	Conductance standard deviation (σ_C)	Solution conductance (µS/cm)
0.08	10	56.32	41.05	
0.31	40	49.06	41.53	
0.54	70	17.55	13.23	
0.77	100	5.20	5.56	
1.01	130	2.16	0.51	
0.85	110	2.62	3.50	129.3
0.70	90	7.90	7.01	
0.39	50	42.69	25.46	
1.16	150	5.63	0.19	
1.01	130	0.00	0.13	
0.93	120	1.72	0.19	
0.77	100	4.52	7.38	

Table C2: Setpoint, Normalised setpoint. Valve position standard deviation, conductance standard deviation and solution conductance during the 16 ml/min – low conductance experiment (Data plotted in figures 4.25 & 4.28(a)).

16ml/min - Low conductance

Normalised Setpoint	Setpoint	Valve position standard deviation (σ_V)	Conductivity standard deviation (σ_C)	Solution conductivity (μS/cm)
0.05	10	53.18	16.47	
0.22	40	56.28	31.59	
0.38	70	57.56	41.10	
0.55	100	34.57	29.24	
0.71	130	16.87	19.18	182.6
0.88	160	8.85	13.36	
1.04	190	3.54	3.97	
1.20	220	11.41	1.20	

Table C3: Setpoint, Normalised setpoint. Valve position standard deviation, conductance standard deviation and solution conductance during the 4 ml/min – high conductance experiment (Data plotted in figures 4.25 & 4.28(a)).

4ml/min - High conductance

Normalised Setpoint	Setpoint	Valve position standard deviation (σ_V)	Conductivity standard deviation (σ_C)	Solution conductivity (μS/cm)
0.01	100	47.20	2714.77	
0.11	1000	49.23	2686.19	
0.32	3000	47.47	2623.37	
0.53	5000	51.82	2692.44	
0.64	6000	34.11	1855.63	9396
0.74	7000	13.50	871.34	
0.85	8000	7.60	665.70	
0.96	9000	1.79	198.60	
1.17	11000	22.33	74.18	

Table C4: Setpoint, Normalised setpoint. Valve position standard deviation, conductance standard deviation and solution conductance during the 16 ml/min – high conductance experiment (Data plotted in figures 4.25 & 4.28(a)).

16ml/min - High conductance				
Normalised Setpoint	Setpoint	Valve position standard deviation (σ_V)	Conductivity standard deviation (σ_C)	Solution conductivity (μS/cm)
0.01	100	49.04	765.57	
0.11	1000	54.36	2077.04	
0.34	3000	58.05	2778.49	
0.57	5000	49.54	2377.53	8750
0.69	6000	32.45	1692.10	
0.80	7000	14.67	932.35	
0.91	8000	5.38	568.67	
1.03	9000	6.70	89.00	

Table C5: Valve position and conductance standard deviation at different flow rates after the setpoint has been initialise for the low conductivity solution (Data plotted in figure 4.27 (a)).

	Low conductivity solution			
flow rate (ml/min)	Valve position standard deviation (σ_V)		Conductivity standard deviation (σ_C)	
	no filter	filter	no filter	filter
1	1.9	1.9	2.1	6.4
4	5.3	4.6	5.7	13.9
8	6.2	6.7	5.9	18.7
12	5.6	8.6	5.8	22.3
16	6.2	9.4	6.2	23.9

Table C6: Valve position and conductance standard deviation at different flow rates after the setpoint has been initialise for the high conductivity solution (Data plotted in figure 4.27 (a)).

	High conductivity solution			
flow rate (ml/min)	Valve position standard deviation (σ_V)		Conductivity standard deviation (σ_C)	
	no filter	filter	no filter	filter
1	1.8	1.5	203.8	155.4
4	2.4	3.0	240.8	325.5
8	3.0	4.6	308.6	446.4
12	3.1	6.2	328.5	562.4
16	3.0	7.4	311.9	641.2

C1.1.2 Pump controlled system

Table C7: Setpoint, Normalised setpoint. Pump flow rate standard deviation, conductance standard deviation and solution conductance during the 4 ml/min – low conductance experiment (Data plotted in figures 4.26 & 4.28(b)).

						4ml/min - low conductivity
Normalised setpoint	Setpoint	flow rate standard deviation (σ_P)	Normalised flow rate standard deviation (σ_P)	Conductance standard deviation (σ_C)	Normalised conductance standard deviation (σ_C)	Solution conductivity (µS/cm)
0.51	50	0.61	0.24	28.96	0.29	
0.10	10	0.74	0.29	10.29	0.10	
0.30	30	0.60	0.24	12.75	0.13	
0.51	50	0.53	0.21	15.60	0.16	98.91
0.71	70	0.32	0.13	12.58	0.13	
0.91	90	0.07	0.03	2.84	0.03	
1.11	110	0.19	0.07	3.21	0.03	

Table C8: Setpoint, Normalised setpoint. Pump flow rate standard deviation, conductance standard deviation and solution conductance during the 16 ml/min – low conductance experiment (Data plotted in figures 4.26 & 4.28(b)).

						16ml/min - low conductivity
Normalised setpoint	Setpoint	flow rate standard deviation (σ_P)	Normalised flow rate standard deviation (σ_P)	Conductance standard deviation (σ_C)	Normalised conductance standard deviation (σ_C)	Solution conductivity (µS/cm)
0.12	10	1.42	0.36	14.02	0.17	
0.36	30	1.20	0.31	16.46	0.20	
0.59	50	0.43	0.11	8.95	0.11	84.14
0.83	70	0.12	0.03	3.27	0.04	
1.07	90	0.36	0.09	4.78	0.06	

Table C9: Setpoint, Normalised setpoint. Pump flow rate standard deviation, conductance standard deviation and solution conductance during the 4 ml/min – high conductance experiment (Data plotted in figures 4.26 & 4.28(b)).

						4ml/min - high conductivity
Normalised setpoint	Setpoint	flow rate standard deviation (σ_P)	Normalised flow rate standard deviation (σ_P)	Conductance standard deviation (σ_C)	Normalised conductance standard deviation (σ_C)	Solution conductivity (µS/cm)
0.06	500	0.24	0.10	69.23	0.01	
0.19	1500	0.34	0.13	282.22	0.04	
0.39	3000	0.32	0.13	524.43	0.07	
0.58	4500	0.38	0.15	943.96	0.12	7740
0.78	6000	0.19	0.08	639.46	0.08	
0.97	7500	0.03	0.01	120.53	0.02	
1.16	9000	0.18	0.07	25.34	0.00	

Table C10: Setpoint, Normalised setpoint. Pump flow rate standard deviation, conductance standard deviation and solution conductance during the 16 ml/min – high conductance experiment (Data plotted in figures 4.26 & 4.28(b)).

16ml/min - high conductivity

Normalised setpoint	Setpoint	flow rate standard deviation (σ_P)	Normalised flow rate standard deviation (σ_P)	Conductance standard deviation (σ_C)	Normalised conductance standard deviation (σ_C)	Solution conductivity (µS/cm)
0.07	500	0.19	0.05	39.30	0.01	
0.21	1500	0.26	0.07	157.99	0.02	
0.41	3000	0.30	0.08	334.45	0.05	
0.62	4500	0.33	0.08	556.49	0.08	7293
0.82	6000	0.04	0.01	100.57	0.01	
0.72	5250	0.22	0.06	463.80	0.06	
1.03	7500	0.62	0.16	744.38	0.10	

Table C11: Pump flow rate and conductance standard deviation at different flow rates after the setpoint has been initialise for the low conductivity solution (Data plotted in figure 4.27 (b)).

Low conductivity solution

flow rate (ml/min)	Pump flow rate standard deviation (σ_P)		Pump flow rate standard deviation normalised (σ_P)		conductivity standard deviation (σ_C)	
	No filter	Filter	No filter	Filter	no filter	filter
1	0.04	0.12	0.04	0.13	5.22	11.05
4	0.13	0.17	0.05	0.07	5.82	9.03
8	0.19	0.26	0.05	0.07	6.49	8.78
12	0.12	0.24	0.03	0.06	3.81	8.50
16	0.15	0.31	0.04	0.08	3.48	10.19

Table C12: Pump flow rate and conductance standard deviation at different flow rates after the setpoint has been initialise for the high conductivity solution (Data plotted in figure 4.27 (b)).

High conductivity solution

flow rate (ml/min)	Pump flow rate standard deviation (σ_P)		Pump flow rate standard deviation normalised (σ_P)		conductivity standard deviation (σ_C)	
	no filter	filter	no filter	filter	no filter	filter
1	0.14	0.10	0.15	0.12	1030.20	1132.21
4	0.16	0.14	0.06	0.06	841.35	654.53
8	0.15	0.14	0.04	0.04	466.17	644.08
12	0.26	0.11	0.07	0.03	738.77	507.11
16	0.32	0.16	0.08	0.04	702.62	553.02

C1.2 Results tables from Chapter 5

In this section are the tables used to create the pore size distribution graphs 5.1 – 5.5. The tables used to fill table 5.10 and figure 5.17 are also given.

C1.2.1 Pore size results tables

Table C13: Pore size data from sample 1 (Plotted in figure 5.1).

Pressure (bar)	Wet curve (Flow (l/min))	Interpolated dry curve (Flow (l/min))	Diameter (um)	Cumulative filter flow (Percent flow)	Differential filter flow (Percent flow)	Pore size flow distribution (Percent flow)
0	0	0				
0.002036	0.004056	9.892	266.9	0.041	0.041	
0.003208	0.004056	12.04	169.4	0.03368	0	0
0.004463	0.02756	14.36	121.7	0.1919	0.1582	0.001225
0.005893	0.06118	19.75	92.22	0.3098	0.118	0.001474
0.007206	0.1178	24.73	75.41	0.4763	0.1665	0.003654
0.008573	0.2234	30.36	63.38	0.7357	0.2595	0.007964
0.009819	0.3567	35.46	55.34	1.006	0.2704	0.01241
0.01108	0.8915	39.88	49.05	2.236	1.229	0.07212
0.01238	1.961	44.47	43.88	4.41	2.174	0.1551
0.01372	4.112	48.73	39.6	8.439	4.029	0.3474
0.01503	5.262	52.9	36.15	9.946	1.507	0.1611
0.0164	7.313	57.01	33.14	12.83	2.882	0.3534
0.01769	9.438	60.89	30.72	15.5	2.672	0.4078
0.01901	12.07	64.82	28.58	18.63	3.128	0.5405
0.02035	18.51	68.79	26.71	26.9	8.274	1.626
0.02167	24.31	72.14	25.08	33.7	6.797	1.54
0.02297	28.27	75.45	23.66	37.47	3.772	0.9805
0.0243	32.82	78.62	22.36	41.75	4.275	1.221
0.02565	38.15	81.85	21.18	46.61	4.868	1.524
0.02697	43.05	84.67	20.15	50.84	4.226	1.5
0.02829	48.76	87.48	19.21	55.74	4.901	1.93
0.02956	53.59	90	18.38	59.54	3.8	1.693
0.03091	57.74	92.67	17.58	62.3	2.763	1.27
0.03224	61.88	95.15	16.86	65.04	2.732	1.398
0.03358	65.13	97.65	16.18	66.7	1.662	0.9124
0.03485	69.86	99.77	15.59	70.02	3.323	2.067
0.03616	74.68	101.9	15.03	73.26	3.236	2.115
0.03752	78.17	104	14.48	75.13	1.876	1.277
0.03886	81.11	106.1	13.98	76.45	1.312	0.9699
0.04014	84.42	108	13.54	78.16	1.719	1.419
0.04146	87.66	110	13.11	79.72	1.551	1.325
0.04283	90.29	112	12.69	80.61	0.8921	0.7886
0.04413	92.66	113.9	12.31	81.32	0.7071	0.697
0.04543	95.78	115.7	11.96	82.78	1.465	1.533
0.04675	99.94	117.5	11.62	85.08	2.296	2.518
0.04809	102.2	118.8	11.3	86.04	0.9629	1.096
0.0494	104	120.1	11	86.62	0.58	0.716
0.05071	105.9	121.2	10.71	87.42	0.8002	1.033
0.05206	108.6	122.3	10.44	88.77	1.353	1.802
0.05335	110.5	123.4	10.19	89.51	0.7334	1.074

0.05472	112.7	124.6	9.93	90.47	0.9625	1.387
0.05601	115	126.2	9.703	91.19	0.7259	1.18
0.05735	117.3	127.8	9.476	91.78	0.5858	0.9529
0.05872	118.8	128.8	9.253	92.19	0.406	0.6738
0.05996	119.9	129.8	9.063	92.42	0.2308	0.4463
0.06131	121.2	130.8	8.864	92.6	0.1878	0.3488
0.06259	122.8	131.9	8.682	93.14	0.533	1.081
0.06391	124.2	133.1	8.502	93.31	0.1713	0.3518
0.06523	125.7	134.3	8.33	93.63	0.32	0.686
0.06662	127.3	135.4	8.156	94.05	0.4167	0.8859
0.0679	128.5	136.3	8.003	94.27	0.2278	0.5494
0.0692	129.5	137.3	7.853	94.3	0.02228	0.05449
0.07059	130.7	138.4	7.698	94.47	0.1784	0.4252
0.07186	132.6	139.4	7.562	95.12	0.6463	1.754
0.07318	133.8	140.5	7.426	95.22	0.1027	0.2781
0.07449	134.5	141.3	7.295	95.15	0	0
0.0759	135.2	142.3	7.16	95	0	0
0.07715	135.9	143.4	7.044	94.76	0	0
0.07847	137.5	144.7	6.925	95.03	0.2675	0.8277
0.07979	138.6	145.5	6.81	95.28	0.2534	0.8182
0.08113	139.8	146.3	6.698	95.56	0.2736	0.9013
0.08245	140.8	147.4	6.59	95.56	0.002856	0.009767
0.08376	141.6	148.5	6.487	95.36	0	0
0.08509	142.5	149.3	6.386	95.47	0.1101	0.4026
0.08641	144.3	150.1	6.289	96.07	0.6045	2.287
0.0877	145.3	151	6.196	96.24	0.1639	0.6513
0.08905	146.2	152	6.102	96.22	0	0
0.09034	147.1	153	6.015	96.14	0	0
0.09171	148.2	154	5.926	96.21	0.06918	0.2849
0.09305	149.3	155.2	5.84	96.19	0	0
0.09431	150	156.3	5.762	95.93	0	0
0.09564	151.4	157.2	5.682	96.3	0.3658	1.685
0.097	152.7	158.2	5.602	96.56	0.2558	1.178
0.09833	153.7	159.1	5.526	96.61	0.05493	0.2679
0.09959	154.6	160	5.456	96.58	0	0
0.1009	155.4	160.8	5.385	96.63	0.04681	0.2425
0.1023	156.5	161.7	5.312	96.82	0.1919	0.9737
0.1036	157.6	162.4	5.246	97.03	0.2089	1.156
0.1049	158.6	163.1	5.18	97.23	0.2032	1.152
0.1062	160.5	163.9	5.117	97.91	0.6796	3.947
0.1075	161.2	164.7	5.053	97.91	0	0
0.1089	162	165.9	4.992	97.67	0	0
0.1102	162.7	167.1	4.931	97.35	0	0
0.1115	163.9	167.8	4.872	97.65	0.3041	1.895
0.1128	165	168.5	4.816	97.88	0.2265	1.498
0.1141	165.7	169.6	4.761	97.7	0	0
0.1155	166.7	170.8	4.706	97.62	0	0
0.1168	167.3	171.7	4.653	97.44	0	0
0.1181	168.1	172.5	4.601	97.43	0	0
0.1195	168.9	173.1	4.549	97.57	0.1391	0.9846
0.1208	170.1	173.7	4.5	97.91	0.3403	2.565
0.122	171.1	174.7	4.452	97.92	0.0171	0.1324
0.1234	171.9	175.7	4.403	97.87	0	0
0.1247	173	176.3	4.358	98.11	0.2383	1.925

0.1261	173.9	177	4.311	98.27	0.1588	1.256
0.1274	174.8	177.9	4.267	98.26	0	0
0.1287	175.6	178.9	4.224	98.18	0	0
0.13	176.8	179.7	4.181	98.34	0.1601	1.381
0.1313	177.9	180.6	4.138	98.51	0.1705	1.462
0.1327	178.5	181.3	4.096	98.46	0	0
0.134	179.2	182	4.056	98.43	0	0
0.1353	180.2	182.8	4.017	98.56	0.1214	1.144
0.1366	181.3	183.6	3.979	98.76	0.204	1.982
0.1379	181.8	184.4	3.939	98.6	0	0
0.1393	182.4	185.2	3.901	98.45	0	0
0.1405	183.2	186	3.866	98.48	0.03069	0.3262
0.1419	184.2	186.8	3.829	98.6	0.1193	1.18
0.1432	185.3	187.7	3.794	98.68	0.08379	0.8717
0.1446	186.2	188.7	3.759	98.71	0.02733	0.2932
0.1459	186.9	189.3	3.724	98.73	0.02045	0.2154
0.1472	187.6	190	3.692	98.74	0.005698	0.06529
0.1485	188.4	190.7	3.659	98.8	0.06273	0.7071
0.1498	189.6	191.5	3.627	99.01	0.213	2.457
0.1512	190.2	192.3	3.595	98.9	0	0
0.1525	190.9	193	3.564	98.88	0	0
0.1538	191.5	193.7	3.533	98.87	0	0
0.1551	192.5	194.3	3.503	99.04	0.1747	2.11
0.1565	193.3	195.3	3.473	98.95	0	0
0.1578	194	196.4	3.444	98.78	0	0
0.1591	194.6	196.9	3.416	98.82	0.04713	0.63
0.1604	195.4	197.5	3.388	98.96	0.1321	1.719
0.1617	196.3	198.4	3.361	98.95	0	0
0.163	197	199.3	3.333	98.84	0	0
0.1644	197.8	199.8	3.305	99.01	0.1662	2.245
0.1657	199	200.4	3.28	99.33	0.3184	4.544
0.167	199.8	201.1	3.254	99.36	0.03314	0.4832
0.1683	200.4					
0.1697	201					
0.171	201.6					

Table C14: Pore size data from sample 2 (Plotted in figure 5.2).

Pressure (bar)	Wet curve (Flow (l/min))	Interpolated dry curve (Flow (l/min))	Diameter (um)	Cumulative filter flow (Percent flow)	Differential filter flow (Percent flow)	Pore size flow distribution (Percent flow)
0	0	0				
0.001918	0.0003769	9.759	283.3	0.003862	0.003862	
0.003302	0.01335	13.94	164.6	0.09578	0.09192	0.0003015
0.004591	0.04564	17.72	118.4	0.2576	0.1618	0.001363
0.005883	0.09719	22.63	92.37	0.4296	0.172	0.002576
0.007224	0.1937	27.72	75.22	0.6988	0.2692	0.00611
0.00851	0.3189	32.65	63.86	0.9767	0.2779	0.009521
0.009842	0.4593	37.72	55.21	1.218	0.2411	0.01086
0.0111	0.8438	41.88	48.97	2.015	0.7968	0.04968
0.01239	2.138	46.16	43.86	4.632	2.617	0.1997
0.01373	4.161	50.6	39.58	8.223	3.591	0.3264
0.01503	5.21	54.92	36.15	9.487	1.264	0.1434
0.01641	6.907	59	33.12	11.71	2.22	0.2855

0.01769	9.222	62.81	30.71	14.68	2.974	0.4799
0.019	12.4	66.37	28.59	18.68	4.002	0.7363
0.02032	18.35	69.96	26.74	26.22	7.542	1.581
0.02166	24.47	73.48	25.09	33.31	7.082	1.673
0.023	29.51	77	23.63	38.33	5.02	1.338
0.02429	34.29	79.96	22.37	42.88	4.556	1.409
0.02565	38.99	83.07	21.18	46.94	4.056	1.328
0.02696	43.49	85.85	20.15	50.65	3.715	1.405
0.02824	48.53	88.56	19.24	54.8	4.149	1.777
0.0296	54.05	91.33	18.36	59.18	4.375	1.925
0.03093	58.15	94.04	17.57	61.84	2.658	1.308
0.03226	62.29	96.55	16.85	64.51	2.68	1.444
0.03357	66.31	99.04	16.19	66.96	2.441	1.441
0.03486	70.81	101.4	15.59	69.83	2.875	1.876
0.03622	75.1	103.9	15	72.28	2.45	1.626
0.0375	79.13	105.8	14.49	74.81	2.525	1.914
0.03881	82.06	107.7	14	76.18	1.376	1.098
0.04013	85.09	109.3	13.54	77.84	1.662	1.406
0.04146	88.03	110.9	13.11	79.37	1.528	1.373
0.04281	92.4	112.4	12.69	82.24	2.871	2.691
0.0441	95.49	113.7	12.32	83.96	1.72	1.803
0.04543	98	115.3	11.96	84.98	1.021	1.104
0.04675	100.2	116.9	11.62	85.72	0.7403	0.8513
0.04811	102.7	118.8	11.3	86.5	0.7715	0.9178
0.04939	104.5	120.6	11	86.72	0.224	0.2981
0.05071	107.8	121.9	10.72	88.45	1.734	2.347
0.05202	110.2	123.2	10.45	89.49	1.036	1.497
0.05342	112	124.6	10.17	89.87	0.3831	0.5448
0.05468	113.9	126	9.939	90.45	0.5732	0.9559
0.05607	115.9	127.3	9.691	91.04	0.5887	0.9263
0.05731	117.5	128.4	9.482	91.53	0.498	0.9288
0.05866	119.2	129.6	9.263	91.99	0.4554	0.8089
0.05997	120.7	130.7	9.061	92.35	0.3601	0.6934
0.06137	122	131.7	8.854	92.6	0.2488	0.4687
0.0626	123.2	132.6	8.681	92.92	0.3178	0.713
0.06394	125	133.9	8.499	93.32	0.4066	0.8704
0.0653	127	135.2	8.322	93.89	0.5718	1.255
0.06658	128.1	136.3	8.161	93.97	0.07393	0.1795
0.06792	129.4	137.5	8	94.11	0.1415	0.3422
0.06924	130.8	138.3	7.848	94.53	0.4192	1.073
0.07054	132	139.2	7.703	94.84	0.3139	0.8423
0.07187	133.4	140.2	7.561	95.17	0.325	0.8921
0.07316	134.8	141.1	7.427	95.53	0.3634	1.056
0.07451	135.9	142.1	7.293	95.61	0.07975	0.2309
0.07585	136.8	143.1	7.164	95.59	0	0
0.07715	137.6	144.1	7.043	95.51	0	0
0.0785	138.4	145.1	6.922	95.37	0	0
0.07978	139.8	146	6.811	95.75	0.3835	1.34
0.08115	140.9	146.9	6.696	95.93	0.181	0.615
0.08245	141.7	147.8	6.591	95.84	0	0
0.08378	142.6	148.8	6.486	95.83	0	0
0.08508	143.9	149.8	6.387	96.12	0.2871	1.127
0.08644	144.9	150.8	6.286	96.14	0.02294	0.08901
0.0877	145.5	151.9	6.196	95.76	0	0

0.08905	146.5	153.2	6.102	95.63	0	0
0.09038	147.7	154.1	6.012	95.88	0.2522	1.09
0.09171	149	155	5.926	96.11	0.2287	1.024
0.09301	149.9	156.1	5.842	96.02	0	0
0.09432	151.6	157.2	5.761	96.43	0.4097	1.965
0.09564	152.6	158	5.682	96.6	0.1634	0.8057
0.09697	153.5	158.7	5.604	96.7	0.1095	0.5467
0.09828	154.5	159.6	5.529	96.79	0.08471	0.4387
0.09959	155.4	160.5	5.457	96.84	0.05051	0.2723
0.1009	156.5	161.7	5.385	96.76	0	0
0.1023	157.7	163	5.313	96.78	0.01545	0.08429
0.1036	158.8	163.7	5.247	97.02	0.2447	1.441
0.1049	159.6	164.4	5.178	97.06	0.03671	0.2066
0.1062	160.5	165.3	5.116	97.11	0.05461	0.3448
0.1075	161.3	166.1	5.054	97.08	0	0
0.1088	163.3	167.2	4.993	97.68	0.5926	3.758
0.1102	164.2	168.2	4.932	97.58	0	0
0.1115	164.9	169	4.873	97.59	0.00616	0.0406
0.1128	165.4	169.8	4.817	97.44	0	0
0.1142	166.3	170.9	4.76	97.29	0	0
0.1154	167.5	172	4.707	97.41	0.1149	0.8453
0.1168	168.8	172.7	4.653	97.75	0.3371	2.443
0.1181	169.6	173.3	4.6	97.86	0.1165	0.8549
0.1194	170.4	174.3	4.55	97.78	0	0
0.1208	171	175.2	4.5	97.63	0	0
0.1221	172.1	176	4.451	97.76	0.1309	1.042
0.1234	172.9	176.8	4.403	97.76	0.001194	0.009818
0.1247	174	177.5	4.356	98.02	0.2576	2.124
0.126	175.7	178.1	4.312	98.64	0.6254	5.499
0.1274	176.5	179.2	4.266	98.5	0	0
0.1287	177.3	180.3	4.222	98.33	0	0
0.13	177.9	181.2	4.179	98.17	0	0
0.1313	178.6	182.1	4.138	98.1	0	0
0.1326	179.2	182.7	4.097	98.08	0	0
0.134	180.3	183.4	4.056	98.32	0.2441	2.302
0.1353	181.4	184.2	4.015	98.49	0.1671	1.609
0.1366	182	184.9	3.978	98.43	0	0
0.1379	182.9	185.6	3.94	98.56	0.1285	1.309
0.1393	184.1	186.3	3.902	98.82	0.262	2.737
0.1405	185.2	187.2	3.866	98.93	0.1151	1.247
0.1419	186.2	188.2	3.83	98.93	0	0
0.1432	186.8	188.8	3.795	98.95	0.01701	0.1888
0.1446	187.5	189.4	3.758	98.96	0.01105	0.1165
0.1459	188	190.1	3.724	98.88	0	0
0.1472	188.7	190.8	3.692	98.9	0.02344	0.2882
0.1485	189.4	191.8	3.659	98.74	0	0
0.1498	190.5	192.8	3.626	98.78	0.03835	0.4574
0.1512	191.4	193.4	3.595	98.98	0.2023	2.492
0.1525	192	193.9	3.563	99.04	0.05573	0.6891
0.1538	192.7	194.5	3.534	99.07	0.03726	0.4882
0.1552	193.6	195.1	3.502	99.21	0.141	1.761
0.1564	194.4	196.1	3.474	99.14	0	0
0.1578	195.3	197.2	3.445	99.04	0	0
0.1591	196	198	3.415	99	0	0

0.1604	196.9	198.7	3.388	99.11	0.1048	1.51
0.1617	197.7	199.3	3.36	99.23	0.1227	1.706
0.163	198.3	199.8	3.333	99.26	0.02521	0.3627
0.1643	199	200.4	3.307	99.28	0.01788	0.2615
0.1657	199.6					
0.1671	200.4					
0.1683	201.1					
0.1696	201.6					

Table C15: Pore size data from sample 3 (Plotted in figure 5.3).

Pressure (bar)	Wet curve (Flow (l/min))	Interpolated dry curve (Flow (l/min))	Diameter (um)	Cumulative filter flow (Percent flow)	Differential filter flow (Percent flow)	Pore size flow distribution (Percent flow)
0	0	0				
0.001926	0	8.641	282.1	0	0	
0.003278	0.02799	12.64	165.8	0.2214	0.2214	0.0008255
0.004627	0.07049	16.68	117.4	0.4226	0.2012	0.001807
0.006039	0.1393	22.79	89.98	0.611	0.1884	0.002975
0.007427	0.2181	28.63	73.17	0.762	0.1509	0.003894
0.008743	0.3087	33.56	62.15	0.92	0.158	0.006224
0.01003	0.4133	38.3	54.2	1.079	0.1592	0.008685
0.01109	0.6093	42.03	49.01	1.45	0.3703	0.03093
0.01244	1.662	46.75	43.69	3.555	2.106	0.1719
0.01371	3.53	50.56	39.62	6.981	3.425	0.365
0.01504	6.114	54.53	36.12	11.21	4.232	0.5247
0.01637	6.114	58.86	33.2	10.39	0	0
0.01769	8.67	63.22	30.71	13.71	3.327	0.5793
0.01899	11.43	67.1	28.61	17.03	3.317	0.685
0.02031	17.1	71.05	26.75	24.07	7.036	1.64
0.02165	23.55	74.29	25.09	31.7	7.63	1.997
0.02296	29.41	77.43	23.66	37.99	6.289	1.907
0.02431	36.08	80.25	22.36	44.96	6.971	2.314
0.02563	40.35	83.03	21.2	48.6	3.641	1.369
0.027	44.51	86.14	20.13	51.67	3.071	1.239
0.0283	49.83	89.1	19.2	55.93	4.263	1.996
0.02956	54.24	91.56	18.38	59.23	3.302	1.75
0.03094	59.47	94.28	17.56	63.08	3.848	2.029
0.03223	64.75	96.91	16.86	66.81	3.734	2.316
0.03354	69.11	99.59	16.2	69.39	2.58	1.7
0.03489	73.09	101.5	15.57	72	2.605	1.798
0.03617	76.07	103.3	15.03	73.63	1.629	1.288
0.03754	80.32	105.7	14.48	75.99	2.361	1.863
0.03887	84.39	108	13.98	78.14	2.151	1.881
0.04016	87.01	109.7	13.53	79.33	1.192	1.151
0.04152	90.86	111.4	13.09	81.54	2.204	2.166
0.04278	94	113.1	12.7	83.12	1.579	1.77
0.04415	96.36	114.9	12.31	83.89	0.7736	0.8558
0.04541	98.86	116.2	11.97	85.11	1.225	1.546
0.04675	101.3	117.5	11.62	86.2	1.089	1.38
0.04814	103.5	119.2	11.29	86.83	0.6217	0.8025
0.04941	106	120.8	11	87.76	0.9332	1.399
0.05071	107.9	122.2	10.72	88.31	0.5494	0.8424
0.05208	110.2	123.7	10.43	89.12	0.8138	1.252
0.05338	112.7	124.8	10.18	90.28	1.161	1.994

0.05468	114.8	126	9.937	91.15	0.8697	1.551
0.05601	116.8	127	9.702	91.93	0.7766	1.43
0.05731	118.5	128.1	9.482	92.5	0.5708	1.124
0.05863	119.8	129.2	9.268	92.76	0.2598	0.5287
0.05998	121.7	130.3	9.06	93.44	0.6813	1.418
0.06129	123.7	131.8	8.867	93.86	0.4207	0.9446
0.06264	125.5	133.3	8.675	94.12	0.2551	0.5777
0.06398	126.6	134.5	8.493	94.13	0.01521	0.03629
0.06534	127.6	135.6	8.317	94.06	0	0
0.06657	128.6	136.6	8.163	94.18	0.1164	0.328
0.06788	129.7	137.6	8.005	94.24	0.06428	0.1768
0.06924	132.1	138.9	7.848	95.09	0.8459	2.333
0.07059	133	140.1	7.698	94.91	0	0
0.07187	133.9	140.8	7.561	95.13	0.2225	0.702
0.0732	135.3	141.5	7.423	95.66	0.5306	1.672
0.07451	136.4	142.5	7.293	95.77	0.1074	0.3571
0.07585	137.5	143.5	7.164	95.87	0.1059	0.3576
0.07713	138.8	144.5	7.045	96.08	0.2087	0.7627
0.07848	140	145.6	6.924	96.17	0.08526	0.3049
0.07978	140.9	146.6	6.811	96.09	0	0
0.08112	141.7	147.6	6.699	95.99	0	0
0.08244	143	148.4	6.592	96.34	0.3554	1.439
0.08375	144.1	149.2	6.488	96.6	0.2551	1.068
0.08505	145.1	150.2	6.389	96.61	0.01052	0.04601
0.08645	146.2	151.3	6.286	96.61	0	0
0.08773	147	152.3	6.194	96.54	0	0
0.08906	148.3	153.3	6.101	96.76	0.2225	1.043
0.09038	149.4	154.3	6.012	96.85	0.08547	0.4159
0.09171	150.6	155.3	5.925	96.96	0.1122	0.5596
0.09298	151.7	156.2	5.844	97.16	0.2028	1.087
0.09435	152.6	157.1	5.76	97.16	0	0
0.09565	153.8	158.1	5.681	97.29	0.1212	0.6691
0.09696	155.1	159.2	5.604	97.4	0.1121	0.6331
0.09834	156	160	5.526	97.48	0.07871	0.4361
0.0996	156.8	160.8	5.456	97.51	0.03613	0.2232
0.1009	158	161.9	5.385	97.6	0.09216	0.5622
0.1022	159.1	163	5.315	97.58	0	0
0.1036	160	163.9	5.246	97.6	0.02116	0.1323
0.1049	161.1	164.8	5.18	97.72	0.1197	0.7867
0.1062	162.2	165.8	5.115	97.81	0.08715	0.5837
0.1076	162.8	166.8	5.05	97.6	0	0
0.109	163.9	167.6	4.987	97.76	0.1573	1.084
0.1102	164.4	168.4	4.93	97.62	0	0
0.1115	165.5	169.2	4.873	97.83	0.2137	1.606
0.1129	166.9	170.1	4.814	98.12	0.2878	2.116
0.1141	167.8	170.9	4.761	98.22	0.1061	0.8779
0.1154	168.6	171.7	4.707	98.23	0.005391	0.04294
0.1168	169.6	172.6	4.652	98.25	0.02104	0.1658
0.1181	170.5	173.6	4.601	98.21	0	0
0.1195	171.3	174.4	4.549	98.21	0.005845	0.04884
0.1207	172	175.2	4.5	98.18	0	0
0.1221	172.7	176.1	4.452	98.09	0	0
0.1234	173.7	177	4.404	98.1	0.01082	0.09832
0.1247	174.7	177.8	4.358	98.28	0.1845	1.717

0.126	175.4	178.4	4.312	98.31	0.02269	0.2164
0.1273	176.8	179.5	4.267	98.49	0.1888	1.815
0.1287	177.8	180.6	4.222	98.47	0	0
0.13	178.7	181.3	4.18	98.54	0.07055	0.7241
0.1314	179.2	182.1	4.136	98.39	0	0
0.1326	180.2	182.9	4.097	98.5	0.1151	1.274
0.134	181.5	183.7	4.057	98.83	0.3306	3.583
0.1353	182.3	184.2	4.017	98.96	0.1219	1.333
0.1366	183	184.7	3.978	99.05	0.09255	1.04
0.1379	183.7	185.6	3.94	98.95	0	0
0.1393	184.4	186.6	3.901	98.84	0	0
0.1406	185.1	187.5	3.864	98.73	0	0
0.142	185.7	188.4	3.828	98.59	0	0
0.1432	186.4	189.1	3.794	98.56	0	0
0.1445	188.3	189.8	3.76	99.24	0.6762	8.57
0.1458	189	190.5	3.726	99.24	0.0006006	0.007808
0.1472	189.5	191.2	3.692	99.11	0	0
0.1485	190.2	191.8	3.659	99.16	0.04796	0.6404
0.1499	190.8	192.5	3.625	99.14	0	0
0.1512	191.7	193.5	3.594	99.07	0	0
0.1525	192.3	194.4	3.564	98.93	0	0
0.1538	193.1	195	3.533	99	0.07653	1.066
0.1551	193.7	195.6	3.503	99.05	0.04171	0.6035
0.1565	194.4	196.3	3.473	99.04	0	0
0.1577	195.2	196.9	3.445	99.1	0.06049	0.962
0.1591	196	197.8	3.416	99.12	0.01238	0.1854
0.1604	197	198.6	3.387	99.2	0.08815	1.305
0.1618	197.7	199.3	3.359	99.17	0	0
0.1631	198.2	200	3.332	99.08	0	0
0.1644	198.7	200.7	3.306	99.02	0	0
0.1657	199.6					
0.167	200.4					
0.1683	201.1					

Table C16: Pore size data from sample 4 (Plotted in figure 5.4).

Pressure (bar)	Wet curve (Flow (l/min))	Interpolated dry curve (Flow (l/min))	Diameter (um)	Cumulative filter flow (Percent flow)	Differential filter flow (Percent flow)	Pore size flow distribution (Percent flow)
0	0	0				
0.001956	0	7.822	277.9	0	0	
0.003148	0	10.04	172.6	0	0	0
0.004493	0.0001438	12.58	120.9	0.001143	0.001143	8.32E-06
0.005829	0.09135	18.19	93.22	0.5022	0.5011	0.006794
0.007261	0.2058	24.23	74.83	0.8494	0.3472	0.007099
0.008455	0.3445	29.48	64.27	1.169	0.3194	0.01137
0.009872	0.5212	35.57	55.05	1.465	0.2963	0.01207
0.01118	0.8021	39.8	48.6	2.015	0.5501	0.03208
0.0124	1.528	43.74	43.82	3.493	1.478	0.1163
0.01371	2.863	48.59	39.64	5.891	2.398	0.2157
0.01504	5.777	53.54	36.13	10.79	4.898	0.5248
0.0164	6.268	57.81	33.13	10.84	0.05354	0.00669
0.01769	8.053	61.82	30.73	13.03	2.184	0.342
0.01902	10.73	65.7	28.57	16.32	3.297	0.5747
0.02035	15.41	69.56	26.71	22.16	5.833	1.178

0.02166	21.66	72.93	25.09	29.7	7.546	1.752
0.02299	27.07	76.34	23.63	35.46	5.757	1.488
0.02429	32.15	79.6	22.37	40.39	4.929	1.463
0.02563	36.42	82.93	21.2	43.92	3.529	1.138
0.02697	41.25	85.53	20.15	48.23	4.308	1.539
0.02828	46.29	88.04	19.22	52.57	4.346	1.756
0.02962	51.55	90.5	18.35	56.96	4.383	1.89
0.03094	55.4	92.92	17.56	59.62	2.665	1.279
0.03222	59.18	95.32	16.86	62.09	2.47	1.329
0.03356	64.26	97.82	16.19	65.69	3.602	2.009
0.03487	69.34	99.88	15.58	69.43	3.734	2.314
0.03622	73.79	102	15	72.33	2.905	1.873
0.03754	77.55	104.3	14.48	74.36	2.025	1.447
0.03887	81.31	106.6	13.98	76.28	1.929	1.467
0.04016	83.71	108.1	13.53	77.44	1.159	0.9685
0.04151	87	109.7	13.09	79.33	1.888	1.613
0.04278	88.99	111.3	12.7	79.99	0.6582	0.6361
0.04414	92.28	113	12.31	81.69	1.699	1.632
0.04541	95.27	114.5	11.97	83.18	1.493	1.623
0.04675	99.13	116.2	11.62	85.33	2.148	2.362
0.04811	101.9	117.8	11.3	86.48	1.149	1.319
0.04938	103.9	119.3	11.01	87.03	0.5535	0.715
0.05077	105.8	120.8	10.7	87.59	0.5601	0.6988
0.05204	108.1	122.1	10.44	88.57	0.9769	1.403
0.0534	110.8	123.4	10.18	89.76	1.185	1.672
0.05468	112.4	124.6	9.939	90.19	0.4353	0.6909
0.05599	114	125.9	9.705	90.61	0.4178	0.6722
0.05731	115.9	127.1	9.481	91.18	0.5718	0.9611
0.05863	118	128.2	9.269	92	0.8235	1.455
0.06002	119.5	129.4	9.054	92.32	0.3206	0.5605
0.06131	120.6	130.3	8.864	92.57	0.2408	0.4764
0.06266	121.9	131.3	8.672	92.85	0.2861	0.56
0.06392	123.8	132.5	8.502	93.37	0.5213	1.154
0.06524	125.6	133.9	8.33	93.85	0.477	1.043
0.06659	127.1	135	8.16	94.14	0.2906	0.6445
0.06789	128.1	136.2	8.004	94.04	0	0
0.0693	129	137.1	7.842	94.12	0.07491	0.1738
0.07053	130.1	137.9	7.705	94.39	0.2704	0.7417
0.07191	131.5	138.8	7.557	94.73	0.3408	0.8688
0.07319	133	139.6	7.424	95.25	0.5155	1.459
0.07449	134.5	140.9	7.295	95.42	0.1704	0.4944
0.07584	135.4	142.3	7.165	95.2	0	0
0.07715	136.4	143.2	7.043	95.21	0.01389	0.04292
0.07846	137.4	144.2	6.926	95.3	0.08987	0.2873
0.0798	138.8	145.2	6.809	95.57	0.2705	0.8724
0.08113	139.7	146.3	6.698	95.5	0	0
0.08244	140.8	147.2	6.592	95.62	0.12	0.4255
0.08374	142.1	148.2	6.489	95.9	0.2794	1.022
0.08506	143	149.1	6.388	95.88	0	0
0.08639	143.8	150	6.29	95.86	0	0
0.08772	145.1	150.9	6.195	96.13	0.274	1.08
0.08903	146.3	151.8	6.103	96.38	0.2455	1.007
0.0904	147.3	153.1	6.011	96.19	0	0
0.09167	148.2	154.3	5.928	96.09	0	0

0.09299	149.4	155.2	5.844	96.25	0.1669	0.7462
0.09431	150.6	156.1	5.762	96.48	0.2287	1.053
0.09568	151.5	157	5.679	96.48	0.002437	0.01107
0.09696	152.4	158	5.604	96.46	0	0
0.09829	153.3	159	5.529	96.42	0	0
0.0996	154.7	160.1	5.456	96.63	0.2111	1.094
0.1009	155.5	160.8	5.384	96.75	0.119	0.6247
0.1022	156.6	161.4	5.314	97	0.2558	1.375
0.1036	157.5	162.6	5.247	96.9	0	0
0.1049	158.6	163.7	5.181	96.87	0	0
0.1062	159.4	164.5	5.116	96.89	0.02821	0.163
0.1075	160.2	165.2	5.054	96.96	0.06289	0.3807
0.1089	162	166	4.992	97.59	0.6315	3.803
0.1102	162.8	166.8	4.931	97.61	0.02105	0.1307
0.1115	163.7	167.8	4.874	97.53	0	0
0.1129	164.6	168.9	4.815	97.48	0	0
0.1142	165.3	169.7	4.759	97.44	0	0
0.1155	166.2	170.5	4.704	97.49	0.04271	0.2951
0.1168	167.1	171.5	4.653	97.42	0	0
0.1181	168	172.6	4.602	97.28	0	0
0.1195	169.2	173.7	4.547	97.42	0.1366	0.9463
0.1208	169.9	174.6	4.498	97.31	0	0
0.1221	170.8	175.3	4.452	97.42	0.1087	0.8786
0.1234	171.8	176	4.403	97.6	0.1799	1.387
0.1247	172.9	176.8	4.357	97.83	0.228	1.858
0.1261	173.7	177.5	4.31	97.86	0.02836	0.2305
0.1273	174.7	178.3	4.268	97.97	0.1126	0.985
0.1287	175.3	179.1	4.224	97.87	0	0
0.13	176.4	180	4.181	98	0.1301	1.135
0.1313	177.5	180.9	4.139	98.13	0.1318	1.185
0.1327	178.2	181.8	4.096	98.01	0	0
0.134	179.1	182.7	4.055	98.03	0.02012	0.1843
0.1353	179.8	183.2	4.015	98.13	0.09248	0.8879
0.1366	180.4	183.8	3.977	98.16	0.03758	0.3685
0.1379	181.1	184.7	3.94	98.05	0	0
0.1393	182.5	185.7	3.902	98.31	0.2546	2.533
0.1406	183.6	186.2	3.866	98.57	0.2636	2.705
0.1419	184.3	186.8	3.83	98.67	0.09517	1.014
0.1432	185.1	187.7	3.794	98.61	0	0
0.1446	185.9	188.6	3.759	98.56	0	0
0.1459	186.9	189.3	3.725	98.74	0.1795	1.972
0.1472	187.7	189.9	3.692	98.84	0.1016	1.167
0.1485	188.4	190.9	3.658	98.67	0	0
0.1498	189.2	191.9	3.627	98.57	0	0
0.1512	190.1	192.6	3.595	98.68	0.1038	1.221
0.1525	190.6	193.3	3.564	98.6	0	0
0.1538	191.3	194.1	3.533	98.56	0	0
0.1551	191.8	194.8	3.504	98.47	0	0
0.1564	192.9	195.4	3.474	98.76	0.2931	3.696
0.1577	194.3	196	3.445	99.18	0.4148	5.307
0.1591	194.9	196.8	3.415	99.03	0	0
0.1604	195.4	197.6	3.387	98.91	0	0
0.1617	195.9	198.3	3.36	98.81	0	0
0.163	196.6	199	3.333	98.82	0.01224	0.1707

0.1643	197.4	199.7	3.306	98.89	0.06405	0.8908
0.1657	198.1	200.3	3.28	98.88	0	0
0.167	198.9	201	3.254	98.95	0.06526	0.9357
0.1683	199.8	201.7	3.228	99.05	0.1076	1.556
0.1697	200.6					
0.1709	201.3					
0.1723	201.9					

Table C17: Pore size data from sample 4 (Plotted in figure 5.4).

Pressure (bar)	Wet curve (Flow (l/min))	Interpolated dry curve (Flow (l/min))	Diameter (um)	Cumulative filter flow (Percent flow)	Differential filter flow (Percent flow)	Pore size flow distribution (Percent flow)
0	0	0				
0.002033	0.0002743	7.928	267.3	0.003461	0.003461	
0.00324	0.0002743	9.324	167.7	0.002942	0	0
0.004485	0.01357	10.86	121.2	0.125	0.1221	0.001006
0.0059	0.05464	16.87	92.11	0.3238	0.1988	0.002626
0.007135	0.09831	22.13	76.16	0.4442	0.1204	0.002896
0.008421	0.154	27.28	64.53	0.5646	0.1204	0.003972
0.009842	0.2549	32.95	55.21	0.7738	0.2092	0.008615
0.01123	0.4078	37.88	48.38	1.077	0.3028	0.01699
0.01241	1.002	42.06	43.77	2.381	1.305	0.1088
0.01371	1.813	46.29	39.63	3.916	1.534	0.1421
0.01505	4.285	50.65	36.11	8.46	4.544	0.4955
0.0164	5.087	54.66	33.14	9.305	0.8452	0.1091
0.01767	6.637	58.47	30.75	11.35	2.047	0.3283
0.01905	9.164	62.31	28.52	14.71	3.355	0.5781
0.02034	12.85	65.88	26.72	19.51	4.799	1.023
0.02166	18.6	70.01	25.09	26.57	7.06	1.656
0.02299	23.84	74.13	23.64	32.16	5.592	1.485
0.02434	28.18	77.11	22.33	36.55	4.387	1.284
0.0256	32.02	79.91	21.22	40.08	3.529	1.223
0.02697	36.68	82.49	20.15	44.46	4.385	1.562
0.02825	42.12	84.89	19.23	49.62	5.157	2.167
0.02958	47.2	87.11	18.37	54.18	4.563	2.027
0.0309	51.26	89.31	17.59	57.39	3.212	1.574
0.03224	55.64	91.86	16.86	60.57	3.178	1.668
0.03355	60.12	94.37	16.2	63.71	3.136	1.825
0.03485	63.74	96.98	15.59	65.73	2.021	1.285
0.03621	67.83	99.7	15.01	68.03	2.302	1.509
0.03751	71.24	101.4	14.49	70.25	2.223	1.637
0.03884	75.08	103.1	13.99	72.79	2.537	1.965
0.04018	79.24	105.1	13.52	75.4	2.614	2.153
0.0415	82.88	107	13.09	77.45	2.047	1.825
0.04282	85.34	109.1	12.69	78.26	0.8078	0.7679
0.04411	87.87	111	12.32	79.13	0.8688	0.8973
0.04543	90.28	112.6	11.96	80.18	1.054	1.129
0.04677	93.66	114.1	11.62	82.05	1.873	2.103
0.04811	96.73	115.5	11.29	83.78	1.727	2.035
0.04942	99.24	116.7	11	85.02	1.236	1.589
0.05073	101.3	118.1	10.71	85.71	0.6889	0.9315
0.05206	103.4	119.6	10.44	86.47	0.7625	1.068
0.05338	105.2	121	10.18	86.9	0.4278	0.6355
0.05471	108	122.5	9.933	88.14	1.24	1.93

0.05604	110.2	123.8	9.696	88.99	0.8499	1.374
0.05731	111.5	125.1	9.482	89.14	0.1564	0.2812
0.05864	113.7	126.1	9.266	90.15	1.005	1.783
0.05998	115.6	127.2	9.059	90.9	0.7514	1.395
0.06131	116.9	128.2	8.863	91.15	0.2459	0.4793
0.06264	118.3	129.3	8.676	91.48	0.336	0.689
0.06394	119.8	130.3	8.498	91.92	0.4406	0.9521
0.06526	121.4	131.3	8.327	92.42	0.4959	1.112
0.06661	122.8	132.5	8.158	92.7	0.2803	0.6382
0.06791	124.4	133.7	8.002	93.06	0.3624	0.8904
0.06923	125.9	134.9	7.849	93.32	0.262	0.6559
0.07055	126.9	136.2	7.703	93.23	0	0
0.07188	127.8	137.1	7.56	93.18	0	0
0.07322	129.3	138.1	7.421	93.64	0.4583	1.268
0.07455	130.8	138.9	7.289	94.19	0.5511	1.6
0.07581	131.9	139.7	7.168	94.45	0.2648	0.8415
0.07712	133.3	140.8	7.046	94.66	0.2051	0.6416
0.0785	134.4	141.9	6.923	94.67	0.01177	0.03664
0.07981	135.4	142.9	6.809	94.79	0.1226	0.4129
0.08112	136.5	143.8	6.699	94.95	0.1536	0.5364
0.08245	137.8	144.7	6.591	95.23	0.2822	1.005
0.0838	139.1	145.6	6.484	95.53	0.2976	1.071
0.08509	140.1	146.6	6.386	95.61	0.08763	0.3434
0.08637	141	147.5	6.291	95.54	0	0
0.08775	142.2	148.6	6.193	95.7	0.1517	0.5903
0.08903	143.3	149.6	6.103	95.82	0.1222	0.5261
0.0904	144.3	150.6	6.011	95.81	0	0
0.09167	145.2	151.6	5.927	95.82	0.0173	0.07924
0.09308	146.4	152.7	5.838	95.93	0.1043	0.4479
0.09433	147.4	153.6	5.76	95.93	0	0
0.0957	148.2	154.4	5.678	95.93	0.007803	0.03629
0.097	149.4	155.2	5.602	96.25	0.3117	1.571
0.09831	150.2	156.3	5.528	96.09	0	0
0.09966	151.4	157.4	5.453	96.17	0.07135	0.3654
0.1009	152.7	158.2	5.384	96.5	0.3314	1.839
0.1022	153.5	159	5.315	96.56	0.06143	0.3447
0.1036	154.7	160	5.247	96.72	0.1657	0.9284
0.1049	155.8	161	5.179	96.78	0.05431	0.3077
0.1062	156.6	161.7	5.116	96.89	0.1073	0.6504
0.1075	157.3	162.4	5.053	96.9	0.01943	0.1185
0.1088	158.6	163.6	4.993	96.93	0.02845	0.1817
0.1102	159.8	164.9	4.931	96.9	0	0
0.1115	160.5	165.6	4.872	96.93	0.02451	0.1581
0.1128	161.3	166.3	4.815	96.98	0.05921	0.4021
0.1142	162.4	167.3	4.76	97.11	0.1231	0.8514
0.1155	163.6	168.2	4.704	97.27	0.1625	1.11
0.1168	164.6	168.9	4.652	97.43	0.157	1.154
0.1181	165.3	169.7	4.6	97.4	0	0
0.1194	166.1	170.6	4.55	97.34	0	0
0.1208	166.7	171.6	4.5	97.12	0	0
0.1221	167.7	172.3	4.45	97.34	0.2135	1.659
0.1234	168.6	173	4.404	97.46	0.1216	1.007
0.1247	169.6	174	4.357	97.52	0.05702	0.4679
0.1261	170.8	174.9	4.31	97.62	0.1091	0.8893

0.1273	171.4	175.7	4.267	97.53	0	0
0.1287	172.4	176.5	4.223	97.67	0.1425	1.23
0.13	173.4	177.5	4.18	97.69	0.01932	0.1752
0.1313	174.2	178.4	4.139	97.66	0	0
0.1326	175.4	179.1	4.097	97.94	0.2736	2.516
0.134	176.4	179.8	4.056	98.14	0.2049	1.902
0.1353	177.5	180.5	4.016	98.32	0.1805	1.769
0.1366	178.2	181.3	3.977	98.33	0.004635	0.04456
0.138	178.9	182	3.937	98.31	0	0
0.1392	179.3	182.6	3.902	98.22	0	0
0.1406	180.2	183.4	3.866	98.26	0.04802	0.4997
0.1419	181.5	184.2	3.829	98.53	0.2697	2.822
0.1432	182.1	185.2	3.794	98.33	0	0
0.1445	182.9	186.2	3.759	98.21	0	0
0.1459	183.6	187	3.726	98.2	0	0
0.1472	184.4	187.8	3.692	98.15	0	0
0.1485	185.3	188.4	3.659	98.33	0.1744	2.05
0.1498	186	189.1	3.626	98.38	0.0502	0.5914
0.1511	186.8	189.7	3.595	98.47	0.0913	1.134
0.1525	187.6	190.3	3.564	98.55	0.08133	0.9798
0.1538	188.5	191.1	3.533	98.62	0.07626	0.9525
0.1551	189.4	191.8	3.504	98.75	0.13	1.704
0.1564	190.2	192.6	3.474	98.76	0.008449	0.1084
0.1577	191.1	193.4	3.445	98.79	0.02927	0.3924
0.1591	191.8	194.3	3.415	98.73	0	0
0.1604	192.4	195	3.388	98.63	0	0
0.1617	193.2	195.8	3.36	98.66	0.02816	0.3827
0.1631	193.9	196.5	3.333	98.69	0.03214	0.4525
0.1643	194.6	197.2	3.307	98.7	0.01466	0.2163
0.1657	195.4	197.9	3.28	98.74	0.03595	0.521
0.167	196.4	198.6	3.253	98.87	0.1291	1.833
0.1683	197.1	199.3	3.228	98.9	0.03304	0.5015
0.1696	197.5	199.9	3.204	98.79	0	0
0.1709	198	200.6	3.179	98.71	0	0
0.1723	198.6	201.3	3.154	98.7	0	0
0.1736	199.4	201.9	3.131	98.75	0.04808	0.7781
0.175	200.1					
0.1763	201					
0.1776	201.7					

C1.2.2 Pixel length measurements – Pure systems

The vertical pixel that corresponded to the top of the organic phase and the bottom of the organic phase in each sample and the top of the aqueous phase and bottom of the aqueous phase from each sample was recorded. The number of pixels between the top and bottom of each phase were calculated. The % of each phase in each outlet was then calculated from this. Tables C18-C21 present this data for the coalescing separator samples and tables C22-S25 present this data for the membrane separator samples. The calculated values in these tables were used to create table 5.10 in Chapter 5.

Table C18: Pixel measurements of Toluene-water samples from coalescing separator.

	Top - Org	Bottom - Org	Pixel Length	Top - Aq	Bottom - Aq	Pixel Length	Vial total (pixels)	% Organic	% Water
Toluene - 2 ml/min - F	498	684	186	0	0	0	186	100	0
Water - 2 ml/min - F	0	0	0	496	682	186	186	0	100
Toluene - 5 ml/min - F	492	678	186	0	0	0	186	100	0
Water - 5 ml/min - F	0	0	0	498	678	180	180	0	100
Toluene - 8 ml/min - F	490	678	188	0	0	0	188	100	0
Water - 8 ml/min - F	0	0	0	494	676	182	182	0	100
Toluene - 2 ml/min - PR = 0.25	640	684	44	0	0	0	44	100	0
Water - 8 ml/min - PR = 0.25	0	0	0	500	682	182	182	0	100
Toluene - 8 ml/min - PR = 4	488	678	190	0	0	0	190	100	0
Water - 2 ml/min - PR = 4	0	0	0	638	676	38	38	0	100

Table C19: Pixel measurements of Ethyl acetate-water samples from coalescing separator.

	Top - Org	Bottom - Org	Pixel Length	Top - Aq	Bottom - Aq	Pixel Length	Vial total (pixels)	% Organic	% Water
Ethyl Acetate - 2 ml/min - F	492	686	194	0	0	0	194	100	0
Water - 2 ml/min - F	0	0	0	494	680	186	186	0	100
Ethyl Acetate - 5 ml/min - F	488	682	194	0	0	0	194	100	0
Water - 5 ml/min - F	0	0	0	490	680	190	190	0	100
Ethyl Acetate - 8 ml/min - F	486	680	194	0	0	0	194	100	0
Water - 8 ml/min - F	0	0	0	490	674	184	184	0	100
Ethyl Acetate - 2 ml/min - PR = 0.25	634	682	48	0	0	0	48	100	0
Water - 8 ml/min - PR = 0.25	0	0	0	488	680	192	192	0	100
Ethyl Acetate - 8 ml/min - PR = 4	480	678	198	0	0	0	198	100	0
Water - 2 ml/min - PR = 4	0	0	0	632	674	42	42	0	100

Table C20: Pixel measurements of 1-Butanol-water samples from coalescing separator.

	Top - Org	Bottom - Org	Pixel Length	Top - Aq	Bottom - Aq	Pixel Length	Vial total (pixels)	% Organic	% Water
Butanol- 2 ml/min - TF	502	686	184	0	0	0	184	100	0
Water - 2 ml/min - TF	0	0	0	486	684	198	198	0	100
Butanol - 5 ml/min - TF	498	680	182	0	0	0	182	100	0
Water - 5 ml/min - TF	0	0	0	488	680	192	192	0	100
Butanol - 8 ml/min - TF	484	660	176	660	680	20	196	89.7959184	10.2041
Water - 8 ml/min - TF	0	0	0	496	676	180	180	0	100
Butanol - 2 ml/min - PR = 0.25	636	686	50	0	0	0	50	100	0
Water - 8 ml/min - PR = 0.25	0	0	0	482	682	200	200	0	100
Butanol - 8 ml/min - PR = 4	474	660	186	660	680	20	206	90.2912621	9.70874
Water - 2 ml/min - PR = 4	0	0	0	654	680	26	26	0	100

Table C21: Pixel measurements of DCM-water samples from coalescing separator.

	Top - Org	Bottom - Org	Pixel Length	Top - Aq	Bottom - Aq	Pixel Length	Vial total (pixels)	% Organic	% Water
DCM - 2 ml/min - NF	430	594	164	0	0	0	164	100	0
Water - 2 ml/min - NF	0	0	0	420	592	172	172	0	100
DCM - 5 ml/min - NF	420	596	176	0	0	0	176	100	0
Water - 5 ml/min - NF	0	0	0	410	590	180	180	0	100
DCM - 8 ml/min - NF	424	588	164	0	0	0	164	100	0
Water - 8 ml/min - NF	0	0	0	408	586	178	178	0	100
DCM - 2 ml/min - PR = 0.25	552	594	42	0	0	0	42	100	0
Water - 8 ml/min - PR = 0.25	0	0	0	432	590	158	158	0	100
DCM - 8 ml/min - PR = 4	430	536	106	0	0	0	106	100	0
Water - 2 ml/min - PR = 4	0	0	0	536	590	54	54	0	100

Table C22: Pixel measurements of Toluene-water samples from membrane separator.

	Top - Org	Bottom - Org	Pixel Length	Top - Aq	Bottom - Aq	Pixel Length	Vial total (pixels)	% Organic	% Water
Toluene - 2 ml/min - Phob	540	724	184	0	0	0	184	100	0
Water - 2 ml/min - Phob	0	0	0	540	726	186	186	0	100
Toluene - 5 ml/min - Phob	538	722	184	0	0	0	184	100	0
Water - 5 ml/min - Phob	0	0	0	532	722	190	190	0	100
Toluene - 8 ml/min - Phob	544	728	184	0	0	0	184	100	0
Water - 8 ml/min - Phob	524	546	22	546	724	178	200	11	89
Toluene - 2 ml/min - PR = 0.25 - phob	688	732	44	0	0	0	44	100	0
Water - 8 ml/min - PR = 0.25 - phob	0	0	0	546	728	182	182	0	100
Toluene - 8 ml/min - PR = 4 - phil	522	726	204	0	0	0	204	100	0
Water - 2 ml/min - PR = 4 - phil	0	0	0	688	722	34	34	0	100

Table C23: Pixel measurements of Ethyl acetate-water samples from membrane separator.

	Top - Org	Bottom - Org	Pixel Length	Top - Aq	Bottom - Aq	Pixel Length	Vial total (pixels)	% Organic	% Water
Ethyl Acetate - 2 ml/min - Phob	560	726	166	0	0	0	166	100	0
Water - 2 ml/min - Phob	512	530	18	530	724	194	212	8.490566	91.5094
Ethyl Acetate - 5 ml/min - Phob	542	722	180	0	0	0	180	100	0
Water - 5 ml/min - Phob	0	0	0	532	718	186	186	0	100
Ethyl Acetate - 8 ml/min - Phob	540	720	180	0	0	0	180	100	0
Water - 8 ml/min - Phob	0	0	0	532	720	188	188	0	100
Ethyl Acetate - 2 ml/min - PR = 0.25 - phob	682	728	46	0	0	0	46	100	0
Water - 8 ml/min - PR = 0.25 - phob	0	0	0	540	726	186	186	0	100
Ethyl Acetate - 8 ml/min - PR = 4 - phil	530	726	196	0	0	0	196	100	0
Water - 2 ml/min - PR = 4 - phil	0	0	0	686	722	36	36	0	100

Table S24: Pixel measurements of 1-Butanol-water samples from membrane separator.

	Top - Org	Bottom - Org	Pixel Length	Top - Aq	Bottom - Aq	Pixel Length	Vial total (pixels)	% Organic	% Water
Butanol - 2 ml/min - Phob	530	600	70	600	610	10	80	87.5	12.5
Water - 2 ml/min - Phob	374	448	74	448	612	164	238	31.09244	68.9076
Butanol - 5 ml/min - Phob	516	566	50	566	608	42	92	54.34783	45.6522
Water - 5 ml/min - Phob	374	482	108	482	608	126	234	46.15385	53.8462
Butanol - 8 ml/min - Phob	512	558	46	558	608	50	96	47.91667	52.0833
Water - 8 ml/min - Phob	372	492	120	492	610	118	238	50.42017	49.5798
Butanol - 2 ml/min - PR = 0.25 - phob	570	584	14	584	610	26	40	35	65
Water - 8 ml/min - PR = 0.25 - phob	438	472	34	472	612	140	174	19.54023	80.4598
Butanol - 8 ml/min - PR = 4 - phil	470	578	108	578	610	32	140	77.14286	22.8571
Water - 2 ml/min - PR = 4 - phil	542	592	50	592	608	16	66	75.75758	24.2424

Table C25: Pixel measurements of DCM-water samples from membrane separator.

	Top - Org	Bottom - Org	Pixel Length	Top - Aq	Bottom - Aq	Pixel Length	Vial total (pixels)	% Organic	% Water
DCM - 2 ml/min - Phob	572	682	110	0	0	0	110	100	0
Water - 2 ml/min - Phob	0	0	0	524	681	157	157	0	100
DCM - 5 ml/min - Phob	540	680	140	0	0	0	140	100	0
Water - 5 ml/min - Phob	0	0	0	510	678	168	168	0	100
DCM - 8 ml/min - Phob	554	678	124	0	0	0	124	100	0
Water - 8 ml/min - Phob	0	0	0	506	678	172	172	0	100
DCM - 2 ml/min - PR = 0.25 - phob	654	680	26	0	0	0	26	100	0
Water - 8 ml/min - PR = 0.25 - phob	0	0	0	508	680	172	172	0	100
DCM - 8 ml/min - PR = 4 - phil	554	686	132	0	0	0	132	100	0
Water - 2 ml/min - PR = 4 - phil	0	0	0	652	684	32	32	0	100

C1.2.3 Pixel length measurements – emulsion systems

The vertical pixel that corresponded to the top of the organic phase and the bottom of the organic phase and the top and bottom of the aqueous phase in the organic samples was recorded. The number of pixels between the top and bottom of each phase was calculated from this. The % of each phase in each outlet was then calculated from this using the knowledge that a 10 ml sample is 214 pixels long. Tables C26-C29 present this data for each HLD value and each different number of filter layers tested. The data presented in these 4 tables were used to plot figure 5.17(a) and (b).

Table C26: Pixel measurements of Toluene-SDBS solution samples from coalescing separator outlets at HLD = -3.35.

HLD value	NacL concentration (M)	NaCl concentration (g/L)	Outlet	No Filter layers	Top - Org	Bottom - Org	Pixel Length	Top - Aq	Bottom - Aq	Pixel Length	Vial total (pixels)	% Organic	% Aqueous
-3.35	0.01	0.52	Organic	0	0	0	0	0	0	0	0	0	0
-3.35	0.01	0.52	Organic	0	818	832	14	0	0	0	14	7	0
-3.35	0.01	0.52	Organic	0	0	0	0	0	0	0	0	0	0
-3.35	0.01	0.52	Organic	1	700	832	132	0	0	0	132	62	0
-3.35	0.01	0.52	Organic	1	698	832	134	0	0	0	134	63	0
-3.35	0.01	0.52	Organic	1	700	830	130	0	0	0	130	61	0
-3.35	0.01	0.52	Organic	5	660	832	172	0	0	0	172	80	0
-3.35	0.01	0.52	Organic	5	668	830	162	0	0	0	162	76	0
-3.35	0.01	0.52	Organic	5	644	832	188	0	0	0	188	88	0
-3.35	0.01	0.52	Organic	10	662	834	172	0	0	0	172	80	0
-3.35	0.01	0.52	Organic	10	660	832	172	0	0	0	172	80	0
-3.35	0.01	0.52	Organic	10	660	830	170	0	0	0	170	79	0

Table C27: Pixel measurements of Toluene-SDBS solution samples from coalescing separator outlets at HLD = -0.97.

HLD value	NacL concentration (M)	NaCl concentration (g/L)	Outlet	No Filter layers	Top - Org	Bottom - Org	Pixel Length	Top - Aq	Bottom - Aq	Pixel Length	Vial total (pixels)	% Organic	% Aqueous
-0.97	0.18	10.50	Organic	0	0	0	0	0	0	0	0	0	0
-0.97	0.18	10.50	Organic	0	0	0	0	0	0	0	0	0	0
-0.97	0.18	10.50	Organic	0	0	0	0	0	0	0	0	0	0
-0.97	0.18	10.50	Organic	1	754	806	52	0	0	0	52	24	0
-0.97	0.18	10.50	Organic	1	746	804	58	0	0	0	58	27	0
-0.97	0.18	10.50	Organic	1	742	802	60	0	0	0	60	28	0
-0.97	0.18	10.50	Organic	5	682	802	120	0	0	0	120	56	0
-0.97	0.18	10.50	Organic	5	672	802	130	0	0	0	130	61	0
-0.97	0.18	10.50	Organic	5	670	800	130	0	0	0	130	61	0
-0.97	0.18	10.50	Organic	10	650	806	156	0	0	0	156	73	0
-0.97	0.18	10.50	Organic	10	656	798	142	0	0	0	142	66	0
-0.97	0.18	10.50	Organic	10	648	796	148	0	0	0	148	69	0

Table C28: Pixel measurements of Toluene-SDBS solution samples from coalescing separator outlets at HLD = -0.26.

HLD value	NacL concentration (M)	NaCl concentration (g/L)	Outlet	No Filter layers	Top - Org	Bottom - Org	Pixel Length	Top - Aq	Bottom - Aq	Pixel Length	Vial total (pixels)	% Organic	% Aqueous
-0.26	0.38	22.02	Organic	0	0	0	0	0	0	0	0	0	0
-0.26	0.38	22.02	Organic	0	0	0	0	0	0	0	0	0	0
-0.26	0.38	22.02	Organic	0	0	0	0	0	0	0	0	0	0
-0.26	0.38	22.02	Organic	1	0	0	0	0	0	0	0	0	0
-0.26	0.38	22.02	Organic	1	0	0	0	0	0	0	0	0	0
-0.26	0.38	22.02	Organic	1	766	790	24	0	0	0	24	11	0
-0.26	0.38	22.02	Organic	5	766	792	26	0	0	0	26	12	0
-0.26	0.38	22.02	Organic	5	768	788	20	0	0	0	20	9	0
-0.26	0.38	22.02	Organic	5	752	786	34	0	0	0	34	16	0
-0.26	0.38	22.02	Organic	10	760	790	30	0	0	0	30	14	0
-0.26	0.38	22.02	Organic	10	748	788	40	0	0	0	40	19	0
-0.26	0.38	22.02	Organic	10	734	784	50	0	0	0	50	23	0

Table C29: Pixel measurements of Toluene-SDBS solution samples from coalescing separator outlets at HLD = -0.03.

HLD value	NacL concentration (M)	NaCl concentration (g/L)	Outlet	No Filter layers	Top - Org	Bottom - Org	Pixel Length	Top - Aq	Bottom - Aq	Pixel Length	Vial total (pixels)	% Organic	% Aqueous
-0.03	0.47	27.68	Organic	0	636	786	150	0	0	0	150	70	0
-0.03	0.47	27.68	Organic	0	650	782	132	0	0	0	132	62	0
-0.03	0.47	27.68	Organic	0	640	782	142	0	0	0	142	66	0
-0.03	0.47	27.68	Organic	1	670	786	116	0	0	0	116	54	0
-0.03	0.47	27.68	Organic	1	668	782	114	0	0	0	114	53	0
-0.03	0.47	27.68	Organic	1	666	778	112	0	0	0	112	52	0
-0.03	0.47	27.68	Organic	5	698	780	82	780	788	8	90	38	4
-0.03	0.47	27.68	Organic	5	714	784	70	0	0	0	70	33	0
-0.03	0.47	27.68	Organic	5	556	724	168	724	784	60	228	79	28
-0.03	0.47	27.68	Organic	10	610	784	174	0	0	0	174	81	0
-0.03	0.47	27.68	Organic	10	622	782	160	0	0	0	160	75	0
-0.03	0.47	27.68	Organic	10	616	780	164	0	0	0	164	77	0

C1.3 Results tables from Chapter 6

In this section the tables used to create figures 6.18 and 6.22 are presented. This includes the pump and conductivity standard deviation data for two stage and three stage counter-current control depending on the flow rate, setpoint and flow rate limit.

Table C30: Setpoint, Normalised setpoint. Pump flow rate standard deviation, conductance standard deviation and solution conductance during the 4 ml/min and 16 ml/min experiments using two stage counter-current arrangement (Data plotted in figure 6.19(a)).

Flow rate (ml/min)		Setpoint	Normalised Setpoint	Solution conductivity (µS/cm)	Pump 1 standard deviation (σ_P)	Pump 2 standard deviation (σ_P)	Cpnductivity 1 standard deviation (σ_C)	Cpnductivity 2 standard deviation (σ_C)
4 ml/min	4	100	0.25	400	1.71	1.55	154.70	68.23
		200	0.50		1.58	1.29	123.64	58.06
		322	0.81		0.91	0.89	58.44	47.02
		350	0.88		0.80	0.77	43.10	41.16
		380	0.95		0.32	0.35	17.72	20.84
		500	1.25		0.18	0.14	2.53	4.28
16 ml/min	16	100	0.28	363	1.92	1.78	104.47	65.14
		200	0.55		1.28	1.22	48.38	45.70
		250	0.69		1.35	1.15	60.57	45.26
		300	0.83		0.46	0.70	19.03	29.76
		400	1.10		0.27	0.22	4.03	8.66

Table C31: Pump flow rate and conductance standard deviations at different flow rates after the setpoint has been initialise while in a two stage counter-current arrangement (Data plotted in figure 6.19(b)).

Flow rate (ml/min)	Setpoint	Normalised Setpoint	Solution conductivity (µS/cm)	Pump 1 standard deviation (σ_P)	Pump 2 standard deviation (σ_P)	Cpnductivity 1 standard deviation (σ_C)	Cpnductivity 2 standard deviation (σ_C)
2	331	0.83	400	0.39	0.32	26.95	23.17
4	331	0.83		0.72	0.60	38.96	31.47
8	331	0.97		0.57	0.50	27.00	26.34
12	331	0.97		0.30	0.41	13.07	16.98
2	280	0.82		0.23	0.55	12.17	32.73
4	280	0.82	340	0.32	0.74	13.61	35.58
8	280	0.82		0.27	0.67	12.99	33.78
12	280	0.82		0.92	0.82	44.01	35.29
16	280	0.82		0.84	0.95	57.82	43.12

Table C32: Pump flow rate and conductance standard deviations at different flow rates after the setpoint has been initialise while in a three stage counter-current arrangement and using the flow limit functionality (Data plotted in figure 6.23(a) & (b)).

Flow rate (ml/min)	Flow rate limit	Setpoint	Normalised Setpoint	Solution conductivity (µS/cm)	Pump 1 standard deviation (σ_P)	Pump 2 standard deviation (σ_P)	Pump 3 standard deviation (σ_P)	Cpnductivity 1 standard deviation (σ_C)	Cpnductivity 2 standard deviation (σ_C)	Cpnductivity 3 standard deviation (σ_C)
4	±2	100	0.33	300	1.67	1.64	1.60	108.82	71.11	64.31
		150	0.50		1.61	1.56	1.47	112.75	68.31	62.42

		200	0.67		1.26	1.30	1.25	101.01	48.05	48.01
		250	0.83		0.62	0.31	0.71	21.55	12.22	25.66
		100	0.33		1.91	1.91	1.87	97.57	80.89	70.43
10	±2	150	0.50	300	1.80	1.80	1.72	110.74	92.10	76.54
		200	0.67		1.42	1.62	1.60	84.29	84.89	57.37
		250	0.83		0.90	1.19	1.12	41.04	49.18	37.88
		100	0.33		0.36	0.38	0.39	74.97	58.34	54.15
4	±0.5	150	0.50	300	0.29	0.35	0.33	80.61	48.68	43.10
		200	0.67		0.19	0.29	0.27	58.79	46.63	31.26
		250	0.83		0.12	0.23	0.17	20.60	45.74	26.76
		100	0.33		0.31	0.44	0.45	54.96	67.64	60.94
10	±0.5	150	0.50	300	0.35	0.45	0.40	90.00	82.66	53.94
		200	0.67		0.24	0.41	0.28	73.09	70.82	29.94
		250	0.83		0.11	0.22	0.18	13.91	35.78	21.98

C1.4 Results tables from Chapter 7

This section presents the results tables from the acetone extraction experiments and the benzoic acid extraction experiments. The acetone extraction results were used in figure 7.6. The benzoic acid extraction results were used in figures 7.8 & 7.9, 7.11 - 7.17, and 7.19 – 7.22.

C1.4.1 Acetone extraction results

Table C33: Results from the batch extraction of acetone from toluene (Results plotted in figure 7.6).

Aqueous volume (ml)	Organic volume (ml)	Aqueous weight (mg)	Organic weight (mg)	Phase Ratio (Aq/Org)	Acetone Concentration (mg/ml)	Acetone weight in toluene after extraction (mg)	Initial acetone weight in toluene (mg)	% acetone extracted
5	5	4985	4335	1	219.75	1551.07	2492.50	62.23
6.66	3.33	6640.02	2887.11	2	299.59	1673.75	3320.01	50.41
7.5	2.5	7477.5	2167.5	3	344.93	1659.44	3738.75	44.38

Table C34: Results from the UNIFAC model extraction of acetone from toluene and the in flow extraction of acetone form toluene (plotted in figure 7.6).

	Feed flow rate (aq) (ml/min)	Feed flow rate (org) (ml/min)	Time to reach 8 ml volume (org stream)	Organic outlet flow rate (ml/min)	Acetone Concentration (mg/ml)	% acetone extracted	% acetone extracted UNIFAC
S1PR1	1.5	1.5	268.19	1.79	250.04	67.98	73.05
S1PR2	2	1	340.58	1.41	335.86	53.93	54.08
S1PR3	2.25	0.75	410.09	1.17	369.35	43.78	41.61
S2PR1	1.5	1.5	234.25	2.05	303.33	94.41	91.05
S2PR2	2	1	319.45	1.50	394.18	67.48	69.61
S2PR3	2.25	0.75	364.39	1.32	438.93	58.55	51.19
S3PR1	1.5	1.5	199.91	2.40	262.37	95.69	96.98
S3PR2	2	1	227.82	2.11	351.63	84.40	76.43
S3PR3	2.25	0.75	247.81	1.94	401.22	78.70	53.97

C1.4.2 Benzoic acid extraction results

Table C35: Time it took the top interface in each vial to reach 90 % of its final height depending on the phase ratio and extractant concentration in the vial (plotted in figure 7.9)

Phase ratio (Org/Aq)	Extractant concentration (M)					
	0	0.05	0.1	0.2	0.3	0.4
	Time to reach 90% of final height (sec)					
0.5	8370	4230	51	39	36	133
0.75	8260	6030	50	40	36	35
1	8840	1740	458	41	38	37
1.25	6180	800	677	584	286	38
1.5	14	1350	832	575	268	171

Table C36: Time it took the bottom interface in each vial to reach 90 % of its final height depending on the phase ratio and extractant concentration in the vial (plotted in figure 7.10)

Phase ratio (Org/Aq)	Extractant concentration (M)					
	0	0.05	0.1	0.2	0.3	0.4
	Time to reach 90% of final height (sec)					
0.5	8370	4230	51	39	36	133
0.75	8260	6030	50	40	36	35
1	8840	1740	458	41	38	37
1.25	6180	800	677	584	286	38
1.5	14	1350	832	575	268	171

Table C37: Single stage extraction efficiency and purity data from benzoic acid extraction experiments (plotted in figures 7.12 – 7.18).

Base Concentration (M)	Phase ratio (Org/Aq)	pH	Extraction efficiency			Aqueous Purity		
			Benzoic acid	2-Chlorobenzoic acid	2,6-Dichlorobenzoic acid	Benzoic acid	2-Chlorobenzoic acid	2,6-Dichlorobenzoic acid
0.65	0.66	12.78	0.99	0.99	1.00	0.30	0.56	0.14
0.21	1.45	5.36	0.07	0.31	0.74	0.06	0.55	0.39
0.02	0.64	3.63	0.02	0.02	0.08	0.18	0.43	0.39
0.73	1.50	6.69	0.64	0.90	0.96	0.21	0.62	0.17
0.49	1.14	6.31	0.43	0.82	0.95	0.17	0.64	0.19
0.17	1.03	5.13	0.06	0.26	0.66	0.07	0.56	0.37
0.33	0.58	6.67	0.68	0.91	1.00	0.26	0.59	0.15
0.77	1.10	12.33	0.99	0.99	1.00	0.30	0.56	0.14
0.01	1.32	2.53	0.02	0.01	0.01	0.35	0.53	0.12
0.49	0.86	7.12	0.79	0.94	0.97	0.27	0.58	0.15
0.65	0.58	12.73	1.00	1.00	1.00	0.30	0.56	0.14
0.24	1.19	5.46	0.10	0.37	0.75	0.08	0.59	0.33
0.46	1.50	6.01	0.25	0.66	0.90	0.11	0.64	0.25
0.44	1.50	5.94	0.23	0.63	0.89	0.10	0.64	0.26
0.56	1.32	6.41	0.46	0.82	0.93	0.17	0.64	0.19
0.50	1.34	6.18	0.35	0.76	0.94	0.14	0.65	0.21
0.64	0.96	12.56	0.99	0.99	0.98	0.30	0.56	0.14
0.54	1.23	6.43	0.47	0.83	0.95	0.17	0.64	0.19

0.70	1.33	7.03	0.76	0.94	0.97	0.24	0.60	0.16
0.49	0.58	12.72	0.98	0.98	0.98	0.30	0.56	0.14
0.54	1.50	6.25	0.34	0.75	0.94	0.13	0.65	0.22
0.25	0.93	5.55	0.13	0.47	0.82	0.10	0.63	0.28
0.28	1.22		0.09	0.35	0.75			
0.54	1.04		0.61	0.88	0.95			
0.00	1.60		0.02	0.02	0.03			
0.26	0.94		0.11	0.40	0.80			
0.46	0.89		0.67	0.93	0.98			
0.07	1.76		0.02	0.05	0.22			
0.23	1.50		0.06	0.23	0.64			
0.36	1.54		0.11	0.42	0.81			
0.19	0.63		0.05	0.22	0.62			
0.33	0.58		0.33	0.75	0.94			
0.10	0.79		0.03	0.08	0.33			
0.50	1.88		0.15	0.50	0.84			
0.60	1.91		0.25	0.67	0.92			
0.16	1.15		0.04	0.16	0.52			
0.44	1.40		0.20	0.60	0.89			

Table C38: two stage counter-current extraction efficiency and purity data from benzoic acid extraction experiments (plotted in figures 7.21 – 7.24).

Base Concentration (M)	pH	Extraction efficiency			Aqueous Purity		
		Benzoic acid	2-Chlorobenzoic acid	2,6-Dichlorobenzoic acid	Benzoic acid	2-Chlorobenzoic acid	2,6-Dichlorobenzoic acid
0	1.86	0.01	0.01	0.01	0.40	0.47	0.13
0.1	4.79	0.04	0.12	0.55	0.07	0.43	0.50
0.2	5.39	0.06	0.29	0.84	0.05	0.53	0.42
0.3	6.03	0.10	0.56	0.97	0.06	0.65	0.29
0.4	6.29	0.15	0.71	1.00	0.07	0.69	0.24
0.5	6.99	0.37	0.91	0.99	0.15	0.67	0.18
0.6	12.51	0.81	0.97	1.00	0.28	0.57	0.14

Table C39: three stage counter-current extraction efficiency and purity data from benzoic acid extraction experiments (plotted in figures 7.21 – 7.24).

Base Concentration (M)	pH	Extraction efficiency			Aqueous Purity		
		Benzoic acid	2-Chlorobenzoic acid	2,6-Dichlorobenzoic acid	Benzoic acid	2-Chlorobenzoic acid	2,6-Dichlorobenzoic acid
0.1	4.51	0.04	0.12	0.59	0.08	0.41	0.52
0.2	4.99	0.06	0.27	0.91	0.06	0.47	0.47
0.3	5.30	0.09	0.52	0.99	0.06	0.61	0.34
0.4	5.48	0.09	0.71	1.00	0.04	0.71	0.25
0.5	5.67	0.32	0.80	1.00	0.13	0.72	0.16
0.6	5.90	1.00	1.00	1.00	0.16	0.68	0.16
0.7	6.20	1.00	1.00	1.00	0.35	0.52	0.13
0.8	12.79	1.00	1.00	1.00	0.30	0.56	0.14